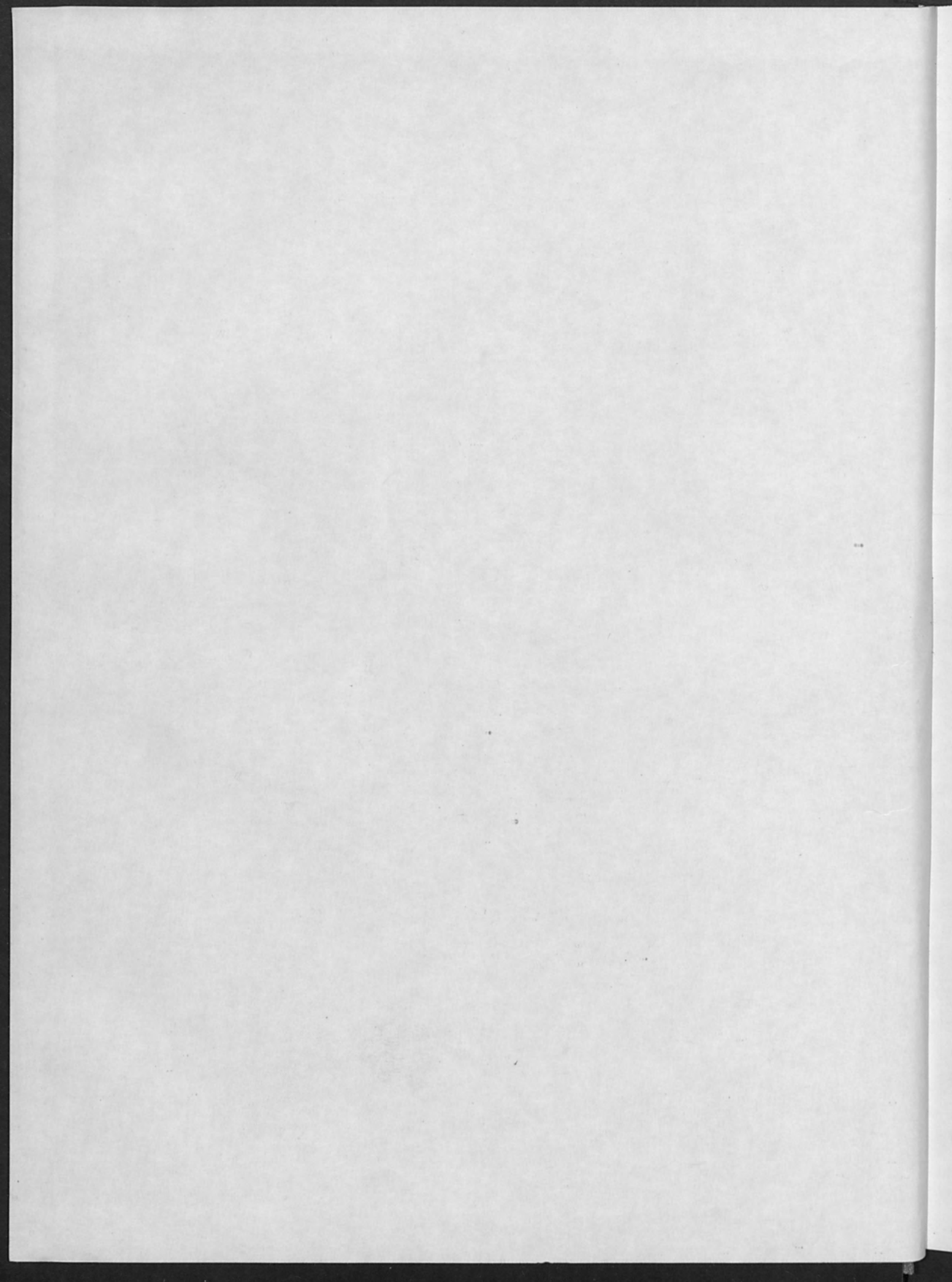




San Francisco, Cal., Inc.



RECORD
of the
IEEE 9th Annual Symposium on
Electron, Ion, and Laser Beam Technology

Berkeley, 9-11 May 1967

R. F. W. PEASE
Editor

IEEE Catalog No. F-79

Sponsored by
Group on Electron Devices of the
Institute of Electrical and Electronics Engineers, Inc.
and the
College of Engineering, University of California



San Francisco Press, Inc.

255 12th Street, San Francisco, California

RECORD

Copyright © 1967 by Institute of Electrical and Electronics Engineers, Inc.

All rights reserved

Berkeley, 9-11 May 1967

R. F. W. Pease
Editor

IEEE Catalog No. F-73

Sponsored by
Group on Electron Devices of the
Institute of Electrical and Electronics Engineers, Inc.
and the
College of Engineering, University of California

Library of Congress catalog card 62-51780

Printed in the United States of America

San Francisco Press, Inc.

255 12th Street, San Francisco, California

PREFACE

THE FIRST MEETING on electron-beam technology was organized in Boston, Massachusetts, by the Alloyd Corporation; the discussions were primarily concerned with the thermal effects of electron beams on metals, i.e., melting, refining, welding, and cutting of metals. In recent years non-thermal interactions have occupied an increasing portion of the symposia and other types of beams, ion beams and laser beams, have also been discussed.

The 9th Annual Symposium was held at the Claremont Hotel in Berkeley, California, under the chairmanship of Charles Süsskind. The Symposium was sponsored by the Professional Group on Electron Devices of the Institute of Electrical and Electronics Engineers, with the cooperation of the College of Engineering of the University of California at Berkeley. Partial support was also received from the U. S. Department of Defense (Office of Naval Research and Army Research Office). As a result of that support, several distinguished visitors from overseas participated in the Symposium, including S. Namba of the Institute for Physical and Chemical Research, Tokyo; K. H. Steigerwald of K. H. Steigerwald GmbH in Munich; and P. R. Thornton of the University College of North Wales.

The keynote address was given by James Hillier, vice president of the RCA Laboratories in Princeton, N. J., who had developed a scanning electron microscope in 1942 and has been prominent in electron microscopy for thirty years. Dr. Hillier described some of the advances in electron-beam technology during that time and stressed the difference between a laboratory demonstration of any given technique and its successful commercial use.

The banquet speaker was John H. Bloomer, who speculated on the possible space-propulsion applications of laser of terawatt power. Many slides were shown describing possible spaceship configurations.

A special lecture was given by Dr. L. Marton on the early history of the electron microscope. The material presented will form the basis for a separate volume, to be issued in the series of History of Technology Monographs published by San Francisco Press.

The technical sessions were concerned with the physics of electron, ion, and light beams, nonthermal interactions, thermal interactions, interference effects and measurements, information recording, and biomedical applications. They appear in the present volume in the above grouping.

Considerable emphasis on nonthermal interactions and on the physics of electron beams was one of the features of the Symposium. One paper described a long-life (1000-hr) cathode for use in apparatus such as an electron microscope. Another described a method of collecting secondary electrons from a surface in a strong magnetic field; this technique removes certain restrictions on the present performance of scanning electron microscopes. A method of making micron-sized transistors using electron-optical techniques was also described and two papers were concerned with ion implantation in semiconductors.

There were two sessions on biomedical applications, largely concerned with the effects of laser beams on biological tissue. Some of these effects are harmful, others are beneficial.

As program chairman I should like to thank the authors of the papers for their contributions and the following people who served on the program committee and moderated the various sessions: Robert Bakish, George R. Brewer, Thomas E. Everhart, L. Marton, Donald E. Rounds, Charles F. Spitzer, Robert G. Wilson, and H. C. Zweng.

R. F. W. PEASE

Berkeley, California, 1967

NOTE

The papers presented at the Symposium have been grouped for convenience in the following categories:

- Physics of beams, pp. 1 - 93
- Nonthermal interactions, pp. 94 - 205
- Thermal interactions, pp. 206 - 286
- Interference effects, measurements, pp. 287 - 326
- Information recording, pp. 327 - 362
- Biomedical applications, pp. 363 - 411
- Scanning electron microscope bibliography, pp. 412 - 438

TABLE OF CONTENTS

| | Page |
|--|------|
| PHYSICS OF BEAMS | 1 |
| Broers, "Electron gun using long-life lanthanum hexaboride cathode," 1; Brewster, Barbour, Charbonnier, Grundhauser, "Twelve joules in 3 nanoseconds with 600-keV electrons," 7; Everhart, "Point-cathode electron sources," 15; Wilson, "Ion implantation sources," 22; Motz, Sparrow, "A simple device for the energy and current measurement of an accelerator electron," 34; Banas, Brown, "Magnetic current control for hollow cathodes," 42; Penner, "Handling high-energy high-power electron beams," 50; Tamura, Kimura, "New electron gun for electron-beam evaporator," 62; Graham, Hutchison, Benedick, "Pulsed electron beam calorimetry utilizing stress wave measurements in solid absorbers," 70; Link, Sloan, "10 ¹² -Watt electron beam," 77; Namba, Kim, Itoh, Arai, Schwarz, "Ion emission from metal surface irradiated by giant-pulse laser beam," 86. | |
| NONTHERMAL INTERACTIONS | 94 |
| Thornley, Hatzakis, "Electron-optical fabrication of solid-state devices," 94; Kleinfelder, Johnson, Gibbons, "Experimental distribution of ions implanted into single-crystal silicon," 101; Johnson, Kleinfelder, Gibbons, "Projected range calculations from a statistical model," 108; Miller, Pease, "An ultrahigh-vacuum surface electron microscope," 118; Chang, Nixon, "Limits of electron-beam nonthermal interactions," 123; Wolf, "Low-energy electron beam interactions with ion-implanted semiconductor surfaces," 135; Thornton, Neve, Sulway, Wayte, "Oil-free scanning electron microscopy," 145; Varker, Juleff, "The application of scanning electron microscopy to imperfection analysis in silicon integrated circuits," 157; Pease, "Low-voltage scanning electron microscopy," 176; Gonzales, "Semiconductor secondary-electron detector," 188; Kimura, Tamura, "New method of detecting secondary electrons on scanning electron microscope," 198. | |
| THERMAL INTERACTIONS | 206 |
| Dreikorn, Levy, Saunders, "Circuit deposition by energy-beam irradiation of certain metal-containing materials to base metal," 206; Schollhammer, "Status of electron-beam welding for in-space applications," 215; Lienau, Lowry, Hassan, "Adaptation of a battery-powered electron beam device to perform an in-orbit welding experiment," 239; Davis, "Differentially pumped electron beam system for micro-zone processing of thin layers," 254; Dean, McDonald, Leitten, "High-purity shape casting with an electron-beam furnace," 262; Smith, Thompson, "Metalworking lasers in engineering service applications," 268; Emery, "Electron-optical control for electron beam deflection in welding and cutting," 278. | |
| INTERFERENCE EFFECTS, MEASUREMENTS | 287 |
| Stroke, "Interference effects in electron microscopy: some theoretical considerations," 287; Thompson, "Applications of Fraunhofer holograms," 295; Herrmannsfeldt, Spranza, Lee, Trigger, "The laser alignment system for the Stanford 3-km-long accelerator," 304; | |

TABLE OF CONTENTS (Cont'd)

| | Page |
|---|------------|
| Smathers, Lesley, Tomlinson, Boyne, "Distance measurements with a laser geodimeter," 313; Scherer, "Use of lasers in Raman spectroscopy of natural products," 321. | |
| INFORMATION RECORDING | 327 |
| MacDonald, Everhart, "An electron-beam-activated charge storage device and memory," 327; Becker, "UNICON-coherent light data processing," 333; Loeffler, "An electron-beam system for digital recording," 344; Kurzweil, Jr., Barber, Dost, "Automatic control of an electron-beam column," 350. | |
| BIOMEDICAL APPLICATIONS | 363 |
| Rounds, Olson, Johnson, "Wavelength specificity of laser-induced biological damage," 363; Hu, Lauridson, Barnes, "Thermal damage to biological materials," 371; Parr, Peacock, Fisher, "Laser effects on the corneal epithelium," 379; Wilde, Kobylnyk, "Arthropods as experimental media for laser investigations," 385; Storb, Amy, Wertz, Bessis, "Ruby laser micro-irradiation of single tissue culture cells vitally stained with Janus green B: an electron microscope study," 391; Zweng, "Clinical experience with laser photocoagulation of ocular tissue," 396; Peabody, "Treatment of macular disease," 397; Stern, Sognaes, "Laser-induced alteration of surface enamel," 402; Brown, Rockwell, Jr., "The argon laser: its effects in vascular and neural tissue," 407. | |
| SCANNING ELECTRON MICROSCOPE BIBLIOGRAPHY | 412 |
| Wells, "Bibliography on the scanning electron microscope," 412. | |

ELECTRON GUN USING LONG-LIFE LANTHANUM HEXABORIDE CATHODE

A. N. BROERS

IBM Watson Research Center, Yorktown Heights, N. Y.

INTRODUCTION

The tungsten hairpin cathode is an excellent electron source for use in laboratory electron beam instruments like electron microscopes. Such instruments are operated by skilled technicians and there is little need for long-term, stable, and unattended operation. However, with the recent application of high-performance electron-beam apparatus to industrial situations such as the microfabrication of integrated circuits, and the recording of digital information, the need for an electron source with better lifetime and stability than the tungsten hairpin has become of great importance. The comparatively poor vacuum conditions found in these instruments has obviated the use of the various oxide and dispenser cathodes, and no suitable alternative to the tungsten hairpin has been found. The possible use of the rare earth borides, particularly lanthanum hexaboride, as cathode materials, was pointed out by Lafferty¹ in 1951. He showed that higher ratios of electron emission density to evaporation rate exist for LaB₆ than for tungsten, and that the electron emission from LaB₆ is maintained under the vacuum conditions (10⁻⁶mm Hg) found in demountable vacuum systems using elastomer O-rings and oil diffusion pumps. The major difficulty that has prevented the application of LaB₆ as a cathode material in electron beam apparatus is its high reactivity with almost all substrate materials at the elevated temperatures required for electron emission. To a certain extent this difficulty was overcome by Favreau² who used rhenium as the substrate material. Favreau cathodetically coated rhenium hairpins with LaB₆ and used the resulting cathode in an ion gage. However, his cathodes were only operated at a few tens of milliamperes per square centimeter. When an attempt was made in this laboratory to operate similar cathodes in the region of 10 A/cm², the LaB₆ coating appeared to break up, and emission was only obtained for a few hours before cathode failure. Kapitza³ et al. have reported a technique for brazing LaB₆ to tantalum which renders the LaB₆ inactive at high operating temperatures. However, to date, this technique has not been adapted successfully to the fabrication of a cathode suitable for use in the standard electron microscope gun.

This paper describes a high-brightness electron gun suitable for electron microscopes and electron-probe apparatus which uses a LaB₆ rod cathode. The cathode has approximately two orders of magnitude greater lifetime than the conventional 0.005-in. tungsten hairpin at a given emission density, and has much better mechanical stability.

The cathode is similar to the Bolt cathode developed by Bas⁴ except that the cathode material is LaB₆ instead of one of the refractory metals, and also, as will be shown later, the heating power can be applied to the cathode by simple radiation without the added complexity of electron bombardment.

DESCRIPTION OF LANTHANUM HEXABORIDE CATHODE

The cathode is a small rod of solid LaB_6 typically 1 mm square in cross section and 1.6 cm long. The rod is spark-machined from bulk LaB_6 . The end of the rod from which the electron emission is drawn is ground to a fine point, and the other end brazed into a copper heat sink. This heat sink is maintained at approximately ambient temperature. The cathode is heated by a tungsten coil which is located around, but not in contact with, the emitting end of the rod. A heat shield surrounds the coil. The heated portion of the cathode is not in contact with the cathode support so the problem of the high reactivity of LaB_6 is eliminated. Heat can be applied to the cathode by radiation or electron bombardment from the heater coil. Electron bombardment heating is more efficient because the coil operates at a lower temperature and the electron bombardment power is delivered directly to the cathode rod. However, it requires an extra power supply and additional controlling electronics, and therefore lacks the simplicity of radiant heating. Typically, the total power required to heat the tip of the cathode to 1600°C , corresponding to an emission density of 8 A/cm^2 , is 60 Watts for radiant heating, and 50 Watts for electron bombardment heating. The exact power required depends, of course, on the length and cross section of the cathode rod.

ESTIMATED LIFETIME OF LaB_6 CATHODE

If it is assumed that the heater coil has infinite life, the life of the cathode is set by the time it takes the LaB_6 rod to evaporate away at its hottest point. In effect, the coil has infinite life when electron bombardment heating is used because the temperature of the coil can be held below 2100°C for all cathode operating temperatures. However, for high cathode temperatures, and radiant heating, the coil temperature can become high enough to make the coil life the limiting factor unless a very efficient heat reflecting shield surrounds the coil. As would be expected, the hottest portion of the cathode rod is not the tip, but that portion of the rod in the center of the heater coil. The temperature difference between the hottest part of the rod and the tip is generally about 150°C , but depends on the distance the tip extends outside the coil. It is possible to estimate the life of one of these cathodes, at a given operating temperature, from the abovementioned temperature difference, the evaporation rate for LaB_6 , and the density of LaB_6 . For a typical case, a 1-mm-square LaB_6 rod, similar to the cathodes tested and operating with tip temperature of 1460°C will last 8000 hr. In making this estimate it is assumed that the rod can be 75% evaporated before its useful life is over. According to Bloomer⁵ a standard 0.005-in. tungsten hairpin has a life of 30 hr at the equivalent emission density (3 A/cm^2).

ELECTRON GUN DESIGN

In order to obtain high brightness from the standard three-electrode electron gun, the configuration of the electrodes should be such that the electrostatic field gradient at the cathode surface is maximized. The effect of space charge on the maximum usable current density is then minimized. In the electron gun under discussion, this goal is achieved by the use of a sharply pointed cathode, and a high potential gradient,

up to 150 kV/cm, between anode and cathode.

In the practical gun design, the major difference from conventional electron guns is the method in which the abnormally high power required to heat the cathode is carried away from the high-voltage cathode region of the gun. This method utilizes several copper rods which pass from the cathode region, through the vacuum wall, into an oil bath which forms an integral part of the gun. The heat is then transferred by convection currents in the oil to walls of the coil container, which are at ground potential, where the heat can be readily dissipated into the air by convection or forced air cooling. The temperature developed at the base of the cathode rod is 200°C for the maximum required cathode input power of 80 Watts. Figure 1 shows a cross-section of the electron gun that has been built and tested.

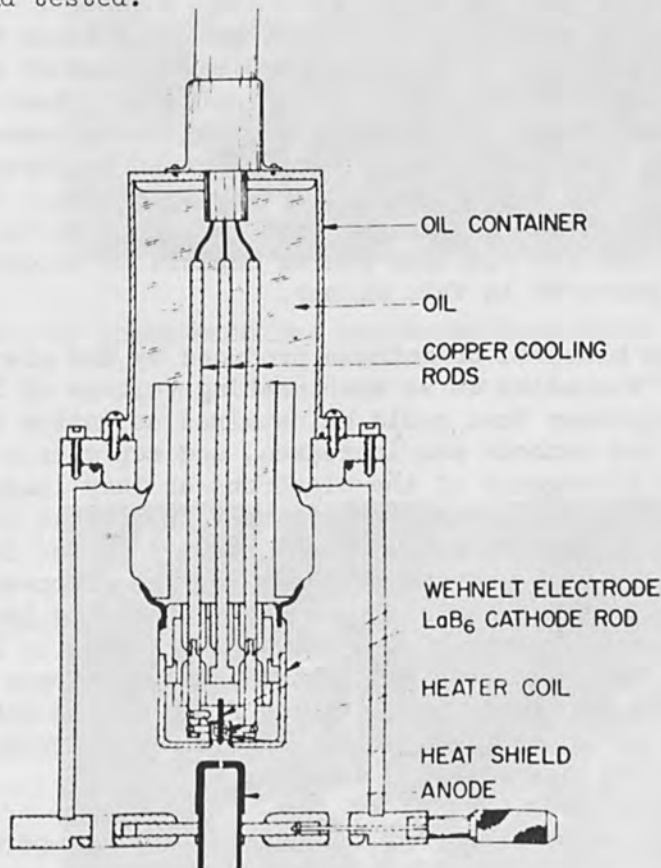


FIG. 1.—Lanthanum hexaboride cathode electron gun.

EXPERIMENTAL RESULTS

To date no cathodes have been tested to failure point so no verification of the optimistic lifetime estimate is available. Two cathodes have been operated for long periods of time, however; one for 1100 and one for 900 hr. In both cases the configuration of the cathodes was apparently unchanged after operation. The brightness of the electron beam was monitored continuously during the lifetime tests at 5×10^4 A/cm²-steradian for an accelerating voltage of 12 kV. The test apparatus used elastomer O-rings and silicon oil-diffusion pumps and had an ultimate

vacuum of 10^{-6} mm Hg. The brightness of the electron beam was measured by using a crossover-defining aperture immediately after the anode and a second aperture outside the electron gun. The crossover-defining aperture set the current density per unit area, and the second aperture the solid angle. For this arrangement, the brightness is given by

$$B = 16IL^2/\pi^2D_1^2D_2^2$$

where

- I is the current through second aperture
- D_1 is the diameter of crossover-defining aperture
- D_2 is the diameter of second aperture
- L is the distance between the apertures

With the particular apertures used, the brightness was measured over a half angle of 2.5×10^{-3} radian. The disadvantage of this method of measuring brightness is that maximum indicated brightness is obtained when the bias conditions are adjusted so that the crossover is formed in the plane of the defining aperture, which has an arbitrary location beyond the anode, which may not be its optimum position. This effect may give a pessimistic value for brightness. However, it can be said that the brightness that the electron gun is capable of producing is at least the brightness measured in this manner.

The maximum measured brightness produced by the electron gun was 5.6×10^5 A/cm²-steradian at an accelerating voltage of 12 kV. This was the maximum brightness that could be obtained no matter how much the temperature of the cathode was increased, and represents the limit set by space-charge divergence of the electrons as they leave the cathode surface. This brightness was approximately twice that obtained when a 0.005-in. tungsten hairpin cathode was operated in the identical electron gun geometry. The most probable reasons for the improvement are first, that the operating temperature of the LaB₆ cathode is lower and therefore the thermal velocity spread of the emitted electrons is likely to be smaller; and second, that the LaB₆ cathode has a sharper point and therefore a higher electrostatic accelerating field at the cathode surface. The radius of the tip of the LaB₆ cathode is 10-15 microns, compared with 125-300 microns for the tungsten cathode.

The mechanical stability of the cathode during operation is remarkably good. During the life test experiments the current through the second aperture of the brightness measuring system remained constant within 10% without realignment, after an initial warm-up period of 10 to 20 min. Repeated exposure of the cold cathode to air had no effect on its emission characteristics.

In order to assess the performance of the electron gun in a practical situation the gun was attached to a Cambridge Instrument Co. scanning electron microscope. Figures 2 and 3 are micrographs of the same area of a lanthanum hexaboride sample at different magnifications taken using the LaB₆ electron gun. A minimum electron probe diameter of 100 ± 30 Å was obtained. A comparison with the standard tungsten hairpin electron gun was made by observing the maximum current that could be focused into

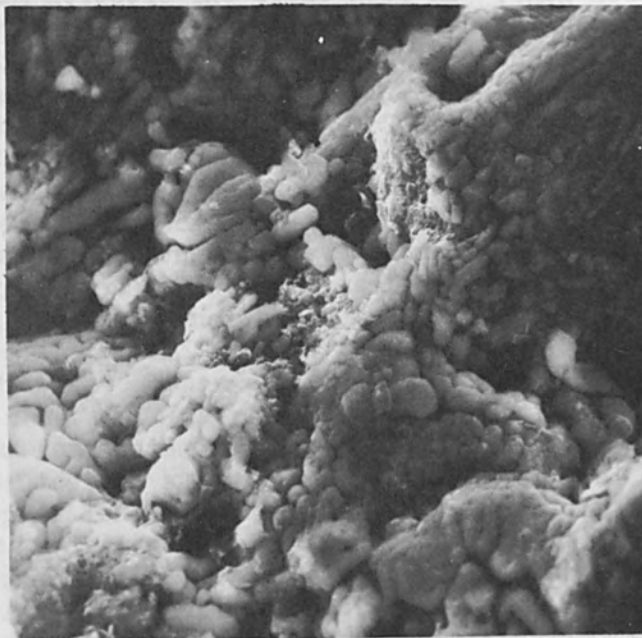


FIG. 2.—Surface of spark-machined lanthanum hexaboride sample (x 3 200).



FIG. 3.—Surface of spark-machined lanthanum hexaboride sample (x 32 000).

an electron probe with a nominal diameter of $250 \pm 50 \text{ \AA}$ using each of the two electron guns. In both cases the electron microscope lenses were operated under identical conditions and the same accelerating potential (20 kV) was used. With the tungsten filament gun the maximum probe current obtained was 4×10^{-12} Amp, and with the LaB₆ gun the maximum current was 1.2×10^{-10} Amp. It should be pointed out, however, that no attempt was made to optimize the spacing and configuration of the electrodes in the standard electron gun. The gun was only adjusted for peak performance with the bias-voltage and filament-current controls. The comparison was not therefore an absolute comparison between the two types of cathode, but an indication of how successfully the LaB₆ gun could be applied to a practical situation.

CONCLUSIONS

Although only a limited number of experimental tests have been completed on the LaB₆ rod cathode, the results indicate that the cathode offers a great improvement over the conventional tungsten hairpin cathode both in terms of lifetime and mechanical stability. The electron gun used to test the cathodes has also shown that the extra power required to heat the cathode can be readily and simply dissipated. To date, a lifetime of 1100 hr has been experimentally confirmed at a brightness of 5×10^4 amp/cm²-steradian for an accelerating voltage of 12 kV, and the condition of the cathode rod after this period of time indicates that a larger fraction of the estimated life of 8000 hr at this brightness should be possible in practice. The electron gun has been used successfully with a scanning electron microscope.

REFERENCES

1. J. M. Lafferty, J. Appl. Phys. 22: 299, 1951.
2. L. J. Favreau, Rev. Sci. Instr. 36: 856, 1965.
3. S. P. Kapitza et al., Soviet Physics—J.E.T.P. 14: 266, 1962.
4. E. B. Bas, Optik 12: 377, 1955.
5. R. N. Bloomer, Proc. IEE 104(B):153, 1951.

TWELVE JOULES IN 3 ns WITH 600-keV ELECTRONS

J. L. BREWSTER, J. P. BARBOUR, F. M. CHARBONNIER, and F. J. GRUNDHAUSER

Field Emission Corporation, McMinnville, Oregon

ABSTRACT. A pulsed electron source which generates a 7000-A beam with a 3-ns pulse duration has been developed. The accelerating voltage can be varied from 200 to 600 kV. Both the total beam energy (12 joules/pulse) and energy density (9 joules/cm²) have been measured with calorimeters. The beam is transmitted through a thin titanium window and can be injected readily into other experimental apparatus. The current density is well in excess of laser thresholds in many substances; electron penetration is substantially greater than that available from vacuum demountable systems.

In addition, an accelerator and focusing system have been developed to generate energy densities of 120 cal/cm² in 50 ns with a 2-MeV electron beam. The energy density can be varied and accurately controlled by the magnetic focusing field. The output is highly reproducible on a pulse-to-pulse basis so that thresholds for spall and other thermomechanical shock damage can be accurately determined.

I. INTRODUCTION

Field-emission cathodes provide electron currents of the order of 10,000 A with rise times as short as 1 ns.

New electron accelerators designed around such cathodes deliver a useful energy in a very short time: 12 joules in 3 ns at 600 keV and 350 joules in 50 ns at 2 MeV. It is thus possible both to activate and to diagnose many high-speed mechanisms with improved time resolution.

The development of sealed-off electron beam tubes with very high vacuum has increased the reproducibility of energy per pulse to within $\pm 3\%$ rms. Thus quantitative measurements can be made, for example of threshold failures of components to radiation effects. The electron beam is transmitted through a thin window for external use in the usual way. The pulse may be repeated at rates up to 10 pps for a few pulses.

The field-emission tube is a diode characterized by short electron transit distance and no heater. Thus the corresponding electron accelerators are relatively small and mobile. A coaxial, shielded design reduces external noise to the order of 1 mV at the pulser face.

The energy density of the external beam is adjustable, at constant electron energy, to densities up to 120 cal/cm² (at 2 MeV). Such densities will explode and spall many materials. Hence, explosive phenomena and high temperature and pressure transients may be studied quantitatively in the laboratory. Electron energy may also be adjusted by voltage control.

This paper briefly describes the field-emission accelerator and its performance and illustrates certain applications.

II. THE HIGH-VOLTAGE PULSERS

The high-voltage pulsers are basically Marx-surge circuits in which capacitors are charged in parallel, then discharged in series through spark gap switches. Several design features have been added: coaxial configuration; the storage is ceramic with epoxy potting for insulation and LC network for wave shape; gas pressure is adjusted in order to vary output voltage (about a factor of 3) with fixed gap spacing; electronic triggering with jitter less than ± 7 ns. The 2.3-MV pulser is shown in Fig. 1; the 600-kV pulser, in Fig. 2. The latter has a 50-ohm Blumlein output circuit which increases current and shortens pulse length to 10,000 A and 3 ns, respectively.

III. THE 600-kV TUBE AND ITS PERFORMANCE

The 600-kV tube has a beam energy of 12 joules/pulse and energy density of 9 joules/cm². These values are measured by calorimeters, metal disks in which a thermocouple junction is imbedded. A uniform temperature is rapidly achieved in the disk after irradiation because of the high thermal conductivity of the metal. The disks are thermally insulated from their surroundings; heat loss is slow and the energy input to the disk is determined from the equilibrium temperature.

Beam characteristics are shown in Fig. 3. The upper two curves were obtained in air; a pronounced beam pinch is observed due to space charge neutralization by ions. The two lower curves were obtained with the electron beam in vacuum where the energy density falls off with distance squared at larger distances.

The penetrating capability of the beam is shown in Fig. 4. The data were obtained by interspersing cellophane dosimeter disks with disks of aluminum and measuring the dose as a function of depth. The dose at a particular point was determined by measuring the change in optical transmittance of the blue cellophane due to irradiation. Curves are shown for two tubes; the upper curve is for the Model 5515 tube and the lower is for the Model 5510. Since the total beam energy is approximately the same for each tube, the beam from the 5510 is appreciably broader than that from the 5515.

The waveform of the transmitted electron beam current is shown in Fig. 5. A 50-ohm Faraday cup was designed for nanosecond response. The collecting cup and current return are coaxial and give a tapered impedance match to a 50-ohm transmission line. The current waveform was displayed on a Tektronix 519 oscilloscope. Figure 6 shows the waveform obtained by allowing the electron beam to impinge on a tungsten target and using a scintillator and photodiode to measure the x-ray output. Both measurements show a pulse width of 3 ns at half amplitude.

The short, intense x-ray burst can be used both in the basic study of transient radiation effects and to obtain x-ray and electron shadowgraphs of very high velocity objects. Motion blur is minimized by the

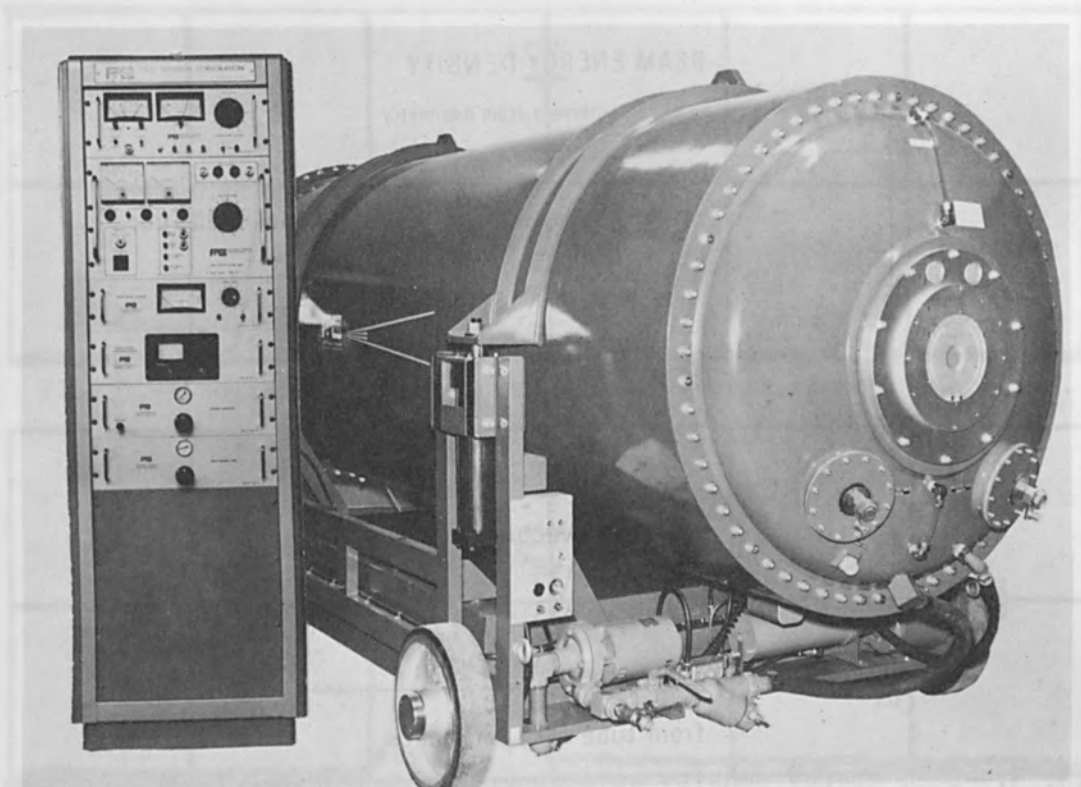


FIG. 1—2.3-MV pulser and control panel.



FIG. 2.—Complete 600-kV system.

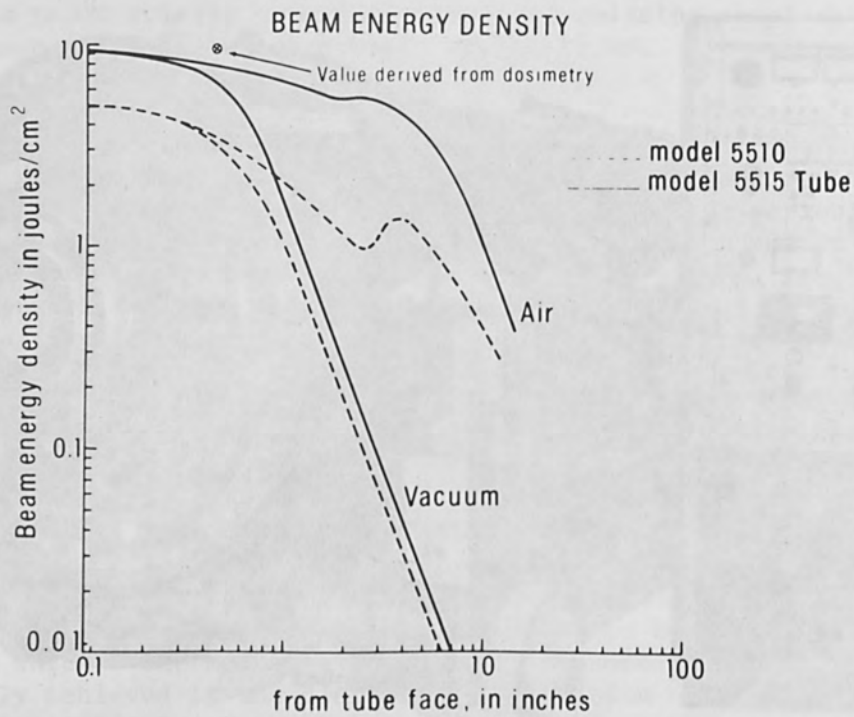


FIG. 3.—Beam energy density as a function of distance from the tube window.

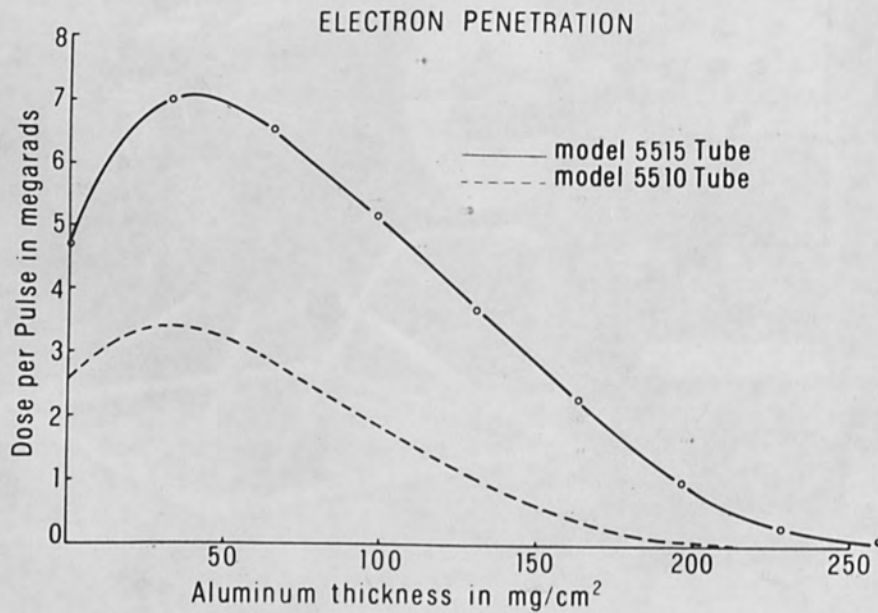


FIG. 4.—Dose-depth curve showing penetrating capability of the beam.

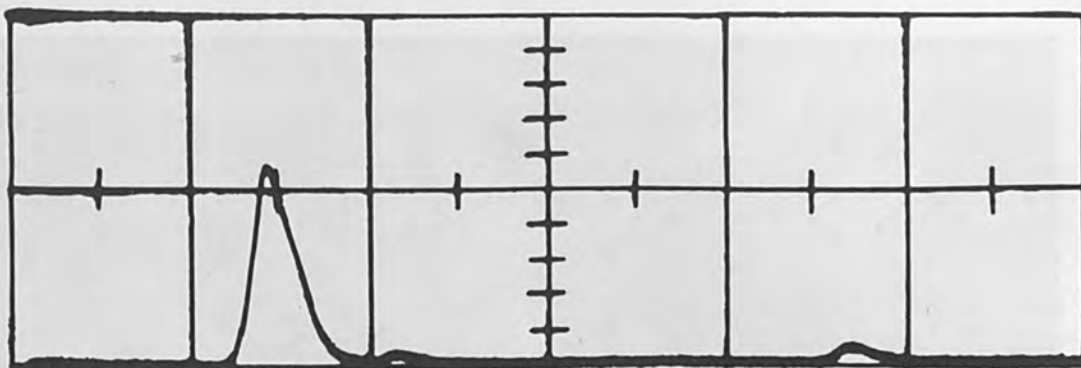


FIG. 5.—Oscilloscope showing variation of beam current with time.

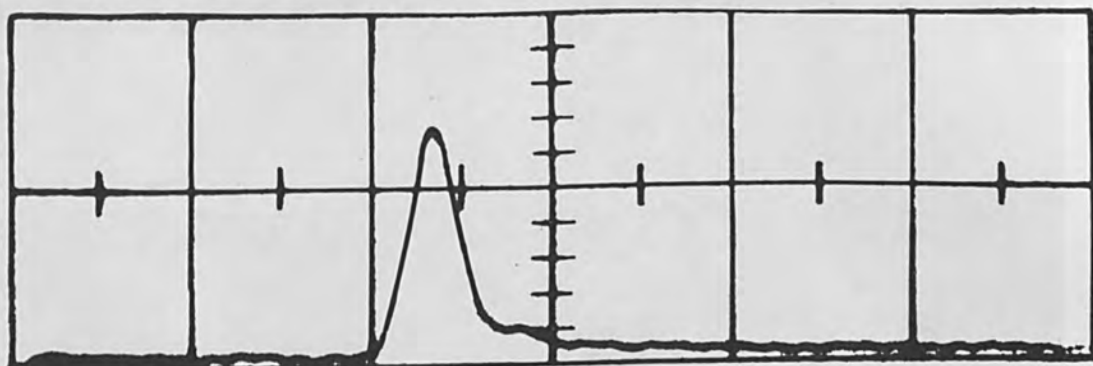


FIG. 6.—Oscilloscope of the x-ray pulse generated by the beam when striking a tungsten target.

short exposure time. Figure 7 shows an electron shadowgraph of 50-micron-diameter glass beads obtained with Kodak Type R film. The beam current density is sufficiently high so adequate exposure can be obtained with a 0.5-mm aperture leading to high geometric resolution.

Glass beads were chosen for the subject since they are used extensively in simulation of micrometeorite effects. Accelerating tunnels have been developed giving velocities of 30,000 to 40,000 ft/sec. Three-nanosecond exposures are required to minimize motion blur so that sharp images can be obtained.

IV. THE POSTFOCUSED 2-MeV ELECTRON BEAM AND ITS PERFORMANCE

The 2-MeV electron beam is generated and accelerated in a field emission diode and is then transmitted through a thin metal window for external use by means of a tube similar to that shown before, but larger.

The external beam is concentrated by injecting it into a strongly converging magnetic field. The field is small at the window (about 4 kilogauss) but large at the target located 10 in. away. The field may be adjusted from 0 to 25 kilogauss to obtain energy densities up to 120 cal/cm²-pulse at the target.

Electron beam current densities are greater than 8000 A/cm² at the target and about 1000 A/cm² at the tube window. Thus it is possible to destroy the target while conserving the electron source. Tube lives up to 1700 pulses are observed.



FIG. 7.—Electron shadowgraph of glass beads 50 microns in diameter.

Figures 8 and 9 show how failure thresholds can be detected in thermo-mechanical shock damage. Figure 8 shows a section through a stainless-steel target. A portion of the front surface was ejected as a high-velocity jet and the series of voids show incipient failure near the rear surface. Figure 9 shows a section through a second target when the energy density was increased to 70 cal/cm^2 . A larger crater was formed at the irradiated surface, and a definite separation line shows a slight increase in energy would result in spall from the rear surface.

The magnetic field is axially symmetric and Busch's theorem can be used to investigate electron trajectories. Angular momentum will not be conserved since azimuthal forces will result from the interaction between electrons and the focusing field. An extended angular momentum is conserved. It is defined by

$$mr^2 \frac{d\theta}{dt} - erA_{\theta} \quad (1)$$

where A is the magnetic vector potential and r is the distance from the axis of symmetry. Equation (1), together with initial injection conditions, can be used to determine changes in angular velocity of an electron as it progresses into the focusing field.

No accelerating voltage is applied outside the tube window, so the sum of the squares of the axial and radial velocity components is $eV_0 - \frac{1}{2}m(r \frac{d\theta}{dt})^2$. The trajectories in the r - z plane have the same form as though the electron moved subject to the equivalent potential

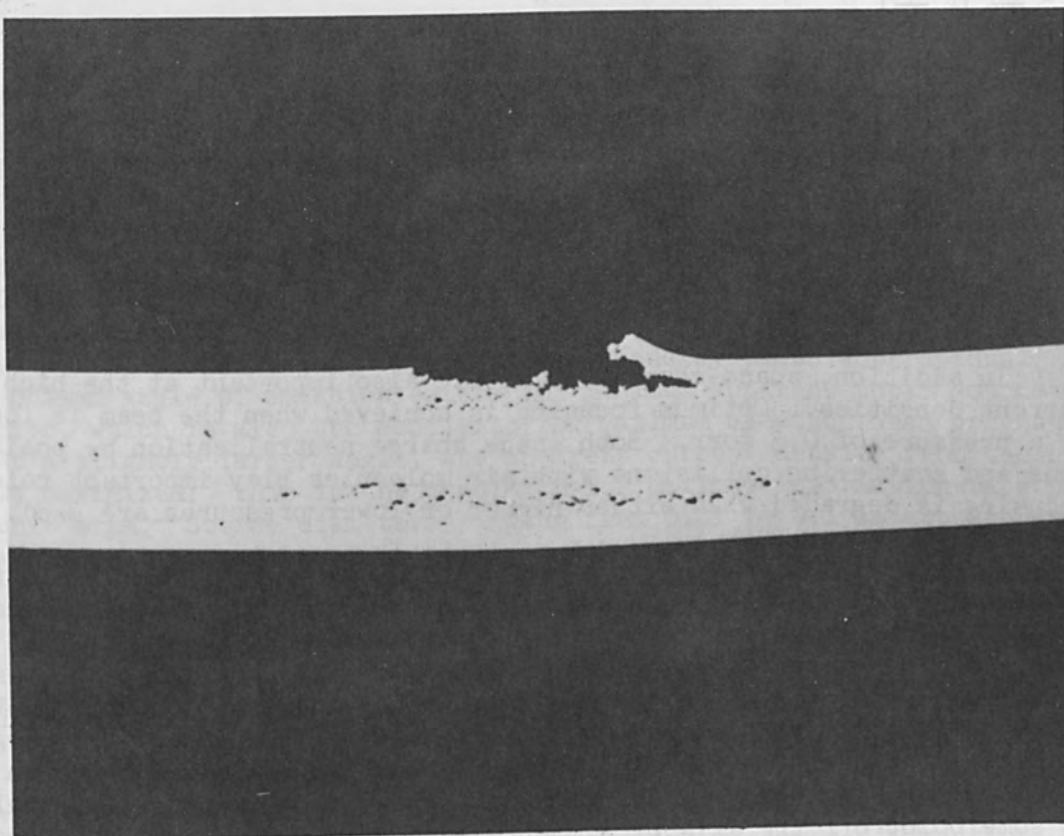


FIG. 8.—Cross section through a stainless steel target after single pulse irradiation.

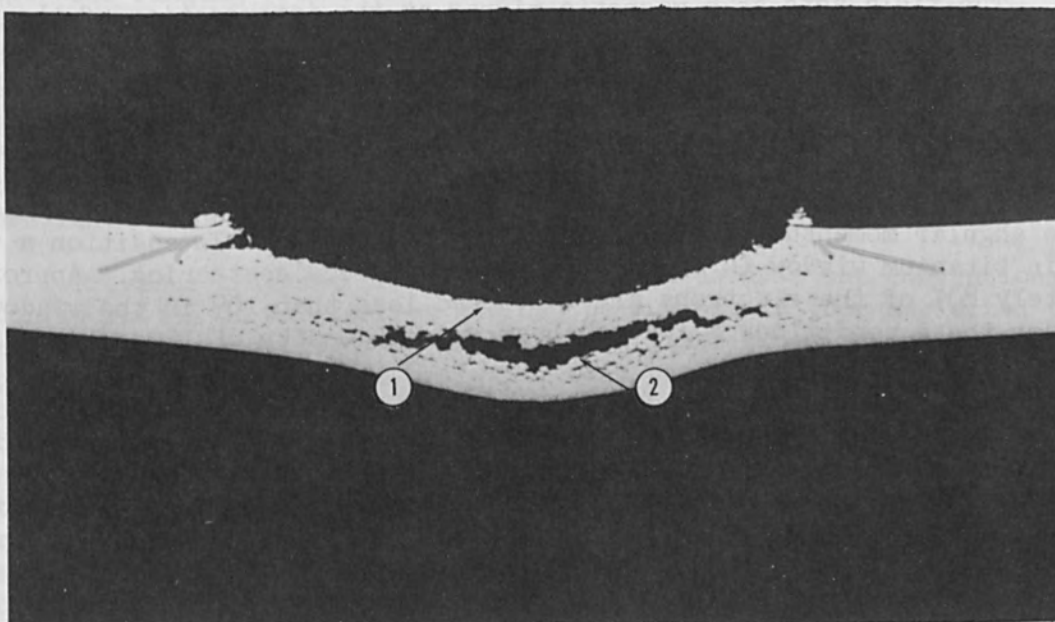


FIG. 9.—Cross section through a stainless steel target after irradiation with a single pulse at 70 cal/cm.

$$V - \frac{m}{2e} \left(r \frac{d\theta}{dt} \right)^2$$

Values of r and $d\theta/dt$ can be derived in any arbitrary $r-\theta$ plane by equating the extended angular momentum at the injection plane to that at each of the arbitrary planes. An equivalent equipotential plot can then be made using the derived values of r and $d\theta/dt$ to determine the voltage correction factor. A different equipotential plot will be obtained for each change in either r or $d\theta/dt$ at the injection plane. Graphical ray tracing can be used to determine trajectories but is cumbersome because of the large number of plots required.

In addition, space-charge fields are also important at the high current densities. Optimum focusing is achieved when the beam is focused at a pressure of 0.3 torr. Both space charge neutralization by positive ions and scattering collisions with air molecules play important roles; focusing is degraded when either higher or lower pressures are used.

To determine exact trajectories would be at best difficult and time consuming. However, the conservation of extended angular momentum can be used to obtain useful information about the beam envelope. There are values of injection conditions and focusing field for which the potential change $\Delta V = \frac{1}{2}(m/e) r (d\theta/dt)^2$ is equal to the accelerating voltage V_0 . These values mark the boundaries of forbidden regions where the energy associated with the azimuthal velocity would have to be greater than the total energy. An electron injected into the converging focusing field at some point off the axis of symmetry is confined within two converging boundaries, the exact positions of which depend on the initial angular momentum. The boundaries converge because the amplitude of the focusing field increases rapidly in the z direction.

The field acts as a magnetic mirror at the intersection of the two boundaries; the electrons are turned back, unable to reach the target. The field strength at which mirroring occurs depends on both the angular velocity and distance from the axis of symmetry at the injection plane. For optimum focusing both r and $d\theta/dt$ should be small.

The cathode and internal focusing system are designed to minimize the angular momentum of the electrons at the window. In addition a very thin titanium window (8 mg/cm^2) is used to reduce scattering. Approximately 80% of the electrons are scattered less than 10° in the window; under these conditions a focused beam energy density of 120 cal/cm^2 is achieved.

POINT-CATHODE ELECTRON SOURCES

T. E. EVERHART*

Institute for Applied Physics, University of Tübingen, Germany

ABSTRACT. A model of the point-cathode electron gun has been analyzed; the results are summarized in this paper. Both the first-order focusing properties of the model are determined, as well as the spherical and chromatic aberration. The source size is limited by the transverse velocities of emission, by diffraction, and by these aberrations. An optimum angle of emission exists for minimum apparent total source diameter, which is also the condition for maximum electron beam brightness. At a slightly larger angle, the apparent current density from the source is maximized: this is the condition for maximum information rate per unit area. Source diameters ranging from 0.01 to 0.1 μm appear possible, with apparent current densities ranging from 100 A/cm^2 (Schottky emission) to 10,000 A/cm^2 (field emission).

INTRODUCTION

Small-diameter, high-intensity electron sources have definite advantages for some uses of the transmission electron microscope, for small-area electron diffraction and scanning electron diffraction, and for high-resolution scanning electron microscopy; and such sources are virtually essential for improved results in electron interference and eventually, for the production of electron holograms. Tungsten point-cathodes ranging from 0.1 to 10 μm in diameter have been suggested for such sources, and have been investigated in several places.¹⁻⁵ Normally the point-cathode is heated and the strong field at the tip produces a lowering of the work barrier (Schottky effect). Field emission from cold point-cathodes has been used successfully in at least two laboratories.^{6,7} Although field emission requires an ultrahigh vacuum for reliable operation, it has definite advantages if small, intense electron sources are desired.

Previous analyses of the point-cathode used in the conventional configuration of an electron microscope gun have either neglected the electric focusing fields^{1,8} or have been first-order analyses.³ This paper summarizes a recent analysis⁹ of a particular model of the point-cathode electron gun, in which the equipotentials very near the point are taken as concentric spheres, and the equipotentials of the converging-lens portion of the gun, which occupy most of the cathode-anode space, are taken as hyperbolas of revolution.¹⁰ The electron motion in the "spherical region" is determined and used as the initial conditions for the electron motion in the "hyperbolic region." The chromatic and spherical aberrations of the hyperbolic region are determined and their influence on the source size is evaluated. This approximate treatment is shown to be valid for

*Permanent address: Department of Electrical Engineering and Computer Sciences, University of California, Berkeley.

the configurations and voltages normally used in electron microscopes and related instruments.⁹

OUTLINE OF ANALYSIS

Ruska has solved the equations of motion for electrons between concentric spherical electrodes.¹¹ If the inner sphere of radius a is the cathode (considered very much smaller than the anode), an electron emitted from point P_a with spherical coordinates (a, θ_a, ϕ_a) and zero transverse energy eV_t (the energy equivalent of all velocity components normal to the radius vector through P_a) has a radial trajectory, whereas an electron with finite transverse energy emitted from the same point has a hyperbolic trajectory. The asymptote to the hyperbolic trajectory cuts the radius vector through P_a at $a/2$, and intersects the plane normal to the polar axis containing the origin at

$$\rho_0 = \frac{a}{\cos \theta_a} \left(\frac{V_t}{aE_a} \right)^{1/2} ; \quad \phi_0 = -\phi_a \quad (1)$$

where E_a is the electric field at the cathode surface. This information is summarized in Fig. 1. If the emission current density from such a

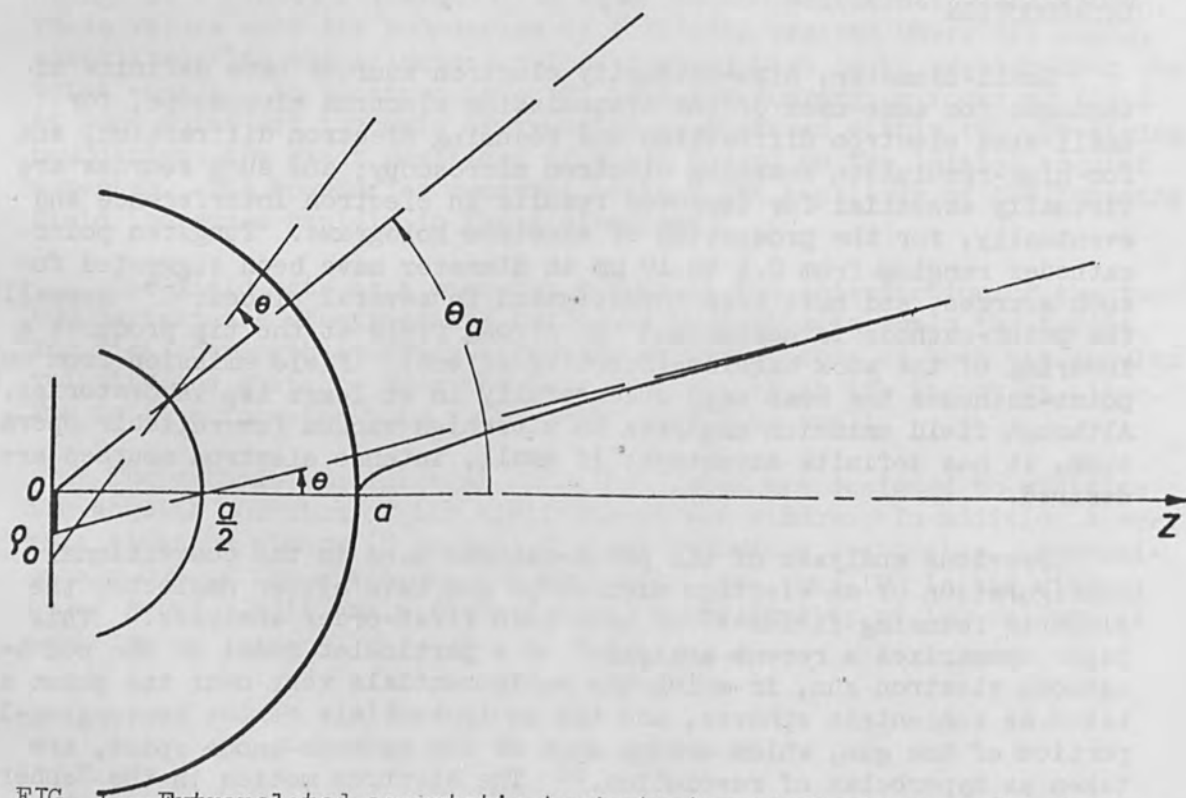


FIG. 1.—Extrapolated asymptotic trajectories of electrons emitted from a spherical cathode in a central-force field.

heated sphere is J_0 , considered uniform for $0 \leq \theta_a \leq \theta_{a1}$ and zero for $\theta > \theta_{a1}$, the current density distribution in the plane $z = 0$ may be written as a function of ρ_0 :⁹

$$J(\rho_0) = J_0 \frac{eaE}{kT} \theta_{a1}^2 \exp\left(-\frac{eaE}{kT} \frac{\rho_0^2}{a^2}\right) = \frac{J_0 \pi a^2 \theta_{a1}^2}{2\pi\sigma^2} \exp\left(-\frac{\rho_0^2}{2\sigma^2}\right) \quad (2)$$

Under the same conditions, the current density at spherical coordinates (r, θ) may be written as

$$J(r, \theta) = J_0 \frac{a^2}{r^2} \left[\exp\left(-\frac{\theta^2}{2\sigma_\theta^2}\right) \int_0^{\theta_{a1}} I_0\left(\frac{\theta\theta'}{\sigma_\theta^2}\right) \exp\left(-\frac{\theta'^2}{2\sigma_\theta^2}\right) d\left(\frac{\theta'}{\sigma_\theta}\right) \right] \quad (3)$$

where the bracketed term contains the effects of initial velocities of emission, I_0 is a modified Bessel function, and $\sigma_\theta \equiv 2\sigma/a \equiv (2kT/eaE_a)^{1/2}$. More general formulas are given in Ref. 9.

Electron motion in the converging field region of the gun is determined here by assuming the "spherical region" gives the electron a certain initial velocity and position in the $z = 0$ plane. The equations of motion are solved in the potential resulting from a superposition of the initial energy $\phi_0 = aE_a$ and the hyperbolic potential:

$$\phi(\rho, z) = \phi_0 + c \left(z^2 - \frac{\rho^2}{2}\right) \quad (4)$$

where c is the "power constant" of the hyperbolic lens.¹² The anode, located at $z = Z$, terminates the electric field of the hyperbolic region; the potential for $z > Z$ is therefore:

$$\phi(0, z > Z) = V = \phi_0 + cZ^2 \quad (5)$$

The first-order solution of the equations of motion in the hyperbolic region yield the lateral magnification M , the angular magnification m , and the axial position x of the cathode image, measured from the anode plane. These first-order properties are summarized in Fig. 2; $x < -Z$ implies a virtual image of the real source, which is located at $z = 0$ ($x = -Z$). To understand the use of Fig. 2 somewhat better, consider the following practical example: Schottky emission from a tungsten point-cathode of tip radius $a = 1 \mu\text{m}$, assumed electric field $E_a = 4 \times 10^6$ V/cm, hence $\phi_0 = aE_a = 400$ V. Final voltage $V = 60$ kV, hence $V/\phi_0 = 150$. The analysis predicts that $M \approx -7$, $m < 0.01$, and $x \approx 8Z$, i.e., an enlarged real image is located in front of the anode, with very low angular divergence. If V_t is taken as 1 volt, then for small θ_a , from (1), $\rho_0 = 500$ AE, in the absence of aberrations.

To determine the actual source size, both diffraction and gun aberrations must be evaluated. This has been done,⁹ and the Gaussian source radius ρ_g , diffraction disk radius ρ_d , chromatic aberration radius ρ_c , and spherical aberration radius ρ_s evaluated in the Gaussian image plane are given by:

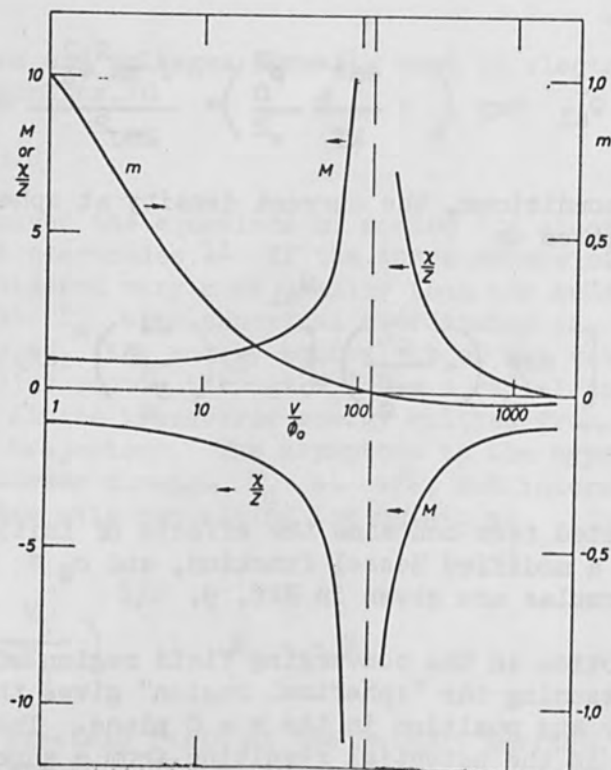


FIG. 2.—Lateral magnification M , angular magnification m , and axial position relative to the anode normalized to the cathode-anode spacing x/Z vs the final energy divided by the initial energy V/ϕ_0 , for an accelerating hyperbolic lens.

$$\rho_g = M\rho_0 ; \quad \rho_d = M (7.5 \times 10^{-8} / \sqrt{aE_a}) \theta^{-1}$$

$$\rho_c = M \left(\frac{Z}{2} \sqrt{\frac{V}{\phi_0}} \right) \frac{\Delta\phi_0}{V} \theta = MC_c \frac{\Delta\phi_0}{V} \theta \quad (7)$$

$$\rho_s = M \left(\frac{Z}{2} \sqrt{\frac{\phi_0}{V}} \right) \theta^3 = MC_s \theta^3$$

The mean-square radius to be expected in the Gaussian image plane can be approximated by adding these radii quadratically. However, if spherical aberration predominates, the minimum radius will be somewhat displaced from the Gaussian image plane, and is given by $\rho_s/4$. Hence, the minimum apparent total source radius ρ_{AT} is better defined as:

$$\rho_{AT}^2 = M^{-2} \left(\rho_g^2 + \frac{1}{16} \rho_s^2 + \rho_c^2 + \rho_d^2 \right) \quad (8)$$

The actual expected mean-square radius located very near to x is $M\rho_{AT}$. This expression has been evaluated for cases of practical interest, namely when $aE_a \ll V$, so that $V \approx cZ^2$, $\phi_0 = aE_a$, and where $\Delta\phi_0$ is determined by the total energy spread of the emitted electrons and V_t is determined by the transverse energy spread.⁹ The results for a

typical case of cold field emission are shown in Fig. 3. For very small values of the divergence angle θ at the cathode, diffraction limits the source radius. As θ increases, the Gaussian disk, then chromatic disk, and finally the spherical aberration disk of confusion become the limiting

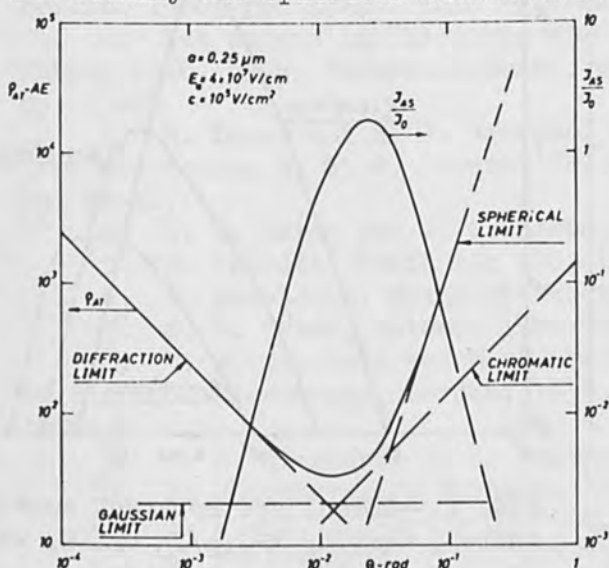


FIG. 3.—Apparent total source radius ρ_{AT} and normalized apparent source current density $M^2 J_{AS}/J_0$ vs. beam aperture angle at the cathode, showing the various limits on the apparent source radius.

factors. For larger values of ϕ_0 , chromatic aberration decreases in importance and spherical aberration increases in importance.

The current density from the point-cathode appears to come from a source of radius $M\rho_{AT}$. If, as is often the case, $\theta < \theta_{a1}/2$, and $l \gg \theta_{a1} > 4\sigma_\theta$, the apparent current density from the source at $z = 0$ is

$$J_{AS} = J_0 \left[\frac{\pi a^2 \theta^2}{\pi \rho_{AT}^2 M^2} \right] = J_0 \frac{a^2 \alpha^2}{\rho_{AT}^2} \left[\frac{V}{aE_a} \right] \quad (9)$$

The apparent brightness of this source (defined as current density per unit solid angle, following Langmuir¹³) follows immediately from Eq. (9), by dividing by $\pi\alpha^2$.

$$B_{AS} = J_0 \frac{a^2}{\pi\rho_{AT}^2} \left[\frac{V}{aE_a} \right] \quad (10)$$

Note that the apparent brightness is maximum when the apparent source radius is minimum, hence the curve of Fig. 3 discussed above also predicts the maximum brightness. The apparent current density is maximized at a somewhat higher value of θ . The choice of which maximum is optimum depends on the application; highest resolution comes at the minimum of ρ_{AT} , highest information rate per unit area comes at the maximum of $M^2 J_{AS}$.

Figures 4 and 5 compare the performance of an oriented tungsten single crystal of $1 \mu\text{m}$ tip radius used as a cold field-emission cathode ($E_a = 4 \times 10^7 \text{ V/cm}$) with the performance of the same tip used as a Schottky-emission cathode ($E_a = 4 \times 10^5$ and $4 \times 10^6 \text{ V/cm}$). The figures

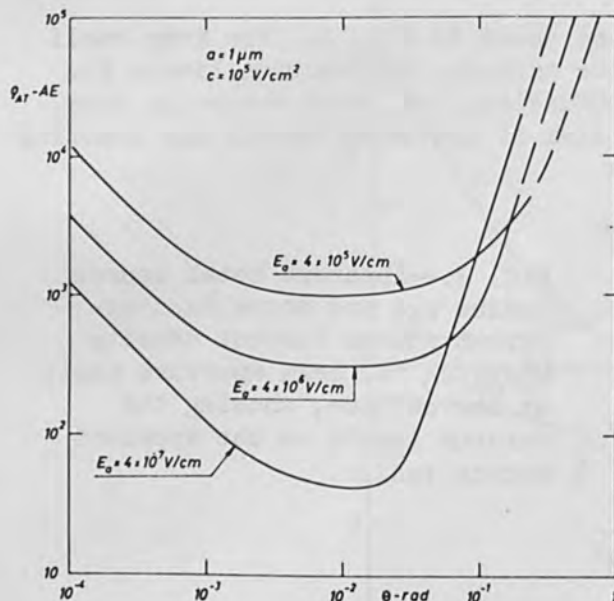


FIG. 4.—Apparent total source radius ρ_{AT} vs θ , with electric field at the cathode as parameter.

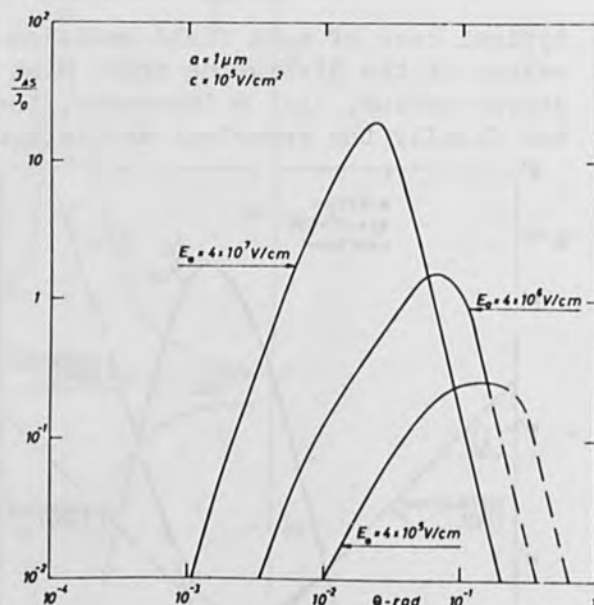


FIG. 5.—Normalized apparent source current density $M^2 J_{AS}/J_0$ vs. θ , with electric field as parameter.

show how the field strength influences the cathode performance. Note that while the field-emission cathode produces a smaller value of ρ_{AT} for smaller values of θ , the Schottky-emission cathodes appear better at larger values of θ . To appreciate the improvement in intensity offered by pointed cathodes, one must realize that J_0 for Schottky emission may be up to 100 times higher than the thermionic-emission value, and J_0 for field emission may be as much as 10^4 times higher than the thermionic emission value for tungsten.

CONCLUSIONS

Quantitative analysis of a particular model shows that strong electric fields at the tip of a pointed cathode produce improved electron brightness and apparent current density from the source. The source diameter is a function of the field, and can approach 100 AE for field emission, and be smaller than 1000 AE for Schottky emission. Since J_0 is higher and ρ_{AT} is lower for the field-emission cathode than for the Schottky-emission cathode, from Eq. (10) and Fig. 4, the brightness of the field-emission cathode is expected to be approximately 10^4 higher than the brightness of the Schottky-emission cathode for $a = 1 \mu\text{m}$. The Schottky-emission cathode, in turn, is expected to have approximately 100 times higher brightness than the normal hair-pin cathode, based on the respective values of J_0 . To achieve this predicted improvement in performance, small aperture angles at the cathode must be used, which make oriented crystals, or other methods of producing the maximum emission density along the polar axis of the electron gun, absolutely necessary.

ACKNOWLEDGMENTS

Helpful discussions with Professor F. Lenz and support from a NSF Senior Post-doctoral Fellowship are gratefully acknowledged.

REFERENCES

1. M. Drechsler, V. E. Cosslett, and W. C. Nixon, Proc. 4th International Conference of Electron Microscopy, Berlin, 1958; Springer-Verlag, Berlin, 1960; pp. 13-20. This reference reviews previous work as well.
2. See papers in "Electron Microscopy," R. Uyeda, ed., Maruzen, Tokyo, 1966, by H. Fernandez-Moran, pp. 27-28; K. Yada and T. Hibi, pp. 25-26.
3. R. Lauer and K. J. Hanssen, *ibid.*; pp. 129-130. See also Electron Microscopy I, S. S. Breese, Jr., ed., Academic Press, New York, 1962; pp. KK-11.
4. D. W. Swift and W. C. Nixon, Brit. J. Appl. Phys. 13: 288, 1962.
5. R. Speidel, Optik 23: 125, 1965/66.
6. K. Shoulders, Stanford Research Institute, private communication.
7. A. V. Crewe, Science 154: 729, 1966.
8. V. E. Cosslett and M. E. Haine, Proc. International Conference on Electron Microscopy, London, 1954, Royal Microscopical Society, London, 1956; p. 639.
9. T. E. Everhart, to be published in J. Appl. Physics.
10. R. Rüdberg, J. Franklin Inst. 246: 311 and 377, 1948.
11. E. Ruska, Z. Physik 83: 684, 1933.
12. K. Schlesinger, Proc. IRE 49: 1538, 1961.
13. D. B. Langmuir, Proc. IRE 25: 977, 1937.

ION IMPLANTATION SOURCES

R. G. WILSON

Hughes Research Laboratories, Malibu, California

Ion implantation doping of semiconductors requires the use of ion beams of a variety of elements with energies from about 10 to 150 keV, or even higher if deeper junctions are desired, although higher energies are less convenient for device manufacturing. Doping is commonly done with elements of the IIB, IIIA, VA, and VIA periods. The IB metals, the rare earth metals, and some transition metals are of interest for special solid state effects, e.g., lifetime reductions, color centers, deep levels, etc. The III and V elements are implanted in Si, Ge, SiC, and the II-VI compounds, and the II and VI elements are used to dope the III-V compounds. A low-energy ion accelerator with versatile ion sources is basic to such a program. Only moderate ion current densities are required to produce appropriate doping concentrations, but good doping uniformity over areas up to 1.5 in. in diameter (wafer size) requires the use of beam scanning techniques which reduce the current density of implanted ions. Good beam parallelism and alignment with single crystal targets are required to cause and study intentional channeling effects. Beam purity is a consideration, and if a mass separator is required, it need only be an element separator. For surface ionization sources, pure enough ion beams may be produced directly from the source, depending on the tolerable impurity level (and the impurity species).

For the various desired ion species, several types of ion sources may be employed. Vapor electron bombardment ionization sources are suitable for many; we are using them for B, N, P, S, Zn, As, etc. Sputter electron bombardment ion sources are practical for the IB metals, Cu, Ag, Au, and for others such as Al.¹ We are employing surface ionization sources for the IIIA metals, Al, Ga, In, and Tl, and they are commonly used for the alkali metals (Li, Na, K, Rb, and Cs) which have been shown to be interstitial dopants in Si,² and for some alkaline earth and rare earth metals.

SURFACE IONIZATION SOURCES

The concept of surface ionization involves the ionization of a low ionization potential element (I) on a high work function surface (ϕ) hot enough to desorb the ions thermally; the electron is lost to surface upon desorption. The ionization efficiency is the most important parameter

$$\beta = \frac{1}{1 + (\omega_0/\omega_+) \exp [(I - \phi)/kT]} \quad T > T_c$$

in which the (I - ϕ) difference is crucial. This equation is derived from the Saha-Langmuir equation. The critical temperature T_c is the temperature for optimum ionization (optimum current density), and is as high

as 2000°K for some metals. Al, Ga, In, Tl, and the rare earths have ionization potentials from about 5.5 to 6 eV, while the alkalis have from about 4 to 5 eV. Refractory metals classically used for the alkalis are W, Mo, Ta, etc. Higher work function surfaces are desirable for ions of higher I. Concepts for higher work function surfaces are: (1) oxygenated surfaces, e.g., W; (2) higher work function metals, e.g., Re, Os, Ir, Pt; and (3) high work function faces of single crystals, e.g., the (110) of W, recently reported to be as high as 7 or 8 eV by Young and Clark.³ Oxygenated surfaces pose several problems: (a) enhancement of emission of inherent impurity ions from the ionizer surface, especially alkalis; (b) emission of other ion species from the ionizer surface in addition to the usual alkalis; (c) deterioration of the ionizer surface from attack by oxygen; (d) chemical reaction between oxygen and the element being ionized at the surface (e.g., Al or Ga), resulting in the gradual deposit of an oxide, e.g., Al₂O₃ on the ionizer surface and possibly in ultimate failure of the ionizer; and (e) deleterious reaction of the oxygen introduced into the system, with other components of the ion source or with other materials in the system such as semiconductor targets. Single crystal ionizers pose problems of obtaining large area single crystal faces and maintaining them at the high surface ionization temperatures.

Our approach has been the use of higher work function metals, Re, Os, Ir, and Pt, whose polycrystalline surface work functions are 4.96, 4.83, 5.27 and 5.6 to 5.8 eV, respectively.⁴ The highest work function metal, Pt, has too low a melting point (below many critical temperatures). The next highest work function metal, Ir, is suitable, so we have employed Ir surfaces. We have done some work on coating porous tungsten ionizers with layers of Ir and Os.

Figure 1 shows the ionization efficiencies which can be obtained for various elements on Ir; the alkalis are near 100% and others are seen down to about 0.1%. Figure 2 shows the critical temperatures (experimental) for surface ionization of several elements on Ir; they are seen to be low for the alkalis and higher for others, e.g., about 2000°K for Al vs about 1000°K for Cs.

Our achievements with such ion sources are: current densities of 10 to 100 $\mu\text{A}/\text{cm}^2$ of In, Ga, and Al in 1-cm diameter beams, or 1 to 10 $\mu\text{A}/\text{cm}^2$ over electronically scanned 10 cm^2 areas. These compare to $\geq 10 \text{ mA}/\text{cm}^2$ of Cs obtainable in surface ionization sources.

An environmental problem with the ionization of Al was encountered and solved. It was found that an Al surface ionization source should be operated in a clean, very high vacuum (about 10^{-8} Torr) to prevent oxidation of the Al on the ionizer surface where a layer of Al₂O₃ building up on the surface eventually inhibits ionization. Another situation which must be prevented is the presence of bulk liquid of In, Ga, or Al on the Ir surface, which results in alloying at surface ionization temperatures and melting of the alloyed region.

Because the ionization process is not highly efficient for these elements, the resulting neutrals must be eliminated from the beam. This is automatically done if mass separation is employed, but can also be

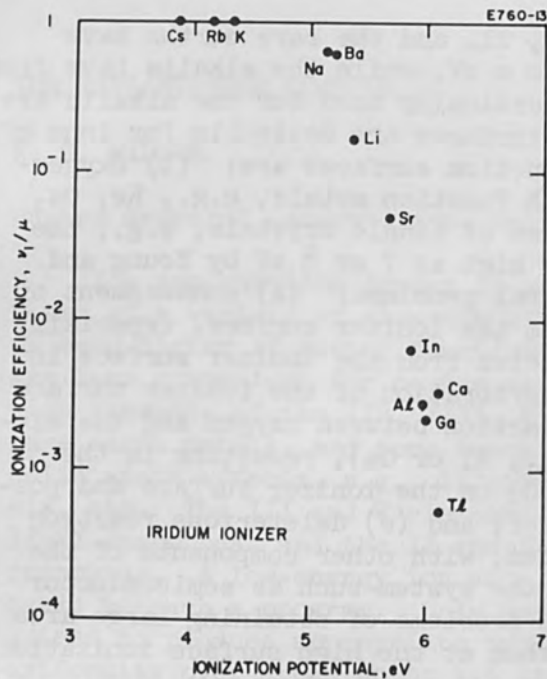


FIG. 1.—Surface ionization efficiencies for various elements on iridium.

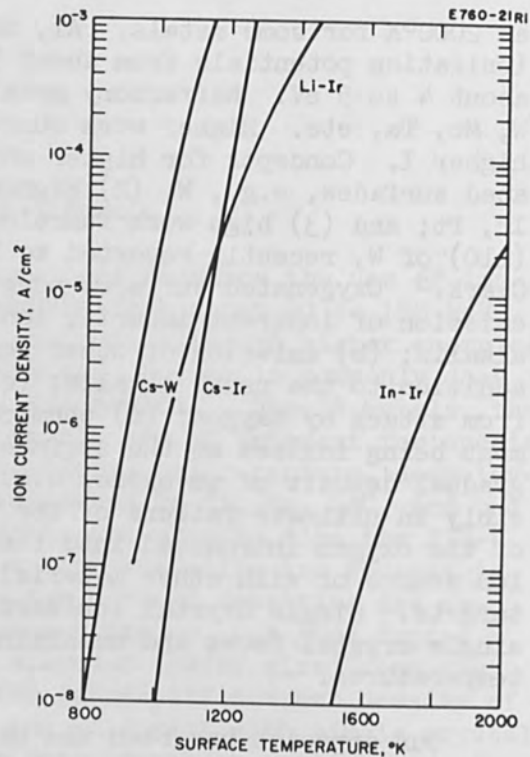


FIG. 2.—Critical temperature envelopes for surface ionization of several elements on iridium.

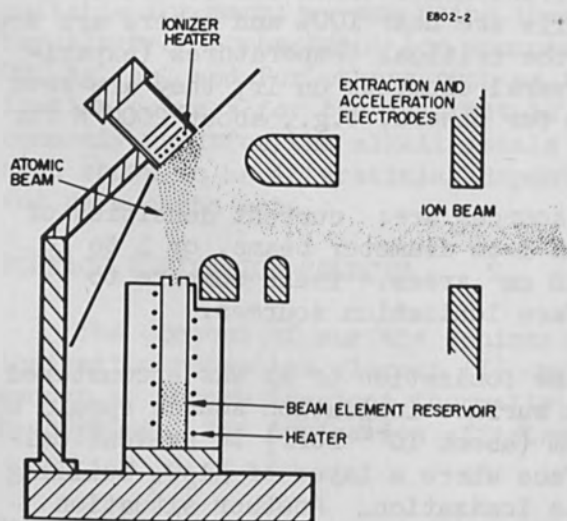


FIG. 3.—Curvilinear surface ionization source.

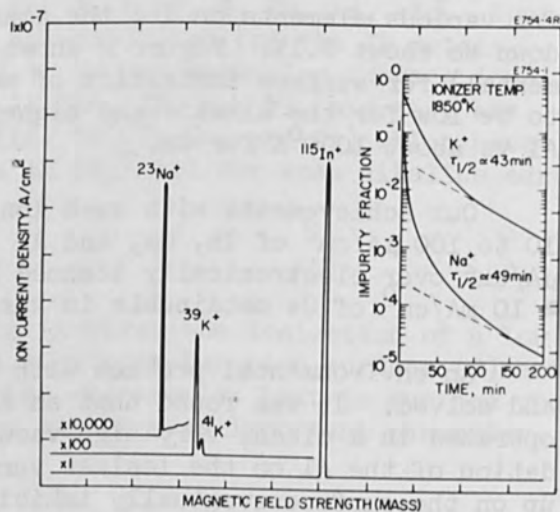


FIG. 4.—Mass spectrum of ion beam from an indium surface ionization source. Insert shows time decay of impurities.

done by electrostatic deflection of the beam or by the use of a curvilinear source (Fig. 3) designed to extract a parallel strip beam at an angle to the ionizing surface.

Ion beams from surface ionization sources have been magnetically mass analyzed here and found to contain impurities of K^+ , Na^+ , and sometimes Li^+ , which decay in time. Impurity levels which can be achieved after some hours of operation for Al, Ga, and In ion sources are shown in Table 1.

TABLE 1.— Typical surface ionization source beam purities.*

| Source | M^+ | Li^+ | Na^+ | K^+ |
|--------|-------|----------------------|--------------------|--------------------|
| Al^+ | 1.00 | 3×10^{-5} | 4×10^{-3} | 2×10^{-3} |
| Ga^+ | 1.00 | $< 1 \times 10^{-6}$ | 5×10^{-5} | 2×10^{-5} |
| In^+ | 1.00 | $< 10^{-7}$ | 6×10^{-6} | 8×10^{-4} |

*After about 10 hr of operation

A spectrum of an ion beam from an In source is shown in Fig. 4 early in its operation, together with the time decay of the K^+ and Na^+ impurity components. A mass spectrum of the beam from a Ga^+ surface ionization source is shown in Fig. 5. Lower impurity levels can be achieved by better outgassing (higher temperature and/or longer time).

ELECTRON BOMBARDMENT IONIZATION SOURCES

There are many types and designs of ion sources which employ electron impact ionization. One of these is the low-voltage modified Penning discharge. The type we employ and for which data are shown below has an ionization chamber composed of a cylindrical anode with the vapor (atoms or molecules) introduced from one end. A hot filament cathode is provided on the axis of the cylinder or at the vapor end, or a cold cathode is located at the vapor end. The cathode design is determined by the vapor species. The ions are extracted from the end of the cylinder opposite the vapor supply through electrodes with one or many matched and aligned apertures. We have successfully used 1, 7, and 700 aperture arrays and anode cylinder diameters as small as 1 cm. The anode is maintained at a positive potential with respect to the ends (electrodes), so that electrons emitted by the cathode are injected through a plasma sheath in an axial potential well. The application of an axial magnetic field prevents the electrons from going directly to the anode and causes them to spiral about the axis in the discharge chamber. As the electrons strike and ionize the vapor particles, they lose energy and are finally collected by the anode, having had long paths in the chamber. The ionized particles and electrons form a neutral plasma which fills the discharge chamber. At the cathode there exists a plasma sheath with sufficient potential drop to the cathode to allow the flow of electrons to the discharge in sufficient quantities to ionize the vapor and maintain the plasma. At the screen electrode or anticathode, located at the opposite

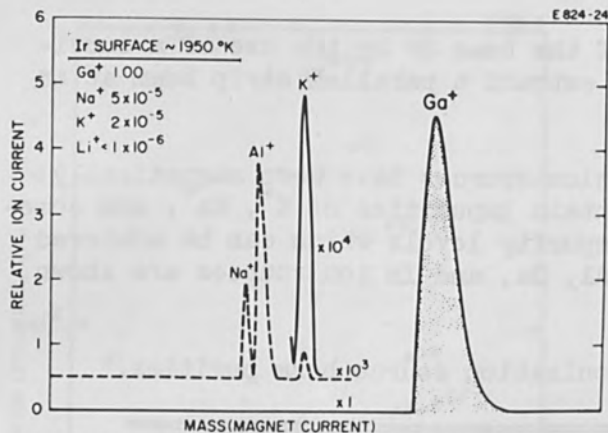


FIG. 5.—Mass spectrum of ion beams from a gallium surface ionization source. The aluminum peak is the result of prior operation as an Al⁺ source and does not exist in the spectrum from a Ga⁺ only source. This spectrum was measured at the target location in an implantation system (Fig. 10) under implantation conditions, explaining the wide peaks.

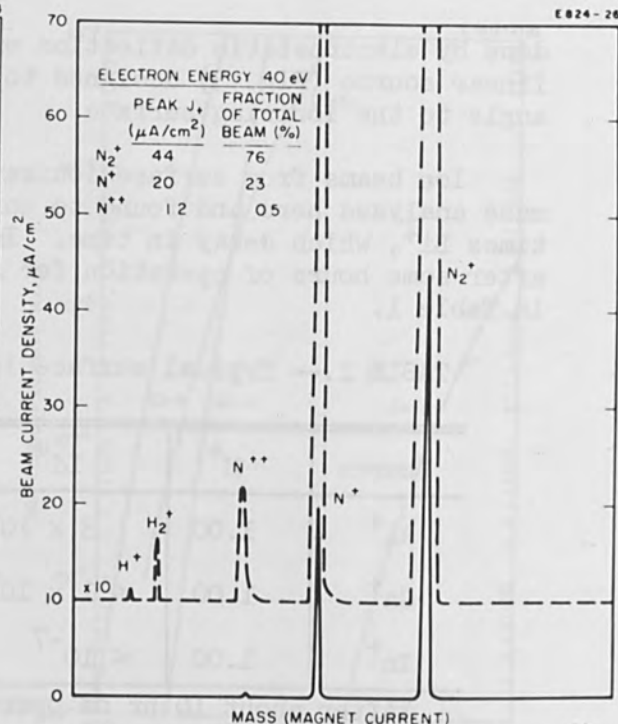


FIG. 6.—Mass spectrum of nitrogen ion beam under implantation conditions.

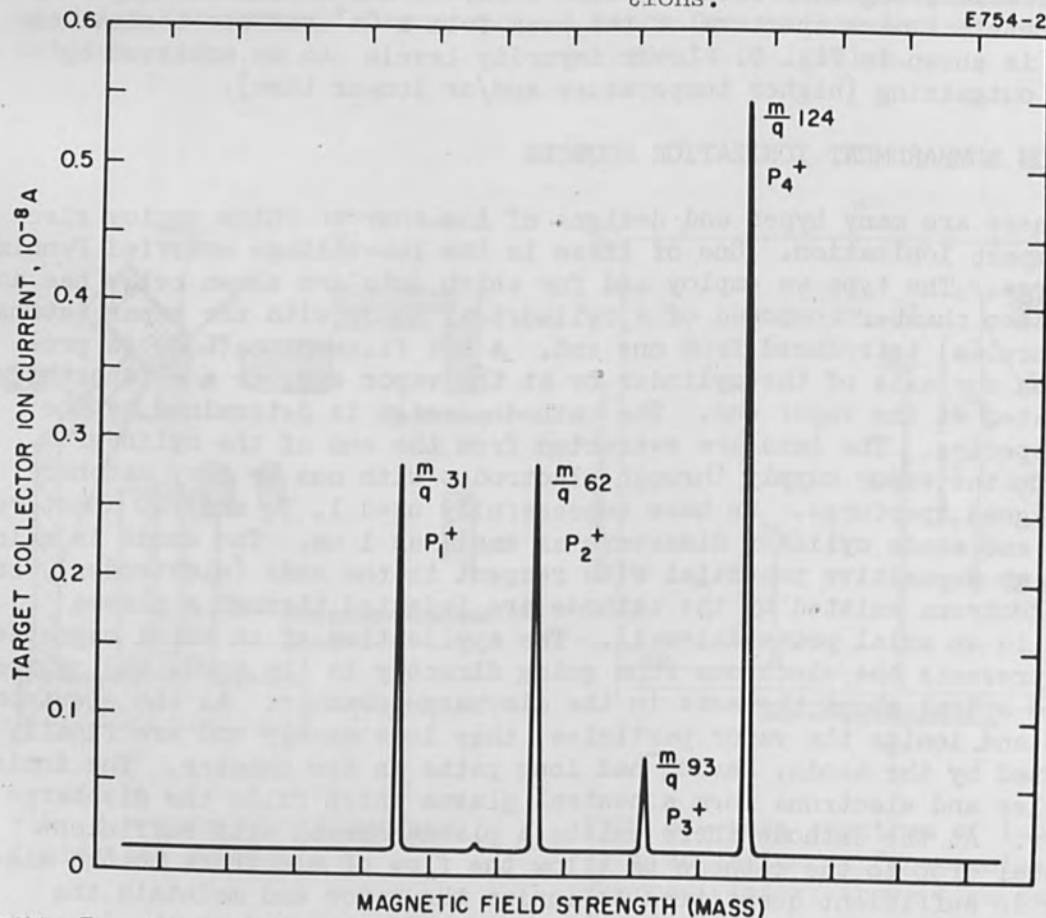


FIG. 7.—Mass spectrum of phosphorus ion beam under implantation conditions.

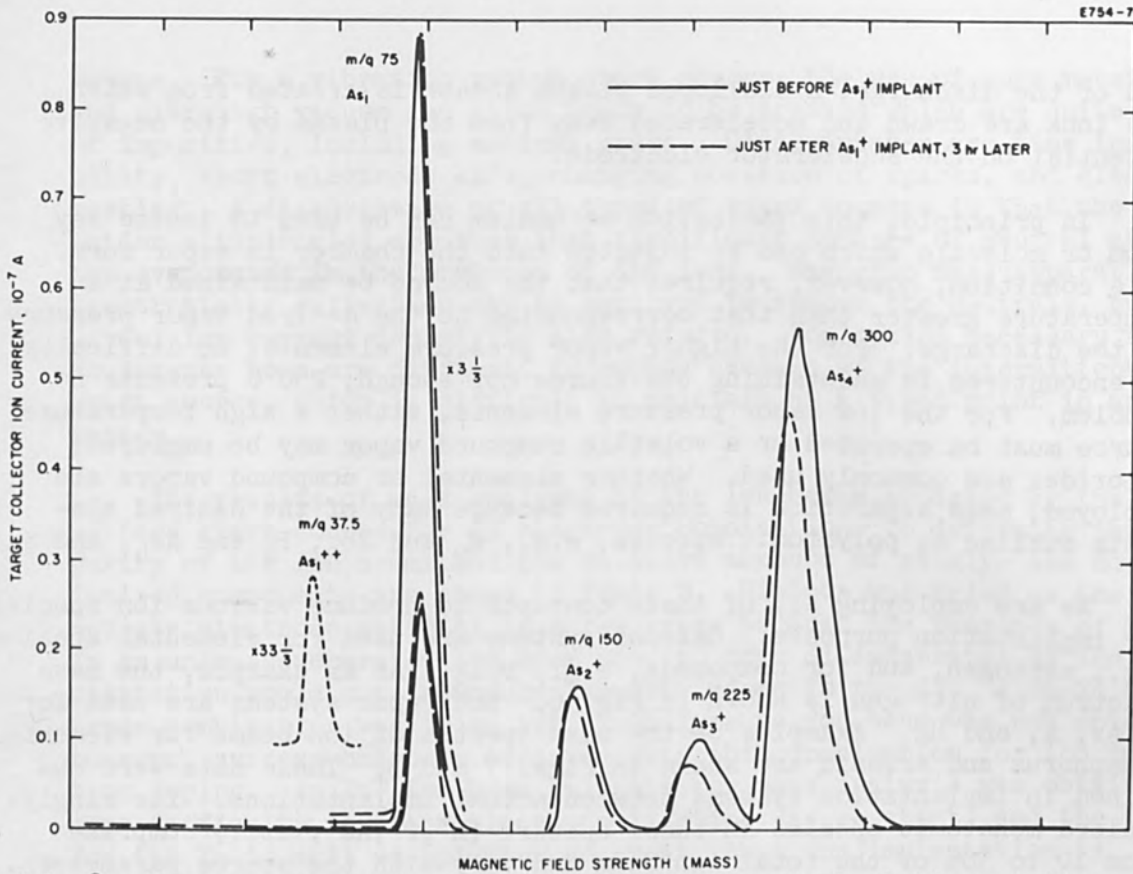


FIG. 8.—Mass spectrum of arsenic ion beam under implantation conditions.

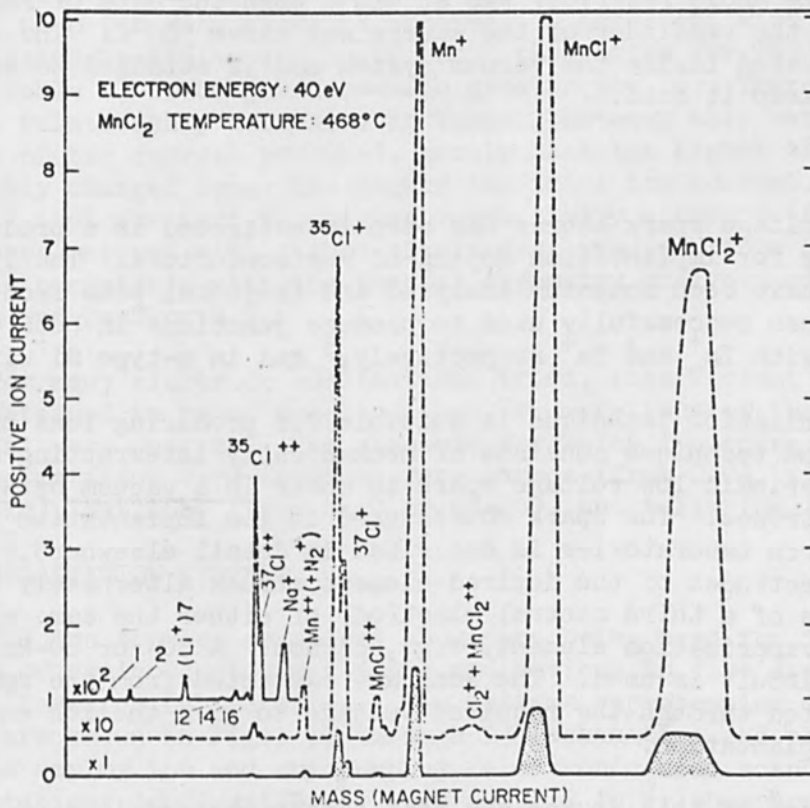


FIG. 9.—Mass spectrum of manganese chloride ion beam under implantation conditions.

end of the discharge, a scalloped plasma sheath is created from which the ions are drawn and accelerated away from the plasma by the negative potential on the accelerator electrode.

In principle, this ionization mechanism can be used to ionize any atom or molecule which can be injected into the chamber in vapor form. This condition, however, requires that the source be maintained at a temperature greater than that corresponding to the desired vapor pressure in the discharge. For the higher vapor pressure elements, no difficulty is encountered in maintaining the source hot enough; 250°C presents no problem. For the low vapor pressure elements, either a high temperature source must be operated or a volatile compound vapor may be employed; chlorides are commonly used. Whether elemental or compound vapors are employed, mass separation is required because many of the desired elements sublime as polyatomic species, e.g., N₂ and Sb₂, P₄ and As₄, and S₈.

We are employing all of these concepts to produce various ion species for implantation purposes. Gaseous systems are used for elemental species, e.g., nitrogen, and for compounds, e.g., BCl₃. As an example, the mass spectrum of nitrogen is shown in Fig. 6. Hot vapor systems are used for P, As, S, and Hg. Examples of the mass spectra of ion beams for elemental phosphorus and arsenic are shown in Figs. 7 and 8. These data were obtained in implantation systems between actual implantations. The singly-ionized monatomic species in these spectra (N⁺, P⁺, As⁺, etc.) comprise from 10 to 30% of the total ion beam and vary with the source parameters. An example of a hot compound vapor system is shown in Fig. 9 for manganese chloride. The metallic Mn⁺ ion can comprise as much as 30% of the total ion beam. The MnCl₂ reservoir was at 468°C when the data of Fig. 9 were obtained and the remainder of the source was above 500°C. The source magnet is located inside the vacuum system and is attached to an LN₂ cryowall to keep it cold.

SPARK SOURCE

A low-voltage spark source has been investigated as a producer of ions suitable for implantation doping of semiconductors. The ions from this source have been momentum analyzed and the total beam from the ion source has been successfully used to produce junctions in both p- and n-type GaAs with Zn⁺ and Te⁺ respectively,⁵ and in n-type Si with Sb⁺.⁶

This ionization technique is suitable for producing ions of solid elements. The technique consists of mechanically interrupting a circuit to cause a periodic low voltage spark to occur in a vacuum between conducting electrodes. The spark source used in ion implantation work at Hughes Research Laboratories is described in detail elsewhere.⁷ It employs two electrodes of the desired element struck alternately against opposite ends of a third central electrode of either the same element, or of a low vaporization element, e.g., carbon. A 50- or 60-Hz interrupted 45-volt dc circuit is used. The ions are extracted from the sparks and are accelerated through the required voltage to give the ion energy desired for implantation.

Advantages of this source are that singly charged ions of a variety of solid elements can be produced in ultrahigh vacuum in the same, simple

source. For a vibrating vacuum spark source, the use of pure materials and ultrahigh vacuum can allow beams to be created which are quite free of impurities, including ambient gases. Disadvantages are time instability, short electrode life, changing position of sparks, and electrode heating. A disadvantage of all types of spark sources is that the ionization efficiencies are such that significant numbers of neutral atoms are evaporated in the presence of the ions. Magnetic mass separation or electrostatic deflection can be employed to remove the neutrals, but the useful ion current density is also reduced. Ion optics necessary to form an intense beam are difficult to employ because of the intermittent nearly point source, which is difficult to maintain at a fixed point in an optics system.

The results of mass analyses of the ion beams produced by the low-voltage spark source for 15 electrode combinations to determine the purity of the ion beams and the relative amounts of singly- and doubly-ionized components are shown in Table 2. Silicon was tried as the intermediate electrode material in a few cases because the presence of Si ions in an un-mass-separated ion beam used to dope Si substrates by ion implantation would not introduce impurity atoms in the Si. A Zn-Zn electrode combination was tried but an analyzable ion beam was not obtained; however, success has been achieved with this combination for ion implantation doping. An In^+ ion beam suitable for mass analysis was obtained with some difficulty, but the electrode lifetime was so short, and the tendency for the In to melt or splatter so great, that ion implantation is impractical.

While the ratios of singly to doubly charged ions are in the range from 2 to 8 for many elements studied, in agreement with the observations of Venkatasubramanian and Duckworth,⁸ the ratios for Te, Sb, and C are seen (Table 2) to be greater—much greater for Te. There seems to be a direct relationship evidenced in Table 2 between this ratio and the magnitude of the current produced, namely that the higher the ratio of singly to doubly charged ions, the higher the total ion current. The data of Table 2 indicate that the higher conductivity elements (Al, Cu, Ag, and Au), when matched with carbon electrodes, produce large C^+ components; that is compatible with the thermal asymmetry analyses of Venkatasubramanian and Duckworth.⁸

For many electrode combinations tried, insufficient ion currents were obtained to be of practical use, or more ions of the undesired material were present. The elements for which ion currents useful for ion implantation were obtained were carbon (from C-C), zinc (from Zn-C or Zn-Zn), antimony (from Sb-C or Sb-Sb), and tellurium (from Te-C).

ION IMPLANTATION SYSTEMS

The ion sources described above are being used for ion implantation doping of semiconductor materials and devices in five systems at the Hughes Research Laboratories. Two systems representing different concepts are shown in Figs. 10 through 13 (schematics and photos). Both systems employ ion and cryopumping, electronic beam scanning to produce implantations doped uniformly over about 2 in.², phosphor display image converters, heated targets, gate valves for maintaining vacuum while

TABLE 2.—Mass analysis of ion beams from a low-voltage spark source employing various electrode combinations.

| Electrode Material A | Electrode Material B | Relative Intensities ^a | | | | | | Miscellaneous | Normal-ization Factor ^b |
|----------------------|----------------------|-----------------------------------|------------------------|-----------------------------|----------------------|------------------------|--|------------------------|------------------------------------|
| | | A ⁺ | A ⁺⁺ | A ₂ ⁺ | B ⁺ | B ⁺⁺ | | | |
| C | C | 1.00 | 5 x 10 ⁻² | g | ... | ... | H ⁺ 5 x 10 ⁻³ , H ₂ O ⁺ 1.4 x 10 ⁻² , (Na ⁺ 3 x 10 ⁻² , Cl ⁺ 7 x 10 ⁻³) ^f | 0.14 | |
| Al | C | 1.00 | < 0.58 ^c | 0.17 | < 0.58 ^c | 1.5 x 10 ⁻² | Al ₂ O ₃ ⁺ 5 x 10 ⁻² , H ₂ O ⁺ 6 x 10 ⁻² | 6 x 10 ⁻³ | |
| Al | Si | ≤ 1.00 ^c | ~ 0.27 ^d | g | < 1.0 ^c | << 0.27 ^d | | 3 x 10 ⁻³ | |
| Al | W | 1.00 | g | trace | 1.0 | g | | 2 x 10 ⁻³ | |
| Mn | C | 1.00 | 0.14 | 0.22 | 0.64 | 4 x 10 ⁻³ | Mn ₃ ⁺ 3 x 10 ⁻² | 5 x 10 ⁻² | |
| Cu | C | 1.00 | 0.65 | g | 1.1 | 8 x 10 ⁻² | | 5 x 10 ⁻⁴ | |
| Zn | C | 1.00 | 0.19 | < 3 x 10 ⁻³ | 6 x 10 ⁻² | 6 x 10 ⁻³ | | 7 x 10 ⁻² | |
| Ag | C | 1.00 | g | g | 1.8 | g | | 2 x 10 ⁻³ | |
| In | C | 1.00 | 0.15 | g | 0.12 | 2 x 10 ⁻² | C ³⁺ 6 x 10 ⁻³ , In ³⁺ 2 x 10 ⁻³ , N ₂ ⁺ 2 x 10 ⁻² | 3 x 10 ⁻² | |
| Sb | C | 1.00 | 7 x 10 ⁻² | g | 3 x 10 ⁻² | 3 x 10 ⁻⁴ | | 0.11 | |
| Sb | Sb | 1.00 | 2.5 x 10 ⁻² | < 10 ⁻³ | ... | ... | | 0.14 | |
| Te | C | 1.00 | < 3 x 10 ⁻⁵ | < 1 x 10 ⁻⁵ | 1 x 10 ⁻³ | 5 x 10 ⁻⁵ | | 1.00 | |
| Te | Si | e | ... | ... | ... | ... | | ... | |
| W | C | g | g | g | 1.00 | 0.21 | | < 5 x 10 ⁻⁵ | |
| Au | C | g | g | g | 1.00 | trace | | < 5 x 10 ⁻⁵ | |

^aNormalized to the A⁺ component of each combination; obtained from relative areas in the peaks in the spectral distributions

^bFor the A⁺ components relative to the Te⁺ peak; obtained using the maximum currents in the A⁺ peaks measured at the collector

^c, ^dPeaks not resolved

^eData unobtainable because Te electrode disintegrated in less than 60 sec

^fAttributed to an avoidable NaCl contamination

^gNot observed, < ~ 10⁻⁴

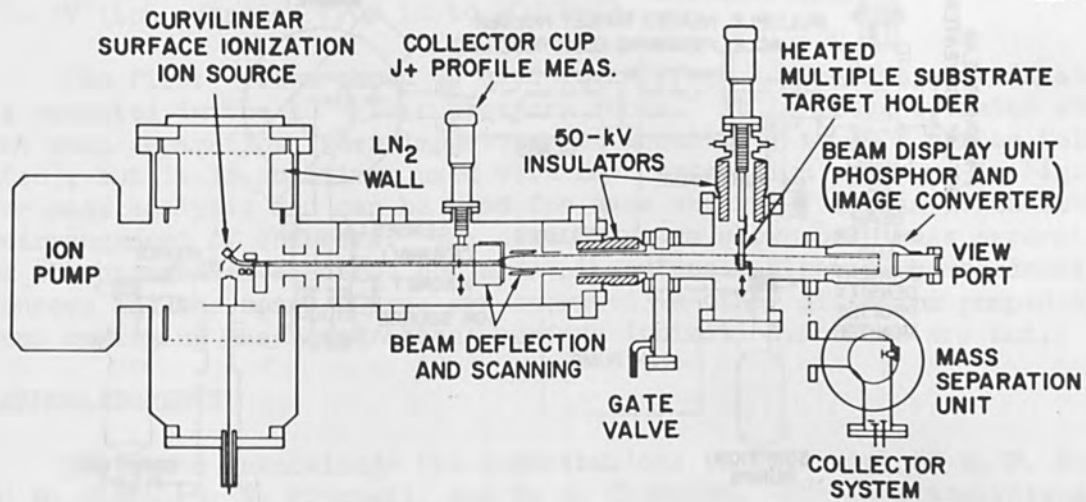


FIG. 10.—Ion implantation system schematic (surface ionization).

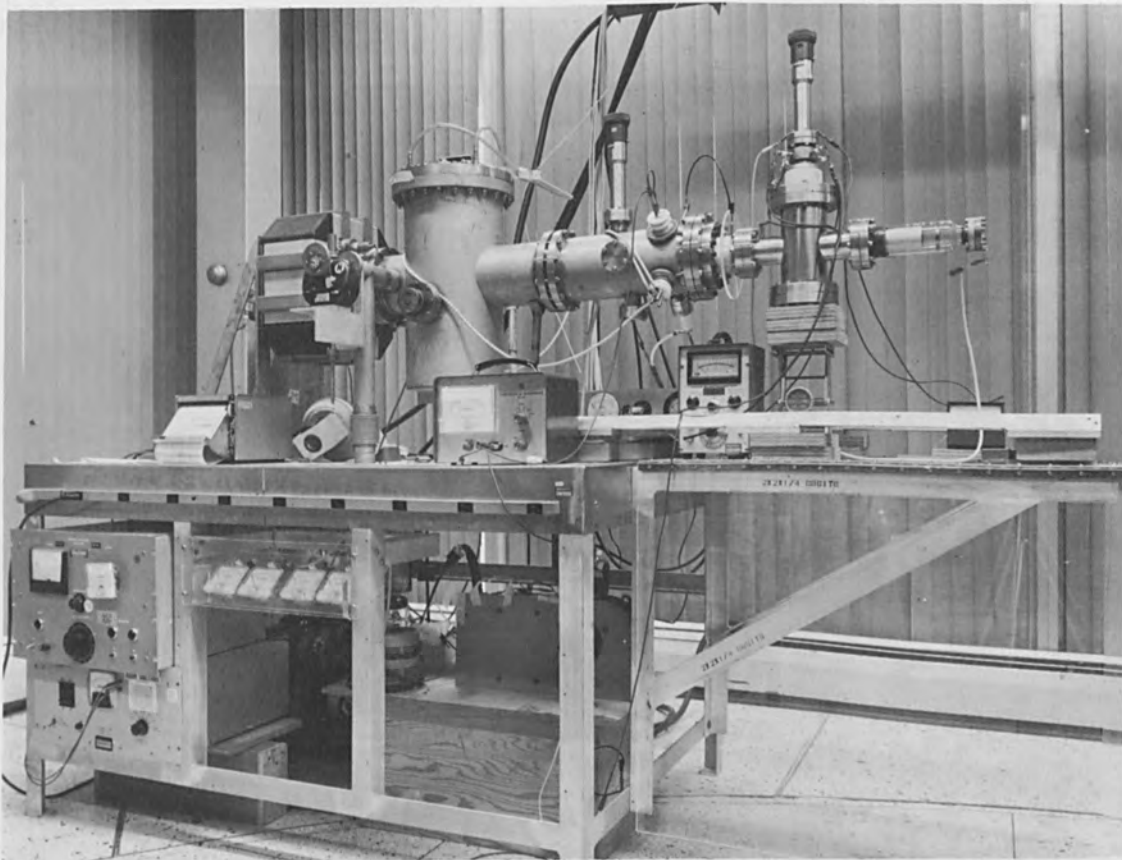


FIG. 11.—Ion implantation system photo (surface ionization).

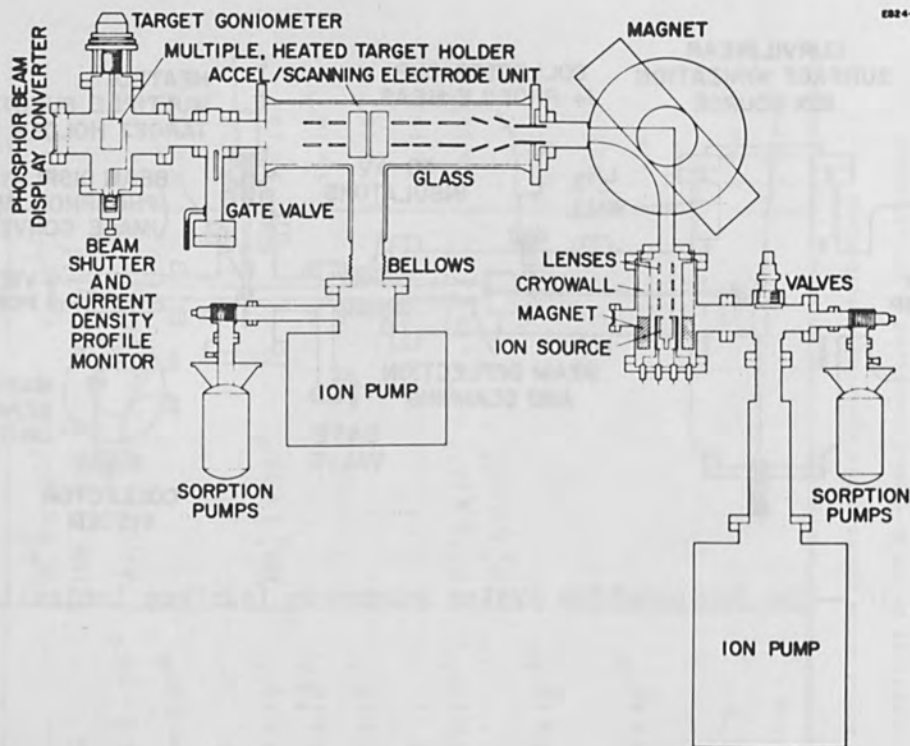


FIG. 12.—Ion implantation system schematic (electron bombardment ionization).

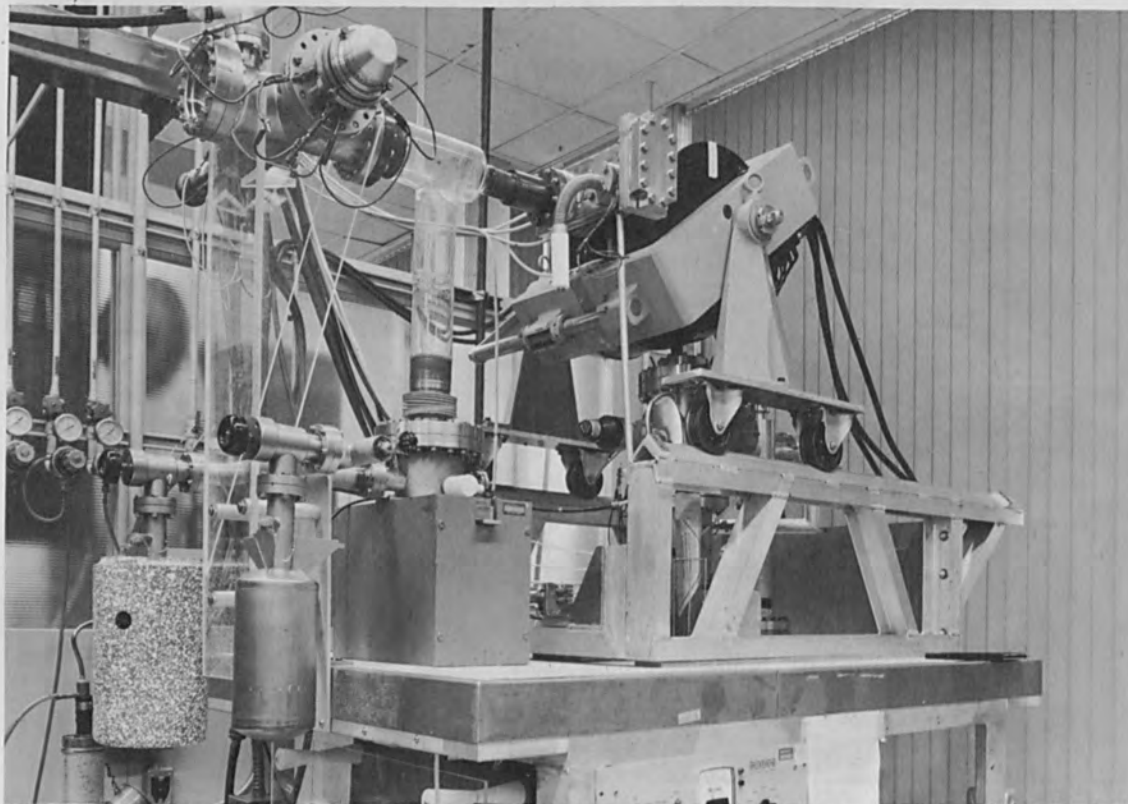


FIG. 13.—Ion implantation system photo (electron bombardment ionization).

quickly changing samples, and are operated at beam voltages from 10 to 150 kV (ion energies from 10 to 300 keV).

The first system shown is used for surface ionization sources and is operated in the 10^{-8} Torr pressure range. It is often operated without mass separation (when impurities of about 10^{-5} to 10^{-4} can be tolerated), but it is sometimes used with mass separation as shown in Fig. 10 for mass analysis and can be used for mass separated implantation with a rearrangement of chambers. The second system shown uses mass separation of the beams from electron bombardment sources. Electron bombardment sources and the spark source are operated in other diffusion pumped systems employing mass separation; surface ionization sources are not.

ACKNOWLEDGMENTS

I wish to acknowledge the contributions to this work of W. P. Fleming, D. M. Jamba, H. P. Mitchell, and S. A. Thompson. The mass analysis data for the spark source were obtained by this group, but it is used by our associates named in Ref. 3.

REFERENCES

1. K. J. Hill and R. S. Nelson, Nuclear Instr. & Meth. 38: 15, 1965.
2. J. O. McCaldin and A. E. Widmer, J. Phys. Chem. Solids 24: 1073, 1963.
3. R. D. Young and H. E. Clark, Appl. Phys. Letters 9: 265, 1966.
4. R. G. Wilson, J. Appl. Phys. 37: 3170, 1966.
5. J. W. Mayer, O. J. Marsh, R. Mankarious, and R. Bower, First Quarterly Progress Report, Contract NAS 12-124, July 1966; also submitted for publication to Journal of Applied Physics.
6. R. W. Bower, R. Baron, J. W. Mayer, and O. J. Marsh, Appl. Phys. Letters 9: 203, 1966.
7. O. J. Marsh, J. W. Mayer, A. J. Mohr, and R. S. Ohl, Submitted for publication in Review of Scientific Instruments.
8. V. S. Venkatasubramanian and H. E. Duckworth, Can. J. Phys. 41: 234, 1963.

A SIMPLE DEVICE FOR THE ENERGY AND CURRENT MEASUREMENT
OF AN ACCELERATOR ELECTRON BEAM

J. W. MOTZ and J. H. SPARROW

National Bureau of Standards, Washington, D. C.

ABSTRACT. A simple apparatus has been developed which permits the simultaneous measurement of the electron energy and current of an accelerator electron beam. This measurement is accomplished with negligible interference of the beam during the continuous operation of the accelerator and applies to electron energies greater than approximately 50 keV. The apparatus consists of a thin aluminum foil which intercepts the beam with a negligible energy loss (less than 1 kV), and two cylindrical aluminum electrodes which are positioned respectively on the incident and exit sides of the foil with axes normal to the foil surface and coincident with the beam direction. With a suitable distribution of electric potentials in this system, the incident electrode current I_i is inversely proportional to the square of the electron velocity and the exit electrode current I_e is inversely proportional to the square of the product of the electron velocity and momentum. Therefore, when an electron beam passes through this system, the electron energy can be determined from the current ratio I_i/I_e and the incident electron current can be determined from the current I_i , as shown in previous measurements with secondary-emission monitors. The energy dependences described above for each electrode has been confirmed over a wide range of electron velocities by measurements carried out with a constant potential electron accelerator in the energy region from 50 to 500 keV.

Various devices are available for measuring the energy¹ or for monitoring the current² of an accelerator electron beam. Compared to these devices, a simple apparatus has been developed with the advantage that it permits the simultaneous measurement of the electron energy and current. This measurement is accomplished with negligible interference of the beam during the continuous operation of the accelerator and applies to electron energies greater than approximately 50 keV.

The apparatus is shown in Fig. 1. The elements in this apparatus consist of a beam collimator, a thin aluminum foil which intercepts the beam with a negligible energy loss (less than 1 kV), and two cylindrical³ electrodes which are positioned respectively on the incident and exit sides of the foil with axes normal to the foil surface. The surfaces of the incident and exit electrodes subtend an angular region respectively from 97 to 168° and from 17 to 23°, as measured with respect to the incident beam direction at the foil center. The system was tested with 50- to 500-keV electron beams from the NBS constant-potential electron accelerator. When the electron beam passes along the axis of this system, each electrode collects a certain fraction of the electrons which are scattered and emitted in various directions from the foil. For a given incident electron energy and beam current, the electrode currents depend on (a) the geometrical and electric-potential configuration in the

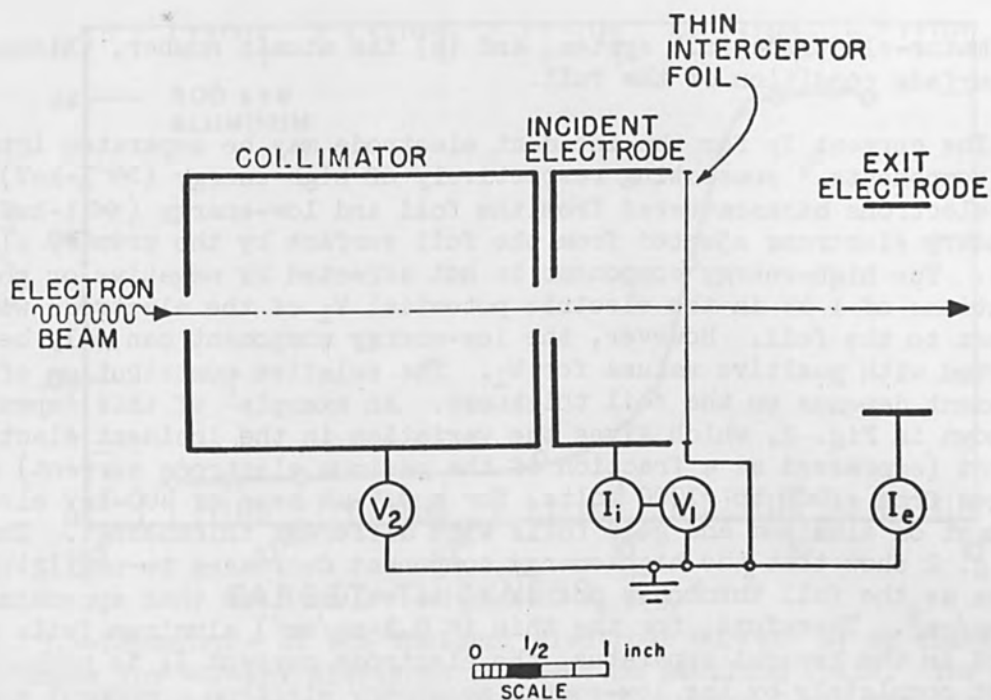


FIG. 1.—Spatial and potential configuration of apparatus used for the simultaneous determination of the energy and current of an electron beam.

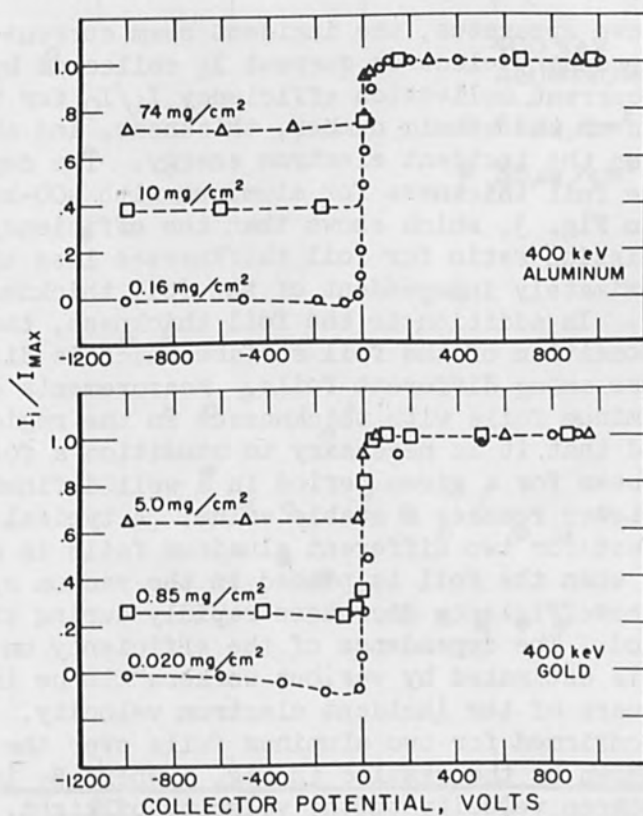


FIG. 2.—Dependence of the incident electrode current I_i on the potential of this electrode with respect to the foil for 400-keV electrons incident on aluminum and gold foils with different thicknesses. The current I_i is expressed in terms of the ratio I_i/I_{max} , where I_{max} is the maximum electrode current for the given potential variation.

collimator-electrode-foil system, and (b) the atomic number, thickness, and surface condition of the foil.

The current I_i for the incident electrode may be separated into two main components,⁴ consisting respectively of high-energy ($\gg 1$ -keV) primary electrons backscattered from the foil and low-energy ($\ll 1$ -keV) secondary electrons ejected from the foil surface by the primary electrons. The high-energy component is not affected by negative or positive variations of 1 kV in the electric potential V_1 of the electrode with respect to the foil. However, the low-energy component can only be detected with positive values for V_1 . The relative contribution of each component depends on the foil thickness. An example⁵ of this dependence is shown in Fig. 2, which gives the variation in the incident electrode current (expressed as a fraction of the maximum electrode current) as V_1 changes from -1000 to +1000 volts, for a 0.5- μ a beam of 400-keV electrons incident on aluminum and gold foils with different thicknesses. The data in Fig. 2 show that the high-energy component decreases to negligible values as the foil thickness decreases to values less than approximately 0.2 mg/cm². Therefore, for the thin (< 0.1 -mg/cm²) aluminum foils employed in the present apparatus, the electrode current I_i is produced almost completely by the low-energy secondary electron component and the apparatus is operated with a positive value of +1000 volts for the potential V_1 .

With the above apparatus, the incident beam current I_0 can be determined from the secondary electron current I_i collected by the incident electrode. The current collection efficiency I_i/I_0 for the incident electrode depends on the atomic number, thickness, and surface condition of the foil and on the incident electron energy. The dependence of this efficiency on the foil thickness for aluminum with 400-keV incident electrons is given in Fig. 3, which shows that the efficiency (expressed as the secondary emission ratio for foil thicknesses less than about 200 μ g/cm²) is approximately independent of the foil thickness in the region below 200 μ g/cm². In addition to the foil thickness, the efficiency depends on the condition of the foil surface which is difficult to control and reproduce among different foils. Measurements carried out with 20 different aluminum foils with thicknesses in the region from 15 to 100 μ g/cm² showed that it is necessary to condition a foil by exposure to the electron beam for a given period in a well defined environment before the efficiency reaches a stable value. A typical example of this conditioning effect for two different aluminum foils is given in Fig. 4, which shows that when the foil is placed in the vacuum system after exposure to air, the efficiency decreases rapidly during the initial irradiation period. The dependence of the efficiency on the incident electron energy is estimated by various workers⁴ to be inversely proportional to the square of the incident electron velocity. This energy dependence was confirmed for two aluminum foils over the region from 50 to 500 keV, as shown by the results in Fig. 5 where β_1 is the ratio of the incident electron velocity to the velocity of light. On the basis of the data in Figs. 3, 4, and 5, it is estimated that the beam current can be determined by this method with an accuracy of approximately 5 per cent and that it is necessary to develop techniques for controlling the foil surface in order to improve this accuracy.

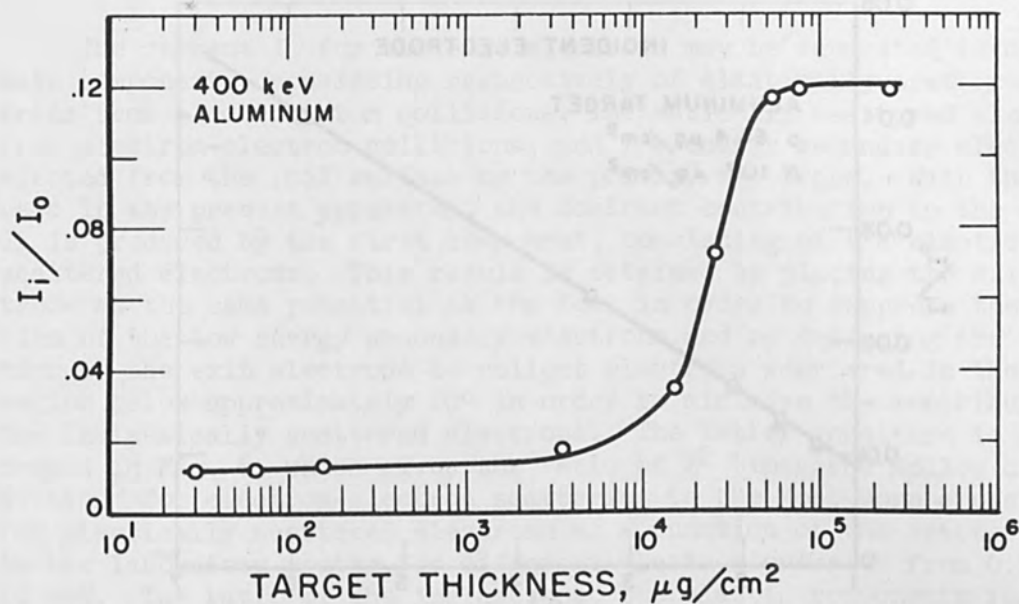


FIG. 3.—Dependence of the incident electrode current I_i on the foil thickness for 400-keV electrons incident on aluminum foils. The current I_i is expressed in terms of the ratio I_i/I_0 , where I_0 is the incident beam current.

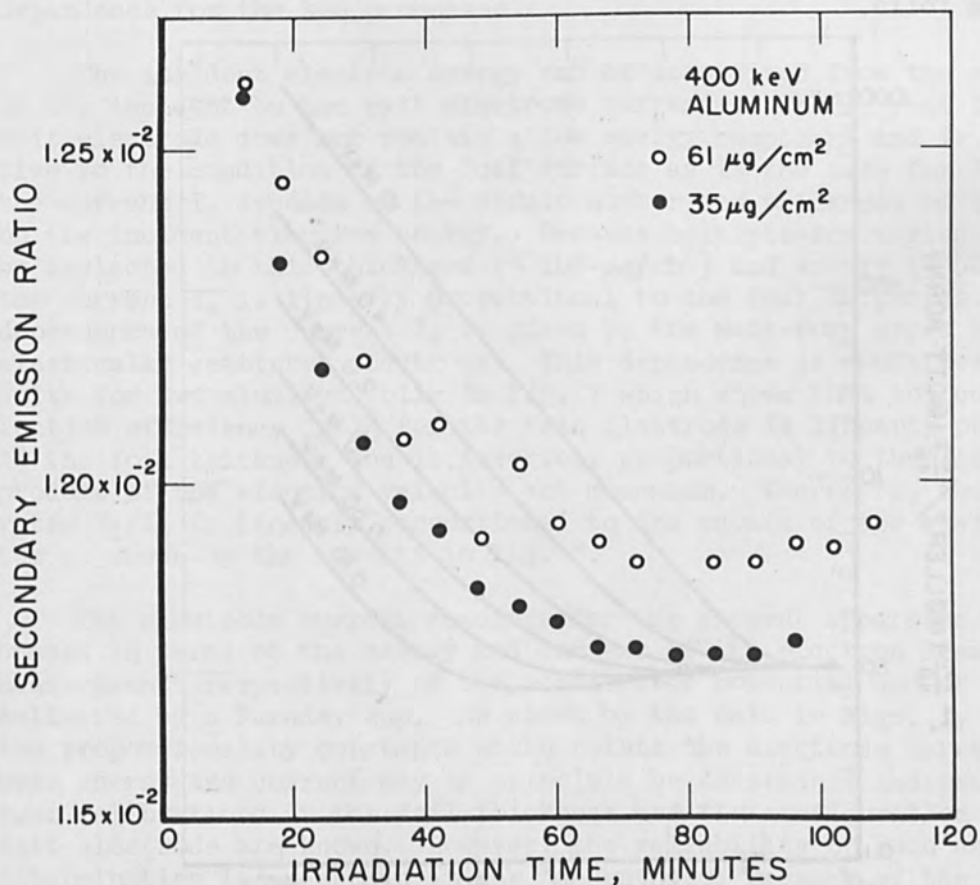


FIG. 4.—Dependence of the secondary-emission ratio on the irradiation time for 400-keV electrons incident on 35- and 61- $\mu\text{g}/\text{cm}^2$ aluminum foils. This ratio is equal to the ratio I_i/I_0 in the present apparatus, where I_i is the incident electrode current and I_0 is the incident beam current.

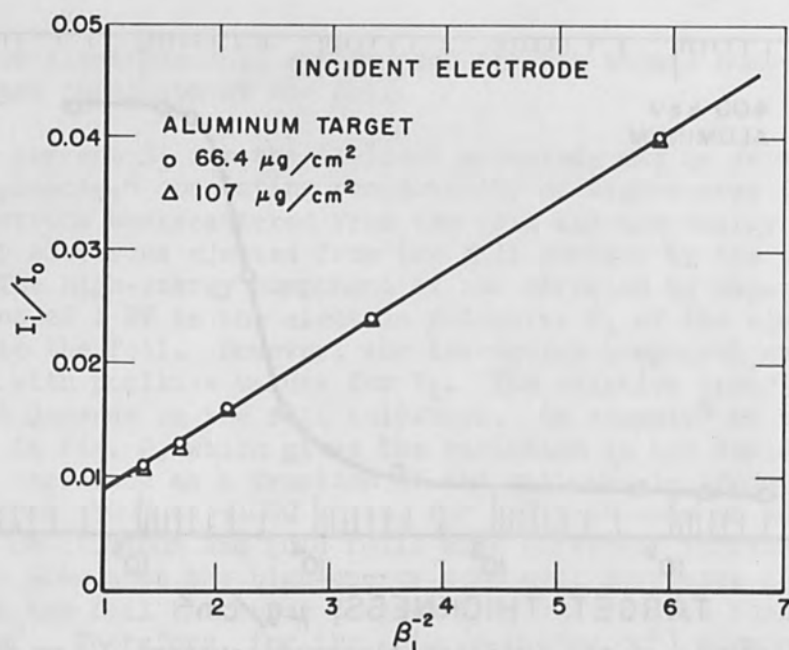


FIG. 5.—Dependence of the current collection efficiency I_i/I_0 for the incident electrode on the quantity β_1^{-2} where β_1 is the ratio of the electron velocity to the velocity of light, for 66.4- and 107- $\mu\text{g}/\text{cm}^2$ aluminum foils.

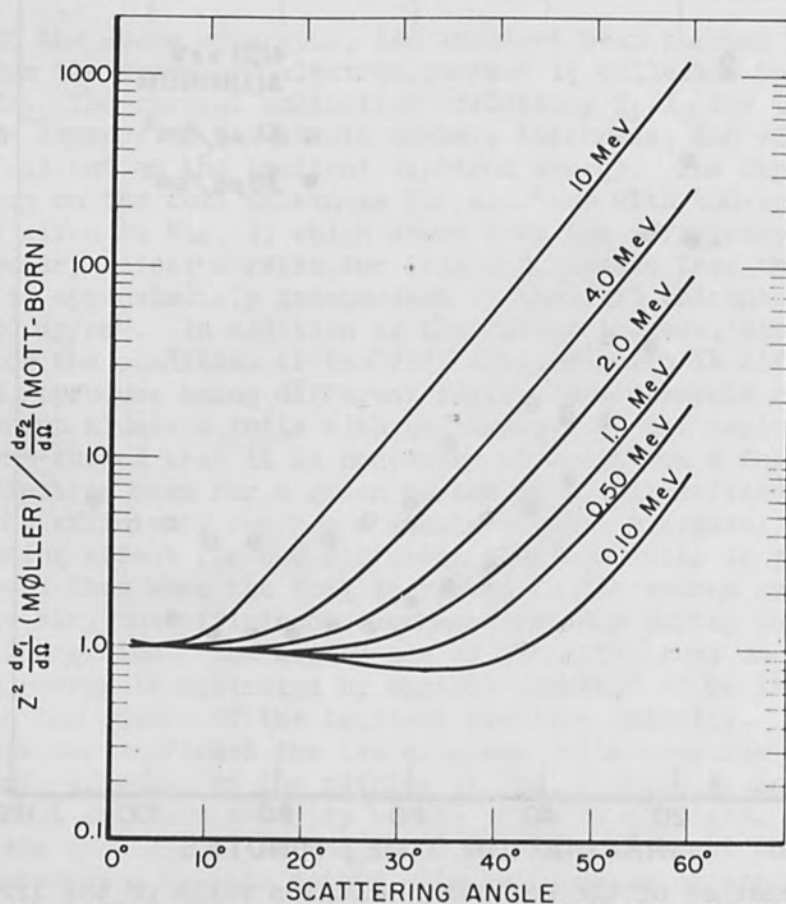


FIG. 6.—Dependence of the cross section ratio for electron-electron (Møller) scattering and for elastic scattering (Mott-Born) on the electron scattering angle for incident electron energies of 0.1, 0.5, 1.0, 2.0, 4.0, and 10 MeV.

The current I_e for the exit electrode may be separated into three main components, consisting respectively of elastically scattered electrons from electron-atom collisions, inelastically scattered electrons from electron-electron collisions, and low-energy secondary electrons ejected from the foil surface by the primary electrons. With the design used in the present apparatus, the dominant contribution to the current I_e is produced by the first component, consisting of the elastically scattered electrons. This result is obtained by placing the exit electrode at the same potential as the foil in order to suppress the contribution of the low energy secondary electrons and by designing the configuration at the exit electrode to collect electrons scattered in the angular region below approximately 20° in order to minimize the contribution of the inelastically scattered electrons. The latter condition is illustrated in Fig. 6, which gives the ratio of Z^2 times the Møller cross section⁶ for electron-electron scattering to the Mott-Born cross section⁷ for elastically scattered electrons as a function of the scattering angle in the laboratory system for different electron energies from 0.1 to 10 MeV. The ratio of the inelastic to the elastic components for I_e is equal to the ratio of the Møller cross section per atom ($Z d\sigma_1/d\Omega$) to the Mott-Born cross section. Therefore, this ratio for aluminum is approximately equal to 1/13 for scattering angles less than 20° and for electron energies less than 0.5 MeV with a negligible difference in the energy dependence for the two processes.

The incident electron energy can be determined from the ratio I_i/I_e of the incident to the exit electrode currents. The current I_e for the exit electrode does not contain a low energy component and is not sensitive to the condition of the foil surface as is the case for I_i . However, the current I_e depends on the atomic number and thickness of the foil and on the incident electron energy. Because multiple-scattering effects may be neglected in this thickness ($< 100\text{-}\mu\text{g}/\text{cm}^2$) and energy ($> 50\text{-keV}$) range, the current I_e is linearly proportional to the foil thickness. The energy dependence of the current I_e is given by the Mott-Born cross section⁷ for elastically scattered electrons. This dependence is confirmed by the results for two aluminum foils in Fig. 7 which shows that the current collection efficiency I_e/I_0 for the exit electrode is linearly proportional to the foil thickness and is inversely proportional to the square of the product of the electron velocity and momentum. Therefore, the current ratio I_i/I_e is linearly proportional to the square of the electron momentum as shown by the results in Fig. 8.

The electrode current readings for the present apparatus were calibrated in terms of the energy and current of the electron beam by accurate measurements respectively of the accelerator potential and of the current collected by a Faraday cup. As shown by the data in Figs. 3, 4, and 8, the proportionality constants which relate the electrode currents to the beam energy and current may in principle be determined independently of such calibrations if the foil thickness and the configuration for the exit electrode are known. However, the reliability of such an absolute determination is uncertain at the present time because of the unpredictable response of the foil surface in different environments. Further, it should be noted that the present apparatus was designed for the energy region from 50 to 500 keV and that the sensitivity for energy measurements decreases with increasing electron energies. It can be expected that with

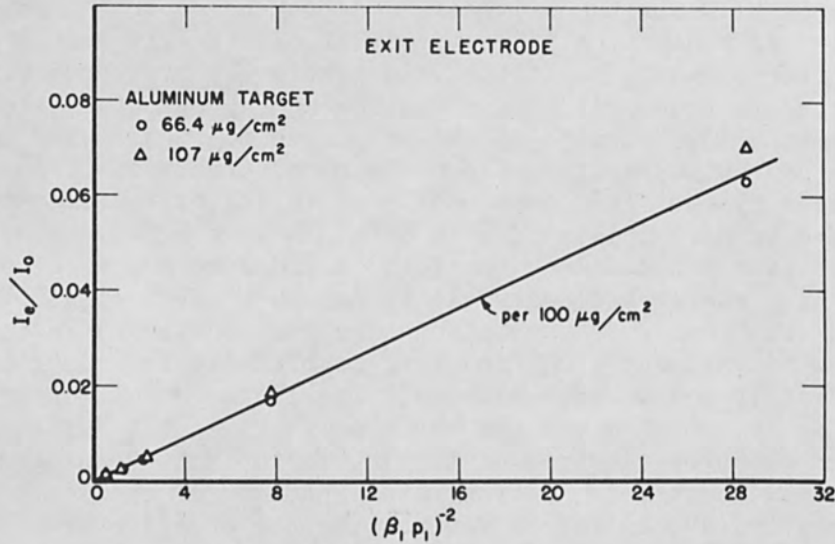


FIG. 7.—Dependence of the current collection efficiency I_e/I_0 for the exit electrode on the quantity $(\beta_1 p_1)^{-2}$, where β_1 is defined in Fig. 5 and p_1 is the incident electron momentum expressed in units of $m_0 c$ with m_0 equal to the electron rest mass and c equal to the velocity of light. The foils are the same as in Fig. 5.

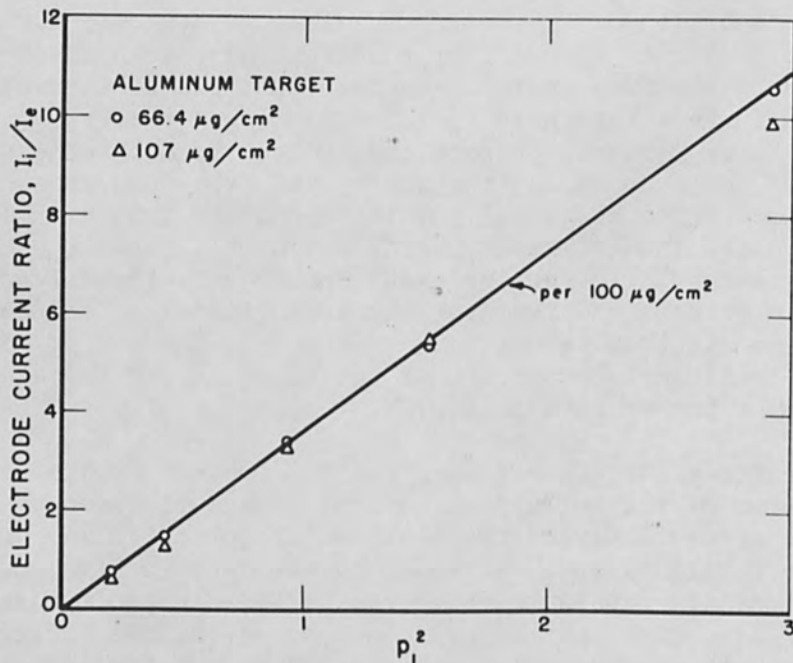


FIG. 8.—Dependence of the electrode current ratio I_i/I_e on the square of the electron momentum p_1^2 , with the same units and foils as defined in Fig. 7.

a suitable modification in the configuration of the exit electrode to improve the current-collection efficiency, this apparatus may be used for measurements over a wide range of electron energies above 500 keV.

ACKNOWLEDGMENT

This work was partially supported by the U. S. Atomic Energy Commission and by the National Aeronautics and Space Administration.

REFERENCES

1. For example, see V. A. Campanile and C. D. Wagner, *Nucleonics* 17 (No. 7): 74, 1959; and M. D. Tang, *Nucl. Inst. and Methods* 39: 181, 1966.
2. For example, see G. W. Tautfest and H. R. Fechter, *Rev. Sci. Instr.* 26: 229, 1955; S. I. Taimuty and B. S. Deaver, Jr., *Rev. Sci. Instr.* 32: 1098, 1961; and V. J. Vanhuysse, E. D. Wattecamps, R. Van De Vijver, and G. Vanpraet, *Nucl. Inst. and Methods* 15: 59, 1962.
3. Data have been obtained with simplified designs for this apparatus, which show that the cylindrical shapes for the collimator and incident electrode can be replaced with flat disk with suitable apertures to permit the passage of the electron beam.
4. Further discussions and studies of these two components are given by A. J. Cohen and K. F. Koral, NASA Technical Note D-2782, National Aeronautics and Space Administration, Washington, D. C., April 1965.
5. For the experimental results given in this paper, the potential V_2 of the collimator with respect to the foil was fixed at a value of -70 volts in order to prevent the loss of the current I_i through the aperture of the incident electrode because of a focusing effect that occurs as V_1 increases to +1000 volts.
6. C. Møller, *Ann. Phys.* 14: 568, 1932; also see J. M. Jauch and F. Rohrlich, "The Theory of Photons and Electrons," Addison-Wesley Press, Reading, Mass., 1955; Eq. (12-15) on p. 255.
7. J. W. Motz, Haakon Olsen, and H. W. Koch, *Rev. Mod. Phys.* 36: 881, 1964; Eq. (1A-101), p. 901.

MAGNETIC CURRENT CONTROL FOR HOLLOW CATHODES

C. M. BANAS and C. O. BROWN

United Aircraft Research Laboratories, East Hartford, Connecticut

ABSTRACT. An experimental investigation of the influence of a magnetic current control technique on the operating characteristics of an axial-beam-forming hollow cathode is described. Details of the cathode-control assembly are shown, and data are presented for a range of conditions within the beam mode of cathode operation. Effectiveness of the control when used in a feedback loop to stabilize hollow-cathode current variations during welding is demonstrated. Advantages and limitations of the technique are discussed.

INTRODUCTION

Investigations of the collimated electron beam mode of operation of hollow cathodes have shown that this type of discharge is potentially useful for electron beam welding and cutting applications.^{1,2} Initially, beam-generating hollow cathodes were formed from metal screen and were usually cylindrical or spherical in shape.³ Metal screen cathodes were, however, found to be relatively inefficient in converting electrical input power to electron-beam power. Insulator-shielded, solid-wall cathode assemblies have subsequently been developed which operate at beam power efficiencies which are often in excess of 80 per cent.⁴ Further, the shielded design has virtually eliminated arcing problems previously encountered at the junction between the insulator and high-voltage feed-through.

A typical insulator-shielded, solid-wall cathode assembly is illustrated in Fig. 1. Although the cathode in this assembly is made of

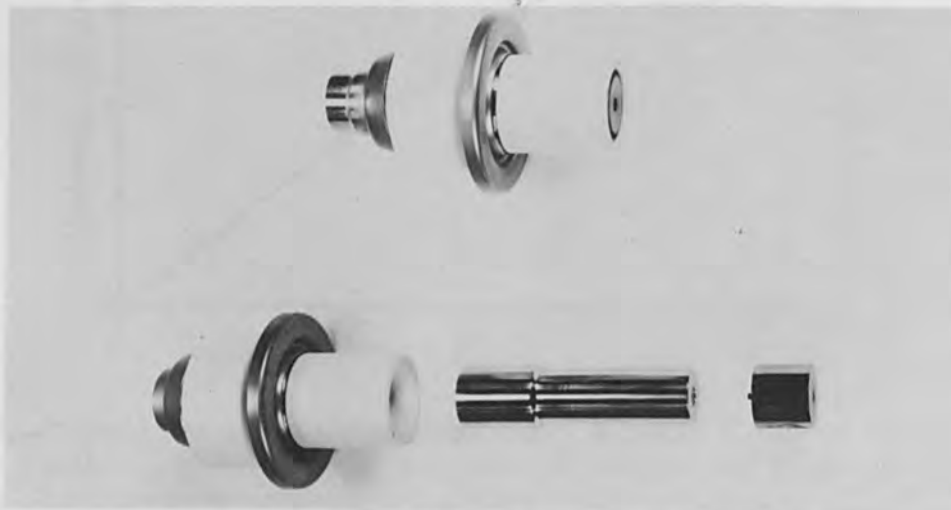


FIG. 1.—Insulator-shielded cathode assembly.

tantalum, many other metals have been used successfully. A standard high-voltage alumina bushing can be used for the shield. The shield serves both to prevent emission from the outer cathode surface and to isolate the junction between the insulator and the high-voltage feed-through from the plasma. The former function leads to higher beam power efficiency; the latter eliminates the arcing encountered in unshielded designs operating at the high voltages and power levels required for electron-beam welding.

The axial-beam hollow cathode may operate in any one of several modes depending on gas type, density, voltage, and cathode design. A set of typical voltage-current curves for operation in the electron-beam mode is shown in Fig. 2. The positive slope is characteristic of the voltage-current behavior of an abnormal glow discharge. Potentials and currents

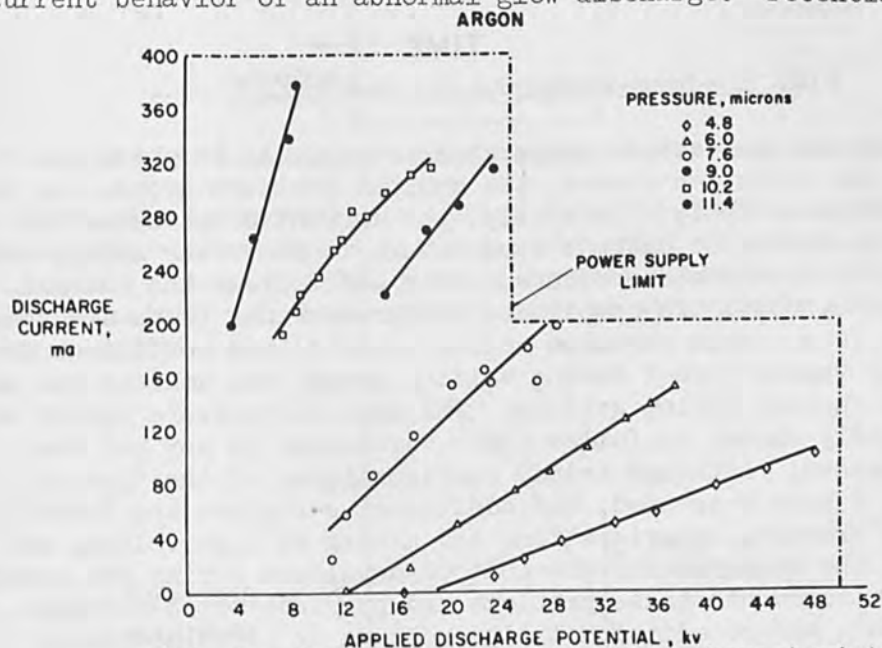


FIG. 2.—Hollow-cathode operating characteristics.

obtained in this mode are normally in the tens of kilovolts and tenths of amperes, respectively. The strong dependence of the operating characteristics on chamber pressure is apparent in Fig. 2. Although this behavior allows choice and control of the I-V characteristic by pressure regulation, it leads to undesirable fluctuations in power, focal length, and power density during welding. These fluctuations are due to pressure variations resulting from gas evolution at the workpiece or gettering by metal vapors.

When the hollow cathode is used for electron-beam welding, changes in ambient pressure level often lead to marked variations in beam power during a weld pass, and hence to variations in penetration and quality along the weld. For example, in a typical weld pass, the current may vary as shown in Fig. 3. Initially, there is a rapid rise in current as the beam impinges on the workpiece and outgassing occurs. The resulting increase in beam power leads to an increase in cathode temperature due to increased ion-bombardment heating at the cathode. Increases in cathode temperature have been observed to decrease both discharge current and efficiency. Hence, as the beam traverses the workpiece, the current

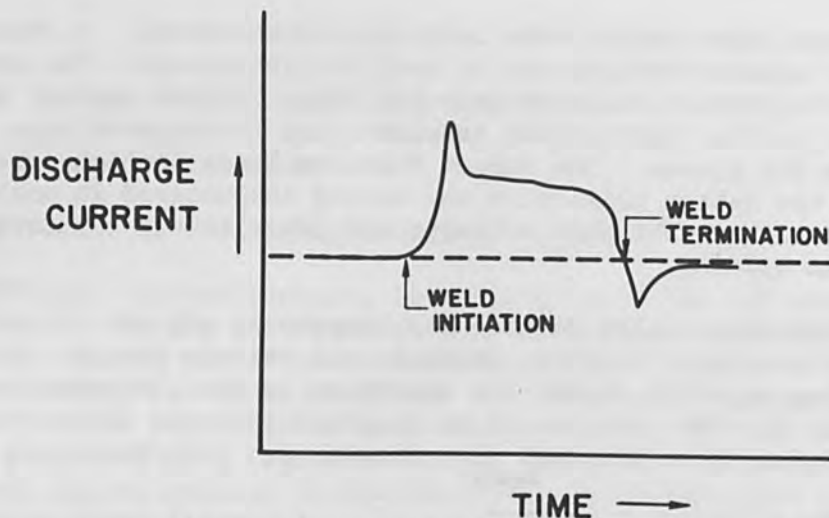


FIG. 3.—Beam-workpiece interaction.

decreases slowly as the cathode temperature rises. As the beam leaves the workpiece gas evolution ceases, the ambient pressure drops, and the beam current drops abruptly. Initially, the current drops below the steady state level because cathode temperature is above the steady state value. Return to steady state occurs slowly and follows the thermal response of the cathode. To complicate matters further there are some weld materials (e.g., high chromium content steels) and conditions for which the metal vapors formed during welding getter the ambient gas and thereby reduce current during welding. The ambient pressure cannot be controlled rapidly enough to follow these variations in any but the slowest weld passes. Although triode configurations of the type described in Ref. 2 have been used, the additional structure and feedthrough are subject to erosion, deterioration, and arcing at high voltage and power levels. The magnetic current control developed during the present investigation circumvents these problems and provides rapid response, positive control, and no additional high voltage or lifetime design limitations.

DESCRIPTION OF CATHODE AND CONTROL SOLENOID

The magnetic current control (Fig. 4) consists of a solenoid placed co-axially with and surrounding the hollow cathode. The axial magnetic field generated by the solenoid substantially reduces the rate at which electrons within the hollow-cathode cavity diffuse toward the cathode centerline. This increased trapping results in an increase in electron production by volume ionization and hence in an increase in electron current migrating to the cathode aperture. Thus, an increase in magnetic field would be expected to provide an increase in beam current.

In the magnetic control employed in the present experiment, the length of the solenoid was approximately one-half the length of the cathode and the inner diameter was approximately twice that of the cathode. The solenoid should be positioned so that the field lines diverge rapidly near the cathode face. This design criterion minimizes the effect of the control field on electron trajectories in the accelerating electrostatic-field region in the vicinity of the cathode aperture. This

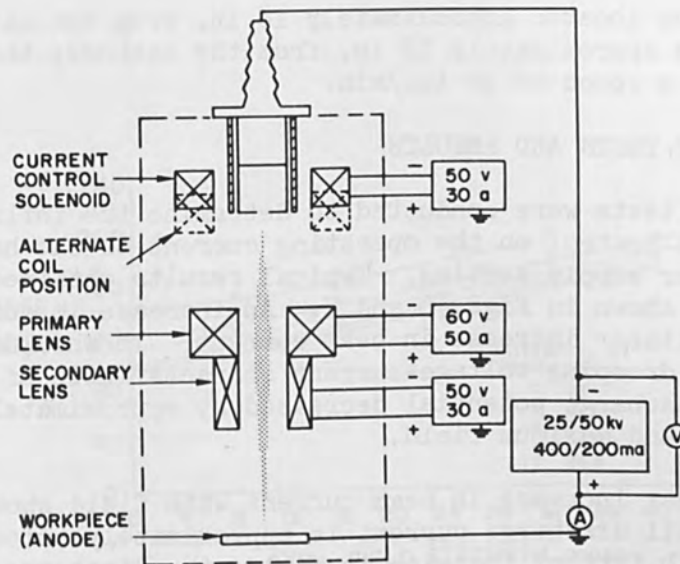


FIG. 4.—Hollow-cathode system with control solenoid.

effect would be undesirable, since it would result in changes in beam focus with control-field setting. The axial variation in magnetic field strength is shown in Fig. 5 for a control solenoid positioned to provide a wide variation in beam current with no appreciable effect on focusing characteristics.

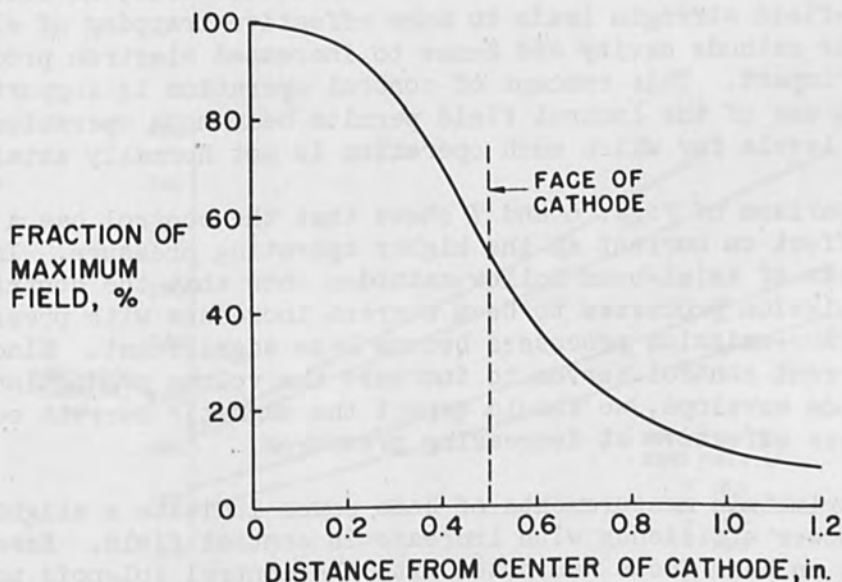


FIG. 5.—Axial variation of control field.

In addition to the control solenoid, a magnetic lens was used in the present tests to focus the electron beam. The lens was located approximately 6 in. from the cathode face. The cathode was a 1-in.-diam. cylinder having a 1/4-in.-diam. aperture and was formed from 0.015-in. tantalum sheet. The cathode was supported within a standard high voltage bushing as shown in Fig. 1. In the 1-in. cathode assembly, a 0.05-in. gap was maintained between cathode and shield; the face of the cathode was positioned flush with the insulating shield. The beam was focused

on a workpiece located approximately 18 in. from the cathode; the workpiece located approximately 18 in. from the cathode; the workpiece was traversed at a speed of 35 in./min.

DISCUSSION OF TESTS AND RESULTS

Initial tests were conducted to determine the influence of the magnetic current control on the operating current of the hollow cathode at constant power supply setting. Typical results obtained for operation in argon are shown in Figs. 6 and 7. An increase in control field results in a nearly linear increase in beam current. It should be noted that owing to the drooping voltage-current characteristic of the beam power supply the discharge potential decreased by approximately 5 per cent between zero and maximum field.

The linear increase in beam current with field shown in Fig. 6 and 7 continues until discharge current is approximately twice the zero-field current. With further increase in field, the discharge becomes unstable as evidenced by a visible flickering of the discharge and by rapid fluctuations in beam current. The onset of this instability limits the beam-current variation which may be obtained by means of the control. The characteristics of this limit are similar to those encountered at operating pressures near the boundary of transition to arc-mode operation. These factors suggest that the magnetic field serves to increase the effective electron pressure within the cathode. In other words, an increase in magnetic-field strength leads to more effective trapping of electrons within the cathode cavity and hence to increased electron production by particle impact. This concept of control operation is supported by the fact that use of the control field permits beam-mode operation at ambient pressure levels for which such operation is not normally attainable.

Comparison of Figs. 6 and 7 shows that the control has a somewhat larger effect on current at the higher operating pressure. In that connection, tests of axial-beam hollow cathodes show that the contribution of volume-emission processes to beam current increases with pressure, and that surface-emission processes become less significant. Since the magnetic current control serves to increase the volume production within the cathode envelope, we should expect the magnetic current control to become less effective at decreasing pressures.

Calorimetric measurements of beam power indicate a slight decrease in beam-power efficiency with increase in control field. Essentially no influence on beam focus was noted with the control solenoid positioned at the axial center of the cathode. With the solenoid centered at the cathode face (as noted by the alternate coil position in Fig. 4) there was a strong effect of control field on focus. In addition, the attainable variation of beam current was substantially reduced with the coil in the alternate position.

To demonstrate the effectiveness of the magnetic current control during welding, the feedback control loop shown schematically in Fig. 8 was assembled. The strength of the magnetic control field was initially set at about the midpoint of the useful range to allow for control in both directions, and the signal to the differential amplifier was nulled

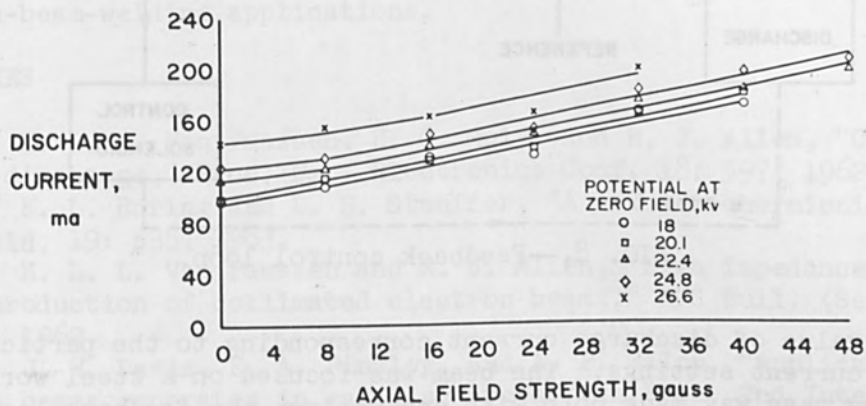


FIG. 6.—Effect of magnetic control field. (Argon at 7 microns.)

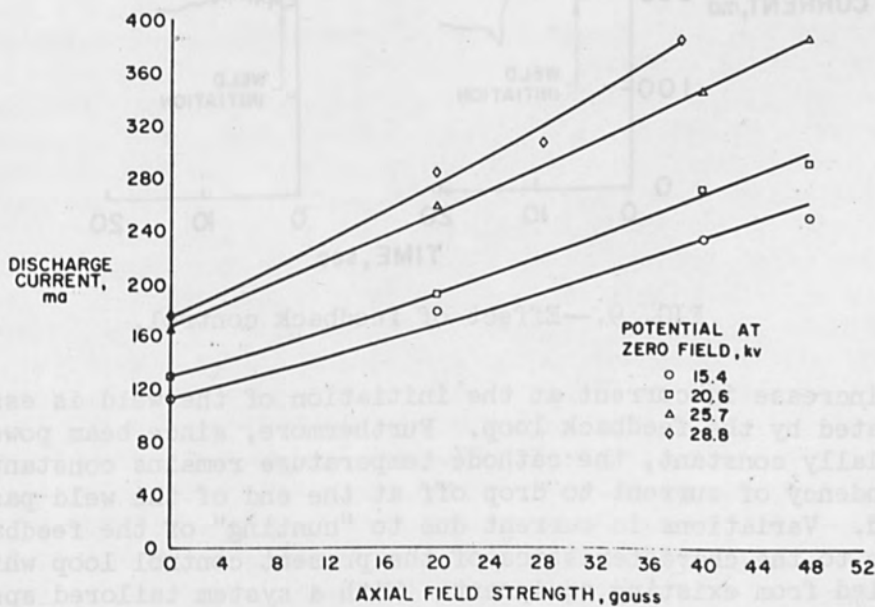


FIG. 7.—Effect of magnetic control field. (Argon at 8 microns.)

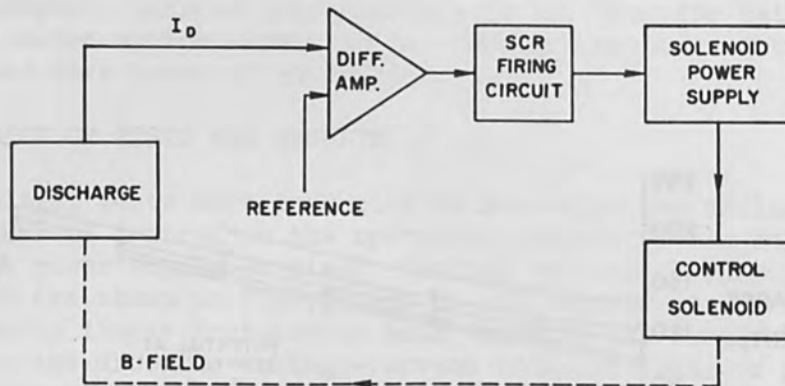


FIG. 8.—Feedback control loop.

for the value of discharge current corresponding to the particular voltage and current settings. The beam was focused on a steel workpiece and a welding pass was made both with and without the feedback loop operative. Typical results of these tests are shown in Fig. 9. It is noted that the

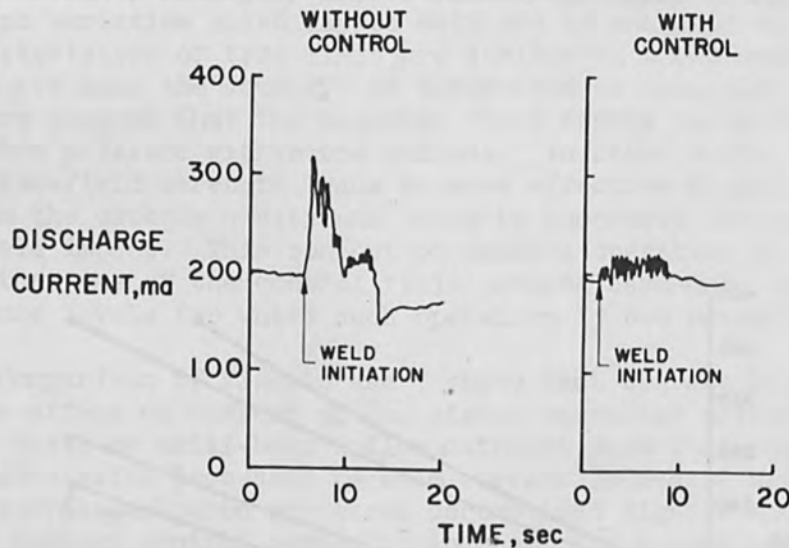


FIG. 9.—Effect of feedback control.

sharp increase in current at the initiation of the weld is essentially eliminated by the feedback loop. Furthermore, since beam power remains essentially constant, the cathode temperature remains constant and, hence, the tendency of current to drop off at the end of the weld pass is also reduced. Variations in current due to "hunting" of the feedback system are due to the characteristics of the present control loop which was assembled from existing equipment. With a system tailored specifically for this application, such oscillations would be eliminated.

CONCLUSIONS

The magnetic current control offers a simple, high-frequency-response technique for reducing hollow-cathode current variations during high-power electron-beam welding. Beam-power efficiency and focus are essentially

unaffected by the control field up to a maximum beam current increase of approximately 100 per cent. Operation of the magnetic current control with a feedback loop using the discharge current fluctuation as an error signal has demonstrated substantial improvement in weld-power uniformity and should improve considerably the utility of the hollow cathode for electron-beam-welding applications.

REFERENCES

1. H. L. L. Van Paassen, E. C. Muly, and R. J. Allen, "Cold hollow cathode discharge," Proc. Nat. Electronics Conf. 18: 597, 1962.
2. K. L. Boring and L. H. Stauffer, "A new non-thermionic electron gun," *ibid.* 19: 535, 1963.
3. H. L. L. Van Paassen and R. J. Allen, "High impedance gas discharge production of collimated electron beams," APS Bull. (Ser. II) 7, Jan. 24, 1962.
4. J. W. Davis, E. A. Pinsley, and A. P. Walch, "Applications of electron beams generated in gas discharges," in Proc. 2nd Internl. Conf. Electron and Ion Beam Science and Technology, New York, 1966 (in press).

HANDLING HIGH-ENERGY HIGH-POWER ELECTRON BEAMS

S. PENNER

National Bureau of Standards, Washington, D. C.

ABSTRACT. Linear electron accelerators (linacs) produce high power pulsed electron beams at energies from a few MeV to 20 GeV. These machines are used in a wide variety of industrial and research applications including radiography, food processing, radiation chemistry, and nuclear physics. Linacs are in use which produce electron beam powers of hundreds of kilowatts and average currents of the order of 1 mA. Existing linacs operate as pulsed devices with peak currents in the ampere range and energy per pulse as high as 300 joules. In the larger laboratories multiple target areas are used. The electron beam is guided from the linac to the target areas by complex ion-optical systems employing numerous deflection and focusing magnets. The beam paths are often hundreds of feet long. Beam spot sizes at the target are often required to be as small as 1 mm^2 . The design of targets, collimators, transmission windows, and absorbers for these high-energy beams is dominated by problems associated with the heat load. The most difficult aspects of these problems are the extremely high heat-transfer rates required and the metal-fatigue problem due to the pulsed nature of the beam.

INTRODUCTION

During the past 15 years the microwave linear accelerator has been developed into a powerful source of high-energy electrons. Linacs are now used in a wide variety of industrial, medical, and research applications. The industrial applications include radiation preservation of foods, sterilization of surgical supplies, curing of plastics, and modification of the properties of semiconductor devices. Research is conducted with linacs in such fields as analytical chemistry (trace analysis), radiation chemistry, reactor engineering, nuclear physics, and elementary-particle physics. Presently operating accelerators range in energy from a few MeV to 20 GeV. Currents of several amperes are achieved in pulses of a few nanoseconds duration. Existing machines operate with beam duty cycles less than 2×10^{-3} , with time-average currents up to about 1 mA and beam power as high as 200 kW.^{1,2} Major problem areas in handling the electron beams from these accelerators include: (1) user's requirements for well-focused, highly resolved, stable beam spots at their targets, often hundreds or thousands of feet from the accelerator in the larger installations; (2) extremely large heat fluxes at points of beam impingement such as collimators and targets; and (3) high radiation levels throughout the accelerator area resulting in potential health hazards for operating personnel and damage to equipment.

ACCELERATOR DESCRIPTION

A microwave linear accelerator consists of one or more sections of disk-loaded circular waveguide. The nine-section NBS machine is shown in Fig. 1. Pulses of coherent microwave power are delivered to the various sections from appropriate sources. The power room for the NBS linac is shown in Figure 2. In this case the microwave power is provided by twelve 1.3-GHz klystrons, each capable of 5 MW peak, 10 kW average output. Pulses of electrons are injected into one end of the accelerator structure in synchronism with the microwave power. Typical injector characteristics are: injection voltage, 100 to 150 keV; maximum pulse current, 1 to 5 amperes; rise time, a few nanoseconds; pulse length, 0.005 to 6 μ sec; microwave phase bunched to a few degrees. The injected electrons are accelerated by the axial electric microwave field and gain energy continuously as they ride along the crest of the traveling wave. One of the outstanding characteristics of the linear accelerator is the extremely efficient coupling between the electron beam and the microwave field. As much as 70% of the microwave power can be transferred to the beam. It follows that the energy achieved in a given machine depends strongly on the current. In fact, maximum power conversion efficiency occurs when the current is so high that the electron energy is one-half of what it would be at very low current. Transverse forces on the electrons during the accelerating process are quite small. Therefore a well-aligned accelerator with a properly designed injector produces a beam with rather good size and divergence characteristics. Typical values are a beam diameter of 5 to 10 mm and an angular spread of 10^{-3} radians or less. The energy spread in the accelerated beam may be anywhere from 1 to over 10% depending on the machine and the mode of operation.

BEAM TRANSPORT

A linear accelerator laboratory is an expensive installation. It should therefore be planned to maximize beam on-time. In most laboratories several different research teams, each having their own experimental equipment, use the accelerator. Often the experimental apparatus is large, complex, and requires many months of setup time. These considerations indicate that it will be more efficient to carry the electron beam to the experiment rather than bring the apparatus to the accelerator. The way that is done is illustrated by Fig. 3, which shows the layout of the NBS linac facility. A number of measurement rooms are grouped around a central magnet room. The beam from the linac enters the magnet room, where it is magnetically switched into a beam tube leading to one of the measurement rooms. Various large experimental setups are semipermanently installed in the measurement rooms. There may be several setups in tandem along the same beam path in each room. Massive shielding walls isolate the measurement rooms from each other and from the magnet room and linac tunnel, so that personnel can work in some measurement rooms while the electron beam is being used in a different room. A great deal of beam off-time for modifications of experimental setups is thus avoided. Personnel may not be present in an area traversed by the electron beam or its secondary radiations. This rule is enforced by a complex system of inspections, warning announcements, and interlocks. Because of the radiation hazard, experimental apparatus as well as the linac and beam-handling system must be remotely controlled and monitored from the

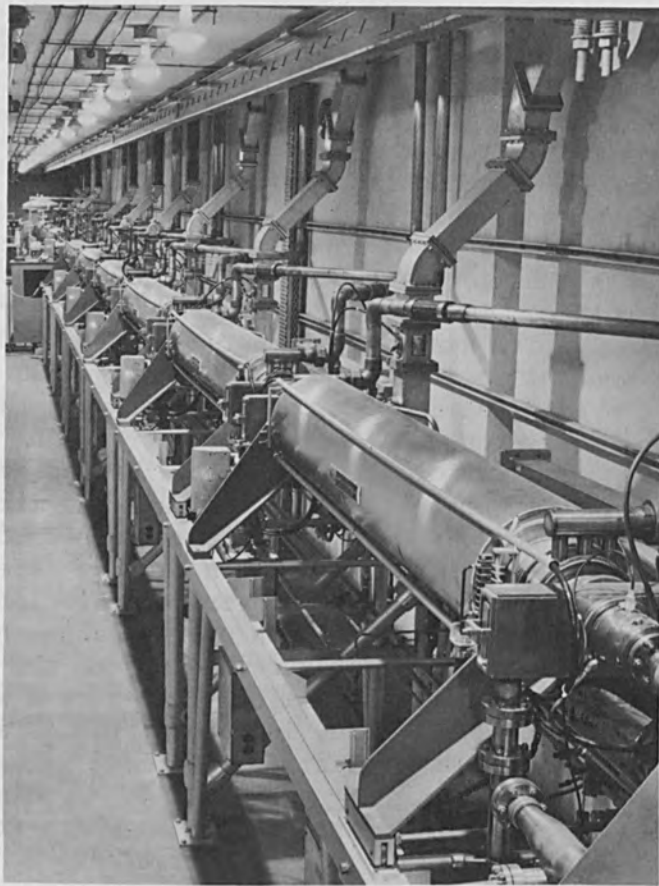


FIG. 1.—The NBS linac viewed from the high-energy end.

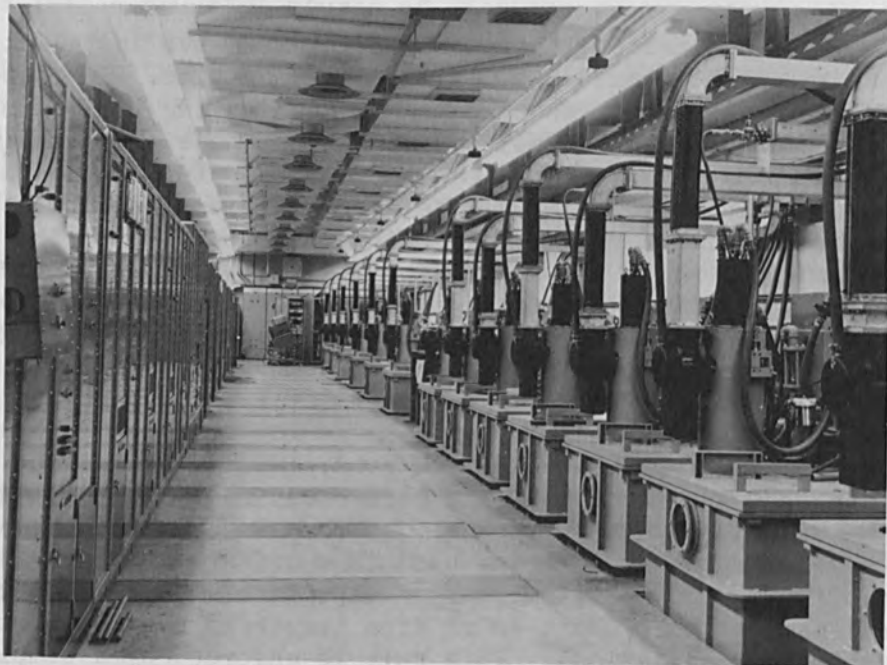


FIG. 2.—Power room for the NBS linac. The cylindrical structures projecting from the tops of the modulator tanks are the high-power klystrons. The microwave power is piped through the rectangular waveguides to the accelerator.

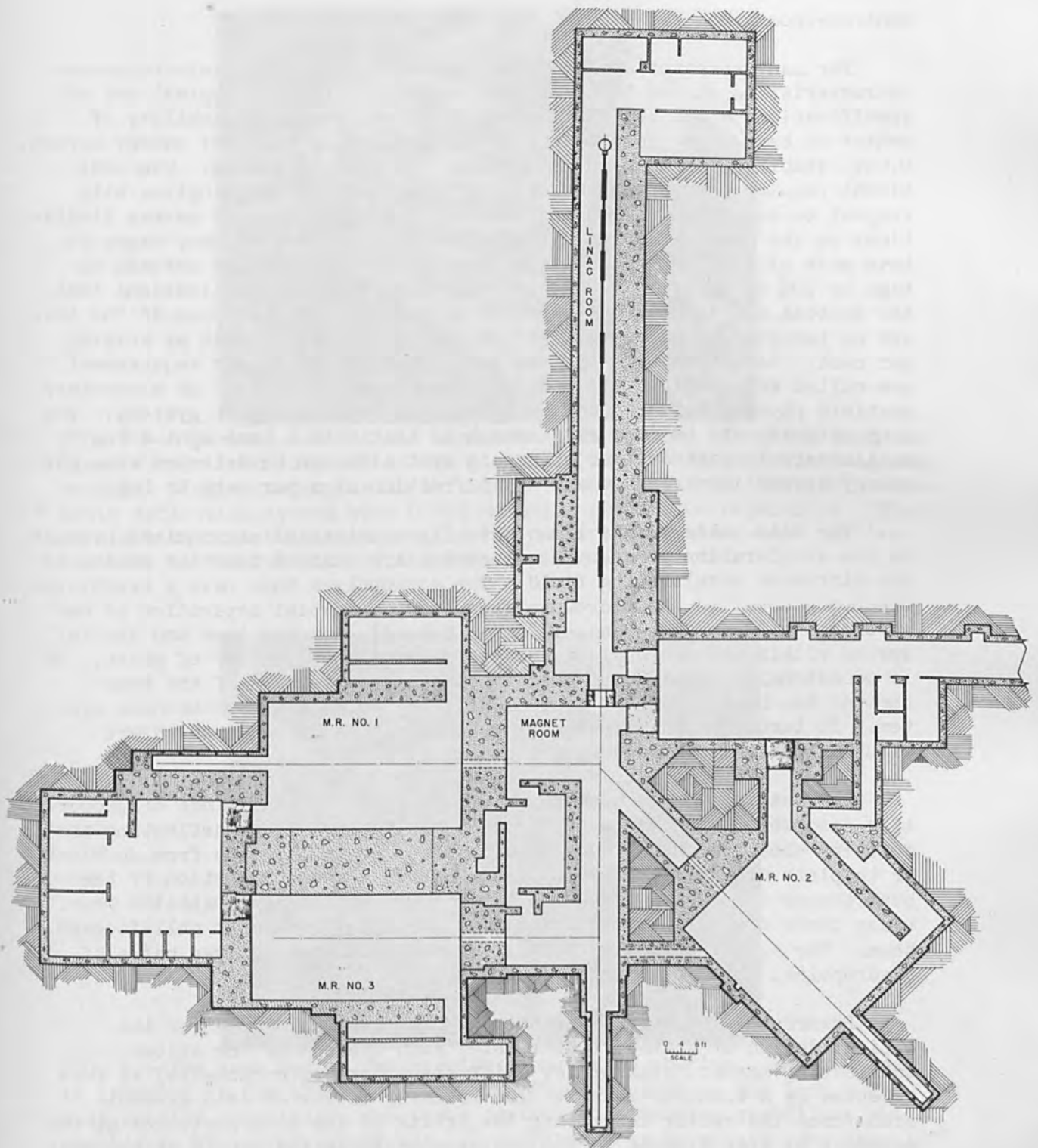


FIG. 3.—Layout of NBS linac facility. Dash-dot lines indicate main beam paths. The entire structure is located about 35 ft below ground level and is covered with a 20-ft-thick earth shield for personnel protection. The distance from the injector end of the linac tunnel to the end of the straight ahead beam path is approximately 300 ft.

control-room area.

For many research applications, precisely controlled electron-beam characteristics at the target location are required. A typical set of specifications might be: spot size, 1 x 5 mm; position stability of center of beam spot, less than 1 mm for periods up to 1 hr; energy spread, 0.05%; stability of mean energy, 0.01% over an 8-hr period. Two additional requirements on the behavior of the beam transport optics with respect to energy spread in the electron beam put the most severe limitations on the optical design. They are (1) the desire of many users to have most of the beam reach their target, even with energy spreads as high as 10% or more; and (2) the requirement for some applications that the spatial and angular distribution of electrons in the beam at the target be independent of energy, for energy spreads of as much as several per cent. Beam transport systems which satisfy the latter requirement are called achromatic. All modern linacs used for nuclear or elementary particle physics research employ achromatic beam-transport systems. The achromaticity can be made good enough so that with a beam spot a few millimeters in diameter, no change in spot size can be detected when the energy spread is varied from a small fraction of a per cent to 10%.

The beam pulse from a linac actually consists of micropulses because in the acceleration process the electrons are bunched near the crests of the microwave accelerating field. The micropulses thus have a repetition frequency equal to the microwave frequency, a spatial separation of one wavelength (23 cm at L-band, 10 cm at S-band), and the time and spatial spread within the micropulse which corresponds to 5 or 10^0 of phase. It is occasionally required to preserve the microstructure of the beam through the beam transport system, that is, to have an isochronous system. It turns out that transport systems can be designed which are simultaneously isochronous and achromatic.

The realization of beam-transport systems with the kinds of properties described above employs precisely built and aligned deflecting and focusing electromagnets. Most of the focusing is obtained from doublets or triplets of magnetic quadrupoles. Figure 4 shows a portion of the beam transport system of the NBS linac. The system now installed provides three energy-analyzed beams plus one undeflected but well-focused beam. The system incorporates six deflecting magnets, seven pairs of quadrupoles, and ten steering elements.

Powerful calculational techniques have been developed for the optical design of transport systems.³ Each element of the system (deflecting magnet, quadrupole, drift space between components) is represented by a transfer matrix. The transfer matrix of each element transforms the vector describing the orbits of the beam particles at the entrance of that element to the vector describing the orbits at the exit of the element. The elements of the orbit vector are the angular, spatial, and momentum displacements of any orbit with respect to a reference orbit along the axis of the system. For many purposes first-order calculations (paraxial-ray approximation) are adequate. Inclusion of higher-order terms is necessary to obtain highly accurate results. Because the higher-order terms make the calculations extremely tedious, computer programs have been written that not only consider the higher-order (optical

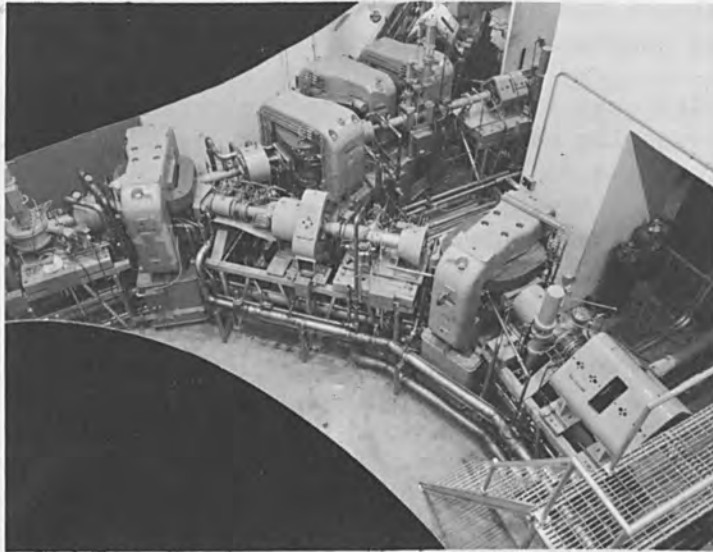


FIG. 4.—A partial view of the beam-transport system. The beam from the linac enters from the left of the picture. The two large deflecting magnets and single quadrupole in the middle foreground comprise a 90° achromatic deflection system with 0.05% momentum-resolution capability. The straight-through beam path and the 45° deflection system which carries the beam to the far side of the facility are also visible.

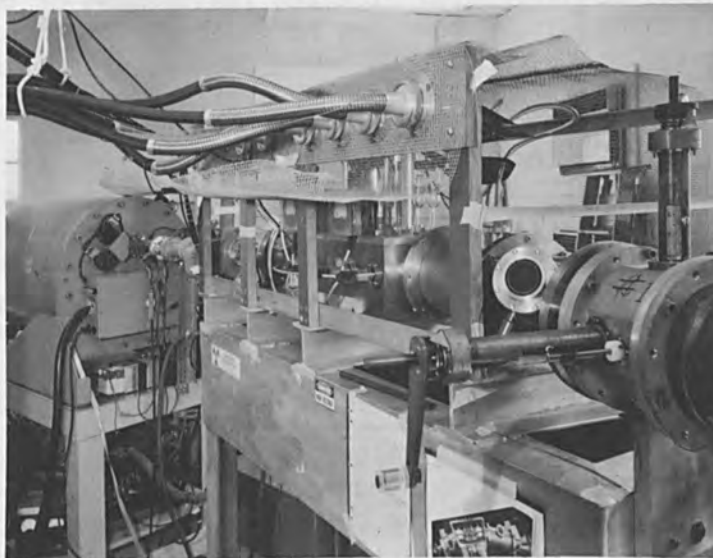


FIG. 5.—Ion beam device for precise beam optics studies. The ion beam is produced in the 400-keV Van de Graaff accelerator at the left. The next section comprises a feed-back controlled direction stabilizer which stabilizes the direction of the $1/2 \times 1/4$ mm beam to within less than 10^{-4} radians. The section within the high voltage cage is an electrostatic energy analyzer in which the beam energy is analyzed with a precision of one part in 10^4 . A feed back system stabilizes the voltage of the accelerator to the same precision. At the extreme right the first of four two-dimensional beam-position micrometers can be seen. Beam positions can be measured to an accuracy of about 0.001 in.

aberration) terms, but allow the study of the effects of apertures in the system and component misalignments.

It is quite easy to write down the transfer matrix of an idealized magnet. The question naturally arises whether a magnet as actually constructed performs as calculated. Several experimental techniques are available for studying the optical properties of magnets, such as: (1) detailed magnetic field mapping (usually with precision Hall effect probes), followed by computer calculation of the resulting orbits; (2) "floating-wire" measurements employing a current-carrying wire under tension as an analog of a particle orbit; and (3) orbit studies with electron or ion beams. An example of the latter technique is the ion-beam setup shown in Fig. 5. In this device, a highly stabilized pencil beam of heavy ions (e.g., argon or klystron) from a 400-keV Van de Graaff accelerator is used for orbit studies.⁴ These ions have the same charge to momentum ratio as the electron beams (up to 250 MeV) with which the magnets will actually be used. The transfer matrices obtained from orbit studies with this device predict electron orbits to an accuracy of one or two thousandths of an inch.

BEAM-POWER HANDLING

THERMAL EFFECTS. Linac beam powers can be in the range of hundreds of kilowatts, with an energy per pulse approaching 1000 joules. Since the beam may have a cross-sectional area of only a few square millimeters, the thermal problems associated with the impingement of beam on components are enormously difficult.⁵ The long range in matter of high energy electrons is helpful, but even so, the power deposited in bulk material can be in the 10- to 100-kW/g region. Components capable of withstanding this kind of bombardment are expensive and complicated. One therefore tries to reduce the number of such components in the beam-transport system. The reduction is accomplished by a combination of two techniques: (1) appropriately locating collimating apertures in the system that can withstand beam impingement and which shadow other parts of the system; and (2) detecting loss of beam in undesired places with suitable monitors and turning the beam off (or reducing intensity) in case of excessive loss.

After carefully minimizing the number of power-handling components as described above, several essential elements remain that must withstand direct beam impingement. These elements include: (1) collimating apertures for the primary beam from the accelerator which serve to limit the spatial and angular extent of the beam presented to the transport system; (2) energy-defining collimators; (3) targets of various sorts; (4) windows through which the beam may emerge from the vacuum system; and (5) beam dumps in which the residual beam is absorbed after passing through targets. Although they may be quite different geometrically, the same types of thermal problems are encountered in the various types of power-handling components. The thermal problems are of three types, any of which may be the limiting factor in the design. We discuss these limitations briefly and give a few examples of practical component design.

The ability to transfer heat to a coolant is obviously one major limitation. For example, in one test a 0.7-mA, 5-mm-diameter beam from the NBS linac incident on a 1.25-mm-thick copper wall required a heat

transfer rate to the coolant of about 8 kW/cm^2 . Heat transfer rates of this magnitude are near the maximum that can be handled over small areas. Wherever possible, we attempt to keep the heat transfer requirement below 3 kW/cm^2 by suitable choice of wall thicknesses and materials. In some cases a component on which the beam impinges may be provided with an oscillating or rotating motion, thus effectively spreading out the beam, and enormously reducing the required heat-transfer rate. In configurations where moving elements can be employed, a reduction of three orders of magnitude may be achieved, permitting the use of thermal radiation as a heat-transfer mechanism. The major advantage of such a device is that a thermal failure does not result in a spill of water into the vacuum system. This type of catastrophe has occurred in several instances with high-powered linacs. An example of a beam collimator incorporating radiation cooled rotating elements is shown in Fig. 6.

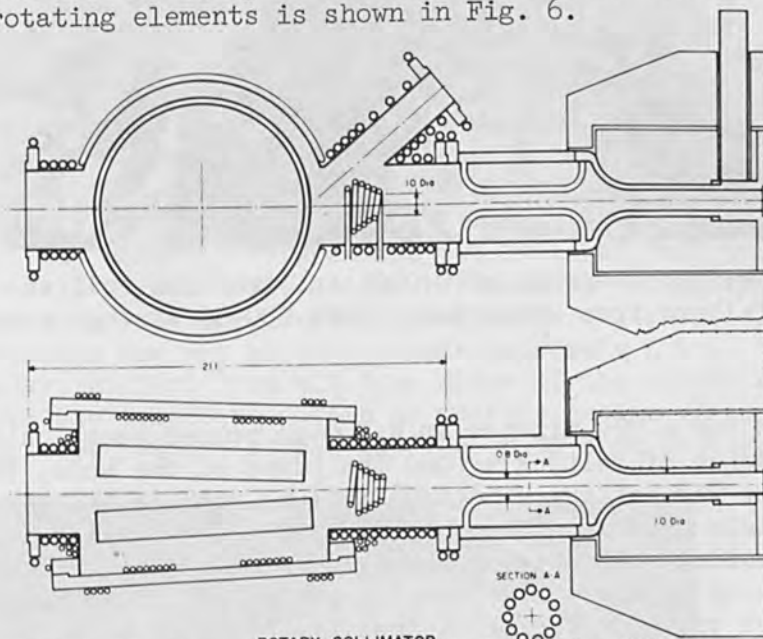


FIG. 6.—One of the complex **ROTARY COLLIMATOR** used in the NBS beam transport system. Beam enters from the left. The first section contains a pair of tantalum-tungsten alloy cylinders which form the variable aperture. The cylinders are rotated at 200 rpm. They can be moved in or out along the axis of rotation to vary the beam aperture by control mechanisms not shown. The next section of the collimator contains a fixed defining aperture built up from several parallel copper tubes utilizing high-velocity water flow to obtain the required heat-transfer rates. The last section is a water cooled lead shield which protects downstream components from scattered and secondary radiations generated in the collimator.

A second possible cause of thermal failure is melting. In the above example of a 1.25-mm copper wall, the temperature on the uncooled surface of the copper reached about 400°C . Any material of poor thermal conductivity such as stainless steel used in this configuration would have melted. There is then a necessity to minimize the path lengths between regions of beam impingement and cooling channels. For this reason many collimators and targets are constructed of multiple elements, particularly for the higher energy machines where electron ranges may be several meters, even in the densest materials.

Because of the pulsed nature of a linac beam, thermal fatigue is a serious problem. Figure 7 shows a 0.0005-in. tantalum foil which was

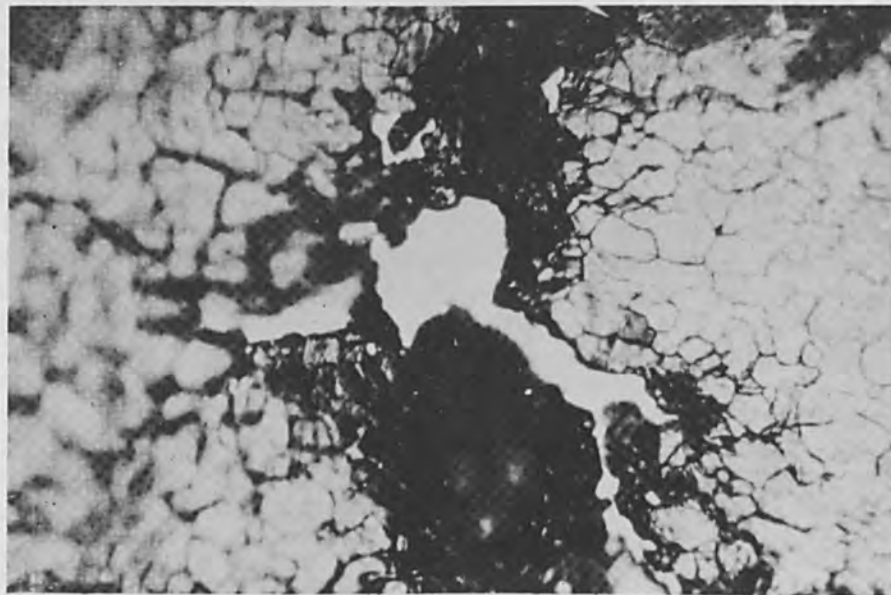


FIG. 7.—Microphotograph of 0.0005-in. tantalum foil showing evidence of fatigue failure from bombardment with 500- μ A average current pulsed beam.

bombarded for a few minutes in a 500- μ A pulsed beam. Although there is some evidence of melting around the edges of the hole, the primary cause of failure was fatigue. Fatigue failure sets an inescapable limitation on materials used in pulsed beams. Since the local heating is a volume effect, making the material thinner does not help. The thermal stress depends only on the charge density per pulse in the beam, and on such properties of the material as density, specific heat, coefficient of thermal expansion, and the elastic moduli. It must be remembered that all of these properties are functions of temperature, so that a foil which can withstand the beam when held near room temperature may fail rapidly at elevated temperatures.

Examples of power handling components are shown in Figs. 6, 8, and 9. Figure 8 shows a beam window which is capable of withstanding the full beam current of the NBS linac with substantial safety factors. The total thickness of this window is less than 0.4 g/cm², or about 0.015 radiation lengths, which causes only moderate perturbations of the 100-MeV beam for which it was designed.

NONTHERMAL EFFECTS. Several nonthermal effects associated with high beam powers must be considered in the design of a linac facility. We briefly mention a few of the more serious problems.

The intense radiation field produced by an electron beam requires that radiation resistant materials be used exclusively throughout beam areas. One employs all metal vacuum systems including valves and ions pumps in order to avoid easily damaged materials such as rubber O-rings and vacuum pump oil. Other means for avoiding radiation-soft organic

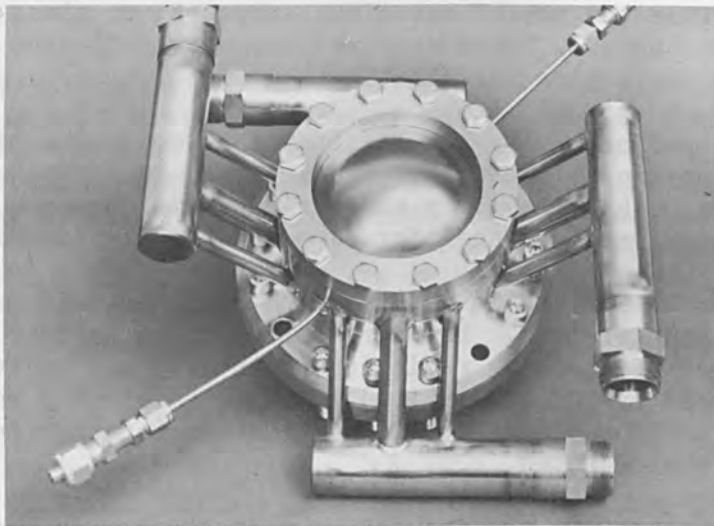


FIG. 8.—High-power beam window. The beam emerges from the domed window which is made of 0.003-in. titanium. The structure contains four of these spherical titanium foils. The foils are arranged in concentric pairs, one pair convex outward, the other pair convex toward the direction of the incident beam. The channels between the two foils of each pair contain water flowing at 15 ft/sec. The volume between the two pairs of foils contains helium at a pressure exceeding the water pressure. Thus all foils are in tension and may safely be made extremely thin. Water inlet and outlet headers project from all four sides of the structure. A mock-up of the device was tested to obtain an orifice design which resulted in a uniform water flow pattern across the region of beam passage.

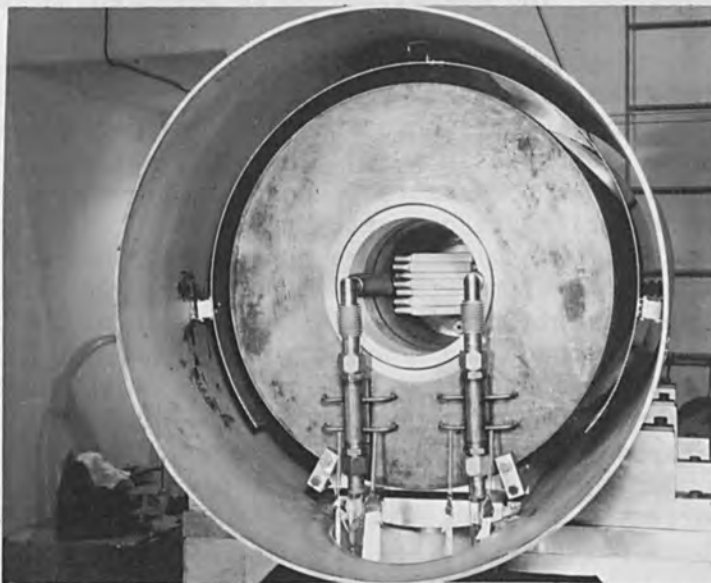


FIG. 9.—High power Faraday cup for 170-MeV electron beam. The front of the vacuum jacket is removed in this view. The large cylindrical structure is a 5-ton lead casting with integral water cooling tubes, supported on ceramic insulators. The central core is made of thin stainless-steel tubing and sheets with high-velocity water flow to insure adequate heat removal. Resistance to ground through the cooling water paths is 400 MOhm in the absence of beam. At beam powers of a few kilowatts the water resistivity drops about two orders of magnitude.

materials include the use of ceramics, asbestos, or glass where electrical insulators are needed. These measures strongly influence the cost and complexity of the entire installation.

Residual radioactivity levels after shut-down of a high-power beam may preclude personnel occupancy of beam areas for hours or days after irradiation.⁶ High reliability and minimized maintenance needs of components in beam areas are therefore important design considerations.

Corrosion in air and in water-cooled components is not a unique problem with accelerators. However, corrosion rates tend to be enhanced by the presence of ionizing radiation (both directly and via the chemical species produced by the ionization). The high-velocity water flow needed to obtain multikilowatt-per-square-centimeter heat-transfer rates also increases corrosion rates.

Chemical reactions are induced by radiolysis when a charged particle beam passes through gases or liquids. In air the major products are nitrous oxide (which combine with water vapor to form nitric acid) and ozone. The nitric acid production rate in humid air has been estimated to be about 70 g/kW-hr of beam dissipated in air. In water, radiolysis liberates hydrogen and oxygen gases and produces substantial quantities of hydrogen peroxide. The hydrogen gas production rate is of the order of 1 liter/kW-hr of beam dissipated in water.

BEAM MONITORING

Monitoring a high-energy electron beam is vastly complicated by the high powers involved. The quantities to be measured include energy, average current, current during the pulse, beam position, and beam size. It is desirable, if not essential, to develop nonintercepting monitors for many of these measurements. For example a zinc sulfide screen used with a closed-circuit television system to determine the location and size of a beam is destroyed in a few minutes by a beam of only 10 μ A. Nonintercepting devices to measure pulsed beam current and position in use in many laboratories are currently under study to determine the accuracy obtainable. Among these are pulse transformers utilizing ferrite cores which respond to either the total pulse current or the product of current and displacement from the axis, depending on the configuration of the device. Both resonant and nonresonant microwave devices, making use of the microstructure in the beam, are practical. Absolute current measurements are probably best performed with Faraday cups. For a beam of 100 MeV, a Faraday cup must be very large, weighing perhaps 5 to 10 tons. At low powers, such devices have been used for many years. At NBS, we are currently studying the properties of a large Faraday cup designed for a beam power of 100 kW.

The power requirement enormously complicates the design. Cooling water must be pumped through the insulated terminal without destroying the insulating properties. Radiochemical processes result in violent changes in the resistance to ground through the cooling water paths when the high power beam is on. Figure 9 shows a view of this Faraday cup taken during assembly.

CONCLUSIONS*

The high-energy, high-current electron linear accelerator is a very useful tool in many areas of industry and scientific research. Powerful beam optical techniques have been developed for handling these beams. Serious problems of thermal, metallurgical, and chemical types are inherent in the handling and targeting of these beams. As machines of even higher power are developed in the next few years, we shall have to push beyond present engineering limits in order to effectively utilize these devices.

REFERENCES

1. J. E. Leiss, "The NBS Linac," Proceedings of the 1966 Linear Accelerator Conference, USAEC Rep. LA-3609, 1966.
2. R. B. Neal, "SLAC: The accelerator," *Physics Today* 20 (No. 4): 27, April 1967.
3. S. Penner, "Calculations of properties of magnetic deflection systems," *Rev. Sci. Inst.* 32: 150, 1961; see also *ibid.* p. 1068.
4. S. Penner and J. W. Lightbody, "Measurements of Ion-Optical Properties of a High Resolution Spectrometer for Electron Scattering," Proc. of the Intern. Symp. Magnet Technology, USAEC Report CONF-650922, 1965.
5. S. Penner, "Handling high power electron beams," *IEEE Trans. Nuclear Science*, in press. A number of detailed references on power-handling problems are given in this reference.
6. J. M. Wyckoff, "Linac Induced Gamma Ray Radioactivities," NBS Accelerator Branch Internal Rep. No. 248-3, 1965.

NEW ELECTRON GUN FOR ELECTRON-BEAM EVAPORATOR

H. TAMURA AND H. KIMURA

Central Research Laboratory, Hitachi Ltd., Tokyo

SUMMARY. Fine cracks and minute irregularities caused by reflected electrons are often observed on the surface of films deposited by conventional electron bombardment heating.

In order to prevent charge accumulation on the film surface a new electron gun has been designed by the present authors for an electron beam evaporator which consists of Pierce gun with an electrostatic deflector. With the new electron gun no flaws are found in films deposited on glass substrate of large area. The construction and characteristics are described.

INTRODUCTION

Many papers have been published on the advantages of electron beam evaporation of refractory metals. The authors have frequently observed fine cracks and minute irregularities on the surface of films deposited by the conventional electron-beam evaporator, a schematic diagram of which is shown in Fig. 1. Figure 2 presents examples of such surface deterioration on silicon, boron and tantalum films deposited by this technique. The deterioration was due to charge accumulation and the subsequent electric discharge over the film surface. In order to prevent charge accumulation, the authors constructed, a few years ago, an evaporator in which the cathode and the metal belljar are grounded and the anode and evaporating material are kept at a high potential. The electrostatic field between the belljar and the trap cylinder prevents the reflected electrons from striking the substrate. Figure 3 illustrates the equipotential lines inside the metal belljar as well as the trajectories of the reflected electrons traced by the resistance-network method. In this device, it is difficult to deposit a uniform metal film on a substrate of large area.

The authors have recently developed a new electron gun which is described in the next section.

CONSTRUCTION AND CHARACTERISTICS OF NEW ELECTRON GUN

Figure 4 shows the sectional diagram of the newly designed electron gun. A thin tungsten plate is used as the cathode consisting of a Pierce-type gun. When the cathode is grounded and both the anode and the crucible are supplied with positive high voltage, uniform films can be obtained even on the glass substrate. The electrons emitted from the cathode are deflected by a set of deflecting electrodes, one of which is at the anode potential and the other at the cathode potential, and bombard the evaporating material in the crucible. The system is named

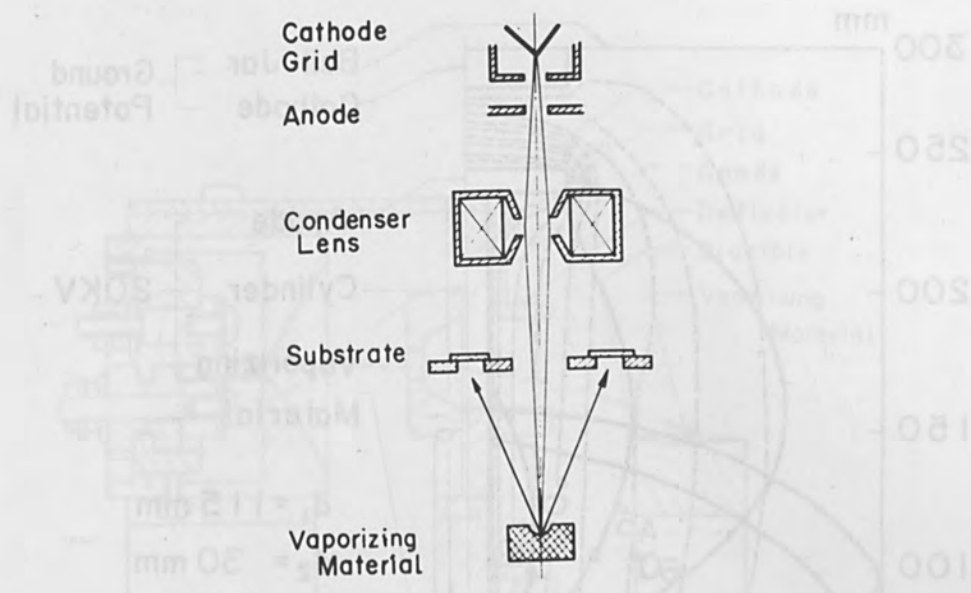
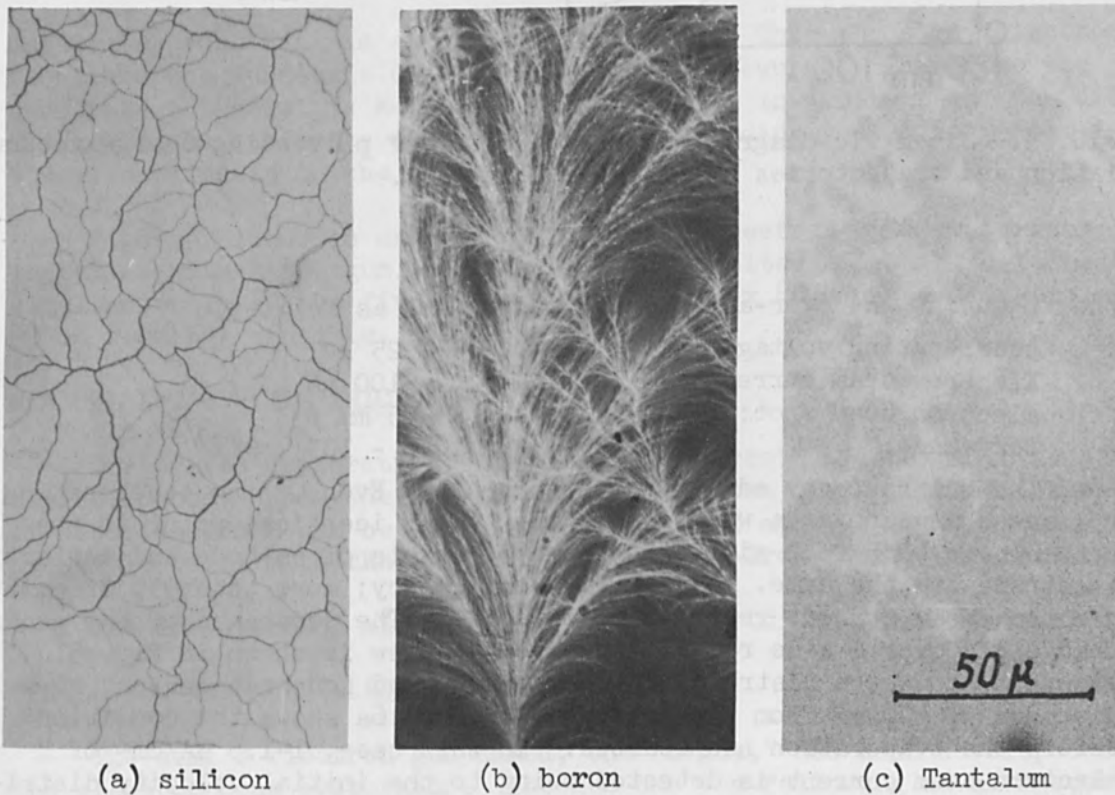


FIG. 1.—Schematic diagram of conventional electron beam evaporator.



(a) silicon

(b) boron

(c) Tantalum

FIG. 2.—Light micrographs of films deposited on glass.

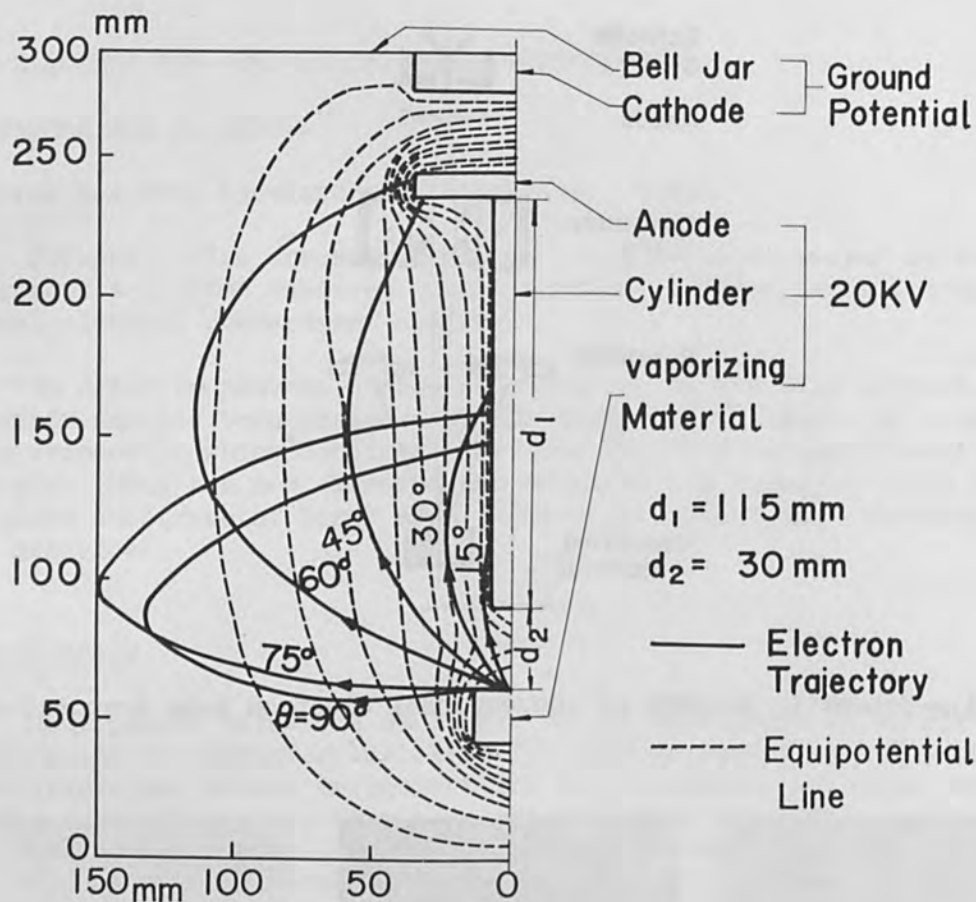


FIG. 3.—Schematic diagram of an evaporator of preventing charge accumulation and trajectories of relected electrons.

the "L-gun." The over-all specifications are as follows.

| | |
|------------------------|---------------------------------------|
| Accelerating voltage: | 0 - 25 kV |
| Electron beam current: | 0 - 100 mA |
| Electron beam spot: | 1 - 5 mm ϕ |
| Perveance: | $10^{-9} - 10^{-7} \text{ A/V}^{3/2}$ |

The gun has many advantageous features. Even if the accelerating voltage changes over a wide range, the almost identical point in the crucible is bombarded since the both potentials of cathode and deflecting electrode are the same. It has high efficiency; more than 95% of emitted electron-beam current reaches the material. The perveance of the gun is changeable over a wide range. An external view is shown in Fig. 5. Figure 6 shows the distribution of electron and ion beam current at a distance of 400 mm from the crucible. Figure 6a shows the condition before the evaporation has started. In this case, 1-1.5 $\mu\text{A}/\text{cm}^2$ of electron beam current is detected owing to the initial velocity distribution of the cathode. During the evaporation, 1.5-5 $\mu\text{A}/\text{cm}^2$ of ion beam current is detected, as shown in Fig. 6b. The detected value varies according to the substrate potential. When the metal is evaporated on an insulator substrate such as glass, the ion beam current reaches the

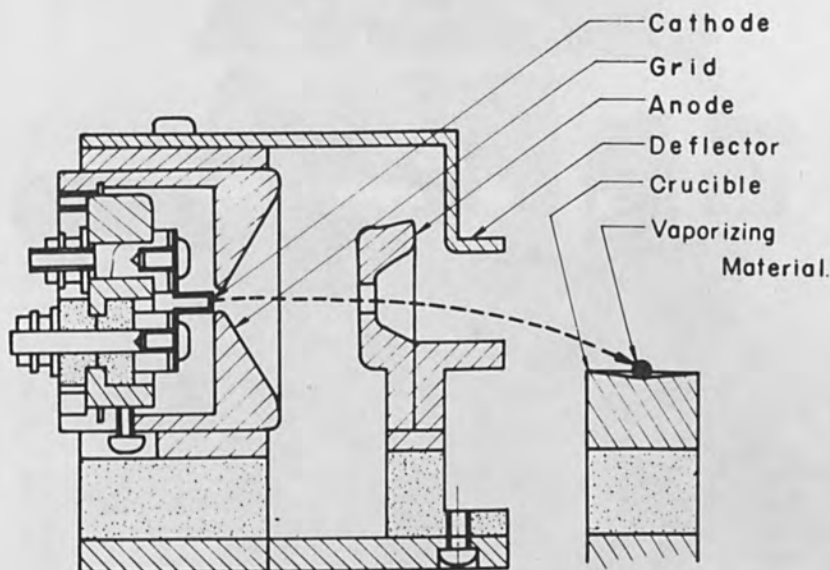


FIG. 4.—Construction of newly designed electron gun.

substrate, resulting in a positive potential. Thus the stray electrons flow into the substrate and its potential is lowered. Therefore the substrate potential is kept at a comparatively low voltage and the discharge on the substrate does not occur. Accordingly a uniform film is always obtainable on the substrate.

Figure 7 shows an external view of the electron beam evaporator installed with a new gun. The uniformly deposited films are obtained simultaneously on the five glass plates of 80 x 80 mm at a distance of 40 mm from the crucible.

MEASUREMENT OF FILM THICKNESS

During the evaporation, the ion beam current is detectable as described above. From the integration of ion beam current the thickness of deposited film can be estimated. Figures 8 and 9 show a measuring principle of film thickness and an example of iron film, respectively.

The interference microscope was used for thickness determination.

CONCLUSION AND ACKNOWLEDGMENT

The simple electron gun named, the "L-gun," has been developed for the electron beam evaporator. The gun has the following advantageous features:

(1) Uniform films can be always obtained, resulting in the elimination of reflected electrons.

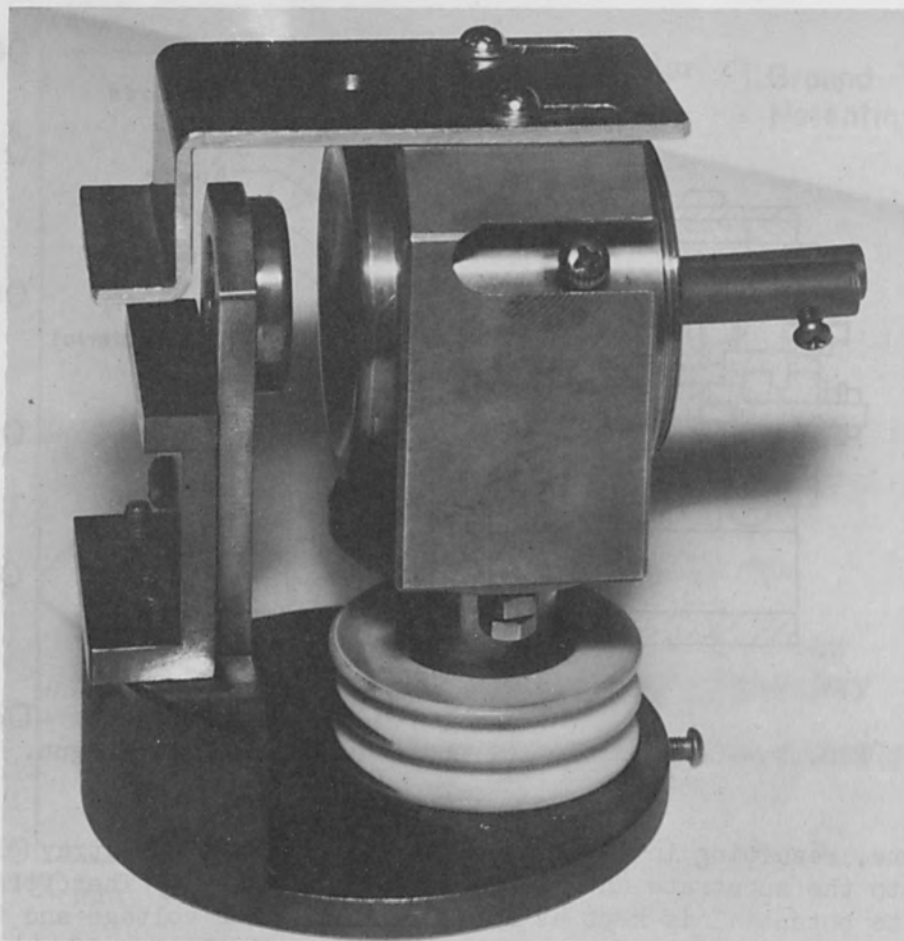


FIG. 5.—External view of "L-gun"

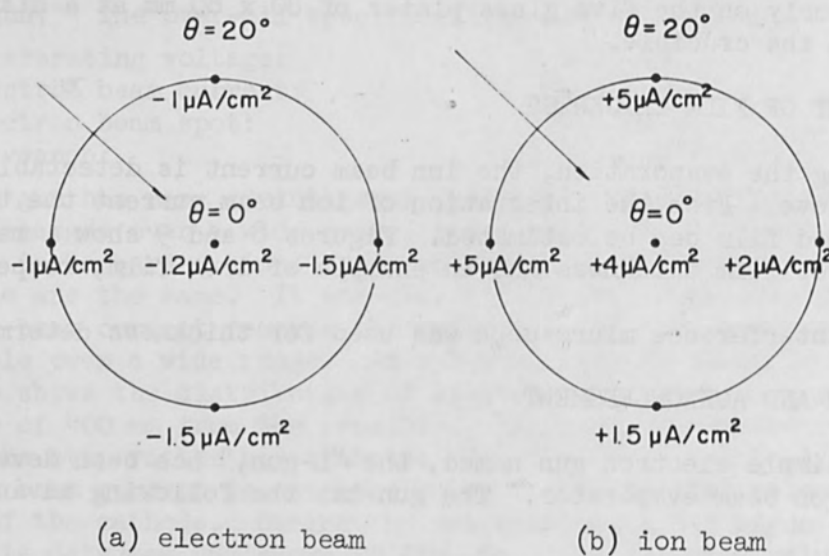


FIG. 6.—Distribution of electron and ion beam current.



FIG. 7.—External view of electron beam evaporator installed with a new gun.

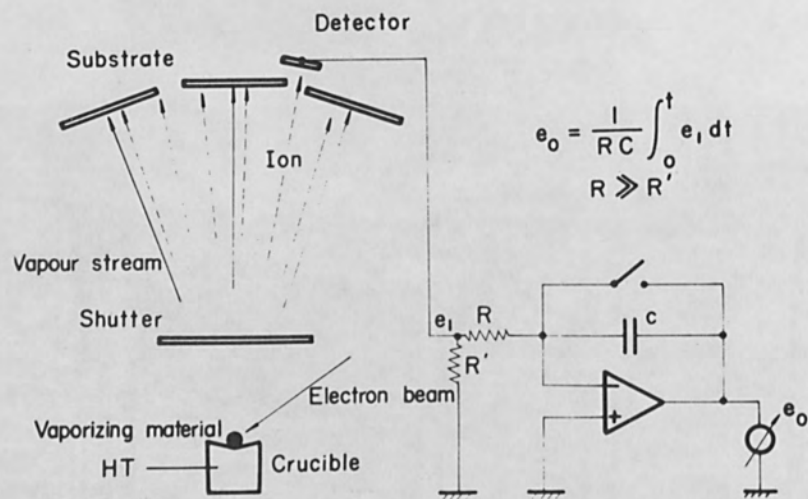


FIG. 8.—Measuring principle of film thickness.

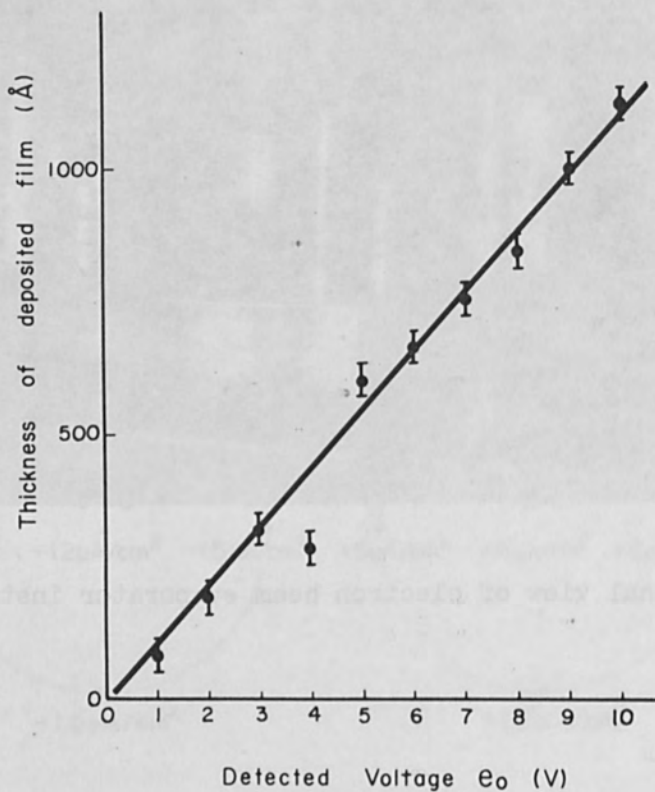


FIG. 9.—Relation of detected voltage and thickness of iron film.

- (2) The same position on the vaporizing material can be always bombarded even under the wide range of accelerating voltages.
- (3) The perveance is variable over a wide range.
- (4) Large-area evaporation is possible.
- (5) High efficiency in electron-beam current is attainable.
- (6) Film thickness is easily monitored by measuring ion beam current.

The new electron gun has one problem. The potential of the crucible should be kept at high voltage in a new gun. The cooling of the crucible is no easier than for the ordinary type. However, this problem can be settled by using zirconium or other special ceramics with good heat conductivity and good electrical insulation as the crucible material.

The authors wish to thank Mr. K. Mori, Hitachi-Koki Co., for his sincere assistance throughout this work.

REFERENCES

1. O. S. Havens, J. Sci. Instr. 36: 95, 1959.
2. J. C. Kelly, J. Sci. Instr. 36: 89, 1959.
3. R. Thun and J. B. Ramsey, Vac. Symp. Trans. 192, 1959.
4. H. Kimura and H. Tamura, Proc. Electron and Laser Beam Symp., Pennsylvania, 369, 1965.
5. H. Tamura and H. Kimura, Japan J. Appl. Phys. 4: 662, 1965.

PULSED ELECTRON BEAM CALORIMETRY UTILIZING STRESS WAVE MEASUREMENTS IN SOLID ABSORBERS

R. A. GRAHAM, R. E. HUTCHISON, and W. B. BENEDICK

Sandia Laboratory, Albuquerque, New Mexico

INTRODUCTION

Pulsed-electron-beam machines which produce currents of thousands of amperes and current durations of the order of 10^{-8} sec are available for transient energy deposition studies. Although extremely short pulse durations are the most characteristic feature of these beams, currently available methods for calorimetric measurements on the beam are adaptations of methods previously employed for steady-state sources. These methods include the passive technique of recovering blue cellophane foils^{1,2} which have been exposed to the beam as well as temperature measurements on thin metallic disks.² It is the object of this paper to propose a new method of calorimetry based on measurements of the stress pulses which result when the beam is absorbed in thick elastic absorbers. In a recent communication we briefly described some of the properties of these thermoelastic stress pulses.³ The stress pulses can be used to determine the intensity, end-point range, and duration of the electron beam.

Previous measurements⁴⁻⁷ of stress pulses produced by radiant energy sources have been accomplished in rod-shaped absorbers with geometrically limited rise-time capabilities. The measurements by White^{4,5} were obtained for conditions in which long duration electron pulses (about 2 μ sec) were absorbed on the surface of a rod.

THERMOELASTIC STRESS WAVES

To understand the operation of the calorimeter we must first consider the properties of the stress pulse which results from the absorption of the beam. The thick elastic absorber is considered to be exposed to an electron beam of uniform areal intensity such that the energy of the beam is deposited within the absorber. If the duration of the incident electron pulse is very short compared to the duration of the resultant stress pulse, the absorption can be assumed to occur instantaneously. From the constant-volume conditions which result from the instantaneous deposition it follows immediately that

$$\sigma_x(x) = \tau_x E(x) \quad (1)$$

where $E(x)$ is the absorbed energy (the x direction taken normal to the disk face), and the resulting normal stress component in the x direction is σ_x . The thermoelastic constant τ_x is defined as $\tau_x \equiv \gamma_x/V \equiv (\partial\sigma_x/\partial E)_V$, where V is the specific volume and γ is the Gruneisen's ratio.⁸ Thus, if the thermoelastic constant of the absorber material is known, a measurement of the stress as a function of position at deposition time provides a direct evaluation of the energy as a function of position.

This evaluation of energy distribution gives the maximum absorbed energy, the electron end-point range, and an absorption coefficient.

If the duration of the electron beam pulse is nonzero but still short compared to the duration of the stress pulse, the stresses in the immediate vicinity of the exposed surface are altered from that predicted by Eq. (1). Normally, however, the stresses at positions remote from the exposed surface are unaffected.

Once the energy is absorbed, a plane compressive stress pulse propagates along the x direction and immediately forms a tensile stress tail to maintain zero total momentum. (The incident electrons have negligible momentum.) While progressing through the disk, the pulse lengthens in time and the peak compressive stress decreases in amplitude. If the absorber is elastic, however, these changes in pulse amplitude and duration can be analyzed as an elastic-wave-propagation problem. Hence, the stress pulse at some position removed from the original deposition site is directly related to the original stress distribution, and this propagated stress pulse is the basis for the proposed calorimeter.

A measurement of the stress pulse requires exceptional time resolution since significant changes in stress occur in times of the order of 10^{-8} sec. The Sandia quartz gage⁹ produces an output current directly related to the instantaneous stress at the input electrode. The time-resolution is limited only by the planarity of the wave and the rise-time of the recording equipment. With this gage it appears feasible to obtain precise measurements of the stress pulses resulting from absorption of the electron beam. The proposed calorimeter, shown in Fig. 1, consists

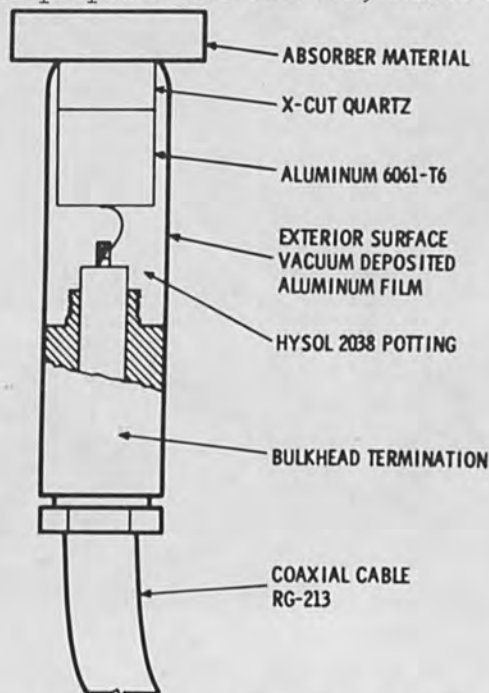


FIG. 1.—Electron calorimeter consisting of a thick elastic absorber and a quartz stress gage. The thickness of the absorber is greater than the electron end-point range. The beam is extracted in a vacuum and impinges on the upper surface of the absorber through an aluminum filter 0.33 mm thick. This calorimeter has been used to study the characteristics of a 2-MeV pulsed-electron-beam machine.

of this gage and an absorber disk of large diameter-to-thickness ratio. The thickness of the absorber is chosen to be greater than the end-point range of the electrons. One plane surface of the disk is exposed to the beam and the resulting stress pulse is detected by the gage located at the opposite surface of the disk.

EXPERIMENTAL

Experiments to study the feasibility of the proposed calorimeter have been performed utilizing electron pulses of 40-ns duration from a 2-MeV pulsed-electron-beam machine.¹ Absorber disks 25 mm in diameter and 6.35 mm thick were exposed to a 12.7-mm-diameter segment of the electron beam in separate experiments in which the nominal characteristics of the beam were unchanged. The experiments were conducted with the absorber 7.6 cm from the window of the machine, which was set on a charging voltage on 30 kV. The quartz gages used were X-cut disks 12.7 mm in diameter and 6.35 mm thick. The relative stress amplitudes were measured with an accuracy of $\pm 5\%$.

A typical stress pulse record obtained on an aluminum absorber is shown in Fig. 2. It is apparent from this record that the stress profile can be measured in considerable detail. The noise encountered at deposition time serves as a convenient marker for deposition time, which in this case occurs 960 ns before arrival of the peak compressive stress. The shape observed is that which would be expected for a radiation-induced thermoelastic stress pulse.

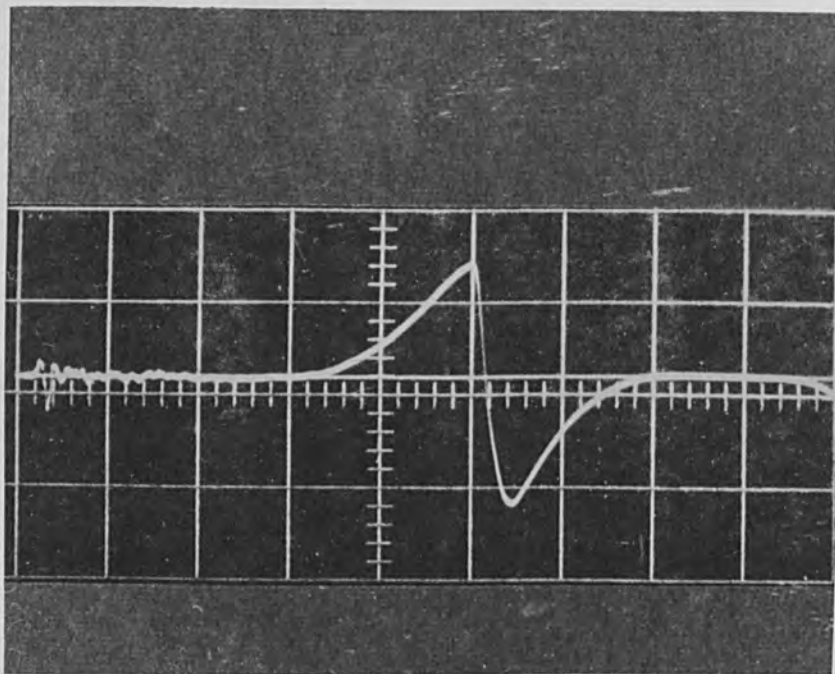


FIG. 2.—Stress-time profile for an aluminum absorber 6.10 mm thick. Time increases from left to right with a scale of 200 ns per major division. The electrical noise accompanying the deposition is shown on the extreme left. The vertical scale is 0.5 Volt per major division. The peak compressive stress indicated by the gage is 0.54 kbar. Such data can be used to study the intensity, energy, and pulse duration of pulsed electron beams.

A wide variety of absorber materials were investigated; all were potentially useful calorimeter absorbers. These materials and their pertinent properties are shown in the first five columns of Table 1

TABLE 1.—Absorber properties and peak stress amplitudes.

| Absorber | Absorber Properties | | | | Relative Stress Amplitudes | |
|-------------------|-----------------------------|------------------------------|------------------------------------|-------------------|----------------------------|--------------|
| | τ_x (a) (bar g/cal) | C_o (b) (mm/ μ sec) | ρ (c) (g/cm ³) | T_o (d) (ns) | Calculated | Observed (e) |
| X-cut quartz | 82 | 5.72 | 2.65 | 590 | 1.00 | 1.00 |
| Z-cut quartz | 66 | 6.36 | 2.65 | 530 | 0.80 | 0.65 |
| Z-cut sapphire | 237 | 11.1 | 3.99 | 200 | 2.80 | 1.60 |
| [111] silicon | 42 | 9.36 | 2.33 | 410 | 0.51 | 0.61 |
| [100] InSb | 116 | 3.44 | 5.8 | 460 | 2.3 | 1.8 |
| [111] germanium | 162 | 5.65 | 5.35 | 300 | 2.0 | 1.4 |
| 6061 T-6 aluminum | 236 | 6.32 | 2.70 | 520 | 2.9 | 3.2 |

(a) The component of the thermoelastic constant, τ , in the x direction is computed by means of the analysis of S. W. Key.⁸

(b) C_o is the dilatational wave velocity along the axis of the disk.

(c) ρ is the density.

(d) T_o is the initial pulse length of the stress pulse calculated as the range for 2-MeV electrons¹⁰ divided by C_o .

(e) The observed stress amplitudes are corrected for the acoustic impedance mismatch between the absorber and the gage.

The materials include dielectrics, semiconductors, and metals with a range of thermoelastic constants of a factor of about six. The dilatational wave velocities C_o and the densities cover a range of values of about a factor of three. All materials have elastic limits high enough so that they remain elastic for the conditions of the experiment.

As previously mentioned, the 40-ns pulse duration of the electron beam causes peak stress amplitudes to be reduced below the values predicted by Eq. (1). The extent of this reduction for a given electron-pulse duration depends on the stress-pulse duration in the absorber. That is, very short stress pulses are reduced in amplitude more than long pulses because the electron-pulse deposition time is a larger fraction of the short pulse. A calculated value for the initial stress-pulse duration T_o resulting from the energy absorption can be obtained by dividing the electron range (expressed as the depth of penetration) by the dilatational wave velocity. Values of T_o are calculated for 1.9-MeV electrons in the various absorbers and shown in Table 1. The 40-ns electron-pulse duration should be compared with the T_o values; the value is 200 ns for sapphire while the value for X-cut quartz is 590 ns.

RESULTS

From records such as that shown in Fig. 2 obtained on the various absorbers the relative amplitudes of the peak compressive stresses may be compared with those calculated from Eq. (1). Both observed and calculated stress amplitudes are normalized to a value of 1.00 for X-cut quartz. This comparison is shown in the sixth and seventh columns of Table 1. With the exception of the germanium and sapphire absorbers, the measurements show a $\pm 20\%$ spread in amplitudes between observed and calculated values (5% of the spread is due to experimental error). This indicates a shot-to-shot variation in the beam of $\pm 15\%$, which is consistent with other measurements. The lowered values obtained in the sapphire and germanium absorbers reflect the influence of the 40-ns electron-pulse duration on these materials with the shorter T_0 values of 200 and 300 ns, respectively. These measurements, as well as repeated experiments on the same absorber at various times, show that the measured stress pulses sensitively reflect the intensity of the beam.

Some difficulty might be expected for the absorption of the energy of charged particles in dielectrics compared with those absorbed in a conductor. The potential accompanying the initial electron deposition may decelerate electrons which arrive somewhat later. In the case of the quartz and sapphire absorbers, no effect was observed on the absorption compared to that in the conductors. Two other dielectrics, tourmaline and a low-thermal-expansion glass,¹¹ were observed to suffer dielectric breakdown which caused major changes in the stress-wave profiles.

The indium antimonide record showed the tensile stress peak to be abnormally reduced in amplitude. Examination of the sample showed that the exposed surface had suffered a tensile stress failure which would cause the change in wave profile.

In addition to the stress amplitude data which reflect the intensity of the electron pulse, the data on the duration of the stress pulse reflect both the electron end-point range and the duration of the beam. The initial stress pulse duration is directly proportional to the electron end-point range and inversely proportional to the dilatational wave velocity. The observed stress pulse durations were used to calculate the range relative to that observed for X-cut quartz with a 1.9-MeV electrons. The results of these range measurements are shown in Table 2. Experimental results are shown for X-cut quartz absorbers at various electron energies and other absorbers at an energy of 1.9 MeV. The observed range values agree with those calculated from the nominal electron energy within $\pm 10\%$. With the pulses reported here it is possible to measure the pulse length within $\pm 5\%$. The remainder of the variation is thought to be the shot-to-shot variation in the energy of the beam. These measurements show that the end-point range of the electrons can be measured without difficulty.

Numerical calculations show that the duration of the electron beam is explicitly shown in the measured stress pulse. The time difference between the peak compressive stress and the zero-stress value immediately following the peak is equal to the beam duration. The record shown in Fig. 2 shows this time to be 35 ns. The pulse duration measurements published by the manufacturer¹ show the main portion of the pulse to last

about 40 ns with a longer low-amplitude tail lasting up to 100 ns. Our measurements on the electron pulse do not show any indication of the long tail, which is apparently associated with low-energy electrons that are absorbed by the thin aluminum filter placed in front of the absorber.

TABLE 2.—Electron-range measurements.

| Absorber | Electron energy (MeV) | Range (mm) | |
|----------------|--------------------------|------------|----------------|
| | | Measured | Calculated (a) |
| X-cut quartz | 1.9 | (b) | 3.36 |
| X-cut quartz | 1.6 | 2.42 | 2.75 |
| X-cut quartz | 1.3 | 2.18 | 2.19 |
| X-cut quartz | 0.96 | 1.44 | 1.58 |
| Z-cut quartz | 1.9 | 3.55 | 3.36 |
| Z-cut sapphire | 1.9 | 2.05 | 2.23 |
| [111] silicon | 1.9 | 3.82 | 3.79 |
| Aluminum alloy | 1.9 | 3.30 | 3.30 |

(a) These values are calculated from conventional energy-vs-range relations.¹⁰

(b) This value is assumed to be 3.36 mm in agreement with the calculated value. Measured values for the other absorbers are computed from the measured pulse lengths relative to that assumed for X-cut quartz with 1.9-MeV electrons.

SUMMARY AND CONCLUSIONS

These measurements show that the stress pulses resulting from the absorption of intense pulsed electron beams can be measured in considerable detail. The stress pulse amplitudes and durations are observed to scale quantitatively with the intensity and energy characteristics of the beams absorbed in various absorbers. In addition, the electron pulse duration is shown as a distinct feature of the stress pulse. It is concluded from this investigation that measurements of the stress pulses in thick elastic absorbers can provide a basis for calorimetry of pulsed electron beams. At present, the measurements are limited to relative values which can be calibrated by more conventional means. Computer solutions of the complex elastic wave propagation problem will permit absolute values to be recovered from these same measured pulses.¹²

It appears that aluminum and X-cut quartz are the best absorber materials for a calorimeter. Aluminum has a much larger thermoelastic constant than quartz and therefore a superior signal-to-noise ratio. Thus, aluminum is preferable for absorbed energies below about 8 cal/g. However, the elastic constants of aluminum are sensitive to the temperature rise and absorbed energies above 8 cal/g cause some nonlinearities in the response of the calorimeter. The temperature-independent properties of

X-cut quartz absorbers make quartz a better material for pulses of higher intensity.

Present measurements show that the most desirable gage for the stress pulse measurements is a guard-ring gage⁹ 31.8 mm in diameter and 6.35 mm thick with an active center-electrode diameter of 12.7 mm. In addition, improvements have led to a considerable reduction in the noise level, which can be observed by comparing the record in Fig. 2 with an earlier published record.³

The stress pulse calorimeter is a unique and promising new device for the study of the characteristics of pulsed electron beams. In fact, the calorimeter seems far more precise and sensitive than needed for currently available sources. Since the physical basis for the operation of the calorimeter is different from that employed in other calorimeters, it is now possible to obtain independent measurements of beam properties. This capability should greatly improve our understanding of pulsed-electron-beam machines.

ACKNOWLEDGMENT

The authors are pleased to acknowledge analysis of the wave propagation problem by J. A. Mogford and helpful discussions with their Sandia Corp. colleagues and C. M. Percival.

REFERENCES AND FOOTNOTES

1. Field Emission Corporation, "Febetron: A high intensity, pulsed source of electrons and x-rays," Vol. 4, No. 1, April 1965.
2. R. B. Oswald, Jr., H. A. Eisen, and E. E. Conrad, "Pulsed electron beam dosimetry," IEEE 1966 Annual Conference on Nuclear and Space Radiation Effects.
3. R. A. Graham and R. E. Hutchison, "Thermoelastic stress pulses resulting from pulsed electron beams," Appl. Phys. Letters (in press).
4. R. M. White, "Elastic wave generation by electron bombardment of electromagnetic wave absorption," J. Appl. Phys. 34: 2123-2124, 1963.
5. R. M. White, "Generation of elastic waves by transient surface heating," J. Appl. Phys. 34: 3559-3567, 1963.
6. C. M. Percival, private communication.
7. W. M. Peffley, "A study of stress waves produced by pulsed high-energy radiation," Appl. Phys. Letters 10: 171-173, 1967.
8. In an isotropic solid the Gruneisen's ratio is a scalar; however, in an anisotropic solid the value depends on the crystallographic direction. For the development of the anisotropic γ see S. W. Key, "The Gruneisen tensor for anisotropic materials," J. Appl. Phys. (in press).
9. R. A. Graham, F. W. Neilson, and W. B. Benedick, "Piezoelectric current from shock-loaded quartz: A submicrosecond stress gauge," J. Appl. Phys. 36: 1775-1783, 1965.
10. L. Katz and A. S. Penfold, "Range-energy relations for electrons and the determination of beta-ray end-point energies by absorption," Revs. Mod. Phys. 24: 28-44, 1952.
11. Cer-Vet composition C-100 Glass Owens-Illinois.
12. D. J. McCloskey has recently obtained solutions describing this problem. (Private communication.)

10^{12} -WATT ELECTRON BEAM

W. T. LINK and D. H. SLOAN

Physics International Co., San Leandro, California

I. PULSED ACCELERATOR FOR ELECTRON BEAMS (D. H. Sloan)

As shown schematically in Fig. 1, a powerful electromagnetic pulse of several megavolts, 50 ns long, can be launched from a pulse-forming line by a spark switch and guided into an evacuated accelerator tube to accelerate an electron beam.

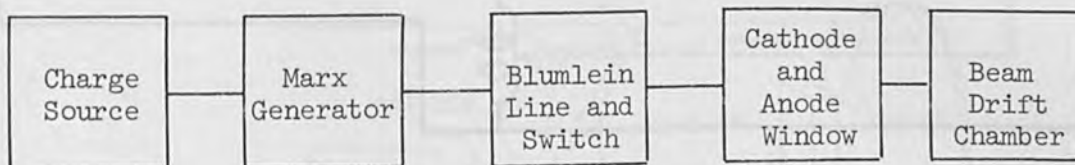


FIG. 1.—Block diagram of pulsed electron accelerator.

If charged slowly, liquid dielectrics fail at low field strength. Fast charging is possible with a reflex Marx generator whose capacitors are charged in parallel and switched to series connection by means of pressurized gas spark gaps. The oil-immersed 4-MV, 100-kJ Marx generators used at Physics International Co. have a capacitance that exceeds by a large factor the capacitance of some of the available oil dielectric pulse-forming lines. This permits the charge to ring up to 6 or 7 MV on the coaxial line within a microsecond, before the single-spark oil dielectric switch launches the pulse wave into the accelerator tube.

If a simple coaxial line is switched to an accelerator tube of equal impedance, both sides of the switch will come to half the voltage of the initial charge. A Blumlein line, Fig. 2, has two co-axes, charged in parallel, with the accelerator connected between their grounded sides. The spark-gap switch is placed at the distant end of one line and shorts it completely, causing ringing and reversal of its voltage. This new polarity adds to the other line and doubles the available voltage. The pulse voltage is thus twice as great as that from a single coax, although its rise time is only half as fast.

The window through which the electromagnetic wave enters the vacuum of the accelerator tube consists of one or more rings of lucite or epoxy. Each epoxy ring lies between flat metal rings or plates. The inner surface of each insulator ring is conical, concave toward the anode, so that free electrons can leave the conical surface and move directly through the vacuum to the more positive metal ring, instead of traveling along the vacuum interface surface and possibly starting breakdown. Each ring can withstand perhaps 1 MV, so a stack of insulator rings and flat metal

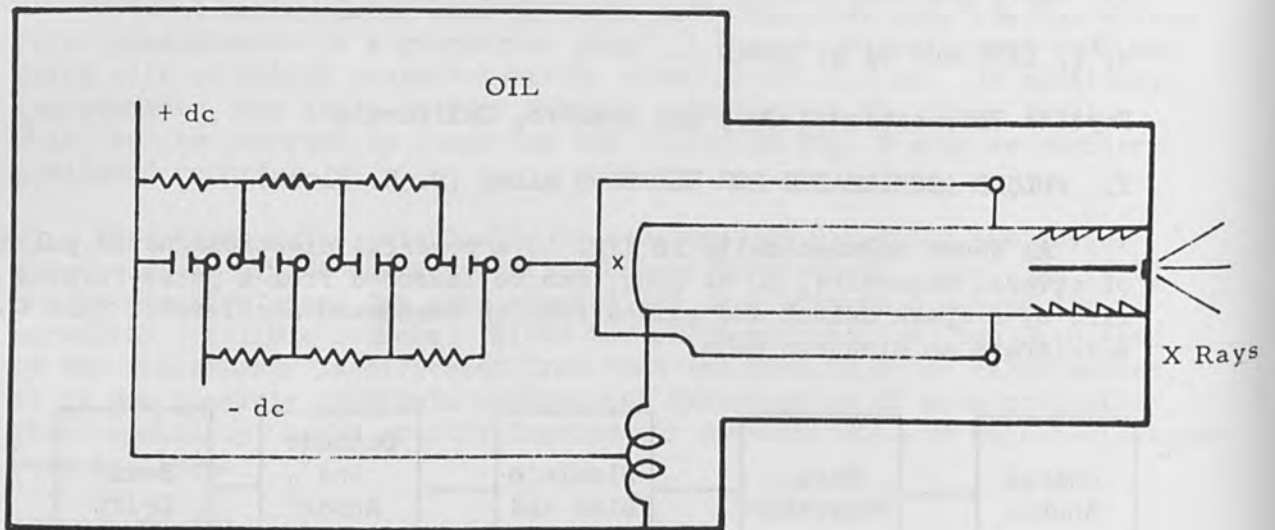


FIG. 2.—Schematic SXR system.

rings are used for higher voltage. For sufficiently low impedance (30 ohms) to guide the pulse wave past the insulator to the cathode, the metal rings must be very wide sheet surfaces, separated only enough to avoid sparking.

If the cathode stem were close enough to the anode structure to provide matched impedance guiding of the pulse wave, electric fields would be so high that field emission would occur almost everywhere. Although it increases the rise time, the separation of cathode stem and anode structure is held larger than suitable for impedance matching, and in this way electric fields at the cathode stem are reduced to a value where only a few random points or whiskers can emit. These points can further be prevented from emitting by coating with dielectric liquid, which reduces electric fields to less than half. The magnetic field around the cathode stem due to 10^5 A of emitted electrons is about 5 000 gauss, easily sufficient to sharply curve electrons emitted from the cathode stem back into it.

The cathode may be a sharpened edge or a cluster of fine wires. In the electron stream, positive ions are needed to reduce space charge repulsion for high current density.¹ Fewer ions are needed as the electron mass γm_0 increases, $\gamma = (1 - \beta^2)^{-\frac{1}{2}}$, and $\beta = v/c$. If the ion charge density reaches the fraction $1 - \beta^2$ of the electron density, radial magnetic attractive forces cancel the radial electric repulsive forces of the electrons.

To complete the pulse wave passage, the 10^5 -A displacement current in the coaxial line becomes a convection current of beam electrons. These electrons disappear from the circuit as they penetrate the anode window.

Continuity demands that an equal current of a much larger number of slow electrons return through the window by metallic conduction and complete the circuit associated with the pulse wave. Because of skin depth, these slow electrons can return through the metal only where the fast ones depart.

II. RELATIVISTIC KILOAMPERE ELECTRON BEAMS (W. T. Link)

THE DRIFTING ELECTRON BEAM. Figure 3 is a schematic diagram of the cathode-anode chamber and the electron beam chamber. Most of the remaining descriptive matter of this paper applies to the Physics International Co. Model 730 electron accelerator. The beam from this machine

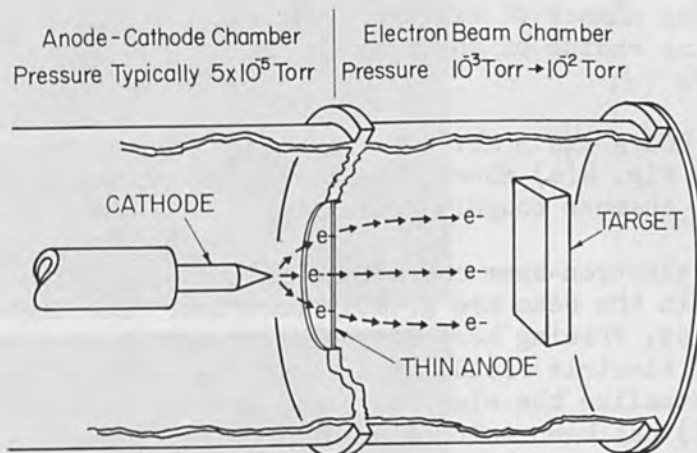


FIG. 3.—Arrangement of anode-cathode and electron-beam chambers.

is a 30×10^{-9} -sec, 50,000-A burst of 3-MeV electrons. This stream of electrons passes through the thin anode window, often breaking it, and is then available for study or use in the electron beam chamber. The diameter of the beam at the anode is typically 5 cm and its phase space area about 0.5 cm radian.

BEHAVIOR OF ELECTRON BEAMS AS A FUNCTION OF THE GAS PRESSURE IN THE ELECTRON BEAM CHAMBER. Figure 4 shows photographs of the electron beam traversing the electron beam chamber at various air pressures. Much of the theory of electron streams is summarized in a general paper by Lawson (1959).¹

The electric, magnetic, and total forces on an electron at the surface of a cylindrical electron beam in a vacuum are

$$F_e = \frac{2Ne^2}{4\pi\epsilon_0 r} \quad (1)$$

$$F_m = \frac{-2Ne^2}{4\pi\epsilon_0 r} \beta^2 \quad (2)$$

$$F = F_e + F_m = \frac{2Ne^2}{4\pi\epsilon_0 r} (1 - \beta^2) \quad (3)$$

where F_e is the radially outward electric force (N)

F_m is the radially inward magnetic force (N)

$F = F_e + F_m$ is the total force (N)

N is the number of electrons per meter

r is the radius of the beam (m)

$\beta = v/c$

For 50 000 A and 3 MeV kinetic energy, the force is large and radially outward. As Fig. 4(a) shows, the beam blows up and a remaining part of it fills the chamber roughly uniformly.

If the electron-beam chamber is filled with a low-pressure gas, the self-forces in the beam are greatly modified. The high-energy electrons ionize the gas, freeing secondary electrons that are then repelled by the large radial electric field. The remaining positive ions tend to electrically neutralize the electron beam; this is represented in Eq. (4), in which Eq. (1) has been multiplied by an electric neutralization factor f_e :

$$F_e = \frac{2Ne^2}{4\pi\epsilon_0 r} f_e; \quad 0 < f_e < 1. \quad (4)$$

The rapid rise of magnetic field when the electron beam passes into the beam chamber produces a large voltage in the backward direction. This backward voltage may, at suitable pressure, produce a backward current that neutralizes or nearly neutralizes the magnetic field, as represented in Eq. (5) obtained by multiplying Eq. (2) by a magnetic neutralization factor f_m :

$$F_m = \frac{-2Ne^2}{4\pi\epsilon_0 r} \beta^2 f_m; \quad 0 < f_m < 1. \quad (5)$$

The total force is then

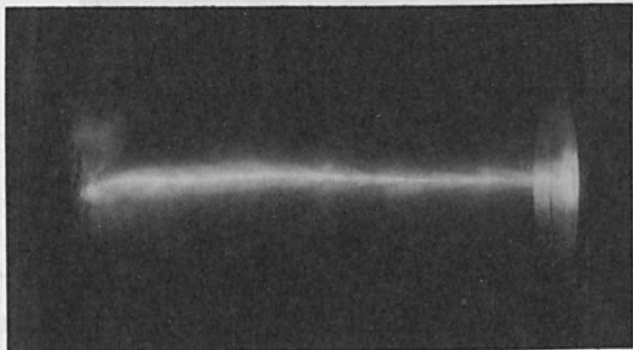
$$F = \frac{2Ne^2}{4\pi\epsilon_0 r} [1 - f_e - \beta^2 (1 - f_m)] \quad (6)$$

Equation (6) assumes a steady-state condition, ignores possible cooperative phenomena in the beam, and ignores possibly large longitudinal forces.

Table 1 summarizes the conditions that can be seen in Figure 4. A continuum of intermediate conditions exists, but we deal here only with



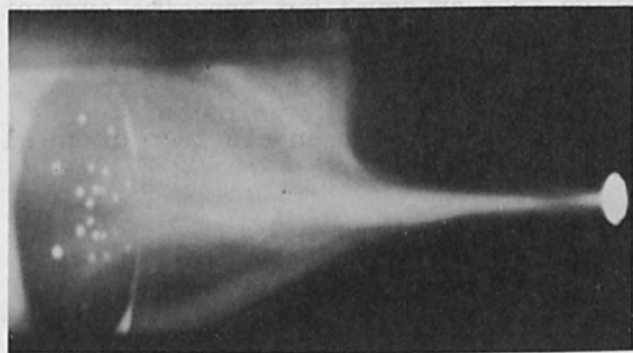
(a)
10⁻³ torr



(b)
10⁻¹ torr



(c)
1 torr



(d)
760 torr

FIG. 4.—Behavior of 3-MeV, 50 000-A electron beams in air at various pressures. The beam chamber is 50 cm long and the camera is about 30 cm from the chamber centerline. The camera shutter is opened 1 sec before and closed 1 sec after the shot.

the four cases shown.

TABLE 1.—Summary of conditions.

| Figure | Chamber pressure (torr) | Observed behavior of beam | Likely values of f_e, f_m | Force on electron* |
|--------|-------------------------|--|-----------------------------|----------------------------|
| 4a | 10^{-3} | Beam blows up | $f_e = 0$ $f_m = 0$ | $1 - \beta^2 \approx 0.02$ |
| 4b | 10^{-1} | Beam pinches a few mm diameter | $f_e = 1$ $f_m = 0$ | $-\beta^2 \approx -1.0$ |
| 4c | 1 | Beam drifts with nearly zero force | $f_e = 1$ $f_m = 1$ | 0 |
| 4d | 760 | Beam pinches; multiple scattering in air finally breaks up pinch | $f_e = 1$ $f_m = 0$ | $-\beta^2 \approx -1.0$ |

* This is the force on an electron at the surface of a beam divided by $2Ne^2/4\pi\epsilon_0 r$.

The values of f_e and f_m assumed in this table are consistent with order-of-magnitude calculations based on primary ionization by the beam, the build-up of large backward currents of low-energy electrons, and finally the suppression of these large backward currents (at high pressure) through the reduction of electron mean free path.

IMAGE FORCES IN A CONDUCTOR. A pulsed electron beam develops a mirror image of itself in a conductor. The rapidly rising magnetic field associated with the beam produces eddy currents and magnetic fields in a conductor that appear to derive from an equal but opposite current equally spaced behind the conductor. Unneutralized charge in an electron beam produces a mirror image charge in the usual way.

The image force from a flat conductor on an electron of an electron beam parallel to the conductor is

$$F_{\text{image}} = \frac{-Ne^2}{4\pi\epsilon_0 r} [1 - f_e - \beta^2 (1 - f_m)] \quad (7)$$

where r is the distance of the beam from the conductor and all other symbols are as defined in Eqs. (3) and (6).

If the electron beam is pinched, f_e equals approximately 1, and the image force should be repulsive. Figure 5 is a side photograph of such a pinched beam. The drawing in Fig. 5 shows why the beam reflects downward after leaving the conducting sheet; it simply "sees" the top of the beam chamber and reflects away from it. The differential equation that governs the motion of the beam in this case is

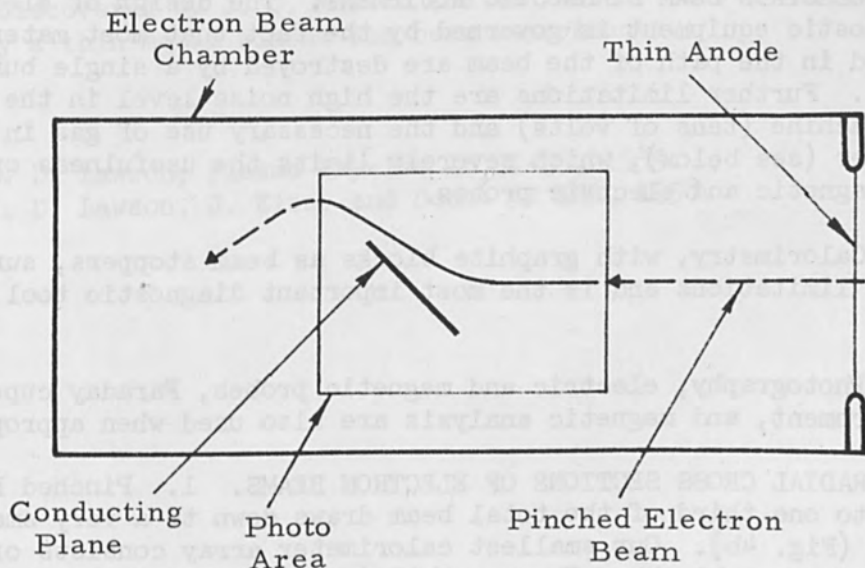
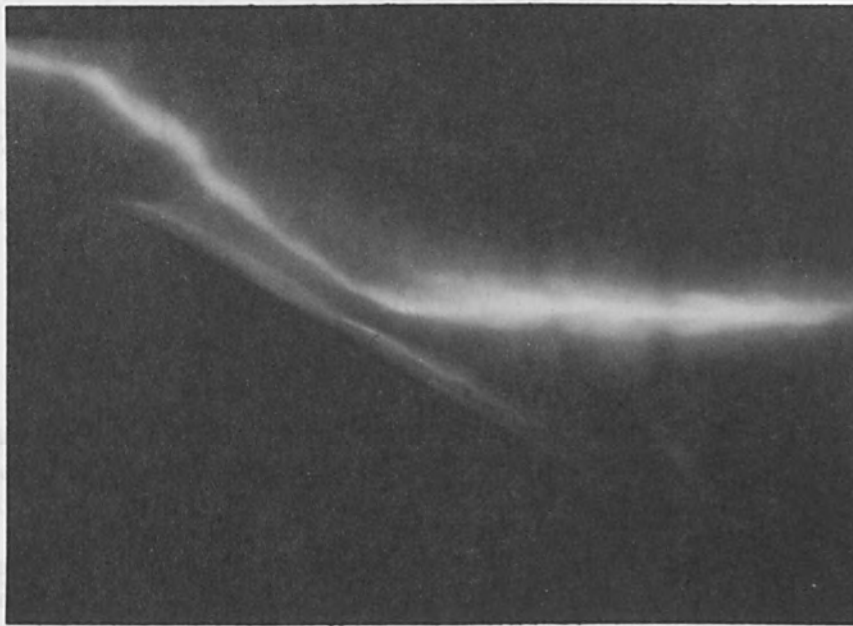


FIG. 5.—A pinched electron beam reflecting from a conducting sheet. The conducting sheet is grounded to the beam chamber. In four shots there was no damage of any sort to the conductor. Had the conducting sheet been normal to the beam a large hole in the sheet would have resulted from each shot.

$$\frac{d^2 r}{dz^2} - \frac{I}{I_0 \gamma} \frac{1}{r} = 0 \quad (8)$$

where I is the total current in the pinch

$$I_0 = \frac{ec}{r_0} \approx 17\,000 \text{ A}$$

$$\gamma = \frac{1}{\sqrt{1 - \beta^2}}$$

The solution of this equation,² when referred to Fig. 5, indicates the beam current in Fig. 5 is about 20 000 A, a reasonable result.

An electrically and magnetically neutralized beam should have no image force ($f_e \sim f_m \sim 1$ in Eq. 7). Experimentally, it has been observed that such a beam shows little or no tendency to reflect from a conducting surface.

ELECTRON BEAM DIAGNOSTIC EQUIPMENT. The design of electron-beam diagnostic equipment is governed by the fact that most material objects, placed in the path of the beam are destroyed by a single burst of electrons. Further limitations are the high noise level in the vicinity of the machine (tens of volts) and the necessary use of gas in the electron chamber (see below), which severely limits the usefulness of Faraday cups and magnetic and electric probes.

Calorimetry, with graphite blocks as beam stoppers, survives all of these limitations and is the most important diagnostic tool currently in use.

Photography, electric and magnetic probes, Faraday cups, x-ray dose measurement, and magnetic analysis are also used when appropriate.

RADIAL CROSS SECTIONS OF ELECTRON BEAMS. 1. Pinched Beams. One half to one third of the total beam draws down to a very small, intense pinch (Fig. 4b). Our smallest calorimeter array consists of twenty-five 0.5-cm-square blocks. The resolution of this array permits only a lower limit to be assigned for the peak current intensity: 20 000 A/cm² (500 cal/cm² for 3-MeV electrons in a 30 x 10⁻⁹-sec burst). The pinch is stable for at least the 50-cm length of the beam chamber and can be bent in a magnetic field with the same deflection as would occur for the individual 3-MeV electrons.

2. Drifting Beams. In this mode the entire beam drifts from the anode to the end of the beam chamber with little indication of internal forces (Fig. 4c). The angular divergence of the electron beam is then 0.2 rad FWHM but this value can be increased to any reasonable value by locating a thin scattering foil at the anode. The electron-beam intensity falls off roughly as the inverse square of the distance from the anode and is observed to have a roughly Gaussian distribution about the center-line of the chamber. One can then write an approximate expression for the

electron beam intensity at any place in the beam chamber,

$$I \approx \frac{200,000}{Z^2} \exp \left[\frac{-13r^2}{Z^2} \right] \text{ A/cm}^2 \quad (9)$$

$$Z > 10 \text{ cm}$$

where I is the beam intensity (A/cm^2)

Z is the distance from the anode (cm)

r is the distance from the beam-chamber centerline (cm)

The drifting electron beam shows pronounced filamentary structure. The filaments are of interest in themselves, and can be completely removed by a thin scattering foil at the anode.

ACKNOWLEDGMENT

The SXR generator (Fig. 2) was built through the efforts of Don Martin, Bernard Bernstein, and Frank Ford. Its insulator design principle was discovered by J. C. Martin and Ian Smith. Its x-ray target is replaced by a thin metal window for beam experiments.

REFERENCES

1. J. D. Lawson, Plasma Physics 1: 31-35, 1959.
2. J. D. Lawson, J. Elec. and Cont. 5: 146, 1958.

ION EMISSION FROM METAL SURFACE IRRADIATED
BY GIANT-PULSE LASER BEAM

S. NAMBA, P. H. KIM, T. ITOH, and T. ARAI

The Institute of Physical and Chemical Research, Bunkyo-ku, Tokyo

H. SCHWARZ

Rensselaer Polytechnic Institute, East Windsor Hill, Connecticut

ABSTRACT. By observing the energy of thermal ions emitted from the metal surface irradiated by a single giant-pulse laser beam, the surface temperatures of some metals are estimated to be several tens of thousand degrees, much higher than the boiling point of each metal.

It is found that ions of two discrete energies are produced, one energy peak corresponding to the thermal energy of the surface, the other peak to an energy of magnitude two orders higher. From the relations of the ion energy to the intensity of the irradiated laser beam and to the intensity of the magnetic field, it is supposed that the thermal ions are accelerated by the interaction with electrons which gain energy from the radiation field of the laser beam by the inverse bremsstrahlung process, and then high-energy ions are produced.

I. INTRODUCTION

As is well known, the focused laser beam can vaporize or melt materials. When the focused laser beam is used in melting refractory materials, e.g., in welding and microprocessing, it is necessary to know the temperature of the material surface irradiated by the laser beam. The surface temperature of metals has been estimated by applying the retarding field to thermal electrons emitted from the surface.¹ By this method, the surface temperature of some metals heated by the normal laser beam was also estimated by the authors and the relation between the surface temperature and the irradiated laser power density was discussed.² When the power density of the laser beam was about 10^6 W/cm², the surface temperatures of W, Mo, Ti, and Ni were below the boiling point of each metal.

However, if an intense laser beam such as a giant-pulse laser beam is irradiated, it is expected that the surface of materials will be heated above the boiling point. When the metal surface is irradiated by a single giant-pulse laser, the surface temperature is estimated by two methods: one is the above-mentioned retarding potential method, and the other is to measure the energy of thermal ions. On the other hand, the measurement of the ion energy is also necessary to examine the possibility of the production of high energy plasma by laser irradiation.

In this paper, the surface temperature estimated by the energy of thermal ions and the production of ions with two discrete energies are

reported in Sec. III-1. And, from the relations of the ion energy to the intensity of the irradiated laser beam and to the intensity of the magnetic field, the mechanism of the production of high energy ions is discussed in Secs. III-2 and III-3.

II. APPARATUS AND EXPERIMENTAL PROCEDURE

The experimental apparatus and its block diagram are shown in Figs. 1 and 2. The vacuum system was evacuated to about 10^{-7} torr by an ion pump. Laser material was a Nd glass rod of 10 cm in length and 6.5 mm in diameter. The peak power of a giant-pulse produced by using a rotating

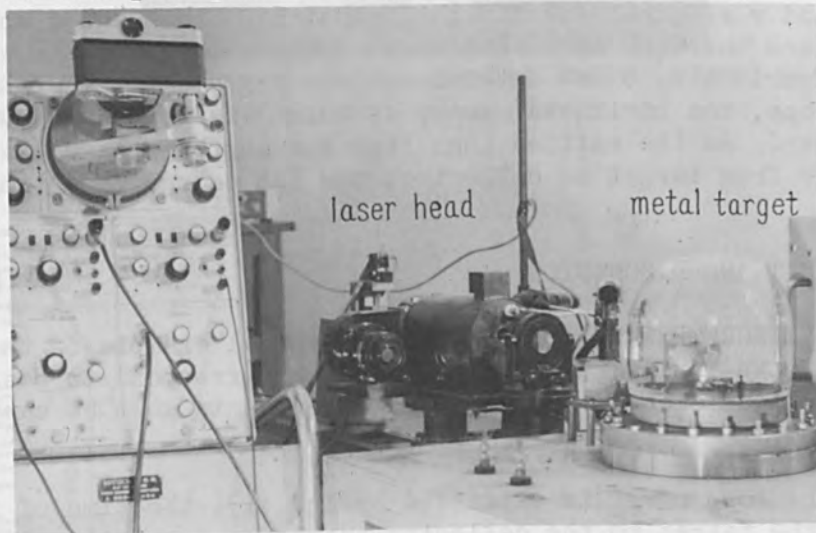


FIG. 1.—Experimental apparatus.

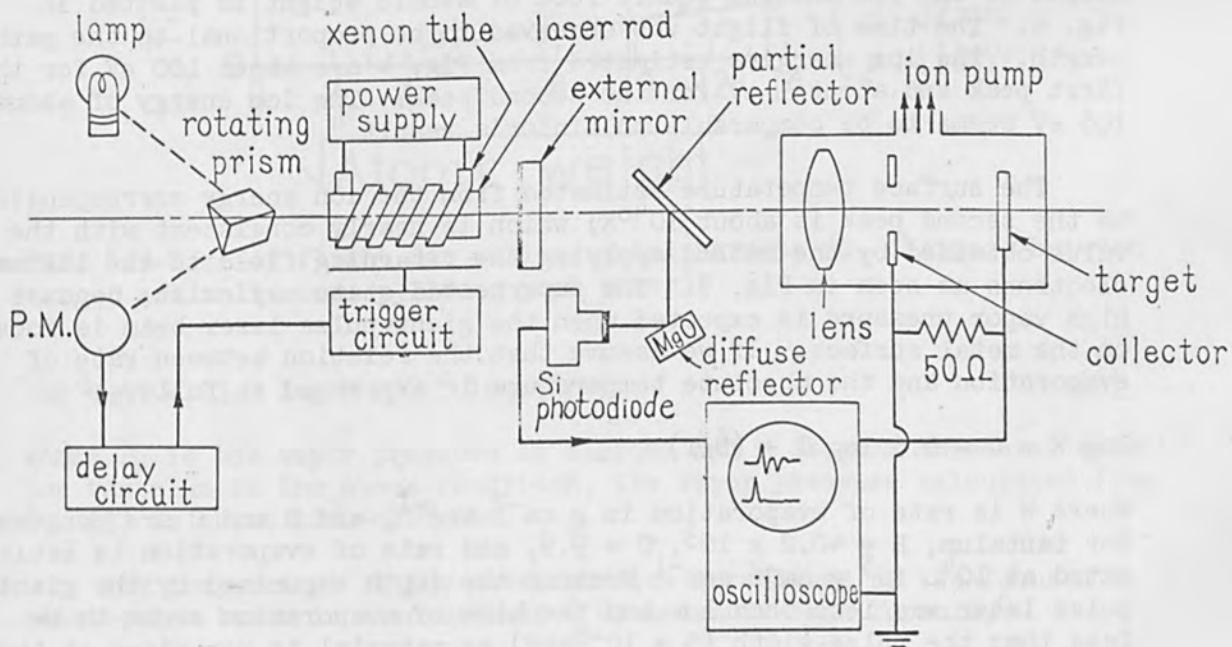


FIG. 2.—Block diagram of experimental system.

prism method was 3 ~ 11 MW, and the pulse width was about 50 ns. The peak power was measured by detecting the partially reflected laser beam by a calibrated Si photodiode. The laser beam was focused on the metal target with a lens of focal length 50 mm and the area of the focal spot was approximately $2 \times 10^{-3} \text{ cm}^2$. Various distances (7 to 32 mm) between the metal target and the collector were used.

The ion energy E at metal surface is given by

$$E = \frac{1}{2}mv^2 = \frac{1}{2}m(d/t)^2 \quad (1)$$

where m and v are the mass and the velocity of ion, and d and t are the distance and the time of flight between the target and the collector. In the experiments, t was determined from signals taken with a fast oscilloscope, the horizontal sweep of which was triggered by the giant-pulse laser. As the emitted ions from the surface travel with initial velocity v from target to collector, the ion energy is estimated from Eq. (1).

III. RESULT AND DISCUSSION

1. MEASUREMENT OF ION ENERGY. A typical example of the oscilloscope trace is shown in Fig. 3. Two peaks which correspond to positive ions³ are observed as seen in Fig. 3. The experiments must be carried out in high vacuum.

As the ion energy is expressed by Eq. (1), the time of flight of the ion from the target to the collector should be proportional to the square root of the atomic weight, if the initial energy of each ion produced by the laser irradiation were the same. The relation between the time of flight of the ion and the square root of atomic weight is plotted in Fig. 4. The time of flight was observed to be proportional to the path length. The ion energies estimated from Fig. 4 are about 100 eV for the first peak and about 1 eV for the second peak. The ion energy of about 100 eV seems to be comparable to Linlor's result.⁴

The surface temperature estimated from the ion energy corresponding to the second peak is about 10^4 OK , which is nearly consistent with the value obtained by the method applying the retarding field to the thermal electrons as seen in Fig. 5. The superheated state may exist, because a high vapor pressure is expected when the giant-pulse laser beam is focused on the metal surface. If we assume that the relation between rate of evaporation and the absolute temperature is expressed as follows,⁵

$$\log W = C - 0.5 \log T - (B/T) \quad (2)$$

where W is rate of evaporation in $\text{g cm}^{-2} \text{ sec}^{-1}$, and B and C are constant. For tantalum, $B = 40.2 \times 10^3$, $C = 9.9$, and rate of evaporation is estimated at $10^4 \sim 10^5 \text{ g cm}^{-2} \text{ sec}^{-1}$ because the depth vaporized by the giant-pulse laser was less than 1μ and the time of evaporation seems to be less than the pulse-width ($5 \times 10^{-8} \text{ sec}$) as material is vaporized at the beginning of the laser pulse. The temperature calculated from Eq. (2) is $10\,000 - 16\,000 \text{ OK}$, which is comparable to the energy for the second peak.

The vapor pressure is calculated by⁵

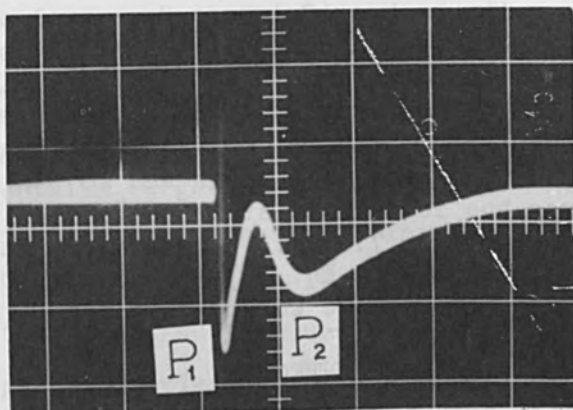


FIG. 3.—Typical oscilloscope trace showing laser induced positive-ion emission from tantalum. Abscissa: 10 μ s/div.

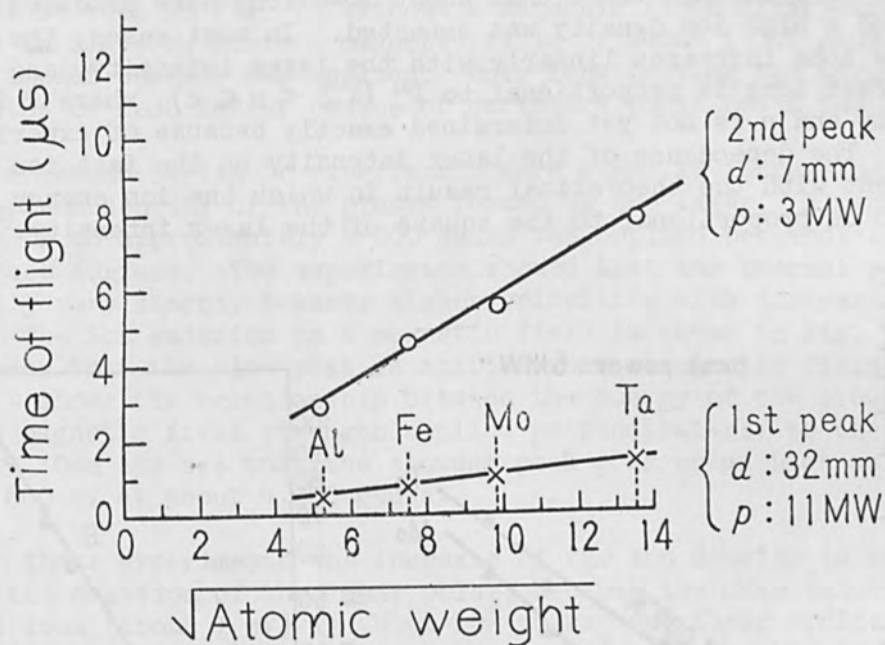


FIG. 4.—Time of flight for various metal targets (d , distance between target and collector; p , laser peak power).

$$\log P_{\mu} = 4.23 + \log W + 0.5 \log (T/M) \quad (3)$$

where P_{μ} is the vapor pressure in microns and M is gram molecular weight. For tantalum in the above condition, the vapor pressure calculated from Eq. (3) is about $10^3 \sim 10^4$ atm.

The temperature of the metal surface irradiated by the focused giant-pulse laser is also estimated by Langmuir-Saha formula,⁶

$$N^+ / N^{\text{II}} = (\alpha + / \alpha_n) \exp [11600(\phi - I_p) / T], \quad (4)$$

where N^+ and N^n are the number of ions and neutral atoms, α is weighting factor for each state and equal to $2J + 1$ where J is the total angular momentum, ϕ is the work function, and I_p is the ionization potential. N^n and N^+ can be estimated from the vaporized volume and the oscilloscope trace showing the charged particle emission. For tantalum, the estimated values of N^n and N^+ are about 10^{15} atoms and $10^{12} \sim 10^{13}$ ions, α_+ and α_n are 3 and 4 because the ion ground state is $5F_1$ and the ground state is $4F_{3/2}$, $\phi = 4.12$ eV and $I_p = 7.7$ eV. With these values for tantalum, the temperature is calculated from Eq. (4) at 6 500 - 10 000°K, which is comparable to the energy for the second peak.

2. ION ENERGY AND LASER INTENSITY.⁷ The relation between the ion energy and the laser intensity is plotted in Fig. 6. The target and the collector materials were tantalum. The laser intensity was changed by using a liquid filter of $CuSO_4$ solution and the maximum intensity of the laser beam was 6 MW. When the laser intensity was 6 MW, it was estimated from the oscilloscope trace that about 10^{12} ions were produced by a single pulse and a high ion density was expected. In most cases, the energy of the slow ions increases linearly with the laser intensity, and the energy of the fast ions is proportional to P^n ($1.5 < n \leq 2$), where P is the laser intensity and n is not yet determined exactly because of experimental errors. The dependence of the laser intensity on the fast ion energy is consistent with the theoretical result in which the ion energy is calculated to be proportional to the square of the laser intensity.⁸

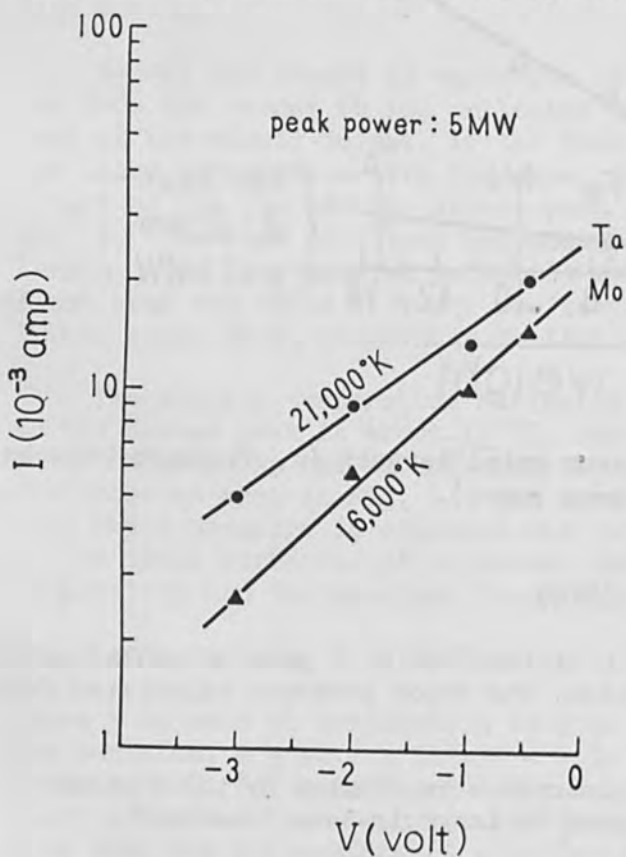


FIG. 5.—Thermionic electron current vs retarding voltage.

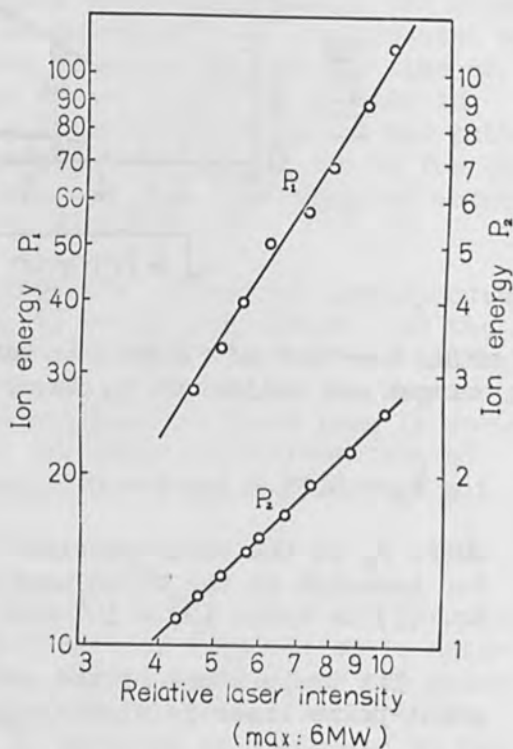


FIG. 6.—Relation between ion energy and laser intensity.

From the above results, it is believed that the slow ions correspond to the thermal ones and the fast ions are produced by the secondary effect as discussed in Sec. III-3 below.

3. ION EMISSION IN MAGNETIC FIELD. Two types of experiments were performed using tantalum target:

(a) At constant laser intensity a variable magnetic field parallel to the impact surface was applied.

(b) Under the same condition as (a), a variable magnetic field perpendicular to the impact surface was applied.

The first type was carried out mainly to prove that the collected charged particles are really ions and not electrons leaving the collector surface. If they were electrons, the radius of curvature of their path would have been so small that they should have returned to the collector electrode. Indeed, as shown in Fig. 7, the very fast peak due to electrons to be seen in Fig. 7a without a magnetic field disappears completely in Fig. 7b, where a magnetic field of about 1 000 gauss parallel to the impact surface was applied. Only ions leaving the target surface with paths of much larger radius of curvature could reach the collector.

The second series of experiments were aimed at increasing the ion and electron density of the plasma formed by the laser. A magnetic field ranging up to approximately 4 000 gauss was applied perpendicularly to the impact surface. The experiments showed that the thermal peak shifts initially very sharply towards higher velocities with increasing magnetic field. The ion emission in a magnetic field is shown in Fig. 8, in which it is seen that the slow peak is shifted when a magnetic field is applied. Figure 9 shows the relationship between the energy of the slowest peak and the magnetic field strength applied perpendicularly to the impact surface. One can see that the slowest peak goes up as high as approximately 600 eV at about 4 000 gauss.

In these experiments the increase of the ion density is negligible within the duration of the laser pulse, because the mean velocity of the thermal ions (about 1 eV) is about 10^5 cm/sec and their cyclotron frequency in a field of 4 000 gauss is 2.1×10^5 rad/sec. On the other hand, the electron density becomes much higher than that of the ion density. It seems that the thermal ions gain energy from the subsequent quantum interaction of the electrons with the radiation field of the laser beam by the inverse bremsstrahlung process.⁹ Already in a field of 100 gauss, the maximum radius of the spiral on which most thermal electrons travel is about 0.3 mm and the cyclotron frequency of the electrons is 1.8×10^9 rad/sec. During the laser pulse duration the majority of the thermal electrons, therefore, stay within the laser beam (spot diameter 0.5 mm), whereas, without a magnetic field, only a small fraction (less than 1%) of the thermal electrons would remain.

After having reached this confinement state of the thermal electrons with a magnetic field in the order of 100 gauss, any further constriction of the electron stream no longer increases the photon-electron interaction so drastically, since the photon density can be considered as unchanged and the electron stream density increases approximately by the same factor as the actual cross section of the electron stream decreases. Only the

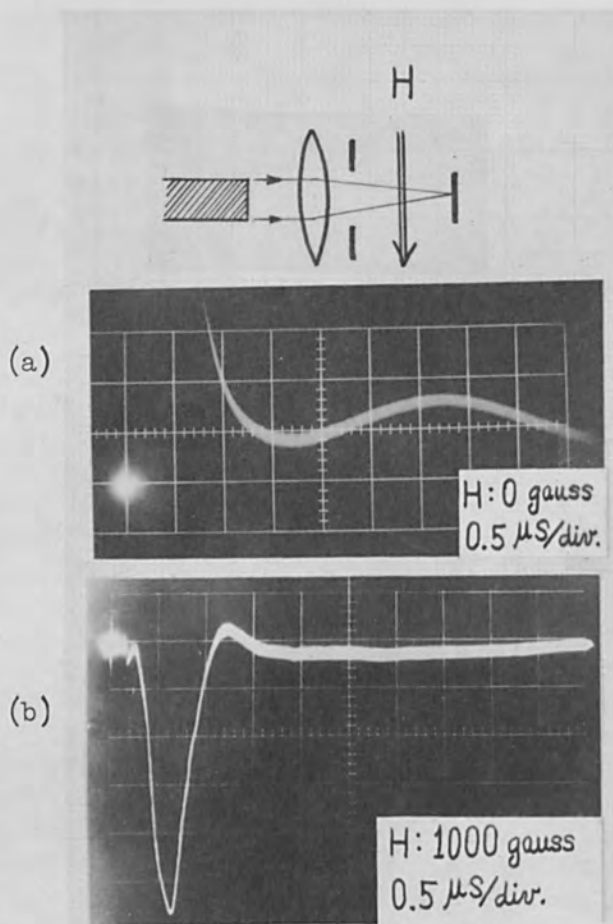


FIG. 7.—Oscilloscope trace of charged particle emission from tantalum in magnetic field.

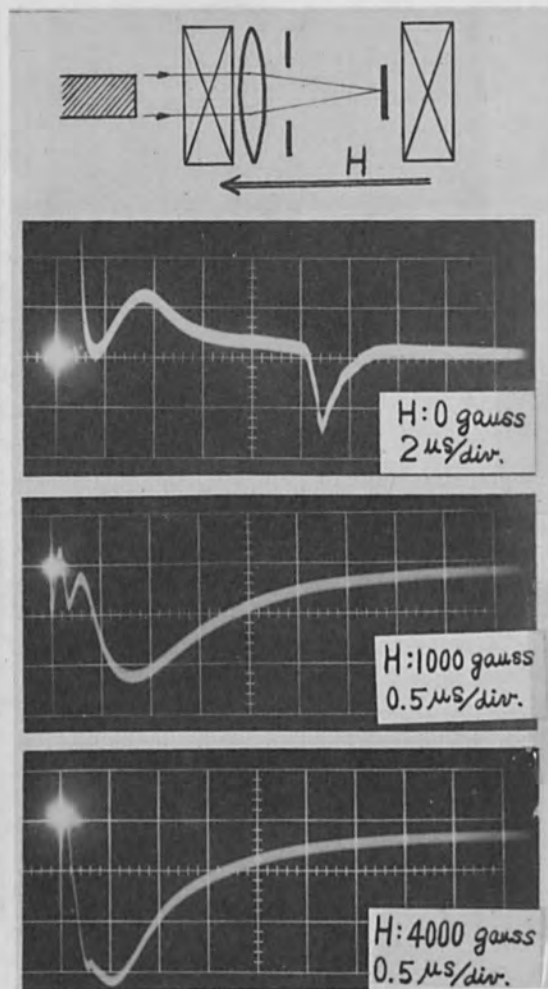


FIG. 8.—Oscilloscope trace of charged particle emission from tantalum in magnetic field.

slight increase of the number of electrons entering the laser beam due to the fast tail of the thermal electron distribution and the slow increase of the ion density seem to be the causes for the continued much slower increase of the ion energy with the magnetic field.

One of the authors (H. Schwarz) would like to thank the Japan Society for Promotion of Science for their generous grant which made it possible to perform part of this work during the 1966 summer vacation.

REFERENCES

1. R. E. Honig, Appl. Phys. Letters 3: 8, 1963; W. L. Knecht: *ibid.* 6: 99, 1965.
2. S. Namba, P. H. Kim, S. Nakayama, and I. Ida, Japan. J. Appl. Phys. 4: 153, 1965.

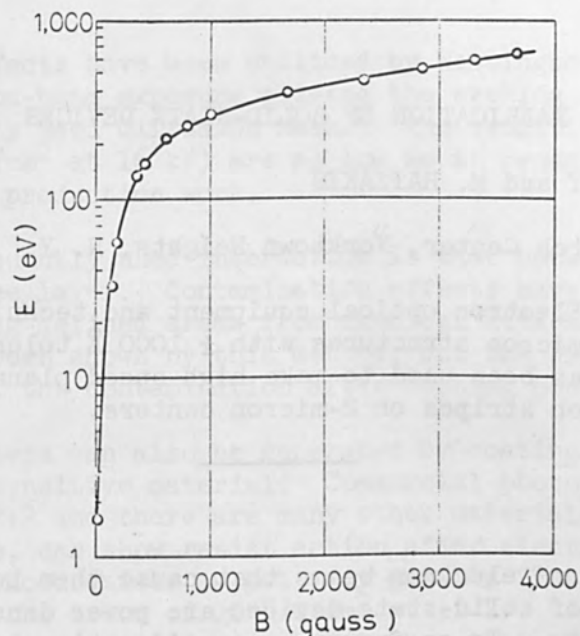


FIG. 9.—Relation between ion energy of second peak and magnetic field strength B applied perpendicularly to impact surface.

3. S. Namba, P. H. Kim, and A. Mitsuyama, *J. Appl. Phys.* 37: 3330, 1966.
4. W. I. Linlor, *Appl. Phys. Letters* 3: 210, 1963; *Phys. Rev. Letters* 12: 383, 1964.
5. S. Dushman, "Vacuum Technique," John Wiley, New York, 1949.
6. K. H. Kingdom and I. Langmuir, *Proc. Roy. Soc.* 107 (A): 61, 1925.
7. S. Namba et al., *Japan. J. Appl. Phys.* 6: 273, 1967.
8. H. Hora, D. Pfirsch, and A. Schlüter, *Z. Naturforsch.* 22a: 278, 1967.
9. J. K. Wright, *Proc. Phys. Soc.* 84: 41, 1964; B. A. Tozer, *Phys. Rev.* 137 (A): 1665, 1965.

ELECTRON-OPTICAL FABRICATION OF SOLID-STATE DEVICES

R. F. M. THORNLEY and M. HATZAKIS

IBM Watson Research Center, Yorktown Heights, N. Y.

ABSTRACT. Electron optical equipment and techniques capable of fabricating sub-micron structures with $\pm 1000 \text{ \AA}$ tolerances are described. The technology has been used to make high-speed planar silicon transistors with 1-micron stripes on 2-micron centers.

INTRODUCTION

The virtues of electron beams that cause them to be considered for the fabrication of solid-state devices are power density, resolution, and deflectability. To go from mere consideration to active utilization requires the electron beam operation to be critically compared with alternative technologies. If this comparison is made, the characteristic that retains its initial promise is that of resolution, since the performance of the competing optical technology is limited by the wavelength of light. This "light barrier" is usually considered to limit device dimensions to greater than 1 to 3 microns, depending on a number of factors such as yield, number of operations, operator skill, and so on. Beyond this barrier, electron optics offer the only known approach to the fabrication of microstructures.

In semiconductor technology, a reduction in device dimensions has always resulted in improved high-frequency performance if the doping parameters are optimized for the new size. Since there is no obvious reason to expect a break in this trend at the light barrier, it appears worthwhile to investigate the characteristics of devices having dimensions beyond this limit.

In any semiconductor structure, it is necessary to form p, n, or intrinsic areas in the bulk of the semiconductor and insulators and metallized areas on the surface. Since the fabrication process is normally a sequential one, one must also be able to locate accurately one part of the structure with respect to those previously made. Current practice uses detail down to about 2.5 microns with registrations of 0.5 micron. Experimental units have been made with stripe widths down to 1 micron.

INTERACTION MECHANISMS

One aspect of electron-beam technology is the high energy density obtainable. This characteristic may be utilized to raise the temperature locally, permitting thermal diffusion of previously deposited surface dopants to take place.¹ The difficulty with this process is the poor resolution obtainable since the lifetime of the hot spot must be sufficiently long (about 1 sec) for significant dopant diffusion to take place. During this period, the heat also diffuses, blurring the boundaries of the active area.

Radiation effects have been utilized by Westinghouse, where it was found that electron-beam exposure altered the etching rate of silicon dioxide, a commonly used diffusion mask.² The sensitivities reported (around 1 coulomb/cm² at 16 kV) are so low as to render the process impracticable for production work.

The most frequently used interaction is that between the beam and a temporary surface layer. Contamination effects have been used to form a resist protecting defined areas from chemical attack.³ The highest resolutions have been shown by this method, but the exposure rate is slow and the removal of the contamination after etching poses severe problems.

A resist pattern can also be generated by coating the semiconductor with a radiation-sensitive material. Commercial photoresists have been used in this way,^{4,5} and there are many other materials which, although not photosensitive, can show resist action after electron exposure. The sensitivities of photoresists do not vary greatly from one material to another, being of the order of 10⁻⁵ C/cm² at 15 kV. Although this sensitivity is approximately 1000 times less than that of the least sensitive silver halide emulsion, it is still sufficient to allow high-production systems to be designed. If the registration adjustments (positioning of the beam relative to detail on the workpiece) are carried out by direct observation of the surface with the electron beam, the use of electron-sensitive coatings may present problems. Any prolonged observation period may result in premature exposure and the coating itself may significantly reduce the contrast and resolution in the observed detail. The work to be described is based on the use of a positive electron resist.

OBJECTIVE

Since there are many possible ways of employing electron beams in microfabrication, it is necessary to define an objective before a reasoned choice of method can be made. The objective established for this paper is a transistor (Fig. 1) having a stripe width of 1 ($\pm 10\%$) micron, based on existing silicon planar technology as far as possible. This target is at the limit of standard optical processes but is not so extreme as to require a completely new semiconductor technology. The reward for success in this program should be an extremely high speed switching transistor, capable of changing states in substantially less than 1 ns.

ELECTRON-BEAM EQUIPMENT

The system is shown schematically in Fig. 2. The electron beam is formed by a two-lens system made up of commercial components. As used, the beam has a diameter of 1000 Å and carries 10⁻¹⁰ A at 10 kV. The silicon wafer is carried on a motor-driven x-y stage and can be rotated to bring a previous exposure line into parallelism with the stage axes. The system is evacuated by a 4-in. oil-diffusion pump without cold traps and operates in the range 10⁻⁵ to 10⁻⁶ torr. The beam is controlled by a synchronously scanned optical scanner viewing an 8.5 x 11-in. hand-cut mask. This size permits us to do our own artwork and avoids problems from dust or fingerprints.

The system can be operated as a scanning electron microscope for the

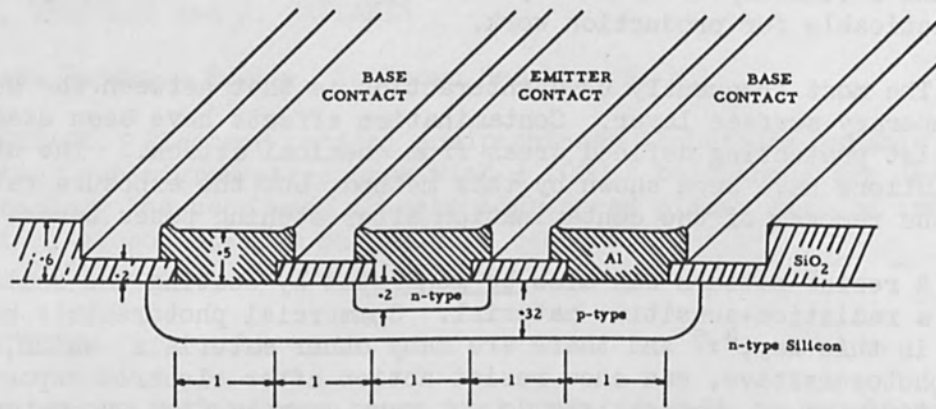


FIG. 1.—All dimensions are in microns.

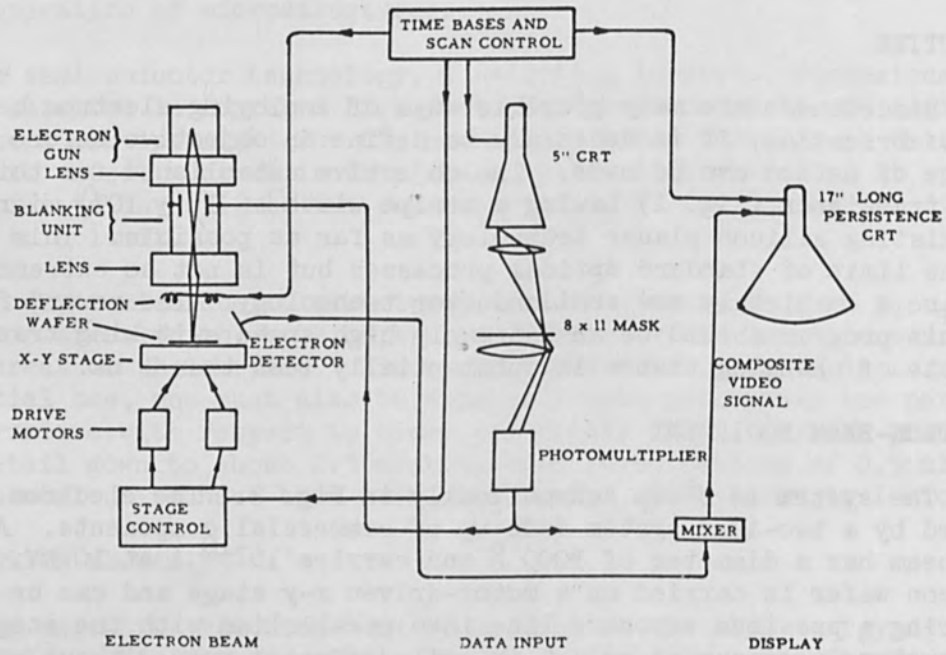


FIG. 2.—Schematic of the electron beam machining system.

registration operation. For this mode, the beam is scanned in a small raster over the semiconductor and the secondary electrons emitted are used to form a magnified picture of existing surface detail on a 17-in. monitor tube.

REGISTRATION

Ideally, each electron exposure should be positioned by reference to the previous operation. This procedure does not appear possible in practice because the varying nature of the operations performed on the semiconductor causes large variations in the contrast and signal-to-noise ratio of the secondary emission signal. In addition, any premature exposure of the resist would produce a false image, destroying the device. To avoid both of these problems, part of the scanned area is reserved for the registration operation. In this area, a suitable structure is formed before any of the device exposure work is initiated. This detail must have suitable secondary-emission characteristics, even when exposed through a resist, and must be compatible with and stable during conventional diffusion operations at about 1000°C. These requirements have been met by forming pedestals of evaporated silicon dioxide through a resist mask, as shown in Fig. 3. The size of the registration area is chosen to be larger than the maximum uncertainty in the position of the mechanical table so that, when the raster size is reduced for registration, the registration pedestal will definitely be scanned and the device area will not. The complete operation is shown in Fig. 4. The control mask in the optical scanner has an aperture in it corresponding to the pedestal on the wafer. The reduced scan is used with the optical scanner gating the electron beam. The secondary emission picture on the display tube then shows a square image generated by the optical scanner and in the square, the registration pedestal can be seen. Registration is performed by moving the beam with auxiliary deflection coils until the pedestal is symmetrically placed with respect to the scanner aperture. The positive resist used is exposed during registration and with normal processing, would expose the pedestal to etchants that would drastically modify or destroy it. This trouble is avoided by a deliberate overexposure of the registration area, which reverses the action of the resist and protects the pedestal. However, round the edge of any overexposed area, there is a narrow, correctly exposed area which does etch, so that the registration pedestal becomes surrounded by a series of fringes as the semiconductor proceeds through successive operations.

Automatic-registration methods based on analysis of the secondary-emission signal have been shown to work but are not currently employed.

RESULTS

Figure 5 is an optical micrograph of a device with 0.001-in.² contact lands. The symmetry of the fingers indicates that a registration accuracy of at least 2000 Å has been achieved. Figures 6 and 7 are electron micrographs showing the registration accuracy and the form of the metalization over the oxide step.

The first devices made in the above manner with a nonoptimized diffusion cycle had f_T 's of 2.2 GHz and current gains up to 25. It is

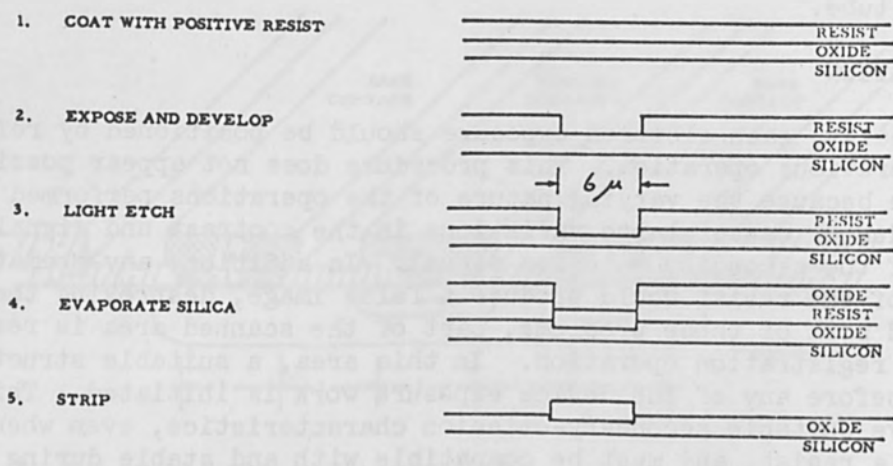


FIG. 3.—Fabrication of registration marks.

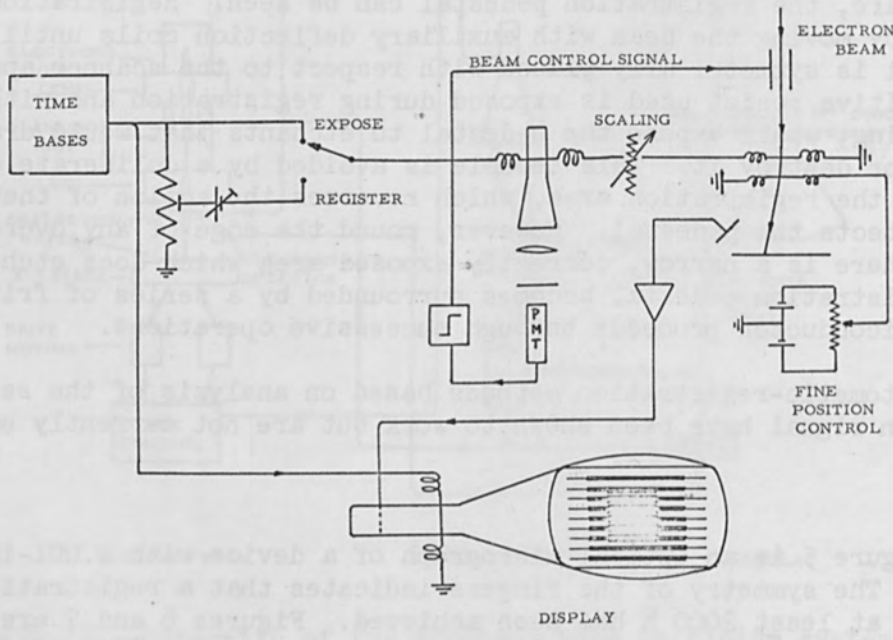


FIG. 4.—Registration.

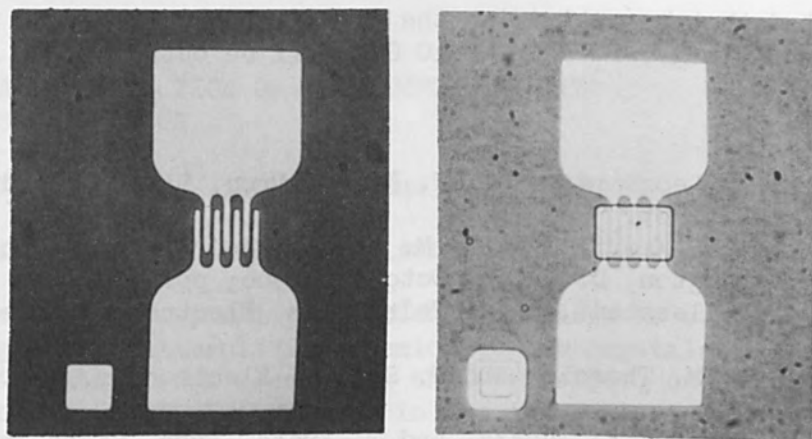


FIG. 5.—Metallized structures (1 in. = 30 μ).

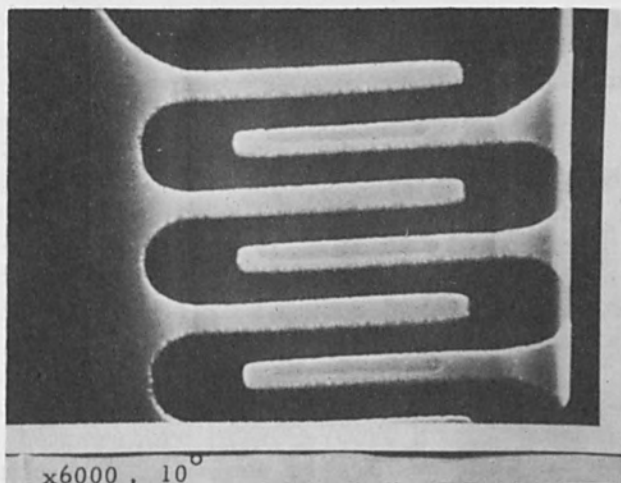


FIG. 6.—Electron micrograph showing registration achieved.

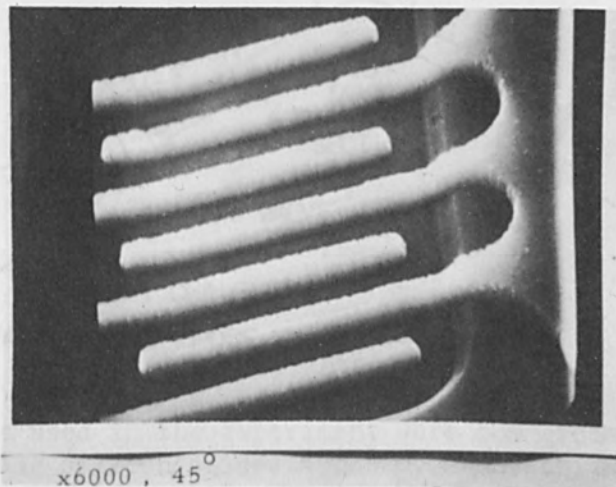


FIG. 7.—Electron micrograph showing metal structure over oxide step.

anticipated that by optimizing the diffusion processes and improving the contact metallurgy, f_T 's up to 10 GHz will be obtainable.

REFERENCES

1. F. W. Leonhard and C. T. Naber, Proc. Electron and Laser Beam Symp.: 97-115, 1965.
2. T. W. O'Keefe, and R. M. Handy, Report of Electron Devices Meeting, Washington, D. C., 17 October, 1966; pp. 125-126.
3. G. Möllenstedt, Proc. Third Symp. Electron Beam Technology, 1961; pp. 340-357.
4. R. F. M. Thornley and T. Sun, J. Electrochem. Soc. 112: 1151-1153, 1965.
5. K. Kanaya, K. Tanaka, and T. Yuasa, Proc. Sixth Intern. Congress Electron Microscopy, Kyoto, 1966; pp. 280-282.

EXPERIMENTAL DISTRIBUTION OF IONS IMPLANTED INTO
SINGLE-CRYSTAL SILICON

W. J. KLEINFELDER, W. S. JOHNSON, and J. F. GIBBONS

Stanford University, Stanford, California

In recent years, ion implantation has arisen as a useful method of introducing doping elements into semiconductor crystals. To be able to design device structures created by this technique, one must know the distribution of the implanted ions in the substrate as a function of the various implant parameters. Among the more important variables are energy, dose, and direction of implant as well as type of dopant and substrate material. With this knowledge, it is a simple matter to synthesize almost any desired distribution by superimposing several implants.

Because of its present technological importance, silicon doped with elements from groups III and V of the periodic table is of great interest. In this paper, we present experimental measurements of impurity distributions resulting from ^{11}B , ^{14}N , ^{31}P and ^{75}As implants in single crystal silicon substrates.

The apparatus used in the experiments was designed and constructed specifically for implantation of ions in semiconductor materials. This apparatus has been described in more detail elsewhere;¹ however, the general construction of this equipment is illustrated in Fig. 1. It is capable of implanting ions into targets under the following conditions:

- (1) Ion energies of 0-100 keV
- (2) Beam alignment of $\pm 3^\circ$ to the target surface
- (3) Target temperature of 20° - 700°C during bombardment
- (4) Monatomic ion beam densities of up to $1 \mu\text{A}/\text{cm}^2$
- (5) Beam uniformity of $\pm 5\%$ over an area of 0.5 cm^2

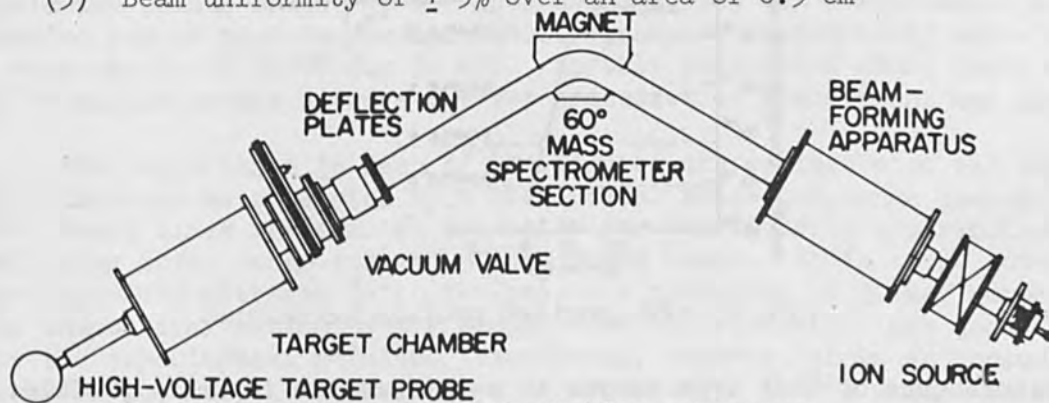


FIG. 1.—Ion implantation apparatus.

The crystals used in the experiment were commercially available semiconductor grade silicon slices about 0.01 in. thick, cut parallel to the $\{111\}$ face to within $\pm 2^\circ$. The material was mechanically and chemically polished so that the resulting surfaces were as smooth as could be obtained and free from residual stress. Just prior to being

bombarded the wafers were chemically cleaned by being washed in HF and then boiled in dilute solutions of $\text{HN}_4\text{OH-H}_2\text{O}_2$ and $\text{HCOOH-H}_2\text{O}_2$. This process results in an oxide of about 50 Å being formed on the silicon surface.

Various methods are available for determining the distribution of the impurities within the silicon wafer. The most successful technique that has been used in the past involves implantation of radioactive isotopes of desired elements. Radioactivity counts made after successive removal of thin layers from the wafer surface serve to determine the distribution of impurities as a function of depth. This method has been used in determining the distribution of ion implanted phosphorus 32 in silicon² and could conceivably be used for other heavy elements in either group III or group V. Unfortunately, there are no useful radioactive isotopes of the lighter group III or group V elements.

Since all group III and group V elements are electrically active in silicon this property can be used in a determination of the distribution of all these elements. There are numerous methods of determining the distribution of impurities based on electrical activity. Most of these methods (e.g., differential conductivity, spreading probe, capacity variation) have been attempted, but the method of pn junction depth measurement to be described has thus far yielded the most significant information.

In this method the impurity profile is generated from a number of pn junction depth measurements made in samples of differing background impurity concentrations but implanted under the same conditions. If a sample of silicon containing a known background concentration is bombarded with a dopant which produces free carriers of a type opposite to that of the background impurity, then a pn junction will be formed at the point where the background impurity concentration is equal to the introduced impurity concentration. As shown in Fig. 2, the combination of many

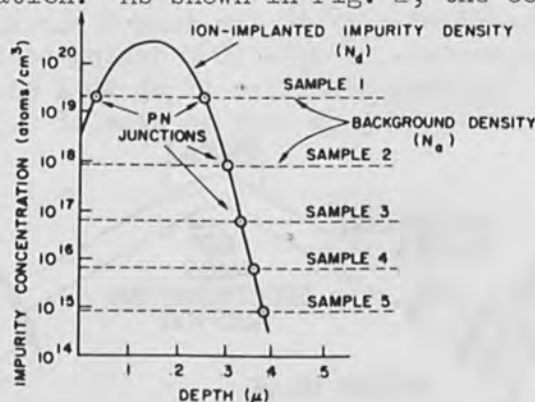


FIG. 2.—PN junction profile technique.

measurements of this type serves to construct the impurity profile. It is to be noted that this method yields accurate results only if the junction is well defined; that is, if the impurity has a maximum concentration significantly above the background concentration of the sample. For this reason, this method is not useful either in locating the peak of the profile accurately or in determining the shape of the distribution within about one order of magnitude of the peak. This method is useful, however, in tracing the impurity profile over six or seven orders of magnitude

below this region.

To use this technique in determining impurity profiles, the depth at which the electrical pn junction is formed within the substrate must be measured very accurately. This measurement may be made by refining a very simple method used in the semiconductor industry for some time. This technique consists of lapping the silicon wafer at a small angle (about 0.1°) to the surface so that the junction in the material is exposed on the lapped surface. The electrical junction may then be made visible by one of two methods: (1) exposing the junction to intense illumination and wetting the surface with a solution of 50% HF to which a small amount (5 drops to 50 ml) of HNO_3 has been added; or (2) applying a solution to the surface similar to the above but with CuNO_3 in place of the HNO_3 and without additional illumination. In either case, a stain is observed that delineates the electropositive from the electronegative material. The depth of the junction may then be determined either by measuring the angle of the lapped surface to the wafer surface and the linear distance from the junction to the edge of the lapped region or by using an optical interference microscope. With the latter method, an accuracy of $\pm 250 \text{ \AA}$ may be obtained.

By this technique the distributions of boron, nitrogen, phosphorus, and arsenic ions implanted at energies of 30 and 50 keV into the $\{111\}$ face of single-crystal silicon have been determined. The results of these measurements are shown in Fig. 3 for boron, Fig. 4 for nitrogen, Fig. 5 for phosphorus, and Fig. 6 for arsenic. The surface concentration in each case was determined by noting the background concentration at which the surface changed conductivity type as measured by a thermoelectric probe. The peak of the 50-keV nitrogen profile was estimated by spreading probe measurements.

In all but one case, the target material was held at a temperature of 625°C during bombardment and for a period of 10 min thereafter to help eliminate the damage introduced during the bombardment process. For the indicated points on the 50-keV phosphorus curve, the bombardments were carried out at room temperature and the samples subsequently annealed at a temperature of 625°C for 30 min. In this particular case, there appears to be no difference between the two processes of bombardment and annealing.

The solid lines in each of the figures are estimates of the impurity distributions as predicted by a statistical projected range theory.^{3,4} The dashed lines are similar estimates for the impurity distributions but using total range instead of projected range. It is to be noted that for boron and nitrogen (with the possible exception of 30-keV boron ions), the theoretical estimates for projected-range statistics are good fits for the experimental results. Phosphorus, however, shows an unusual behavior in that the distribution is exponential ($e^{-\alpha x}$) while the simple theory indicates that the curve should be approximately Gaussian. This exponential behavior of the phosphorus distributions is in agreement with the results reported using a radiotracer technique.² It is not clear yet whether this behavior is due to a diffusion mechanism (which may be suggested by the unusual diffusion constant of phosphorus in silicon at higher temperatures) or by a channeling mechanism which would allow the ions to penetrate to greater distance owing to the regularity

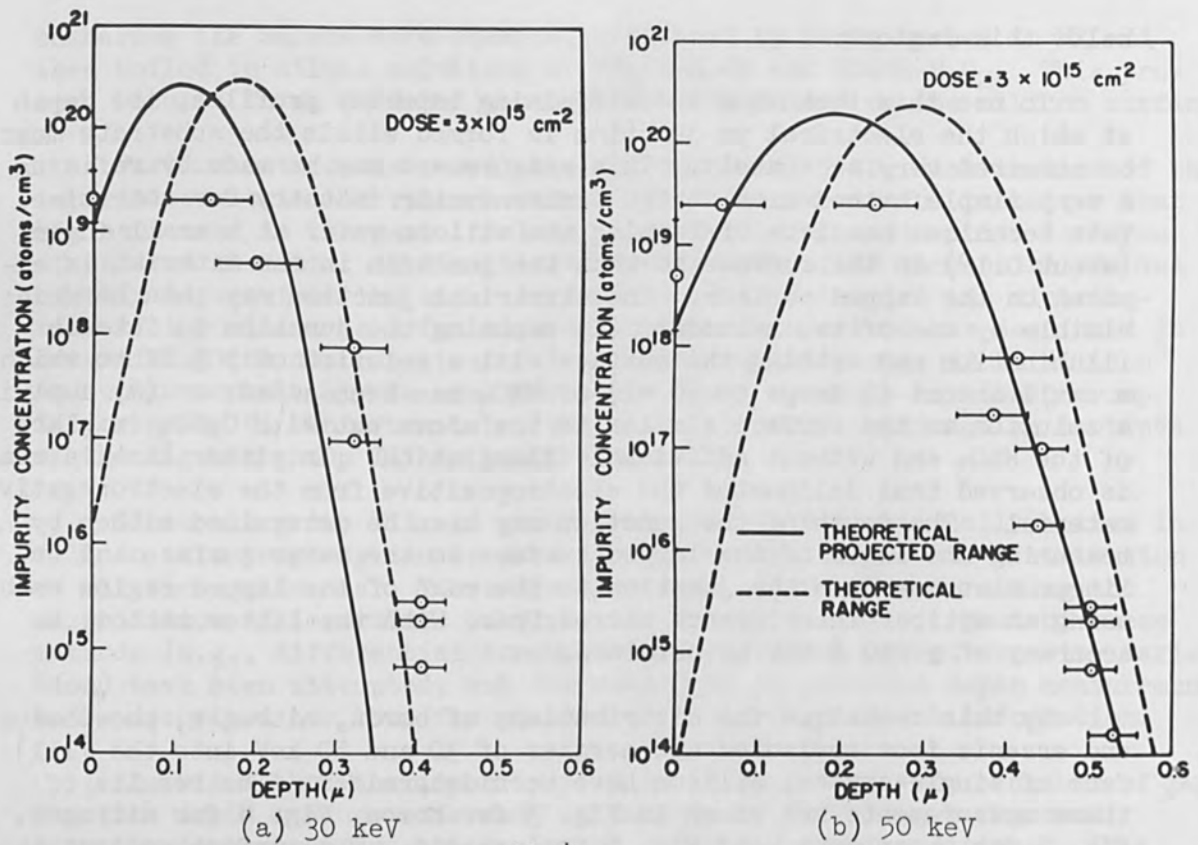


FIG. 3.—Distribution of $^{11}\text{B}^+$ ions in a silicon substrate.

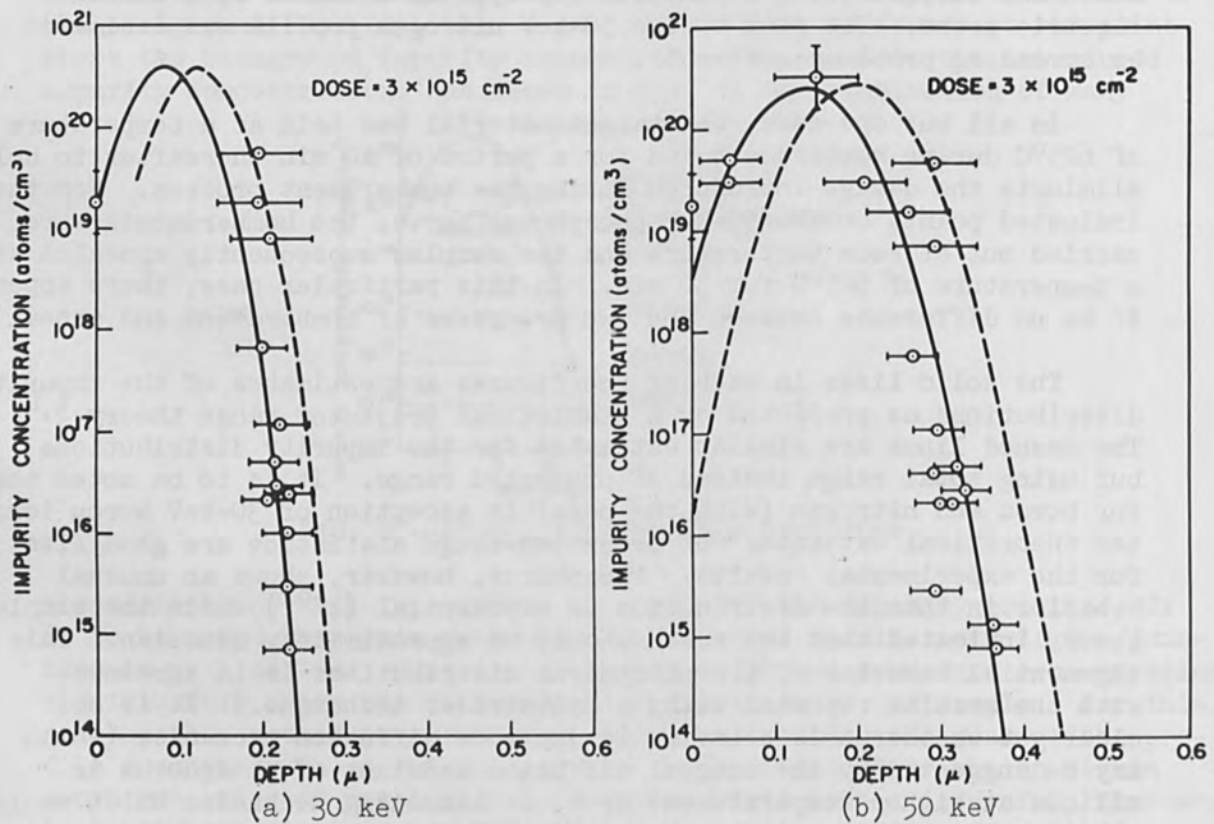


FIG. 4.—Distribution of $^{14}\text{N}^+$ ions in silicon substrate.

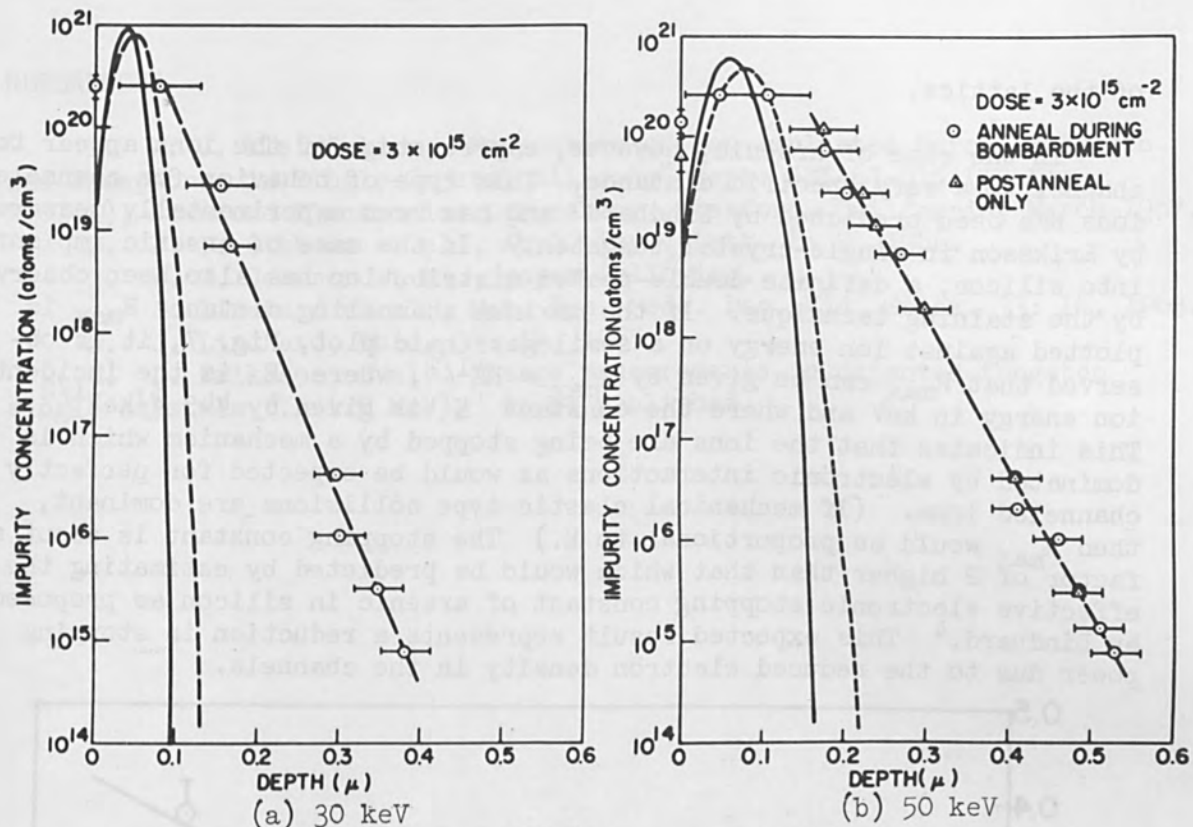


FIG. 5.—Distribution of $^{31}\text{P}^+$ ions in a silicon substrate.

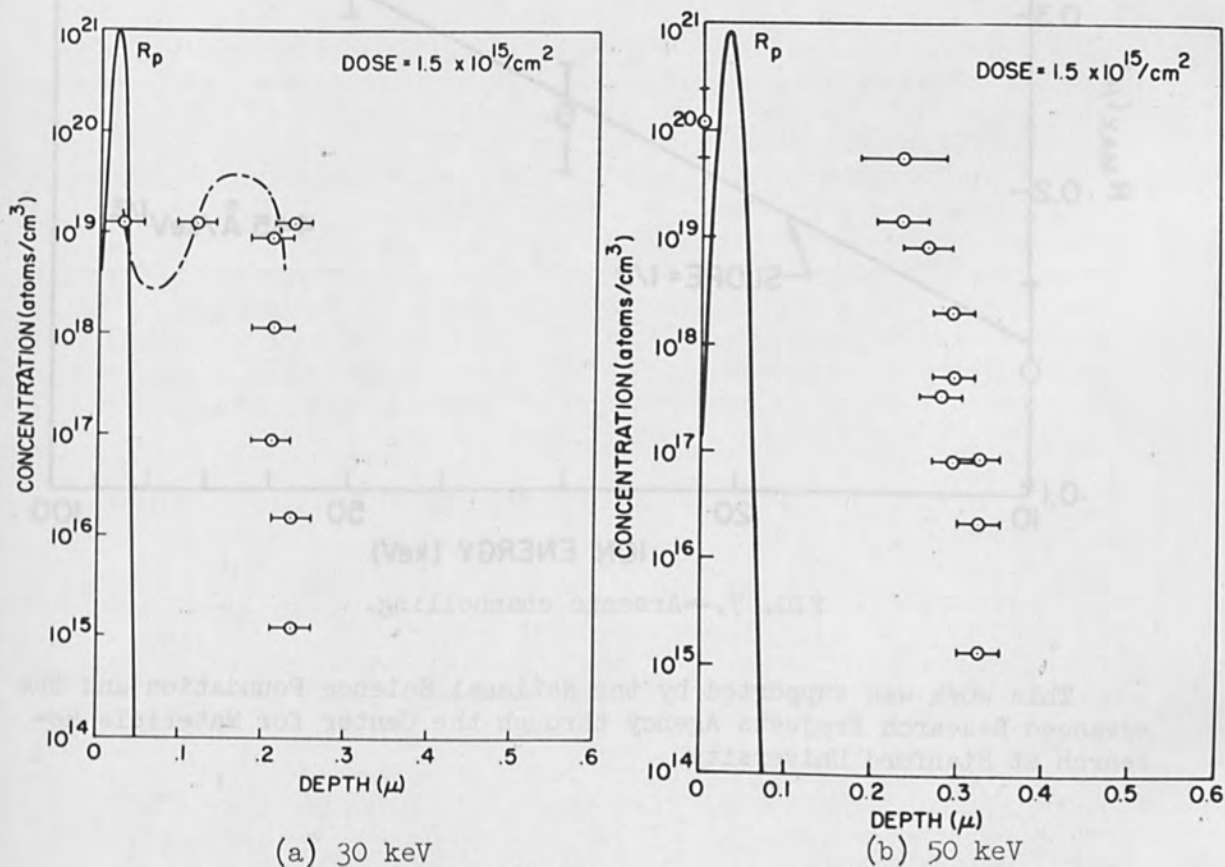


FIG. 6.—Distribution of $^{75}\text{As}^+$ ions in a silicon substrate.

of the lattice.

In the case of arsenic, however, a percentage of the ions appear to channel to a very specific distance. This type of behavior for channeled ions has been predicted by Lindhard⁵ and has been experimentally measured by Eriksson in single-crystal tungsten.⁶ In the case of arsenic implanted into silicon, a definite double-peaked distribution has also been observed by the staining technique. If the maximum channeling distance R_{\max} is plotted against ion energy on a semilogarithmic plot, Fig. 7, it is observed that R_{\max} can be given by $R_{\max} = KE^{1/2}$, where E is the incident ion energy in keV and where the constant K is given by $445 \text{ \AA}/\text{keV}^{1/2}$. This indicates that the ions are being stopped by a mechanism which is dominated by electronic interactions as would be expected for perfectly channeled ions. (If mechanical elastic type collisions are dominant, then R_{\max} would be proportional to E .) The stopping constant is about a factor of 2 higher than that which would be predicted by estimating the effective electronic stopping constant of arsenic in silicon as proposed by Lindhard.⁴ This expected result represents a reduction in stopping power due to the reduced electron density in the channels.

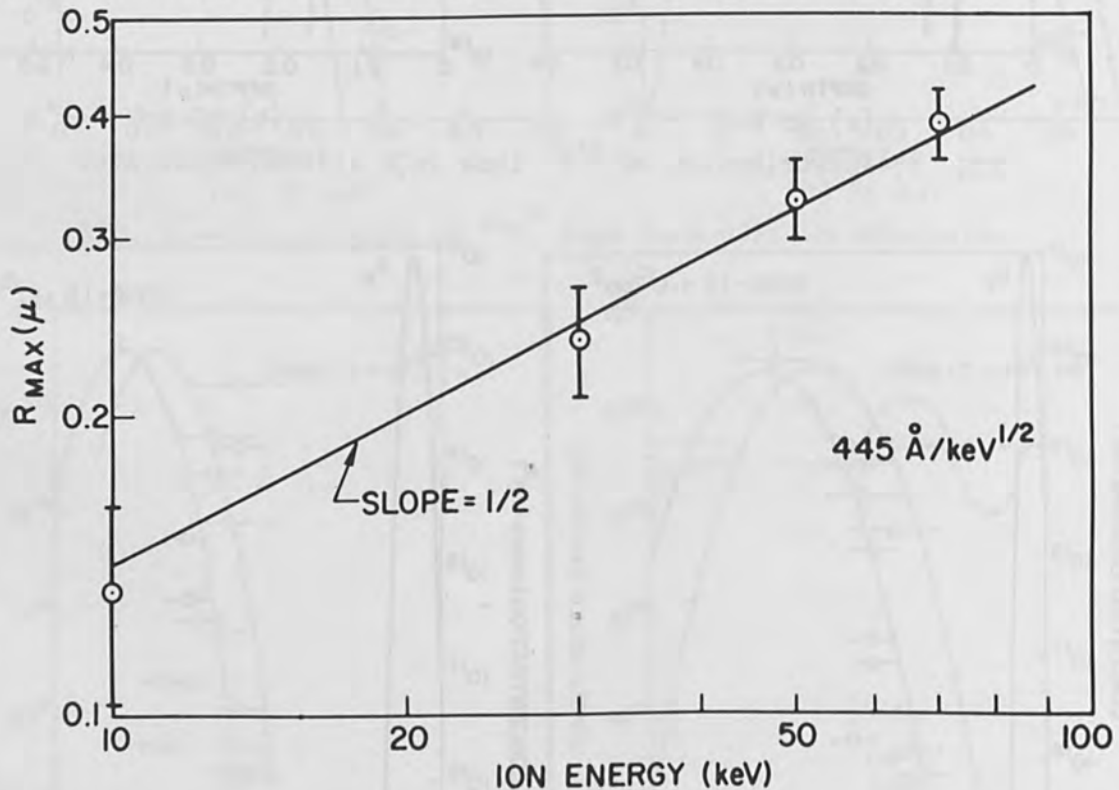


FIG. 7.—Arsenic channelling.

This work was supported by the National Science Foundation and the Advanced Research Projects Agency through the Center for Materials Research at Stanford University.

REFERENCES

1. W. J. Kleinfelder, "Properties of Ion-Implanted Boron, Nitrogen and Phosphorus in Single-Crystal Silicon," Rept. SEL-67-015 (TR-No. K701-1), Stanford Electronics Laboratory, Stanford, California, March 1967.
2. J. F. Gibbons et al., Appl. Phys. Lett. 8: 2, 1966.
3. W. S. Johnson et al., paper following.
4. J. Lindhard et al., Mat. Fys. Medd. Dan. Vid. Selsk. 33: 14, 1963.
5. J. Lindhard, ibid. 34: 14, 1965.
6. L. Eriksson et al., "Range measurements in oriented tungsten single crystals (.1-1.0 MeV)," to be published.

PROJECTED RANGE CALCULATIONS FROM A STATISTICAL MODEL

W. S. JOHNSON, W. J. KLEINFELDER, and J. F. GIBBONS

Stanford University, Stanford, California

INTRODUCTION

Ion implantation is currently being studied as a means for doping semiconductors. To use this technique successfully for device design, one must be able to predict the dopant distributions in the substrate. These distributions can be obtained directly by measurements of implanted specimens. Information obtained by this method is presented in the preceding paper.

In addition, it is useful to be able to make theoretical predictions of impurity profiles based upon physical models. This approach has the advantage of easy extension to new dopants and new substrates for which in some cases direct measurements may be difficult. Such an analysis can also aid in obtaining a better physical understanding of the processes involved in the stopping of ions by matter. In this paper we shall present a statistical theory for implanted profiles.

MODEL

We are interested primarily in two (related) phenomena: how a particle loses energy and how a particle is deflected while traversing a section of material. We shall assume that energy loss can be divided into two independent categories corresponding to collisions with the substrate electrons and collisions with the atomic nuclei. The electronic collisions are represented by a differential cross section $d\sigma_e(E,T)$, where T is the energy transferred in a collision and E is the ion energy before the collision. Electronic encounters are assumed to be symmetrical in that negligible angular deflection is involved. Nuclear encounters are represented by $d\sigma_n(T,E)$ and are elastic in nature. The angular deflection in nuclear collisions is directly related to the energy loss T through conservation of momentum and energy and can be very large, especially for light ions.

The total differential cross section can be written as the sum of its components

$$d\sigma(T,E) = d\sigma_n(T,E) + d\sigma_e(T,E)$$

For the analysis we shall need the first and second moments of this cross section. The stopping cross section is given by

$$S(E) = \int_T T d\sigma(T,E) = S_n(E) + S_e(E)$$

The average square fluctuation in energy loss is

$$\Omega^2(E) = \int_T T^2 d\sigma(T,E) = \Omega_n^2(E) + \Omega_e^2(E)$$

The fluctuation in electronic energy loss is often negligible.

In the statistical model, the mean and squared fluctuations in energy are summed for all collisions. Such a summation requires that the individual collisions be statistically independent. This in turn requires that the substrate atoms be randomly located. Hence, the analysis only applies well to amorphous materials. In crystalline materials high correlation is often observed between consecutive collisions. An ion which initially starts down an open direction in the crystal tends to undergo only low angle scattering thus keeping it in this "channel." Such an ion loses an abnormally small amount of energy per unit distance traveled. The statistical model excludes the above correlations but, nevertheless, it is worthwhile to apply it to crystals for several reasons:

- (1) The model is the only simple analytic one presently available.
- (2) It can be reasonably applied to light ions which do not channel easily.
- (3) It can serve as a starting point for more complex analyses.

Consider a particle traversing a small thickness of matter. The probability for transferring an energy T must be proportional to the density of scattering centers N , proportional to the cross section for that energy transfer $d\sigma$, and proportional to the thickness under consideration δx . Thus we must have as the probability for an energy transfer T , $N\delta x d\sigma$, and as the probability for any collision at all, $N\delta x \int_T d\sigma$ and finally as the probability of no collision at all, $1 - N\delta x \int_T d\sigma$.

As a first approximation to the problem, we might simply use the probabilities above and observe that the expected energy loss in the thickness considered is

$$\langle \delta E \rangle = - \int_T N\delta x T d\sigma$$

Passing to the differential limit gives

$$\left\langle \frac{dE}{dx(E)} \right\rangle = NS(E)$$

Then, since the stopping point for the particle corresponds to $\langle R(E_0) \rangle = \langle x(0) \rangle$, where E_0 is the initial energy, we have

$$\langle R(E_0) \rangle = \int_0^{E_0} \frac{dE}{NS(E)}$$

The distance calculated here does not take into account the angular deflections the particle undergoes and consequently corresponds to the total zig-zag path length traversed. This is known as the (total) range (Fig. 1). Of much greater experimental interest is the distance the particle penetrates beneath the substrate surface—i.e., the projection of the total range upon the normal to the surface. This is the projected range R_p ; associated with that is the perpendicular range, R_\perp , which is

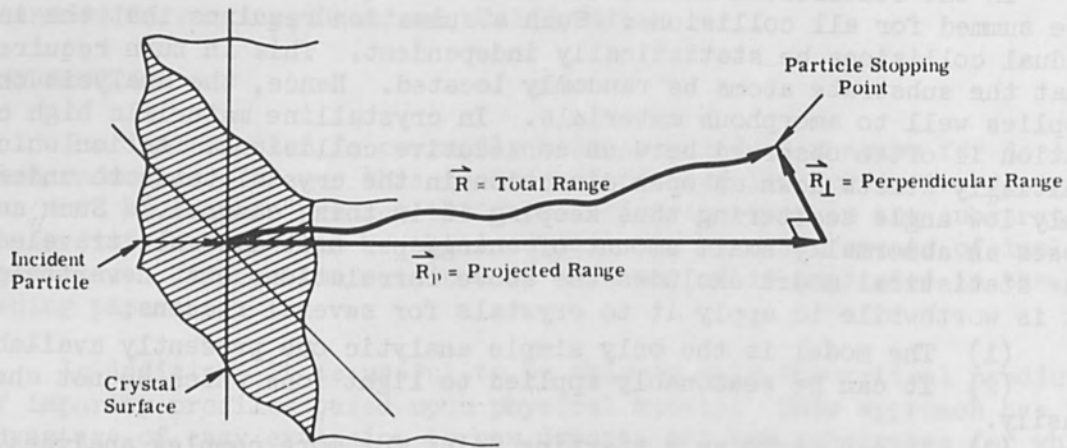


FIG. 1.—Definition of range parameters.

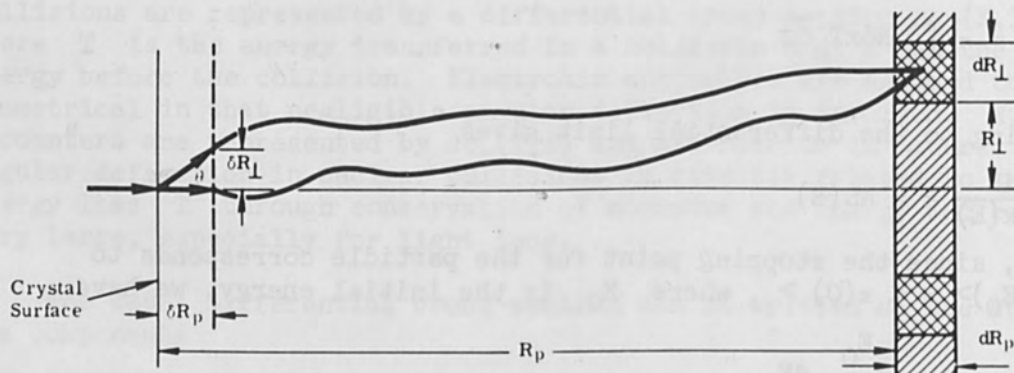


FIG. 2.—Diagram of statistical model.

the projection on a plane perpendicular to the normal.

Calculation of the projected range is somewhat more complicated. Our analysis follows that of Lindhard, Scharff, and Schiøtt^{1,2} and hence is known as the LSS theory. The model is presented in Fig. 2. A brief summary of the important points follows.

ANALYSIS

At left of Fig. 2 is the substrate surface. The arrow represents one particle impinging normally on this surface. The distance δR_p represents a differential layer of material. At right is a differential annular volume which measures dR_p by dR_\perp and is located a distance R_p from the surface. We wish to write down the probability that the particle will terminate its travel in this annulus. We shall use the following notation:

(1) $p(R_p, E)$ is the probability density function for projected range. Thus, the probability that a particle with initial energy E has a projected range between R_p and $R_p + dR_p$ is $p(R_p, E)dR_p$.

(2) Similarly, $q(R_\perp, E)2\pi R_\perp dR_\perp$ is the probability that a particle with initial energy E will have a perpendicular range between R_\perp and $R_\perp + dR_\perp$.

From Fig. 2 we may write down the above probabilities in an alternate way—from the viewpoint of the particle after it has traversed δR_p . Summing the conditional probabilities gives

$$p(R_p, E) = N\delta R_p \int d\sigma p(R_p - \delta R_p, E - T, \cos \theta) \\ + (1 - N\delta R \int d\sigma) p(R_p - \delta R_p, E)$$

and

$$q(R_\perp, E) = N\delta R_p \int d\sigma q(R_\perp, E - T, \cos \theta) \\ + (1 - N\delta R_p \int d\sigma) q(R_\perp, E).$$

The limit of these equations as $\delta R_p \rightarrow 0$ leads to differential equations for the probabilities. Then, multiplying the new equations by $R_p^m dR_p$ and $R_\perp^m dR_\perp$, respectively, and integrating, we obtain differential equations for any desired moments of the projected and perpendicular ranges. In particular, the equations for the first and second moments are

$$1 = \langle R_p(E) \rangle N \int d\sigma (1 - \cos \theta) + \frac{d \langle R_p(E) \rangle}{dE} N \int d\sigma T \cos \theta \quad (1)$$

$$2 \langle R_p(E) \rangle = \langle R_p^2(E) \rangle N \int d\sigma (1 - \cos^2 \theta) - \frac{1}{2} \langle R_\perp^2(E) \rangle N \int d\sigma \sin^2 \theta$$

$$+ \frac{d \langle R_p^2(E) \rangle}{dE} N \int d\sigma T \cos^2\theta + \frac{1}{2} \frac{d \langle R_1^2(E) \rangle}{dE} N \int d\sigma T \sin^2\theta \quad (2)$$

$$0 = \frac{1}{2} \langle R_1^2(E) \rangle N \int d\sigma (\cos^2\theta - 1) - \langle R_p^2(E) \rangle N \int d\sigma \sin^2\theta$$

$$+ \frac{d \langle R_p^2(E) \rangle}{dE} N \int d\sigma T \sin^2\theta + \frac{1}{2} \frac{d \langle R_1^2(E) \rangle}{dE} N \int d\sigma T (1 + \cos^2\theta) \quad (3)$$

The integrals above can all be evaluated simply for the case $T \ll E$. This is no restriction in the sense that if energy transfers approaching the particle's energy were common, then the particle would stop after only very few collisions. In this case, the whole statistical approach would be invalid. The limitations imposed by the above will be discussed later. From conservation of energy and momentum it is found that for nuclear collisions

$$\cos \theta = \frac{1 - \frac{1 + \mu}{2} \frac{T}{E}}{\sqrt{1 - T/E}} \quad (4)$$

where

θ = deflection angle of the particle

$$\mu = \frac{m^2}{m_1} = \frac{\text{mass of substrate atom}}{\text{mass of particle}}$$

For $T \ll E$ we have

$$\cos \theta \approx 1 - \frac{\mu}{2} \frac{T}{E}$$

For electronic collisions $\cos \theta = 0$. The integrals within Eqs. (1), (2), and (3) may be contained in the following definitions:

$$\alpha_1(E) \triangleq N \int d\sigma_n (1 - \cos\theta) \approx \frac{\mu}{2} \frac{NS_n(E)}{E}$$

$$\beta_1(E) \triangleq N \int T d\sigma_e + N \int T d\sigma_n \cos \theta \approx N \left[S_n(E) + S_e(E) - \frac{\mu}{2} \frac{\Omega_n^2(E)}{E} \right]$$

$$\alpha_2(E) \triangleq N \int d\sigma_n \sin^2\theta \approx \mu \frac{NS_n(E)}{E}$$

$$\beta_2(E) \triangleq N \int T d\sigma_e + N \int T d\sigma_n \left(1 - \frac{3}{2} \sin^2\theta\right)$$

$$\approx N \left[S_n(E) + S_e(E) - \frac{3\mu}{2} \frac{\Omega_n^2(E)}{E} \right]$$

If we add to these the definitions

$$\langle R_c^2(E) \rangle \triangleq \langle R_1^2(E) \rangle + \langle R_p^2(E) \rangle$$

and

$$\langle R_r^2(E) \rangle \triangleq \langle R_p^2(E) \rangle - \frac{1}{2} \langle R_1^2(E) \rangle$$

the differential equations become

$$\frac{d \langle R_p(E) \rangle}{dE} + \frac{\alpha_1(E)}{\beta_1(E)} \langle R_p(E) \rangle = \frac{1}{\beta_1(E)}$$

$$\frac{d \langle R_c^2(E) \rangle}{dE} = \frac{2 \langle R_p(E) \rangle}{NS(E)}$$

$$\frac{d \langle R_r^2(E) \rangle}{dE} + \frac{3}{2} \frac{\alpha_2(E)}{\beta_2(E)} \langle R_r^2(E) \rangle = \frac{2 \langle R_p(E) \rangle}{\beta_2(E)}$$

where

$$\langle R_p^2(E) \rangle = \frac{2 \langle R_r^2(E) \rangle + \langle R_c^2(E) \rangle}{3}$$

The solutions to these first-order equations are

$$\langle R_p(E) \rangle = \int_0^E \frac{dE'}{\beta_1(E')} \exp \left[\int_E^{E'} \frac{\alpha_1(E'')}{\beta_1(E'')} dE'' \right] \quad (5)$$

$$\langle R_c^2(E) \rangle = \int_0^E \frac{2 \langle R_p(E') \rangle dE'}{NS(E')} \quad (6)$$

$$\langle R_r^2(E) \rangle = \int_0^E \frac{2 \langle R_p(E') \rangle dE'}{\beta_2(E')} \exp \left[\int_E^{E'} \frac{3}{2} \frac{\alpha_2(E'')}{\beta_2(E'')} dE'' \right] \quad (7)$$

Computer programs have been written that perform these integrations using differential cross sections based on the Thomas-Fermi potential model of the atom. The possibility of multi-element substrates has been

included in these programs. Assuming that the different substrate elements act independently, the only changes necessary in Eqs. (5), (6), and (7) are to replace $\alpha_1(E)$, $\beta_1(E)$, $NS(E)$, $\alpha_2(E)$, and $\beta_2(E)$ by summations of functions of the same form over all elements. A typical set of results is shown in Fig. 3. Further specific results together with comparisons to experimental measurements are given in the preceding paper. We shall discuss here some general properties of the theory.

DISCUSSION

A feel for the effects of various parameters upon the accuracy of the statistical theory can be obtained by means of Fig. 4 which was originally presented by Bohr.³ The variables ζ and χ are defined

$$\zeta \triangleq \frac{b}{a}$$

$$\chi \triangleq \frac{b}{\lambda}$$

where

b = collision diameter

a = screening parameter

λ = deBroglie wavelength of particle divided by 2π .

A detailed discussion of these parameters cannot be presented here. Qualitatively, ζ measures the effect which the screening of the nuclear charge by its electrons has on a collision: $\zeta \gg 1$ implies distant collisions in which screening is important; $\zeta \ll 1$ implies close collisions in which the electrons are unimportant. The factor χ measures the extent of diffraction in the collision, thus indicating the applicability of classical mechanics. The interpretation here is somewhat more complicated; if $\zeta \ll 1$ then $\chi \ll 1$ implies quantum mechanics is necessary, but if $\zeta \gg 1$ then $\chi \ll \zeta$ implies the necessity for quantum mechanics. The parameter ζ varies inversely as the energy of the particle while χ varies inversely as the square root of the energy. Thus, in a full logarithmic plot such as Fig. 4, any particle slowing down by any means traces a straight line of slope 1/2.

Trajectories for several ions in a few substrates are drawn in the figure. The energy limits are all 50 keV to 5 ev. The lower energy is arbitrary except that zero cannot be used because zero energy corresponds to the point at infinity. This fact is immaterial, however, because the statistical theory breaks down well before even 5 ev.

It was mentioned earlier that $T \ll E$ was essential to the analysis. The maximum T occurs in a head-on collision and can be obtained from Eq. (4) by setting $\theta = 0$. This substitution gives

$$T_{\max} = \frac{4m_1 m_2}{(m_1 + m_2)^2} E$$

Therefore it can be seen that $T \ll E$ is satisfied for either extremely

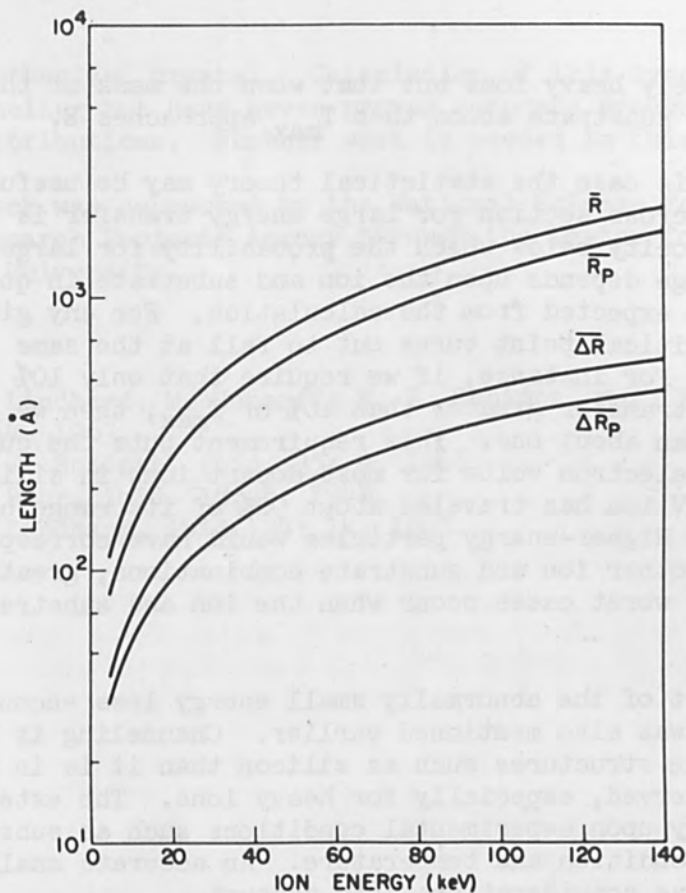


FIG. 3.—Total \bar{R} range \bar{R} , projected range \bar{R}_p , and standard deviation in total range $\Delta\bar{R}$ and in projected range $\Delta\bar{R}_p$ for ^{31}P and ^{28}Si .

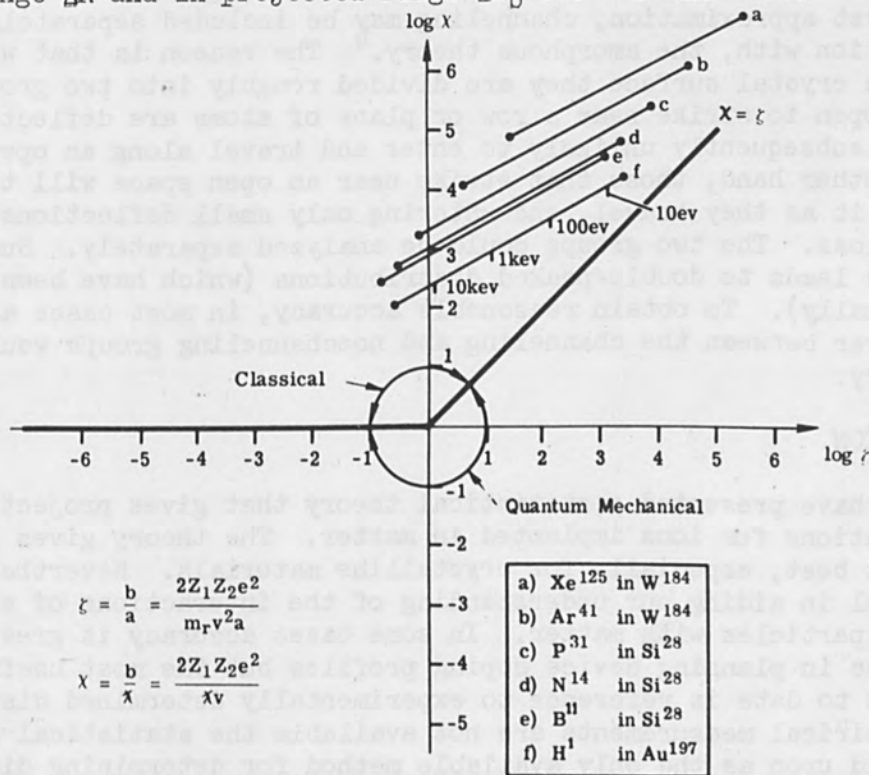


FIG. 4.—Bohr diagram showing trajectories of several combinations of ions and substrates. (Energy limits are 50 keV and 50 ev.)

light or extremely heavy ions but that when the mass of the ion approaches the mass of the substrate atoms then T_{\max} approaches E .

Even in this case the statistical theory may be useful. For large velocities the cross section for large energy transfer is relatively small. The velocity below which the probability for large energy transfer becomes too large depends upon the ion and substrate in question as well as the accuracy expected from the calculation. For any given accuracy, however, the critical point turns out to fall at the same ζ for any ion and substrate. For instance, if we require that only 10% of all collisions have an energy transfer greater than 10% of T_{\max} , then we find that $\log \zeta$ must be less than about one. This requirement puts the cutoff point at a few thousand electron volts for most dopant ions in silicon. Fortunately, a 50-keV ion has traveled about 90% of its range by the time it reaches 5 keV. Higher-energy particles would have correspondingly greater accuracy. For other ion and substrate combinations, great care must be exercised. The worst cases occur when the ion and substrate atoms are heavy.

The neglect of the abnormally small energy loss encountered by channeled ions was also mentioned earlier. Channeling is less severe in open crystalline structures such as silicon than it is in metals. However, it is observed, especially for heavy ions. The extent of channeling depends strongly upon experimental conditions such as substrate orientation, surface condition and temperature. An accurate analysis would have to take all these considerations into account.

Although no complete theory is yet available, there is evidence that as a first approximation, channeling may be included separately, but in conjunction with, the amorphous theory.⁴ The reason is that when ions strike a crystal surface they are divided roughly into two groups. Those that happen to strike near a row or plane of atoms are deflected widely and are subsequently unlikely to enter and travel along an open space. On the other hand, those that strike near an open space will tend to remain in it as they travel, encountering only small deflections and small energy loss. The two groups could be analyzed separately. Such an analysis leads to double-peaked distributions (which have been observed occasionally). To obtain reasonable accuracy, in most cases account of cross over between the channeling and nonchanneling groups would be necessary.

CONCLUSION

We have presented a statistical theory that gives projected range distributions for ions implanted in matter. The theory gives rough results at best, especially for crystalline materials. Nevertheless, it is useful in aiding our understanding of the interactions of energetic charged particles with matter. In some cases accuracy is great enough to be of use in planning device doping profiles but the most useful method for that to date is reference to experimentally determined distributions. When empirical measurements are not available the statistical approach must be relied upon as the only available method for determining distributions. One possible alternative is Monte Carlo calculation. In this method ions are actually followed from encounter to encounter as they traverse a

computer-synthesized crystal. Calculation of this type originally predicted channeling but have never proven accurate enough to give reliable complete distributions. Further work is needed in this area.

This work was supported by the National Science Foundation and the Advanced Research Projects Agency through the Center for Materials Research at Stanford University.

REFERENCES

1. J. Lindhard, M. Scharff, H. E. Schiøtt, Mat. Fys. Medd. Dan. Vid. Selsk. 33: 14, 1963.
2. H. E. Schiøtt, *ibid.* 35: 9, 1966.
3. N. Bohr, *ibid.* 18: 8, 1948.
4. J. Lindhard, *ibid.* 34: 14, 1965.

AN ULTRAHIGH-VACUUM SURFACE ELECTRON MICROSCOPE

D. E. MILLER and R. F. W. PEASE

Electronics Research Laboratory, University of California, Berkeley

INTRODUCTION

In most electron microscope columns the vacuum is of the order of 10^{-4} torr, so that during the course of a single exposure the specimen is continually bombarded with residual gas molecules. Some of these polymerize to form contamination which typically may form a layer¹ whose thickness increases at 5 \AA-sec^{-1} . Successful attempts to reduce the contamination to a level acceptable for the transmission electron microscope have been reported by Heide,² who used a liquid nitrogen trap in the specimen region. For certain examination of surfaces the conditions for cleanliness are considerably more stringent than those described by Heide and for this reason ultrahigh-vacuum techniques are employed.^{3,4} If the surface is to be examined using either secondary-electron emission or photo-electron emission the presence of a monolayer of absorbed atoms can cause gross changes in signal level.

The microscope described here employs ultrahigh-vacuum techniques to obtain a working pressure of 10^{-9} torr. The instrument is designed primarily for scanning electron microscopy but can also be used for electron diffraction and electron emission microscopy. At the time of writing the microscope has been constructed and the parts individually leak tested. Complete vacuum system tests are now under way.

MECHANICAL DESCRIPTION

The vacuum chamber consists of a large (12-in.-dia. x 12-in.-high) specimen area at the top of the column (Fig. 1). This specimen chamber is similar to a satisfactory ultra high vacuum chamber built at this Laboratory by W. G. Oldham.⁵ Stainless steel is used throughout except for a 2.5-in.-diameter quartz viewing window at the top. The large flanges at the top and bottom employ aluminum-foil gasket seals. The other flanges are commercially obtained and use copper gaskets. Although the large chamber is slower to pump, it allows considerable versatility for different specimen arrangements. A total of nine ports is provided.

The "floor" of the specimen chamber is vacuum brazed to an OFHC copper assembly (spray aperture cavity) which forms the vacuum wall in the region of the final lens polepieces. Thus the only part of the final lens inside the vacuum is the final polepiece. The spray aperture cavity is vacuum brazed to 0.5-in.-diameter stainless-steel tube which is heat treated and fits inside the bores of all the other electron lenses. Thus these lower lenses are entirely outside the vacuum. The bottom of the tube is sealed to the initial aperture cavity by a small diameter demountable seal developed in this laboratory (Fig. 2). The demounting of this seal makes it possible for the microscope to be disassembled without breaking any welded or brazed joints. The electron gun is mounted on the bottom of the initial

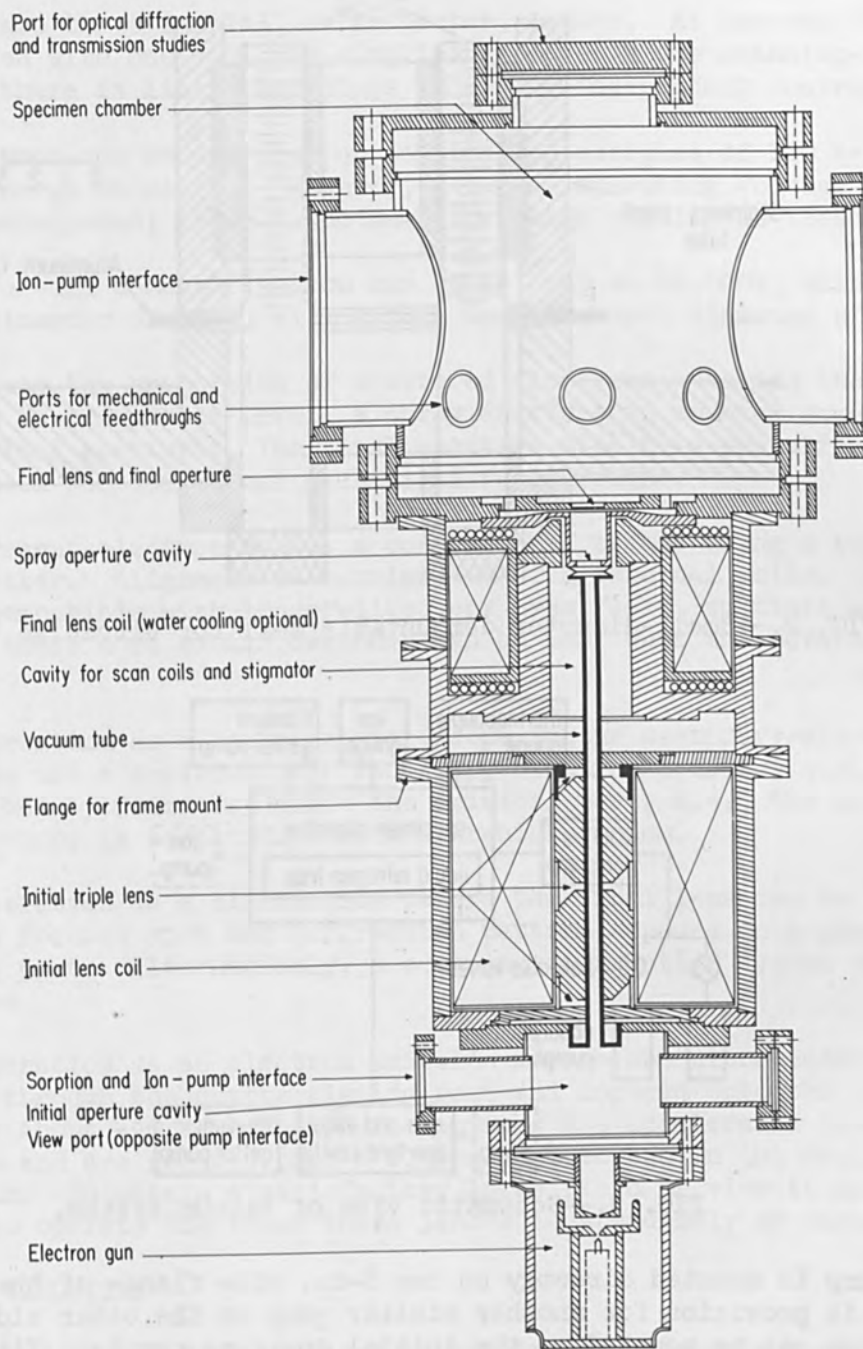


FIG. 1.—Cross section of column of UHV surface electron microscope.

aperture cavity using a commercially obtained flange. The microscope is designed for a bakeout temperature of 200°C.

PUMPING ARRANGEMENT (FIG. 3)

Roughing is carried out with two sorption pumps connected independently to the specimen chamber via bakable valves and an ion pump. This 100 l-sec⁻¹

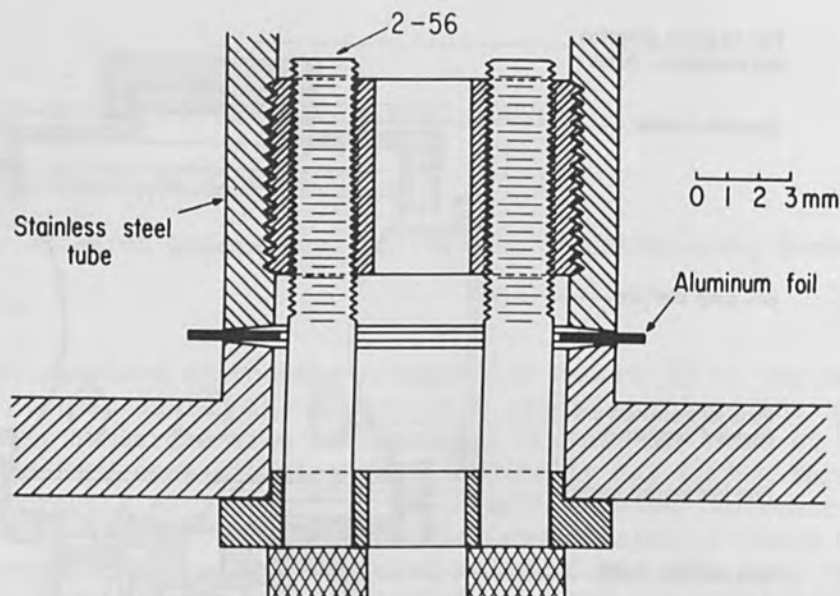


FIG. 2.—Small-diameter demountable seal for ultrahigh vacuum.

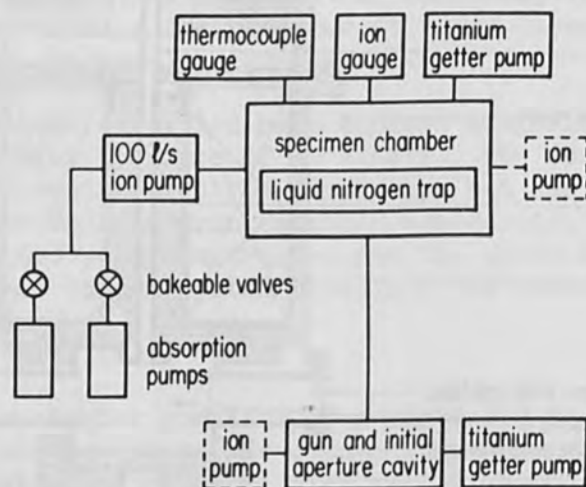


FIG. 3.—Schematic view of vacuum system.

ion pump is mounted directly on one 8-in. side flange of the specimen area. There is provision for another similar pump on the other side. A smaller ion pump can be mounted on the initial aperture cavity. Titanium sublimation pumps are mounted both on the specimen chamber and on the initial aperture cavity. Provision is also made for a liquid nitrogen trap in the specimen chamber.

ELECTRON OPTICAL ARRANGEMENT

The electron optics are similar to those of a high resolution ($100\text{-}\text{\AA}$) scanning electron microscope described by Pease and Nixon.⁶ The crucial item is the final, or objective, lens which employs the "pinhole" design with a spherical aberration coefficient $C = 1$ cm, a working distance of 0.5 cm, and a magnetic flux density of only a few gauss at the specimen.

There are three initial, or projector, lenses. At present these are all energized with one coil for simplicity since in the scanning-microscope mode there is little advantage in having independent control.

All lenses can be operated up to electron energies of 100 keV should such high energy be useful. However, a normal operating voltage of 20 to 30 kV is anticipated; there is no need for water cooling at these energies.

The over-all demagnification can be as high as 40,000x, which for a crossover diameter of 100 μ will give a Gaussian spot diameter of 25 \AA .

To reduce the proportion of scattered electrons entering the final aperture to an acceptable level, a spray aperture is mounted some distance below the final aperture. The final aperture itself is pre-aligned to avoid the need for additional mechanical feedthroughs.

The present electron gun is a conventional triode using a tungsten hairpin emitter. Alignment is carried out with external coils. The vacuum is compatible with longer-lived, or even field, emitters and conversion to these more exotic cathodes can be made when the advantage is practical.

For operation as a scanning microscope in the secondary-electron mode we intend to use a semiconductor secondary electron detector similar to that described by Gonzales⁷ since the critical part, i.e., the semiconductor junction, is compatible with ultrahigh vacuum.

For operation as a diffraction camera the final lens can be weakened so that the focused spot and diffraction pattern appears on a phosphor on the viewing port. Alternatively, a scanning diffraction system can be incorporated.

For operation as an electron emission microscope ultraviolet light is brought through the quartz viewing port and focused onto the specimen which is at about -40 kV. The photoelectrons are accelerated into the lens system and are focused onto a fluorescent screen in the region of the electron gun. To obtain a satisfactory large field of view it may be necessary to operate the lower three lenses independently of each other.

ASSOCIATED CIRCUITRY

Circuitry proven from previous operation has been used throughout. The scan generators, amplifiers, and video amplifier are identical to those described by Everhart, Pease, and Pedersen.⁸ All other circuitry has been obtained commercially.

SUMMARY

A versatile electron microscope has been built employing ultrahigh vacuum techniques. The microscope should enable the surfaces, free from contamination, to be examined using scanning electron microscopy, reflection electron diffraction, or electron-emission microscopy.

ACKNOWLEDGMENT

This work has been supported by the U. S. Air Force Avionics Laboratory under contract AF33(615)-3886 and by the Joint Services Electronics Program.

REFERENCES

1. A. E. Ennos, Brit. J. Appl. Phys. 4: 101, 1953.
2. H. G. Heide, in Proc. 5th International Congress on Electron Microscopy, Philadelphia 1962 (S. Breese, ed.), New York, Academic Press, 1962.
3. J. B. Marsh and H. E. Farnsworth, Surface Sci. 1: 3, 1964.
4. J. J. Lander, *ibid.* 1: 124, 1964.
5. W. G. Oldham, University of California (Electronics Research Laboratory), Semi-Annual Progress Report No. 1, 1965; p. 132.
6. R. F. W. Pease and W. C. Nixon, J. Sci. Inst. 42: 82, 1965.
7. A. J. Gonzales, see p. of the present volume.
8. T. E. Everhart, R. F. W. Pease, S. R. Pedersen, University of California (Electronics Research Laboratory), Technical Memorandum No. 66-11-4, 1965.

LIMITS OF ELECTRON-BEAM NONTHERMAL INTERACTIONS

T. H. P. CHANG

Cambridge Instrument Co., Cambridge, England

W. C. NIXON

Cambridge University, Cambridge

INTRODUCTION

In recent years, processes utilizing properties other than the thermal properties of an electron beam have shown promising applications in many aspects of microcircuit fabrication and of microrecording. These processes rely on the ability of an electron beam to produce a surface chemical reaction and can be divided into two main categories, polymerization processes and activated chemical deposition processes. In the first category, the electron beam is used to produce a polymer film by irradiating the surface in the presence of an organic compound. The organic compound used may be in the form of a vapor, such as silicone oil vapor, or it may be in the form of a solid, such as triphenylsilanol or a photoresist coating. The polymer film can be used as an insulator for thin-film microcircuitry or for thin-film cryotron fabrication. Work of this type has been reported by Christy,¹ Mann,² Haller and White,³ Allam, Stoddart, and Stuart,⁴ and Hill.⁵ Alternatively, the polymer film can be used as a mask to protect the underlying material from subsequent etching, a technique that is very useful for the fabrication of microcircuitry and for microrecording. Examples of polymer film used in this manner are the polymerized photoresist coating (Thornhill and Mackintosh,⁶ Thornley and Sun,⁷ and Broers⁸), the polymerized silicone oil film (Broers⁸ and Chang and Nixon⁹), and the polymerized triphenylsilanol (Buck and Shoulder¹⁰). Finally, the polymer film can also be used directly as a microrecording storage element (White and North¹¹). In the second category, a film is formed as a result of direct decomposition by electron-beam bombardment of a suitable chemical compound already present on the target surface. Both metallic and dielectric films have been produced in this way. For metallic films, the chemical used is usually an organometallic compound; a survey has been given by Ryan et al.¹² By using this method, a tin film has been formed from stannous chloride (Christy¹³), tin and lead films from tetrabutyltin and tetraethyllead respectively (Baker and Morris¹⁴), and tungsten film from tungsten hexycarbonyl (Hlavin and Fotland¹⁵). Insulating films such as silicate films have also been formed by this method, from tetraethylorthosilicate (Buck and Shoulder¹⁰).

Most of the work described above was done with a flood beam of electrons to produce a large-area film. This procedure, of course, makes it possible for tests and measurements to be carried out on the film more conveniently. However, the main objective of the process is to produce high-resolution patterns, and for that the ability to employ a very fine electron probe is highly desirable. This paper describes some

experimental results and theoretical considerations regarding the use of a fine electron probe for such applications.

CONTROLLED POLYMERIZATION OF SILICONE OIL VAPOR WITHIN A SCANNING ELECTRON MICROSCOPE

The monomer was placed outside the microscope and its vapor was bled into the specimen chamber through a needle valve and directed to the specimen by a small tube. The vapor pressure was varied by varying the monomer temperature or by the needle valve setting. The temperature of the specimen could be controlled.

A number of experiments on polymerization of silicone oil vapor were carried out. The main object of these experiments was to study the variation of line width and the structure of the polymer film produced as a function of the accelerating voltages and sweep velocities of a fine electron probe.

The silicone fluids, MS200 0.65 c.s. and MS 704, were chosen for the experiments. The former has a relatively high vapor pressure at room temperature, approximately 30 mm of Hg (see technical data sheet G1, Midland Silicones Ltd., England, or Dow-Corning equivalent). Well-polished silicon slices were used as substrates. Lines were drawn by single sweep electron probe at 2 to 30 kV, at various vapor pressures and specimen temperatures.

Figure 1 shows scanning electron micrographs of such a series of lines of polymer film produced by an electron probe approximately $200 \pm 50 \text{ \AA}$ in diameter at 5 kV of accelerating voltage.

During the experiments, the specimen was held normal to the incident electron beam and the specimen temperatures were as indicated on the pictures. For a given beam accelerating voltage, six lines were drawn with the probe moving at six different sweep velocities. It can be seen that the line width increases with decrease of sweep velocity. For a given velocity, the width decreases with decrease of beam voltage, as shown by the full range of voltages used in the experiment.

Figure 2 shows a high magnification micrograph of three lines drawn at 15 kV with velocities of 1.4, 0.87, and $0.5 \mu/\text{sec}$, respectively. The polymer film appears considerably darker than the silicon surface. It can be seen that in the middle of each dark line there is a very much narrower line structure running continuously along the length of the line. The width of this line structure is approximately 400 \AA and remains practically the same for all three sweep velocities. This narrow line structure appears much lighter in contrast with the polymer lines and this suggests that it stands proud of the surrounding film.

Figure 3 shows a micrograph of films formed with a 25 kV, 150 \AA electron probe. The specimen temperature was -10°C and the monomer temperature was kept at 80°C . The lines were drawn at 1.1, 0.65, and $0.15 \mu/\text{sec}$ respectively and the line width increases with decrease of sweep velocity. In this experiment the specimen surface was inclined at an angle of approximately 60° to the incident beam and it is interesting to

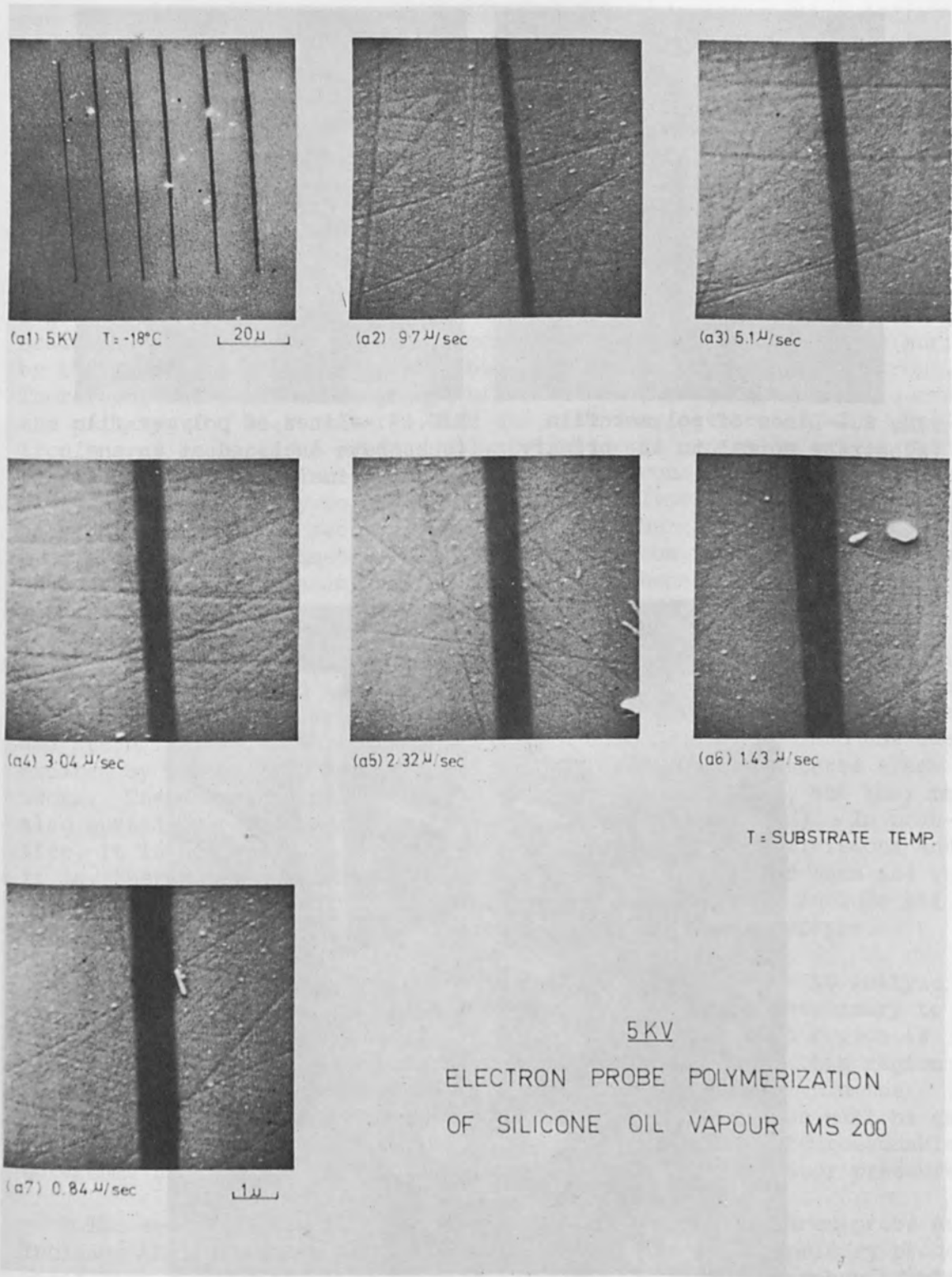


FIG. 1.—Controlled polymerization of silicone oil vapor with a 5-kV electron beam.

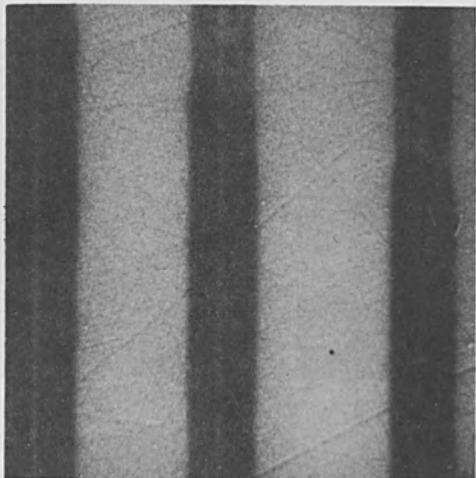


FIG. 2.—Lines of polymer film (substrate normal to the primary beam).

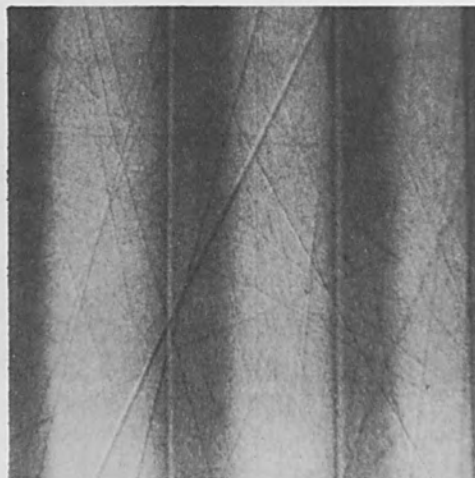


FIG. 3.—Lines of polymer film (substrate inclined at an angle to the primary beam).

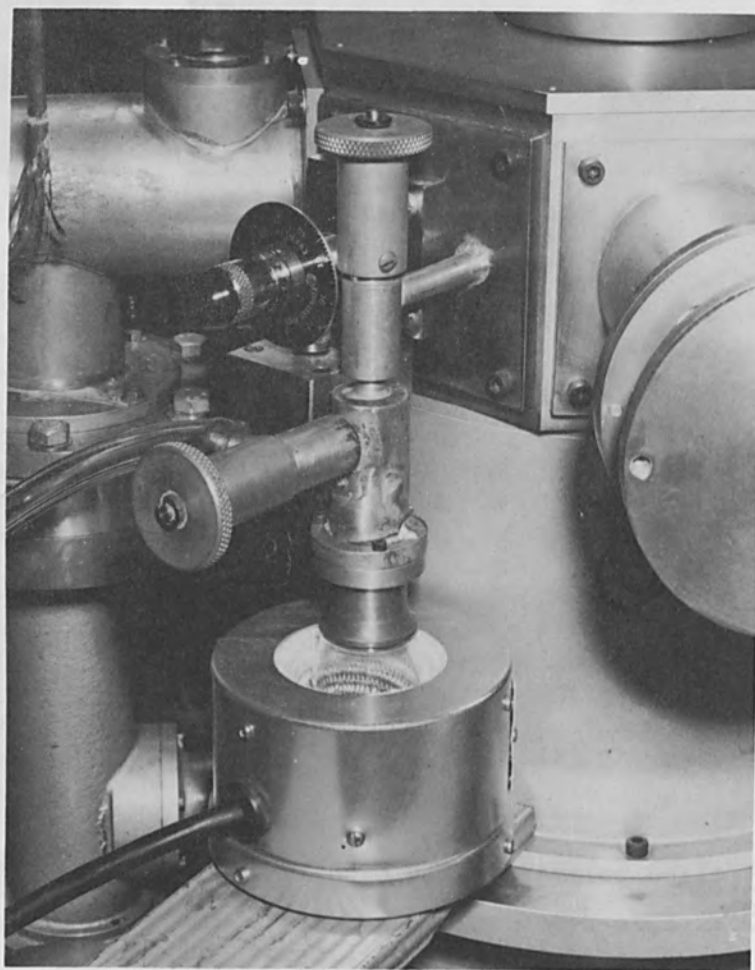


FIG. 4.—The vapor source.

see that the position of the fine line-structure is not in the middle of the film as observed in Fig. 2 but shifted nearer to the lower edge of the film. The picture also shows quite conclusively that the fine line structure within the line was actually standing proud.

THEORETICAL CONSIDERATION OF POLYMERIZATION BY A FINE ELECTRON PROBE

When a fine electron probe bombards a surface, it penetrates into the target and loses energy through inelastic collisions; these collisions cause the primary electrons to deviate from their original directions and to scatter inside the solid. Some of these scattered electrons may suffer a large angle of deflection and re-emerge through the surface as backscattered electrons. Secondary electrons are also produced at the surface by the impact of both the primary beam and the backscattered electrons. Therefore, there are three groups of electrons impinging upon the surface: the primary, the backscattered, and the secondary electrons. The electron energy required to produce polymerization is generally only a few electron volts; therefore, almost all the electrons in these three groups have sufficient energy to participate in the polymerization process. The backscattered and the secondary electrons may emerge from the surface over a much larger diameter than the primary probe, depending on the target material and the accelerating voltage, and hence the resolution or line width of the polymer film produced will be impaired.

Strictly speaking, the backscattered electrons should be divided into two types, elastic and inelastic backscattered electrons, and the latter may have a very wide spectrum of energy (Archard,¹⁶ Everhart,¹⁷ Holliday and Sternglass¹⁸). The secondaries should also be divided into the ones excited by the primary and the ones excited by the backscattered electrons. These are generally at a lower energy level (50 V), but they may also spread over a wide energy range (Bruining,¹⁹ Gibbons²⁰). In practice, it is not possible to differentiate among all these divisions and it is, therefore, convenient to adopt a collective term for them and the name "collective secondary electrons" will be used here to include all the backscattered and secondary electrons that leave the surface.

It may be seen from the above discussion that in order to analyze the polymerization effects of a fine electron probe it is necessary to consider the process separately for two regions. The first region is the one directly under the primary probe; electrons inside this region include the primary probe and the collective secondaries within the primary probe diameter. The electron density in this region will be extremely high, in the order of 100 A/cm^2 , so that it is quite reasonable to assume that the polymerization rate is limited by the vapor pressure.

The second region is the one outside the primary electron probe and includes the collective secondaries on either side of the primary probe, which have a Gaussian distribution of density. The total number of electrons in this region is less than in the first region and these electrons spread out over a considerably larger area; hence the density will be low. Therefore, it may be assumed that the rate of film formation in this region will be governed by both the vapor pressure and electron density. The full theory will appear elsewhere.

Following the above description, one would expect that when a line of polymer film is formed by sweeping a fine electron probe over the surface, it will have a cross-sectional profile as shown in Figs. 2 and 3. The high density electrons will form a relatively thick ridge in the middle, the width of which approximately equals the primary probe diameter; on either side of this ridge there will be a much wider region of thinner film formed by the low-density collective secondaries.

When the specimen is inclined at an angle to the incident probe, the collective secondaries emerge from the surface asymmetrically. It can be seen that the distribution of the intensity is no longer symmetrical about the primary beam diameter and the center of the exit diameter is shifted upwards. Therefore, the resultant film exhibits a profile as demonstrated in Fig. 3.

CONCLUSION

The polymer film formed with an electron probe involves two groups of electrons: (a) the primary plus some secondary electrons which escape from the central region, and (b) the part of the collective secondaries which emerge from the wider region. The first group of electrons produces very fine lines of film, the width of which is of about the same order of magnitude as the probe diameter and relatively independent of speed and beam voltage. The second group of electrons produces much wider lines of film, the width of which depends critically on parameters such as beam voltage, speed, temperature, vapor pressure, etc. Therefore, for really high resolution work, it is important to operate the electron probe with conditions such that only the first group of electrons has a high enough density to produce a useful film.

AN APPLICATION OF HIGH-RESOLUTION ELECTRON-BEAM POLYMERIZATION

A polymer film, in the form of very fine lines, was deposited by the electron probe, in the presence of a silicone oil vapor, to form a protective coating over an evaporated aluminum film. This coating protected the film against subsequent chemical etching. As a result very fine aluminum lines were left on the surface of the substrate.

A thin layer of aluminum film, a few hundred angstroms thick, was evaporated on to a silicon substrate by means of a small evaporator inside the scanning electron microscope specimen chamber. The surface was examined with the system operated in the microscopy mode to select a particular area for the experiment. The electron beam was switched off and the specimen surface cooled. Experiments were carried out for a range of temperatures between +10° and -20°C. A silicone fluid was contained in a glass envelope placed outside the system and the vapor was admitted to the specimen chamber through a needle valve and directed via a fine nozzle to the specimen surface. The actual set-up is shown in Fig. 4. The glass envelope and transmission pipework were evacuated separately from the system; during evacuation, the silicone fluid had to be kept frozen by surrounding the glass envelope with liquid nitrogen. The nozzle was placed close to the specimen so that only a small amount of the vapor needed to be admitted. The exact vapor pressure at the specimen surface was not known, but its relative value could be monitored by an ionization

gage placed in the chamber. The vapor pressure was varied by controlling the temperature of the silicone fluid container and the transmission pipework including the needle valve. During the operation the specimen chamber was isolated vacuumwise from the rest of the system apart from the small aperture in the final lens. With this arrangement, it was possible to fill the specimen chamber to a vapor pressure of 10^{-3} torr without hampering the electron beam operation in the rest of the system. The electron beam, which had previously been focused and positioned during the inspection stage, was switched on and used to lay down a polymer film in a predetermined pattern. The speed at which the electron beam was moved could be controlled.

At any stage of the experiment the surface could be re-examined to check the continuity and positioning of the polymerized film. This procedure merely required the shutting off of the vapor source, heating the specimen to approximately 100°C , and pumping for a short while. The experiment could be continued again after this examination.

After the polymerization was completed the specimen was removed from the specimen chamber and the aluminum film etched by a conventional chemical-etch process. By carefully timing the etching, the areas protected by the polymer film could be preserved on the specimen surface, and these protected areas appeared in the form of very fine high-definition aluminum lines and patterns.

EXPERIMENTAL RESULTS

Lines 600 \AA wide and with good edge definition were obtained and a micrograph is shown in Fig. 5 which demonstrates that patterns can be formed with this technique and that the lines are uniform and continuous. The experimental conditions were (see also Ref. 21):

| | |
|----------------------|---|
| Beam voltage | 25 kV |
| Probe diameter | $150 \pm 50 \text{ \AA}$ |
| Probe current | $2 \times 10^{-10} \text{ A}$ |
| Specimen | Silicon |
| Specimen temperature | $-5^{\circ} \pm 1^{\circ}\text{C}$ |
| Monomer employed | MS704 at a vapor pressure below 10^{-6} torr |
| Writing speed | 4 μ /sec |

PATTERN GENERATION AND ELECTRON-BEAM POLYMERIZATION

In order to apply this technique of producing fine lines to the full range of microcircuits, microfabrication, and microrecording, some form of pattern generator is needed. Two versions have been tried so far: (1) an x-y pen recorder used in reverse as an electrical pantograph with reduction, and (2) a flying-spot cathode-ray-tube mask scanning system using the scanning microscope photographic recording tube in reverse.

The principle of the x-y pen recorder technique is demonstrated in Fig. 6. The pattern was first engraved in a master and the tracing pin of the recorder was moved manually along the engraved lines of the master. The movement of the pin was imparted, through a system of pulleys, to two

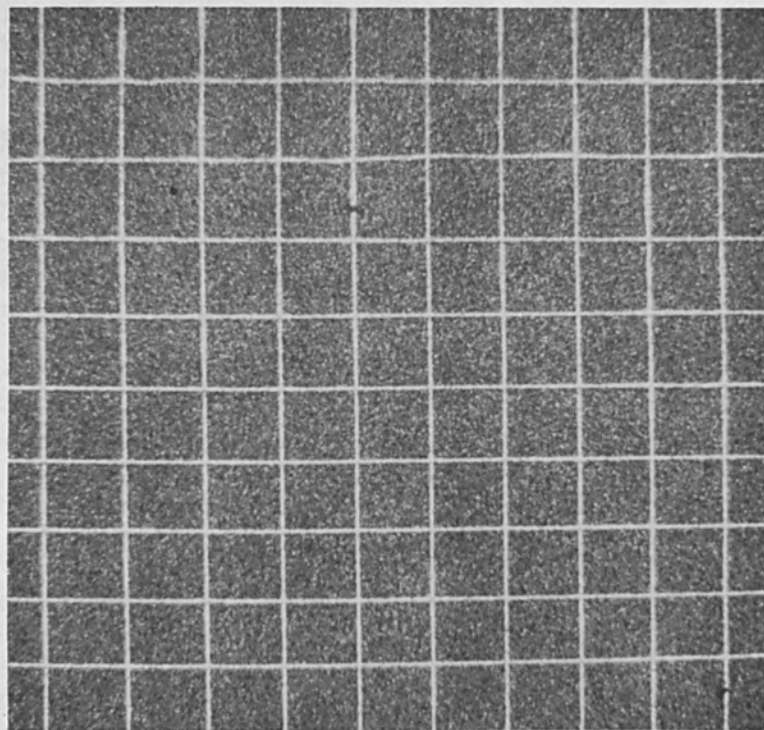


FIG. 5.—Patterns of fine aluminum lines (line width = 500 Å).

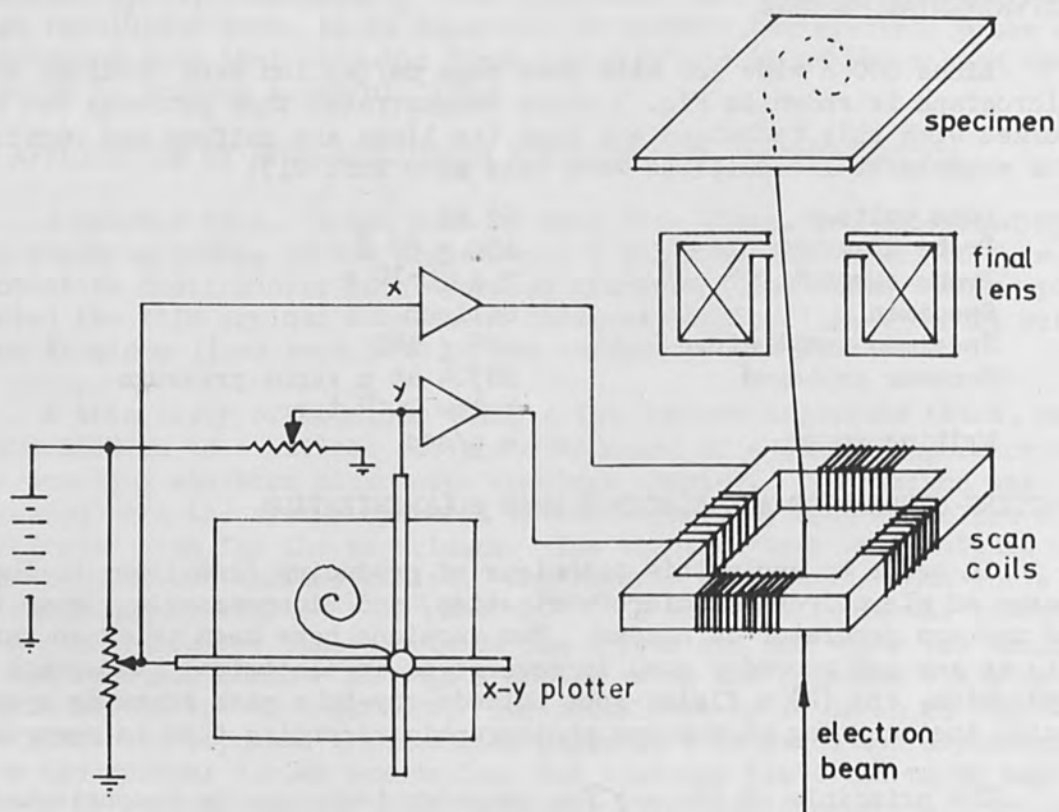


FIG. 6.—Principle of the x-y pen-recorder technique.

potentiometers and electric signals proportional to the x-y movements were produced and fed into the column scan coils after suitable amplification. The electron probe inside the microscope was thereby made to follow the same pattern as prescribed on the master. By adjusting either the dc voltages applied to the potentiometers or the amplification of the signal to the scan coils, the pattern could be reproduced scale.

This is a slow, yet extremely versatile, analog control technique and is most suitable for the tracing of patterns composed of continuous lines. The speed of the pin head can be controlled by a servomechanism to achieve very uniform movement. The process can be speeded up if the x-y signals are first recorded with a tape recorder running at slow speed and the information is then fed to the deflection system with the tape recorder running at a much higher speed.

Figure 7 is an example of patterns produced by this technique. The electron beam was used to produce a pattern of polymerized film which protected the underlying aluminum film against subsequent chemical etching. The lines are black because the polymerized film still remains on the surface.

The letters are a few microns high and the line width is about 1500 \AA in this very preliminary result which does not yet show the full resolution of the technique as seen in Fig. 5.

The flying-spot-scanner technique is based on the fact that the movement of the electron probe in the column is synchronized with that of the electron beam in the crt. By placing a mask in front of the crt and picking up the light passing through the transparent parts of the mask, one obtains a series of signals defined by the pattern in the mask. This light signal is converted into an electrical signal by a photomultiplier and used to switch the electron probe in the column on and off. Hence, a demagnified pattern as defined by the mask can be traced inside the system. The amount of demagnification can be easily calibrated by changing the system to microscopy operation. The block diagram of Fig. 8 demonstrates the principle of this technique.

This technique allows complicated patterns to be traced and the shape of the pattern can be easily varied by simply changing the mask. High speed operation can be obtained by using high scan frequencies and the whole operation is automatic. The main drawback of this method is that it does not trace out the pattern continuously, which results in some loss of resolution.

The cathode-ray tube was a 5-in.-diameter Ferranti (5/04 PM) short-persistence tube; a Shackmann AC/25 35-mm oscilloscope camera was used to image the crt spot. The mask was placed at the focal plane of the camera lens, but for work not requiring very high resolution, the mask was placed immediately in front of the crt. It was found that ordinary high-contrast negative films are reasonably good material for the preparation of the mask. The camera had a detachable window placed very conveniently behind the negative carrier and a photomultiplier (type 9524B) was coupled via a light pipe to the mask through this window. The output of the photomultiplier was fed into a variable-gain dc amplifier.

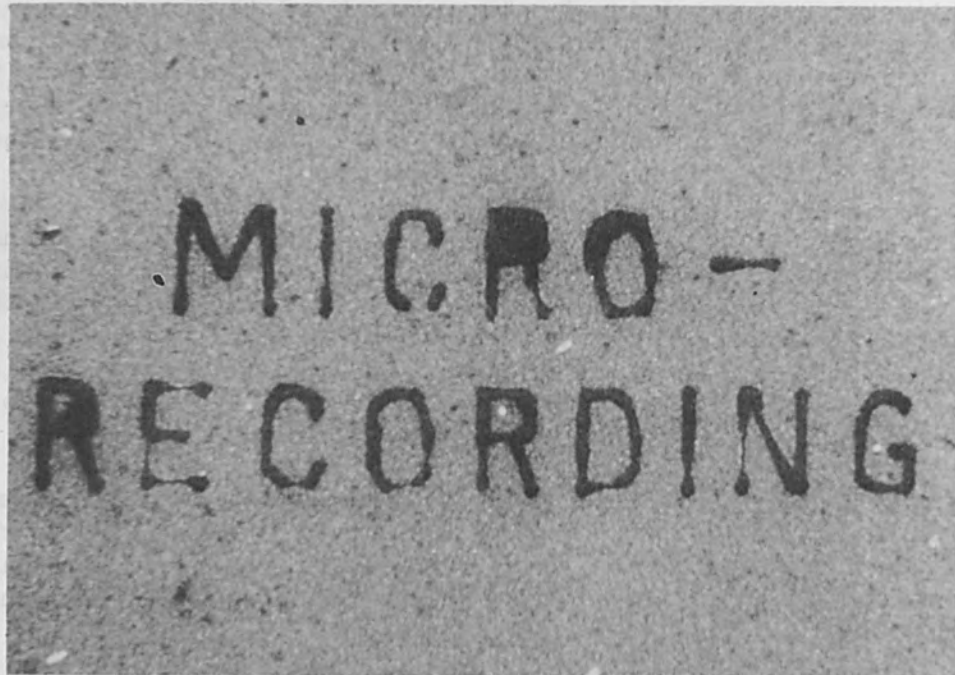


FIG. 7.—Patterns produced by the x-y pen recorder technique.

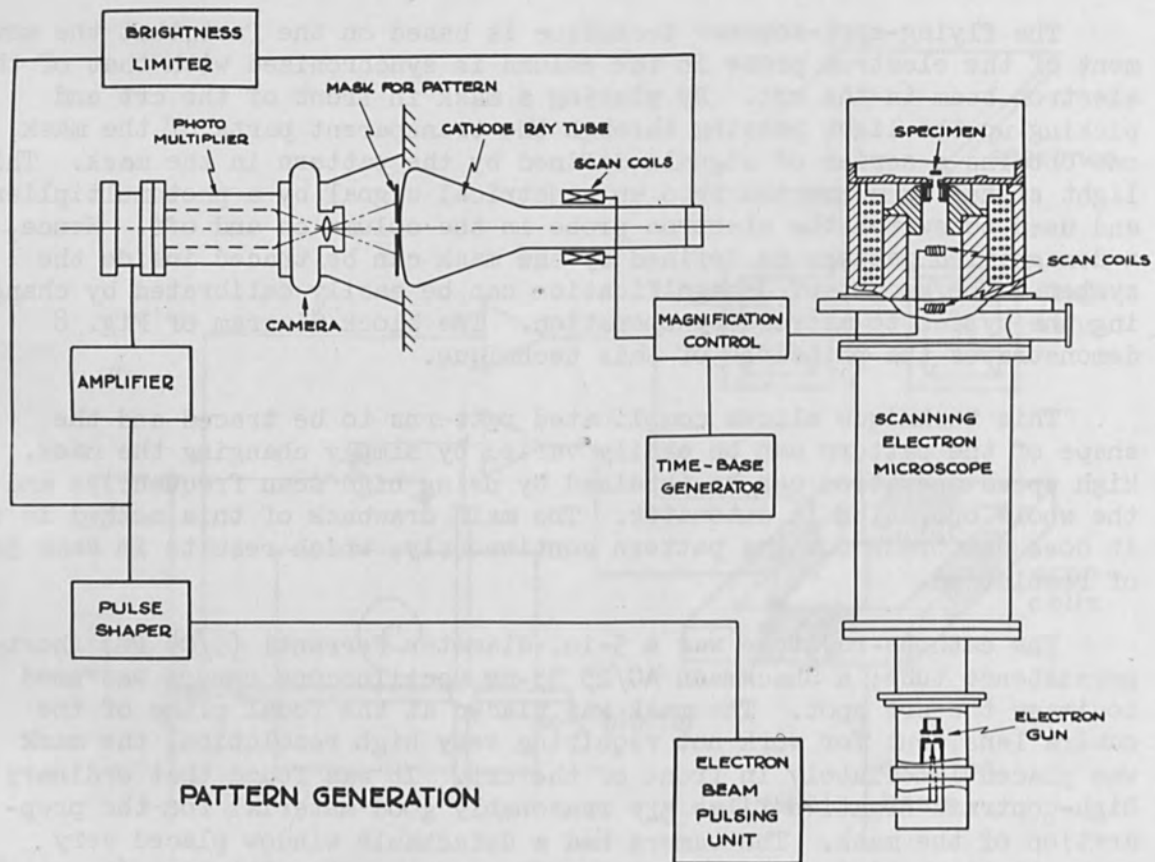


FIG. 8.—Principle of the flying-spot scanner.

As the waveform of the output signal from the amplifier did not have sufficiently fast rise and decay times to be used directly for triggering the electron gun switching circuit, a pulse shaper was required. This is basically a two-stage comparator, the reference level of which was set by the first stage and the second stage was used to speed up the switching process. The output signal was 50 V with a rise time of 2 μ s, and was connected to the trigger-input port of the electron beam pulsing unit.

A brightness limiter was found necessary to compensate for the build-up of signal due to afterglow on the crt. The function of the limiter was to prevent the output signal from the amplifier exceeding a specified level by controlling the brilliance of the spot on the crt.

Figure 9(a) shows the original mask used for 9(b). This pattern was produced by thermal machining of silicon coated with an oxide. The line-scan frequency was 60 Hz and frame time was 5 sec. The probe diameter of the electron beam used was approximately 3 μ m.



FIG. 9.—Patterns produced by the flying-spot-scanner technique.

This thermal process is limited in resolution and cannot be compared to the quality of the lines produced in Fig. 5. However, thermal machining does have a place in electron-beam technology and the pattern generator may be the same for both thermal and nonthermal processes. Fuller details of the silicon thermal etching are reported in Chang and Nixon⁹ and by Chang.²¹

REFERENCES

1. R. W. Christy, "Formation of thin polymer films by electron bombardment, *J. Appl. Phys.* 31: 1680-1683, 1960.
2. H. T. Mann, "Electrical properties of thin polymer films: Part I, thickness 500-2500 Å," *J. Appl. Phys.* 35: 2173, 1963.
3. I. Haller and P. White, "Polymerization of butadiene gas on surface under low energy electron bombardment," *J. Phys. Chem.* 67: 1784, 1963.
4. D. S. Allam, C. T. H. Stoddart, and P. R. Stuart, *Microelectronics & Reliability*, 5: 19-25, 1966.
5. G. W. Hill, "Electron beam polymerization of insulating films," *Microelectronics & Reliability* 4: 109-116, 1965.
6. J. W. Thornhill and I. M. Mackintosh, *Microelectronics & Reliability*, 4: 97, 1965.
7. R. F. M. Thornley and T. Sun, "Electron beam exposure of photoresists," *J. Electrochem. Soc.* 112: No. 11, 1965.

8. A. N. Broers, "Selective Ion Beam Etching in a Scanning Electron Microscope," Ph. D. Dissertation, Cambridge University, 1965.
9. T. H. P. Chang and W. C. Nixon, "Electron beam machining of silicon observed with the scanning electron microscope," IEE Conference on Thin Films, London, July, 1966; and "Scanning electron microscopy and electron beam effects on silicon surfaces," 6th Intern. Conf. Electron Microscopy, Kyoto, September 1966.
10. D. A. Buck and K. R. Shoulder, "An Approach to Microminiature Printed Systems," Special Publication T-114, Proc. Eastern Joint Computer Conf., Dec. 1958.
11. P. W. White and D. W. North, "An electron-beam memory utilizing some properties of polymer films," 1st Intern. Conf. Electron & Ion Beam Science & Technology, 1965.
12. D. Ryan, L. J. Rigby, and M. W. Jones, Progress Report on the Formation of Microcircuit Element by Photocatalysed Surface Reactions, Ministry of Aviation, Contract no. KH/F/7286/C.B.19(C)3.
13. R. W. Christy, "Conducting thin films formed by electron bombardment of substrate," *ibid.* 33: 1884, 1962.
14. A. G. Baker and W. C. Morris, "Deposition of metallic film by electron impact: Decomposition of organic vapour," *Rev. Sci. Instr.* 32: 458, 1961.
15. J. M. Hlavin and A. Fotland, "The fabrication of electronic components using low-energy electron beams," 1st Intern. Conf. Electron & Ion Beam Science & Technology, 1965; p. 231.
16. G. D. Archard, "Back scattering electrons," *J. Appl. Phys.* 32: 1505-1508, 1961.
17. T. E. Everhart, "Contrast Formation in the Scanning Electron Microscope," Ph. D. Dissertation, Cambridge University, 1958.
18. J. E. Holliday and E. J. Sternglass, "New method for range measurements of low-energy electrons in solids," *J. Appl. Phys.* 30: 1428, 1959.
19. H. Bruining, "Physics and Applications of Secondary Electron Emission," Pergamon Press, 1954.
20. D. J. Gibbons, "Secondary electron emission," in "Handbook of Vacuum Physics" A. H. Beck, ed., Pergamon Press, 1966.
21. T. H. P. Chang and W. C. Nixon, "Electron beam formation of 800 Å wide aluminium lines," *J. Sci. Instr.* 44: 231, 1967; and "Combined Microminiature Processing and Microscopy using a Scanning Electron Probe System," Ph. D. Dissertation, Cambridge University, 1967.

LOW-ENERGY ELECTRON BEAM INTERACTIONS WITH ION-IMPLANTED SEMICONDUCTOR SURFACES

E. D. WOLF

Hughes Research Laboratories, Malibu, California

ABSTRACT. Electron beam induced (EBI) current response of shallow ion-implanted p-n junctions in silicon were investigated using a low-voltage (0- to 1000-V) scanning electron beam (about 3 microns in diameter). Implant boundaries, implant uniformity, and imperfections such as "pipes" and implant damage within the implant regions were displayed on a synchronously scanned cathode-ray oscilloscope. The surfaces were imaged using the secondary electron emission current for intensity modulation of the display cathode-ray tube. This mode of operation revealed many surface topographical details. The work function and externally applied potential distributions were measured in regions adjacent to biased p-n junctions by the retarding potential technique (0- to 5-V electron beam). The measurements were made locally at a fixed position and recorded directly with an x-y recorder, or an entire region was displayed on the monitor. Specific examples of these low-voltage probing techniques and some of their advantages and limitations are discussed.

INTRODUCTION

The electrical responses of semiconductor surfaces to high-voltage electron bombardment have been studied for many years and many of these responses have been displayed as a spatial function of the surface in a two-dimensional television image with high magnification. Both the scanning electron microscope¹⁻⁴ and the microprobe analyzer,^{5,6} particularly the former with its greater spatial resolution, have been very successfully employed in this manner. Notably, Everhart and associates⁷⁻¹² have used the scanning electron microscope for investigating semiconductor devices and integrated circuits. Minority-carrier lifetime measurements¹³ have been made with the scanning electron microscope and inversion layers have been observed by several investigators.^{12,14,15} The microprobe analyzer has been used by Wittry and Kyser^{16,17} for studying cathodoluminescence response of p-n junctions and infrared radiative recombination processes. Lander et al.¹⁸ has reported the observation of lattice defects "shadowed" on shallow planar p-n junctions.

This brief summary of effects observed when an electron beam interacts with a semiconductor surface is not intended to be inclusive, but indicative of the information that can be obtained.

It is the purpose of this paper to describe a unique combination of low-voltage (0- to 1000-V) scanning techniques embodied in one ultrahigh-vacuum low-energy scanning electron microscope. By describing some recent measurements on ion-implanted semiconductor surfaces, it will be shown that within the limitations of resolution and primary electron beam penetration

most of the phenomena referenced above can be observed, and in addition, retarding potential measurements, i.e., work functions and externally applied potentials can be obtained. An earlier paper¹⁹ presented data using a mechanically scanned low voltage beam which was a forerunner to the present low-voltage scan system.

In the present method, as in the operation of the scanning electron microscope and the microprobe analyzer, a small-diameter electron beam is scanned over the surface and the resulting signal which is generated on the target is amplified and used as a video signal to modulate a synchronously scanned cathode-ray tube.

In the work reported here the final electron spot diameter at the device surface was about 3μ and the beam current was 10^{-8} to 10^{-7} A. The advantages of the technique to be described are large area scan (1.5×1.5 cm); the ability to scan in three different modes of operation: retarding potential current, inverse secondary-emission current and electron beam induced junction current; large secondary-emission signals because the secondary-electron emission coefficient is a maximum for most materials in the 20- to 500-V range, in particular silicon and silicon dioxide. The limitations to the method are obviously resolution and primary beam penetration. The latter, however, is not so important and, in fact, may be undesirable for very shallow ($\leq 0.1\mu$ deep) nonpassivated ion-implanted junctions. A description of the experimental apparatus and a more thorough analysis of these and other results will appear elsewhere. A brief explanation of the modes of signal generation is given, followed by a discussion of experimental data illustrative of the operational modes of the low energy scanning electron microscope.

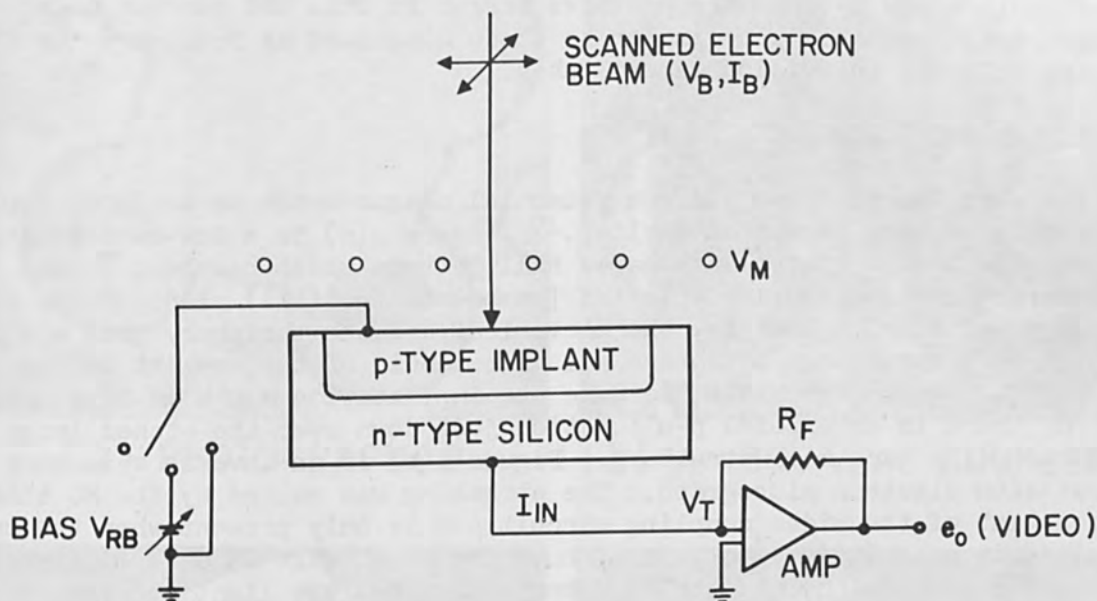
PRINCIPLES OF SIGNAL GENERATION

In Fig. 1 the target configuration, signal pick-up, and modes of operation are illustrated. The amplifier is a unity gain current amplifier which maintains the target voltage $V_T = 0$ by feedback current through the feedback resistor R_F . The other terms are mesh voltage V_M , reverse bias voltage V_{RB} , beam current I_B , target current I_T and I_{IN} , secondary-electron current I_{SEC} , back scattered electron current $I_{BACK\ SCAT}$, electron beam induced current I_{EBI} , reverse bias junction current I_{JN} , the electron-gun emitter temperature T_e , surface potential ϕ , electron charge e , and Boltzmann constant k .

RETARDING POTENTIAL CURRENT MODE (Switch Open). In this mode of operation the input current I_{IN} is simply the target current with the functional relationship indicated in Fig. 1. In the absence of an externally applied bias potential, ϕ is the work function. The distance between mesh and target is as small as possible (about 100μ minimum) to maintain a high field at the target surface. Haas and Thomas²⁰ and Bauer²¹ have used similar experimental techniques to measure and display the work function distribution of refractory materials. We have applied this technique not only to work function measurements, but also to externally applied potentials and have developed two other modes of operation.

INVERSE SECONDARY CURRENT MODE (Switch Open). Because the secondary electron emission coefficient is a maximum for both silicon and silicon

dioxide at low voltages, the modulation present on the target current is great when the mesh potential V_M is fixed so that the secondary electrons from the target are collected. This modulation is opposite in sign and can vary from zero to more than the primary beam current. The polarity change is important for interpretation of the secondary electron emission micrographs because a decrease in secondary emission will brighten the display in this mode. The role of the backscattered electron in image formation is not fully understood at present.



Modes of Operation

- (1) Retarding Potential Current

$$I_{IN} = I_T = I_B e^{-\frac{(\phi - eV_B)}{kT_e}} = I_B$$

$$V_T \equiv 0, I_{IN} = e_o/R_F$$

$$V_M \gg V_B \sim V_T$$

$$eV_B < \phi$$

$$eV_B > \phi$$

- (2) Inverse Secondary Electron Current

$$I_{IN} = I_B - I_{SEC} - I_{BACK\ SCAT.}$$

$$V_B \gg V_M > V_T$$

- (3) Electron Beam Induced Diode Current

$$I_{IN} = I_{EBI} + I_{JN}(V_{RB})$$

$$V_B \gg V_T \gg V_M$$

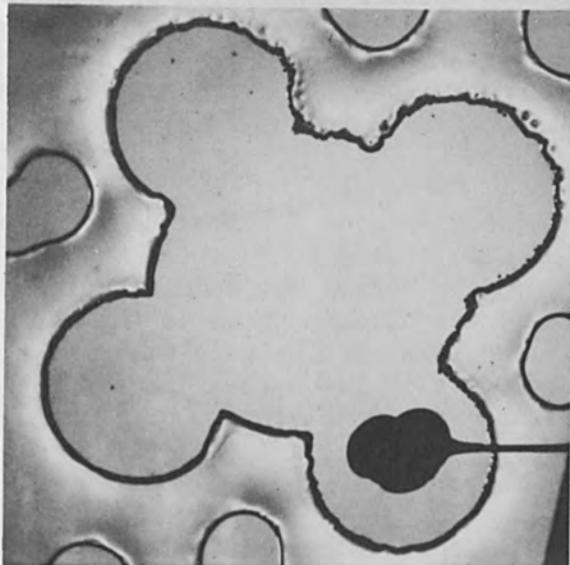
FIG. 1.—Signal generation and operational modes of the low-energy scanning electron microscope.

ELECTRON BEAM INDUCED DIODE CURRENT (Switch closed to ground or bias). In this mode of operation the electron beam generates hole-electron pairs in the surface and if they are produced in or near a depletion region a current pulse will be observed as the generated carriers are collected in that depletion region. If the amplifier is dc coupled to the display monitor, then the reverse bias junction current is also part of the video signal. The efficiency of carrier generation and the local recombination rate greatly influence the EBI current mode display. One complication imposed by the presence of the mesh, which is essential for the other two modes of operation, is that of secondary electron emanation from the mesh and collection by the more positive target in this EBI current mode. The associated problems are similar to those discussed by Dresner²² for high-beam-velocity television camera tubes.

RESULTS AND DISCUSSION

Work function and surface potential measurements on antimony implants in silicon were presented earlier.¹⁹ Figure 2(a) is a low-magnification photograph of a cloverleaf-shaped Hall pattern which has been etched from a large area gallium implantation [normal to the (111) plane of 200 Ω -cm n-type silicon]. That is, the cloverleaf and the periphery pads are 10- μ high-mesa structures which are all that remain of the implant on the original n-type material. Because the implantation depth is less than 1 μ , there is an exposed p-n junction just down over the etched ledge surrounding each mesa structure. Figure 2(b) is an inverse secondary emission electron micrograph. The streaking was caused by the RC time constant of the video coupling circuit and is only present when the coupling is ac. It is important to note the mesa ledge is dark (increased secondary emission) and the periphery scratches are light (decreased secondary emission). The small dark squares in the right-hand lobe are areas of increased secondary electron emission which resulted from earlier, high-magnification scans in those areas. This effect is probably not caused by beam contamination (pressure about 10^{-8} Torr) and suggests some alteration in the electrical properties of the surface. Figures 2(c) and (d) are EBI current-mode displays to show the collection of generated carriers not only at the periphery of the mesa as expected, but also throughout the implanted area. It is obvious in the EBI mode displays that the implant was truncated in two of the lobes; however, Fig. 2(a) does not yield this information.

As the primary beam voltage was increased from 100 to 1000 V, the EBI current in the implant region became very significant and several important features were observed. Increased EBI current in the truncated lobes was pronounced as was an increase in the density and intensity of "pipes" within the implant region. In order to observe the brushmark-like structures emanating from the left lobe, the periphery junction EBI signal was allowed to saturate. The large-area streaks are a probable indication of either decreased hole-electron pair generation efficiency, variations in the underlying junction depth, or enhanced recombination in these areas. Many of the bright "pipes" (sizes range from a few microns to several mils) and dark spots invert in display intensity under inverse secondary-emission imaging. The so-called "pipes" are areas in which the underlying n-type silicon is probably very close (relative to the average implantation depth) to the surface.



(a) PHOTOGRAPH, 9x

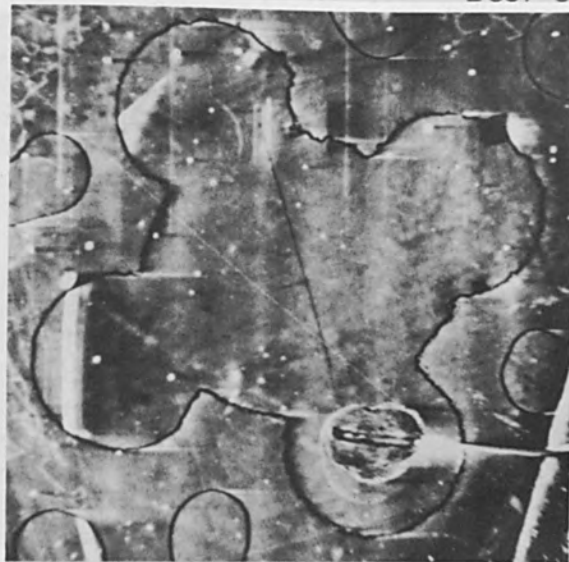
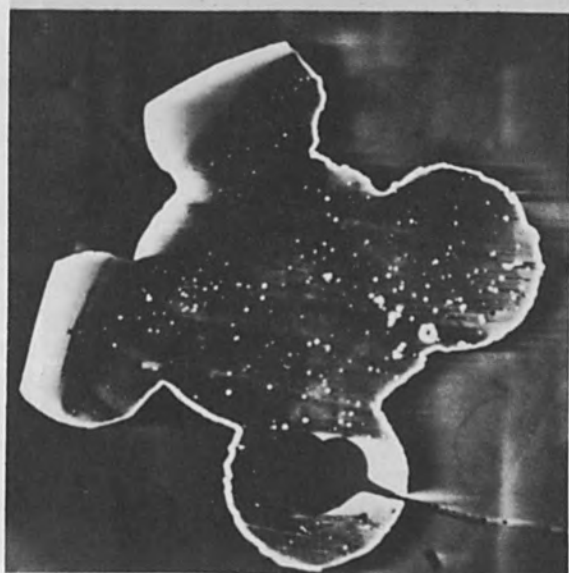
(b) $V_B = 300$ V, AC COUPLED(c) $V_B = 900$ V, DC COUPLED(d) $V_B = 900$ V, AC COUPLED

FIG. 2.—Gallium implanted silicon Hall pattern (a) photograph, (b) inverse secondary emission display, (c) and (d) EBI current displays.

A "ripple" effect in the left lobe is shown under higher magnification in Fig. 3. Included also are two line scans (A-scope displays) which indicate the relative EBI current collection at the shallow and probably uneven implant. The line scans were at the position indicated in (b). Combining the observations of high EBI current and low secondary emission (Fig. 2) in this area, suggests sputter deposition of a molybdenum mask which was positioned on top of the sample during ion implantation or of some electrode structure upstream in the ion beam. Alternatively a decrease in implant ion current in this area is possible. The gross effect and particularly the "ripple" are not fully understood at present.

Figure 4 shows higher magnification displays of EBI current. Both displays show small ($10\ \mu$ deep x $50\ \mu$ dia) etched holes where there were holes in the etch-resist mask near the mesa edge. The communication of the bottom of one hole with the n-region is clearly shown in the horizontal line scan in Fig. 4(b). The signal inside the hole was at the same level as outside the implant region which is to the right of the meandering p-n junction. The line scans were made at the locations indicated in (a) and (c) and the video response in (b) and (d) include the constant beam current in addition to the EBI current.

Figure 5 is a comparison of an EBI current signal displayed as an intensity-modulation (television) image (b) and as a deflection-modulation image (c) referenced to a photomicrograph (a). The area of interest was an etched hole near the mesa edge and a nearby hole intercepted by the mesa edge. The deflection-modulation display was a series of line scans displaced vertically in synchrony with the vertical sweep. This type of display carries considerably more information than the intensity modulation display provided the line density of the raster is not too high.

CONCLUSION

The low-energy scanning electron microscope has been shown to be a very versatile research instrument within the limitations of resolution and beam voltage. The three modes of operation are: retarding potential current, inverse secondary electron current, and electron beam induced junction current. The combination of these operational modes is unique to this system and the data that can be obtained is similar to and complements that of the high-energy scanning electron microscope.

Several unusual effects have been observed in defective ion implanted structures and this suggests the utility of the low energy scanning electron microscope for quality control of ion implanted semiconductors.

ACKNOWLEDGMENT

Several helpful discussions with R. G. Wilson and O. J. Marsh of these laboratories, the consultation of Prof. T. E. Everhart during the early design stages of the scan electronics, and the technical assistance of P. J. Coane are gratefully acknowledged.

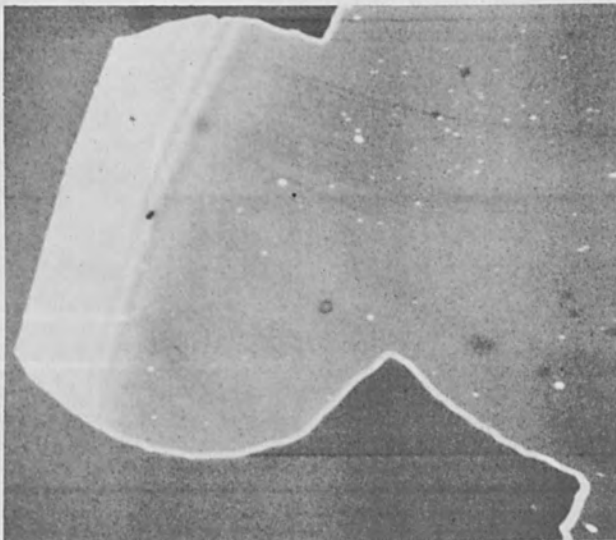
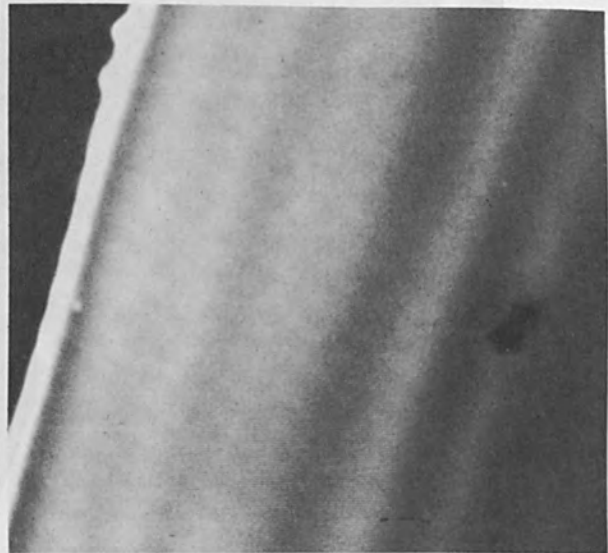
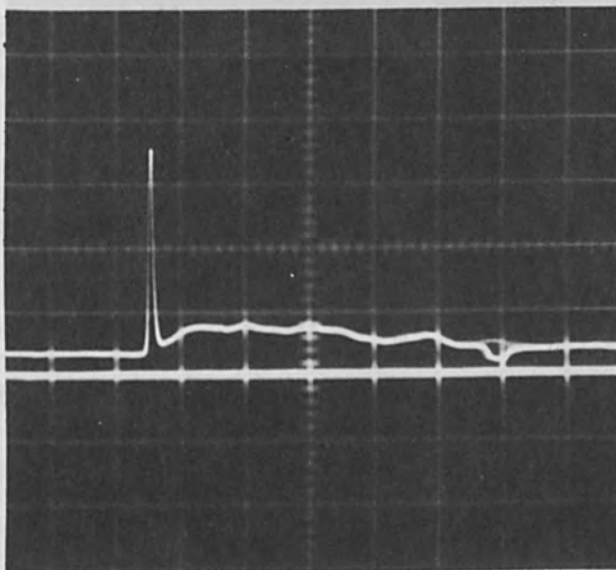
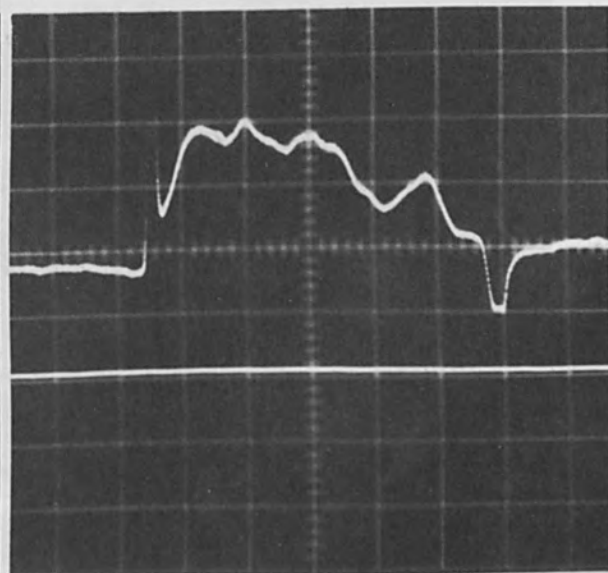
(a) $V_B = 900\text{ V}$ (b) $V_B = 900\text{ V}$ (c) LINE SCAN; $V_B = 800\text{ V}$
 $x = .08\text{ mm/DIV.}$; $y = 1.0\text{ V/DIV.}$ (d) LINE SCAN; $V_B = 800\text{ V}$
 $x = .08\text{ mm/DIV.}$; $y = 0.2\text{ V/DIV.}$

FIG. 3.—EBI current displays of truncated lobe (a) over-all view, (b) higher magnification near center of lobe, (c) line scan at position indicated in (b), (d) line scan with increased video gain.

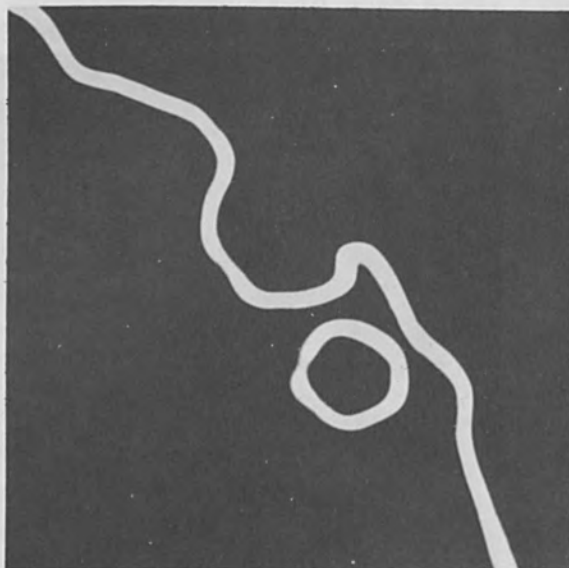
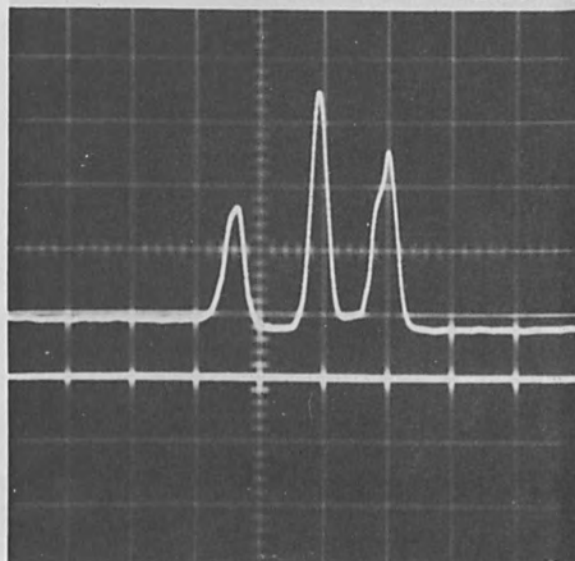
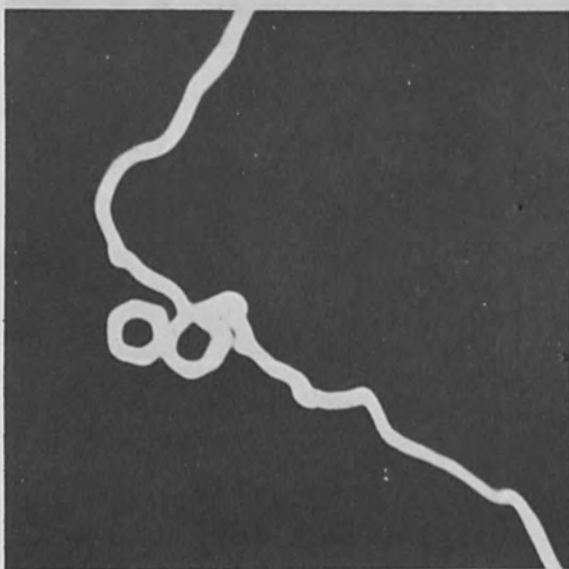
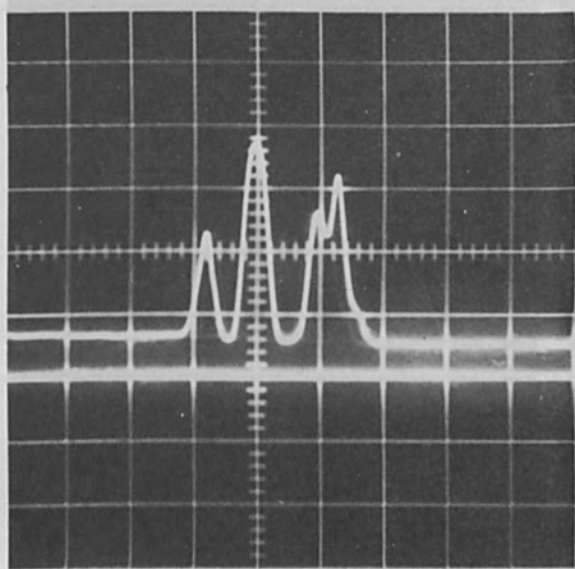
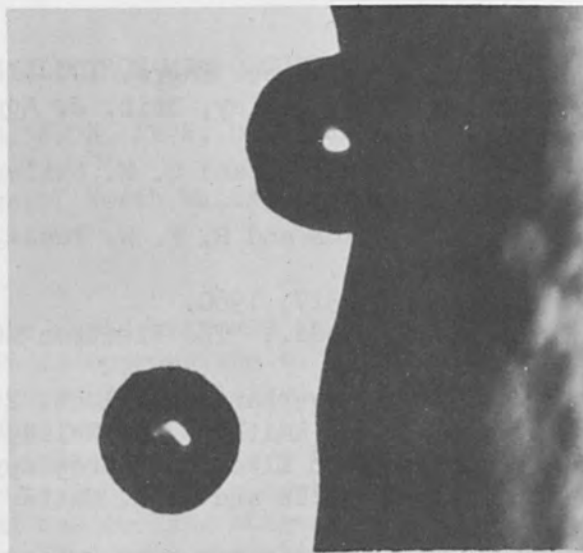
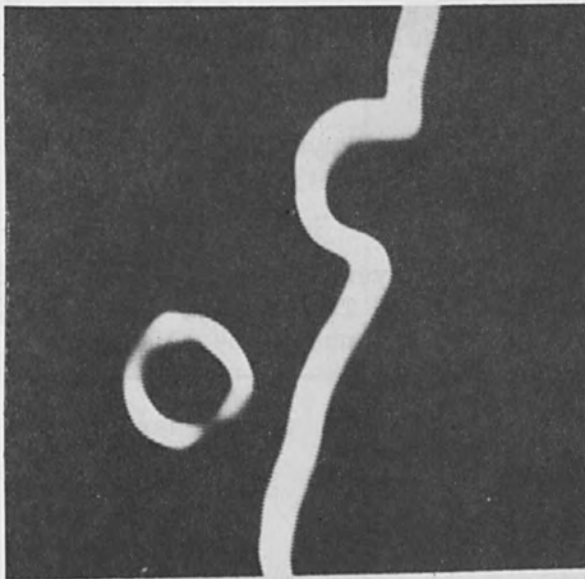
(a) $V_B = 700$ V(b) LINE SCAN ; $V_B = 1000$ V
 $x = 39\mu/\text{DIV.}$; $y = 0.5$ V/DIV.(c) $V_B = 700$ V(d) LINE SCAN ; $V_B = 900$ V
 $x = 39\mu/\text{DIV.}$; $y = 1.0$ V/DIV.

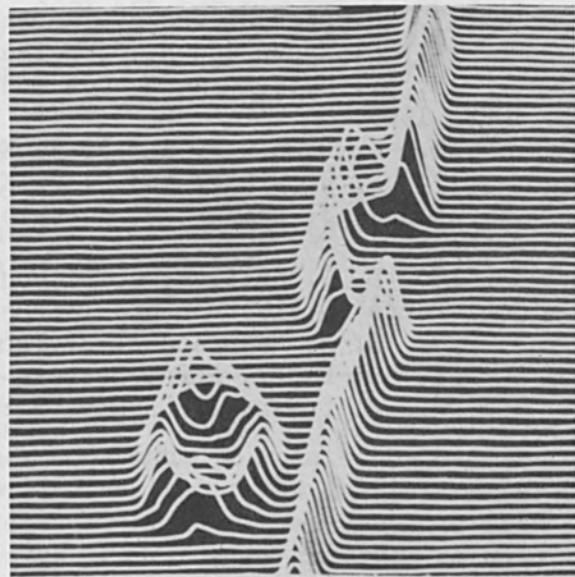
FIG. 4.—EBI current displays at imperfections near the pattern boundary (a) and (b) $10\ \mu$ deep and $50\ \mu$ diameter etch hole (c) and (d) etched hole and irregular p-n junction.



(a) PHOTOGRAPH, 300x



(b) TELEVISION DISPLAY



(c) DEFLECTION
MODULATION DISPLAY

FIG. 5.—Comparison of display modes (a) photograph, (b) intensity modulation, (c) deflection-modulation.

REFERENCES

1. D. McMullan, Proc. Inst. Elec. Engrs. 100 (II): 245, 1953.
2. K. C. A. Smith and C. W. Oatley, Brit. J. Appl. Phys. 6: 391, 1955.
3. T. E. Everhart, O. C. Wells, and C. W. Oatley, J. Electron and Control 7: 97, 1959.
4. C. W. Oatley, W. C. Nixon and R. F. W. Pease, Adv. Electronics and Electron Phys. 21: 181, 1965.
5. R. Castaing, *ibid.* 13: 317, 1960.
6. T. D. McKinley et al., eds., "The Electron Microprobe," John Wiley and Sons, New York, 1966.
7. C. W. Oatley and T. E. Everhart, J. Elect. 2: 568, 1957.
8. T. E. Everhart, K. C. A. Smith, O. C. Wells, and C. W. Oatley, Fourth International Conference on Electron Microscopy, Berlin, 1958.
9. T. E. Everhart, O. C. Wells and R. K. Matta, J. Electrochem. Soc. 111: 929, 1964.
10. T. E. Everhart, O. C. Wells, and R. K. Matta, Proc. IEEE 52: 1642, 1964.
11. C. J. Varker, T. E. Everhart, and A. J. Gonzales, Second International Conference on Electron and Ion Beam Science and Technology, New York, 1966.
12. T. E. Everhart, A. J. Gonzales, P. H. Hoff, and N. C. MacDonald, Sixth International Congress for Electron Microscopy, Kyoto, 1966.
13. H. Higuchi and H. Tamura, Japan J. Appl. Phys. 4: 316, 1965.
14. D. Green and H. C. Nathanson, Proc. IEEE 53: 183, 1965.
15. Y. Matsukura, J. Oda and S. Koreeda, Japan J. Appl. Phys. 4: 1022, 1965.
16. D. B. Wittry and D. F. Kyser, J. Appl. Phys. 36: 1387, 1965.
17. D. B. Wittry and D. F. Kyser, *ibid.* 35: 2439, 1964.
18. J. J. Lander, H. Schreiber, Jr., and T. M. Buck, Appl. Phys. Letters 3: 206, 1963.
19. E. D. Wolf, R. G. Wilson and J. W. Mayer, Second International Conference on Electron and Ion Beam Science and Technology, New York, 1966.
20. G. A. Haas and R. E. Thomas, Surf. Science 4: 64, 1966.
21. K. Bauer, Phys. Letters 7: 179, 1963.
22. J. Dresner, RCA Rev. 22: 305, 1961.

OIL-FREE SCANNING ELECTRON MICROSCOPY

P. R. THORNTON, N. F. B. NEVE, D. V. SULWAY, and R. C. WAYTE

University College of North Wales, Bangor, U. K.

INTRODUCTION

In view of the rapid increase in the application of scanning electron microscopy it is appropriate to assess some of the limitations in the technique as currently exploited. In addition to limitations imposed by source brightness we can list (1) difficulties in interpretation and (2) experimental limitations, i.e., the absence of versatile hardware in hygienic environments. Until the contamination problem is eliminated and a range of heating and cooling stages are available unnecessary difficulties hinder detailed interpretation. Some of the more immediate needs, particularly in the microelectronics materials and devices field, are listed and commented on in Table 1.

TABLE 1.—Some present limitations of scanning electron microscopy.

| Current need | Comment |
|---|--|
| More versatile specimen stages | Need to heat, cool and perform experiments in the SEM (e.g., ion etch, evaporate, melt, anneal, mechanically deform, and carry out complex electrical measurements) |
| Use of high vacuum and hygienic handling conditions | In order to eliminate surface contamination with its inherent specimen degradation and its complication of contrast interpretation; rapidity of pump down and ease of specimen changing to be considered |
| A valid assessment of the radiation damage introduced by SEM beam | No systematic data available, only indications; no attempt has been made to relate the nature and extent of the damage to the initial properties of the device, nor have measurements been made at elevated temperatures in order to minimize the damage |
| Development of more versatile detector systems | To allow multiple-mode operation with cooled detectors which can be operated in conjunction with a modulated beam, sampling and storage facilities |

This paper describes one approach to these problems and can be divided into two main parts: a description of the system used and a brief discussion of some recent applications including avalanche noise studies, breakdown at diffusion-induced dislocations, and the possibilities of examining the localized variations at the silicon-silicon oxide interface. We begin by describing the properties of an ion-pumped adaptation of the Cambridge Instrument Co. SEM.

GENERAL

Working within constraints imposed by the existing specimen chamber, by the need for a rapid pump-down and by the need to change specimens, say, ten times in one day we designed an ion-pumped system with the necessary specimen stages. This system, which is currently unbaked, has properties which can be summarized as follows:

(1) Pump-down time (without cryogenics in the specimen chamber):

| | |
|----------------------------------|------------|
| (a) to $< 5 \times 10^{-6}$ torr | < 20 min |
| (b) to $< 10^{-6}$ torr | 2 hr |
| (c) to $< 10^{-7}$ torr | 5 to 6 hr |

Pump-down time with cryogenics, to 10^{-7} in circa 3 hr (Note: the present limitation is a rotary seal on the aperture changer, currently being replaced by a bellows seal.) This system has been cycled from atmospheric to better than 5×10^{-6} torr ten times in one day with no detrimental effect.

(2) Resolution - better than 300 \AA proven (Fig. 1a).

(3) Contamination—has not been eliminated in any absolute sense (see below) but has been reduced so that no interference with specimen examination occurs. A measure of the improvement can be seen from Fig. 1, which illustrates results on GaAs and Ge, both susceptible to contamination. Figure 1(b) shows a GaAs laser which has been etched after somewhat extensive SEM examination. The electron beam has made the oil film sufficiently coherent to resist acid attack so that the scanning raster and "line scan" lines are made visible. Such coherent contamination can be formed within 2 min with specimens at low temperatures subjected to beam current levels suitable for cathodoluminescent studies. Figure 1(c) shows a different type of contamination which is invisible on emissive micrographs unless a bias is applied to the diode and which renders both the voltage-contrast mechanism and charge-collection micrographs useless as means of determining junction position; i.e., the contamination charges up positive, inverts the p-type layers, and obscures the diffused p-n junction position. Such contamination can be formed in 20 sec at room temperature. In the oil-free version contamination films on GaAs take much longer to form depending on the cleanliness of the system. In an uncleaned system the films take about 10 times longer to form, interfere slightly with specimen observation, and interfere with subsequent etching. In a well-cleaned system such films can be observed with difficulty after about 2 hr and they do not interfere with etching. On Ge with a clean system, diodes similar to that shown in Fig. 1(c) can be examined for hours at 100°K with no beam induced changes in contrast (Figs. 1d-f).

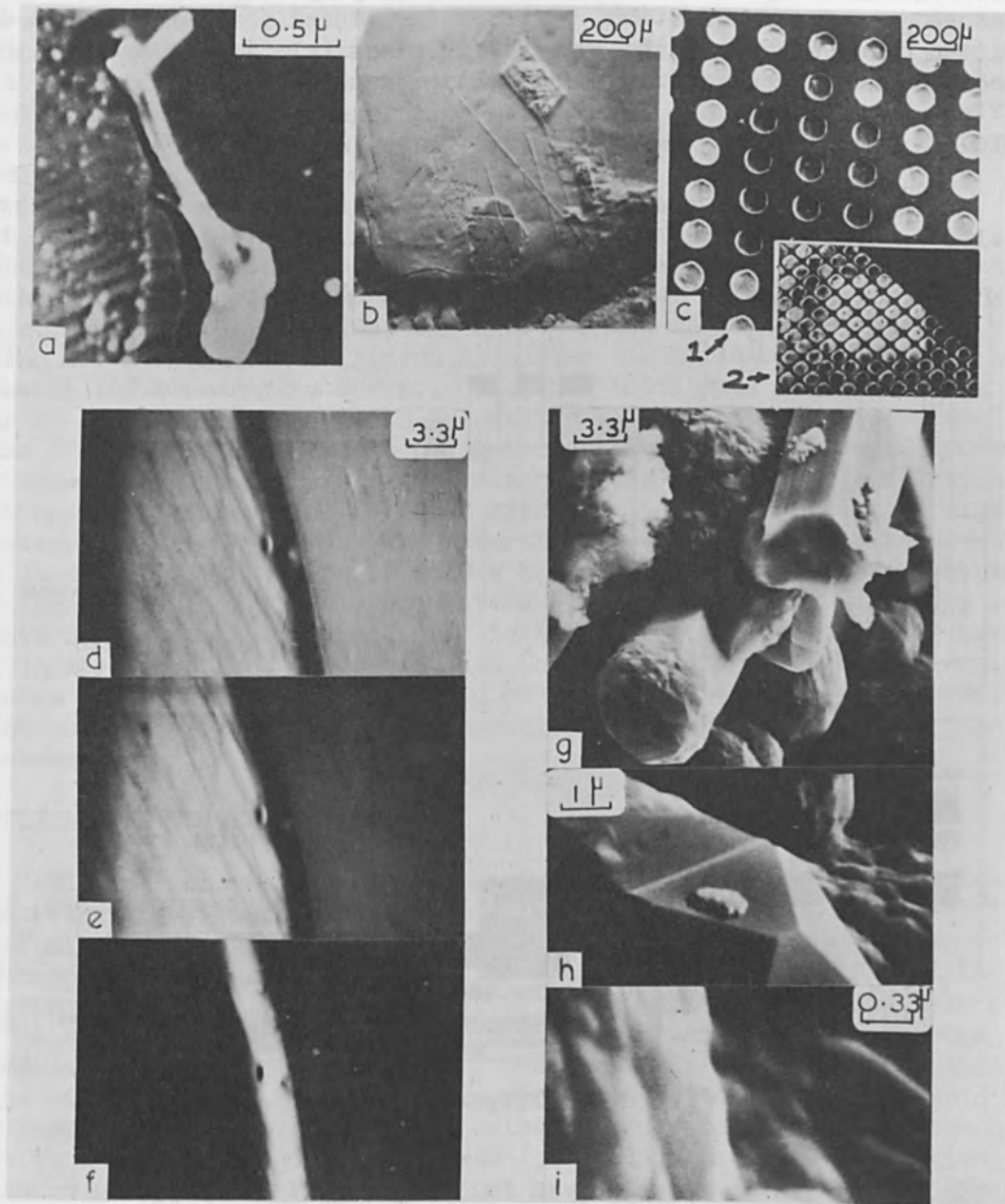


FIG. 1.—Micrographs illustrating the properties of an ion pumped SEM. (a) Micrograph of a dust particle showing the available resolution; (b) effect of oil contamination on the etching of a GaAs laser; (c) oil induced contamination on "dimpled" Ge diode which renders junction location impossible both on emissive (1) and conductive (2) micrographs; (d), (e) and (f), near complete elimination of contamination in ion-pumped SEM; junction location at moderate magnification by emissive [(d) and (e) diode bias 0 and 6V] and by conductive (f) micrographs; (g) to (i) emissive micrographs of Si whiskers showing the resolution obtainable with the multipurpose stage described in the text.

If an unclean stage is used some visible contamination occurs but is different in nature to that observed in oil-pumped systems and does not obscure junction observation. Often beam-induced contamination is difficult to observe because the contrast it gives relative to that of the specimen is beam-current and beam-voltage dependent.

SPECIMEN STAGES

One multipurpose stage is shown in Fig. 2. Such a stage is essentially several stages in modular form. The aims of this stage are implied

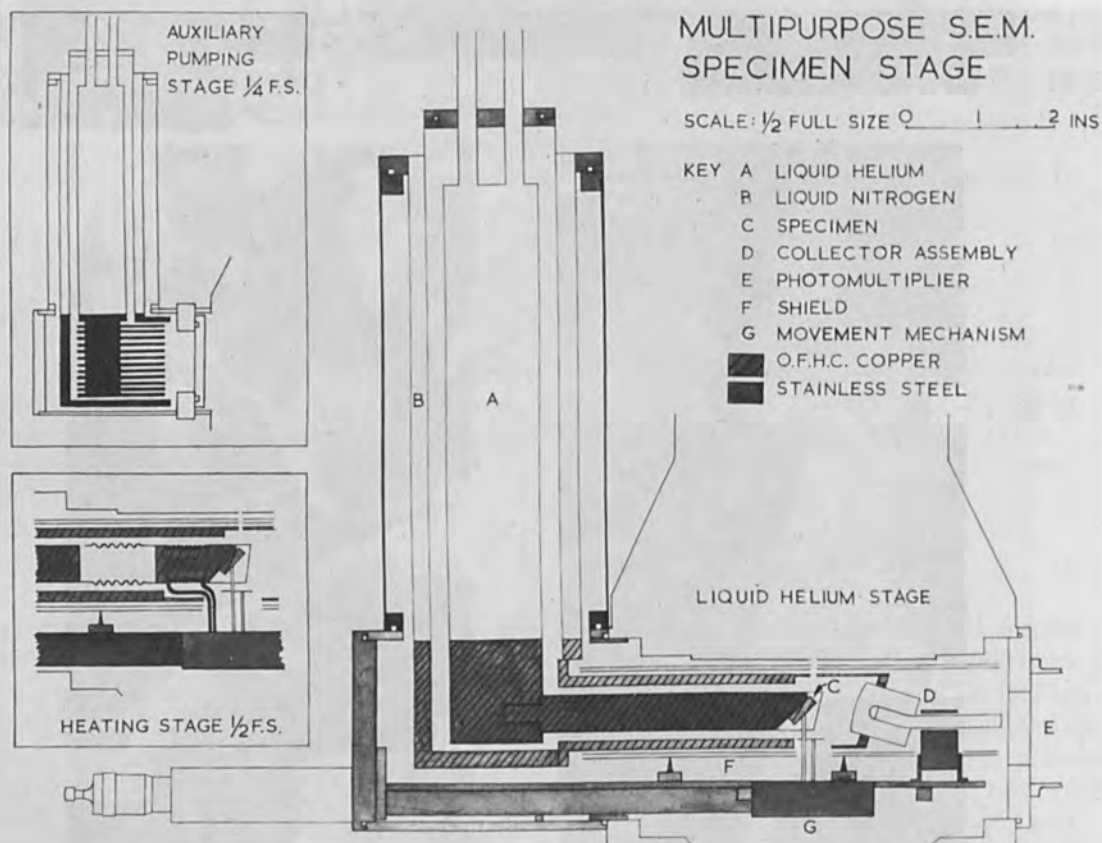


FIG. 2.—Multipurpose stage.

in Fig. 2 and can be summed up as follows.

(a) To provide a stage with which specimens can be examined at liquid He temperatures (i.e., $< 16^{\circ}\text{K}$). Here the motives are to examine luminescent materials under conditions of high efficiency, to cool the radiation detectors, and to see if it is possible to locate and observe the superconductor filaments in type II superconductors by observing changes in secondary-emission yield.

(b) To provide a rapid, auxiliary pumping system to speed up the pumping rate, particularly with regard to condensable vapors.

(c) To provide shielding for specimens from pump oil and from chamber contamination.

(d) To enable specimens to be studied up to temperatures (circa 800°C) at which physical mechanisms such as photon or thermionic emission start

to limit the immediate application of the SEM.

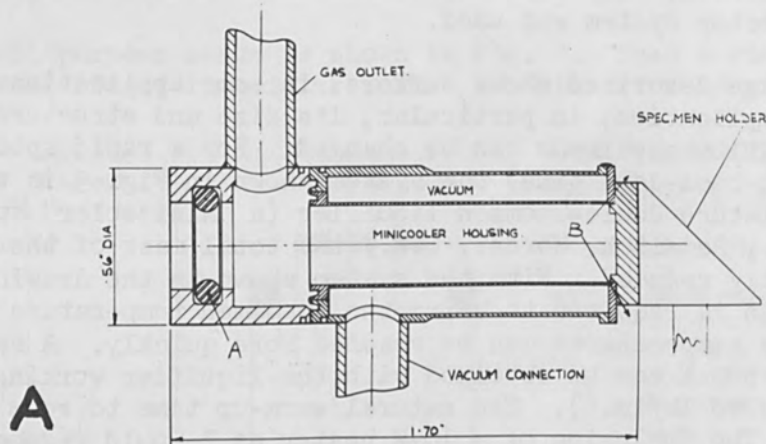
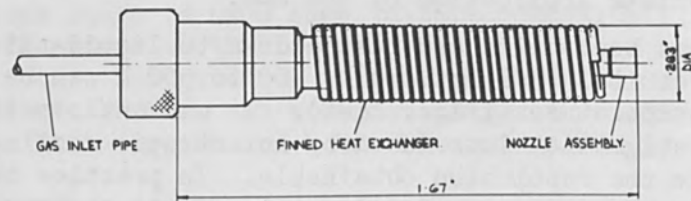
This stage has been built and tested down to liquid-nitrogen temperatures with good results. Resolutions of 400 to 500 Å can be obtained at liquid-nitrogen temperatures (Figs. 1g-i). It was anticipated that vibrations and/or astigmatism introduced by anisotropic cooling of the final lens would degrade the resolution obtainable. In practice these effects were not observed. Nor were any detrimental effects observed while a cooled collector system was used.

The stage described above suffers, in some applications, from its inherent complication; in particular, its size and structure limit the speed with which specimens can be changed. For a rapid specimen change (i.e., short cool-down time) the system shown in Fig. 3 is useful. By using a miniature Joule-Thomson liquifier (a "Minicooler" supplied by Hymatic Ltd., Redditch, Worcs., U.K.) the total mass of the coolant system can be greatly reduced. With the system shown in the drawing a cool-down time of 4 min is required to bring the specimen temperature to 100°K. Intermediate temperatures can be reached more quickly. A resolution of better than 500 Å can be obtained with the liquifier working at high pressure (2,250 lb/in.²). The natural warm-up time to room temperature is 14 min. The inclusion of a 10-W heater at B would reduce this time to less than 4 min. The steady-state temperature can be varied by increments of 5°K and the temperature stability is $\pm \frac{1}{2}$ °K for the time needed to locate, focus on, and photograph the required area several times. The system is economical, more than 20 hr running at the lowest temperature from one gas cylinder. A full assessment of this stage will be reported elsewhere.¹

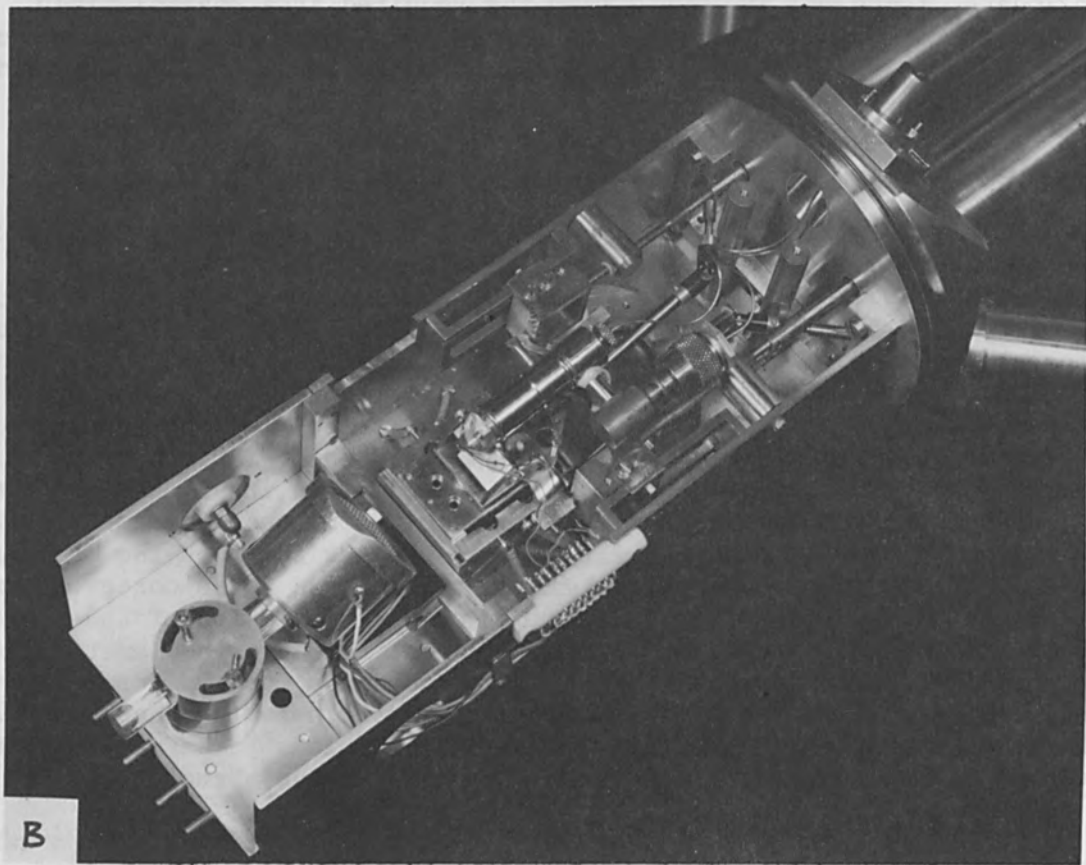
APPLICATIONS OF OIL-FREE SEM

Figure 4 shows quantitative estimates of the current multiplication occurring in avalanche diodes, in particular of that occurring at diffusion-induced dislocations. Although these defects have been well documented^{2,3} this is the first time that it has been shown that their presence leads to localized breakdown. The quantitative data were obtained by passing the charge collection signal after amplification through a comparator which can be set at a fixed signal level (0 to 5 V) with a gate width of 30 mV. In the oil-pumped system, the relatively rapid film buildup while the information is being recorded can invalidate the quantitative information as a significant (probably nonlinear) correction has then to be applied. Figure 5 illustrates the way in which the SEM can be used to study the physical origins of the excess noise observed⁴ in avalanche diodes. The figure shows the spatial variation of the current multiplication as a function of diode current for a large-diameter diode. As the diameter is decreased the breakdown becomes more uniform (Fig. 6). This behavior is reflected to some extent in the noise characteristics shown in Fig. 7, which also shows how some anomalous peaks may be related to breakdown occurring in the guard ring part of the structure.

Figure 8 illustrates another situation in which contamination can obscure the observations. There is a possibility that the properties of the subsurface Si-SiO₂ interface can be studied in the SEM by using low beam voltages so that the oxide layer charges up to an extent determined



A



B

FIG. 3.—Rapid cooling specimen stage based on miniature Joule-Thomson liquifier. (a) The cooler itself; (b) the cooler in use.

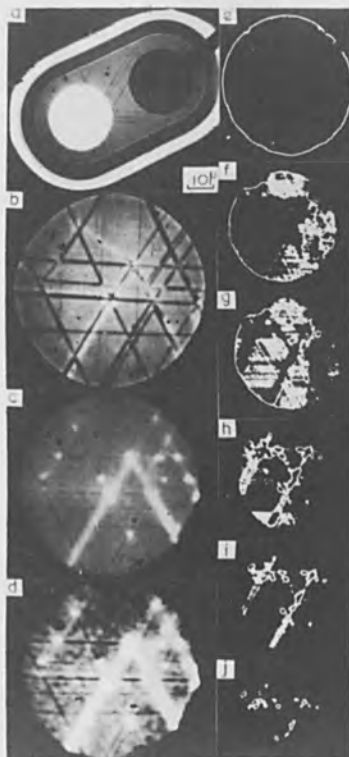


FIG. 4.—Charge collection maps of an avalanche diode showing (1) localized current multiplication at diffusion induced dislocations, with (a) to (d) micrographs taken at 0, 0, 8.43, and 8.52 V diode reverse bias, respectively; (2) use of a comparator to obtain quantitative estimates of current multiplication. Micrographs (e) to (j) are charge collection maps taken with the comparator set at 2.00, 3.23, 3.30, 3.40, and 3.52 V, respectively. Bias on diode, 7.49 V.

by the local variations in insulator resistivity and thickness. The way in which this "charge-up" contrast can reveal features lying below the oxide (or nitride) surface is shown in Fig. 8. As the beam voltage is increased from 1.5 to 20 kV additional contrast first becomes apparent and then fades. Such additional contrast is absent in conventional optical micrographs taken at similar magnifications (Fig. 8f). We have observed contrast of this type having the characteristics of drying marks, of faults in photoresist, of scratches, and of plausible extensions of visible surface faults. In an environment which produces an insulator-like contamination film, the contrast due to variations in the specimen insulator film can be complicated or obscured by effects due to contamination.

We have also used the oil-free system to study: (1) the way in which the contrast observed using surface-barrier counters depends on film thickness, on target atomic number, and on the beam parameters; and (2) a temperature-sensitive contrast observed on a multifinger power transistor when run at high powers. In neither case has contamination interfered with observation.

CONCLUSIONS

It should be stressed that much can be done to reduce contamination interference with a far simpler system than used here. Oil-pump systems

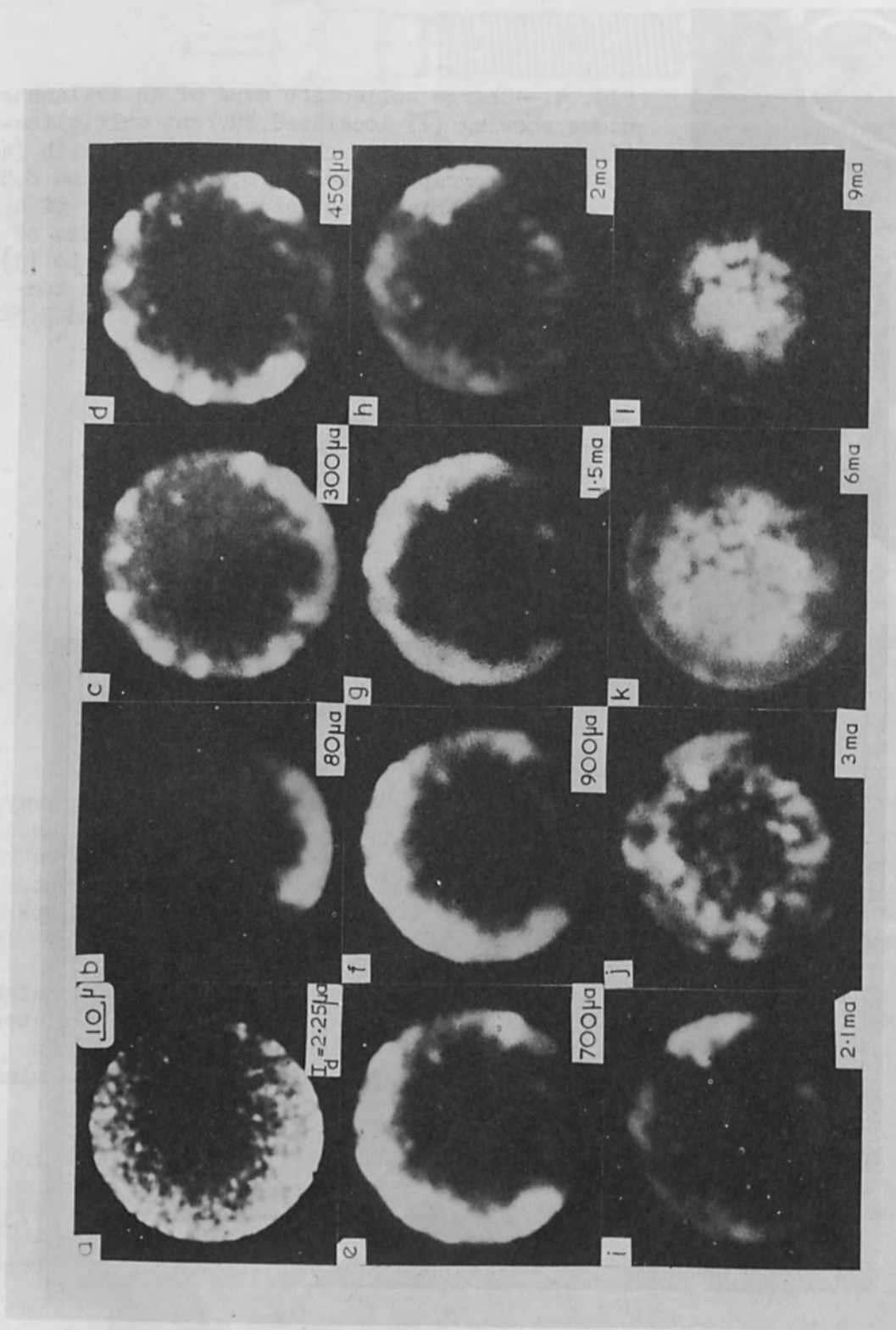


FIG. 5.—Charge collection maps of a large-area avalanche diode run at very high currents showing the nonuniformity of the device behavior.

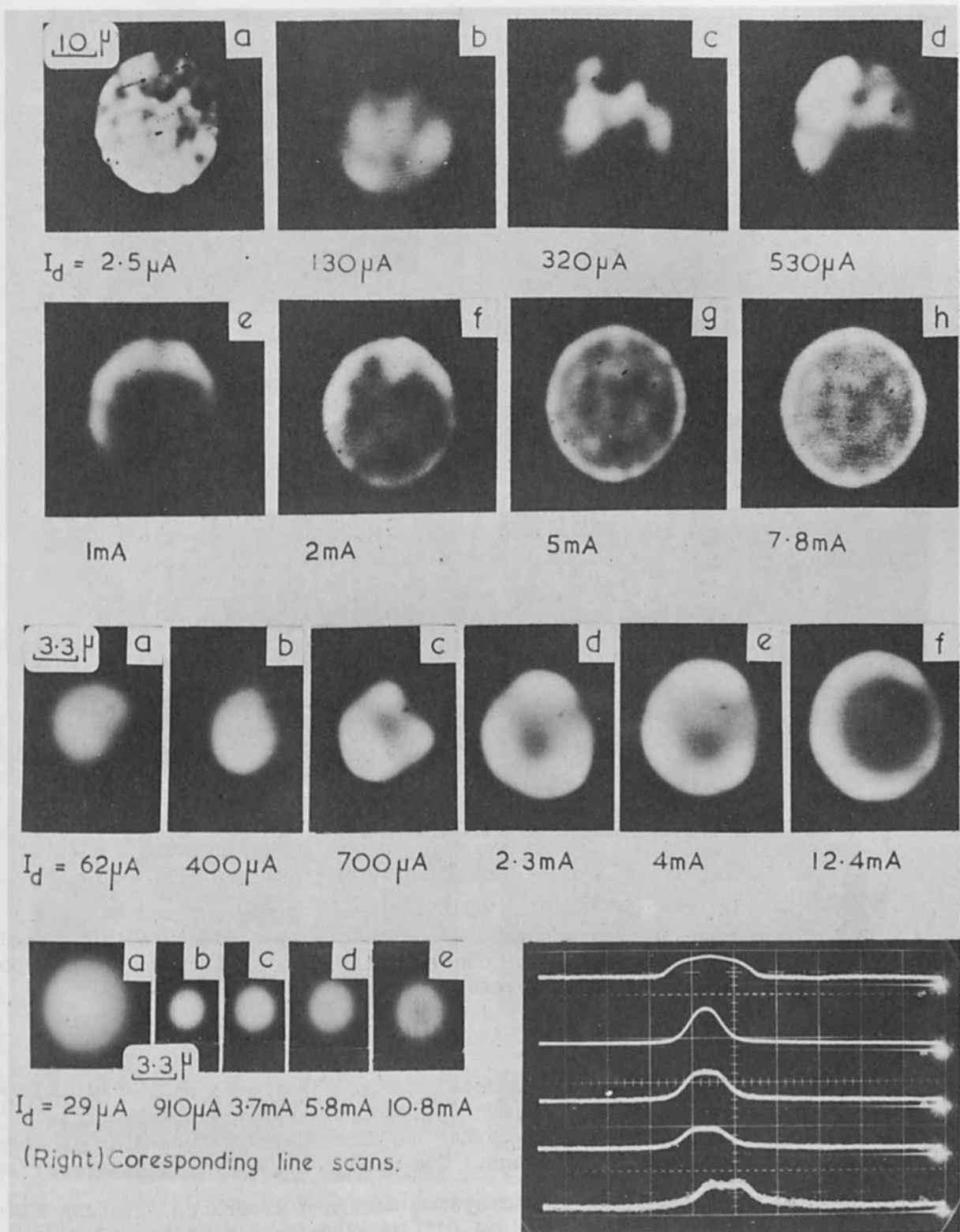


FIG. 6.—Micrographs similar to those of Fig. 5 but for smaller device diameters, showing the increase in uniformity and symmetry of the charge collection. The line scans shown correspond to the charge collection "maps" of the smallest diode. The micrograph lettering corresponds to that shown in Fig. 7.

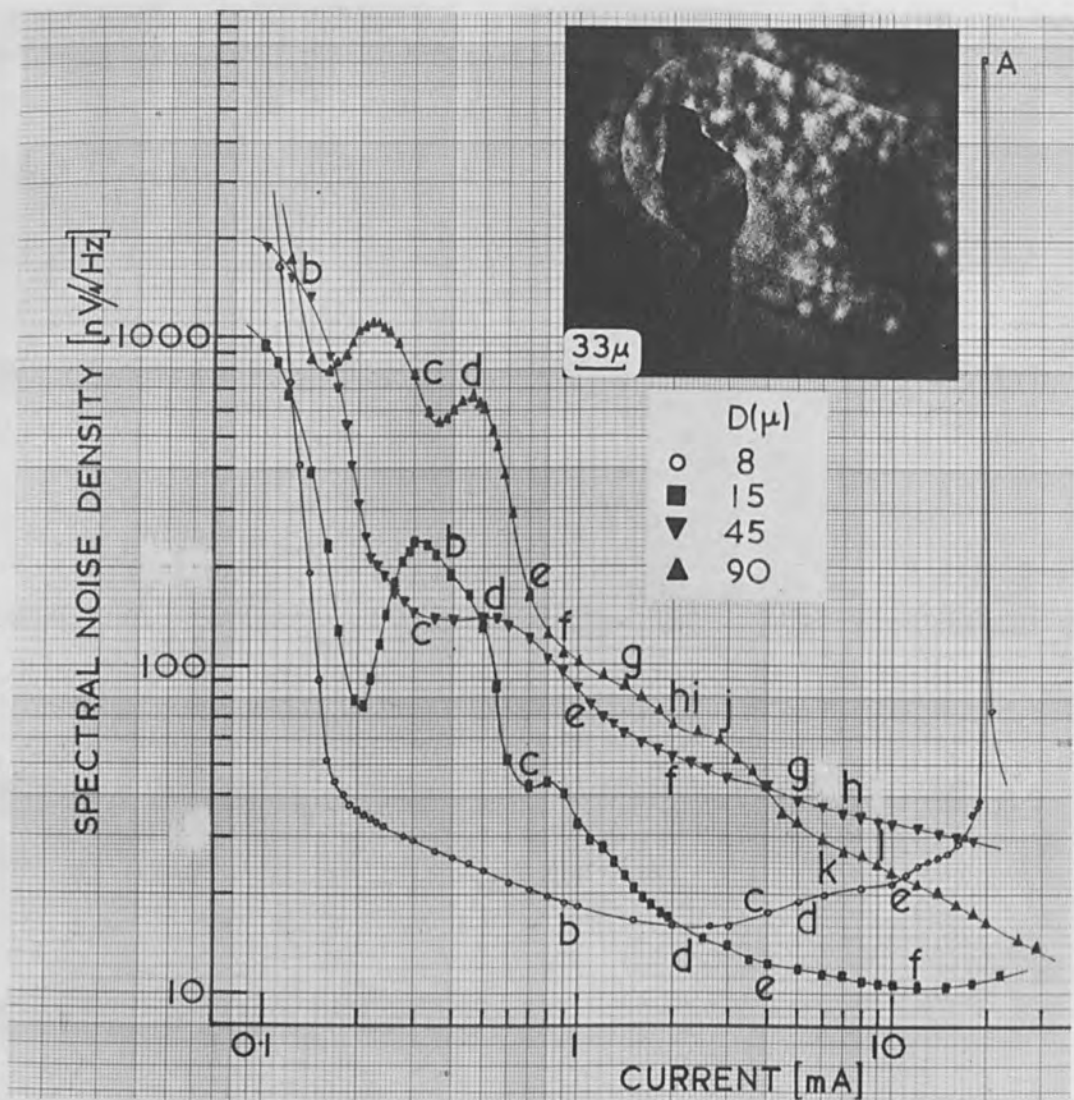


FIG. 7.—Noise characteristics of the diodes of Figs. 5 and 6. The lettering on the curves corresponds to that on the micrographs in Figs. 5 and 6. The insert shows the charge collection at a current corresponding to the anomalous peak marked A.

with baffles and strict cleanliness go some way toward achieving this aim. The present system is aimed ultimately at providing a versatile ultrahigh vacuum system suitable for surface physics studies and a very wide range of other applications. The main conclusions to date are:

- (1) An unbaked ion pumped system designed around an existing SEM can give a vacuum of the order of 10^{-7} torr in an acceptable time and can be cycled to ambient pressure at least ten times in one day.
- (2) There is no significant degradation of the resolution or contrast due to the use of ion pumps close to the column.
- (3) Vibration due to high-pressure gas flow, boiling refrigerant, or lack of mechanical coupling between the stage and the final lens is

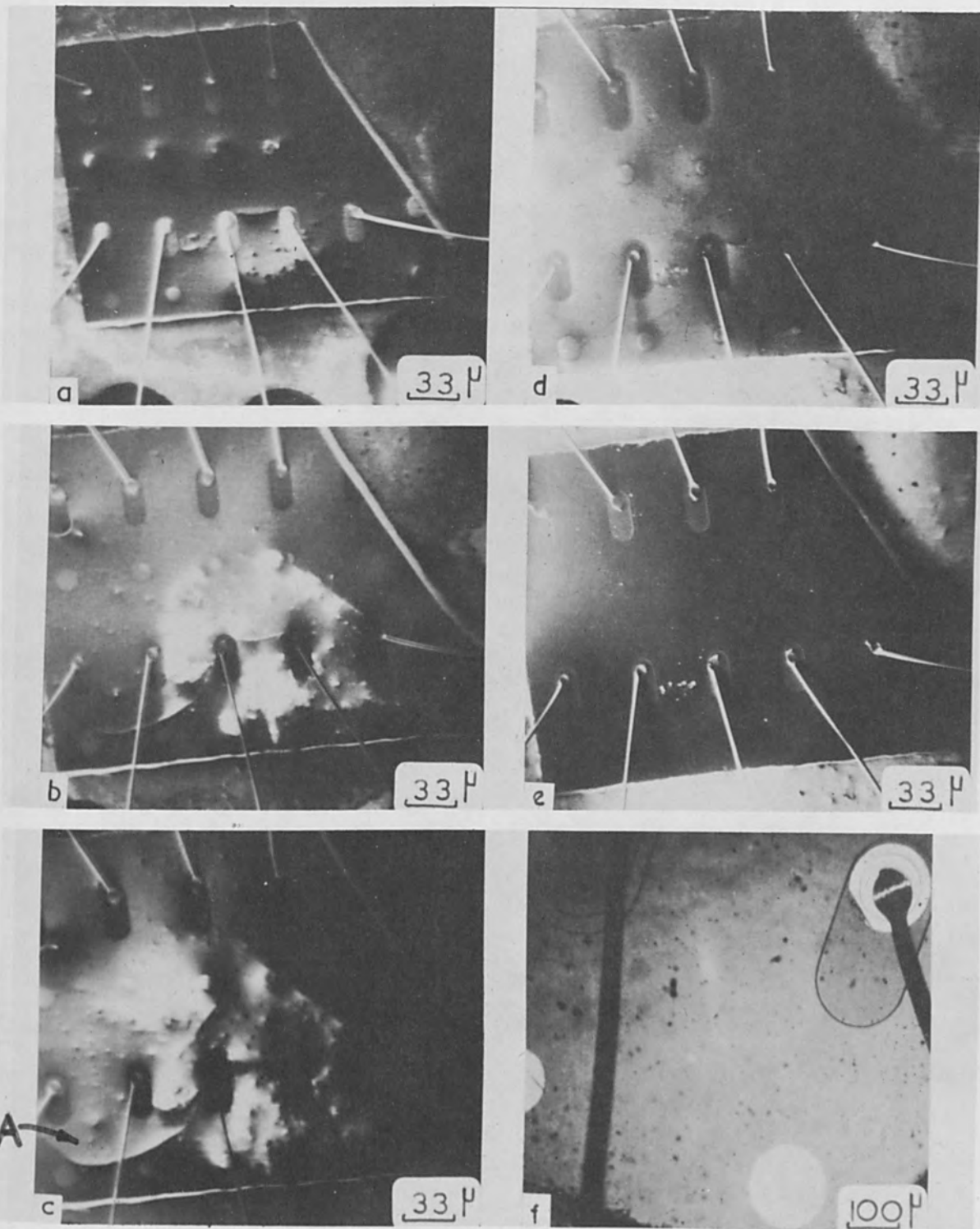


FIG. 8.—Additional contrast observed on insulator specimens at low beam voltages. Specimen: passivated SiO₂-Si device chip, emissive micrographs (a) to (e) taken at 1, 2.5, 3, 5, and 20 kV, respectively. Figure 8(f) is an optical micrograph of the region marked A in figure 8(c), but rotated through 180°.

not a problem at present; i.e., resolutions approaching 300 Å can be obtained.

(4) Earlier suggestions⁵ that contamination arises both from pump oil and from absorbed films on the specimen stage and on the chamber walls have been confirmed. The elimination of oil pumps greatly reduces the contamination deposition rate. The residual contamination from cleaned chamber walls does not impede a wide use of the SEM at high magnifications for prolonged times. Baking would lead to further reduction.

ACKNOWLEDGMENTS

The writers wish to thank W. A. Evans, D. A. Shaw, and C. Millward for technical help in support of this work. The financial assistance of the Science Research Council and of the Ministry of Defence (Navy Department) is gratefully acknowledged.

REFERENCES

1. R. C. Wayte and P. R. Thornton, Brit. J. Appl. Phys. (in preparation).
2. G. H. Schwuttke and H. T. Queisser, J. Appl. Phys. 33: 1540, 1962.
3. J. J. Lander, H. Schreiber, T. M. Buck, and J. R. Mathews, Appl. Phys. Letters 3: 206, 1963.
4. R. H. Haitz and F. W. Voltmer, Appl. Phys. Letters 9: 381, 1966.
5. G. C. Stewart (private communication).

THE APPLICATION OF SCANNING ELECTRON MICROSCOPY TO IMPERFECTION ANALYSIS IN SILICON INTEGRATED CIRCUITS

C. J. VARKER and E. M. JULEFF

Westinghouse Electric Corp., Elkridge, Maryland

ABSTRACT. This paper provides preliminary results on the application of scanning electron microscopy to the observation of imperfections induced in silicon integrated circuits by standard manufacturing procedures. Measurement and inspection masks for integrated circuits (MIMIC) are used to provide a test wafer capable of scanning electron microscope evaluation, initially as a silicon wafer single unit (30 mm diameter), and subsequently as 12 discrete test dies (3 mm square) containing a variety of integrated circuit devices. The electron beam induced current mode (EBIC) is found to be the most suitable for revealing and interpreting surface and bulk imperfections induced by standard manufacturing procedures. MIMIC test wafers are evaluated at various critical stages in the fabrication of standard integrated circuits. Imperfections revealed and discussed include diffusion pipes, dislocations, slip lines, and precipitates.

INTRODUCTION

In the manufacture of integrated circuits, silicon substrates are subjected to a variety of processing conditions which induce considerable physical damage in the final product. These processes include epitaxial growth, diffusion, and oxidation. At our laboratory, interest has been focused on the scanning electron microscope as a relatively nondestructive tool for investigating process-induced imperfections. In recent years numerous investigators using various techniques have revealed the extent of imperfections such as dislocations, slip, and precipitates which result from the diffusion of boron and phosphorus into silicon. However, much of this research was restricted to basically destructive analytical methods and to conditions which are not typical of those generally applied to the manufacture of integrated circuits. Although these results are desirable and informative, it is our objective to obtain information concerning the application of the scanning electron microscope to the problems associated with real manufacturing processes.

It is the purpose of this paper to describe a technique for utilizing the scanning electron microscope as an inspection tool for silicon wafers processed according to standard manufacturing procedures. The method relies on the fabrication of test-vehicle wafers processed through standard manufacturing lines, but utilizing measurement and inspection masks for integrated circuits (MIMIC). These masks provide the capability for scanning electron microscope evaluation by various information-display modes, initially as silicon wafer single units (30 mm diameter) and subsequently as 12 discrete test dies (3 mm square) containing a variety of integrated-circuit devices. The ability of the scanning electron microscope to reveal process-induced imperfections such as diffusion pipes,

dislocations, slip, and precipitates are illustrated and discussed.

THE MIMIC TEST PATTERN

Present investigations with the scanning electron microscope reveal that optimum display conditions for observing imperfections in silicon are not provided in conventional small area integrated circuit structures, particularly when utilizing electron beam induced current signals. The effective utilization of the scanning electron microscope for imperfection analysis in integrated circuit manufacture requires a test vehicle which is compatible with both integrated circuit processing and the design requirements of the scanning electron microscope. This test vehicle is fabricated in the MIMIC pattern. It is designed primarily to overcome some of the technical problems associated with the complexity and small dimensions of present integrated circuits, when utilizing the various scanning techniques to reveal material imperfections induced by manufacturing processes.

A typical completed MIMIC test wafer is illustrated in Fig. 1 and

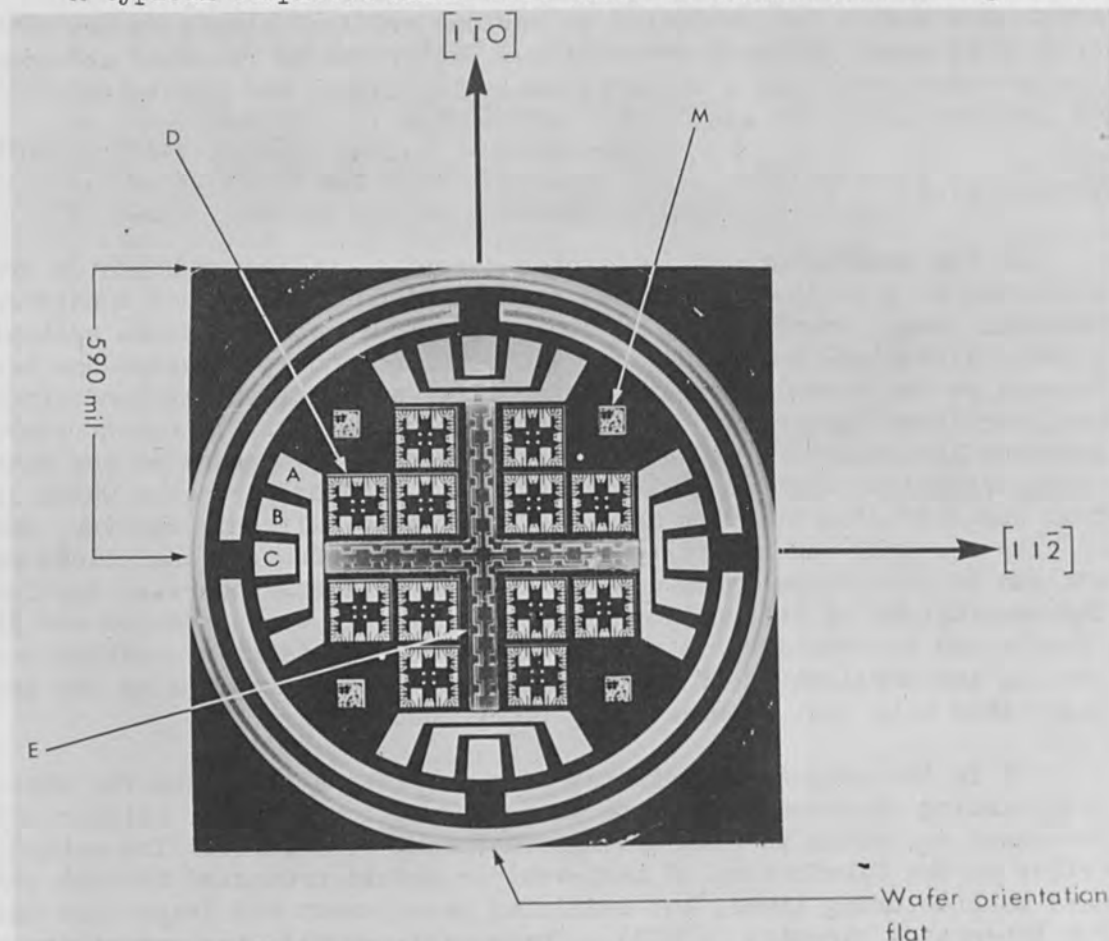


FIG. 1.—Typical processed MIMIC wafer.

provides the following components for process evaluation and electrical measurements:

- (1) A large area transistor cross E of arm length 7.5 mm and oriented in $\langle 110 \rangle$ and $\langle 211 \rangle$ directions relative to the (111) wafer surface

and reference flat. The contacts A, B, and C correspond to the emitter, base, and collector regions, respectively. Thus, the wafer can be evaluated with the SEM as a single unit over the large transistor cross.

(2) Test die distributed in triplets between the arms of the large transistor cross, for example, at D. An enlargement of the test die is illustrated in Fig. 2, and it is seen to be composed of the following elements:

(a) A small transistor cross e of arm length 0.8 mm and oriented with the transistor cross E. The contacts are identified as E, B, and C, corresponding to the emitter, base, and collector, respectively. A cross section through X reveals the structural profile in Fig. 3.

(b) Bipolar transistor pairs with a common collector and distributed in the four quadrants of the test die. These pairs are identified in Fig. 2 by the contacts e, b, and, c corresponding to the emitter, base, and collector regions, respectively. The geometrical dimensions of these transistors are comparable to those of standard integrated circuit transistors.

(c) Unipolar MOS field-effect transistors distributed in the four quadrants of the test die and identified by the contacts d, g, and s, corresponding to the drain, gate, and source contacts, respectively.

(d) MOS capacitors distributed in the four quadrants of the test die and identified by the contacts 1 and 2.

(3) Measurement and test circuit (see M in Fig. 1), distributed in the four quadrants of the large transistor cross, E.

The purpose of the large and small transistor crosses E and e illustrated in Figs. 1 and 2, respectively, is to provide large areas for scanning electron microscope evaluation of diffused regions to determine the extent of process-induced damage. The devices in the test die, however, are provided to examine the effect of electron bombardment on electrical characteristics, for example, β -degradation in the bipolar transistor pairs and unipolar MOSFETs. The capacitors are provided to investigate the SiO₂ insulator material. The work reported in this paper was performed on the large and small transistor cross areas described above, but we propose to extend the investigations to test die devices in a later publication.

PROCESSING CONDITIONS

MIMIC wafers were fabricated utilizing two standard integrated circuit manufacturing processes. The process sequence is provided in Tables 1 and 2 for these types of circuit. Surface concentrations assuming ERFC distributions were determined from measurements of diffusion depths by angle lapping and staining and from the sheet-resistance measurements.

TEST VEHICLE PREPARATION. The initial point in integrated circuit manufacture where the scanning electron microscope (SEM) can be utilized effectively as a process analysis tool is following the isolation diffusion cycle. This process sequence provides a continuous electrical path between the silicon surface and the underlying P substrate, thus providing direct access to the epitaxial substrate junction. Ohmic contacts are formed to the epitaxial material using the standard N⁺ emitter diffusion. Subsequently, the wafer is metallized and etched to form the interconnect pattern. In this manner, MIMIC test vehicles which have been incorporated

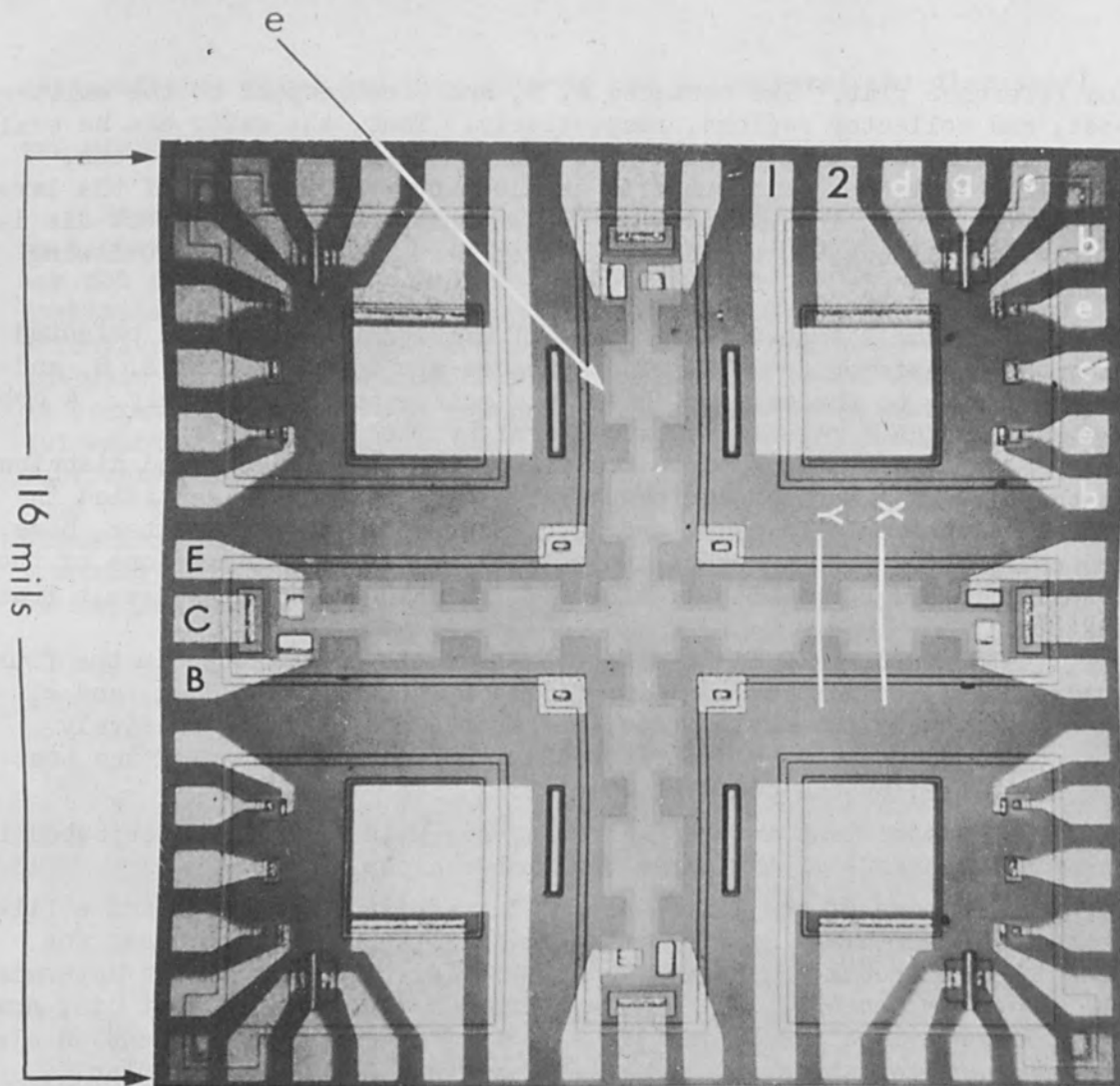


FIG. 2.—Test die using MIMIC pattern.

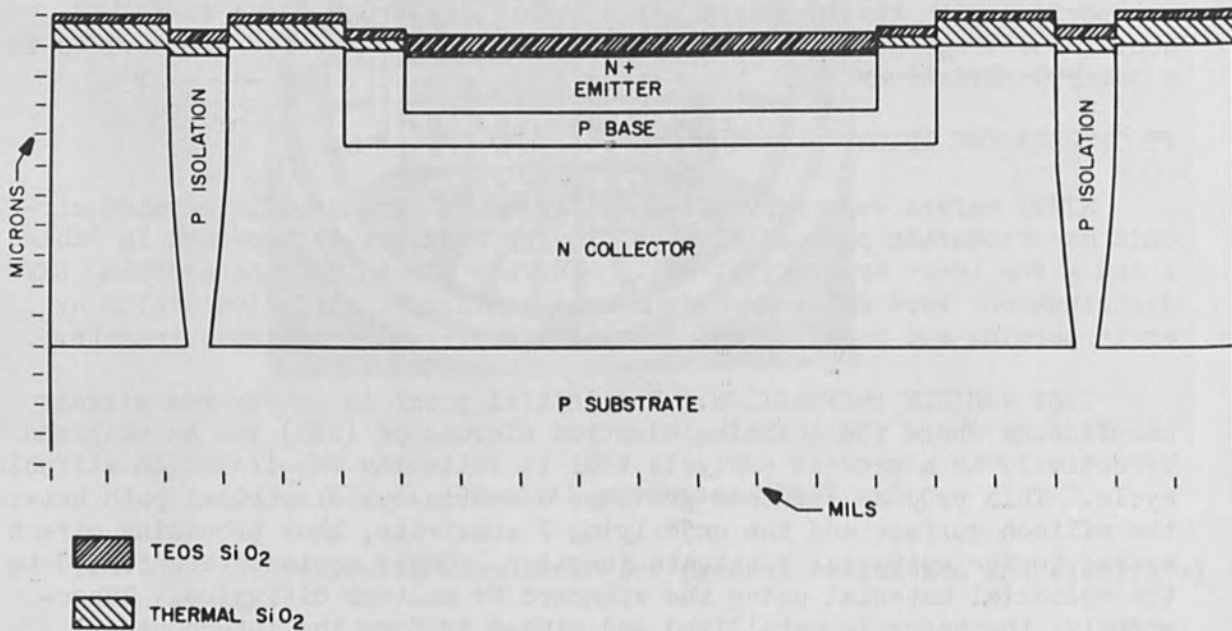


FIG. 3.—Typical MIMIC device profile (transistor cross).

| PROCESS STAGE | TABLE 1. ---Target parameters for process A. | | | | | | | | MASK |
|-------------------------|--|------|-----------------------------------|--------------------------|---|-------------------------------------|---|--|---------------|
| | DOPANT | TYPE | RESISTIVITY ρ Ω CM | THICKNESS t MICRONS | SHEET RESISTIVITY ρ_s Ω / \square | DIFFUSION DEPTH x_j MICRONS | BULK DOPANT CONCENTRATION N_1 ATOM CM ⁻³ | SURFACE DOPANT CONCENTRATION C_s ATOM CM ⁻³ | |
| POLISHED WAFERS | BORON | P | 10-40 | 200 | | | .4-1.5x10 ¹⁵ | | |
| EPITAXIAL LAYERS | 1 ARSINE | N+ | 0.085 | 4.2 | | | 10 ¹⁷ | | |
| | 2 ARSINE | N | 0.9 | 11.8 | | | 6x10 ¹⁵ | | |
| OXIDATION (THERMAL) | | | | 0.8 | | | | | |
| ISOL. DIFFUSION DEPOSIT | BBr ₃ | P+ | | | 4.5 | | | | ISOLATION |
| DRIVE | | | | | 5 | 13 | | 5.5x10 ¹⁹ | |
| OXIDATION (THERMAL) | | | | 0.35 | | | | | |
| B&R DIFFUSION DEPOSIT | BBr ₃ | P | | | 63 | | | | B&R |
| DRIVE | | | | | 200 | 3.7 | | 2.5x10 ¹⁸ | |
| OXIDATION (THERMAL) | | | | 0.40 | | | | | |
| EMITTER DIFF. DEPOSIT | POCl ₃ | N+ | | | 3 | | | | EMITTER |
| DRIVE | | | | | 2.5 | 2.8 | | 2.9x10 ²⁰ | |
| OXIDATION (THERMAL) | | | | 0.15 | | | | | |
| OXIDATION (TEOS) | | | | 0.25 | | | | | |
| EMITTER DIFF. DEPOSIT | BBr ₃ | P+ | | | 4.5 | 2.0 | | 5x10 ²⁰ | EMITTER |
| OXIDATION (TEOS) | | | | 0.25 | | | | | |
| ALUMINUM EVAP. | | | | | | | | | CONTACT |
| SINTER | | | | | | | | | INTER-CONNECT |

| PROCESS STAGE | TABLE 2. ---Target parameters for process B. | | | | | | | | MASK |
|----------------------|--|------|-----------------------------------|--------------------------|---|-------------------------------------|---|--|---------------|
| | DOPANT | TYPE | RESISTIVITY ρ Ω CM | THICKNESS t MICRONS | SHEET RESISTIVITY ρ_s Ω / \square | DIFFUSION DEPTH x_j MICRONS | BULK DOPANT CONCENTRATION N_1 ATOM CM ⁻³ | SURFACE DOPANT CONCENTRATION C_s ATOM CM ⁻³ | |
| POLISHED WAFERS | B | P | 10-40 | 200 | | | .4-1.5x10 ¹⁵ | | |
| EPITAXIAL LAYER | AsH ₃ | N | 0.3 | 9.0 | | | 2.5x10 ¹⁶ | | |
| OXIDATION (THERMAL) | | | | 0.8 | | | | | |
| ISOL. DIFFUSION DEP. | BBr ₃ | P+ | | | 4.2 | | | | ISOLATION |
| DRIVE | | | | | 5.0 | | | | |
| OXIDATION (THERMAL) | | | | 0.35 | | | | | |
| B&R DIFFUSION DEP. | B ₂ H ₆ | P | | | 30 | | | | B&R |
| DRIVE | | | | | 105 | 1.2 | | 3.5x10 ¹⁹ | |
| OXIDATION (THERMAL) | | | | 0.04 | | | | | |
| EMITTER DIFF. DEP. | PH ₃ | N+ | | | 6 | 0.9 | | 1x10 ²¹ | EMITTER |
| DRIVE | | | | | | | | | |
| OXIDATION (THERMAL) | | | | 0.15 | | | | | |
| OXIDATION (TEOS) | | | | 0.25 | | | | | |
| ALUMINUM EVAP. | | | | | | | | | CONTACT |
| SINTER | | | | | | | | | INTER-CONNECT |

in standard process lots can be selected at random and removed from on-line processing following critical manufacturing stages and subsequently prepared for SEM analysis.

A fully processed wafer is then positioned directly onto a specially designed target pedestal Fig. 4 and subsequently inserted into the specimen chamber for analysis. The pedestal incorporates the mechanical contacts and signal leads required for withdrawing display signals directly from the silicon wafer.

The alternative method, which is used for a detailed examination of smaller regions and for devices measurements, requires the standard circuit assembly operations. The test dies are normally mounted in 12-pin 3/8-in. square integrated-circuit FLAT PAKs and the desired device terminals are then selected for wire bonding. The assembled unit is positioned onto a target pedestal designed particularly for integrated circuits and inserted directly into the SEM. The majority of samples discussed here were prepared by this latter method, since the FLAT PAK pedestal permits smaller target to lens spacing, thereby improving display resolution.



FIG. 4.—Target pedestal for MIMIC wafer.

DISPLAY CONDITIONS. The scanning electron microscope utilized in this investigation comprises a three-lens system, incorporating a double deflection beam scanning assembly. A digital scan generator provides line sweep rates of 512 μ sec to 16.8 sec at typically 1000 lines/raster. The nominal instrument conditions applied in this study are the following;

| | |
|------------------------|--------------------------|
| Beam voltage | 15 KV |
| Target current | 10^{-10} - 10^{-8} A |
| Sweep rate | 64 ms/line |
| Target-to-lens spacing | 0.5-5.0 cm |
| Chamber pressure | About 10^{-6} torr |

The information displays obtained with the scanning electron microscope utilize the electron beam induced current mode (EBIC) exclusively, since it is the most informative display technique for revealing process induced semiconductor imperfections. A schematic representation of this mode applied to n+ emitter evaluation is provided in Fig. 5. In this illustration the base-emitter pn junction collects the electron-hole pairs generated in the emitter region by the scanning electron beam. It has been established that imperfections in the Si lattice in the path of the

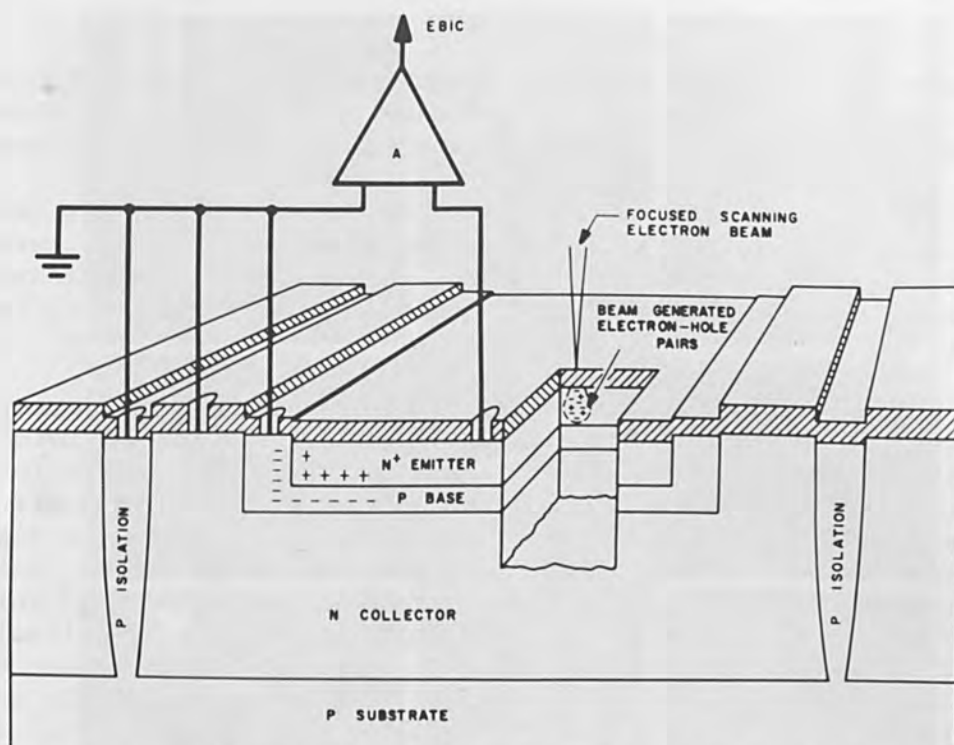


FIG. 5.—EBIC mode using the emitter-base pn junction.

diffusing electron-hole pairs enhance carrier recombination with a resultant decrease in the junction current. Thus, imperfections appear as reduced current signals when suitably amplified and displayed on a CRT scanned in synchronism with the primary beam.

PROCESS ANALYSIS. To distinguish imperfections generated by the relevant process from those previously existing in the substrate and subsequent epitaxial layer, an initial evaluation using techniques other than scanning electron microscopy is necessary.

A determination was made of the extent of imperfections in the original substrate by selecting a wafer for Lang scanning x-ray diffraction analysis. The technique is capable of a resolution of about 1-2 microns and reveals Si lattice strain fields associated with dislocations, precipitates, clusters, etc., by enhanced diffraction of an x-ray beam in the neighborhood of the imperfection.

From the results of this analysis, it is evident that the original Si substrate is relatively dislocation and damage free. To confirm this, several substrate wafers were subjected to the Sirtl etching technique and, in general, it was found that 90% of the wafer area indicated a dislocation density of less than 10 cm^{-2} .

The initial stage in the Process B logic manufacturing process (Table 2) excluding the floating collector diffusion, requires the growth of an epitaxial layer, of resistivity $\rho = 0.3 \text{ ohm-cm}$ and thickness $t = 9.0$ micron, by the standard $\text{SiCl}_4:\text{H}_2$ reduction process. Several wafers were withdrawn from the process at this stage and destructively analyzed for imperfections using a Sirtl etch and interference contrast microscopy. It was found that the center 90% of these wafers also indicated a

dislocation density of less than 10 cm^{-2} and a stacking fault density of less than 1 cm^{-2} . However, the 10% edge region revealed a stacking fault distribution generally associated with scratches on the substrate surface.

The results presented in the following sections concern imperfections directly associated with the manufacturing method which are revealed with the scanning electron microscope and confirmed with other techniques, following both the P isolation-diffusion and the N emitter-diffusion processes.

POSTISOLATION DIFFUSION. The electron-beam induced current (EBIC) analysis of epitaxial material following the isolation diffusion utilizes the current generated at the epitaxial substrate PN junction for the information signal. The display technique requires a carrier diffusion length comparable to the depth of the epitaxial layer. For optimum display conditions, one desires low resistivity and relatively thin epitaxial layers. Since the integrated-circuit process revealed in Table 2, to which we refer as process B, requires a thin epitaxial layer of relatively low resistivity, this process was selected initially in preference to Process A, which requires a double epi-layer. This choice was partly a result of the poor display conditions which resulted from the "floating" collector layer associated with Process A.

Initial investigations using the EBIC mode indicated a time-dependent charge-storage effect when scanning the relatively low-surface-concentration epitaxial material. During the examination the image tends to darken gradually reducing the ability to distinguish imperfections. It was found that this effect can be minimized by control of the charge density over the area scanned by the beam. Results indicate that for this material, the charge density should not exceed $10^{-6} \text{ coul-cm}^{-2}$ to prevent excessive image decay. Thus, since the charge density is dependent on the magnification, it is necessary to reduce the target current proportionately for smaller scan areas when operating at higher magnifications.

Although the display conditions utilizing the epi-substrate junction are not optimum for revealing crystalline defects, the EBIC display mode has revealed several process-induced imperfections in the epitaxial material. Figure 6 reveals the isolation junction surrounding the small cross inside a test die. In addition to the vertical isolation wall pn junction, several bright rings with dark centers are visible, A and B. These rings are associated with pinholes in the SiO_2 layer which are revealed by optical microscopy using a Nomarski prism for interference contrast (Fig. 7). Now, if the diameter of the SiO_2 holes observed in Fig. 7 is d and the isolation diffusion produces a junction depth x_j , then the surface diameter D of the rings observed in the EBIC mode is $D \approx 2x_j + d$, assuming the lateral diffusion is approximately equal to the vertical diffusion depth x_j . Detailed measurements on several displays confirm this result. Thus, these imperfections are isolation diffusion pipes extending to the substrate-epitaxial pn junction. In general, the ring diameter is about 25 microns and the hole d is about 5 microns (compare A and B in Figs. 6 and 7).

It should be emphasized that since the penetration depth of a diffusion pipe depends on the initial diameter of the oxide hole, below a

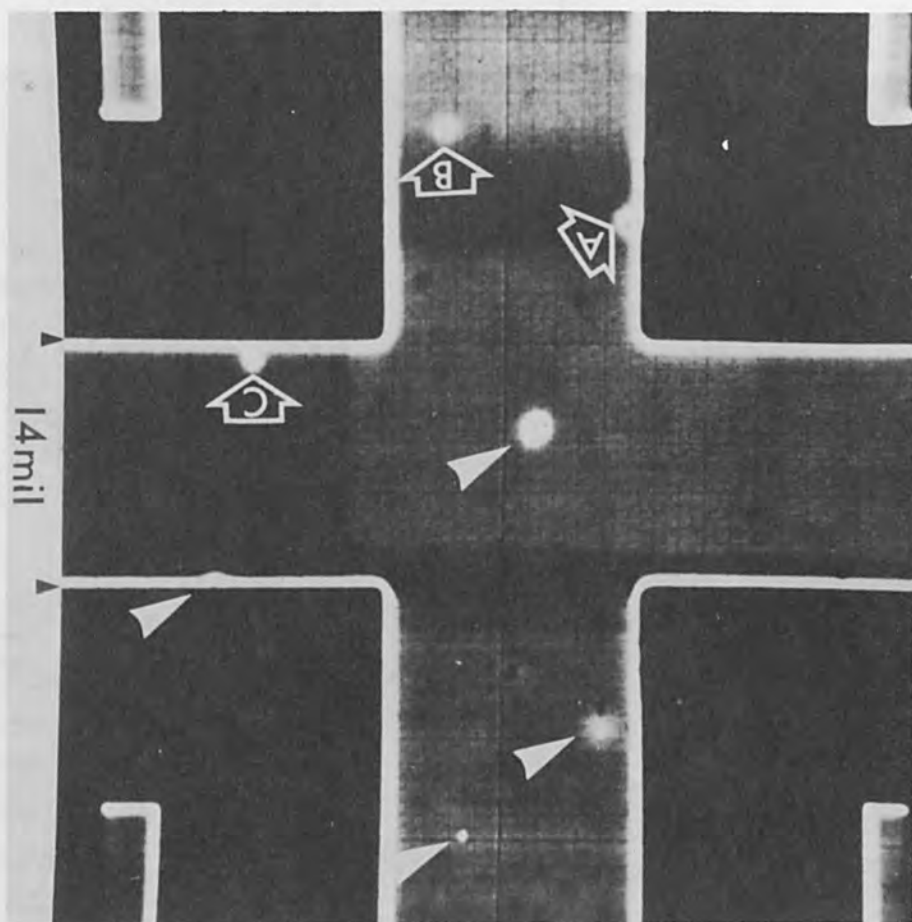


FIG. 6.—EBIC micrograph showing isolation diffusion pipes.

certain size range, this method of display will reveal only those pipes which penetrate the epitaxial layer completely (Fig. 8). However, the distribution of pipes at intermediate depths, which range between the base-collector junction depth and the epitaxial layer depth can be determined by utilizing the base-collector junction as the signal source.

The density of oxide pinholes on fully processed MIMIC wafers was determined by interference contrast microscopy. For defects larger than several microns in diameter the density ranged from $300 - 1500 \text{ cm}^{-2}$ for different processed lots. It was also observed that the density recorded on individual wafers increased with each subsequent processing step. The evidence suggest that the oxide pinholes are associated with the photochemical masking operations. Figure 6 displays a diffusion pipe density of approximately 800 cm^{-2} which falls within the range observed using interference contrast microscopy, and therefore represents a typical sample. The previous results apply only to SiO_2 holes over relatively perfect bulk silicon. If the SiO_2 mask defect is associated with a stacking fault (Fig. 9a), then diffusion apparently can occur preferentially along the $\{111\}$ walls of the fault (Fig. 9b). Confirmation that these defects were p-type diffusion pipes is determined by 30° angle-lapping and stain procedures (Fig. 9c). The stacking fault case may be unique, but since the stacking fault density is very low in these wafers further investigations are necessary to confirm whether they always give rise to diffusion pipes. A sketch illustrating the structure of diffusion

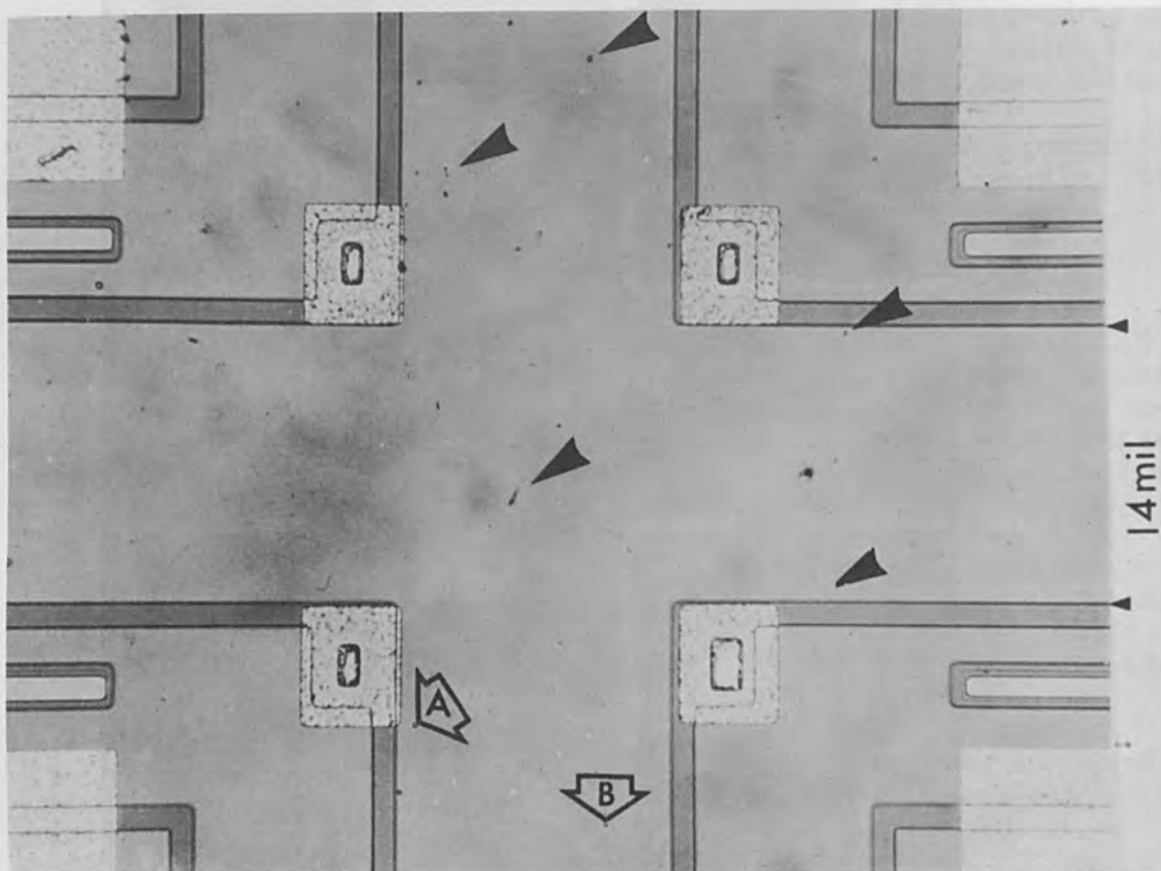
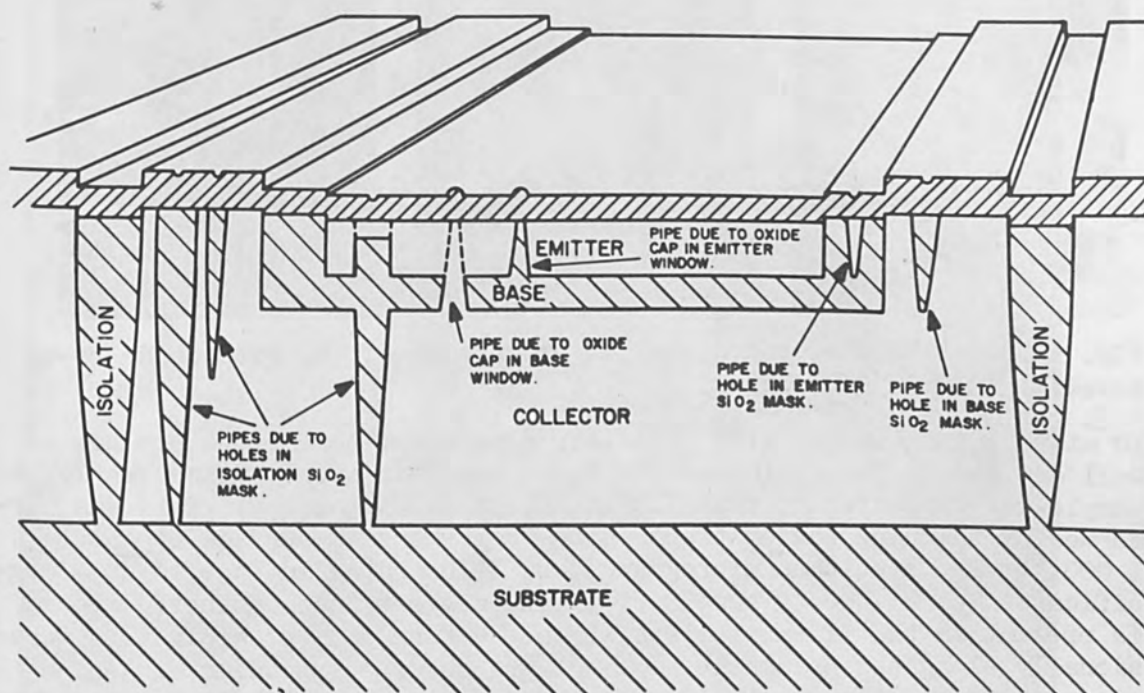


FIG. 7.—Interference contrast micrograph showing oxide holes.

pipes in a completed MIMIC wafer is shown in cross section in Fig. 8. It is evident that not all isolation diffusion pipes are detrimental to device performance. However, those that penetrate the epitaxial layer to the substrate, depending on the diameter of the SiO_2 defects, can cause base electrical shorting to the substrate. In addition, "negative pipes" are formed by residual oxide "caps" prior to base and emitter diffusions. An example of this type will be presented in the section on emitter analysis.

POSTEMITTER DIFFUSION ANALYSIS—PROCESS B. In a similar manner, information displays are obtained from the phosphorus diffused regions, of the transistor cross contained in the MIMIC test die, by utilizing the emitter-base junction. Results obtained on typical process B lots reveal the following details, as shown in Fig. 10(a). Dark rings with bright centers are observed which measure approximately 1 micron in diameter with a density of about 10^6 cm^{-2} . These imperfections are evident as small surface pits after oxide removal (Fig. 10b), and appear as well-defined oriented triangular etch pits following a Sirtl etch (Fig. 10c). The comparison illustrated in Fig. 10 reveals the degree of information contained directly in the SEM display. The etch pits in Fig. 10(c) suggest dislocations with a strong edge component intersecting the $\{111\}$ wafer surface.

The other imperfections consist of dense dark spots, approximately





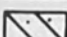
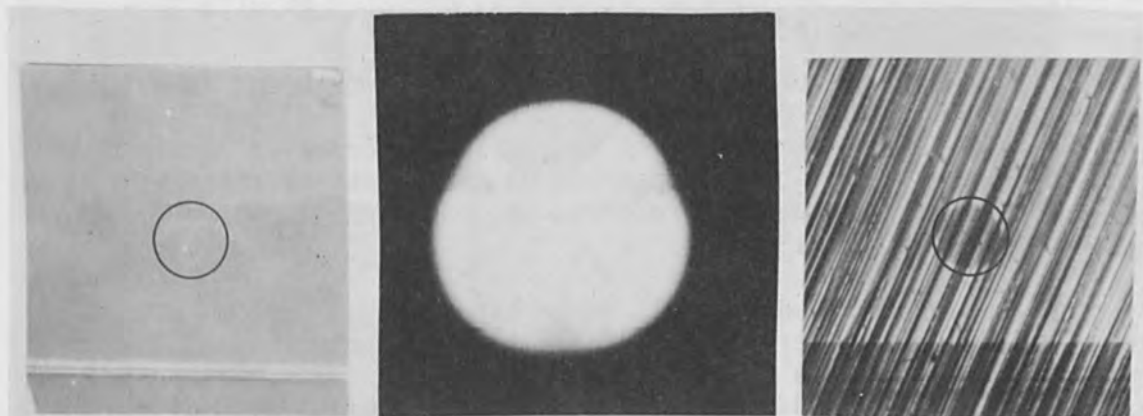
-  SiO₂
-  N-TYPE Si
-  P-TYPE Si

FIG. 8.—Diffusion pipes formed by improper masking procedures.



(a)

(b)

(c)

FIG. 9.—(a) Interference contrast micrograph of stacking fault (magnification 450 x); (b) EBIC micrograph (magnification 2000 x); (c) interference contrast following lap and p-stain (magnification 450 x).

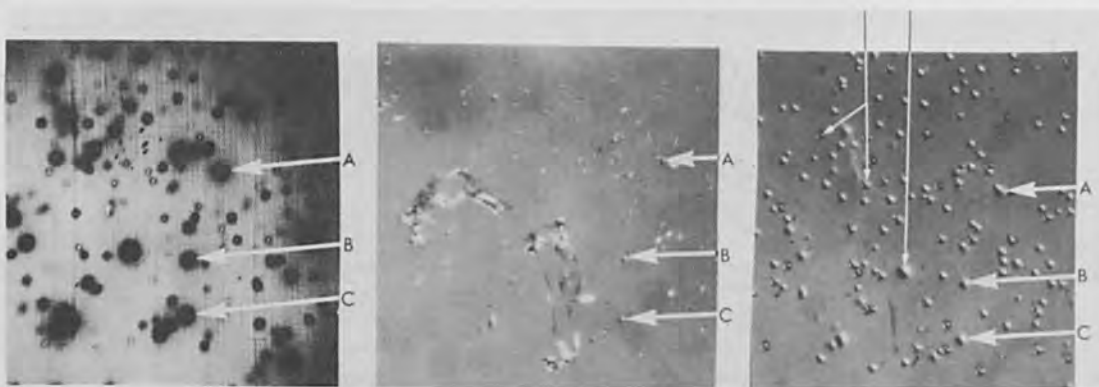


FIG. 10.—(a) EBIC micrograph of V_3 emitter area; (b) with oxide removed; (c) 1-min Sirtl etch.

10 microns in diameter with a similar density. These spots are not as well defined in Fig. 10(c) as are the triangular pits. Consequently, a sample was subjected to transmission electron microscopy. This was performed by thinning the emitter region from the back surface to about 1 000 Å. The resultant micrographs are illustrated in Fig. 11 at a magnification of 25,000. These micrographs suggest that another compound is present in the Si emitter region in the form of a precipitate. Occasionally elongated prismatic crystals are observed which are oriented along $\{110\}$ relative to the Si lattice, and possess clearly defined facets (Fig. 11a). In general, however, the structures appeared as equidimensional particles of less than 0.5 micron diameter and with an average density about 10^6 cm^{-2} (Fig. 11b). At present this compound has not been identified but it is believed to be a form of SiP precipitated as a result of the presence of a high concentration of inactive phosphorus near the emitter surface. Similar precipitates have been reported¹² in high concentration phosphorus diffused regions.

POSTEMITTER DIFFUSION ANALYSIS—PROCESS A. In contrast to the previous results, the process A wafers reveal oriented imperfections of three general types (Fig. 12).

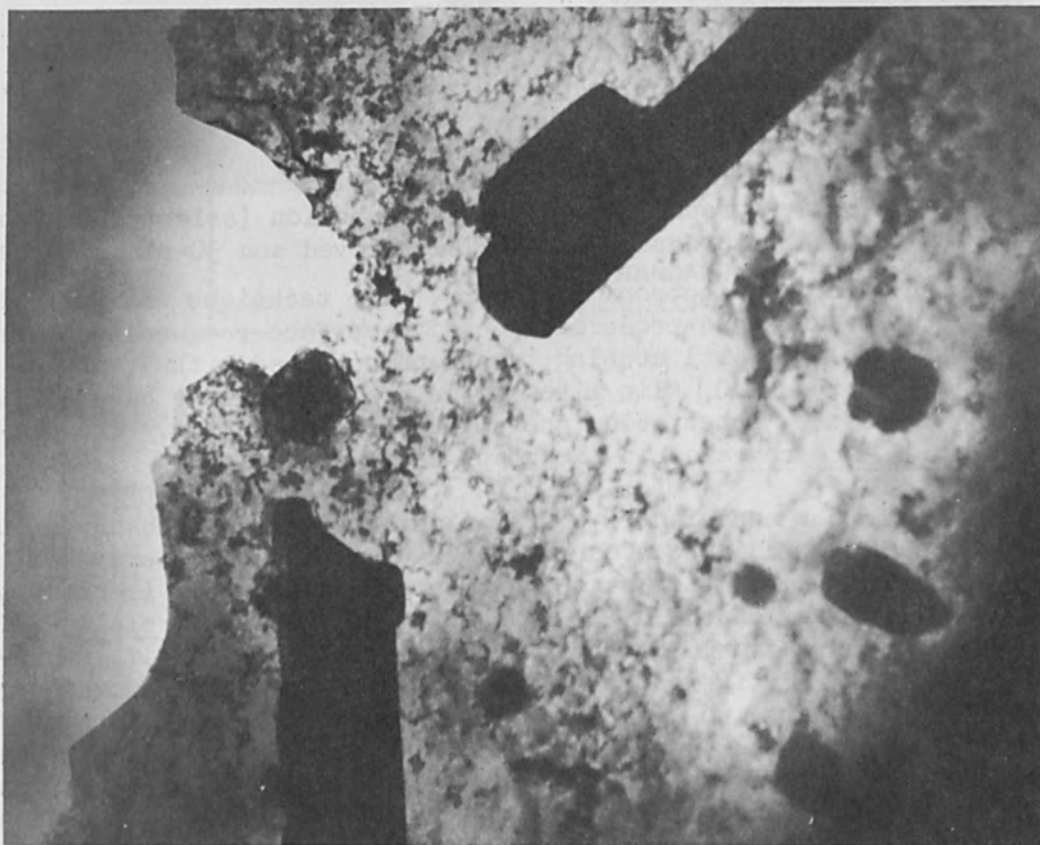
(a) $\{110\}$ oriented lines several mils in length and an estimated average density of $12\ 000 \text{ cm}^{-2}$

(b) $\{211\}$ oriented lines of length in the order of 12 microns

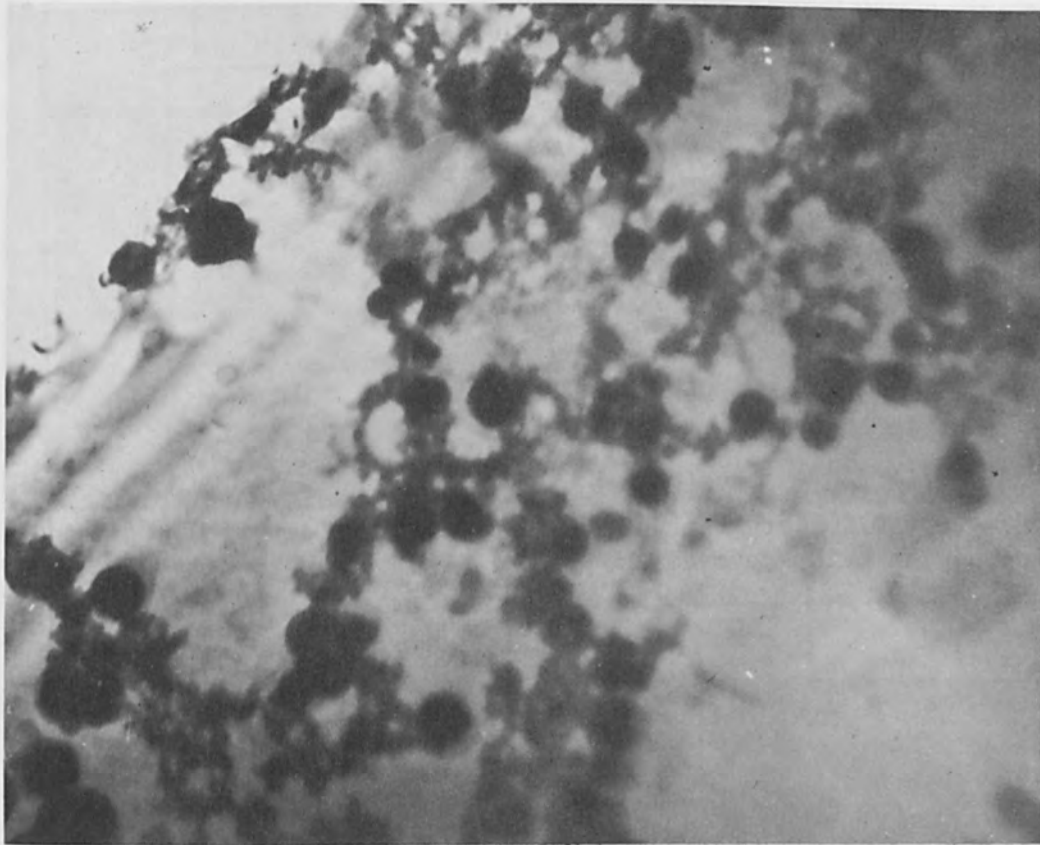
(c) edge dislocations appearing as dark spots of approximately 1 micron diameter (not clearly resolved but identified by Sirtl etching (see 1 and 2 in Fig. 13))

It was established that all three types are associated with the double-diffused emitter process (Table 1) and correspond to adjustments in the Si lattice as a result of the diffusion drive. Furthermore, it was observed both by SEM analysis and optical microscopy that in some cases variation in the distribution and density of the $\{110\}$ lines occurred across a wafer in the $\{110\}$ direction.

Accurate determination of the depth of $\{110\}$ slip lines in the emitter region is under investigation. Initial results indicate the slip density is related to the surface dopant concentration and distribution in agreement with other investigators.^{2,11} However, it is desirable to determine accurately the depth of the induced slip which often appears to penetrate into the base region. This determination was attempted initially on the process A lots using an anodization-dissolution



(a)



(b)

FIG. 11.—Electron transmission micrograph emitter area (magnification 25,000 x).

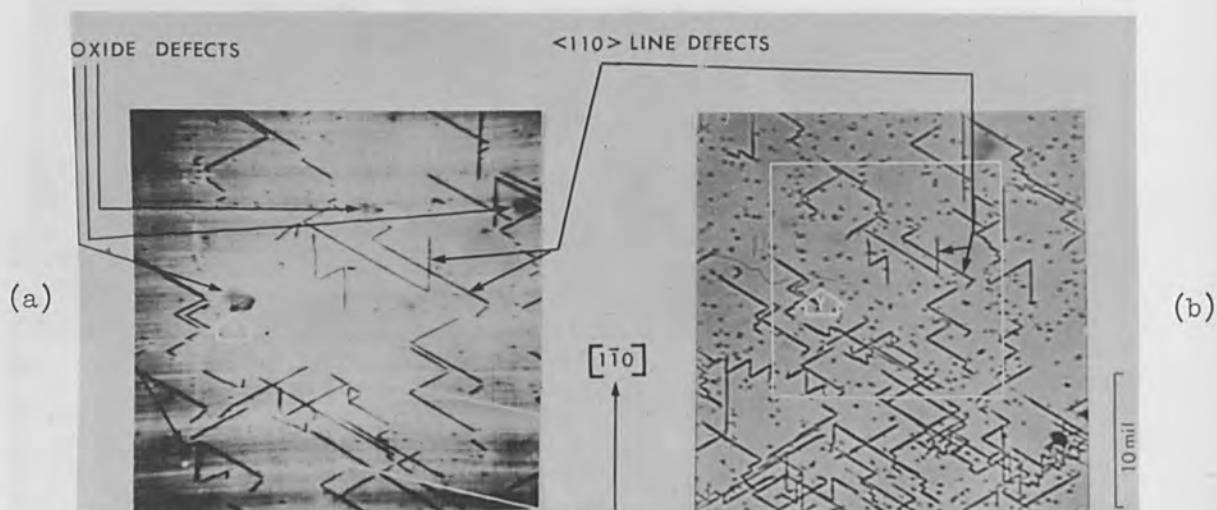


FIG. 12.—(a) EBIC micrograph at emitter-base junction; (b) optical micrograph with oxide removed and 30-sec Sirtl etch.

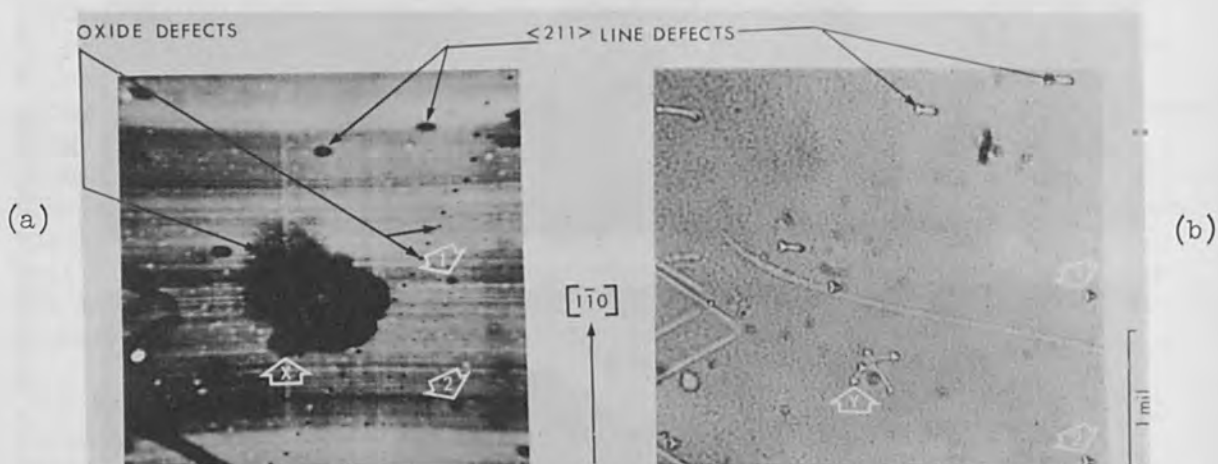


FIG. 13.—(a) EBIC micrograph at emitter-base junction (selected region of Fig. 12a); (b) optical micrograph with oxide removed and 30-sec Sirtl etch.

technique with scanning electron microscopy. The technique was found to be entirely too tedious and produced excessive surface roughening. More recently, a controlled Sirtl etching technique combined with 3° angle lapping has shown the $\{110\}$ slip lines to be near and in the base diffused region, and therefore, penetrating the emitter-base junction. The preliminary results are revealed in the graph shown in Fig. 14.

Less conspicuous nonoriented circular defects are also observed in the emitter region which appear as light rings with dark centers when examined by SEM at the emitter-base junction. Here the SiO_2 is present (Fig. 15). On removal of the SiO_2 , however, they appear as relatively uniform light spots (Fig. 16). This effect can be explained if, subsequent to the emitter diffusion, the SiO_2 was not completely removed in the area to be subjected to phosphorus diffusion; i.e., small caps of oxide remained preventing phosphorus diffusion from occurring in these regions; see dark centers in Fig. 15(b) resulting in "negative type" pipes as shown in Fig. 8. Thus, areas under the SiO_2 caps remain p-type (base diffusion), whereas the surrounding regions are n-type (emitter

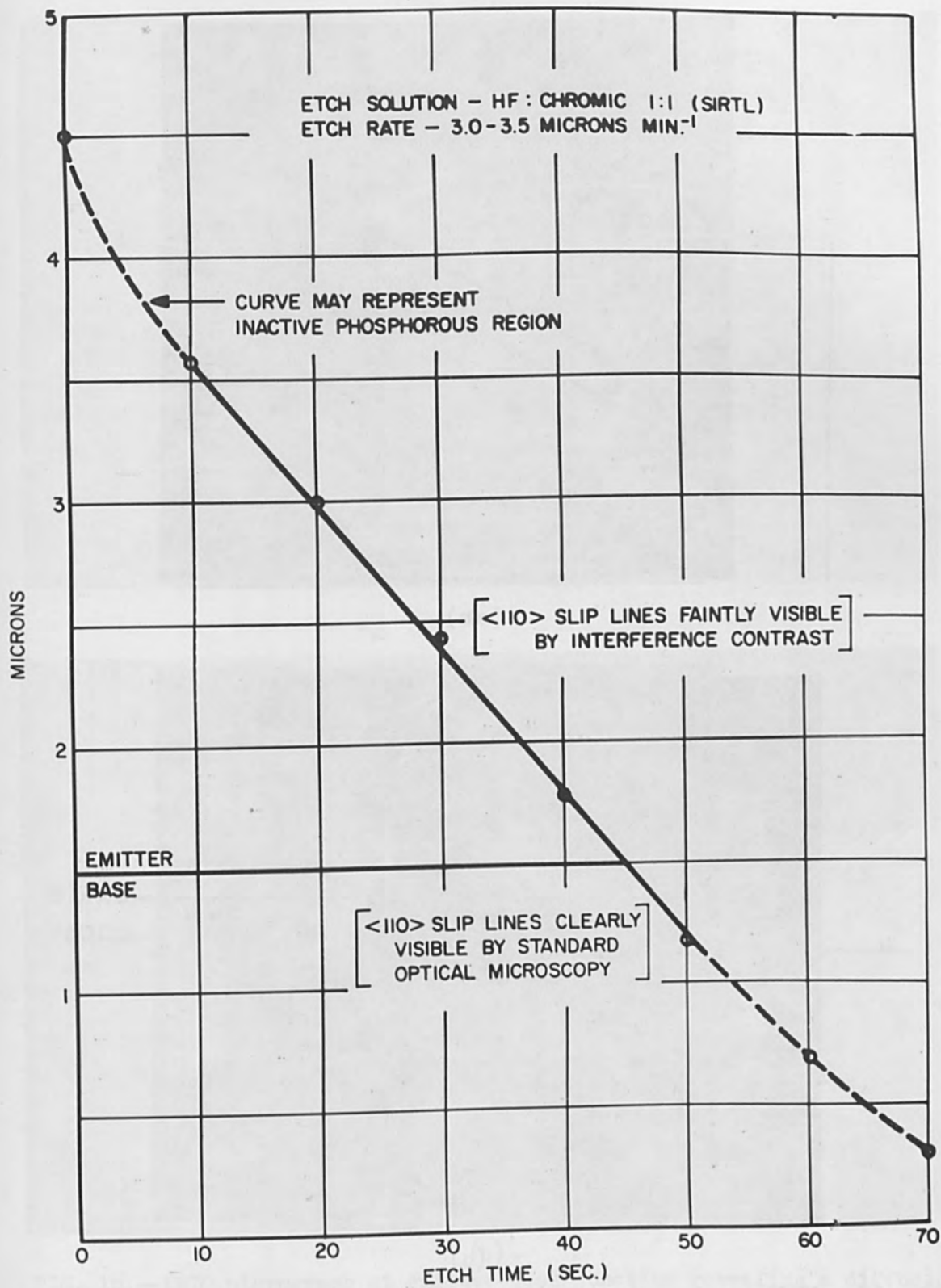
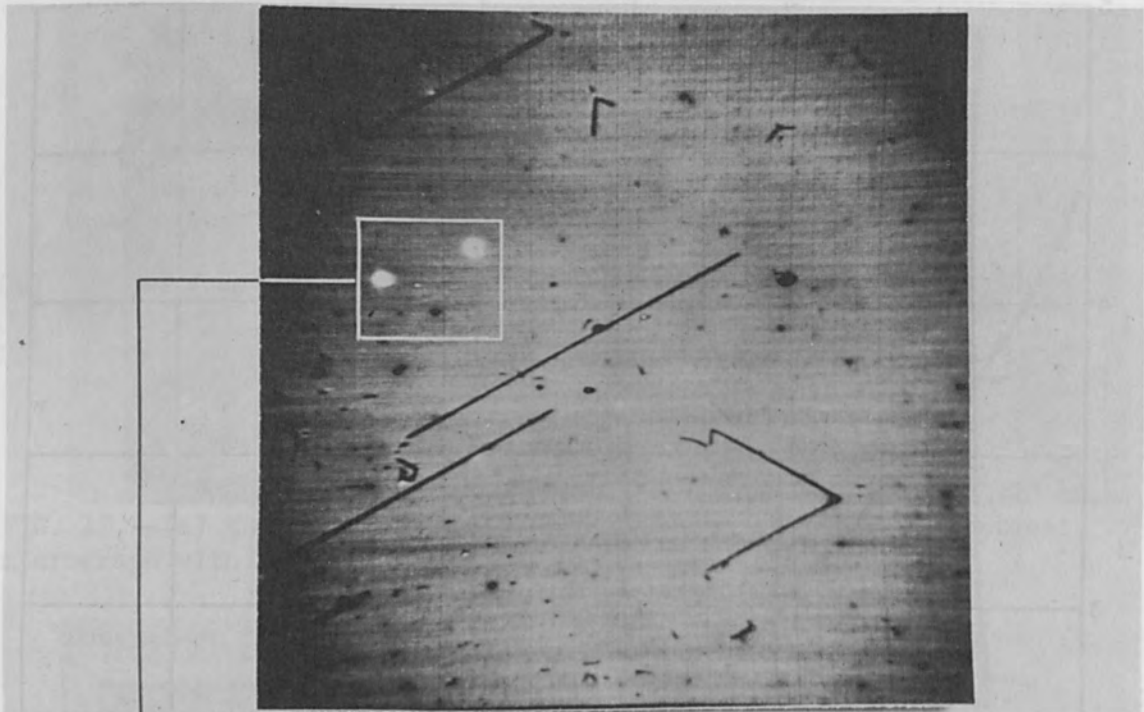
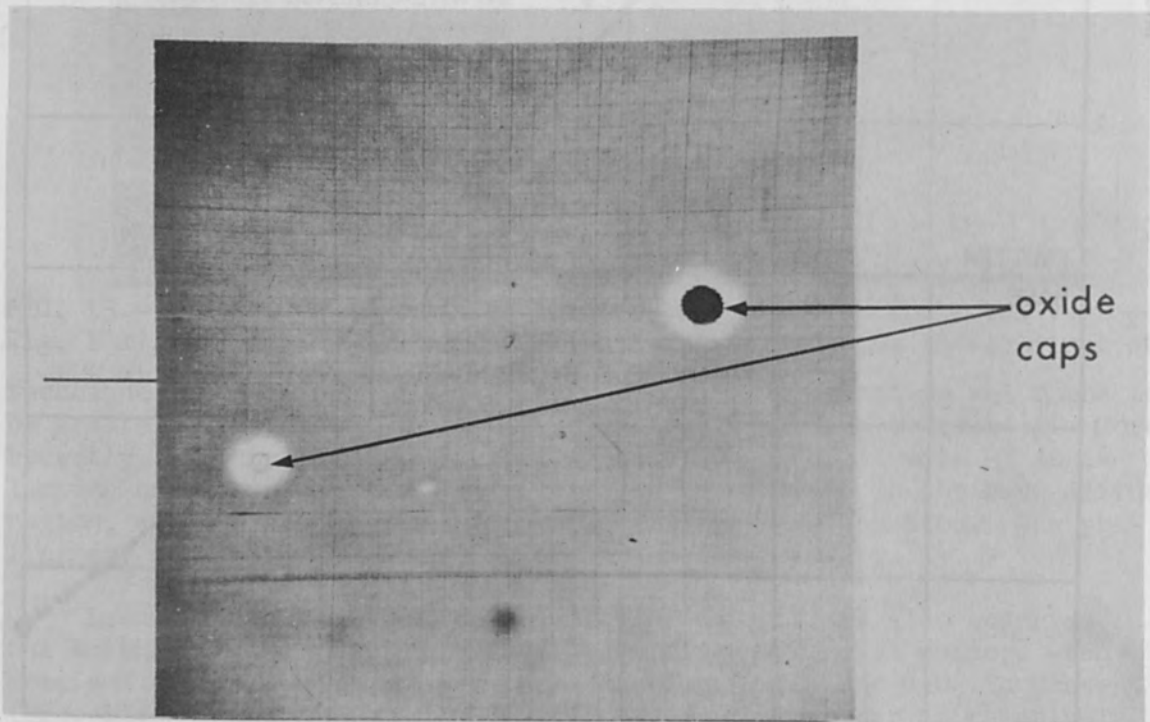


FIG. 14.—Sirtl etch graph revealing depth of diffusion induced slip.

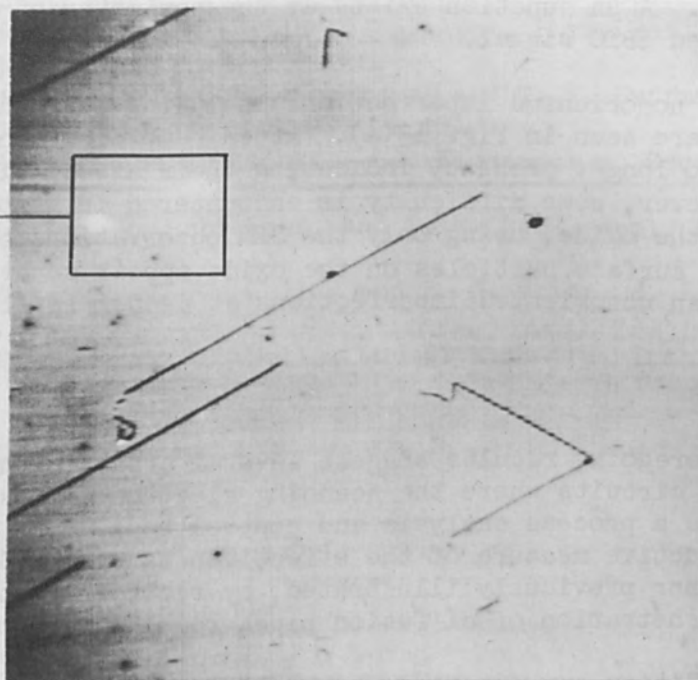


(a)

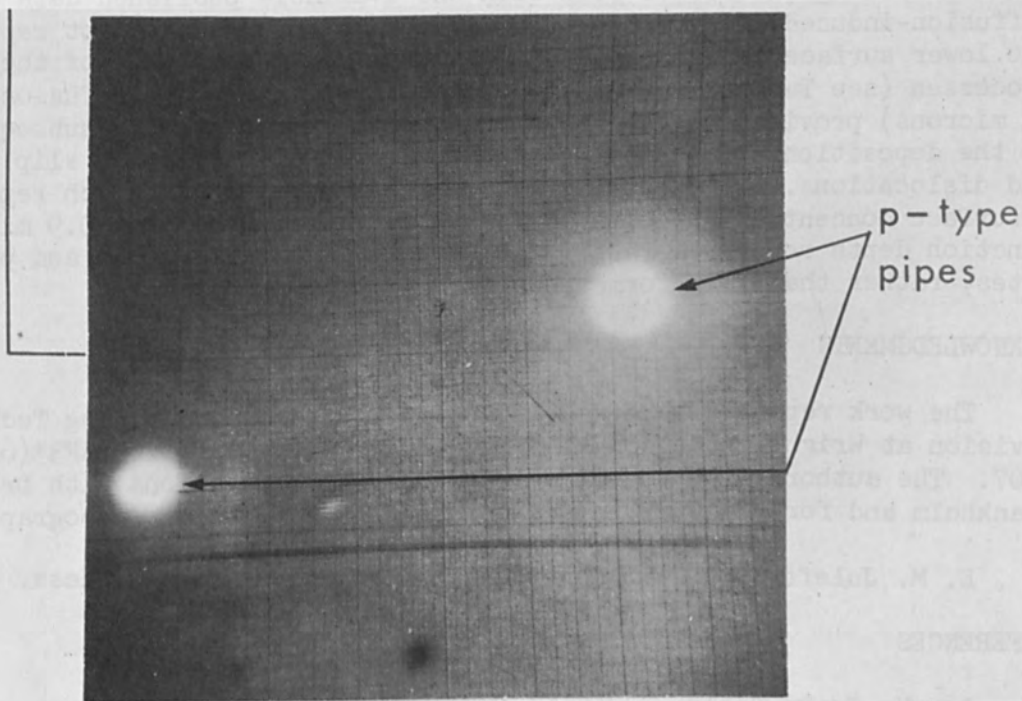


(b)

FIG. 15.—EBIC micrograph at emitter-base junction revealing a diffusion void ("negative pipe") - oxide present.



(a)



(b)

FIG. 16.—EBIC micrograph at emitter-base junction revealing a diffusion void - oxide removed.

diffusion). A pn junction exists at the perimeter of the caps producing an increased EBIC signal.

Other nonoriented imperfections including foreign particles and scratches are seen in Fig. 13(a). After removal of the SiO₂, however, they are no longer present, indicating their association with the oxide film. However, some difficulty is encountered in associating their presence with the oxide, using only the SEM observations before removal. Generally, surface particles on the oxide appear to be more sharply focused than nonoriented imperfections at deeper levels in the Si lattice.

CONCLUSIONS

The foregoing results suggest several areas in the manufacture of integrated circuits where the scanning electron microscope can be applied directly as a process analysis and control tool. SEM analysis provides a nondestructive measure of the effectiveness of the SiO₂ diffusion mask, in the manner previously illustrated, by recording both the density and range of penetration of diffusion pipes resulting from oxide imperfections.

In addition, as a process control tool it can be used to monitor nondestructively the diffusion-induced imperfections which result from each major diffusion processing step. The results obtained on Process A and B lots agrees rather well with the available published data on diffusion-induced imperfections in silicon. The process A lot represents the lower surface concentration (about 5×10^{20} atoms cm⁻³) of the two processes (see Tables 1 and 2) and represents the deeper diffusion front (2 microns) provided by the phosphorus redistribution drive subsequent to the deposition. The imperfections observed are primarily slip lines and dislocations. On the other hand, the process B lot, which represents a surface concentration about 10^{21} atom cm⁻² with a shallow 0.9 micron junction depth reveals a rather high density of dislocations and precipitates, rather than slip formations.

ACKNOWLEDGMENTS

The work reported here was sponsored by the Manufacturing Technology Division at Wright-Patterson Air Force Base under Contracts AF33(615)-5107. The authors wish to acknowledge helpful discussions with Dr. M. Frankholm and for his work in preparing the transmission micrographs.

E. M. Juleff is now at Honeywell, Inc., in Framingham, Mass.

REFERENCES

1. H. J. Queisser, J. Appl. Phys. 32: 1776, 1961.
2. S. Prussin, *ibid.* 32: 1876, 1961.
3. G. H. Schwuttke and H. J. Queisser, *ibid.* 33: 1540, 1962.
4. J. Washburn, C. Thomas, and H. J. Queisser, *ibid.* 35: 1909, 1964.
5. R. J. Jaccodine, Appl. Phys. Letters 4: 414, 1964.
6. W. Czaja and G. H. Wheatley, J. Appl. Phys. 35: 2782, 1964.
7. G. H. Schwuttke and H. Rupprecht, Bull. Am. Phys. Soc. 9: 649, 1964.

8. M. L. Joshi and F. Wilhelm, J. Electrochem. Soc. 112: 185, 1965.
9. M. L. Joshi and F. J. Wilhelm, J. Appl. Phys. 36: 2593, 1965.
10. W. Czaja, *ibid.* 37: 3441, 1966.
11. R. A. McDonald, C. G. Ehlergerger, and T. R. Huffman, Solid-State Electronics 9: 807, 1966.
12. P. F. Schmidt and R. Stiekler, J. Electrochem. Soc. 111: 1188, 1964.
13. J. J. Lander, H. Schreiber, and T. M. Buck, Appl. Phys. Letters 3: 206, 1963.
14. T. E. Everhart, O. C. Wells, and R. K. Matta, J. Electrochem. Soc. 3: 8, 1964.
15. T. E. Everhart, O. C. Wells, and R. K. Matta, Proc. IEEE 52: 1642, 1964.

LOW-VOLTAGE SCANNING ELECTRON MICROSCOPY

R. F. W. PEASE

Electronics Research Laboratory, University of California, Berkeley

INTRODUCTION

Most electron probe instruments (e.g., electron microprobe, x-ray analyzer, scanning electron microscope) have a region of constant potential between the final lens and the target. This feature does not offer any serious disadvantage when the final electron energy is of the order of 20 keV and places little restriction on specimen configuration. For certain applications, however, it is desirable that the final electron energy should be 1 keV or less. Such energies are desirable when a high secondary emission coefficient is desired, as when insulators are to be bombarded without charging¹; or when penetration is to be kept to a minimum, as in scanning electron microscopy of specimens of low atomic number or when it is desired to keep the energy input to a specimen to a minimum. Low energies are particularly useful when examining living specimens in the scanning electron microscope.²

Under these circumstances there are several advantages to employing a system in which the electrons have an energy of about 40 keV throughout most of the column and are only retarded to the required final energy by an electric field just in front of the specimen.

First of all there are a number of practical advantages. Electrons at 40 keV are much less sensitive to stray fields due to charged contamination or dust in the column than are, say, 100-eV electrons; and the higher-energy electrons are less affected by stray alternating magnetic fields arising from transformers or chokes. There are also a number of advantages on grounds of spherical aberration, chromatic aberration, and diffraction; and there is a resulting indirect advantage in current density.

The main disadvantage is that the specimen should be fairly flat so that there is no serious distortion of the retarding field. This restriction is also shared by emission and mirror electron microscopes.

Several workers (e.g., Zworykin, Hillier, and Snyder³ and Wolf⁴) have employed retarding-field systems for obtaining low energy probes. This paper presents a simple analysis to indicate the performance which might be achieved by use of such a system and also shows some experimental results.

ANALYSIS OF RETARDING FIELD SYSTEM

The system described consists of a standard scanning electron microscope column with the specimen held near cathode potential (Fig. 1). The final lens is of the asymmetric type often used in electron probe instruments.⁵ On the outside of the final polepiece is placed a small aperture

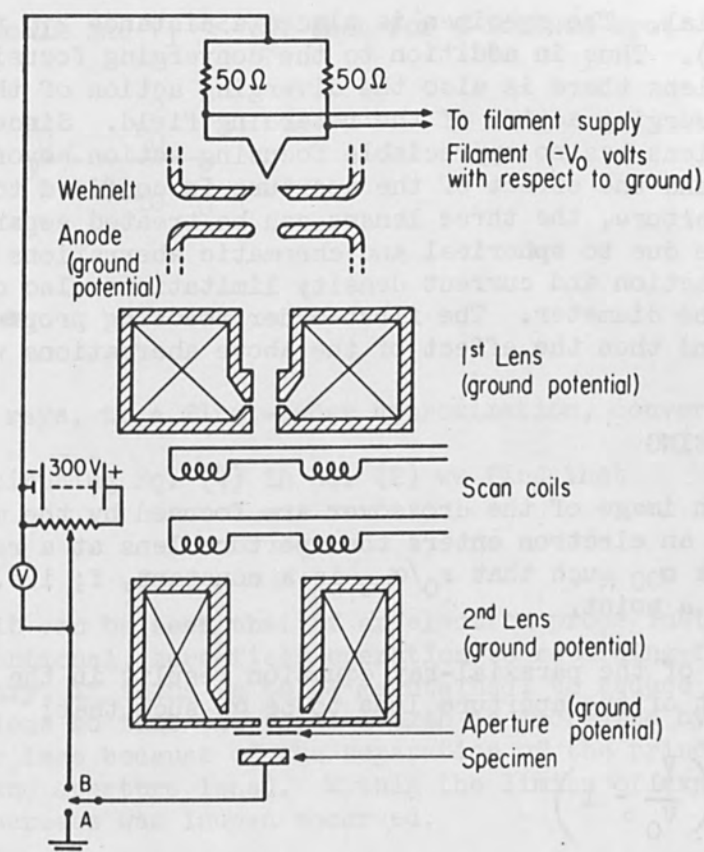


FIG. 1.—Schematic view of electron probe system. For retarding field operation the specimen is connected to B.

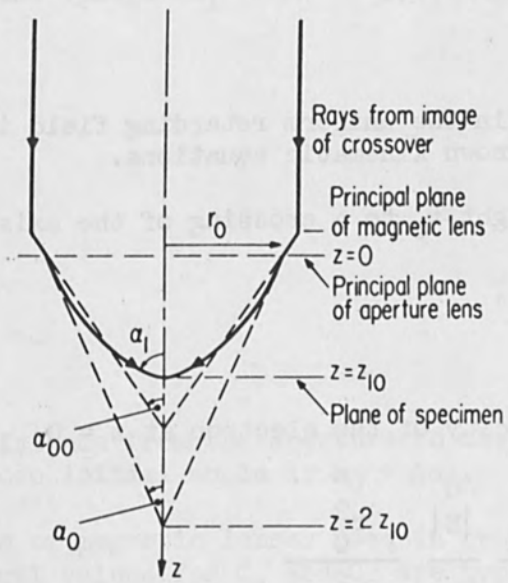


FIG. 2.—Ray diagram for retarding-field operation.

at ground potential. The specimen is placed a distance Z_{10} from the aperture (Fig. 2). Thus in addition to the converging focusing action of the magnetic lens there is also the diverging action of the aperture lens and the converging action of the retarding field. Since the asymmetric magnetic lens has no appreciable focusing action beyond the final polepiece bore, and the effect of the aperture is confined to a region very near the aperture, the three lenses can be treated separately. Aberrations arise due to spherical and chromatic aberrations of all three lenses and diffraction and current density limitations also contribute to the over-all probe diameter. The first-order focusing properties will be analyzed first and then the effect of the above aberrations will be examined.

FIRST ORDER FOCUSING

Rays from an image of the crossover are focused by the magnetic lens (Fig. 2) so that an electron enters the aperture lens at a radius r_0 and convergence angle α_{00} such that r_0/α_{00} is a constant, f ; i.e., all rays converge towards a point.

Integration of the paraxial-ray equation results in the convergence angle at the exit of the aperture lens to be α_0 such that:

$$\alpha_{00} - \alpha_0 = \frac{-r_0}{4z_{10}} \left(\frac{V_1}{V_0} - 1 \right) \quad (1)$$

where z_{10} is the distance between the aperture and the specimen.

If the specimen potential V_1 is much lower, with respect to the cathode, than the aperture potential, then

$$\alpha_0 = \alpha_{00} - \frac{r_0}{4z_{10}} \quad (2)$$

The trajectory in the uniform retarding field is a parabola and can be found from well known kinematic equations.

The time of flight t_0 to a crossing of the axis at z_1 is

$$t_0 = \frac{r_0}{v_0 \sin \alpha_0}$$

where v_0 is the velocity of the electron at $z = 0$

$$\text{and } z_1 = \frac{r_0 \cos \alpha_0}{\sin \alpha_0} - \frac{|E|}{4V_0} \frac{r_0^2}{\sin^2 \alpha_0} \quad (3)$$

If α_0 is small and $V_1 \ll V_0$, then for a focused spot

$$Z_1 = Z_{10} = \frac{r_0}{\alpha_0} - \frac{r_0^2}{4Z_{10}\alpha_0^2}$$

$$Z_{10} = r_0/2\alpha_0 \quad (4)$$

Hence all rays, to a first-order approximation, converge to a point.

Substituting Eq. (4) in Eq. (2) we find that

$$\alpha_0 = \frac{2}{3} \alpha_{00} \quad (5)$$

From (5) it can be seen that if an electron probe instrument is switched from conventional, zero-field operation to retarding-field operation it is necessary, if focus is to be maintained, to reduce the current in the magnetic lens so that the focal length is increased by a factor of 4/3 (or rather less because of the separation of the principal planes of the magnetic and aperture lens). Within the limits of experimental error such an increase was indeed observed.

EFFECT OF ABERRATIONS OF MAGNETIC LENS AND APERTURE LENS

Such aberration gives rise to a spread $\Delta\alpha_0$ about the initial angle α_0 at the entrance to the retarding field.

From Eq. (3) the spread ΔZ_1 in Z_1 is given by

$$\frac{\Delta Z_1}{\Delta\alpha_0} = \frac{-r_0}{\alpha_0^2} + \frac{|E|r_0^2}{2V_0\alpha_0^3}$$

Therefore

$$\Delta Z_1 = \frac{-V_1}{V_0} \frac{r_0}{\alpha_0^2} \Delta\alpha_0 \quad (6)$$

Z_1 refers to the distance from the aperture to the intersection of the axis with a ray whose initial angle is $\alpha_0 + \Delta\alpha_0$.

The aberration of magnetic lenses used in probe instruments is well known.⁶ Typical values for C_s and C_c are typically 2 cm for each case when the focal length $f = 2$ cm. Hence for spherical aberration of the magnetic lens

$$\Delta\alpha_0 = \frac{c_s \alpha_0^3}{f} = 125 \times 10^{-9} \text{ radian, if } \alpha_0 \approx 5 \times 10^{-3} \text{ radian}$$

from which

$$\frac{\Delta z_1}{z_{10}} = \frac{-V_1}{V_0} \frac{\Delta\alpha_0}{\alpha_0}$$

If $z_{10} = 0.5 \text{ cm}$, then the ray crosses the Gaussian image plane at a radius

$$\alpha_1 \Delta z_1 = -2 \sqrt{\frac{V_1}{V_0}} \Delta\alpha_0$$

If $V_1/V_0 = 1/100$ the least disk of confusion has a diameter of 1 \AA . Therefore spherical aberration of the magnetic lens is negligible compared with the aberration of the retarding field calculated later.

For chromatic aberration of the magnetic lens

$$\Delta\alpha_0 = \frac{\Delta V_0}{V_0} \frac{c_c \alpha_0}{f}$$

If we take $V_0 = 40\text{kV}$ and $\Delta V_0 = 1 \text{ V}$, then owing to this energy spread

$$\Delta\alpha_0 = \frac{1}{4 \times 10^4} \times 1 \times 5 \times 10^{-3} = 10^{-7} \text{ radian and the least disk of confusion}$$

has diameter d_c given by

$$d_c = -\frac{1}{10} \times 10^{-7} \text{ cm} \approx 1 \text{ \AA}$$

Therefore chromatic aberration of the magnetic lens is negligible. The effect of the aberration of the aperture lens could be similarly calculated but in view of the extremely small effect of the aberration of the magnetic lens it is highly unlikely that the aperture lens aberrations would be comparable with the effect of the retarding-field aberrations discussed in the next section.

ABERRATIONS OF THE RETARDING FIELD

Equation (3) gives the exact expression for Z_1 . The spherical aberration of the retarding field can be calculated by using the first two terms in the power-series expansions of $\sin \alpha_0$ and $\cos \alpha_0$:

$$\Delta Z_1 = \frac{r_0}{\alpha_0} \left(\frac{-\alpha_0^2}{2!} + \frac{\alpha_0^2}{3!} \right) - \frac{E}{4V_0} \frac{r_0^2}{\alpha_0^2} \left(\frac{+2\alpha_0^2}{3!} \right)$$

$$= \frac{r_0}{\alpha_0} \frac{-\alpha_0^2}{2}$$

$$\Delta z_1 = \frac{r_0}{\alpha_0} \frac{\alpha_0^2}{2}$$

The diameter d_s of the least disk of confusion is then given by

$$d_s = \frac{1}{4} \frac{r_0}{\alpha_0} \alpha_0^2 \alpha_1 = \frac{r_0}{4\alpha_0} \alpha_0^3 \sqrt{\frac{V_0}{V_1}} = \frac{1}{2} Z_{10} \sqrt{\frac{V_0}{V_1}} \alpha_0^3$$

This expression is in terms of the convergence angle α_0 . Note that d_s is reduced if Z_{10} is reduced. For a uniform retarding field α_0 and α_1^s are related by Snell's law; hence

$$d_s = \frac{1}{2} Z_{10} \frac{V_1}{V_0} \alpha_1^3$$

This result could be compared with the more normal formula for d_s for a zero-field system in which

$$d_s = \frac{1}{2} C_s \alpha^3$$

Hence in terms of the final convergence angle the retarding field lens enjoys an advantage in terms of spherical aberration roughly by a factor of V_0/V_1 . For the retarding-field system with $\alpha_0 = 10^{-2}$, $V_1 = 100$ V, $Z_{10} = 0.5$ cm,

$$d_s = \frac{1}{4} \times 20 \times 10^{-6} = 500 \text{ \AA}$$

To find the chromatic aberration of the retarding field we find the distance ΔZ_1 at which an electron with initial energy $V_0 + \Delta V_0$ and initial convergence angle α_0 crosses the axis, then the least disk of confusion d_c is given by the radius at which this electron crosses the Gaussian image plane.

Differentiating Eq. (3) we get

$$d_c = \alpha_1 \Delta z_1 = \frac{-r_0}{2\alpha_0} \frac{\Delta V_0}{V_1} \left(\frac{V_1}{V_0} \right) \alpha_1 = \frac{-Z_{10} \Delta V_0}{\sqrt{V_0 V_1}} \alpha_0$$

This result could be compared with the zero-field system in which $d_c = C_c (\Delta V/V) \alpha$. Note that in terms of α_1 the retarding field system enjoys an advantage over the zero field system by a factor of about V_0/V_1 .

In terms of α_0 it can be seen that the aberration reduces for decreasing z_{10} and increasing V_0 and V_1 .

For $V_1 = 100$ V, $V_0 = 40$ kV, $\Delta V_0 = 1$ V, $Z_{10} = 0.5$ cm, and $\alpha_0 = 10^{-2}$ radian, we obtain $d_c = 250$ Å.

CURRENT-DENSITY LIMITATION

The current density J that can be focused into a spot by an electron-optical system depends on the final energy of the beam V , the convergence angle α_1 , and the cathode current density J_c , and is given by an expression derived by Langmuir:⁷

$$J = \left(\frac{eV}{kT} + 1 \right) J_c \sin^2 \alpha_1$$

for beam voltages as low as 10, $eV/kT \gg 1$ and typically $\alpha \leq 1/10$, so that $\sin \alpha \approx \alpha$; therefore

$$J = (eV/kT) J_c \alpha_1^2$$

If we define the spot diameter d_0 as that diameter within which 80% of the current is contained, then

$$i = 0.62 \frac{\pi}{4} d_0^2 J$$

$$d_0^2 = \frac{2i kT}{J_c eV_1} \frac{1}{\alpha_1^2}$$

$$d_0 = \frac{1}{\alpha_1} \sqrt{\frac{2i kT}{J_c eV_1}} = \frac{1}{\alpha_0} \sqrt{\frac{2i kT}{J_c eV_0}}$$

Thus in terms of the final convergence angle α_1 there is no advantage in the retarding field system. In terms of the convergence angle α_0 , however, it can be seen that the required Gaussian spot diameter d_0 is independent of the final voltage V_1 . For $V_0 = 40$ kV, $\alpha_0 = 10^{-2}$, $i = 10^{-12}$ A, and $J_c = 5$ A-cm⁻¹,

$$d_0 = 10^2 \frac{2 \times 1 \times 10^{-12}}{5 \times 16 \times 10^4} = \frac{10^{-6}}{6.5} \approx 15 \text{ Å}$$

DIFFRACTION

A similar relation holds for diffraction. An electron beam, converging at an angle α_0 , has an Airy disk whose diameter d_f is given by

$$d_f = \frac{15}{V_1} \frac{1}{\alpha_1} \overset{\circ}{\text{A}} = \frac{15}{V_0} \frac{1}{\alpha_0} \overset{\circ}{\text{A}}$$

For $V_0 = 40$ kV and $\alpha_0 = 10^{-2}$ radian, $d_f = 7 \overset{\circ}{\text{A}}$.

Note that both the diffraction disk diameter and the Gaussian disk diameter are proportional to $1/\alpha_0$.

In Fig. 3 are plotted as functions of α_0 the various (significant) contributions to the over-all disk diameter for three different final voltages V_1 and for three different current values: $i = 10^{-12}$ A, which is about the minimum required for scanning microscopy; $i = 10^{-9}$ A, which is about the minimum required for x-ray microanalysis; and $i = 10^{-6}$ A, which may be regarded as a minimum for thermal micromachining. Voltage V_0 is 40 kV, J_c is 5 A-cm⁻², Z_{10} is 5 mm. Also on Fig. 3 are marked in dotted lines the equivalent limitations for a zero field system with a final lens with $C_s = C_c = 2$ cm.

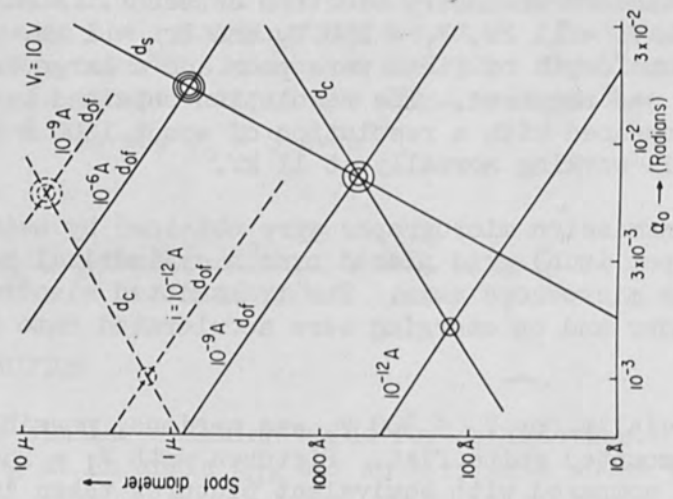
As would be expected the improvement is most marked at low voltages. For instance for $V_1 = 10$ V the minimum spot diameter for $i = 10^{-12}$ A is about two orders of magnitude less than the spot diameter for a zero-field system. When $V_1 = 1000$ V the difference is only one order of magnitude. For higher currents the improvement is slightly smaller because the spherical aberration of the retarding field system becomes appreciable. This is most marked for the higher V_1 . It is perhaps worth noting that even for V_1 as low as 10 V it should be possible to obtain electron-probe diameters of only about 300 Å, which is about the minimum probe diameter of present day commercial scanning electron microscopes—but without the attendant problems of electron penetration into the sample—so that a retarding field may well be an advantage for examining specimens with constituents of low atomic numbers.

EXPERIMENTAL RESULTS

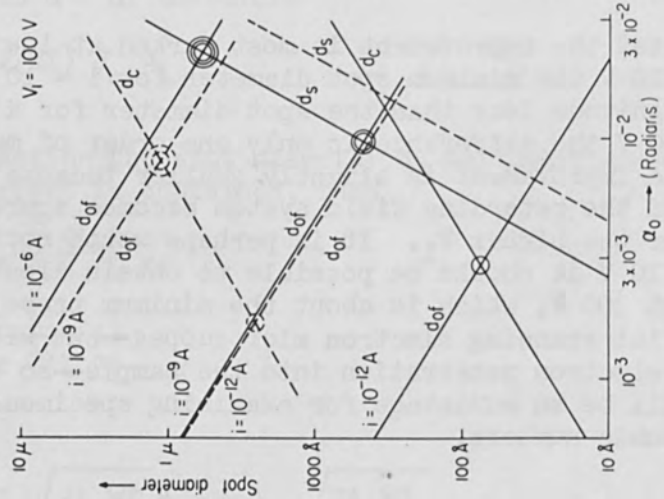
Three sets of experiments have been run. In the first the specimen was inclined at 80° to the axis so that some secondary electrons could be detected by use of a standard secondary electron detector. A micrograph is shown in Fig. 4 with $V_0 = 11$ kV, $V_1 = 250$ V, and $Z_{10} = 1$ cm. Both the collection efficiency and depth of field were poor and a large degree of astigmatism correction was required. The resolution obtained was about 2000 Å, which can be compared with a resolution of about 1000 Å when this particular instrument is working normally at 11 kV.

Some scanning transmission micrographs were obtained by using as a specimen a 2000-mesh (per inch) grid placed over a cylindrical hole which was concentric with the microscope axis. The transmitted electrons then drifted down the cylinder and on emerging were accelerated onto a scintillator.

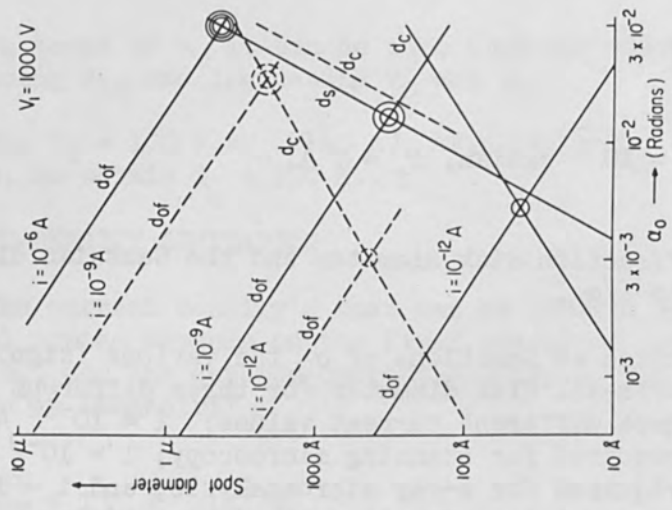
Astigmatism, especially for $V_1 < 300$ V, was serious, possibly owing to the grid not being mounted quite flat. Pictures with $V_1 = 250$ V were obtained (Fig. 5a) and compared with equivalent pictures taken in the



(a)



(b)



(c)

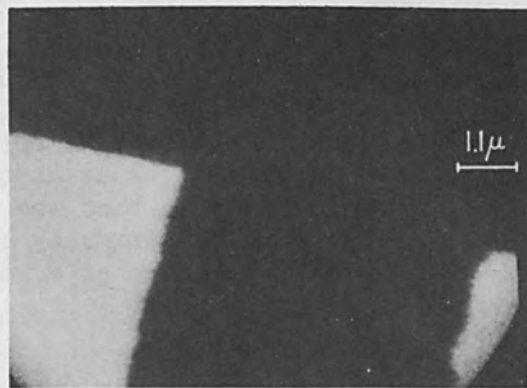
FIG. 3.—Values of d_c , d_s , and $d_0 + d_f$ plotted as functions of initial convergence angle α_0 . The circled intersections correspond to about half the total minimum spot diameter. The continuous lines correspond to a retarding field system with $V_0 = 40$ kV, $J_c = 5$ A-cm $^{-2}$, $Z_{10} = 0.5$ cm. (a) $V_1 = 10$ V; (b) $V_1 = 100$ V; (c) $V_1 = 1000$ V.



FIG. 4.—Low-voltage ($V_1 = 250$ V) scanning electron micrograph of a piece of aluminum.



(a)

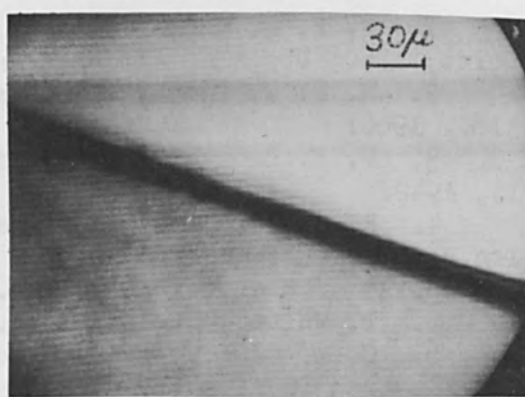


(b)

FIG. 5.—(a) Low-voltage ($V_1 = 200$ V) scanning transmission electron micrograph of a 2000-mesh (per inch) grid; (b) conventional ($V_0 = 11$ kV) scanning transmission electron micrograph of the same grid.



(a)



(b)

FIG. 6.—Low-voltage ($V_1 = 100$ V) scanning electron micrograph of a cracked quartz cover slip: (a) $V_1 = 100$ V; (b) similar area at $V_1 = 10$ V.

normal mode of operation (Fig. 5b). The comparison is quite good and again a probe diameter of about 2000 Å was obtained.

Finally some pictures were obtained by depositing P-11 phosphor around the aperture and viewing the phosphor with a large-diameter light pipe and photomultiplier. The specimen was a quartz cover slip lightly covered with evaporated carbon. The cover slip cracked as a result of mounting, which gave a useful reference line. The phosphor unfortunately entered the aperture, causing severe astigmatism, but it was possible to obtain micrographs with V_1 as low as 100 V (Fig. 6 A) and even with $V_1 = 10$ V (Fig. 6b); the probe diameters were estimated to be about 2000 Å and 1 μ at these respective voltages. With very low V_1 it was difficult to obtain uniformly efficient detection of secondary electrons from the surface since the secondaries tend to be imaged on the aperture and hence a picture of the aperture appears when a large field is viewed.

CONCLUSION

A simple electron-optical analysis of a retarding field probe system indicates that it should be possible to obtain focused probes a few hundred angstroms in diameter at voltages down to 10 V. For best results the retarding field should be as strong as is practical. Some preliminary experiments demonstrate that the values of probe diameter at voltages down to 100 V are only worse by a factor of two than the values obtained in conventional operation at a voltage of 11 000.

ACKNOWLEDGMENT

The research reported herein was supported wholly by the Electronic Technology Division, Air Force Avionics Laboratory, Research and Technology Division, Wright-Patterson Air Force Base, Ohio under Contract AF 33(615) - 3886.

REFERENCES

1. R. F. M. Thornley, Proc. 2nd Reg. Conf. on Electron Microscopy, Delft, 1960; Uppsala, Almqvist and Wiksell, 1961; vol. 1, p. 173.
2. R. F. W. Pease, T. L. Hayes, and A. Camp, N. Amer. Science 154: 1185, 1966.
3. V. K. Zworykin, J. Hillier, and R. L. Snyder, ASTM Bull. 117: 15, 1942.
4. E. D. Wolf, papers presented at 2nd Intern. Conf. Electron and Ion Beam Science and Technology, New York, 1966; to be published. (See also p.135 of the present volume.)
5. T. Mulvey, J. Sci. Inst. 36: 350, 1959.
6. C. W. Oatley, W. C. Nixon, R. F. W. Pease, Adv. in Electronics and Electron Physics (L. Marton, ed.), New York, Academic Press, 1965.
7. D. B. Langmuir, Proc. IRE 25: 977, 1937.

LIST OF SYMBOLS

Z_{10} , distance between final aperture and the target on which the beam is focused

r_0 , radial distance of a ray in the plane of the aperture
 α_∞ , the convergence angle of a ray at r_0 in the aperture plane before entering the aperture lens
 α_0 , the convergence angle of the above ray just after emerging from the aperture lens
 α_1 , the convergence angle of the above ray at the target
 V_1 , the potential of the specimen with respect to the cathode
 V_0 , the potential of the aperture and final lens with respect to the cathode
 t_0 , the time of flight to the target of a ray at radial distance r_0 in the aperture plane
 E , the field between the target and aperture
 C_s, C_c , the respective coefficients of spherical and chromatic aberration of the final lens
 f , the focal length of the final magnetic lens
 $\Delta\alpha_0$, the spread in α_0 as a result of aberration in the magnetic lens
 ΔZ_1 , the longitudinal distance from the target at which a ray with convergence angle $\alpha_0 + \Delta\alpha_0$ (after emerging from the aperture lens) crosses the axis
 d_c , the diameter of least disk of confusion due to chromatic aberration
 d_s , the diameter of least disk of confusion due to spherical aberration
 J , the current density in the final spot
 J_c , the emission-current density of the cathode
 d_0 , the diameter of the Gaussian image of the crossover
 d_f , the diffraction-disk diameter
 d_{of} , the combined value of d_0 and d_f
 i , the spot current

SEMICONDUCTOR SECONDARY-ELECTRON DETECTOR

A. J. GONZALES

Electronics Research Laboratory, University of California, Berkeley

One of the most important modes of observation with the scanning electron microscope is secondary electron emission. This mode gives information concerning the topography and surface potential of the specimen.

A common method of secondary-electron detection uses a scintillator-photomultiplier combination as proposed by Everhart and Thornley.¹ This system consists of a collector and rigid light pipe mounted a fixed distance from the final lens aperture. Under most conditions the fixed position of the collector is adequate for good collection of the secondary electrons.

Fields and objects near the sample may influence the efficient collection of secondary electrons by modification of the electron trajectories. In most commercial semiconductor devices, insulators and metallic leads surround the device being studied; metallic leads and packaging often obstruct the collection of secondary electrons from the specimen. The surrounding insulators may be bombarded when initially aligning the specimen, or secondary and backscattered electrons may strike the insulators and cause them to accumulate charge. Since the conductivity of the insulators is low, the accumulation of charge produces a large negative potential which interferes with the fields from the secondary-electron collector. The charged insulators may either hamper or completely prevent a normal secondary-electron presentation. The size of the sample and the proximity of the lens surface also obstructs secondary electron collection. These effects may be reduced by moving the sample away from the lens surface and tilting the sample surface toward the collector.

In order to study possible improvement in collection efficiency, a detector which allows flexibility of mechanical motion was constructed. The initial test results of the system are described.

A p-n junction diode was chosen as the electron detection element. By proper choice of diode structure and acceleration voltage, a current multiplication of the input signal is obtained. The electrical nature of the diode output allows a flexible cable coupling to a subsequent amplifier. The wide range of diode configurations allows considerable freedom in collector design.

To evaluate the merits of this system, a scintillator detector, which is normally used in the Berkeley SEM, is used as a reference. The scintillator detector is mounted a fixed distance from the lens to allow ample clearance for the passage of the specimen stage.

Figure 1 illustrates the configuration of the diode and scintillator detectors. The scintillator detector is axially symmetric about the axis

of the light pipe. A wide-mesh metal grid is used to attract the secondary electrons; these electrons pass through the grid and are attracted by the high potential of the aluminized scintillator. The metal cylinder which supports the collector grid contains a crude focusing electrode that guides the electrons to the scintillator. A rigid light pipe guides the light output of the scintillator to a photomultiplier.

The upper portion of Fig. 1 illustrates the diode-detector configuration. A metal grid covers the face of the detector; the grid is at a sufficient potential to attract secondary electrons. Electrons passing through the grid are attracted by and strike the pn junction diode which is at a high positive potential. The electrical output of the diode is carried by a flexible insulated cable to the input of an amplifier.

A commercial diffused silicon planar diode was used in the initial testing of this system. As indicated in Fig. 1, the area of the diode was rather large. Use of this system has shown that the area of the diode may be considerably reduced.

With a diode potential of 10 kV, the collected secondary electrons penetrate approximately 1 micron into the silicon diode. Owing to this small penetration, the p-n junction must lie close to the diode surface in order to collect efficiently the carriers generated by the impinging high energy electrons. Another important parameter of the diode is the thickness of material through which the energetic electrons must pass before entering the semiconductor diode. For maximum current multiplication the surface material must be kept thin. The diode used exhibited a gain of 2000 for an acceleration potential of 10 kV. The multiplication is approximately 70% of the theoretical maximum.

In many detectors of high energy particles a reverse bias is applied to increase the collection efficiency and to decrease the transit time of the generated carriers. However, by the use of a shallow diffused diode, the built in field of the p-n junction allows good collection efficiency with no applied bias. Moreover, by the use of a low input impedance amplifier at the diode output, it was found that the diode signal was not significantly increased by application of a diode bias. Owing to modest frequency requirements the transit time of the carriers in the diode is no problem.

Figure 2 is a schematic diagram of the diode detector system. A flexible cable couples the output signal of the diode to the amplifier. Then the amplified signal passes through a high-frequency chopper which permits transformer decoupling of the amplified signal from the 10 kV potential of the diode and amplifier. The amplitude detector restores the chopped signal to its original form and provides an output signal near ground potential. By using the chopper and the amplitude detector, we obtain dc coupling from the diode to the output. The transformer coupling allows the high-voltage portion of the system to have a low capacitance to ground. With the use of a current limiting resistor of 10 megohms in the 10-kV line, any point of the system may be shorted to ground without producing permanent damage.

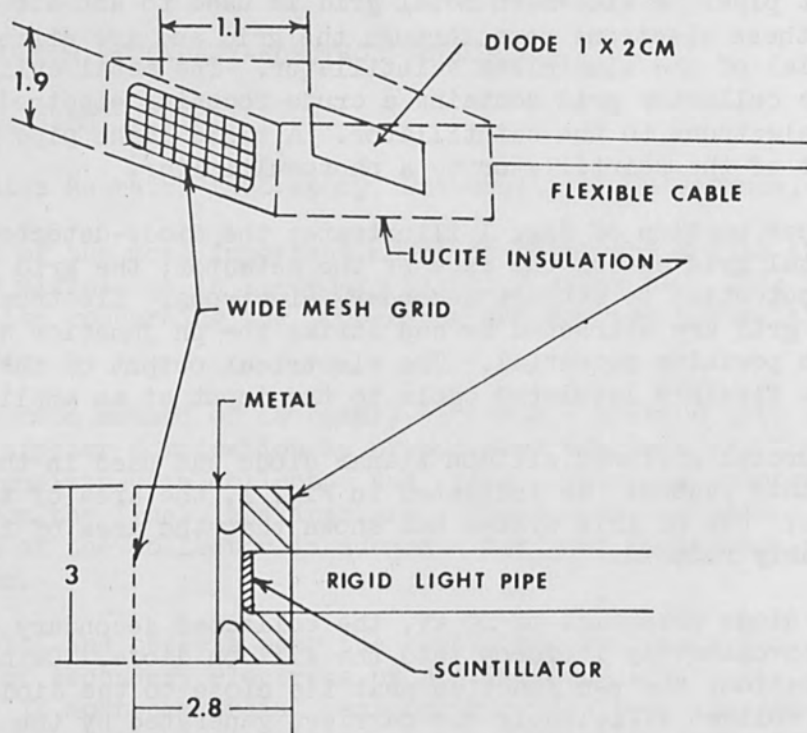


FIG. 1.—Scintillator and diode detector configurations. (All dimensions in centimeters.)

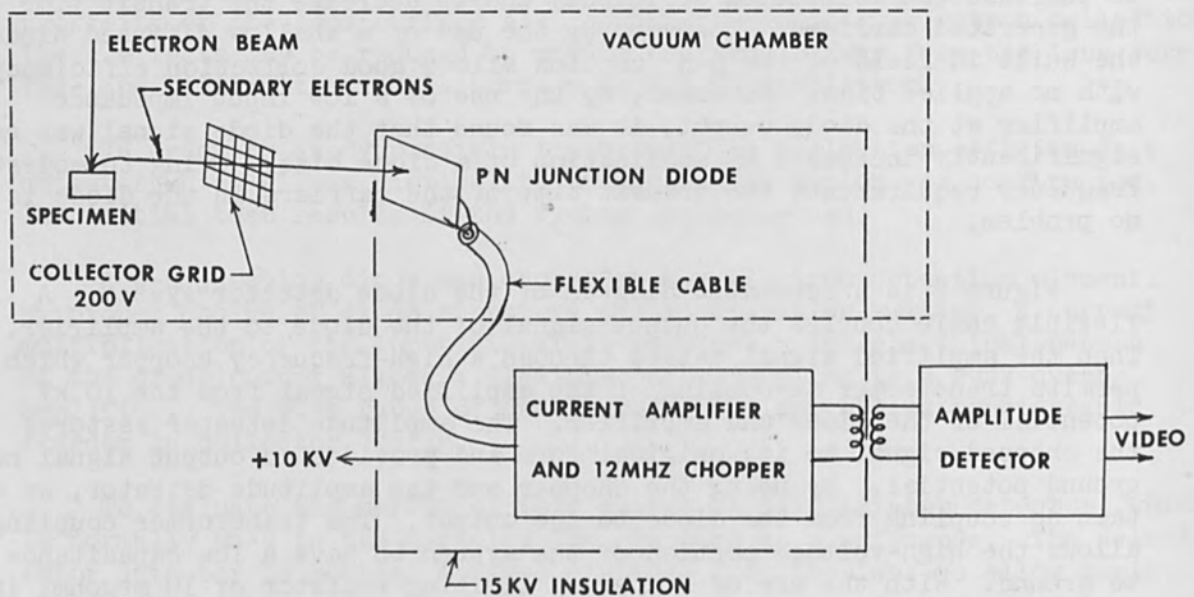
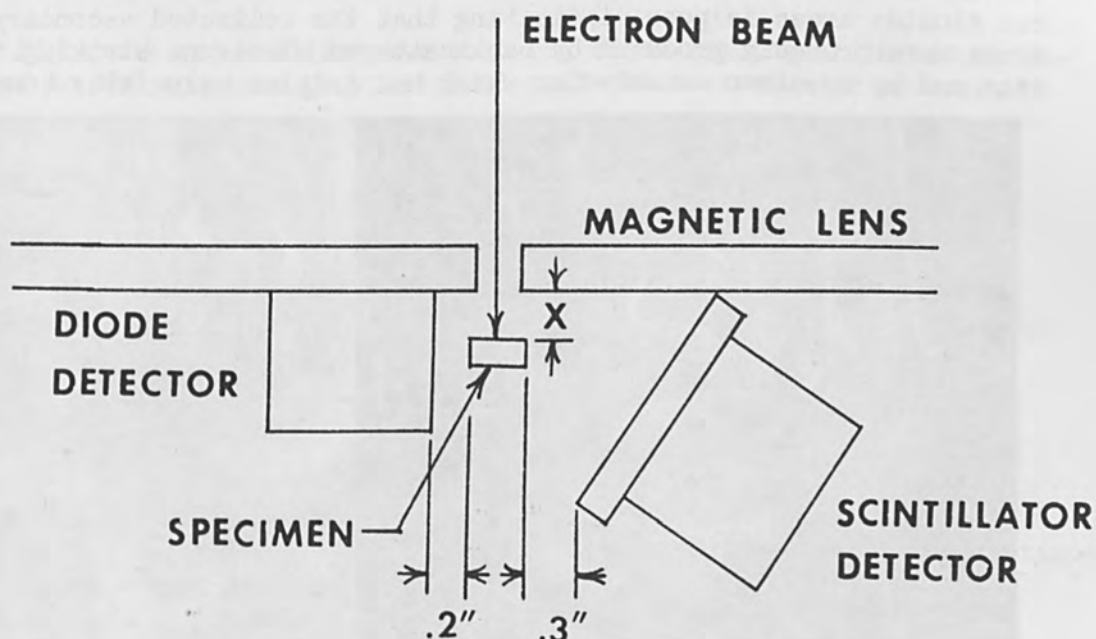


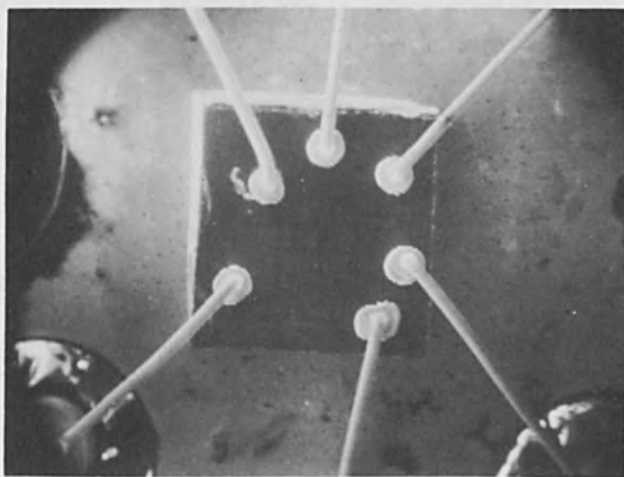
FIG. 2.—Schematic diagram of diode detector system.

The amplifier in use has a bandwidth of 150 kHz and a noise input equivalent of 1 nanoamp. The calculated minimum discernible signal is 0.5 picoamp.

The specimen-lens-detector geometry has been varied to study the collection efficiency of the two systems. To permit simultaneous comparison, the detectors were located at opposite sides of the specimen, as indicated in Fig. 3(a). The collector grid potentials of both systems could be controlled to prevent any interaction of the two detectors. Except as noted, the following experiments were conducted with the specimen surface normal to the electron beam.



(a)



(b)

FIG. 3.—Specimen-lens-detector configuration and integrated-circuit specimen.

A commercial integrated circuit was used to illustrate a specimen configuration that would interfere with secondary-electron collection. In Fig. 3(b) the integrated circuit is seen to be surrounded by insulated glass posts which provide terminals for the gold bonding leads.

To provide disturbing fields in the vicinity of the specimen, the insulators surrounding the integrated circuit were bombarded by the electron beam to produce charging of the insulators to some negative potential.

Figure 4(a) is a micrograph obtained using the scintillator detector with a specimen-lens distance of 0.15 in. A portion of the integrated circuit is shown. The contrast between the aluminum, silicon, and silicon dioxide areas is poor, indicating that the collected secondary electrons were probably produced by backscattered electrons striking the final lens and by specimen secondaries which had initial velocities toward the



(a) scintillator detector

Specimen - lens distance
0.15"



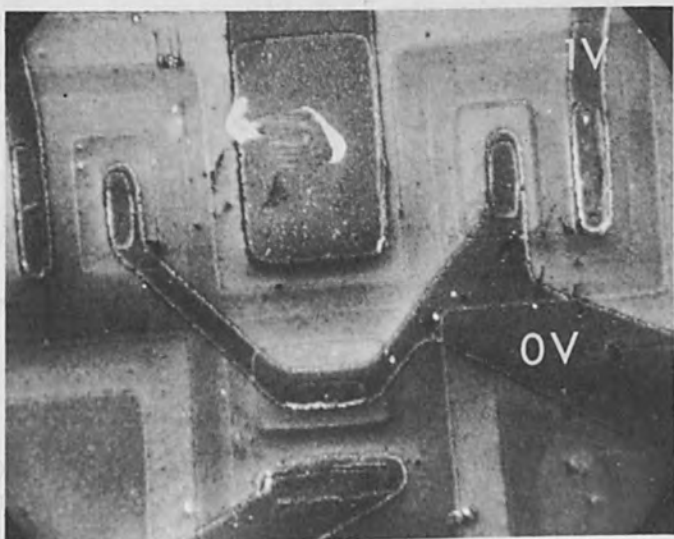
(b) diode detector

FIG. 4.—Secondary-electron information comparison of the scintillator and diode-detector systems for a small specimen-lens distance.

detector. The collector grid potential is ineffective in providing adequate collection fields and no voltage contrast is observed. The diode detector output shown in Fig. 4(b) illustrates a normal secondary electron display of the specimen.

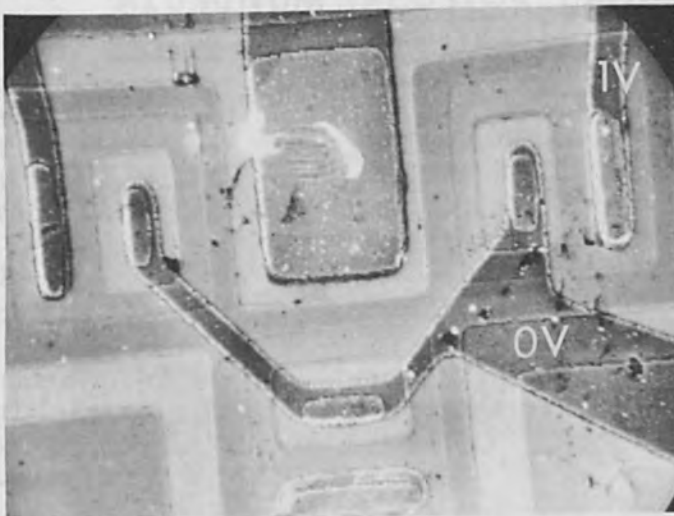
In Fig. 5(a) the specimen-lens distance has been increased to 0.35 in., and a small bias has been applied between two aluminum leads. The scintillator detector displays improved contrast, and some voltage contrast is discernible. The poor quality of the display is attributed to the disturbing effect of the charged insulators, since subsequent coating of the insulators with a conductive material eliminated the hazy appearance of the micrograph.

Figures 4 and 5 illustrate that the close spacing of the diode detector to the specimen provides good collection even under adverse



(a) scintillator detector

Specimen - lens distance
0.35"



(b) diode detector

FIG. 5.—Secondary-electron information comparison of the scintillator and diode-detector systems for a large specimen-lens distance.

secondary-electron collection conditions. The close lens-sample spacing had little effect on the diode-detector collection efficiency.

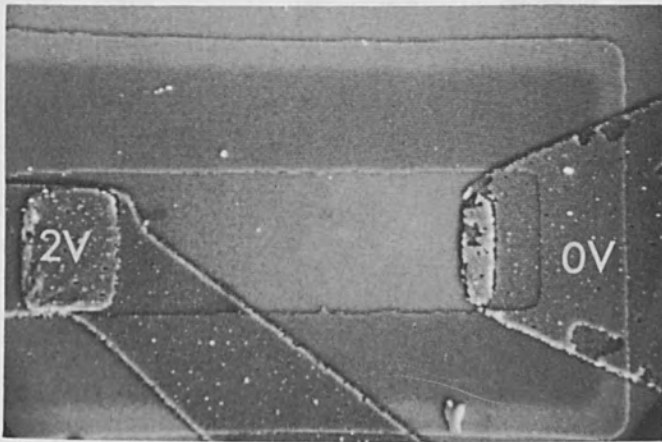
Close spacing of the detector and lens may produce an asymmetric field at the lens aperture, and thereby cause aberrations in the electron beam. The beam diameter used in these experiments was less than 0.1 micron. No noticeable loss of resolution was produced when the collector was mounted near the final lens. It should be possible to construct an axially symmetric collector which should improve collection efficiency and reduce any collection field induced aberrations.

To have a fair comparison of the voltage contrast sensitivity of the two systems, all exposed insulators were covered with a conductive coating. In Fig. 6 a comparison is made of the voltage contrast which is observed across a diffused silicon resistor. The peak video signals were held at a comparable level. In both micrographs the isolation region and the voltage gradient across the resistor are evident. The close sample-diode-detector spacing provided greater voltage contrast than the more distant scintillator detector.

Figure 7 illustrates the video signals from both systems for a single scan across the center of the resistor. The video signals with and without applied resistor bias are shown. The diode detector exhibits a well-defined signal gradient across the resistor, and a noticeable signal change is detected when the resistor bias is removed. The scintillator detector signal changes are less pronounced, as previously indicated in Fig. 6. The response of the right-hand aluminum edge is shown to be equal for both detectors.

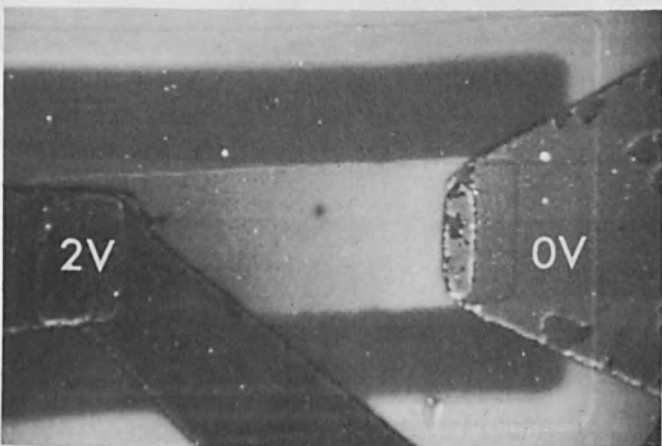
The absolute voltage contrast sensitivity is a strong function of the collector-specimen configuration, as shown by Everhart.² A potential of 100 mV has given usable contrast with the diode collector mounted close to the sample. As an example of contrast of small potentials, Figs. 8 and 9 illustrate voltage contrast produced by the electron beam induced "photovoltage" of the integrated circuit's junctions. Figure 8 is a large-area micrograph which indicates voltage contrast of the resistor and transistor isolation walls. Since the isolation wall was not available for electrical contact, the field of view was reduced to a small portion of the transistor, as shown in Fig. 9. In the upper portion of the figure, the emitter, base and collector were shorted together to eliminate any induced voltages. In the lower portion of the figure the open-circuited base produces 300 mV of photovoltage. The shading of the two portions of the base indicates the contrast produced by this small voltage.

The diode detector has been directly bombarded by a 10-kV electron beam and has produced a minimum detectable signal of 0.3 picoamp. The sensitivity is presently limited by the noise developed in the signal amplifier. Figure 10 is a micrograph of a failed silicon transistor. The sample was tilted 45° , and the collector was positioned to minimize the collection of backscattered electrons. The beam and target currents indicate that a maximum of 2 picoamps of secondary electron current was produced from the silicon dioxide areas. The contrast produced by the silicon dioxide steps, indicated by arrows, shows that the detector is faithfully following the secondary signal and not merely outlining areas



(a) scintillator detector

Specimen - lens distance
0.35"



(b) diode detector

FIG. 6.—Voltage-contrast comparison of the scintillator and diode-detector systems.

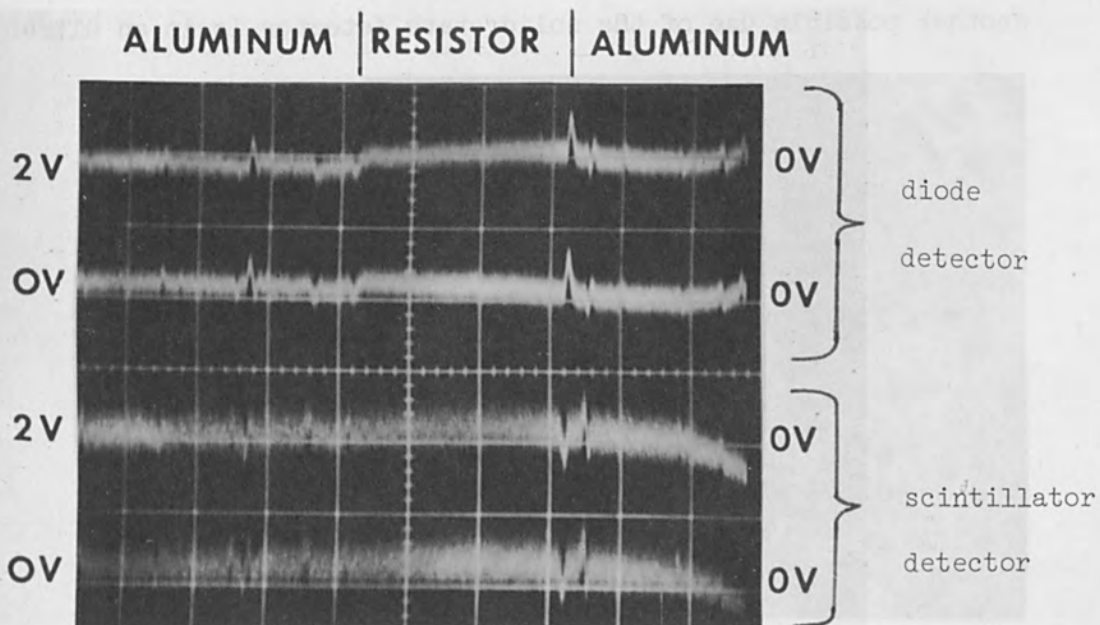


FIG. 7.—Comparison of the video output of the scintillator and diode-detector systems.

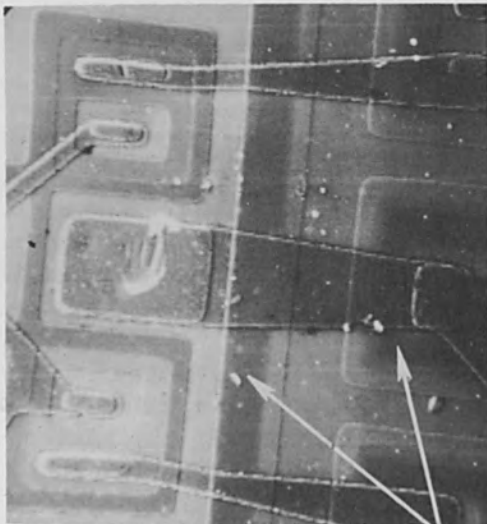


FIG. 8.—Photo voltage contrast of isolation junctions. (Arrows show isolation walls.)

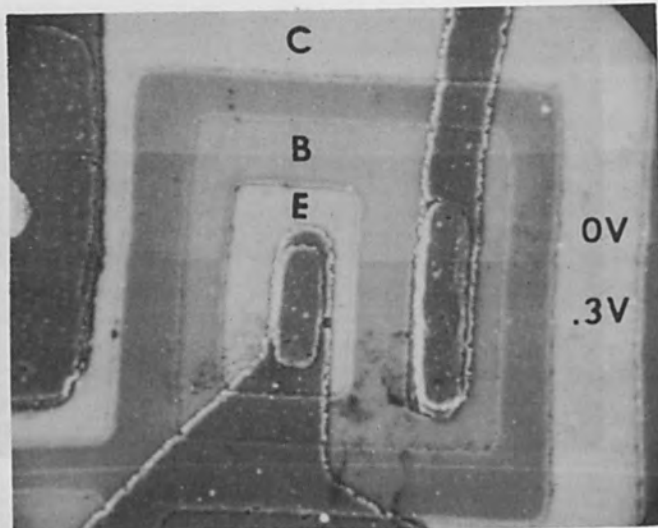


FIG. 9.—Voltage contrast at low voltage.

of higher secondary output.

A flexible light pipe, from scintillator to photomultiplier, could have been used to perform similar experiments. The diode detector was constructed in order to explore some of its advantages. However, the flexibility of size and shape of the diode allows fabrication of detectors of more exotic shapes without light optical limitations.

Another possible use of the solid state detector is in an ultrahigh-



V_B 18 KV

I_B 5 pA

I_T 3 pA

FIG. 10.—Micrograph taken at low electron beam current.

vacuum microscope. The high vacuum would require that the collector and cable be of low vapor pressure materials.

Although the absolute sensitivity of the diode detector is lower than the conventional scintillator detector, it has proved to be adequate for the present study. As indicated earlier, the high collection efficiency of this system may allow a higher over-all sensitivity in difficult circumstances.

REFERENCES

1. T. E. Everhart and R. F. M. Thornley, "Wide-band detector for micro-microampere low-energy electron currents," J. Sci. Instr. 37: 246-248, 1960.
2. T. E. Everhart, Ph. D. dissertation, Cambridge University, 1958.

NEW METHOD OF DETECTING SECONDARY ELECTRONS
ON SCANNING ELECTRON MICROSCOPE

H. KIMURA and H. TAMURA

Central Research Laboratory, Hitachi Ltd., Tokyo

SYNOPSIS. A new method of detecting secondary electrons has been developed and found to be advantageous for a scanning electron microscope. In this method the secondary electrons from a specimen are confined by an additional magnetic field and led to a detector installed above the focusing lens for the primary beam. Accordingly the focal length of the lens can be very short so that the primary beam may have a small diameter and high intensity on a specimen. The efficiency of collecting secondary electrons has been actually improved by this method and pictures showing surface and potential topographs of specimens were taken with an electron microscope equipped with such a device.

1. INTRODUCTION

Many papers have already reported on the construction, image quality, and resolving power of scanning microscopes. Biological specimens and semiconductor elements have been hitherto observed by many researchers with scanning electron microscopes.

In the secondary-electron image of a scanning microscope, it is possible to observe surface and material topography as well as voltage topography. In this paper, a new detection method is described. The method has many advantageous features such as that the image of a specimen can be observed just as a front view and that a fine beam spot and higher current density are available since the focusing lens has a short focal length.

2. PRINCIPLE OF NEW METHOD

Figure 1 (a) shows the method proposed by T. E. Everhart and adopted in many instruments to detect secondary electrons. The secondary electrons emitted from a specimen are selected by the electrostatic field between the collector and lower plate of the focusing lens and the electrons within some energy band are captured by the scintillator. A light signal is detected by the photomultiplier and led to the amplifier.

The authors have developed a new method in which the secondary electrons from a specimen are confined in a magnetic field and led to a collector. The principle is shown in Fig. 1 (b). The electrons with energy V move in a circle in the uniform magnetic field H and the radius of the circle ρ is given by

$$\rho = \frac{3.37 \sqrt{V}}{H} \sin \alpha$$

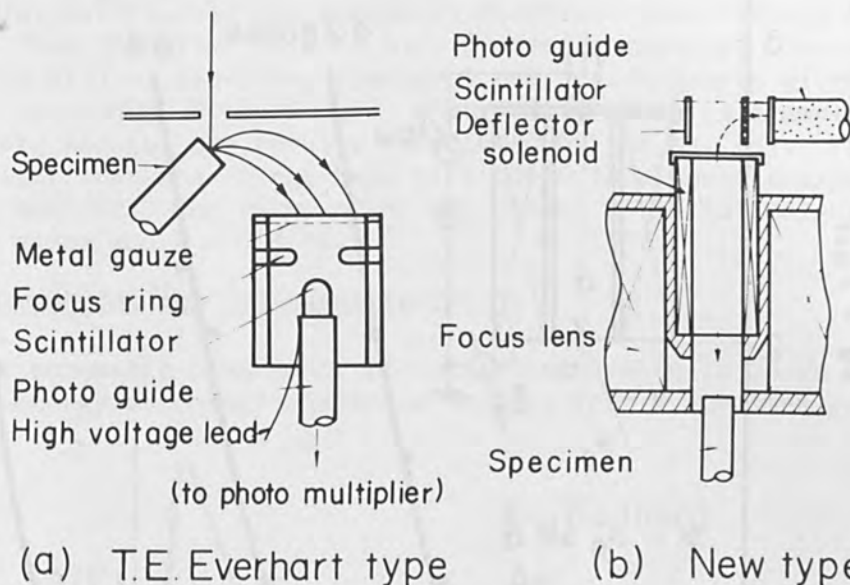


FIG. 1.—Diagram showing secondary electron collectors.

where α is the incident angle of an electron.

Accordingly the electron energy is selected by using a variable aperture and the magnetic field of constant strength or by using a fixed aperture with the magnetic field of variable strength.

The preliminary test of our method was tried as follows. Electrons emitted from a videcon gun with accelerating voltage of 10-50 V were led into a solenoid coil. The Faraday cage was kept at a voltage 0-50 V higher than the accelerating voltage to prevent the emission of secondary electrons from the cage. The relations between the electron beam current I_{Det} detected with a Faraday cage and the beam current I_g captured on the solenoid wall were investigated under various magnetic-field strengths of the solenoid coil. Figure 2 shows our result that I_g/I_{Det} became larger with the increase of the incident energy; in other words, the radius of the electron trajectories became larger and the electron beam current into the Faraday cage decreased. In addition, the energy of electrons reaching Faraday cage became higher with the increase of magnetic field.

3. ENERGY ANALYSIS OF SECONDARY ELECTRON WITH MAGNETIC FIELD

The condition that an electron of energy V can be passed through the aperture of radius R are given by the following equation.

$$\rho = \frac{3.37}{H} \sqrt{V} \sin \alpha < \frac{R}{2} \quad (1)$$

The secondary electron density is a function of the angle α and the energy V :

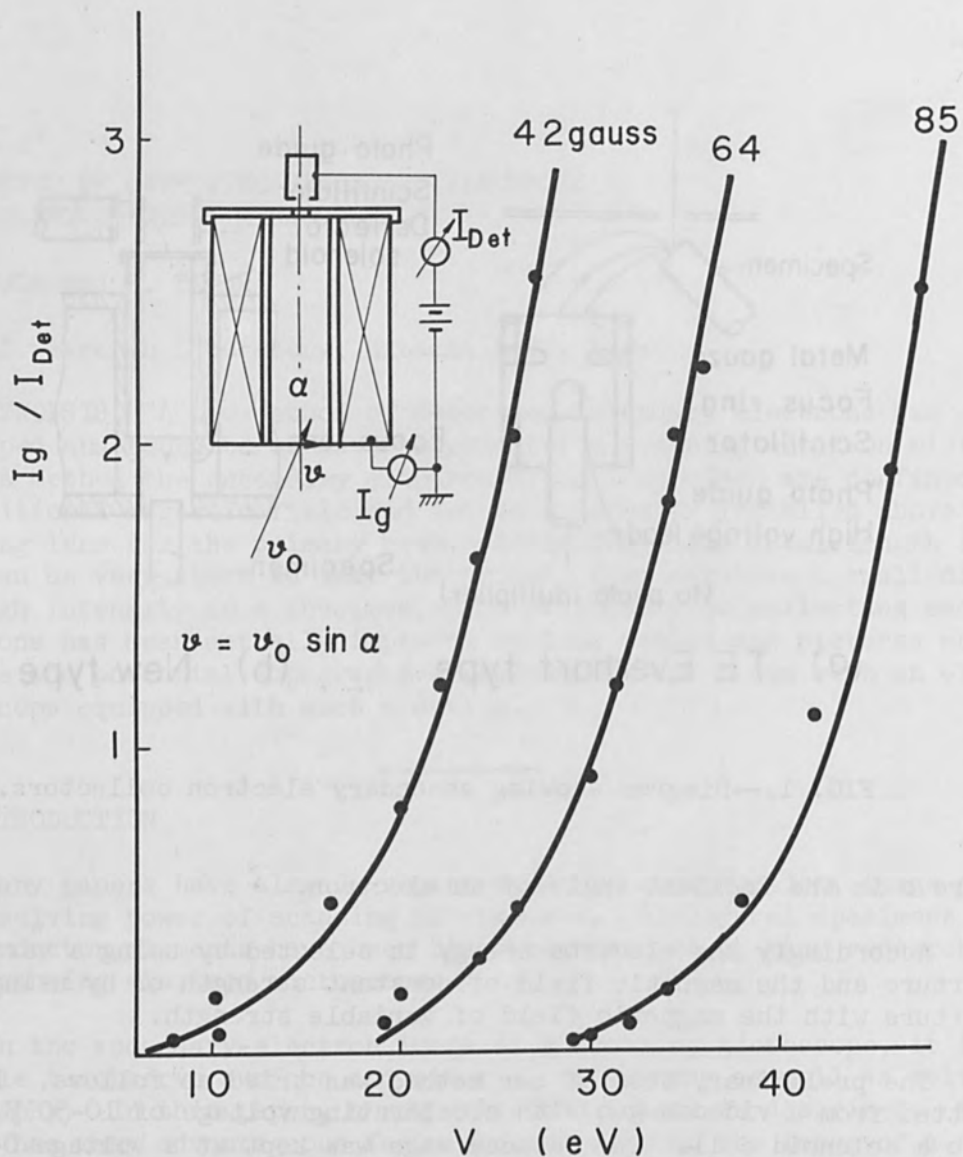


FIG. 2.—Relation between I_g/I_{Det} and incident energy.

$$I(\alpha, V) \sin \alpha \, dV \quad (2)$$

The angular distribution of the secondary electrons may be assumed to obey the so-called cosine-law; i.e.,

$$I(\alpha, V) = A(V) \cos \alpha \quad (3)$$

where $A(V)$ is a function of only V .

Then we obtain the energy distribution $J(R, H, V)$ of the electrons passing through the aperture of diameter $2R$ as an integral of (3) over α .

$$J(R, H, V) = \left\{ \begin{array}{l} \frac{1}{2} A(V) \sin^2 \alpha \quad \sin \alpha \equiv \frac{HR}{6.74 \sqrt{V}} < 1 \\ \frac{1}{2} A(V) \quad \frac{HR}{6.74 \sqrt{V}} \geq 1 \end{array} \right\} \quad (4)$$

When $HR/6.74\sqrt{V} \geq 1$, all the secondary electrons pass through the aperture, whereas when $HR/6.74\sqrt{V} < 1$, $J(R,H,V)$ decreases rapidly. The energy distribution $A(V)$ of secondary electrons has been hitherto given only in the case of low-energy bombardment. Figure 3(a) shows an example measured by E. Rudberg and (b) the results calculated by the Eq. (4). From this curve it is clear that the energy band is limited to a lower energy region as HR becomes smaller. The value of HR was chosen as 15 in designing our device. ($H = 50$ gauss and $R = 0.3$ cm.)

4. CONSTRUCTION AND ITS CHARACTERISTICS

The schematic diagram of focusing lens system is shown in Fig. 4. The low-energy secondary electrons emitted from a specimen are led to the

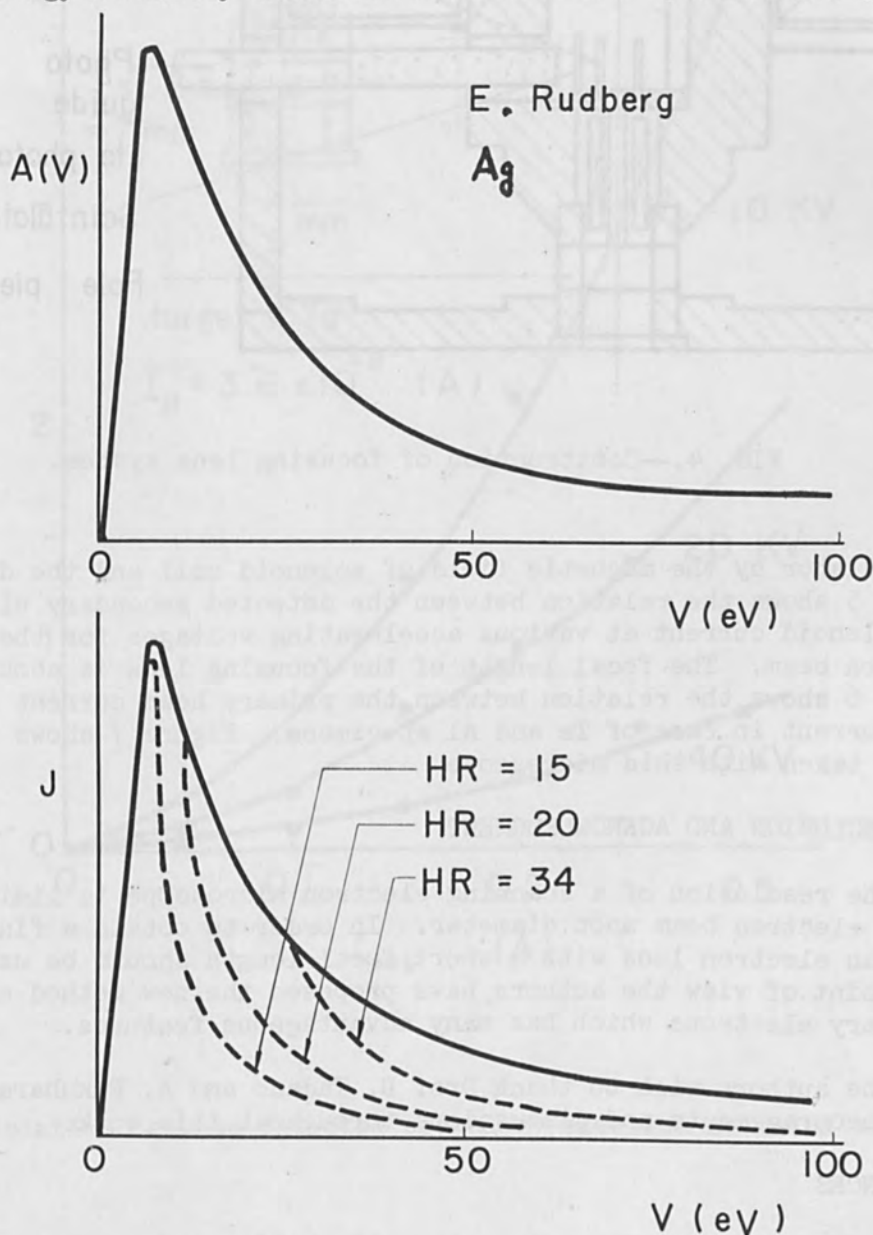


FIG. 3.—Energy analysis of secondary electron with magnetic field.

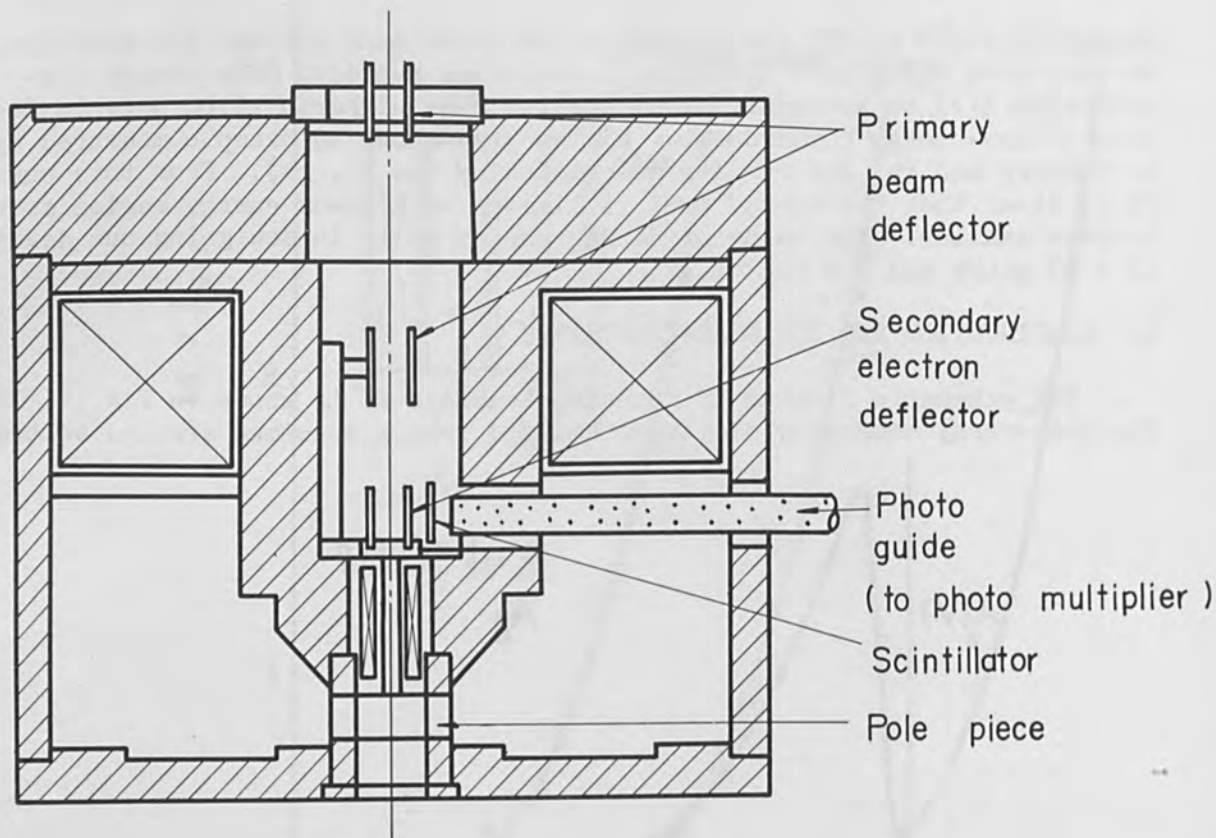


FIG. 4.—Construction of focusing lens system.

scintillator by the magnetic field of solenoid coil and the deflector. Figure 5 shows the relation between the detected secondary electron beam and solenoid current at various accelerating voltages for the primary electron beam. The focal length of the focusing lens is about 7 mm. Figure 6 shows the relation between the primary beam current and detected beam current in case of Ta and Al specimens. Figure 7 shows the photographs taken with this microscope.

5. CONCLUSION AND ACKNOWLEDGMENT

The resolution of a scanning electron microscope is limited mainly by the electron beam spot diameter. In order to obtain a fine electron beam, an electron lens with a short focal length should be used. From this point of view the authors have proposed the new method of detecting secondary electrons which has many advantageous features.

The authors wish to thank Drs. B. Tadano and A. Fukuhara for their kind encouragements and discussions throughout this work.

REFERENCES

1. E. Rudberg, Phys. Rev. 50: 138, 1936.
2. T. E. Everhart and R. F. M. Thornley, J. Sci. Instr. 37: 246, 1960.

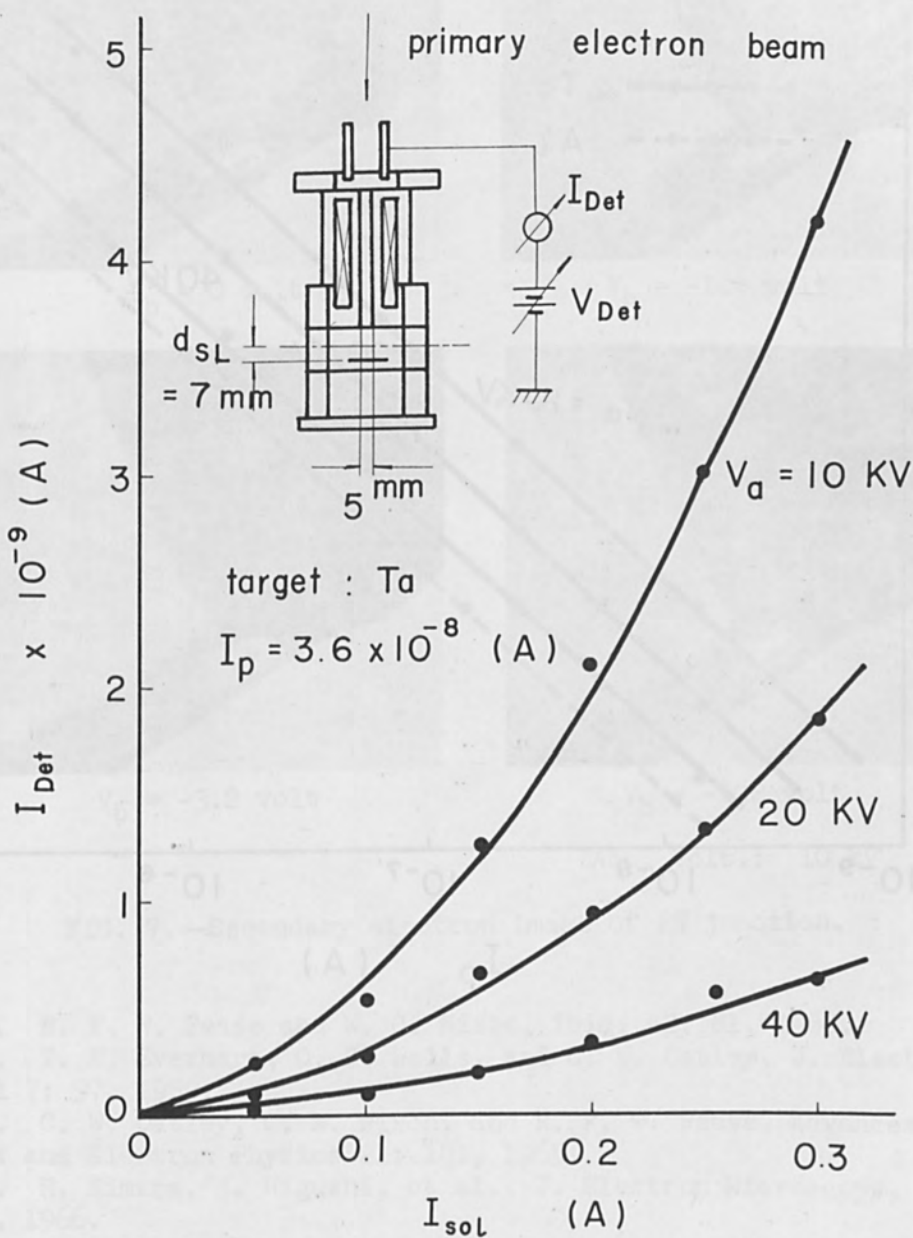


FIG. 5.—Relation between detected secondary electron beam and solenoid current.

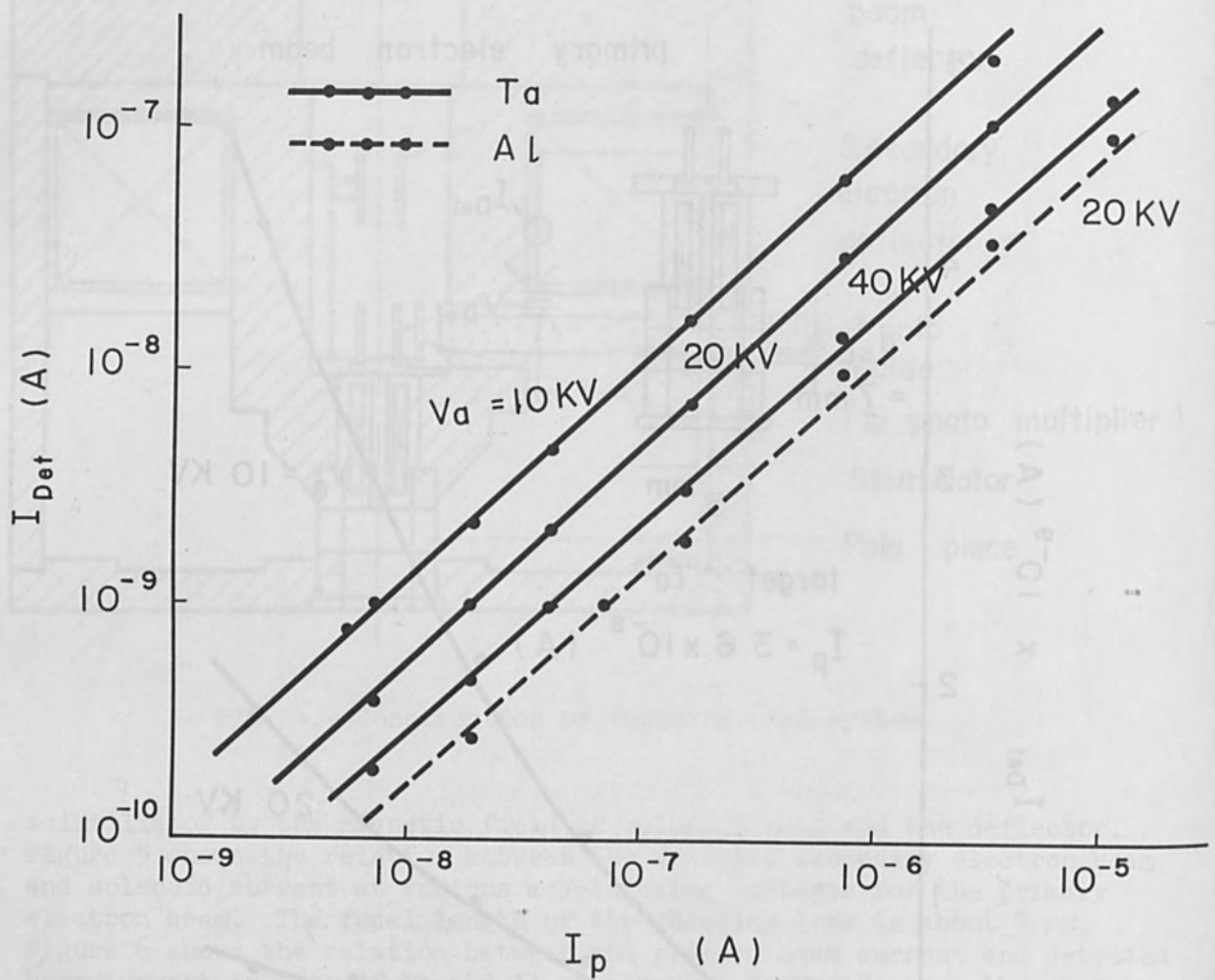
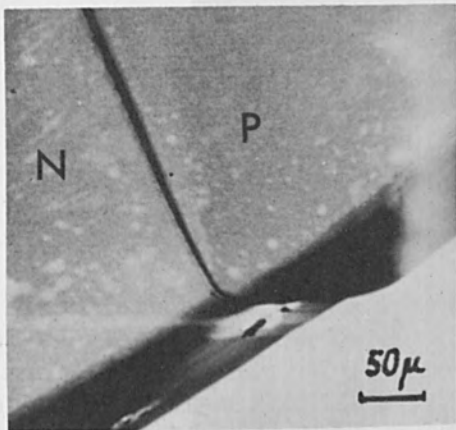
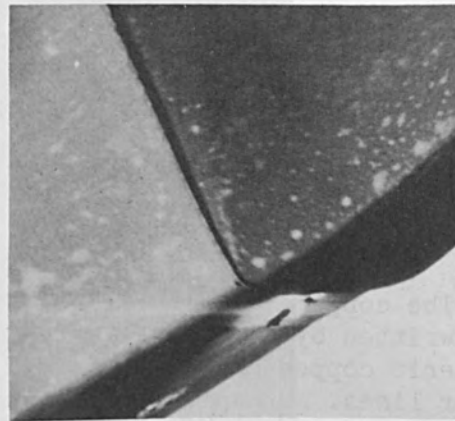


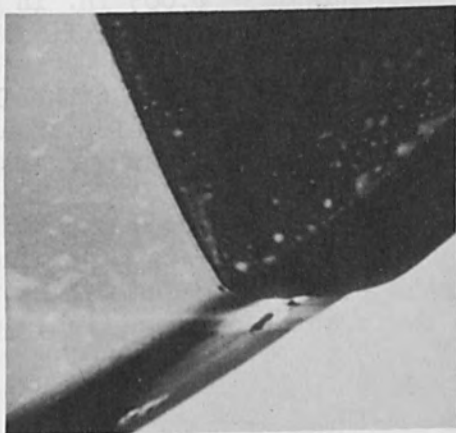
FIG. 6.—Relation between primary beam current and detected beam current.



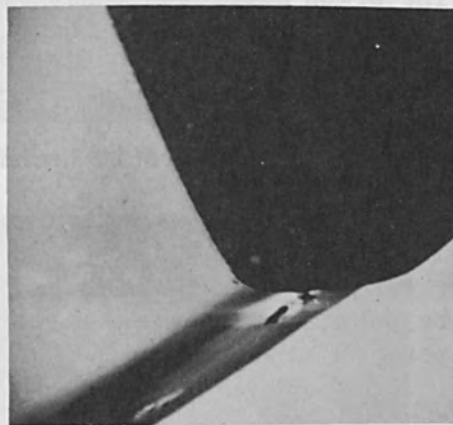
$V_b = 0$ volt



$V_b = -1.6$ volt



$V_b = -3.2$ volt



$V_b = -6.2$ volt

Acc. Volt.: 10 kV

FIG. 7.—Secondary electron image of PN junction.

3. R. F. W. Pease and W. C. Nixon, *ibid.* 42: 81, 1965.
4. T. E. Everhart, O. C. Wells, and C. W. Oatley, *J. Electron. and Control* 7: 97, 1959.
5. C. W. Oatley, C. W. Nixon, and R. F. W. Pease, *Advances in Electronics and Electron Physics* 21: 181, 1965.
6. H. Kimura, H. Higushi, et al., *J. Electron Microscopy, Japan* 15: 21, 1966.

CIRCUIT DEPOSITION BY ENERGY-BEAM IRRADIATION OF CERTAIN METAL-CONTAINING MATERIALS TO BASE METAL

R. E. DREIKORN, M. F. LEVY, and T. F. SAUNDERS

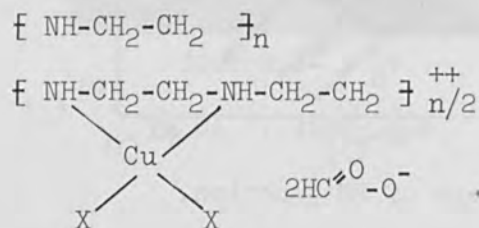
IBM Components Division, Endicott, N. Y.

The copper conductor lines shown in Fig. 1 on the dielectric substrate were written by an argon laser. The material between the lines is a polymeric copper chelate that was decomposed by the laser to form the copper lines. The dielectric substrate is Nomex (registered trademark of E. I. DuPont Co., Wilmington, Del.), a fully aromatic polyamide.

The argon laser beam that wrote these lines is 0.005 in. in diameter and has power levels comprising a few to several hundred milliwatts.

This presentation is a report of research performed at the IBM Manufacturing Research Laboratory at Endicott, N. Y., to develop an additive process for printed-circuit technology. Electron and laser beams were used in this study.

The following are the idealized formulas of polyethyleneimine and of copper formate-polyethyleneimine. The latter is representative of the metal chelate polymers that were decomposed by irradiation with either electron or laser beams.



These polymeric chelates are water-soluble containing in excess of 20 per cent solids as copper. To make conductor lines, these moderately viscous aqueous solutions were applied to the substrates by dipping and then air drying. After irradiation, the undecomposed chelate, between the lines, was removed by washing with water for reuse.

The application of energetic beams to decompose an organic material is not new. However, the use of a low-cost, water-soluble chelate with a high concentration of metal that is nonvolatile, and easily applied in any thickness through spraying or dipping, represents a new process for the manufacture of printed conductor lines.

Figure 2 illustrates a palladium spiral conductor produced by irradiating a palladium polyethyleneimine chelate with the electron beam. Figure 3 shows why spiral patterns are useful. The energy input varies with exposure velocity; therefore, from the center of one spiral to the edge, the exposure can vary approximately 300 per cent. An optical and electrical inspection of the entire spiral permits selection of the best

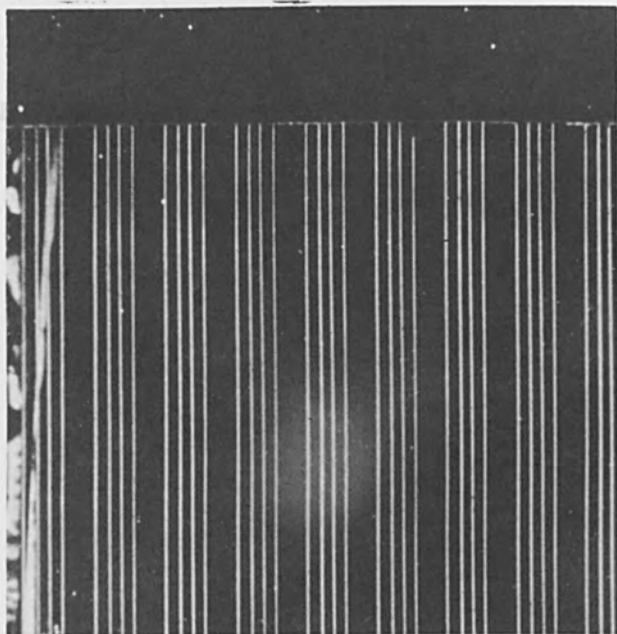


FIG. 1.—Copper conductors written with Argon laser in polymeric chelate.

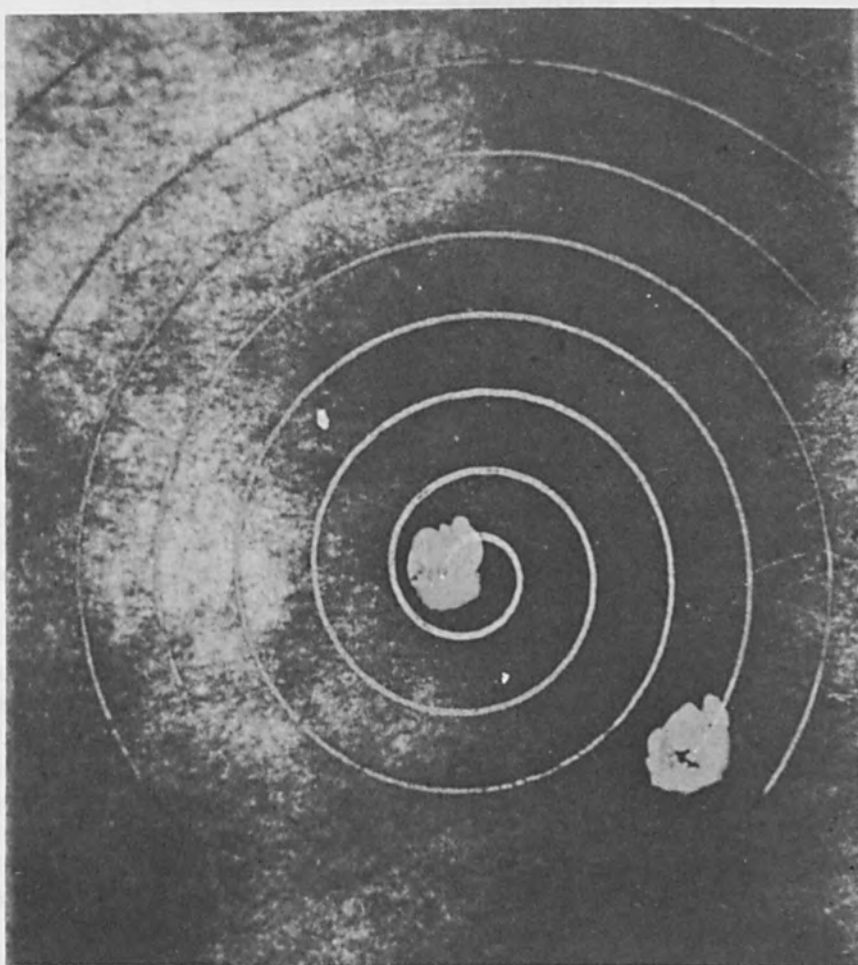


FIG. 2.—Spiral conductor made by electron beam in Palladium chloride polyethylenimine on a Nomex substrate.

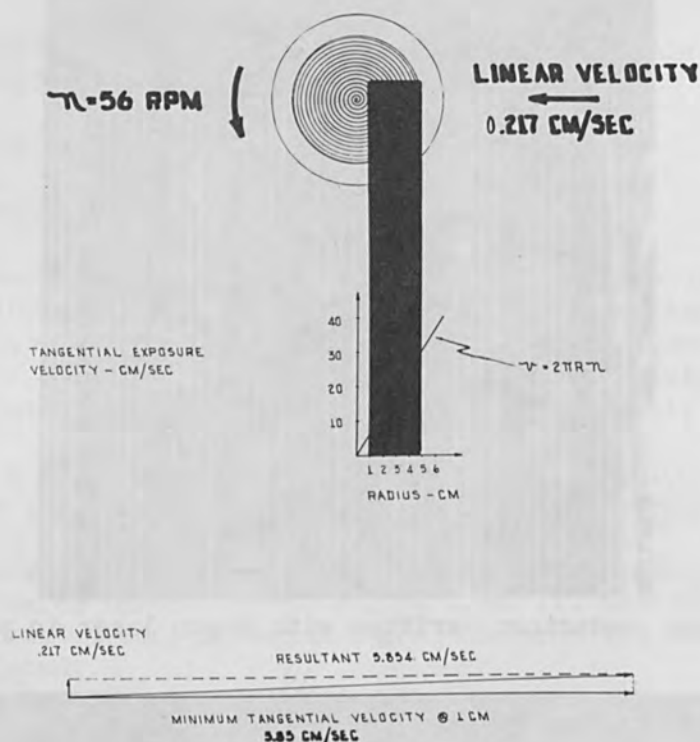


FIG. 3.—Variation of exposure velocity across spiral.

section of the spiral. The energy density of the section is then calculated. Confirmation of the energy density given by these calculations is accomplished by a linear traversing mechanism that makes straight lines 3 in. long, as seen in Fig. 1. These lines are convenient to measure.

The range of electron-beam energy densities that were used in this study extended from 2 to approximately 100 joules/cm^2 . By varying the accelerating voltage, electron-beam current, and revolutions per minute of the sample, any density range required could be obtained. From the results of this wide variation in power input, the following generalizations could be made pertaining to the influence of electron-gun parameters on the conductivity of the printed conductor formed in the exposed chelate (Fig. 4).

The resistance of a printed conductor line formed on irradiation of a polymeric chelate with an electron beam is plotted against energy density. The idealized result would be "U" shaped as illustrated in Fig. 4. This shape means that conversion from high resistance chelate to low resistance conductors occurs only after a critical energy density is applied to the chelate. The curve further shows that low-resistance conductors can be obtained through a wide range of energy densities and that after an excessive energy density has been exceeded, all the copper is evaporated and a high-resistance residue remains.

However, the experimental data form a parabolic curve and show that the conductor becomes increasingly resistive and critical (a narrower

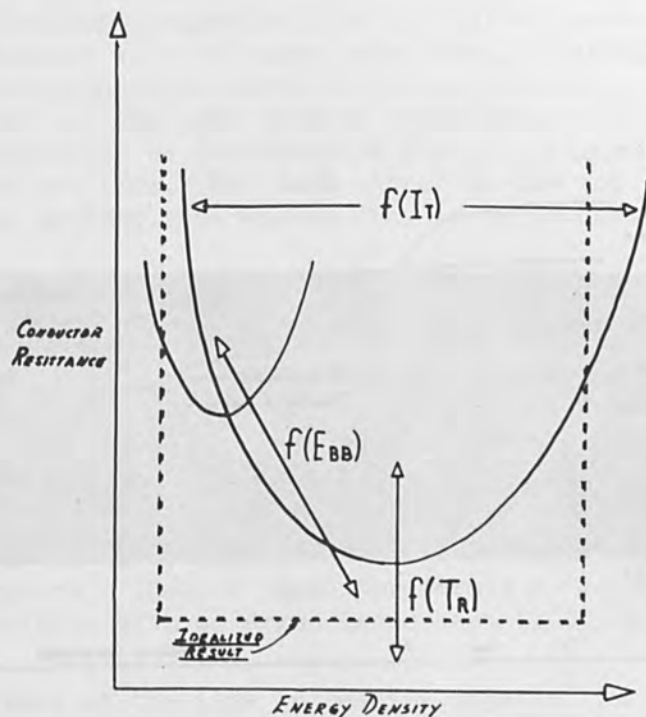


FIG. 4.—Trends of parameters of copper polyethyleneimine chelates on electron irradiation.

range of energy density for approximately the same resistance) with an accelerating potential (E_{BB}). Increased accelerating voltage leads to deeper penetration or more material to convert per unit charge. At increased energy densities and decreased voltages, the beam could penetrate the coating more deeply, performing the greater conversion, which is manifested by decreased resistance.

Similarly, an increase in the time that a beam dwells at a given location causes an increase in the conversion to copper and a decrease of the resistance. This relationship explains the effect of residence time (T_R) on the resistance. Finally, with an increased current, the increased flux of electrons blunts the parabola because the I^2R effect increases the conversion to copper and thereby lowers the resistance.

The choice of inorganic salt to formulate the polymeric chelate is based on the desired metal conductor and the vigor of the decomposition reaction when irradiated. Some systems, such as copper nitrate-polyethyleneimine, produced poor printed conductor lines at all tested energy densities; however, other systems produced consistently fair-to-good lines. The exothermic character of the nitrate system led to ejection of copper metal from the line during the decomposition. A Thermal Gravimetric Analysis (TGA) Survey was made of many possible systems as an aid in selection of the chelate that would produce better conductors.

Figure 5 shows the TGA traces of copper nitrate and copper formate polyethyleneimine chelates as well as polyethyleneimine itself. The TGA is a plot of weight of remaining sample against temperature as the sample

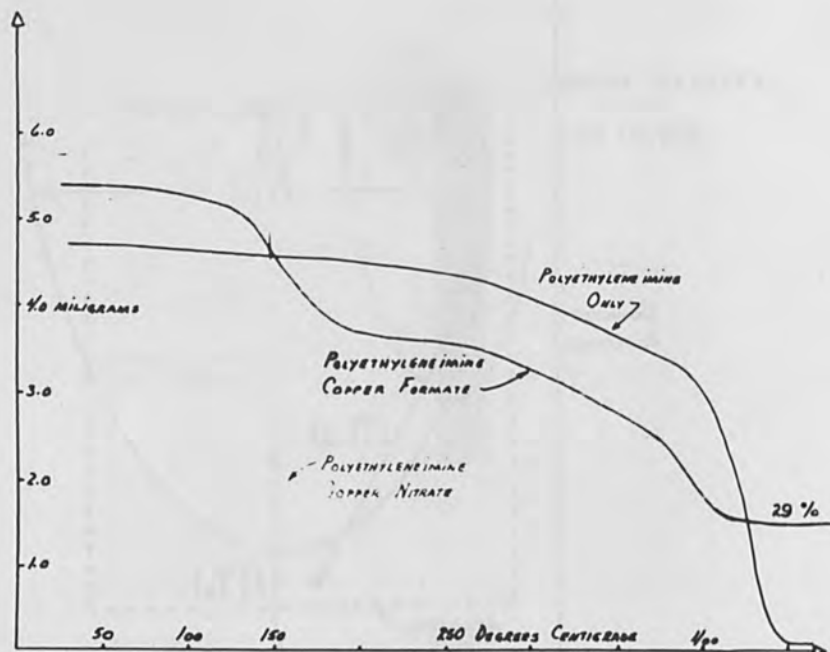


FIG. 5.—Thermal gravimetric analysis of polyethyleneimine and chelates of copper salts (25°C/min).

is heated. These TGAs were accomplished in vacuum with a heating rate of 25°C/min. The slope of the weight-loss curve indicates the vigor of the decomposition. These curves show that the poor printed conductors that resulted with the nitrate are due to the explosive nature of the decomposition. The formate trace is typical of a very mild evolution of gaseous products and almost parallels the endothermic decomposition of the polyethyleneimine.

The residue after TGA decomposition of the formate chelate agrees with the theoretical amount of copper plus a small quantity of char resulting from the organic portion of the chelate. The small residue in the nitrate chelate supports the conclusion that the copper was ejected from the substrate. The TGA survey permitted an evaluation of the degree of dependency of the decomposition rate with power input. The copper formate polyethyleneimine chelate was the most controllable system evaluated.

After considerable electron beam work was done, an argon laser was made available and used because of its convenience and because it represented only thermal energy. Working in vacuum systems requires pumpdown time and the installation of machinery and apparatus in constrained volumes. The use of a laser eliminated the rapid expansion of the hot gaseous decomposition products with vacuum. This can be destructive to the conductor. Further, the laser is electrically neutral, so an electrical charge is not accumulated on the dielectric substrate to cause unknown side effects. Lastly, in working with the electron beam, the electrons are easily stopped, so that the coating thickness is more critical for electron reduction.

Calculations based upon exposure velocity spirals made in copper formate-polyethyleneimine with an argon laser beam, 0.005-in. in diameter, indicated good printed conductor lines at energy densities of approximately 100 joules/cm²; so straight printed conductor lines were produced at various energy densities as indicated in Fig. 1. Figure 6 illustrates a photomicrograph of one line. The dark streak on the top of the line is a condensed reaction product that washed away in water during the development process.

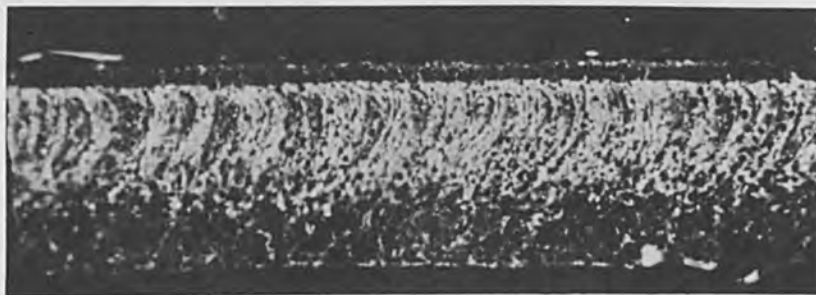


FIG. 6.—Photomicrograph of copper conductor formed by decomposition copper formate polyethyleneimine with an Argon laser beam (100j/cm²)

The grainy texture of the line is readily apparent in Fig. 6; the resistance values of the best lines obtained prior to development ranged from 20 to 30 ohms/inch. The data indicated that approximately 100 joules/cm² produced printed conductor lines of highest conductivity and that the conductivity depended on the energy input. The lines were approximately 0.015 in. wide and both the width and depth of conversion were reduced with reduced energy input.

Metallographic cross sections were made of some printed conductors and the resistivity of the conductor was calculated to be approximately 600 times greater than bulk copper. This is indicative of the open grainy-structure in the metal. During the development in water, normally used to remove the unaffected chelate located between the printed conductor lines, the major portion of the copper was also removed because of poor adhesion to the substrate.

This poor adhesion of the decomposed copper to the substrate had been predicted. Two methods were tested in an effort to improve the adhesion. One method required incorporating a material in the substrate surface that reacted with the decomposed copper, as illustrated in Fig. 7. In this instance, a slurry of copper oxide powder and epoxy resin was coated on the substrate. The blue-colored-chelate was coated over this undercoating with the intention that the hot metal would form a bond with the imbedded oxide. Unfortunately, the resulting oxide-epoxy surface was rough, and the heat loosened the oxide particles, causing open gaps in the copper printed conductor. The second method, illustrated in Fig. 8, was a precoating of the plastic substrate with a Neoprene or polysulfone that would lock copper to the substrate by adhesion. And substrates treated with these organic materials produced the best adhesive surface for the copper lines formed.

The lines that had greatest survival in the development process were those formed in the 100-joule/cm² range. Thus, a feasible method of

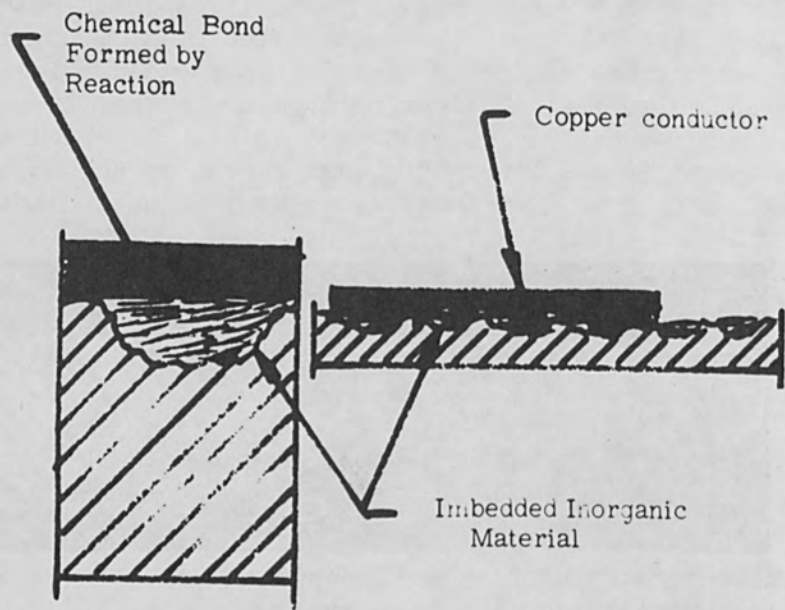


FIG. 7.—Adhesion obtained through reaction with material imbedded in substrate.

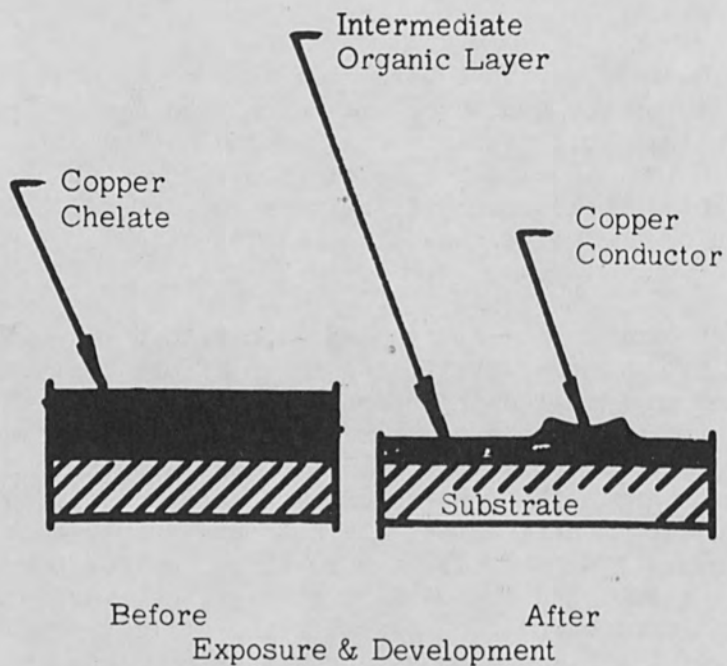


FIG. 8.—Adhesion obtained through a thermally activated intermediate layer which grips the conductor.

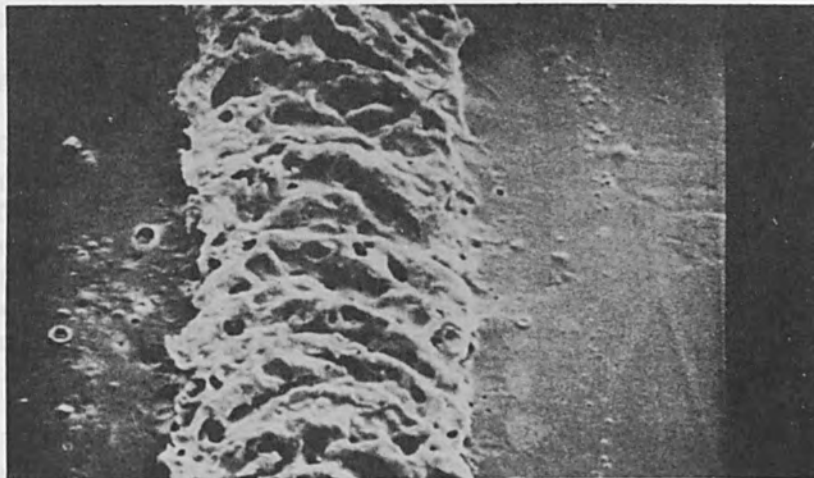


FIG. 9.—Scanning electron micrograph of copper conductor made by Argon beam irradiation of copper formate polyethyleneimine chelate 200x.

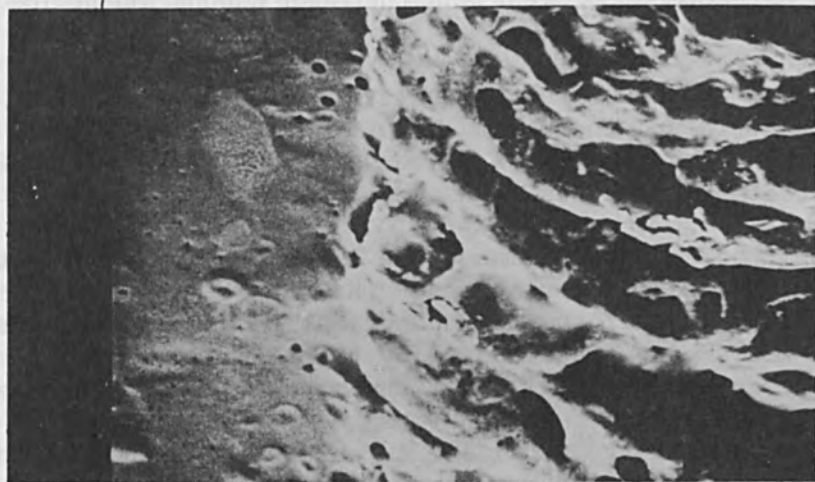


FIG. 10.—Scanning electron micrograph of copper conductor made by Argon beam irradiation of copper formate polyethyleneimine chelate 500x.

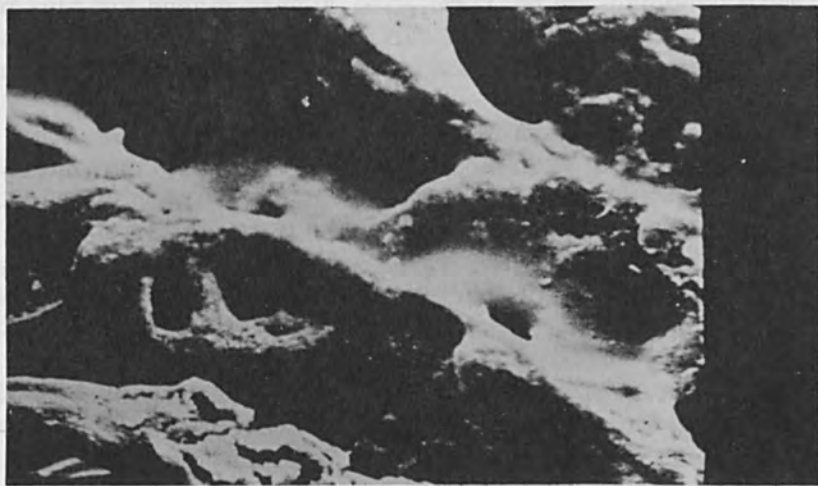


FIG. 11.—Scanning electron micrograph of copper conductor made by Argon beam irradiation of copper formate polyethyleneimine chelate 1000x.

promoting copper-line adhesion to the substrate was now at hand.

The high resistance of the printed conductors that survived development was the next consideration.

Tests indicated that the printed conductor lines were brittle and it was difficult to make connections to them by soldering. These characteristics suggested impure copper or imperfect sintering. Printed conductor lines were examined with a scanning electron microscope. This instrument, with its large depth of field, can show the character of the copper in the printed conductor that was produced by laser irradiation of the chelate.

Figures 9 through 11, inclusive, produced by a scanning electron microscope, illustrate a copper conductor produced after an argon laser beam exposed copper formate polyethyleneimine. The magnifications are 200, 500, and 1000x. The blue chelate between the lines has been removed during the development process and the open porous structure of the metal is shown.

This type of structure can result from the evolution of the gaseous reaction products and the rapid solidification of the copper that occurs after the laser passes. These factors and the dissolved gases could produce a brittle, high-resistance conductor.

The printed conductor lines were electroplated to fill the voids and gaps and reduce the resistance. The resulting printed conductor lines were of good quality, but economically unsound. Electroless plating of printed lines made of palladium by the electron beam was successful too, but the cost of the palladium chelate limits its application. Finally, multiple sweeps of a laser beam on a copper conductor line were tested at various energy densities to obtain additional sintering and purification. The results may be summarized by stating that if the energy input is sufficient to remelt or resinter the metal, the substrate is burned and adhesion of the copper is lost. Also, the surface tension of the liquid metal caused it to form into a ball ahead of the beam and spill over the edges of the slot; if melting did not occur on the subsequent sweeps of the beam, the resistance and brittleness would be unchanged.

Finally, an economic analysis indicates that if greater energy densities were available with more powerful lasers than those in existence at this time, and the probable speed of printed conductor line writing were significantly increased, then reasonable conductors could be formed in copper polyethyleneimine chelates. However, the process would be more costly than the current subtractive process used in the industry.

The authors are grateful to their colleagues in the IBM Manufacturing Research Laboratory whose work has contributed to these results: O. Abolafia for the TGA analysis, E. C. Baldwin for the electron beam irradiation and analysis of results, and T. J. Stewart for photography, metalographic cross sections and x-ray analysis, B. J. Serafin for conducting tests and offering suggestions, and especially Dr. G. S. Kozak, Manager of Advanced Chemical Technology.

STATUS OF ELECTRON-BEAM WELDING FOR IN-SPACE APPLICATIONS

F. R. SCHOLLHAMMER

Hamilton Standard, Windsor Locks, Connecticut

INTRODUCTION

The success of space exploration will, to a large extent, depend upon the presence of man as part of the space mission. Because of his presence, the problem of maintaining a habitable environment for long periods within a space vehicle assumes primary importance. However, before extended missions can be realized, the problems of crew safety and minimal air leakage from a space system first must be solved. Therefore, the capsule must exhibit a high degree of structural integrity and meet leakage standards approaching those of a hermetic seal.

It becomes evident that a completely welded system has many advantages in the fabrication of advanced hermetically tight space systems. In order to fabricate such a system, the first series of space stations must be assembled as an integral unit and then launched into orbit. However, large spacecraft and stations will have to be assembled while in orbit after the substations have completed a suitable in-space rendezvous. It is here that an in-space welding tool will be required. This tool obviously must be light and compact, easy to operate, highly reliable in performance, and efficient in use of energy.

Commercial welding techniques have not been developed for gravity-free, atmosphere-free use. In addition, most of the present techniques are difficult to apply to thin materials. The solution to in-space welding thus lies in a true fusion process which can be adapted to a space environment while exhibiting minimal heat input. Extensive studies indicate that electron-beam welding is well suited to fabricating the range of materials and joint configurations encountered in the assembly of space stations and spacecraft. Furthermore, this process is ideal for repairing damage which could occur during a rendezvous or while orbiting in space.

Electron-beam welding has several unique attributes that make it well suited to the problems of joining material in space. First, electron-beam welding utilizes a vacuum environment that enhances the process as the pressure decreases, i.e., higher vacuum. For this reason, the hard-vacuum environment of space can be a great advantage. Second, the electron-beam welding process is characterized by high power densities and low total power input. These characteristics permit single-pass welding of a wide variety of material combinations with minimum distortion and shrinkage. In addition, electron-beam welding has essentially no reaction force, an important consideration in outer space.

The use of an electron beam as a heat source for melting and joining is relatively old. However, in the late 1950's, the so-called "deep-weld" effect was discovered by K. H. Steigerwald, greatly enhancing the

utility and value of the process. Taking advantage of the techniques of this invention, Hamilton Standard has, during the past 7 years, developed advanced electron-beam gun designs that now make it technically possible and feasible to apply electron-beam welding manually to the joining of space materials and structures. Significant advances have been made in developing a hand-held gun which can be used to weld materials in nearly all attitudes. A description of some of the operational considerations for in-space welding, subsequent equipment development, and welding results achieved at Hamilton Standard in these special areas are discussed below.

IN-SPACE JOINING CONSIDERATIONS

The importance of producing sound joints for spacecraft or space stations having load-bearing members and pressure compartments cannot be overestimated. A large segment of American technology is currently involved, directly or indirectly, with equipment or facilities to produce a space system that will exhibit a high degree of structural reliability. However, after achieving this reliability through exhaustive and proven welding methods, the habitable environment and structural integrity of the spacecraft must be maintained for the duration of the mission through repair and maintenance techniques. In addition, extension of existing space structures and new construction in space undoubtedly will be required as space missions become even longer, more complex, and more demanding.

MATERIAL JOINING REQUIREMENTS

An optimum process for joining different types of aerospace materials under extraterrestrial conditions should meet the following requirements.

- (1) The welding process must be adaptable to operation in a vacuum.
- (2) It should not cause distortion in the structure as a result of the heat applied.
- (3) It must produce joints free from internal stresses.
- (4) It must not depend upon the use of filler metal.
- (5) It must produce minimal metallurgical transformation.
- (6) It must produce joints in which the mechanical properties equal or approach those of the base metal.
- (7) It must produce sound weld metal across or around the entire joint.
- (8) It must be a rapid and easily performed process.

These requirements for joining have been used to briefly evaluate several different joining processes. Table 1 shows that each of these processes is deficient in one or more areas. For example, shielded metal-arc welding produces a high degree of distortion and very frequently, a high degree of residual stress. Also, the high heat input of this welding process produces detrimental metallurgical effects.

Gas-shielded tungsten arc welding, commonly referred to as TIG, provides an improvement over the shielded metal-arc process. However, with this process at very low pressures, broadening of the arc occurs causing the power in the arc to dissipate and the heat input to the

TABLE 1.---Comparison of joining processes.

| Process | Adaptable to High Vacuum | Distortion | Internal Stresses | Filler Material Required | Metallurgical Transformation | Weld Joint Uniformly Equal Base Metal | Sound Metal | Weld Speed |
|-----------------------------------|--------------------------|----------------|-------------------|--------------------------|------------------------------|---------------------------------------|-------------|------------|
| Shielded metal-arc welding | Questionable | High | High | Yes | Yes | Seldom | Seldom | Very Slow |
| Gas-shielded tungsten-arc welding | Questionable | Medium to high | Medium to high | (1) | Yes | Sometimes | Sometimes | Slow |
| Gas-shielded metal-arc welding | Questionable | Moderate | Moderate | Yes | Yes | Sometimes | Sometimes | Slow |
| Brazing | Yes | Varies | Varies | Yes | Yes & no | No | Sometimes | Varies |
| Soldering | Yes | Low | Low | Yes | No | No | Sometimes | Slow |
| Flash and upset welding(2) | Yes | Low | Low | No | Yes | Frequently | Yes | Fast |
| Adhesive bonding | Yes | Low | Low | Yes | No | No | No | Very slow |
| Laser | Yes | Low | Low | (3) | Yes | Sometimes | Sometimes | Slow |
| Electron beam | Yes | Low | Low | (3) | Yes | Frequently | Yes | Very fast |

(1) Depends upon thickness.

(2) Process produces a large amount of flash or upset around the joint which can be troublesome to remove.

(3) Depends on tightness of fit. Wire may be needed for surface fill.

workpiece to spread. Thus, the formation of a molten pool is difficult. In addition, this process results in poor energy utilization, which is important for in-space welding (i.e., the use of minimum power is desirable to conserve power that is drawn from fuel cells or batteries).

Gas-shielded metal arc welding (MIG) is undesirable since this process depends upon the addition of filler metal. Again, the disadvantage of this system is similar to that cited for the tungsten-arc welding process.

Present brazing alloys and methods for melting these alloys—torch, induction, furnace, resistance, etc.—do not lend themselves to in-space fabrication. In addition, suitable brazing alloys for the joining of magnesium or aluminum are not readily available. Even the adaptability of thermochemical brazing in lieu of conventional brazing techniques will not readily lend this process to the joining of in-space materials. Cleanliness and tolerance requirements for fit-up of the components to be joined are as critical for exothermic brazing as they are for any other brazing process.

Soldering, like brazing, utilizes a filler material except that in the case of soldering, the filler metal melts below 800°F. Again, the disadvantages of this joining method are similar to those of brazing with the added problem of low joint strength.

Both flashing and upset welding require high pressures and heavy equipment, not readily available in outer space. In addition, the process has a high electrical-power requirement with instantaneous demand. These disadvantages make this process unsuitable for in-space joining.

Adhesive bonding, like soldering, does not provide a metallurgical bond. The speed of this process as well as its temperature and aging characteristics limit its use for joints having high structural and hermetic requirements.

Laser welding is a fusion welding process which has several major drawbacks as a space repair and fabrication technique. First, lasers with sufficiently high power output are pulsed devices and short pulse lengths tend to vaporize the target rather than melt it. Second, a laser is basically an inefficient device from an electrical energy utilization standpoint. Third, the basic physical properties of the metals to be welded affect the quality of the weld. For example, best results have been obtained with metals having a high thermal diffusivity, e.g., copper and aluminum. Metals such as stainless steel and titanium limit the flow of heat, thus increasing the possibility of vaporizing rather than melting the material.

When compared with these other joining processes, electron-beam welding shows itself to be best suited for in-space joining. Some advantages of the electron beam process are as follows:

- (1) Minimum energy requirements.
- (2) Minimum operating and maintenance cost.
- (3) Low distortion.

- (4) Low residual stresses produced.
- (5) High joint strength.
- (6) Uniformly sound joints.
- (7) Minimum metallurgical effects.
- (8) Ability to weld without filler metal.
- (9) High speed.
- (10) Ability to use for on-site pre- and postweld heating if required.
- (11) Single-pass welding.

This process does not require a high degree of operator skill, thereby increasing the reliability of the joint. When fully developed and proven by man-rated chamber and flight evaluation tests, this process should be acceptable for the majority of in-space welding and joining requirements.

OPERATIONAL CONSIDERATIONS

Since in-space joining will be accomplished in environments vastly different from earth environments, modifications of normal electron beam equipment and welding techniques are required. These modifications should not require preweld equipment checking or prebaking of system prior to commencing welding operations. During emergency in-space conditions such a tool must be available for immediate use. Therefore, new design approaches to joining problems had to be investigated. Early studies of an in-space system indicated that certain design parameters had to be resolved prior to selecting or evaluating an optimum system. Parameters particularly unique to electron beam welding which required study are: welding mode, heat transfer from the gun assembly, electrostatic charging, x-ray emission from the workpiece, and movement of the gun during welding operations. Basic studies were conducted relative to these factors. In addition, items such as weight, envelope definition, moment, equipment safety, workpiece viewing, and operational dexterity as related to manipulation of the welding gun and its associated controls had to be considered.

MATERIAL THICKNESS. Some of the typical structures considered for in-space fabrication are shown in conceptual form in Fig. 1. Assembly of these structures by electron-beam welding now is considered possible and practical. Typical materials being considered include the more common aerospace materials such as aluminum, titanium, and stainless steel. Of these three materials, aluminum appears to be the predominant choice. Some high-temperature requirements also exist which may require the joining of refractory materials. Some 65 thicknesses of typical structures have been tabulated and are shown in Figure 2. From this graph, it is evident that over 90 per cent of the applications involve materials less than 0.125 in. in thickness. Furthermore, approximately 80 per cent of the applications involve thicknesses of 0.075 in. or less. These criteria were used to determine, in general, the power required by an electron beam in-space welding system.

WELDING MODE. Initial design studies indicate that a time-limited on-off welding technique is preferred over welding in a pulsed mode or welding for long periods of time in an uninterrupted or continuous mode.

ELECTROSTATIC CHARGING. Another operational consideration of importance is the electrostatic charging that could occur during the operation of an electron beam device. When an electron beam impinges on a workpiece, secondary emission produces free electrons and ions. Most of these particles go to ground or are neutralized when proper precautions are taken. In order to ascertain whether or not an electrostatic potential could build up around neighboring components or on the space suit of an astronaut, tests were conducted with tufted swatches on the outer spacesuit garment. Tests conducted with and without a radiation-vapor shield mounted on the end of the gun indicated that when the object was suspended (not grounded) and exposed to the beam and to secondary emission, some charging of the tufts on the instrumented swatches occurred. With the object suspended and exposed to a beam, but with the vapor shield mounted on the end of the gun, no electrostatic charging occurred. With the object grounded but unshielded from the beam, no electrostatic charging was observed. These tests confirmed similar work conducted at NASA-Houston and operational tests conducted in a man-rated chamber. During the man-rated chamber tests, the test subject, electron-beam gun, and workpiece all were grounded. The space-suited technician who performed the tests was instrumented with special nylon tufts to observe visually any electrostatic charging that occurred during the test. No charging was observed.

SPLATTER. Consideration also had to be given to the problem of material splatter which emanates from the weld zone during welding. Even though the particles are minute and the amount of weld splatter is less than that of other welding methods, shielding is considered mandatory to preclude possible puncture of the space suit by hot particles. In addition, migration of particles and deposition into other pieces of space equipment must be prevented. Therefore, it was necessary to include a deposition shield which could be mounted on the end of the electron-beam gun. This shield contains the vapor and particles as they are emitted from the weld zone. Transparent windows were designed into the shield to permit viewing the workpiece during most welding operations.

RADIATION. X-radiation is another factor that must be considered when using an electron beam device because the operator is closely linked to the welding operation. Normally, electron-beam welding equipment includes integral shielding which is sufficient to protect the operator from exposure to the x rays associated with electron-beam devices. For most in-space applications, particularly in extravehicular operation, it is impractical to shroud the workpiece completely, although the gun can be shielded. A possible solution is the use of a "hardened" space-suit design; however, this would make the suit very cumbersome. The best solution appears to be to place a shield around the beam and such an arrangement was incorporated successfully into the vapor-deposition shield mentioned previously. A radiation investigation then was conducted which indicated that 0.31-in. minimum thickness of steel (in the hand gun and radiation shield) would adequately attenuate x radiation at 20 kV at a safe level of less than 2 mR/hr. However, the study indicated that a strong x-ray emission pattern could be expected in the forward direction, that is, in the direction of the beam. Therefore, x-ray shielding may be required on the reverse side of the weld joint, depending on the

proximity of personnel. Adequate shielding in this case could be provided with approximately 0.040 in. of steel.

In order to confirm the various theoretical calculations of x-ray attenuation, radiation tests were performed with the hand gun in an experimental chamber. For radiation testing, a Mylar window 0.003 in. thick was installed in the chamber. A tungsten target, tilted toward the window, was then placed in the chamber and the electron beam (at various energies) was allowed to impinge upon the tungsten target. The radiation passing through the Mylar window was monitored in ambient using a Victoreen S/N 214 Model 440 rf-shielded radiation meter. Various thicknesses of shielding materials, particularly stainless steel, were placed in front of the Mylar window, and the attenuated x ray beam was monitored. The results shown in Table 2 indicate that 0.040-in.-thick steel shielding is adequate for the Hamilton Standard hand-held gun.

TABLE 2.—Radiation test data (0.003-in. Mylar window).

| Beam Setting | Shielding | Measured radiation (mr/hr) | | | |
|-----------------|-----------|----------------------------|---------------------|---------------------|---------------------|
| | | No ss shield | 0.008-in. ss shield | 0.017-in. ss shield | 0.025-in. ss shield |
| 12 kV 0.2 mA | 300 | --- | --- | --- | --- |
| 12 kV 50 mA | --- | 0.2 | --- | --- | --- |
| 15 kV 50 mA | --- | 87 | 0.1 | 0.05 | --- |
| 15 kV 100 mA | --- | 90 | 0.1 | 0.1 | --- |
| 20 kV 75 mA | --- | --- | --- | 3.6 | --- |
| 20 kV 100 mA | --- | --- | --- | 7.2 | --- |
| 15 kV 75 mA | --- | --- | --- | --- | 1.8 |

HUMAN ENGINEERING. During the design study of the hand-held gun, special attention was devoted to the handle assembly. One of the problems that had to be considered was the handle configuration, including the angle at which it is attached to the housing; also, the optimum configuration of the handle cross section for gripping by a gloved astronaut had to be evaluated. All of these questions were answered by building a model of the handle and gun assembly and then testing the model in a small portable high vacuum chamber for acceptability. A glove and arm section from a space suit was used for these tests.

WELDING EQUIPMENT

In developing special or unique equipment, the design is evaluated continuously for improvements. The first electron-beam gun developed under Air Force sponsorship is shown in Fig. 3. The over-all dimensions of this first-generation device, excluding the optical viewing attachment, were approximately 9 in. in diameter and 18 in. in length. The electron gun was designed to operate at 80 kV and 12.5 mA. It was used to conduct many of the first reliability studies, weld analyses, and design investigations for defining the next generation of electron beam in-space welding systems. Although this first device can be considered large and bulky by today's standards, it nevertheless pointed out those items which needed special attention in developing a lightweight hand-held gun.

Accordingly, a lightweight breadboard electron beam gun was conceived (Fig. 4). This gun measured 3.5 in. in diameter and approximately 7 in. in length. Size and weight were the paramount design objectives for this hand-held system. A reduction in accelerating potential from 80 to 20 kV was made to reduce significantly the intensity of radiation emitted from the workpiece. At the same time, an increase in power from 1.0 to 1.5 kW was deemed necessary since the accelerating potential had been reduced. As shown in Fig. 5, the electron-optical portion consisted of a triode-type gun. This electron optical configuration was selected because of the excellent performance obtained in similar commercial electron-beam welding systems.

Several preliminary concept sketches then were considered from the results of the breadboard gun studies. These were evaluated from the standpoint of the gun's use as a practical tool while meeting anticipated in-space fabrication requirements. The configuration selected for a prototype gun is shown in Fig. 6. The basic internal features of this gun are shown in Fig. 7. As can be seen, the prototype gun does not have the vapor-radiation shield. This illustration also shows the assembly of the gun components in the housing with the high-voltage cable entering through the connector-handle assembly. The electron-optical section of the prototype gun was similar to that used for the breadboard gun.

The radiation-vapor shield design for the prototype gun is cylindrical, with rectangular bosses that support flat viewing windows of leaded glass on two adjacent sides (Fig. 6). These windows permit the operator to view the weld area. The end of the gun is within the enclosed area, and adjustment of the gun to work distances can be made by loosening the height adjustment clamp and sliding the gun housing up or down as required and then retightening the clamp.

The lightweight hand-held gun described was used in the man-rated chamber (Fig. 8) for all welding evaluations. The gun and handle assembly and radiation-vapor shield weigh less than 10 lb. This gun has been successfully operated at 2 kW (20 kV and 100 mA).

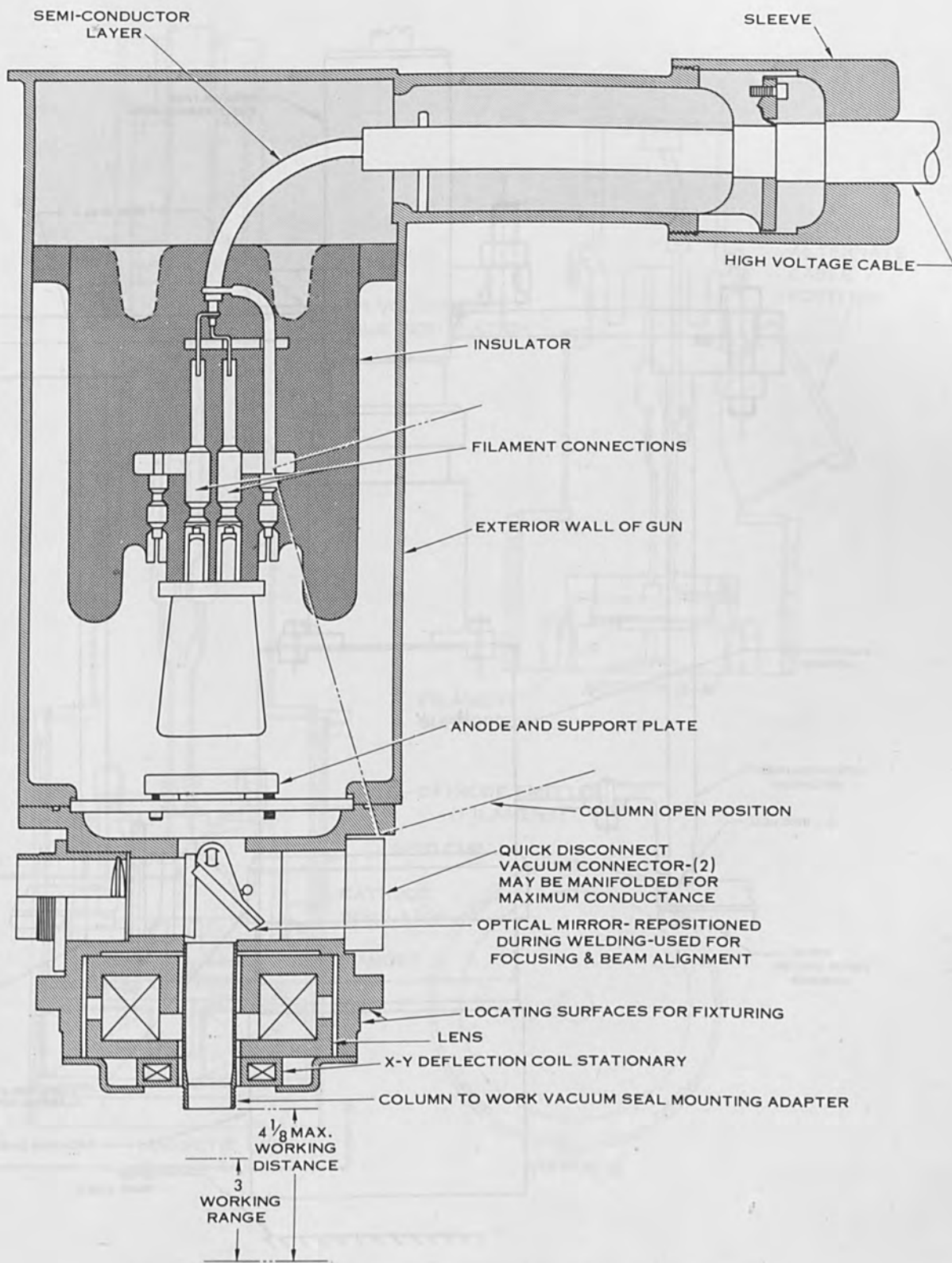


FIG. 3.—Preliminary electron-beam gun.

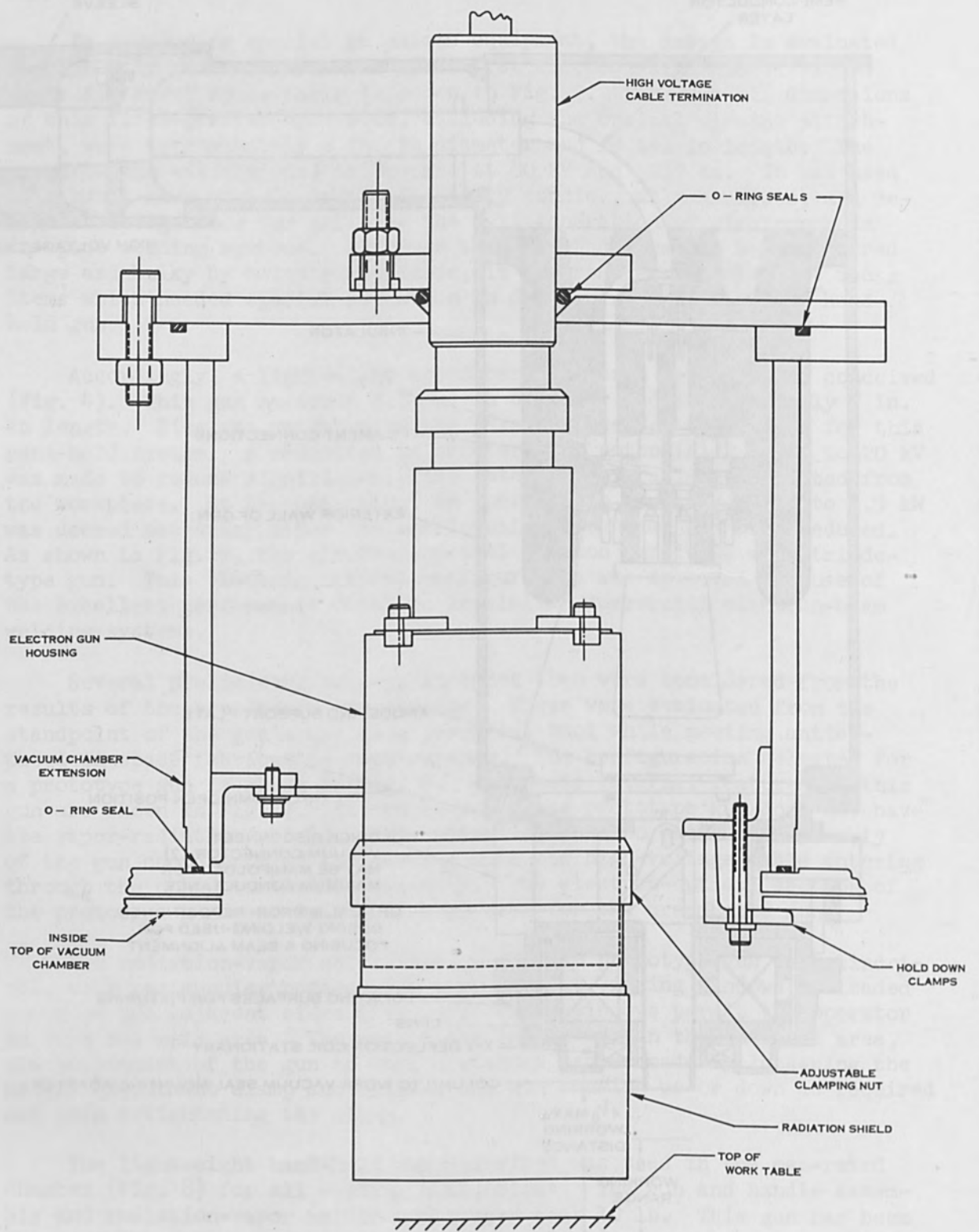


FIG. 4.—Breadboard gun assembly for test.

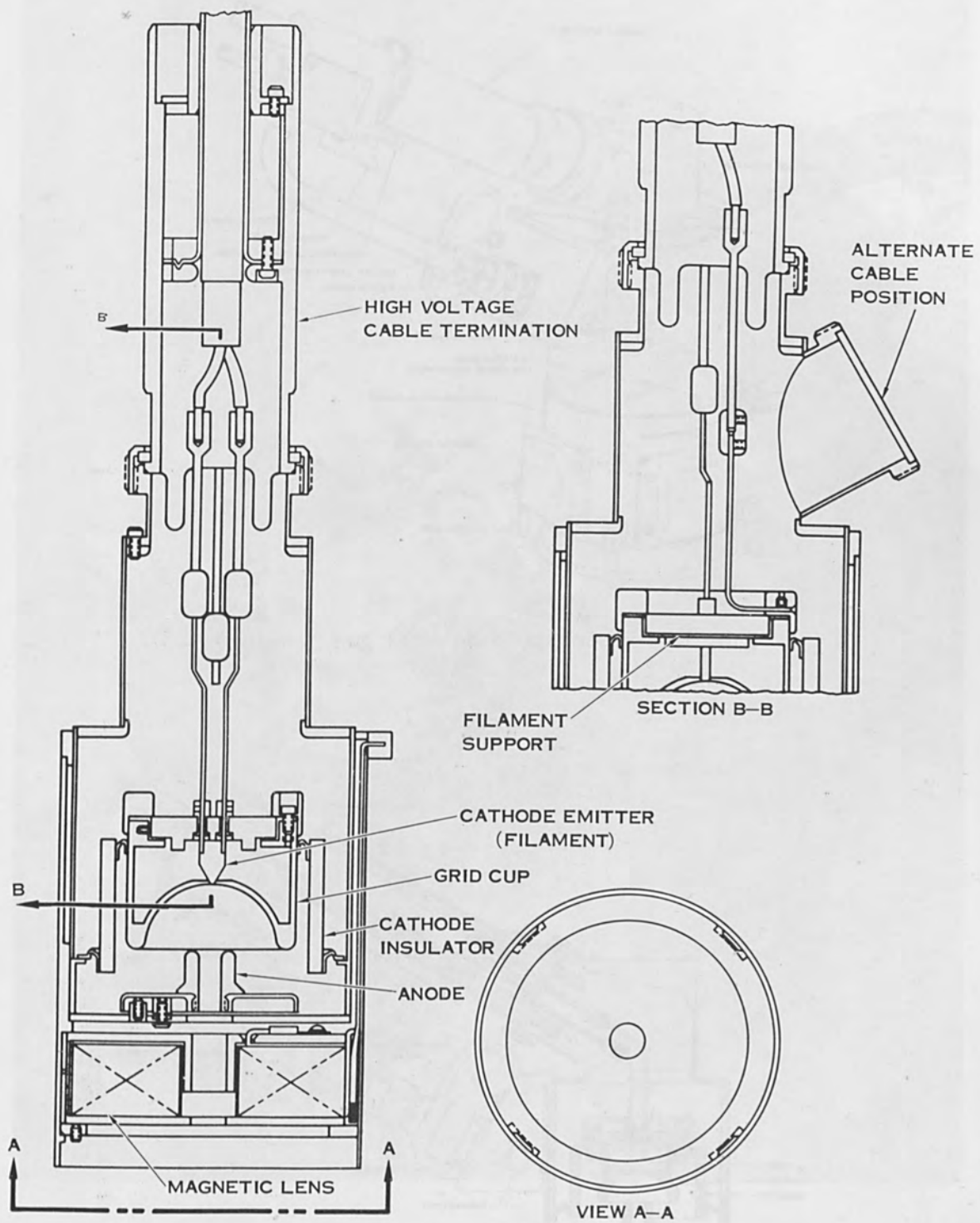


FIG. 5.—Hand-held gun—breadboard test hardware.

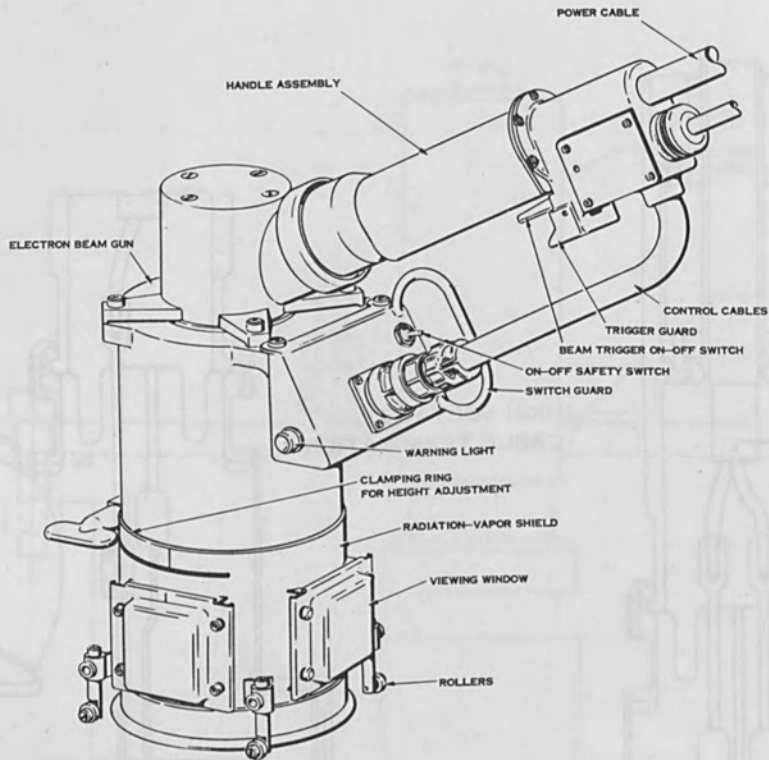


FIG. 6.—Prototype hand-held gun concept.

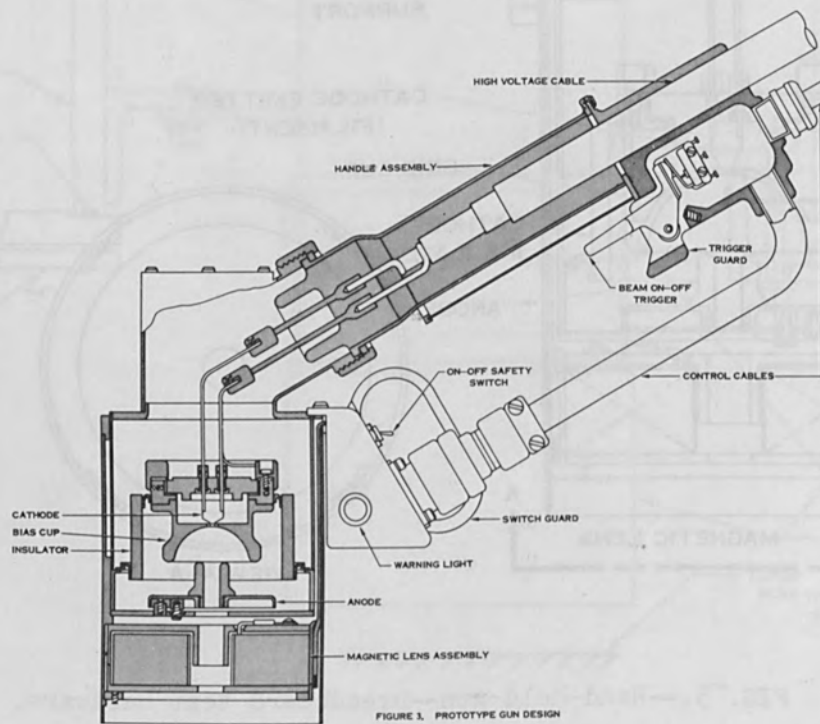


FIG. 7.—Prototype gun design.

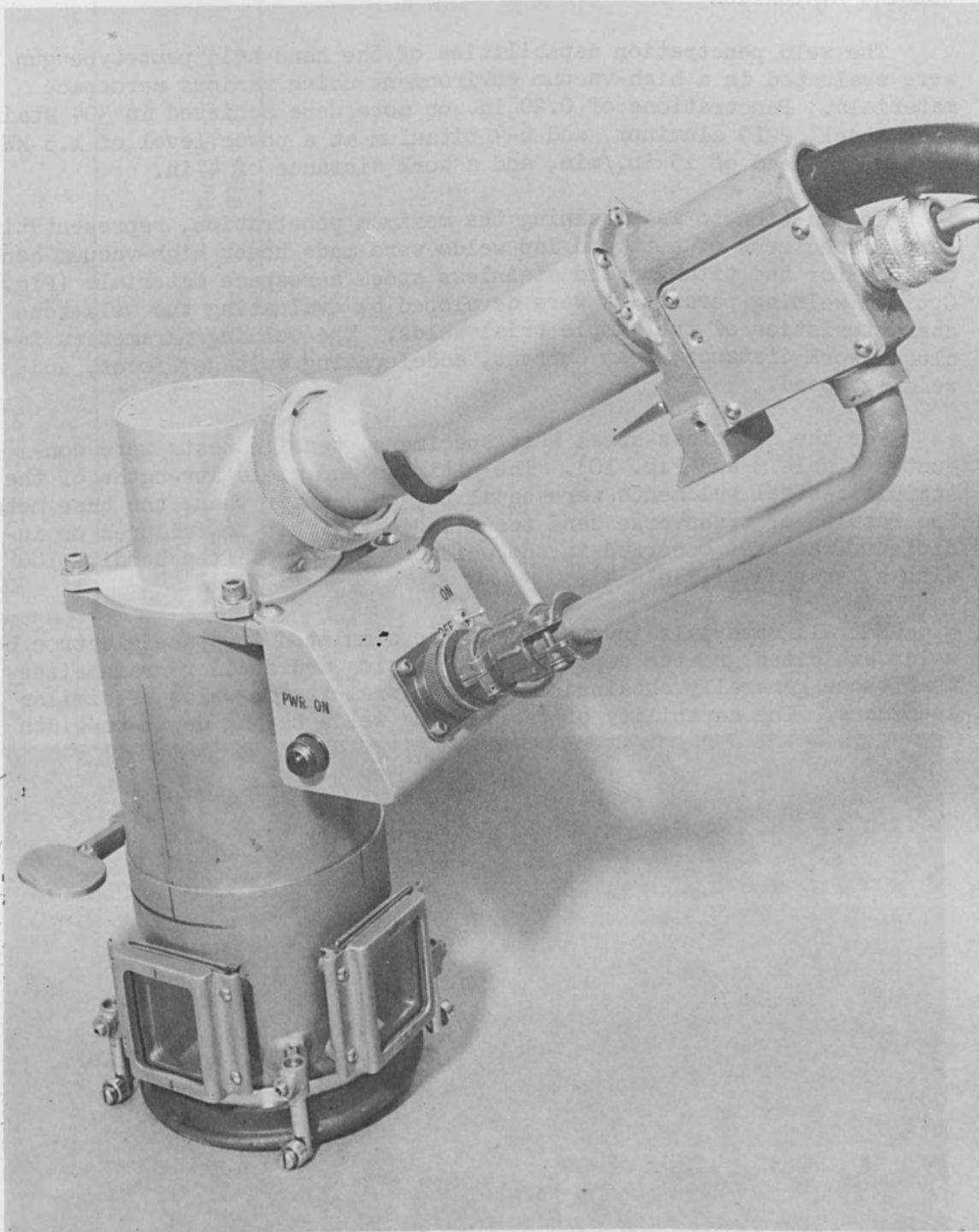


FIG. 8.—Hand-held electron-beam gun.

WELDING EVALUATION

The weld penetration capabilities of the hand-held prototype gun were evaluated in a high-vacuum environment using various aerospace materials. Penetrations of 0.20 in. or more were achieved in 304 stainless steel, 2219 aluminum, and 6-4 titanium at a power level of 1.5 kW, a welding speed of 15 in./min, and a work distance of 4 in.

In addition to ascertaining the maximum penetration, representative sample specimens of butt and lap welds were made under high-vacuum conditions for the titanium and stainless steel aerospace materials (Fig. 9). Optimum welding parameters were developed by evaluating the weld zone characteristics of the sample trial welds. The welding parameters included work distance, beam current, accelerating voltage, focus, and welding speed.

For the stainless-steel test specimens, tensile tests were conducted (Table 3 and Fig. 10). The ultimate and yield strengths of the stainless-steel weldments were equal to, or greater than, the base metal. The results of transverse bend tests indicated that no failures or incipient fractures occurred in the weld or weld zone after bending 180° with a 1-t radius (Table 4).

For all materials investigated, the simulated in-space electron beam welds exhibited greater depth-to-width ratios and smaller grain sizes than those generally obtained in conventional fusion welds of similar specimens. The capability of fabricating welds having depth-to-width

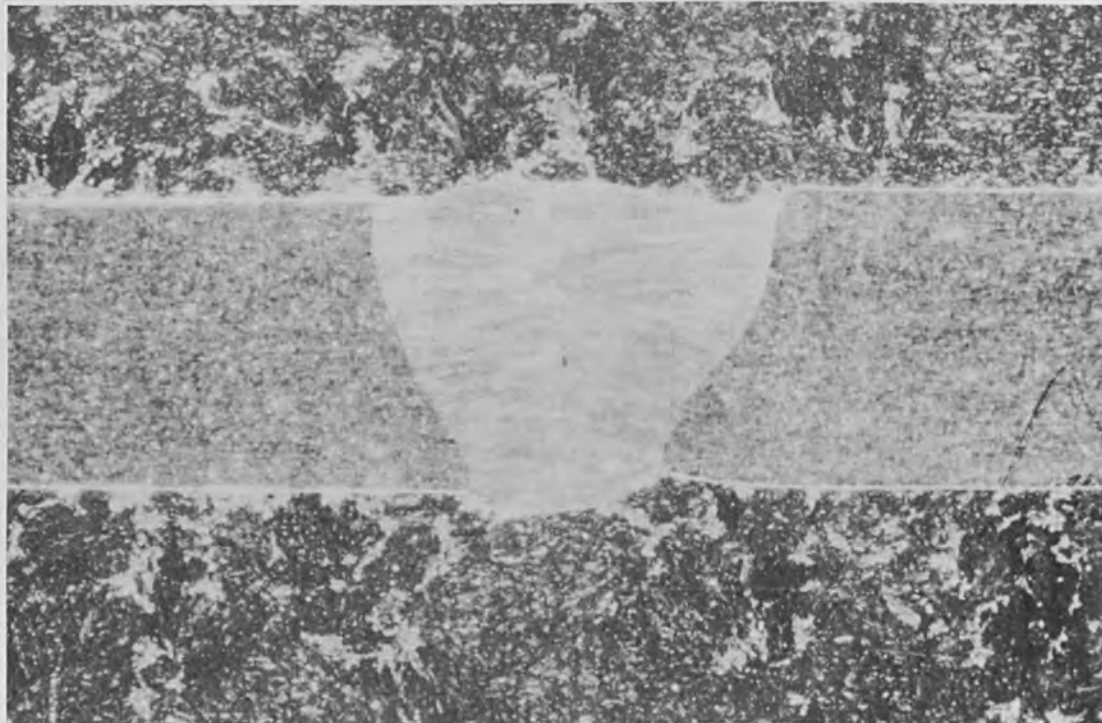


FIG. 9.—Electron-beam butt weld. (Power, 945 W; speed, 36 in./min; material, 304 SS; magnification, 20 x.)

TABLE 3.—Tensile properties of AISI 304 stainless-steel welds.

| Thickness (in.) | Heat Treat Condition | Test Temp. (°F) | Ultimate Tensile Strength (psi) | Yield Strength at 0.2% Offset (psi) | Percent Elongation in 1 in. | Location of Failure | Radiographic Classification |
|--------------------|----------------------------|-----------------------|--|---|-----------------------------------|---------------------------|--------------------------------|
| 0.062 | BM | RT | 82 259 | 43 333 | 38 | — | — |
| 0.062 | BM | RT | 84 258 | 46 296 | 37 | — | — |
| 0.043 | A, W | RT | 98 576 | 54 762 | 31.5 | W | 0 |
| 0.043 | A, W | RT | 87 429 | 55 714 | 23 | " | " |
| 0.041 | A, W | RT | 86 700 | 57 400 | 31 | " | " |
| 0.040 | A, W | RT | 86 000 | 50 500 | 30 | " | " |
| 0.056 | A, W | RT | 85 358 | 47 680 | 21 | " | " |
| 0.057 | A, W | RT | 92 142 | 54 250 | 32 | " | " |
| 0.049 | A, W | RT | 86 000 | 47 800 | 29.5 | " | " |
| 0.058 | A, W | RT | 78 824 | 46 138 | 42.5 | BM | " |

Legend: 0 - No porosity
 A - Annealed
 W - Vacuum electron beam welded
 RT - Room Temperature
 BM - Base Metal
 HAZ - Heat-affected zone

TABLE 4.—BEND test results of AISI 304 stainless-steel welds.

| Thickness (in.) | Heat Treat Condition | Test Temp. (°F) | Bend Span (in.) | Bend Radius (in.) | Bend Radius (degrees) | Location of Failure | Radiographic Classification |
|--------------------|----------------------------|-----------------------|-----------------------|-------------------------|-----------------------------|---------------------------|--------------------------------|
| 0.053 | A, W | RT | 1 | 0.0625 | 180 | None | 0 |
| 0.057 | A, W | RT | 1 | " | " | " | " |
| 0.054 | A, W | RT | 1 | " | " | " | " |
| 0.056 | A, W | RT | 1 | " | " | " | " |
| 0.058 | A, W | RT | 1 | " | " | " | " |
| 0.050 | A, W | RT | 1 | " | " | " | " |
| 0.059 | A, W | RT | 1 | " | " | " | " |
| 0.057 | A, W | RT | 1 | " | " | " | " |
| 0.054 | A, W | RT | 1 | " | " | " | " |
| 0.053 | A, W | RT | 1 | " | " | " | " |
| 0.062 | A, BM | RT | 1 | " | " | " | " |
| 0.062 | A, BM | RT | 1 | " | " | " | " |

Legend:

- O - No porosity
- W - Vacuum electron beam welded
- RT - Room temperature
- T - Thickness of specimen
- BM - Base metal
- HAZ - Heat-affected zone
- FZ - Fusion zone
- A - Annealed

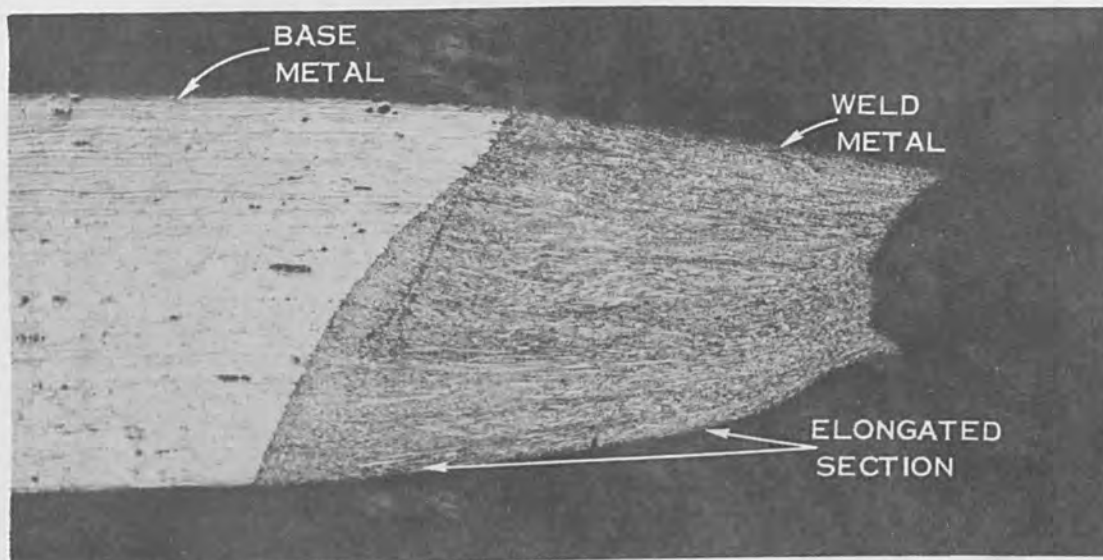


FIG. 10—Specimen after tensile test. (Material: AISI 304; magnification 15x.)

ratios of approximately 10 is extremely important for in-space joining considerations, because the fusion area is a direct representation of the amount of energy and power required. Therefore, it is obvious that maximum weld efficiency and minimum in-space power requirements are afforded by electron-beam welding.

SPACE-CHAMBER TESTS

To prove the usefulness, operational reliability, and safety of the Hamilton Standard hand-held welding tool, the prototype gun was tested and evaluated in a man-rated chamber (Fig. 11). The tests included performing acceptable welds in a repeatable manner. Space chamber tests are still being conducted to study manual welding under vacuum conditions. The first two test objectives, the welding and evaluation portions, have been met. The latter item, the further evaluation of hand-held equipment, is currently in process.

During the space-chamber tests, the prototype gun was manually operated in a vacuum of 2.6×10^{-5} torr. Power to the electron beam gun was supplied from a conventional power supply located exterior to the chamber. Interconnection between the electron-beam gun and the power supply were made by ducting a high-voltage cable through the chamber wall. Several 6-in.-long weldments were made by the operator (Fig. 12). The quality and smoothness of the welds exceeded expectations, especially for the first welds produced under manual operation. Earlier laboratory mockup tests indicated that when the speed is manually controlled, large fluctuations occur over minute increments (Fig. 13). However, when a simple speed indicator was used, relatively smooth control of the gun would be achieved with some practice, as was demonstrated during the welding operations. This test also demonstrated that a hand-held electron beam gun is capable of being used for fabrication and repair of special equipment located in large evacuated test chambers.

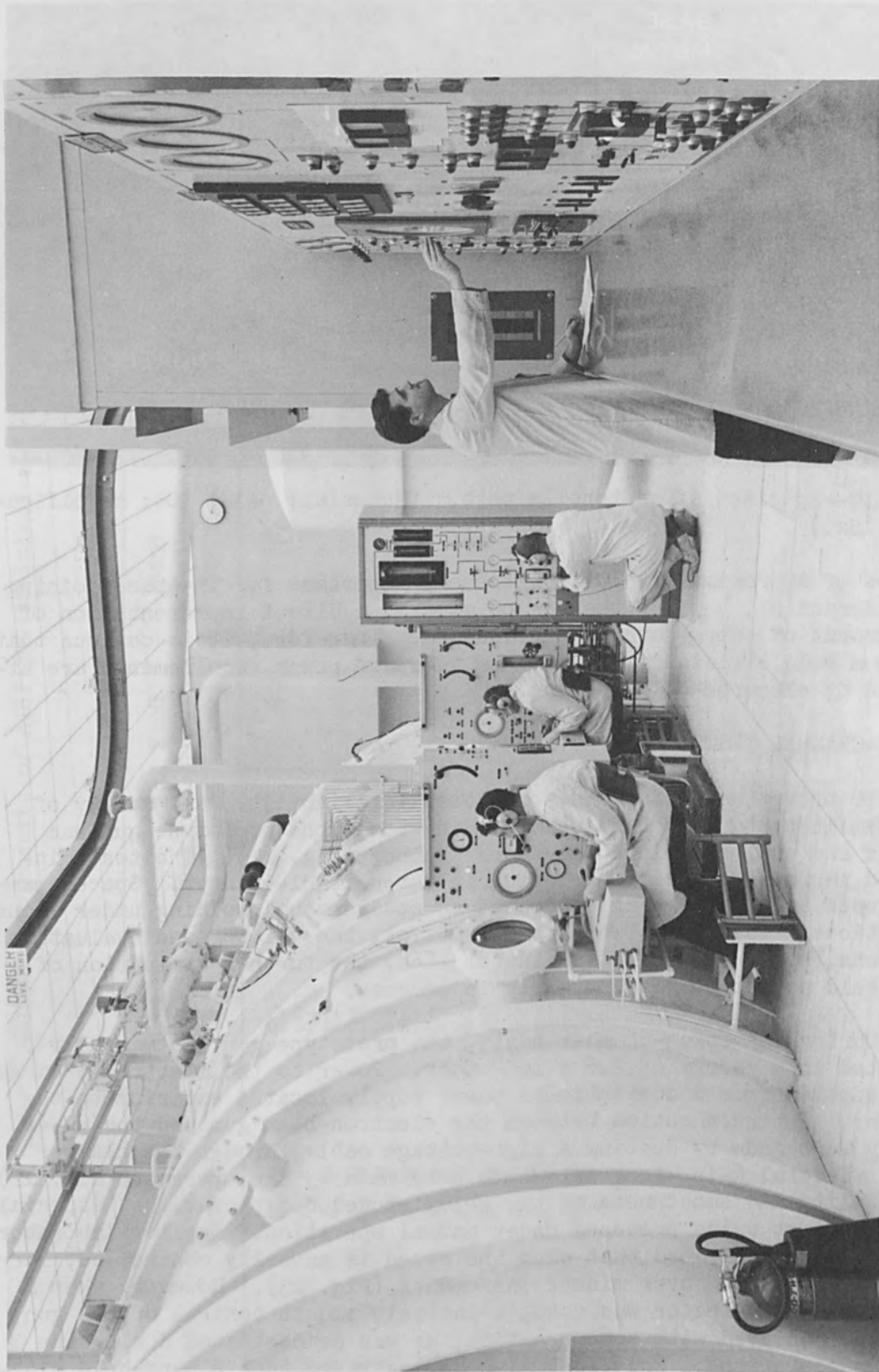


FIG. 11.—Man-rated space simulation.

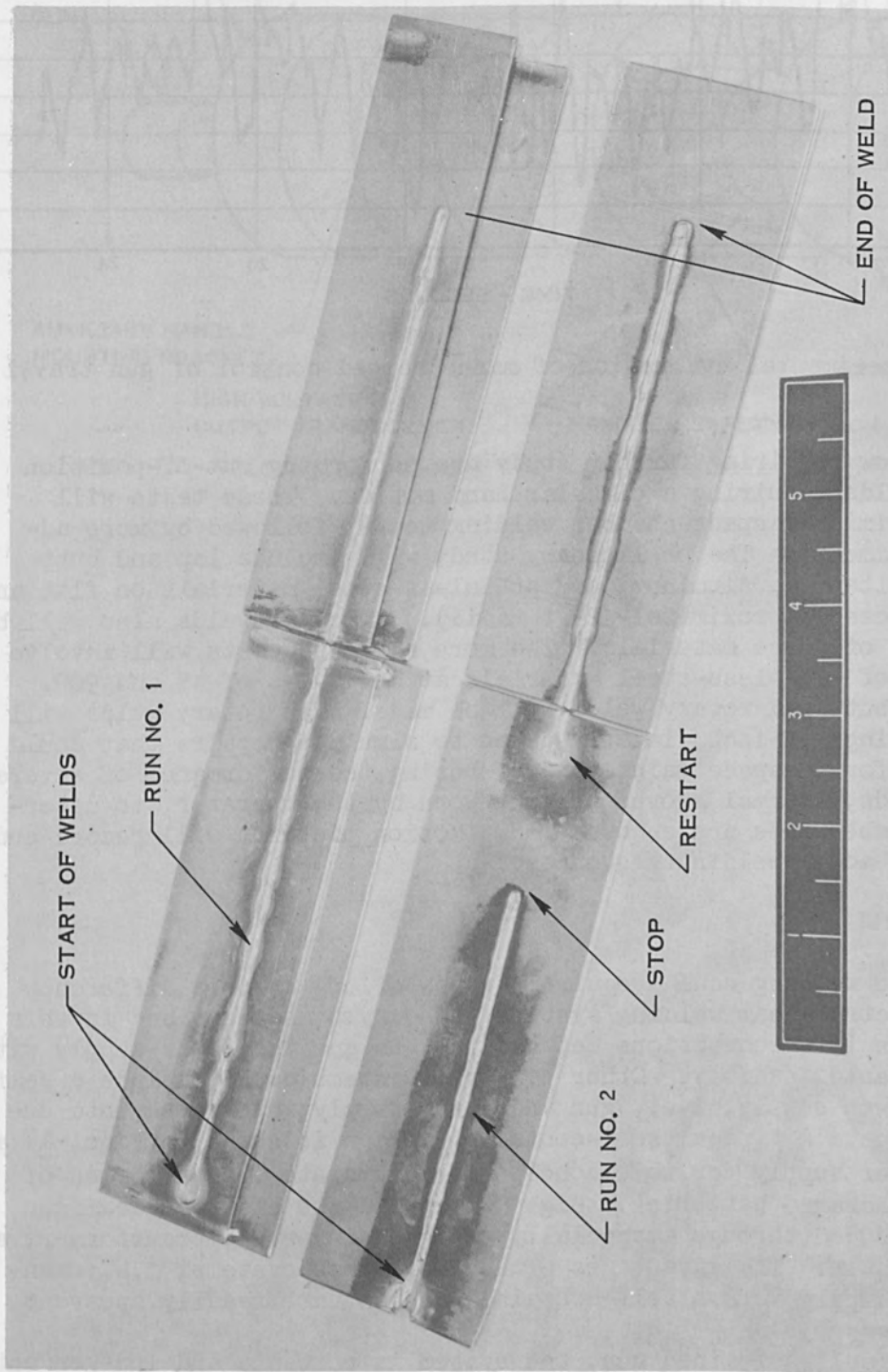


FIG. 12. --Electron-beam welds made by hand-held gun.

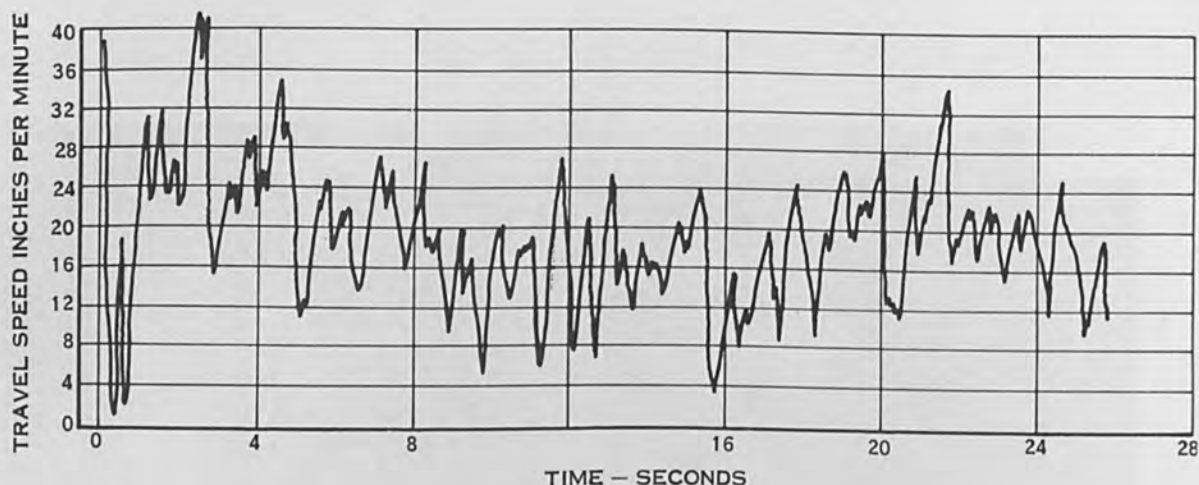


FIG. 13.—Experimental evaluation of manned speed control of gun travel.

Areas now requiring further study are performing out-of-position welds and welds requiring a circular hand motion. These tests will involve preliminary space-chamber welding tests, followed by more advanced experiments. The preliminary study will include lap and butt welding of titanium, aluminum, and stainless-steel materials on flat and curved surfaces (approximately 2-ft radii). Circular welds also will be made on some of these materials. The more advanced tests will involve the welding of stainless-steel materials at attitudes of 45 and 90°. Again, lap, butt and rotary welds will be made. The rotary welds will include welding a 3-inch diameter patch to simulate repairs that could be required for in-space maintenance. During the performance of several of these welds, thermal gloves will be worn by the operator, to determine if encumbrances are encountered. Motion pictures will record and document the above welding sequences.

FUTURE SYSTEMS

In-space welding could require the use of one or more different types of electron-beam welding systems. The systems described in this paper require interconnections between the gun and the power supply with a flexible cable assembly. Other possible systems could include a self-contained power supply, i.e., gun and power supply integrated into one common package. A typical self-contained design is shown in Figs. 14 and 15. The power supply for this concept would operate from a series of internally packaged batteries. High voltage to the electron beam gun would be produced through a specially designed inverter, transformer, and rectifier system. The advantages of each of these systems, i.e., gun-cable-power supply versus self-contained design, are readily apparent.

For the self-contained gun, the system is portable and independent of spaceship power schedules and demands. Therefore, this design lends itself to emergency repairs, particularly those which might be required during a lunar exploration mission. The disadvantage of a self-contained gun is its bulkiness because it must include the source of power. Another

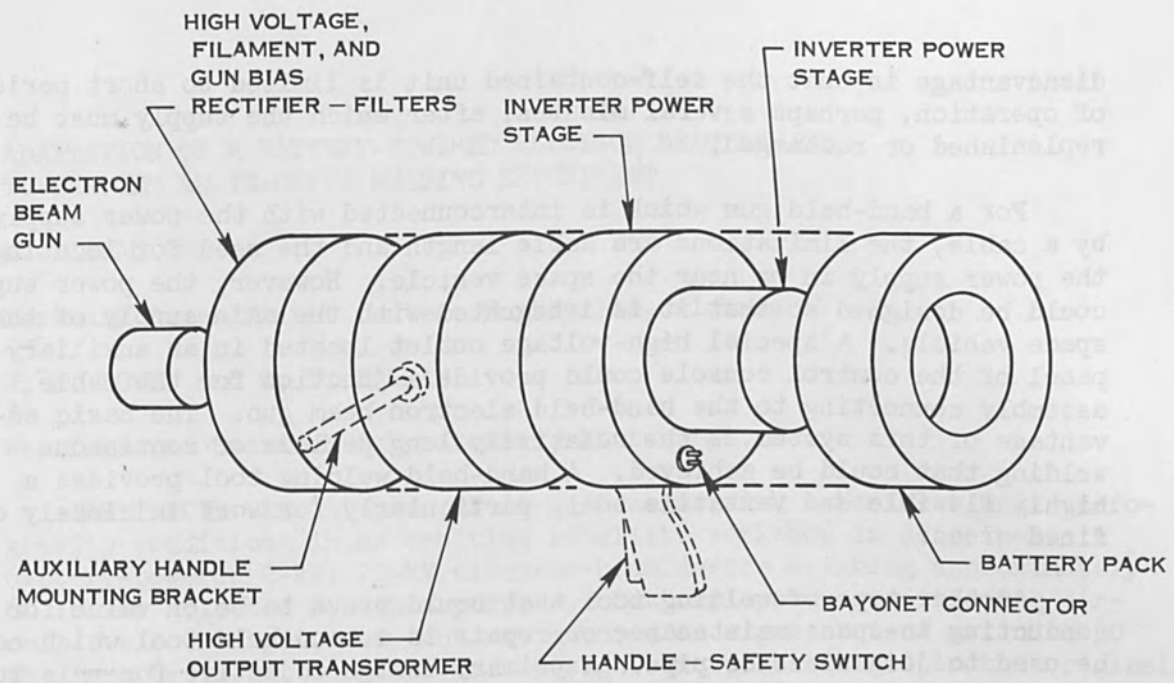


FIG. 14.—Packaging concept for a self-contained 0.5-kW welder.



FIG. 15.—Space-suited engineer and 0.5-kW welder.

disadvantage is that the self-contained unit is limited to short periods of operation, perhaps several minutes, after which the supply must be replenished or recharged.

For a hand-held gun which is interconnected with the power supply by a cable, the limitations are cable length and the need for locating the power supply in or near the space vehicle. However, the power supply could be designed so that it is integrated with the main supply of the space vehicle. A special high-voltage outlet located in an auxiliary panel of the control console could provide a junction for the cable assembly connecting to the hand-held electron beam gun. The basic advantage of this system is the relatively long periods of continuous welding that could be achieved. A hand-held welding tool provides a highly flexible and versatile tool, particularly for work in closely confined areas.

Another type of welding tool that could prove to be of value for conducting in-space maintenance or repair is a hand-held tool which could be used to join wires or pipe. A primary design objective for this tool is to fuse material without revolving the device or beam around the joint. An annular or uniformly circumferential electron beam could fulfill this requirement. Concept studies now are being directed toward developing such a tool.

In summary, current space joining efforts have resulted in the successful testing of a compact, lightweight hand-held welding tool that has joined a variety of aerospace materials in a reliable manner with minimum difficulty. However, much still remains to be accomplished relative to further design improvements in equipment and demonstration that this equipment can produce welds in space under conditions of zero gravity.

ACKNOWLEDGMENT

Work reported in this paper was conducted as part of a study for the U. S. Air Force under contract AF33(657)-9926 and also for the NASA-Houston Manned Spacecraft Center under contract NAS 9-4501. The writer wishes to express his appreciation for the technical counsel provided by Dr. Donovan of Hamilton Standard and by Mr. R. Bricker and Mr. D. Medlock of NASA-Houston.

ADAPTATION OF A BATTERY-POWERED ELECTRON BEAM DEVICE
TO PERFORM AN IN-ORBIT WELDING EXPERIMENT

H. LIENAU

Marshall Space Flight Center, Huntsville, Alabama

J. F. LOWRY and C. B. HASSAN

Westinghouse Research Laboratories, Pittsburgh, Pa.

ABSTRACT. An intended electron-beam welding experiment under zero-gravity conditions in an orbiting satellite workshop is described. A battery-powered 2-kW, 20-kV electron-beam device weighing approximately 60 lb was selected for this purpose. Battery, power-conditioning circuits, electron gun, and lens are mounted in a pressurized cylinder 30 in. long by 12 in. in diameter. Design concepts involved in the original laboratory unit along with beam analysis data are discussed, and the resulting advanced electron-beam device for producing an electron beam in space is described.

I. INTRODUCTION

Now that the lunar-oriented Apollo program is well underway, corollary follow-on programs are being planned to provide a greater capability in space with more time in orbit, such as the S-IVB Workshop (see Fig. 1) which is in progress, or others that are being considered. The programs will certainly involve extended-duration flights in space stations that must be considerably larger than anything considered to date. Their size alone may require that components be assembled in space, which in turn will dictate a need for metals-joining capabilities. In anticipation of this need, experiments to develop processes and supporting equipment are in progress or are being considered. They encompass metals-joining techniques such as welding, brazing, and using mechanical fastening devices.

The experiments will be performed in the Apollo Applications Program and will have two prime purposes:

- (1) To determine the extent to which metals-joining methods can be used for fabrication and repair in space.
- (2) To enable future planners to develop and test processes and equipment at one-gravity with an assurance of satisfactory performance at zero-gravity.

Of the various metals-joining processes, one likely candidate is electron-beam welding. Of all the joining methods considered, it has probably the highest potential for use in an extraterrestrial environment. The application of electron beams to welding is fairly well understood; the process can be readily adapted to simplified control; it is applicable to a broad range of materials including all of those used in space-vehicle structures; and because of the steep thermal gradients resulting from the

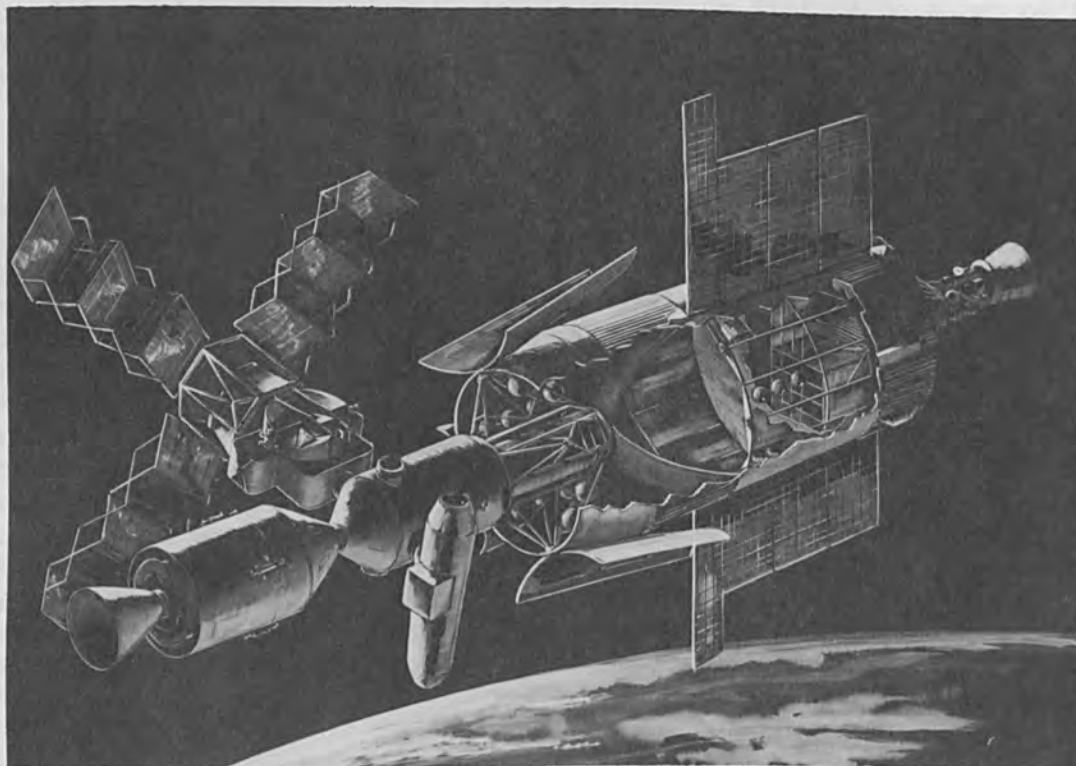


FIG. 1.—Artist's illustration of the Saturn S-IVB Workshop.

high energy densities used, it is probably the most efficient process from the standpoint of energy utilization. The principal problem is the bulk and mass of the power-handling equipment. Now this problem has been solved with the development of a battery-operated, lightweight, portable electron beam generator by Westinghouse Electric Corp., under contract to NASA's Marshall Space Flight Center. This device will be used in the first welding-in-space experiment and is discussed in more detail in Sec. IV.

The design, fabrication, and qualification program for the space-experiment package is in progress at the Marshall Space Flight Center's Manufacturing Engineering Laboratory, Research and Development Division, Welding Development Branch. The primary object of the experiment is to determine and to attempt to understand the effects of weightlessness (the environmental factor unique in space) on the electron-beam welding process. The potentially most severe effect of weightlessness could be "levitation" of the molten weld-metal, causing it to "ball-up" and literally float away during welding. Also, splatter may exist in the form of miniature molten metal projectiles, capable of damaging distant surfaces. Furthermore, the low ambient pressure creates problems such as molten weld-metal sublimation, control of joining temperatures, and waste-heat dissipation. However, these joining problems can be minimized by steep thermal gradients and small melted zones such as can be achieved by electron-beam welding. The vacuum environment facilitates the volatilization of surface oxide films and helps reduce the recontamination of cleaned surfaces. Both of the latter factors contribute to the quality

of the weldments produced. Such weldments should be free of joining defects and should be high strength-to-weight ratios for the welded metal relative to the parent metal.

The experiment is designed to obtain as much useful information as possible without undue complications. All performance parameters (such as welding speed and beam power) and environmental conditions (such as temperature, vacuum, and radiation) will be duplicated in pre-flight tests. These parameters will be fixed during the experiment, leaving weightlessness as the only unknown condition affecting the quality of the weld specimens produced in space.

Simplicity and reliability for consistent performance are being achieved by using specimens formed into rings that can be rotated at a fixed speed through the electron beam. The specimen rings, two or more, are constructed of arc segments of different materials suitable for space applications (alloy aluminum, stainless steel, titanium, etc.). By varying the thickness of each material, welding performance in space ranging from overpenetration to lack of penetration by the electron beam can be recorded and then checked for effects relative to performance in the laboratory at one-gravity.

The weld specimens and motion pictures taken during the experiment will be returned from orbit for laboratory evaluation at Marshall Space Flight Center to compare the characteristics of electron-beam welds made in space with those made in the laboratory under one-gravity conditions, and to formulate materials-joining criteria for the design of space structures.

The potential universal applicability of electron beam welding and its simplicity of operation and high efficiency make it one of the most suitable processes for further development; and with the design data from this experiment for the various materials that lend themselves to electron-beam welding in space, it is reasonable to expect that we may develop electron-beam welding as a manufacturing process under one-gravity conditions and have confidence of successful performance in space.

II. GENERAL DESCRIPTION OF THE EXPERIMENT PACKAGE AND THE WELDING EXPERIMENT

Figure 2 is an artist's illustration of the experiment, showing two cameras on brackets and showing the welding chamber vented to space through the wall of the MDA (Multiple Docking Adapter). The experiment package is mounted to the interior surface of the Multiple-Docking-Adapter portion of the Orbital Workshop. The package is completely self-contained. A single battery provides the energy for welding, sample rotation, lights, and two cameras.

The right-hand portion of the package consists of the electron-beam gun, high-voltage generator, and battery case. The central portion contains the necessary switches, controls, and meters for operation of the experiment. The left-hand portion consists of a vacuum chamber vented to space through the wall of the MDA. This provides the high vacuum of space without subjecting the astronauts to the hazards of EVA (Extra-Vehicular

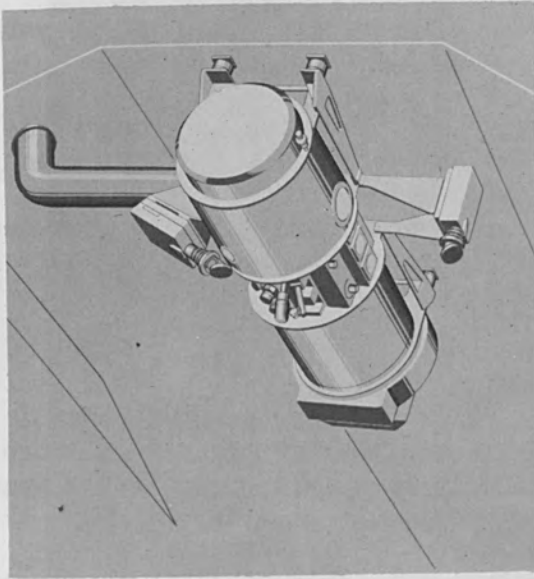


FIG. 2.—Artist's illustration of the experiment package mounted on the interior surface of the Multiple Docking Adaptor.

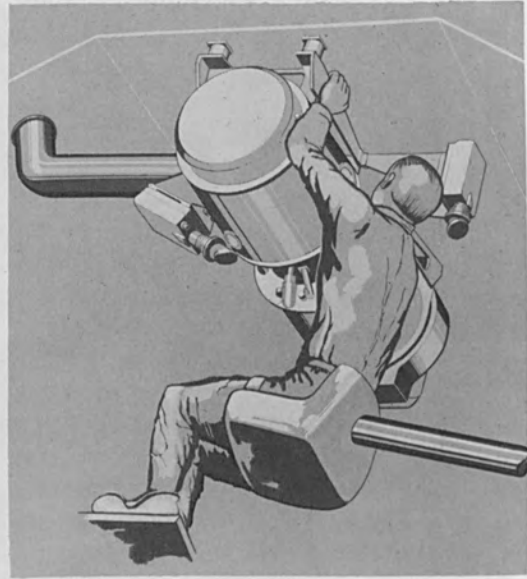


FIG. 3.—Artist's illustration of an astronaut performing a welding experiment.

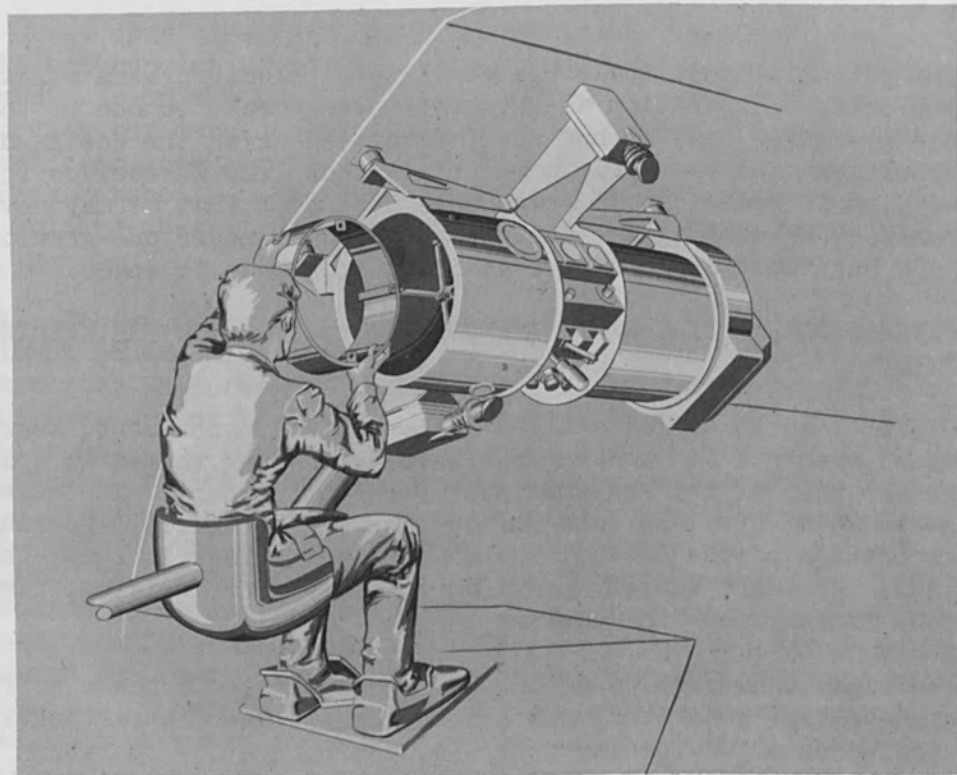


FIG. 4.—Artist's illustration of an astronaut removing a weld specimen from the welding chamber.

Activity) or the welding operation itself.

Figure 3 is an artist's illustration of an astronaut performing a welding experiment. Two cameras will operate during the welding experiment; one camera will view the weld puddle in color, and the other will record meter readings and control settings.

After closing a vacuum vent line valve and admitting oxygen to the vacuum chamber, the latter can be opened to remove the welding specimen for return from orbit. Figure 4 is an artist's illustration of an astronaut removing a weld specimen from the vacuum chamber. A new specimen can then be installed and the chamber re-evacuated.

III. DESCRIPTION OF A LABORATORY BATTERY-POWERED ELECTRON BEAM WELDING DEVICE

A. DESIGN CONCEPTS AND GENERAL DESCRIPTION. Westinghouse Electric Corp. has produced and delivered to Marshall Space Flight Center the battery-powered, self-contained electron beam welding device shown in Fig. 5. This device is intended for laboratory use—to aid in the design of the in-orbit welding experiment described previously. The device is designed to be mounted on a glass or metal cylinder as shown in Fig. 6; or the entire unit may be placed inside a larger vacuum chamber. In either case, welding tests can then be performed in the evacuated chamber.

The laboratory electron-beam welding device is a self-contained, battery-operated, 2-kW electron-beam welder capable of producing a 20-kV, 100 mA, tightly focused electron beam for about 5 min at a time. The complete unit consists of a sealed, pressurized, stainless-steel vessel containing the main battery pack, inverter power supply, filament battery pack, filament control circuit, and electron-beam gun (Fig. 5), a keeper valve and magnetic lens attached to the pressure vessel (Fig. 5), and an external rack-mounted control panel (not shown) connected by a cable to the pressure-vessel circuitry. The control panel is designed for conveniently operating the unit from external power sources (to conserve batteries). In order to use small high-voltage clearances and to minimize the size of the vessel, the latter is designed to be pressurized to 60 psia with sulfur hexafluoride (SF_6), a stable, chemically inert compound commonly used as an insulating medium in high voltage equipment.

Convective cooling by an ambient atmosphere cannot be used to remove heat from power-dissipating electrical components within the pressure vessel, primarily because the entire unit may be operating within a vacuum chamber, and also because some of the power-dissipating components are electrically and thermally insulated from the pressure vessel. Rather, the unit is designed such that the dissipated power is absorbed by the thermal capacity of the mechanical support structure. The temperature rise of this structure limits the operating time of the unit to 5 min (at 2-kW power output).

The unit shown in Fig. 5 weighs 61 lb and is 21 in. long by 12 in. in diameter; the small end of the focus coil protrudes 10 in.

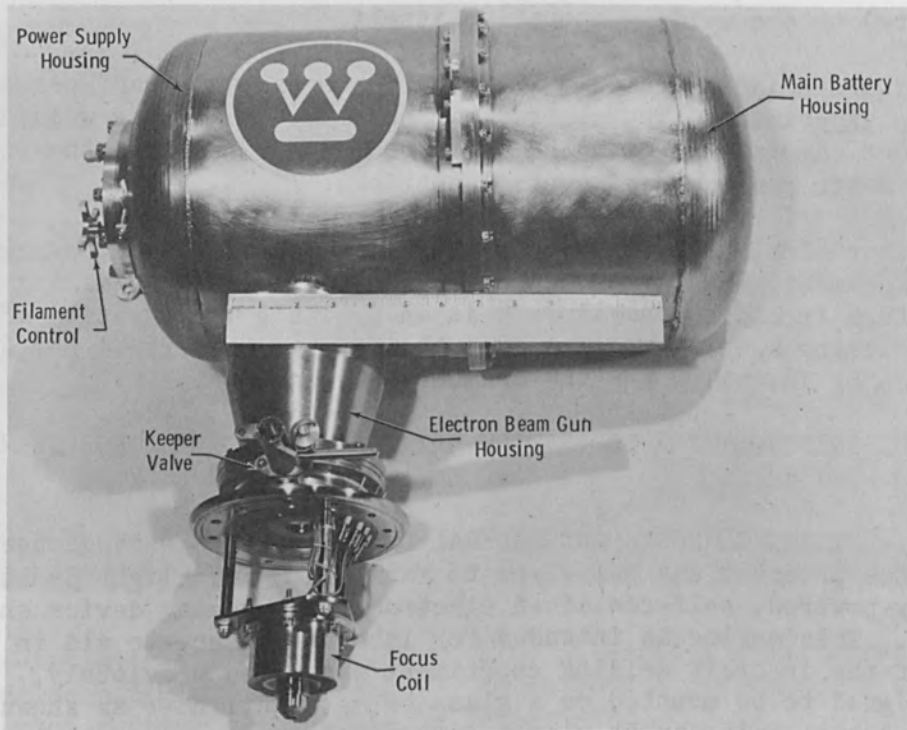


FIG. 5.—The laboratory battery-powered electron beam welding device.

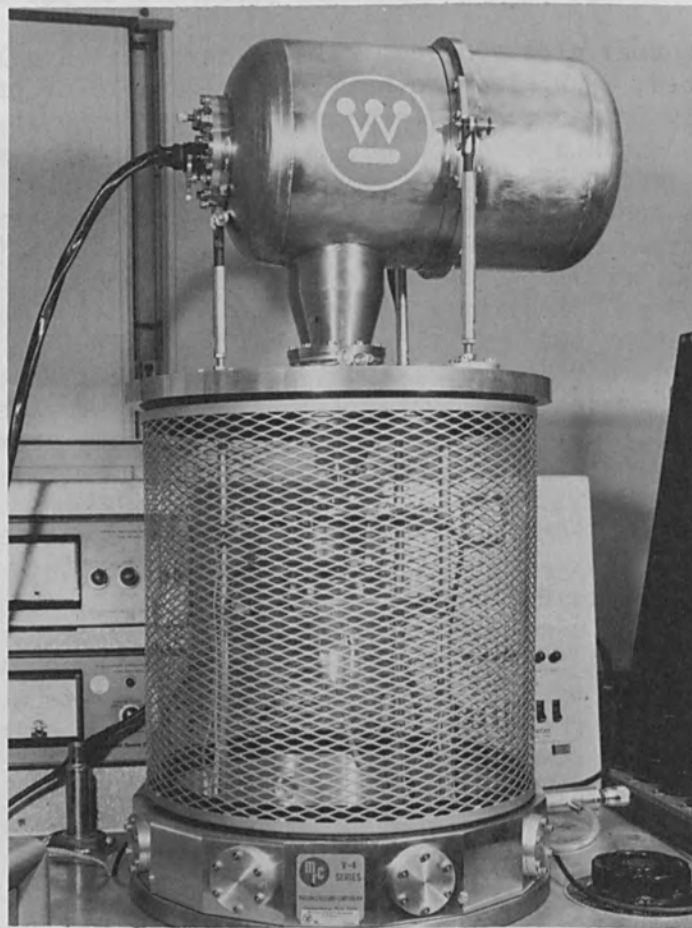


FIG. 6.—The laboratory welding device mounted on a vacuum system for performing welding tests.

B. BATTERY PACK. Figure 7 illustrates the arrangement of the individual cells comprising the main battery pack. This pack consists of 27 Yardney Electric Corp. "Silvercel" batteries, type HR-15VDC, connected in series by means of heavy, silver-plated bars. The open circuit voltage of the pack is about 50 V. Under the nominal 70-A load the battery voltage drops to 35 V. When fully charged the battery stores 525 W-hr of energy.

C. INVERTER POWER SUPPLY. The inverter power supply employs two states: a saturable-inductor power oscillator and a 2-kW inverter consisting primarily of two banks of six parallel germanium power transistors and a high-voltage transformer. Some of the components of the power oscillator and inverter are shown in Fig. 8.

The saturable-inductor power oscillator generates an alternating voltage square wave of approximately 3 kHz which is used to drive alternately the two banks of power transistors in the inverter stage. Each bank is connected between one side of the center-tapped primary of the high-voltage transformer and an aluminum base plate which acts as a mechanical support and heat sink for the power oscillator and inverter components. The transformer centertap is connected to the positive terminal of the main battery; the negative battery terminal is connected to the base plate. Alternately turning "on" and "off" both parallel banks of transistors such that one bank is "on" while the other is "off" is, in effect, applying an alternating voltage square wave across the entire centertapped winding of the transformer.

D. HIGH-VOLTAGE COMPONENTS. The high-voltage transformer steps up the nominal 35-V main battery voltage to the desired 20-kV output voltage. The 20-kV alternating square-wave voltage which appears on the secondary of the high-voltage transformer is applied to a fullwave bridge rectifier made up of four high-voltage, stacked diodes. A filter capacitor smooths the voltage waveform into a nearly pure direct voltage with less than 2% ripple at 100 mA of full load current. The load current is measured by a milliammeter (in the control unit) connected in the ground return lead of the power supply. Beam voltage is measured by a suitably calibrated meter (also in the control unit) operating from series multiplier resistors connected across the 20-kV output of the power supply.

E. FILAMENT BATTERY PACK AND CONTROL CIRCUIT. The filament battery and control circuit "floats" at the negative 20-kV output of the inverter power supply. The filament battery pack consists of three Yardney "Silvercel" cells, type HR-15VDC, connected in series to yield 5.5 V (open circuit) or 4.3 V under the filament load (nominal 15.5 A). The battery is contained in a teflon box for high-voltage insulation and held firmly in place by a strip of polyurethane foam filler. The filament control circuit consists of a transistor in series with the filament, a rheostat connected to vary the transistor emitter-base bias, a switch operating from a cam attached to the rheostat shaft, and a jack for charging the filament battery without opening the pressure vessel. The filament can also be operated from an external power source suitably insulated for high voltage. An insulated extension of the rheostat shaft engages a rotary seal on the pressure vessel endport, enabling an operator to turn the filament on and off and to adjust the filament current with

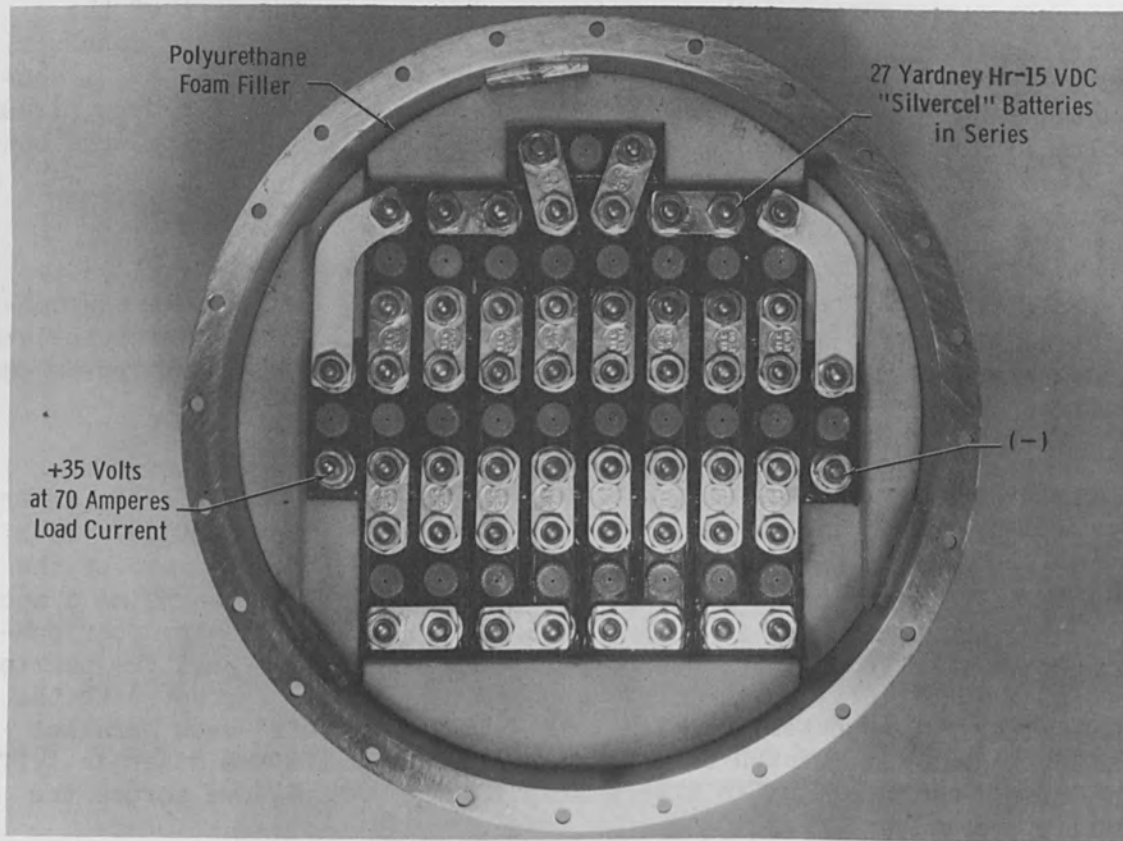


FIG. 7.—The main battery pack of the laboratory welding device.

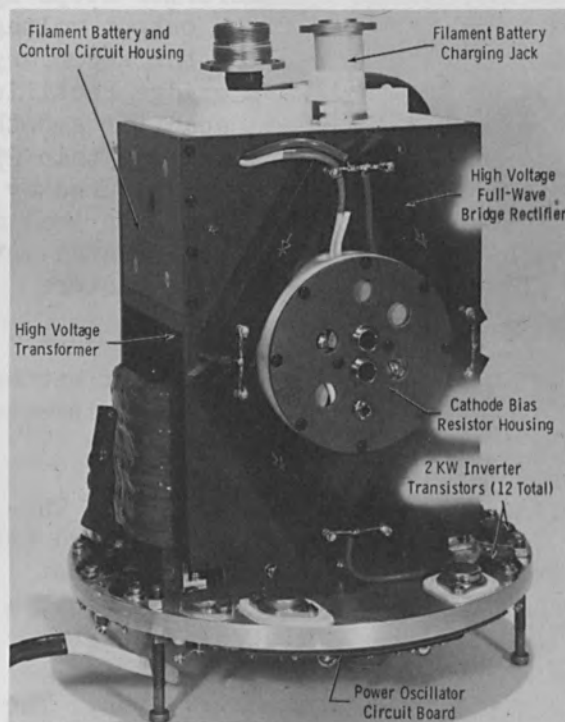


FIG. 8.—The power supply of the laboratory welding device illustrating some of the inverter and high voltage components.

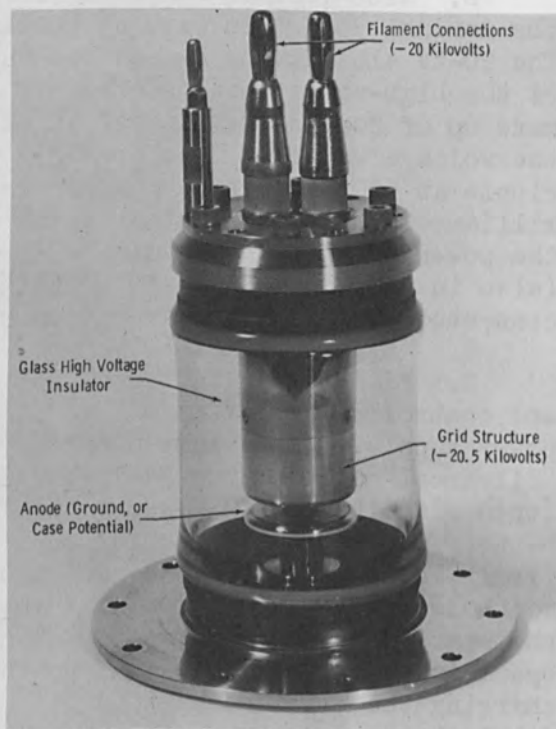


FIG. 9.—The electron-beam gun of both the laboratory and the in-orbit welders.

a control knob external to the pressure vessel.

F. ELECTRON BEAM GUN. The gun (Fig. 9) is a triode consisting of an anode, grid, and filament. The anode is at case (ground) potential; the filament and grid operate at a high negative voltage relative to the anode and are insulated from the anode by the hard glass envelope of the gun. This glass shell serves not only as an insulator but also as a barrier between the pressurized SF₆ in the power supply and the hard vacuum required in the gun. The filament is made from pure tungsten ribbon filament stock and is mounted in such a way as to be electrically insulated from the grid.

Grid bias is required for proper focus of the electron beam gun, but not for current control, which is accomplished by temperature control of the filament. Grid bias is developed by passing the beam current from the power supply through a cathode bias resistor to the filament. Typically, a 4000-ohm resistor may be used, developing 400 V of negative bias (with respect to the filament) at 100 mA of beam current.

No mechanical alignment is required to make the grid, filament, anode, and focus coil coaxial, except that the filament must be centered in the grid structure. Rather, precise machining is relied upon to properly align the various structures.

A double-acting keeper valve seals the high voltage chamber of the electron gun (Fig. 5). Thus a vacuum can be maintained in the gun while welding specimens are changed. When the chamber is again evacuated, the keeper valve must be opened. The pressure in the high voltage chamber must be 10⁻⁴ torr or less for satisfactory operation of the gun.

The final element of the gun is a magnetic lens (Fig. 5), which is used to refocus the electron beam at the work. The beam is refocused approximately 2 in. from the center of the lens or about 0.75 in. below the endshield. The lens weighs less than 1 lb. It requires about 1.3 A of current, which is derived from the main battery. A resistor and Zener diode pre-regulator and a miniature constant-current regulator provide constant current to the coil. A meter and a control potentiometer for the coil are provided on the control panel.

G. ELECTRON-BEAM-GUN CHARACTERISTICS. Figure 10 presents typical characteristic curves of the electrostatic portion of the electron beam gun. The influence of the cathode bias resistor can be seen in the departure of the quasi-space-charge-limited emission current curve (16.0-A filament current) from the 3/2 power law, and the departure of the quasi-temperature-limited-emission current curves (12.0 to 15.5 A) from horizontal straight lines. The former effect is due to the increasing grid bias developed by increasing beam current, and the latter is due to the decreasing effect of grid bias with increasing high voltage at constant temperature-limited emission current.

H. BEAM DIAMETER MEASUREMENTS. Attempts were made to measure the diameter of the beam at a location approximately 2 in. from the center of the magnetic lens. A water-cooled, electrically insulated aperture holder was placed beyond the lens; deflection coils guided the beam into

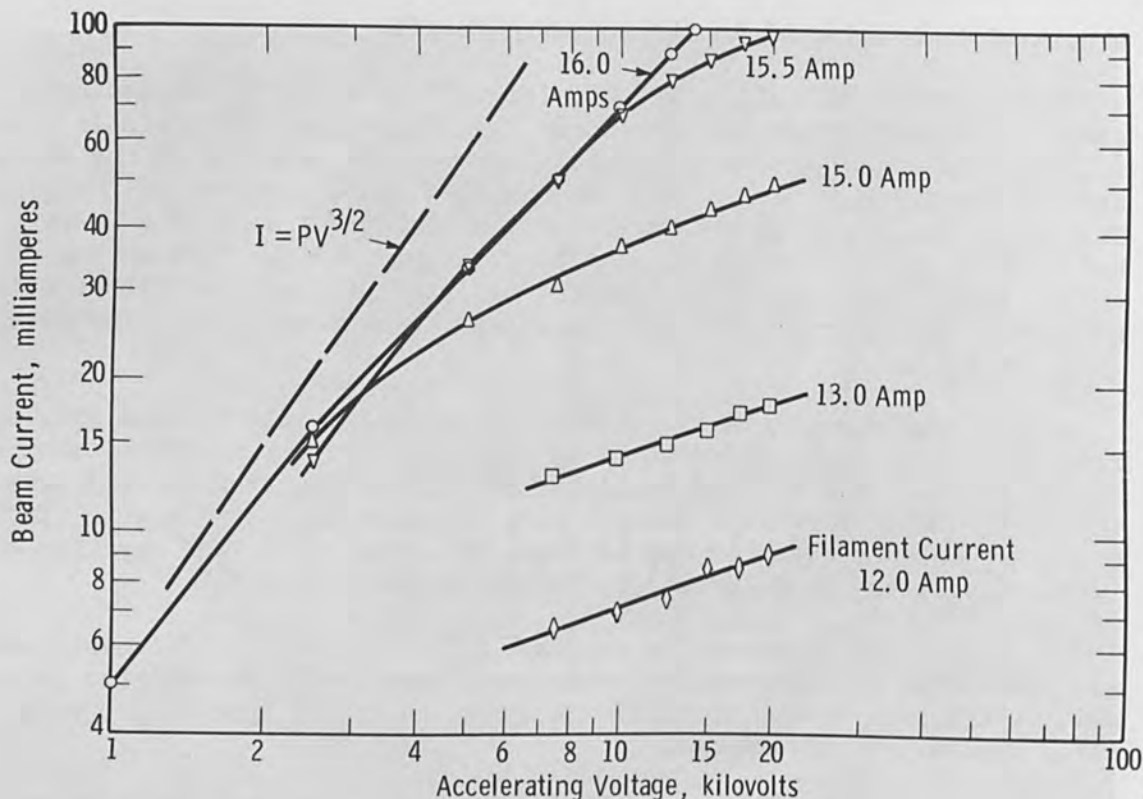


FIG. 10.—Self-contained electron beam welding device--typical electron-beam gun characteristics with 4000-ohm cathode bias resistor.

the aperture, making precise coaxial alignment of the aperture holder with the gun unnecessary. That portion of the beam which passed through the aperture was collected in a water-cooled Faraday cup located a short distance beyond the aperture holder. The aperture current and collector current were both monitored. With the proper values of grid bias and lens current, it was found that 90% or more of a 100-mA, 20-kV beam could be passed through an aperture 0.031 in. in diameter. If it is assumed that the cross-sectional beam current distribution is a Gaussian function, then 50 mA of the 2-kW beam would occupy a disk only 0.015 in. in diameter. For comparison, the calculated diameter of the magnetic lens spherical aberration disk is 0.006 in. Although very little is known about the spherical aberration of the electrostatic lens, it is probably at least as great or greater than that of the magnetic lens. Thus, the measured beam diameter seems to be approaching a value limited by lens aberrations. The weld specimens produced with the beam also attest to the small diameter of the beam.

I. WELD SPECIMENS PRODUCED USING THE BATTERY-POWERED ELECTRON BEAM WELDER. Figure 11 shows a weld (bead-on-plate) produced with the laboratory welder operating completely on battery power. The weld was made in type 304 stainless steel, thickness 0.125 in. at a speed of 36.8 in./min and a beam of 65 mA and 21.5 kV (1.4 kW). The beam was not at optimum focus to produce this weld. The top-bead width is approximately 0.090 in. and the underbead width approximately 0.025 in. The radiograph of this

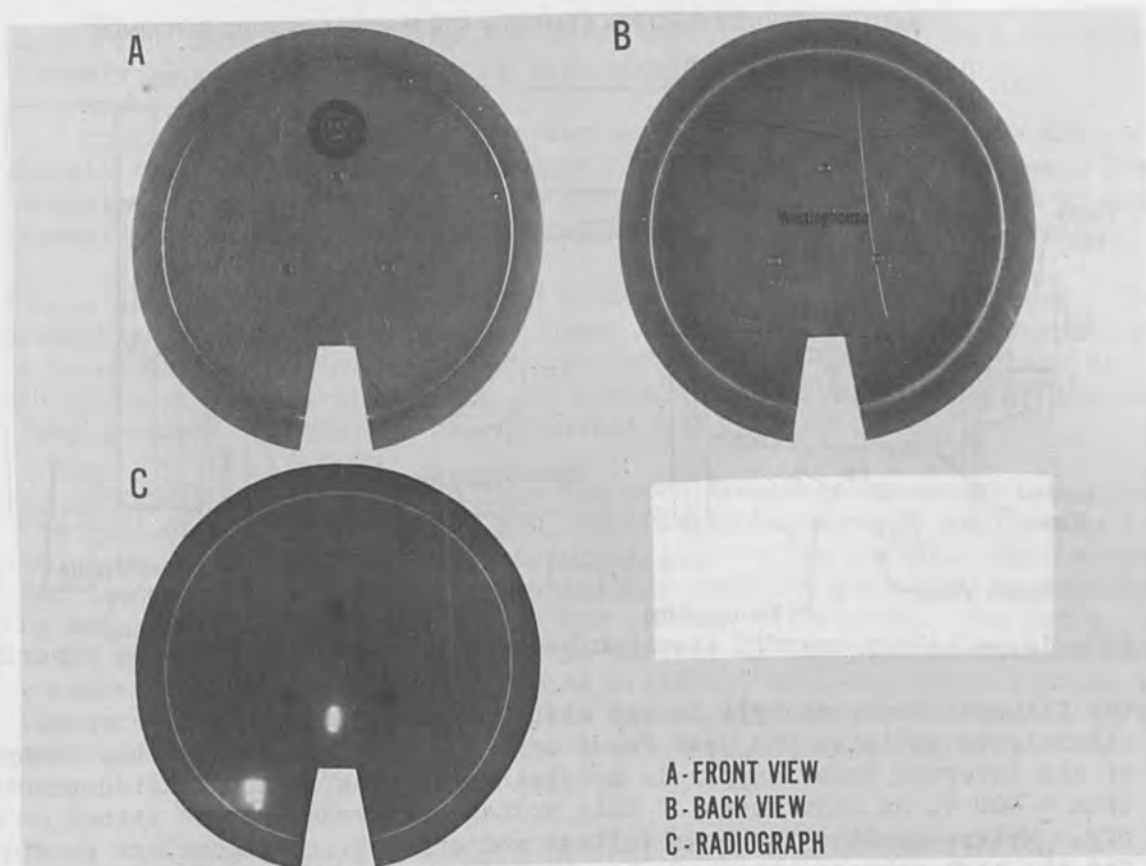


FIG. 11.—Bead-on-plate weld produced with the battery-powered electron beam welder.

weld reveals no discernible porosity. Another weld was made using external power supplies to substitute for the two battery packs. The bead-on-plate weld was made in type 304 stainless steel of thickness 0.188 in., at a speed of 40.4 in./min and a beam of 80 mA and 18 kV (1.44 kW). The magnetic-lens current was varied during the run to find an optimum value; full penetration was achieved over a certain range of lens currents.

IV. ADAPTATION OF THE LABORATORY UNIT TO PRODUCE A COMPLETELY SELF-CONTAINED ELECTRON BEAM GUN FOR THE IN-ORBIT WELDING EXPERIMENT

Figure 12 is a drawing of the completely self-contained electron beam welder now being constructed for use in the in-orbit welding experiment described in Sec. II. The most obvious difference between the two units is the position of the electron beam gun relative to the power supply and battery. The right-angle laboratory unit has been adapted to the in-line configuration of Fig. 12 to produce a more manageable package. The in-line configuration is also mechanically sturdier; during launch the unit will be positioned such that its long axis is parallel to the direction of maximum acceleration.

The second-most obvious difference between the two units is the integral control panel on the in-orbit welder. This panel contains all the controls and meters necessary for the performance of the welding experiments. The astronaut has direct control of the beam current (by varying

BATTERY-OPERATED ELECTRON BEAM GUN FOR IN-ORBIT WELDING EXPERIMENT

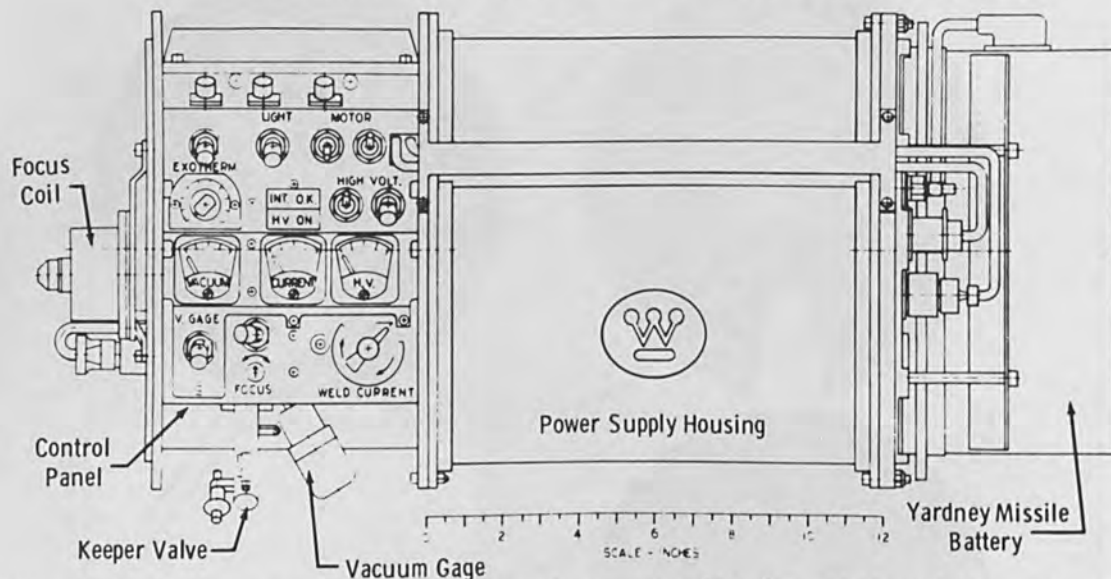


FIG. 12.—Battery-powered electron beam gun for in-orbit welding experiment.

the filament temperature); he can also vary the magnetic lens current slightly to optimize the beam focus on the work. The high-voltage output of the inverter power supply is maintained at 20 kV and regulated to better than ± 400 V; no adjustment of this voltage is needed—it is either on or off. Meters monitor the beam voltage and current. Switches are provided for the high voltage power supply, the magnetic lens, the specimen drive motor, the lights (necessary for photography), and an exothermic brazing experiment located in the welding chamber.

A number of the welder parts have been adapted to the in-orbit unit with very little or no change. Certain items which do not exist in the laboratory unit but are believed to be necessary for the successful performance of the orbital welding experiments have been added.

The electron-beam gun, keeper valve, and focus coil were adapted to the in-orbit unit with only minor changes. Because of the double-acting keeper valve it is possible to evacuate the gun to a high vacuum, close the valve, and maintain a vacuum in the gun during prelaunch storage, launch, and in-orbit storage. When the unit is mounted in the orbital workshop, the valve can again be opened. The valve is interlocked—it must be open for the high voltage to operate.

The filament control circuit has been modified slightly to obtain increased reliability. The new circuit uses only silicon transistors. An additional battery has been added to provide more filament voltage; this battery is needed because of the increased voltage drop across the series silicon transistor compared to the germanium transistor used in the laboratory device. The filament battery pack has been placed in a sealed compartment whose absolute pressure is 760 torr of air; this battery pack can be replaced without depressurizing the power supply.

For increased reliability, the battery pack of the laboratory unit has been replaced with a Gemini-rated Yardney Electric Corp. "missile

battery." This battery provides up to 100 A at a nominal 28 V for approximately 10 min; its capacity is thus about 470 W-hr.

The 2-kW inverter stage is essentially unchanged except for the use of all silicon rather than germanium transistors; in addition, each power transistor is separately fused so that the failure (by shorting) of any transistor will not cause additional failures or trip off the device.

A more reliable, encapsulated filter capacitor has been chosen. The same high-voltage rectifiers are used. The high-voltage transformer has a somewhat higher turns ratio because of the lower battery voltage in the case of the in-orbit unit. In addition, an extra winding in the transformer secondary provides approximately 500 V for grid bias.

The axis of the magnetic lens has been displaced about 3/4 in. from the axis of the electron-beam gun and two electromagnetic deflection coils added to steer the beam from the former axis to the latter. Such a system is needed to minimize the possibility that the gun might be damaged by metal fragments created during the welding experiment. The two deflection coils and lens are all wired in series; an independent battery and a constant-current regulator provide a stable, well-regulated current to the three coils. A shunt across the focus coil enables the astronaut to make up to a $\pm 10\%$ variation in the lens current with no effect on the current through the deflection coils.

A vacuum gage is provided on the in-orbit unit for monitoring the pressure in the chamber housing the double-acting keeper valve. This valve seals against both the high voltage chamber of the gun and the vacuum chamber where the welding is performed. The gun is to be evacuated on earth and the keeper valve closed to seal the gun under high vacuum; by keeping the gun under vacuum the probability of arc-overs occurring will be minimized. Before operating the welder, the astronaut will energize the vacuum gage. If the pressure is satisfactory (approximately 10^{-3} torr or less), he will open the keeper valve (assuming that the welding chamber has been evacuated previously) and operate the welder. For satisfactory operation of the gun, the pressure must be 10^{-4} torr or less after opening of the keeper valve. If this initial check reveals that the pressure is unsatisfactory, he will still open the keeper valve, but in this case he must permit the gun chamber to pump until the pressure reaches 10^{-4} torr.

The vacuum gage is interlocked with the high-voltage circuitry in such a manner that the high voltage cannot be activated unless the pressure is satisfactory. An extraordinary increase in pressure during welding will trip off the high voltage.

Other functions which are interlocked with the high voltage include the following: the position of the keeper valve, which must be open to close the interlock; and the focus and deflection-coil power supply, which must be energized to close the interlock.

Figure 13 is a block diagram of the major electrical circuits comprising the battery-operated electron beam welder. The square blocks indicate main power-handling components or circuits; the round blocks

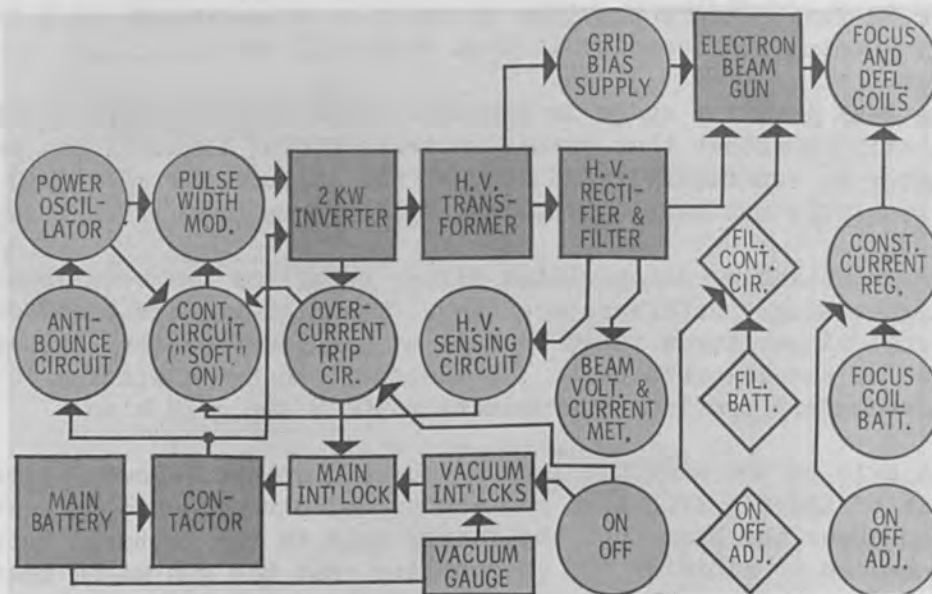


FIG. 13.—Battery-operated electron beam gun: electrical system block diagram.

indicate control or metering circuits; the rectangular blocks indicate interlock circuits; and the diamond-shaped blocks indicate circuitry associated with the gun filament.

Regulation of the beam voltage is required for at least two reasons:

- (1) To maintain beam focus on the work with changing battery input voltage and changing beam current.
- (2) To simplify the astronaut's control task by enabling him to concentrate his attention on the welding current, quickly setting the current to the desired value without having to adjust the high voltage or the beam focus.

Regulation is achieved by varying the pulse width of a square wave used to drive the 2-kW transistor inverter. This driving signal is generated by a square-wave power oscillator. The frequency of the oscillator is determined by a low-power relaxation oscillator; thus the frequency is relatively free from change owing to battery voltage and temperature variations.

Operation of the power supply is initiated by actuating the "on" push-button, thus closing the contactor (assuming that the vacuum and main interlock switches are closed, as is normally true). The antibounce circuit provides a short time delay before applying the battery voltage to the power oscillator circuitry. This time delay is such that the contact bounce associated with the contactor is completed before the termination of the time delay. The power oscillator provides power and synchronization signals for the control circuitry. The control circuitry slowly increases the pulse width of the square wave being supplied from the power oscillator to the 2-kW inverter through the pulse-width modulator. Thus the inverter initially draws no battery current (when the contactor closes), then slowly draws increasing current until approximately 90 A (full-load) current is reached. The actual battery current is determined by the

magnitude of the electron beam current. The high-voltage sensing circuit samples the nominal 20-kV output and compares it with a reference voltage. The difference between these two voltages is fed back into the pulsewidth-modulator control circuit in such a way that the 20-kV output is maintained over wide ranges of load impedance and battery voltage.

Since every electron-beam gun is characterized by erratic and unpredictable momentary arc-overs, self-protection of the power supply circuitry is of major concern. When an overcurrent condition is detected, the pulse width is immediately decreased to zero. Also the main interlock is opened which, in turn, opens the contactor and removes battery power. The phase-back of the pulse width takes only a few microseconds, whereas the opening of the main interlock and contactor requires many milliseconds; thus the contactor does not interrupt the high current of the 2-kW inverter, but only the relatively low current required by the power oscillator. To restart the power supply, the astronaut simply actuates the "on" pushbutton. To turn off the power supply, the "off" pushbutton is actuated; this activates the overcurrent trip, which again opens the contactor under a light-current condition.

ACKNOWLEDGMENTS

The authors wish to acknowledge the contributions of the following to this program: L. R. Carver, F. A. Elder, J. Lempert, J. Manion, J. R. McDowell, R. P. Putkovich, F. A. Reed, B. W. Schumacher, F. D. Seaman, and A. P. Terek.

DIFFERENTIALLY PUMPED ELECTRON BEAM SYSTEM FOR MICRO-ZONE PROCESSING OF THIN LAYERS

N. M. DAVIS

Naval Ordnance Laboratory, Corona, California

ABSTRACT. An electron beam micro-zone scanning system produces a narrow heated zone in elemental or compound films recrystallizing up to 5 x 10-mm areas. The system has an electron-optics column operating in high vacuum and a working chamber in which the sample is processed at pressures up to 200 microns. An orifice allows the electron beam to enter the working chamber. Examples of the use of this system for recrystallizing InSb films are given.

I. INTRODUCTION

A micro-zone electron-bombardment technique for forming an inter-metallic compound from an evaporated film of its constituent metals, and controlling its crystalline structure and morphology, has been reported previously.¹ An electron beam melts a narrow zone which is swept across the film causing the compound to grow from the melt as long dendrites. Two-phase films of InSb-In can be grown by such a recrystallization process. However, InSb films without In inclusions could not be produced because Sb, the more volatile constituent, was lost during electron beam heating. This paper describes a two-stage electron-beam system (Fig. 1) which has been used successfully for producing InSb, without excess In, as well as elemental films which consist of a well-ordered aggregate of large single crystals. The system has a primary chamber operating at 10^{-5} torr containing the electron-gun and beam-focusing elements. A small orifice allows the electron beam to pass from the high-vacuum region into the working chamber in which the sample is processed at pressures as high as 200 microns.

II. ELECTRON OPTICAL SYSTEM

Three electron lenses are used to focus the electron beam onto the sample (Fig. 2). The first lens, located below the anode, accepts a large fraction of the current emitted by the filament of the conventional triode electron gun and produces a magnified image of the electron beam crossover some distance from the lens. The second demagnifies this image to a size such that the beam will pass through a small aperture into the working chamber. The diverging electron beam emerging from the aperture is focused onto the sample by a third lens.

Electrostatic electron lenses were chosen because of previous successful experience with electrostatic optics and their insensitivity to accelerating voltage fluctuations. They are of the three-aperture type (Fig. 3), outer apertures at ground potential and central aperture at some point between ground and cathode potential. The construction of the lens is

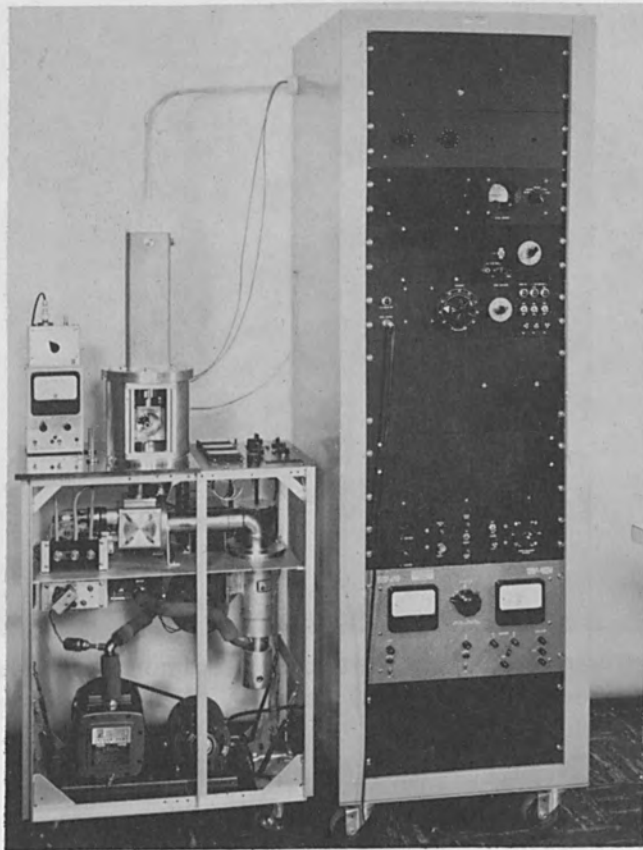


FIG. 1.—Electron beam system with electron beam column on base plate of commercial vacuum system and rack-mounted power supplies.

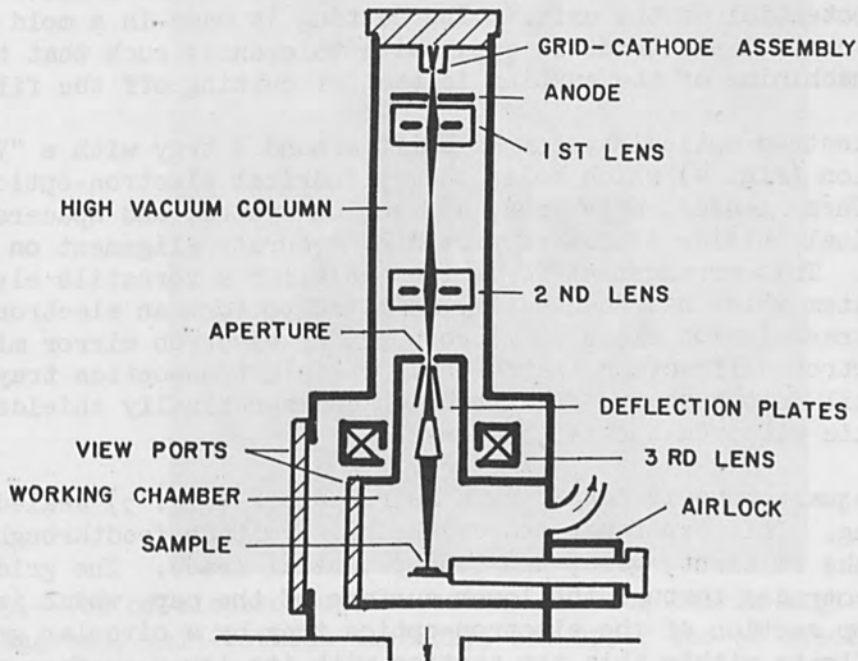


FIG. 2.—Schematic diagram of electron-beam system.

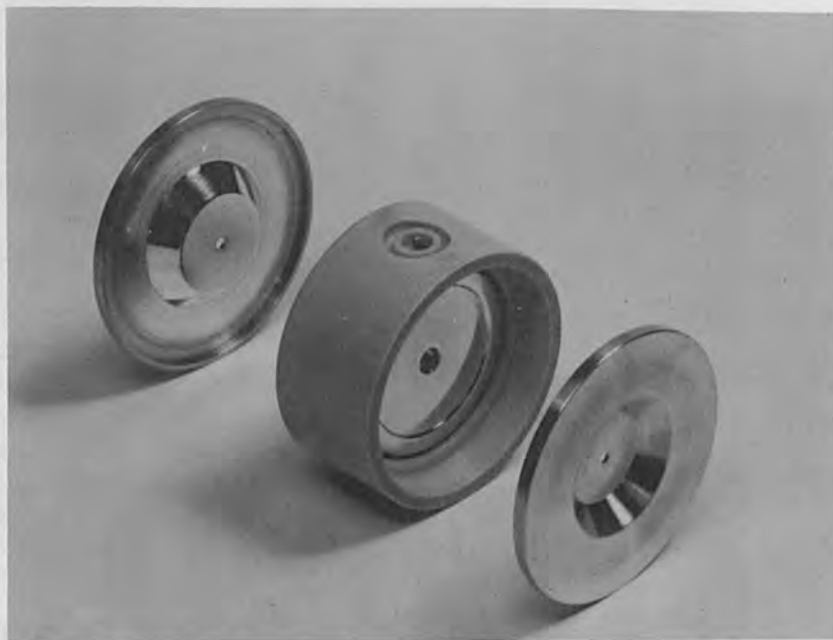


FIG. 3.—Exploded view of electrostatic electron lens showing epoxy-embedded central electrode and end caps.

similar to that used in the electron microscope manufactured by Mikros, Inc. The outer electrodes are caps which fit over the ends of the cylindrical insulator in which the central electrode is embedded. The central electrode is cast in epoxy resin to provide high voltage insulation and rigid mechanical alignment with the two outer electrodes. Care has been taken in the design of the junction between the central electrode and its insulator to minimize the local electric field and thus to raise the breakdown potential of the unit.² The casting is made in a mold which embeds the central electrode in epoxy with tolerances such that the only necessary machining of the casting is that of cutting off the fill plug.

The electron optical system is built around a tray with a "V" shaped cross section (Fig. 4) which holds the cylindrical electron-optical components. These lenses, apertures, deflection system, and spacers all have identical outside diameters providing accurate alignment on the optical axis. This arrangement forms the basis for a versatile electron optical system which has been easily modified to form an electron beam system, a transmission electron microscope, an electron mirror microscope, and an electron diffraction instrument. The electron-optics tray slides on a dovetail into a square steel tube which magnetically shields the electrostatic electron optical elements.

This square tube is capped by a Delrin block (Fig. 5) sealed to it by an O-ring. This cap functions as the high-voltage feedthrough insulator for the filament, grid, and lens potential leads. The grid-cathode assembly protrudes through the lower surface of the cap, which is aligned with the top section of the electron-optics tray by a circular groove. The anode floats within this top section with its lower surface resting on the top of the condenser lens. Two pairs of opposing screws and springs allow external positioning of the anode by vacuum-sealed keys inserted

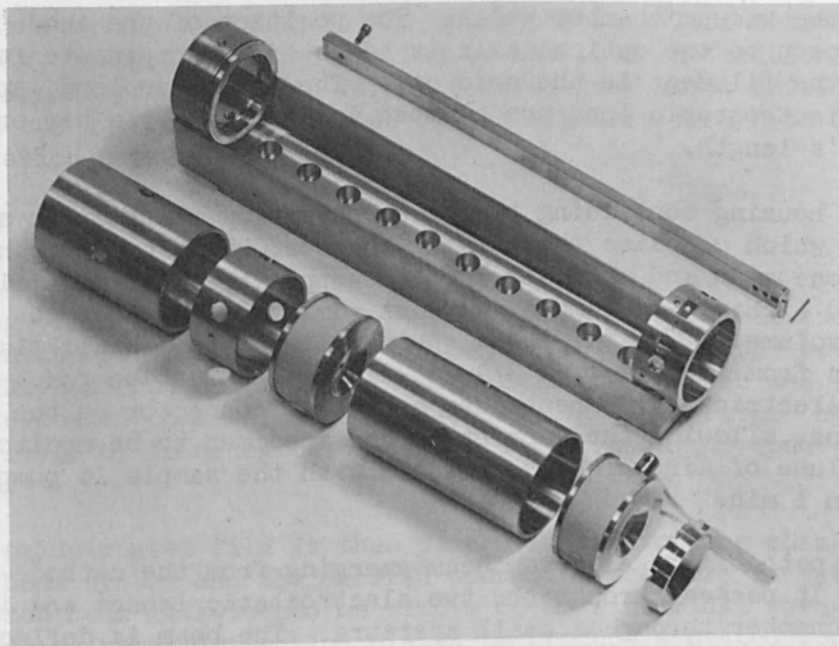


FIG. 4.—Electron optics tray with spacers, electrostatic lenses, and anode in foreground.

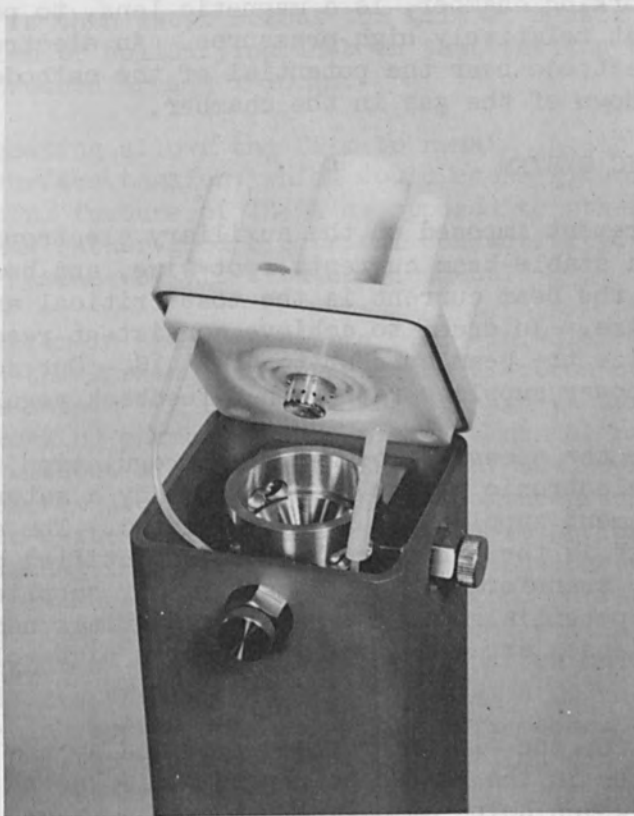


FIG. 5.—Top of electron optics column showing Delrin high-voltage insulating cap, grid-cathode assembly, and upper end of electron optics tray.

through the vacuum chamber walls. The position of the anode aperture with respect to the optical axis is adjusted to compensate for misalignment of the filament in the grid cap. The condenser lens, spacers, and second electrostatic lens are clamped in the tray by a bar extending along the tray's length.

The housing containing the electron optics rests on an aluminum cylinder which contains the working chamber. This cylinder has a view port on one side and an airlock on the opposite side. The airlock permits the rapid exchange of samples without admitting air into the entire working chamber volume.³ The sample is spring clipped to a small platform which protrudes from the end of a 3/4-in.-diameter insertion rod. This platform is electrically connected to a coaxial connector on the exterior end of the rod, allowing the current to the specimen to be monitored. The small volume of air which is admitted with the sample is pumped out in less than 1 min.

The path of the electron beam emerging from the cathode is shown in Fig. 2. It passes through the two electrostatic lenses and into the working chamber through a small aperture. The beam is deflected by a set of deflection plates of conventional cathode ray tube design.

The third electron lens, which acts upon the electron beam after entering the working chamber, is a magnetic lens, to permit the working chamber to be at relatively high pressures. An electrostatic lens with its central electrode near the potential of the cathode could cause dielectric breakdown of the gas in the chamber.

III. ELECTRONIC SYSTEM

The requirement imposed on the auxiliary electronic system is that it must yield a stable beam current, spot size, and beam position. Of these factors, the beam current is the most critical and the most difficult to stabilize. In order to achieve consistent results, it is necessary to stabilize the beam current to about 1%. Our solution has been to use stable power supplies rather than feedback regulation.

To achieve the necessary beam-current regulation, the line voltage to the entire electronic system is regulated by a saturable-core reactor and the ac filament supply is current regulated. The accelerating potential of 20 kV is the unfiltered fullwave rectified output of a high-voltage step-up transformer. A voltage divider supplies the cathode, grid, and lens potentials. The variable potentials necessary for the electrostatic lenses are provided by Victoreen high-voltage potentiometers rated at 10 kV.

Grid bias for the electron gun is provided by the IR drop across a variable resistor in the cathode circuit. This "self" bias feature provides feedback which helps stabilize the beam current.

The electrostatic deflection system consists of two pairs of plates, the upper pair providing the beam deflection to generate the zone, and the lower pair providing zone motion. To position the beam, one plate of each pair is biased by a dc potential. The zone is generated by supplying

a repetitive waveform signal to the upper plates. Zone motion is caused by a slowly rising dc voltage applied to the lower deflection plates. This voltage is produced by a variable-speed gear motor driving a ten-turn potentiometer such that the voltage rises linearly from 0 to 600 V with a sweep duration between 10 and 500 sec.

IV. APPLICATION OF SYSTEM

As an example of the use of this electron beam system, consider the processing of an InSb film. The film is produced by simultaneous evaporation of In and Sb from a single boat onto No. 1 microscope cover slip glass. The 2 micron thick film containing InSb, free Sb and free In is then oxide-coated to a thickness of 250 Å with In_2O_3 either by oxidation of a top layer of In or by the reactive evaporation⁷ or sputtering of In in oxygen.

The oxide-coated film is then placed in the working chamber of the electron beam system and the desired operating pressure is established. The electron beam is switched on with a 60-Hz sinusoidal sweep voltage applied to the upper deflection plates to produce a heated zone near one end of the film. This zone is about 100 microns wide and 3 mm long. The temperature of the zone is allowed to rise until the zone is molten. This typically requires a beam current of 35 μA at 20 kV acceleration potential. The molten zone is then swept across the film at a rate of 100 microns/sec producing a region of solidifying InSb on the trailing edge of the zone and yielding a treated area 3×10 mm.

The oxide coating allows the film to remain intact while molten by decreasing its surface tension, which would cause globules to form. A particularly useful feature of In_2O_3 as opposed to other oxides in this application is its rather good electrical conductivity, which eliminates charging of the surface by electron bombardment.

When the system is operated with a 0.013-in.-diameter by $\frac{1}{4}$ -in.-long aperture between the working chamber and the electron optics column, it is possible to maintain 6×10^{-5} torr in the high-vacuum column and 500 microns in the working chamber. This pressure can be maintained in the working chamber without excessive scattering of the 20-kV electron beam. However, at pressures above 200 microns, arcing occurs in the electrostatic deflection system. The two-chamber system performs its intended function of producing InSb films with no In inclusions when the working chamber is at a pressure of 100 microns of argon. However, it was found that decreased Sb loss could more easily be achieved in high vacuum by a thick oxide overcoat on the film and using a narrow heated zone. The narrow zone minimizes the length of time a region of the film is at a temperature at which appreciable Sb evaporation occurs. Therefore the working chamber view port can be removed and films can be processed at a pressure of 2×10^{-2} torr.

Films of the In-Sb system have been produced by this technique over a range of composition from pure In to the InSb-Sb eutectic (69.5% Sb). In all cases, the resulting structure is a well-ordered aggregate of crystals with the ordering along the direction of zone motion.

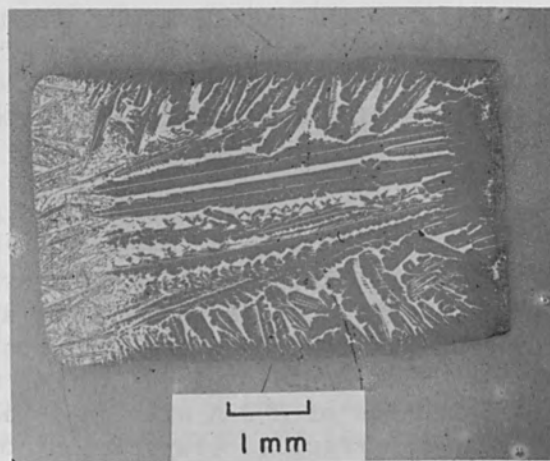


FIG. 6.—Electron beam recrystallized InSb film with excess In inclusions between long InSb crystals.

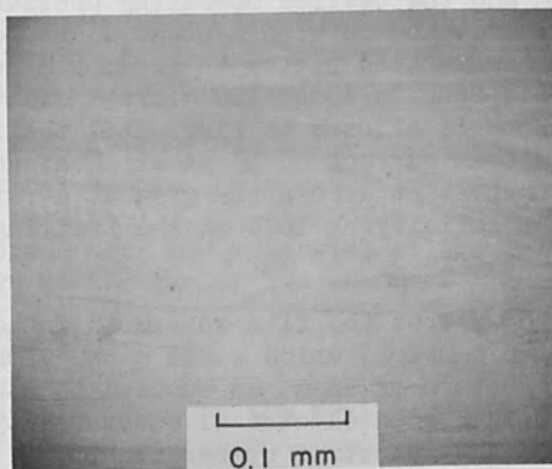


FIG. 7.—Electron beam recrystallized InSb-Sb eutectic film with fine lamellar structure.

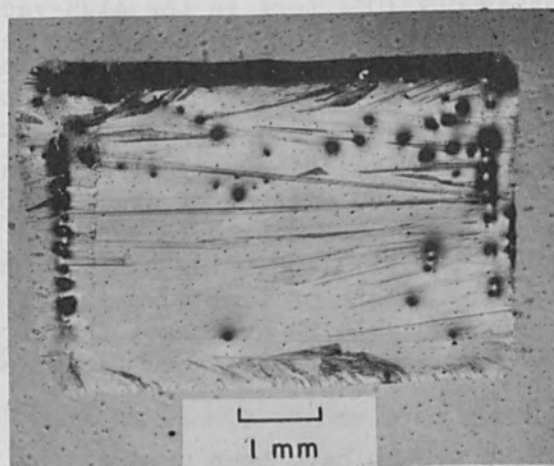


FIG. 8.—Electron beam recrystallized InSb film with no In or Sb excess. Long crystals are delineated by etch. Zone motion from right to left.

A film of InSb with In excess is shown in Fig. 6. The excess In is in the form of narrow inclusions between the long InSb crystals. Such films exhibit high magnetoresistance increasing their resistance by over 10 times when placed in a magnetic field of 10 kilogauss.

Films of InSb-Sb eutectic have a very fine lamellar structure, which is illustrated in Fig. 7.

Of greater importance are InSb films without an In or Sb excess. These are produced in the previously described manner with the additional conditions that the evaporated film contains 52% Sb by weight to compensate for its loss during heating and that the oxide overcoating thickness is increased to 1000 Å.

The resulting recrystallized film, as in Fig. 8, has long parallel crystals aligned in the direction of zone motion. These crystals may extend the full length of the recrystallized area and be up to 100 microns in width. Twinning is quite common with the twin plane running the length of the crystal. The direction of crystal growth lies in the twin plane and the $\langle 211 \rangle$, $\langle 321 \rangle$, and $\langle 110 \rangle$ growth directions are primarily found. The entire recrystallized area of these films has an electron mobility as high as 5.7×10^4 cm²/V-sec at room temperature and a carrier concentration of around 1 or 2×10^{16} cm⁻³.

This technique has also been applied to such materials as Bi, InSb-NiSb eutectic, InSb-MnSb eutectic, and InSb-CdSb with promising results. Efforts are under way to extend these studies to additional intermetallic compound and elemental films.

The appreciation of the author is extended to H. H. Wieder for many helpful suggestions.

REFERENCES

1. N. M. Davis and H. H. Wieder, "Electron beam synthesis and crystallization of InSb films," Proc. 8th Annual Electron and Laser Beam Symposium (University of Michigan), 1966; p. 385.
2. T. J. Holce, "High voltage problems in vacuum," Trans. 9th National Vacuum Symposium, American Vacuum Society, 1962; p. 376.
3. A. Strojnik, "A simple airlock and specimen stage for demountable electron optical systems," J. Sci. Instr. 42: 898, 1965.
4. R. B. Schilling, "Fabrication of ultrathin pinhole-free insulation of aluminum oxide," Proc. IEEE 52: 1350, 1964.

HIGH-PURITY SHAPE CASTING WITH AN ELECTRON-BEAM FURNACE

C. W. DEAN, R. E. MC DONALD, and C. F. LEITTEEN, JR.

Oak Ridge National Laboratory, Oak Ridge, Tennessee

ABSTRACT. An electron-beam melting furnace has been utilized to produce laboratory quantities of high-purity metals for many Oak Ridge National Laboratory research programs. The furnace hearth originally produced pancake-shaped ingots. Although high-purity samples could be produced in this shape, they contained cold shuts, porosity, and a coarse grain structure. Because of the shape and other undesirable properties, rod and wire were difficult to produce from such castings.

To overcome these difficulties, we developed a casting technique that permitted a molten charge of high-purity metal to be drop cast into a cylindrical or rectangular chill mold. Subsequent fabrication was easier and less expensive because of the improved cast structure and more desirable ingot shapes. In addition, a higher material yield was realized. The drop-casting technique and melting equipment have been used to cast fabricable shapes of Ti, Zr, Nb, V, Ta, W, Mo, and their alloys.

INTRODUCTION

The type of research programs at the Oak Ridge National Laboratory requires a casting and melting capability for a variety of metals. Because certain impurities can be vaporized during the melting operation and because there is no contamination from molds or electrodes, the electron-beam furnace is useful for producing many metals and alloys of extremely high purity. In the routine melting of most refractory metals at ORNL, melts are produced with a very low interstitial impurity content. By remelting several times before final casting is attempted, homogeneity is achieved on the high-melting-point, difficult-to-alloy metals. This report covers the development of a drop-casting technique that greatly improved the fabricability of the electron-beam-melted alloys.

EXPERIMENTAL

EQUIPMENT DESIGN. The electron-beam furnace employed in this study is an original NRC design that has undergone considerable modification by ORNL. Although originally designed with one electron gun and one hearth, this furnace is now equipped with two electron guns and hearths. Figure 1 shows the configuration of the furnace before modification, and Fig. 2 shows the furnace after modification. The double-gun and double-hearth configuration allows two melts to be made without opening the furnace.

The cylindrical furnace shell is constructed of 1/2-in.-thick stainless steel plate with a 23-in. inside diameter and a length of 60 in. The evacuation system consists of two 10-in. diffusion pumps, a 5 hp-30 cfm roughing pump, and two 1 hp-30 liter/min backing pumps and is capable of

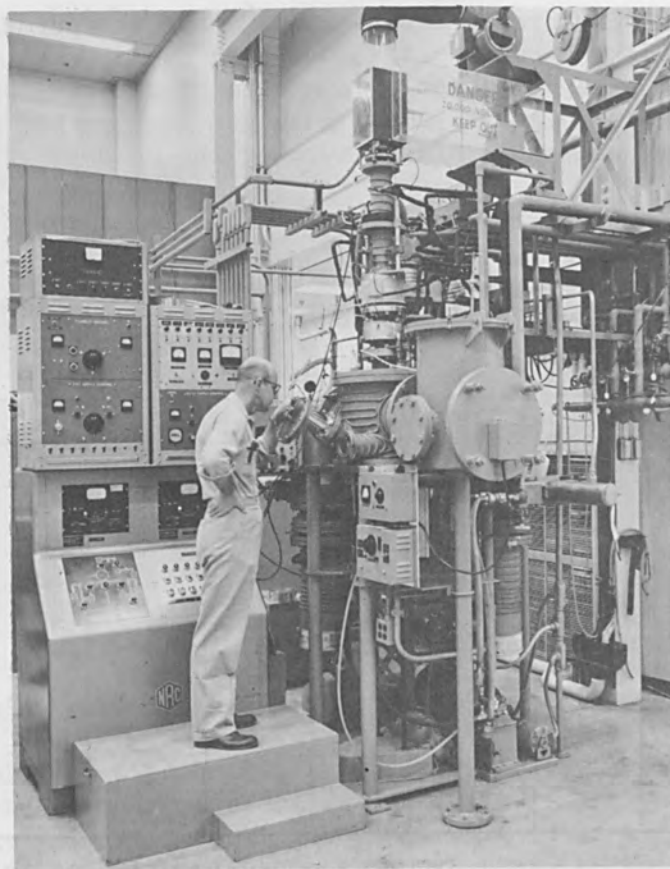


FIG. 1.—Electron-beam furnace: original configuration.

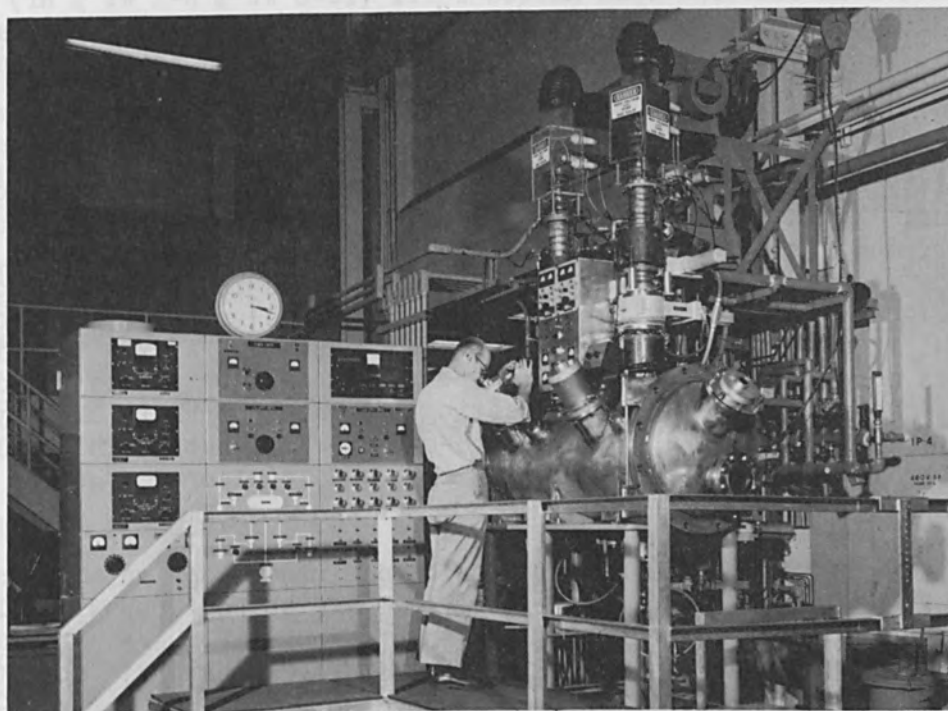


FIG. 2.—Electron-beam furnace: modified configuration.

reducing the internal pressure to 1×10^{-6} torr in approximately 20 min. Unless high outgassing rates are encountered during metal purification, this evacuation system is capable of maintaining a pressure of 5×10^{-6} torr throughout the melting cycle. Each gun chamber has a separate 4-in. short-series diffusion pump that evacuates the chamber to 5×10^{-7} torr.

A measure of the removal of interstitial impurity elements is shown by the chemical analysis in Table 1.

TABLE 1.—Chemical analysis of interstitial impurities before and after electron-beam melting.

| Material | Before, ppm | | | | After, ppm | | | |
|---------------|-------------|------|----|-----|------------|-----|-----|-----|
| | C | O | H | N | C | O | H | N |
| Titanium | 200 | 1090 | 45 | 340 | 160 | 890 | < 1 | 260 |
| Molybdenum | 270 | 710 | 4 | 6 | < 20 | 20 | < 2 | < 2 |
| Vanadium | 400 | 1260 | 8 | 720 | 210 | 880 | 4 | 570 |
| Zirconium | 80 | 1300 | 60 | 25 | 50 | 630 | 2 | 24 |
| Niobium | 40 | 75 | 2 | 45 | < 20 | 38 | 2 | 10 |
| Tantalum | 40 | 25 | 5 | 12 | 30 | 12 | 3 | 4 |
| Tungsten | 30 | 20 | 3 | 5 | < 20 | 5 | < 2 | < 2 |
| Nb-1 wt % Zr | 30 | 71 | 23 | 36 | 30 | 10 | 10 | 15 |
| Ta-10 wt % W | 20 | 29 | 6 | 5 | < 20 | 21 | 4 | 3 |
| W-26 at. % Re | | | | | < 20 | 59 | 5 | 18 |

The furnace is rated at 60 kW (20,000 V and 3 A) which is adequate power for melting most refractory metals and alloys. Cathodes are machined from electron-beam melted T-111 (Ta-8 wt % W-2 wt % Hf) alloy. They are approximately 1 in. in diameter and 1/8 in. thick and have a concave face, for initial focusing, that is polished to a very smooth finish.

To accelerate cooling and minimize contamination, melts are made in a variety of water-cooled copper mold shapes, which consist of four basic designs: for initial consolidation and purification—pancake, button, and finger; and for final casting—either rectangular or cylindrical drop-casting molds. Figure 3 shows some of the molds in use. A button mold is designed specifically for drop casting and is split in half for easy removal from the skull that remains after casting. A 1/2- to 1-in.-diam hole is bored through this mold to permit the metal to flow rapidly into a drop-casting mold. The drop-casting apparatus consists of a cylindrical copper mold that is 2 in. OD and 3.5-6.5 in. in length. This mold is split to facilitate removal of the ingot and is clamped together for casting.

DROP-CASTING PROCEDURE. The original furnace design and associated hearths permitted the melting of only pancake shapes approximately 4 in. in diameter by 3/4 in. thick. Such ingots, however, were not readily amenable to fabrication because of the heterogeneous grain structure resulting from this type of casting arrangement. Demands for high-quality rod and wire products necessitated the development of an electron-beam melting technique capable of producing ingot shapes amenable to swaging



FIG. 3.—Electron-beam furnace: drop-casting molds.

and wire-drawing operations.

The result was a technique which we refer to as drop casting. Drop casting differs in many respects from what is commonly referred to as "drip casting." In drip casting the material is melted in a button hearth with a hole in the bottom in such a manner that the molten metal runs slowly into the vertical mold below. This produces an irregular surface and an inhomogeneous internal condition.

In order to make a drop casting, scrap and/or chop stock is first melted in a conventional button mold. By turning the button from side to side and remelting several times, homogeneous alloying is achieved even for the most hard-to-melt, difficult-to-alloy refractory metals. When consolidation, purification, and homogeneity of the melt are assured, the button mold is removed and the drop-casting apparatus is installed.

The electron beam, broadly focused, traverses the button until the button surface is completely molten. The beam is now "pinpointed" or concentrated while continuing to traverse the molten surface. The button now melts to deeper penetrations until the entire charge is molten except for a thin layer at the bottom. An increase in furnace power rapidly melts the bottom of the button and the molten metal is drop cast into the vertical chill mold.

RESULTS AND DISCUSSION

The rapid drop-casting action prevents cold shuts and gives an internally sound ingot with good surfaces. Because of the differential cooling rate from top to bottom, pancakes and buttons usually contain shrinkage cavities. In a drop casting, the body of the ingot solidifies at a greater rate than does the feeder head. This solidification sequence results in the elimination of shrinkage cavities from the body of the ingot.

The internal structure of pancakes and drop castings differs in many respects. Pancake configurations generally exhibit a fine-grained structure at the bottom and a much coarser grain structure at the top, because of the vast differences in solidification and cooling rates exhibited within these regions. The microstructure of a molybdenum pancake, illustrated in Fig. 4, shows the definite line of demarcation that exists between the grain sizes. In addition, grains extend through the entire thickness of some pancakes. Drop-cast ingots are internally homogeneous and exhibit a uniform grain size throughout, as shown in Fig. 4 for molybdenum.

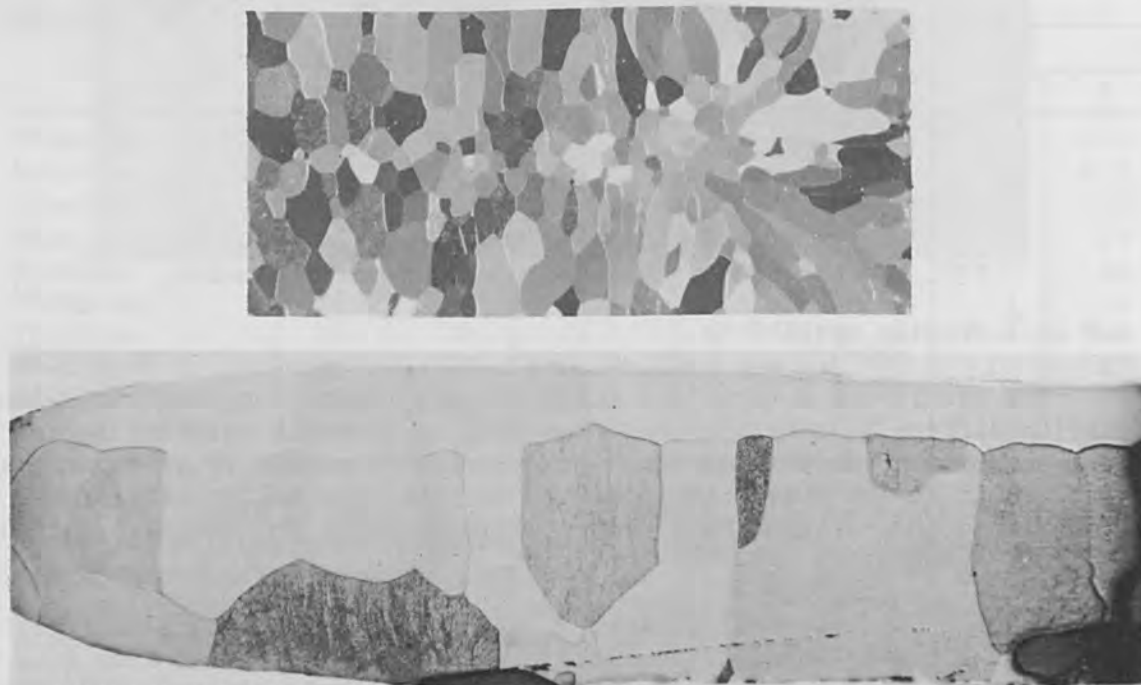


FIG. 4.—Electron-beam melted molybdenum pancake (top) and electron-beam melted molybdenum drop-casting (bottom). Original magnification: 3x.

Not only do drop castings have a more desirable grain structure for fabrication but they are also in a configuration that is much easier to fabricate. A cylindrical drop casting is readily amenable to swaging and drawing operations, whereas sheet, plate, or bar are easily fabricated from ingots with rectangular cross sections. Fabrication of rod or wire from pancake configurations requires a costly cutting operation. Further difficulties are encountered because the sectional strips are rectangular and contain a broad range of grain sizes and therefore are not readily amenable to the formation of cylindrical shapes. For many refractory metals this sectioning operation is not practical because of breakage during cutting operations.

Fabricability improvements afforded by drop casting are also accompanied by a considerable gain in material yield. An average yield for drop-cast ingots is approximately 80% in the ingot condition, but almost 100% yield is attained on fabrication. A drop casting must be overcharged by approximately 20% to allow for the skull and feeder head. Pancakes

attain almost 100% yield on melting, but on fabrication the average yield is considerably lower.

Ingots up to 3/4 in. in diameter and 5.5 in. long of V, Nb, Mo, Zr, Ti, and Nb-1% Zr are routinely drop cast. Refractory alloys such as W-26 at. % Re, W-35 at. % Re-18 at. % Mo, and Ta-10% W have been successfully drop cast in ingots 1/2 in. in diameter and 2.5 in. in length. Figures 5 and 6 show a number of these castings.



FIG. 5.—Electron-beam melted cylindrical drop castings.



FIG. 6.—Electron-beam melted rectangular drop castings.

CONCLUSIONS

The quality of electron-beam melted drop-cast materials is superior to that produced by other methods. The low impurity levels combined with the favorable grain structure obtained by drop casting improve alloy fabricability. In addition, the shapes of the drop-cast ingots are readily amenable to fabrication methods such as swaging, rolling, and wire drawing.

ACKNOWLEDGMENT

This research was sponsored by the U. S. Atomic Energy Commission under contract with the Union Carbide Corporation. Mr. Leitten is now with Union Carbide Corporation, Linde Division.

METALWORKING LASERS IN ENGINEERING SERVICE APPLICATIONS

J. F. SMITH and A. THOMPSON

International Business Machines Corp., Poughkeepsie, N. Y.

ABSTRACT. Applications for which laser metalworking systems have been used as an engineering service in a manufacturing plant are described. The applications include examples of how the laser has been used to assemble development and model parts, to help fabricate tool parts, to repair tools, to produce thermocouple junctions on substrates to be monitored, and to produce highly specialized parts.

In the applications described, the laser showed itself to be a valuable tool capable of performing many specialized metalworking tasks impossible by more conventional techniques. In some of the cases, the laser performed tasks that ordinarily would have required considerable additional equipment and tooling, involved delays, and entailed great expense.

The paper also includes a description of the laser equipment used.

INTRODUCTION

Much has been written and presented on the subject of laser metalworking applications. To a great extent the material was of an experimental nature—laboratory work or theoretical—but little has been published on lasers paying their way within a manufacturing plant. Probably the most publicized exceptions are Western Electric's laser diamond drilling process and assorted resistor trimming operations by several companies.

In the early stages of an IBM project to develop laser metalworking techniques for production, it was realized that the laser could be used as an engineering service tool. This paper describes how a laser has been used by Advanced Manufacturing Engineering to service a production organization, and shows the breadth of possible service applications for laser metalworking.

APPLICATIONS

DEVELOPMENT AND MODEL PARTS. The laser has been a valuable welding tool in programs calling for the fabrication of development and model parts. In several cases the final choice of materials and design configuration for a part determined which of several complicated and expensive bonding processes would be used. Final processes could not be designed and installed until the choice was made on materials and design. The laser—which can vaporize any metal—was used to weld the model parts for evaluation and test of completed assemblies. After the evaluations were complete, final design was established and tooling could begin for conventional bonding processes. Other programs have been established to

design for the laser welding process.

Figure 1 shows an example of a development assembly. The two fingers are beryllium copper 0.080 in. wide and 0.018 in. thick. The L-shaped contacts are 0.024-in.-thick coin silver. The conventional process normally used to make this joint was silver soldering, in which excessive heat was put into the beryllium copper. Position tolerances on the assembly were tight. Laser welding produces a reliable joint with less assembly time and higher yields. The figure shows a weld utilizing a plug welding technique. Initially, not enough energy was available from the laser to weld through the beryllium copper to the coin silver. In the plug welding technique a 0.032-in. pilot hole was punched in the beryllium copper. A 0.040-in.-diameter focused laser spot was used to produce the weld. Later in the project a neodymium-glass laser rod was used to weld the assembly without pre-drilling or punching the beryllium copper.

A solenoid assembly consisting of a 0.125-in.-diameter silicon iron base and 0.040-in.-diameter stainless-steel pin was laser welded. Figure 2 shows the assembly after welding with a single shot through a long focal length lens. The joints produced by the laser in this application pull in excess of 60 lb.

Another example of laser welding of development parts is shown in Fig. 3. A large quantity of oxygen-free copper flange-cap assemblies was required to set up and debug an experimental process line. For this purpose, an hermetic seal was not required but a welded joint was necessary. The assemblies were laser welded with two spot welds on each edge. The thickness of the mated flanges is 0.020 in. The assembly is approximately 1/4 in. square.

A prototype assembly consisting of a 0.030-in.-diameter music wire was laser welded to a 0.212-in.-diameter, 0.070-in.-thick silicon iron disk as shown in Figure 4. The disk is drilled through to accept the wire. The first approach to welding the assembly was to hit the end of the wire and the edge of the disk with the laser beam. The wire was subjected to a higher energy density than the silicon iron and excessive cratering was the result. The final approach as shown in the figure was to weld through the silicon iron into the music wire. This approach produced results which exceeded the assembly specifications.

Laser welding is being considered as a supplementary process for welding an assembly consisting of two copper clad stainless steel spring bars welded on one end to hardened steel and on the other end to silicon iron. Figure 5 shows a weld of the spring bar to the hardened steel component.

PARTS REPAIR. Many different parts repair possibilities exist for laser welding. One of the more unusual ones is shown in Fig. 6. The stud is a 5/16-in.-diameter steel mounting stud. The panel is a special part of thin-gage steel with elaborate artwork on the front side. Conventional welding techniques could not be applied because prolonged heat applied to the panel would damage the artwork. Three studs were laser welded to the special panel to put it into service. The boss at the base of the stud was too thick to laser weld through on the first pass. The first pass was

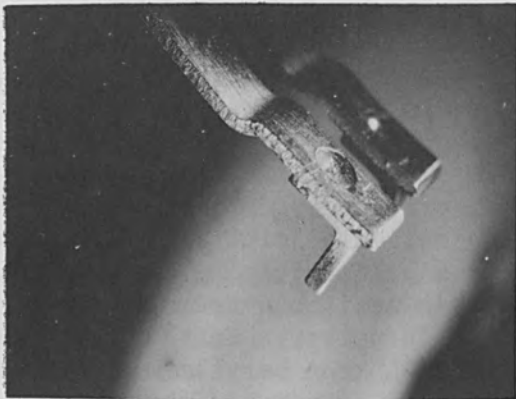


FIG. 1.—Beryllium copper to coin silver contacts.

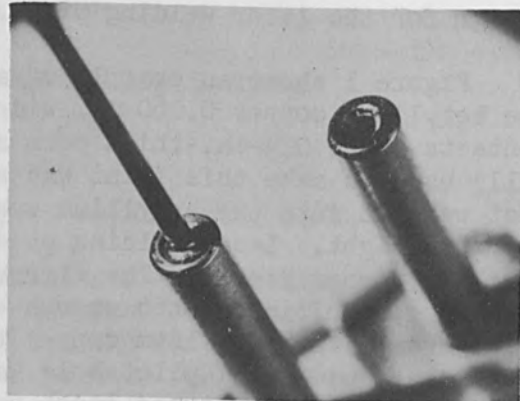


FIG. 2.—0.040-in. stainless-steel pin to silicon iron solenoid.

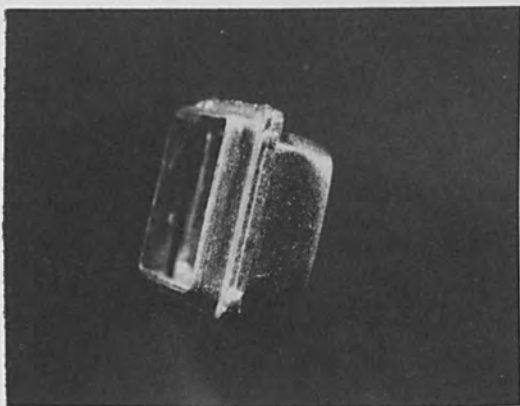


FIG. 3.—Copper-flange cap assembly.

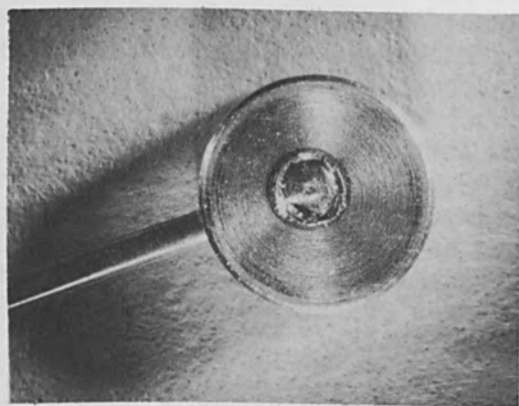


FIG. 4.—Music wire to silicon iron.

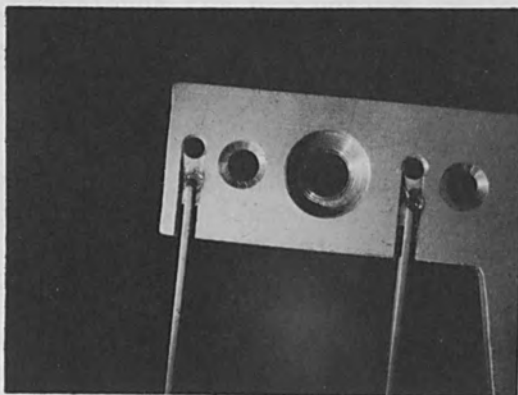


FIG. 5.—Copper-clad stainless to hardened steel.



FIG. 6.—Panel repair, 5/16 in. stud to steel panel.

used to chamfer the edges down. A second pass was made to weld the studs to the panel.

Another repair technique that has been used is laser reflow of gold plated Kovar pins. In one application the Kovar pins are subjected to a process that occasionally creates fissures at the base of the pin. Conventional repair techniques were not applicable. The laser was focused at angles of incidence of 45 and 60 degrees to reflow the Kovar pin at the base. A cross section of a reflow pin is shown in Fig. 7.

TOOL REPAIR. Laser welding is a useful tool in many instances for tool repair. Expensive tools with cracks are often readily welded with a laser. Inserts are easily welded in place to narrow down slot widths or gaps.

Figure 8 shows an example of a die mold cavity repair. This particular tool was in final stages of build when it cracked. The material was a hardened tool steel. Figure 9 shows a closeup of a laser weld repair. A backup insert was used to strengthen the corner where the crack had occurred.

Figure 10 is of a broach nest repaired by laser welding. The tool is of an oil-hardened tool steel. The crack was through the bed of the nest. After welding, the nest was lightly surface ground to remove flashing from the edges of the weld zones and put back into service.

Figure 11 is a cracked cylindrical staking tool of oil-hardened tool steel. The two cracks were laser welded and the tool put back into service.

TOOL FABRICATION. No real emphasis has been put on tool fabrication utilizing the laser, but there are a few areas where it has been used upon request. Welding of inserts in tools and drilling of holes in hard materials are two of these areas. In hole drilling, the laser may be used in some cases to drill finished holes and in other cases to rough drill as a pilot hole for another process, such as ECM (electrochemical machining) or EDM (electrical discharge machining).

Figure 12 shows a 0.060-in.-diameter tungsten carbide probe with a feedhole drilled through with a laser. The entrance diameter is approximately 0.008 in. in diameter with the exit 0.0025 in. in diameter. The angle of incidence on the entry and exit in this case is 45°.

Another application of laser welding in tool fabrication is shown in Fig. 13. The tool is a vacuum deposition mask constructed of two thin sheets of molybdenum. The bottom layer is 0.007 in. thick and the top layer 0.010 in. thick. After alignment of the two layers, two laser spot welds were used to join the sheets and prevent skewing of the assemblies. The rectangular nest areas are 0.600 x 0.360 in. Figure 14 shows a close-up of one of the spot welds. The small slots in the bottom layer are 0.030 x 0.008 in.

TEMPERATURE INSTRUMENTATION. The applications for thermocouples have been reduced in recent years with the improved methods for temperature

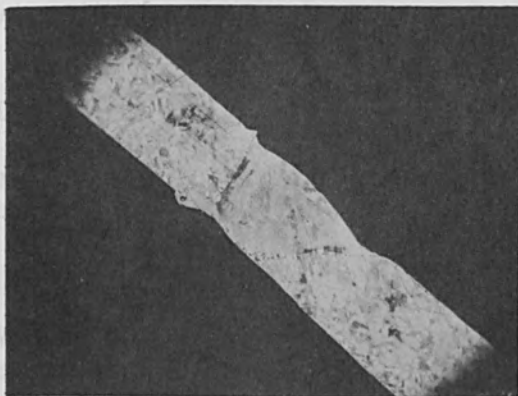


FIG. 7.—Reflow of 0.018-in. diameter kovar pin.

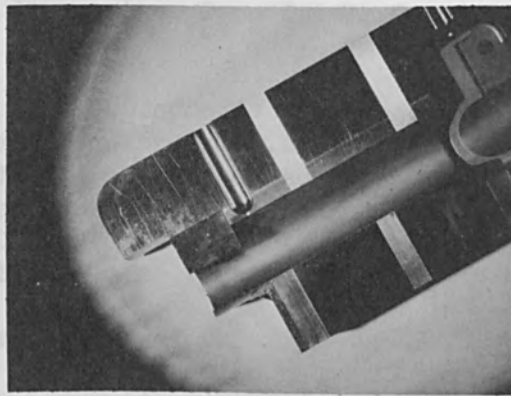


FIG. 8.—Die mold cavity, air hardened tool steel.

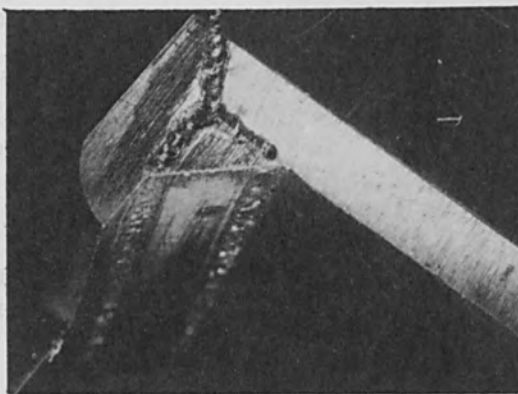


FIG. 9.—Repaired region of die mold cavity.

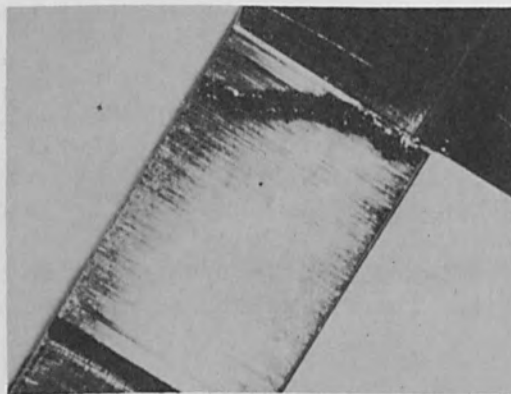


FIG. 10.—Oil-hardened tool steel broach nest repair.

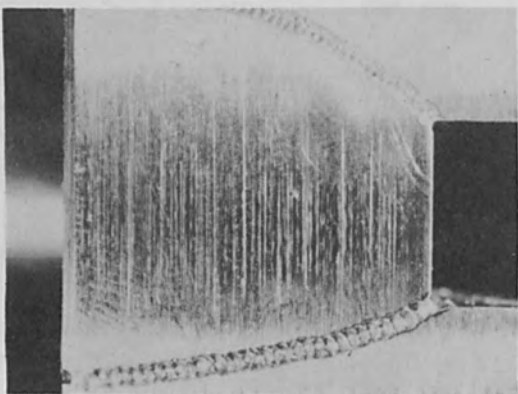


FIG. 11.—Oil-hardened tool steel cylindrical staking tool repair.

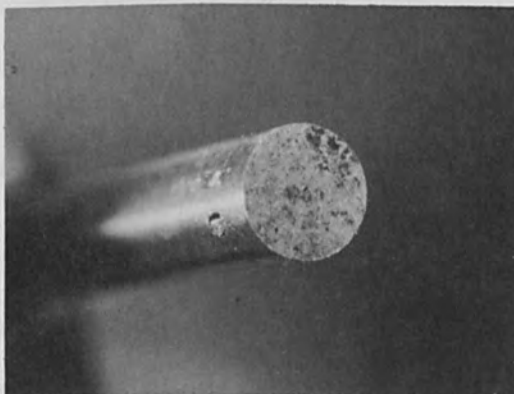


FIG. 12.—Laser-drilled tungsten carbide probe.

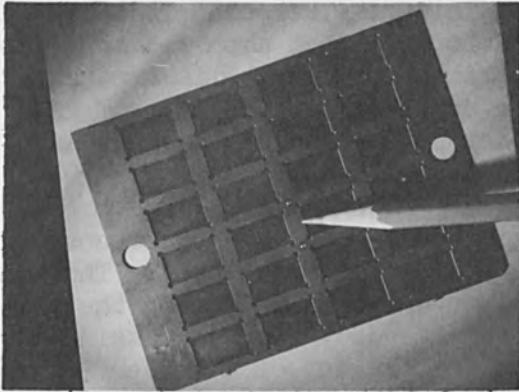


FIG. 13.—Vacuum-deposition mask, 0.010 to 0.007 in. molybdenum.

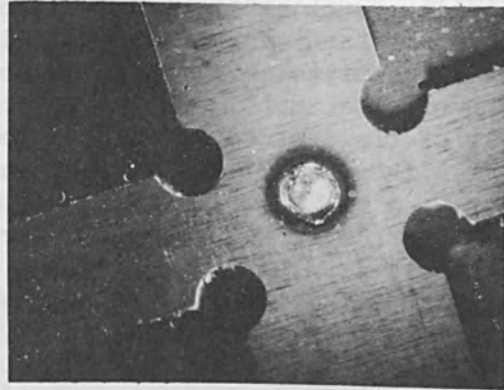


FIG. 14.—Close-up of molybdenum deposition mask weld.

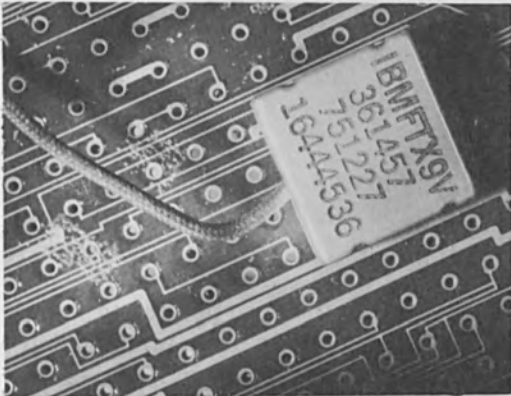


FIG. 15.—Module with thermocouple inserted in card.

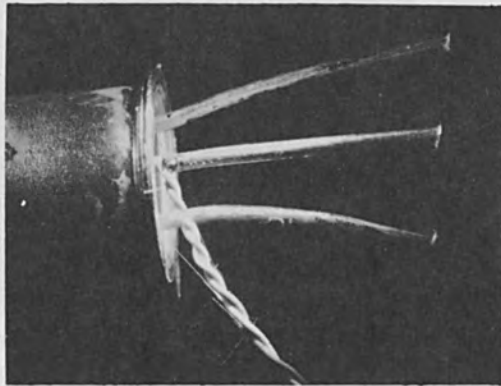


FIG. 16.—No. 36 iron-constantan thermocouple on transistor lead.



FIG. 17.—No. 20 iron-constantan thermocouple to stainless steel.

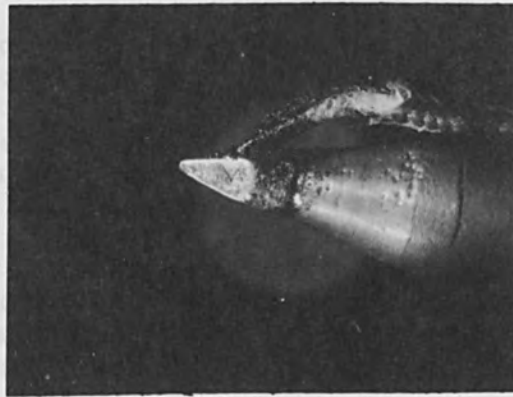


FIG. 18.—No. 20 iron-constantan thermocouple to soldering-iron tip.

monitoring, such as the infrared thermo-plotter. Thermocouples are still used though, and many times it is desirable to attach a thermocouple to a metal substrate. Brazing a thermocouple to a substrate is a common method of attachment, but this procedure usually introduces error as a result of the increase in mass. The laser has been used in many cases to attach a thermocouple to a metal that is to be temperature monitored.

Figure 15 shows a module inserted into a card with a thermocouple attached to lead pin in the region of the glass to metal seal. This particular application of thermocouple welding was for monitoring the temperature of the base of the module pin as a loaded card was passing through a wave soldering machine. Figure 16 shows a closeup of a number 36 iron-constantan thermocouple pair welded to a transistor lead.

Figure 17 shows a number 20 iron-constantan thermocouple welded to a stainless-steel substrate used in vacuum deposition work. Figure 18 is of a number 24 iron-constantan thermocouple laser welded to soldering iron tip. It is an example of many such tips that were prepared for a soldering iron evaluation project to determine the tip temperatures with no-load and solder-load conditions.

EQUIPMENT DESCRIPTION

The laser system used in the work described consists of a commercially available laser metalworking unit slightly modified for our own use.

The head is of a dual elliptical cavity design incorporating two FX-55 xenon flash tubes. Ruby and neodymium laser rods are used interchangeably. The output reflector for ruby is the natural ruby-to-air interface. The neodymium output reflector is an external resonant reflector aligned to the front surface. Both rods incorporate a TIR (total internal reflection) design for the rear reflector.

The flash tubes and laser rod are cooled by a closed loop water system containing a dionizing filter.

The power supply is a 4-kV resonant charging type with a dc output continuously variable from 1.7 to 4.0 kV.

The energy-storage network consists of six identical banks. Each bank contains 200 microfarads of capacitance and 1600 microhenries of inductance, and a control switch.

The control console contains a voltmeter; power, standby, and high-voltage-on switches; and fire button. The modes of firing are: two, manual (panel and remote cable); four, automatic intervals (1, 2, and 5 sec and variable); and by external signal input.

Viewing and focusing the laser beam onto the target is accomplished by a closed-circuit television unit using a common objective lens for focusing and viewing. Twenty-five objective lenses ranging in focal length from 11 to 200 mm are used for coarse spot-size control and producing viewing screen magnification of 18 X to 300 X on a 15-in. TV monitor.

An in-line sampling energy monitor measures the output of the laser head and records the energy in joules on a panel meter. The monitor also has provision for scope monitoring for measuring peak powers, pulse width, and pulse shape.

Figure 19 shows the equipment less the energy storage units. Figure 20 indicates a typical output calibration of the system with ruby and neodymium glass rods.

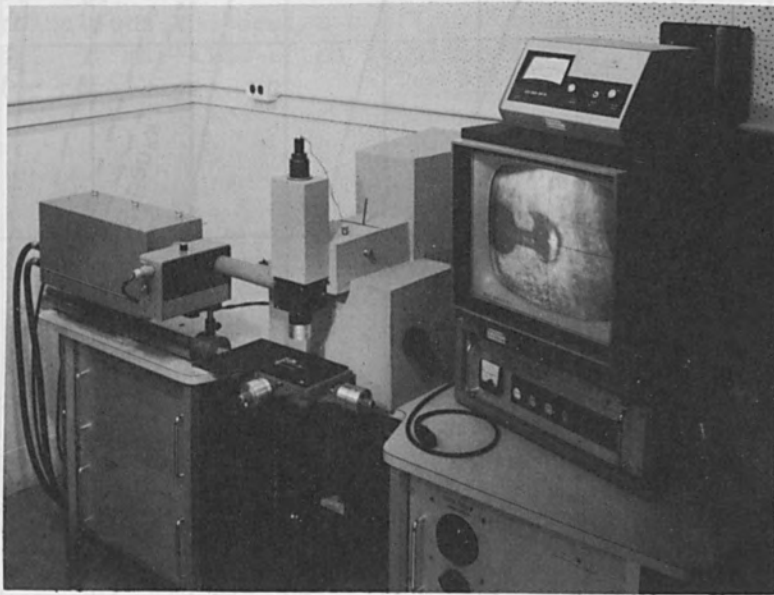


FIG. 19.—Laser metalworking unit with TV-Optics package.

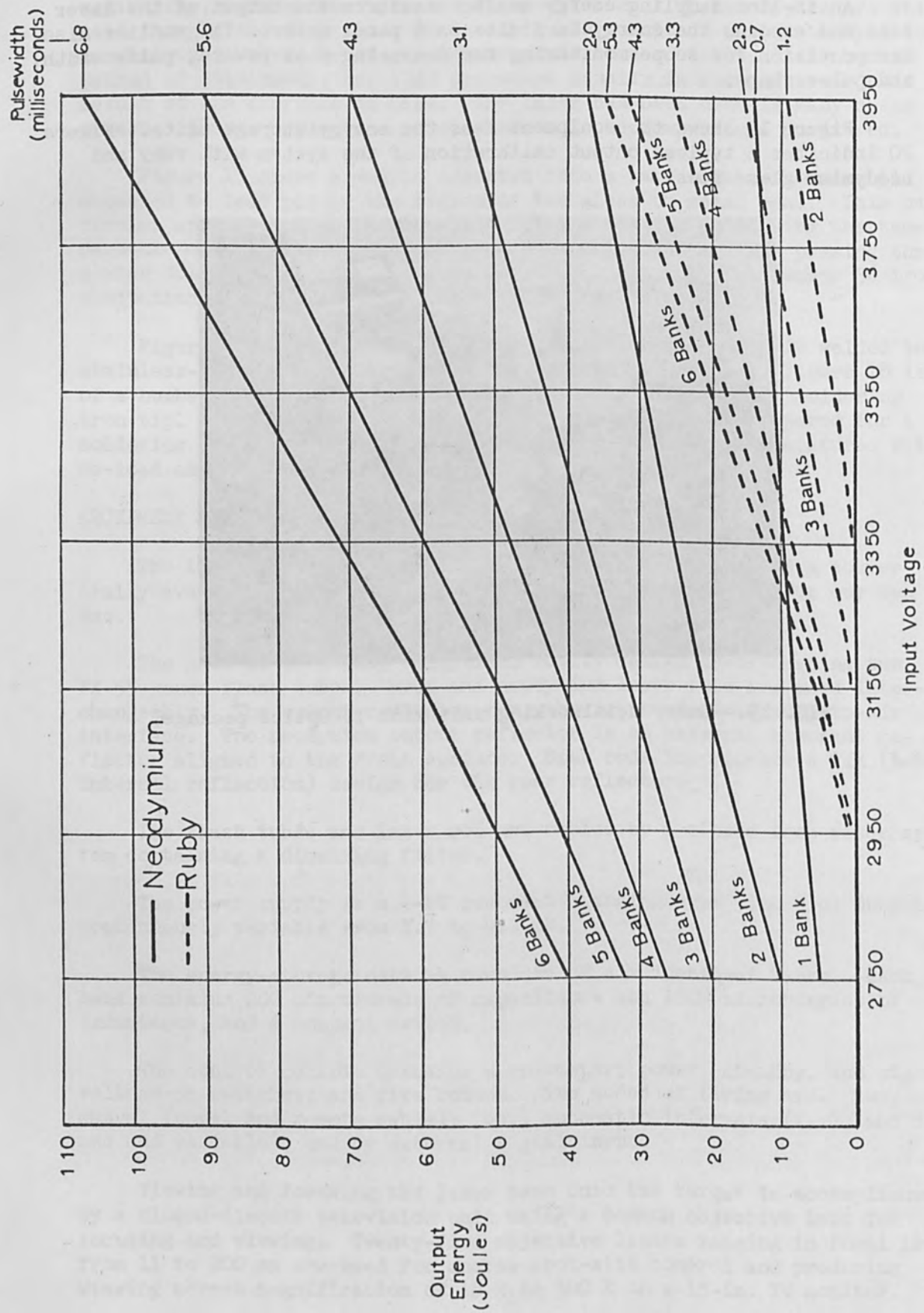


FIG. 20.—Energy output of ruby and neodymium rods.

SUMMARY

The laser is no longer restricted to a laboratory environment. There are many everyday tasks that lend themselves readily to a laser metal-working process. Engineering service applications such as just described are a very important function. The service applications also inform others of the laser's capabilities and potential in a manufacturing plant, and help to bring about additional potential production applications. The laser is not a cure-all, but an additional tool which will broaden the material combinations and design configurations that may be used in modern manufacturing. It may also often supplement other processes to speed up fabrication or assembly.

ELECTRON-OPTICAL CONTROL FOR ELECTRON BEAM
DEFLECTION IN WELDING AND CUTTING

A. EMERY

Hi-G, Inc., Windsor Locks, Conn.

The specific problem outlined in this paper is the sealing of small relay enclosures, such as shown in Fig. 1, with an electron-beam welder. The assembly, shown in Fig. 2, consists of a copper-nickel can with end dimensions of 0.8 by 0.4 in. and wall thickness of 0.009 to 0.013 in., into which is hermetically sealed a steel header. The header has eight glass beads, each of which insulates a steel pin that make connections to the relay within. The beads are 0.030 in. from the edge of the header.

Several methods are currently used to accomplish the weld. Some entail moving the object under the beam, and some use deflection coils to direct the beam around the object. A purely mechanical means is the pantograph (Fig. 3), a mechanical amplifier which follows an oversize pattern with a drive wheel and, by linkages, transmits a congruent but significantly reduced pattern to a table upon which the object sets. The pantograph reduces any errors in the oversized pattern by the same reduction, thus effecting close tolerances in the final table motion.

Other methods produce voltage functions which can be transferred to servo motors to control the table, or to deflection coils to move the beam itself. One such system is the cam-resistor method (Fig. 4) in which motor-driven cams operate high-resolution potentiometers which produce the necessary X and Y voltage functions. The cams can be cut to compensate for all errors in the deflection system. The speed of the weld is controlled by the motor and the size is controlled by the final amplifier. A point-by-point computer function can be generated by assigning two binary numbers to each point on the function and recording the sequence on a digital tape recorder. When the tape is played back through a digital to analog converter to the final amplifiers, the function is repeated. The tape can also operate stepping motors to produce the proper table motion. Straight-line functions can be generated by logic systems and ramp generators but must be used with highly linear deflection methods because there is no way to compensate for irregularities.

Assuming the generated pattern is perfect, there are some manufacturing and positional errors which must be considered. Ideally a minimum beam diameter which covers 0.010 in. on either side of the seam will produce a reliable seal. The beam must also stay 0.020 or more inches from the highly stressed glass insulator to prevent the sharp heat gradient from cracking it. The manufacturing and positional errors are shown in Fig. 5, together with a small cross section of the assembly drawn to scale. If one side of the assembly is referenced to the table, the possible position of the seam and bead due to manufacturing tolerances alone are shown in Fig. 5 in the top bar. It is seen that a 0.025-in.-diameter beam can easily produce the ideal conditions. If the indexing system can only position to ± 0.003 in., the beam will always cover the seam but the

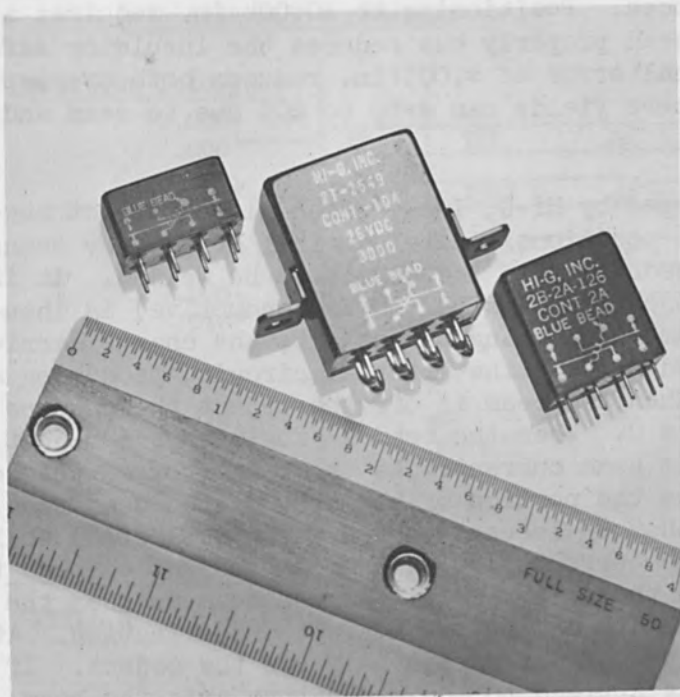


FIG. 1.—Relay enclosures.

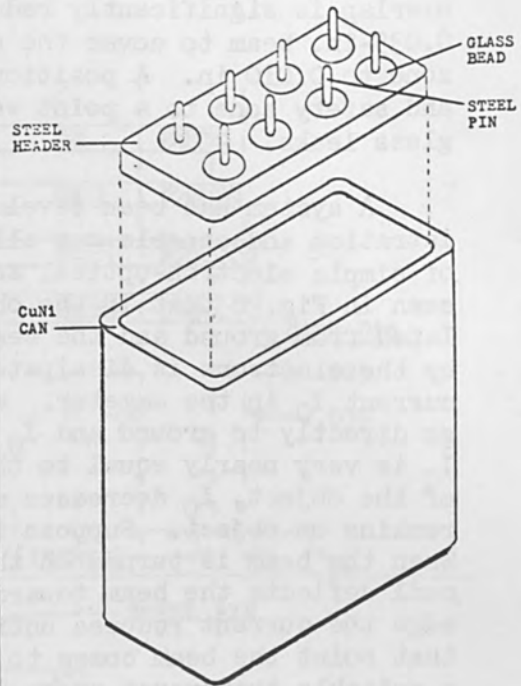


FIG. 2.—Assembly.

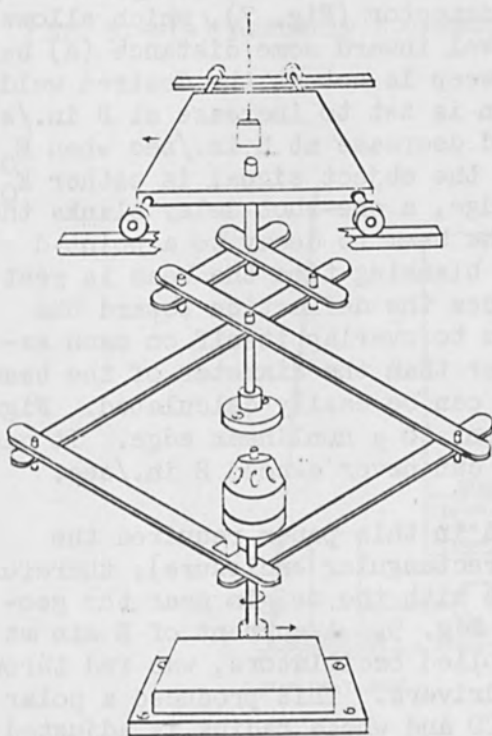


FIG. 3.—Pantograph.

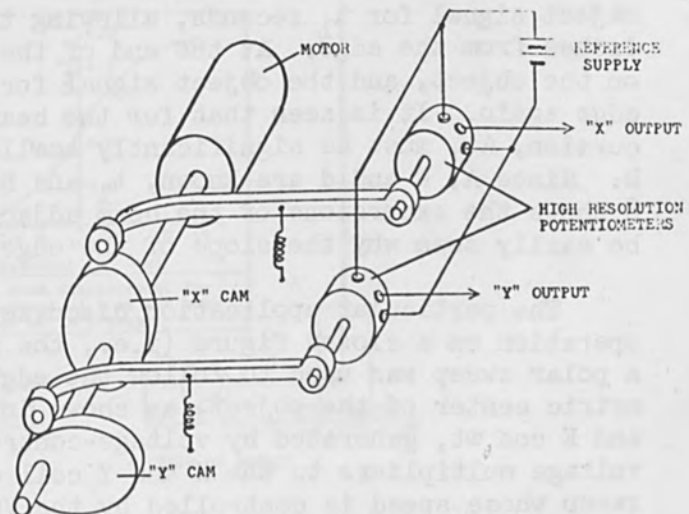


FIG. 4.—Can-resistor function generator.

overlap is significantly reduced. Positioning to ± 0.004 in. requires a 0.035-in. beam to cover the seam properly but reduces the insulator safety zone to 0.010 in. A positional error of ± 0.005 in. reduces both overlap and safety zone to a point where yields can drop to 80% due to seam and glass leaks.

A system has been developed by Hi-G, Inc., which gives perfect registration and cancels out all positional and electrical errors, by means of simple electron-optical feedback from the object to be welded. It is seen in Fig. 6 that if the object (understood to be conductive) is insulated from ground and the beam is touching the object, the charge carried by the electrons is dissipated through the external circuit, producing a current I_0 in the ammeter. When the beam is off the object the charges go directly to ground and $I_0 = 0$. When the beam is fully on the object, I_0 is very nearly equal to the beam current. As the beam crosses the edge of the object, I_0 decreases as the portion of the area of the beam that remains on object. Suppose that I_0 is used to operate a deflection coil. When the beam is turned on the current flowing from the object through the coil deflects the beam toward the object edge. As the beam crosses the edge the current reduces until it can support no further deflection. At that point the beam comes to rest, half on and half off the object. If a suitable transverse sweep is applied to the quadrature axis the beam traverses the edge of the object following every minute deviation independent of location or errors in the deflection system.

The point where the weld must occur, however, is usually displaced from the edge by some distance. The displacement can be accomplished by a logic system, referred to as the edge detector (Fig. 7), which allows the beam, after seeking the edge, to travel inward some distance (d) before re-seeking the edge again. The Y axis sweep is set at the desired welding speed of A in./sec. The X deflection is set to increase at B in./sec when the object signal E_0 is present, and decrease at B in./sec when E_0 is zero. A Schmitt trigger assures that the object signal is either E_0 or 0. As soon as the beam reaches the edge, a one-shot delay blanks the object signal for t_1 seconds, allowing the beam to decay to a point d inches from the edge. At the end of the blanking time the beam is resting on the object, and the object signal forces the deflection toward the edge again. It is seen that for the beam to overlap itself on each excursion, At_1 must be significantly smaller than the diameter of the beam D . Since A , D and d are known, t_1 and B can be easily calculated. Figure 8 shows the excursions of the beam adjacent to a nonlinear edge. It can be easily seen why the slope of the edge can never exceed B in./sec.

The particular application discussed in this paper required the operation on a closed figure (i.e., the rectangular enclosure); therefore, a polar sweep was used to follow the edge with the origin near the geometric center of the object, as shown in Fig. 9. A current of $E \sin \omega t$ and $E \cos \omega t$, generated by voltage-controlled oscillators, was fed through voltage multipliers to the X and Y coil drivers. This produced a polar sweep whose speed is controlled by the VCO and whose radius is adjusted through the multipliers by the edge detector. The speed can be modified by a function generator (as speed is not too critical under ideal conditions) or by an analog system such as shown in Fig. 10, which computes the linear speed of the beam from the X and Y signals. The computer uses

(a) ASSEMBLY TOLERANCES

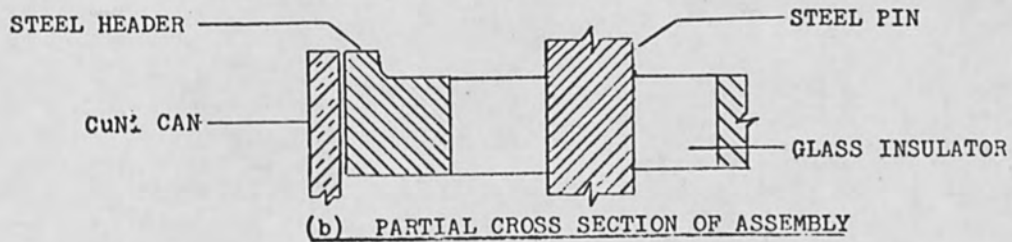
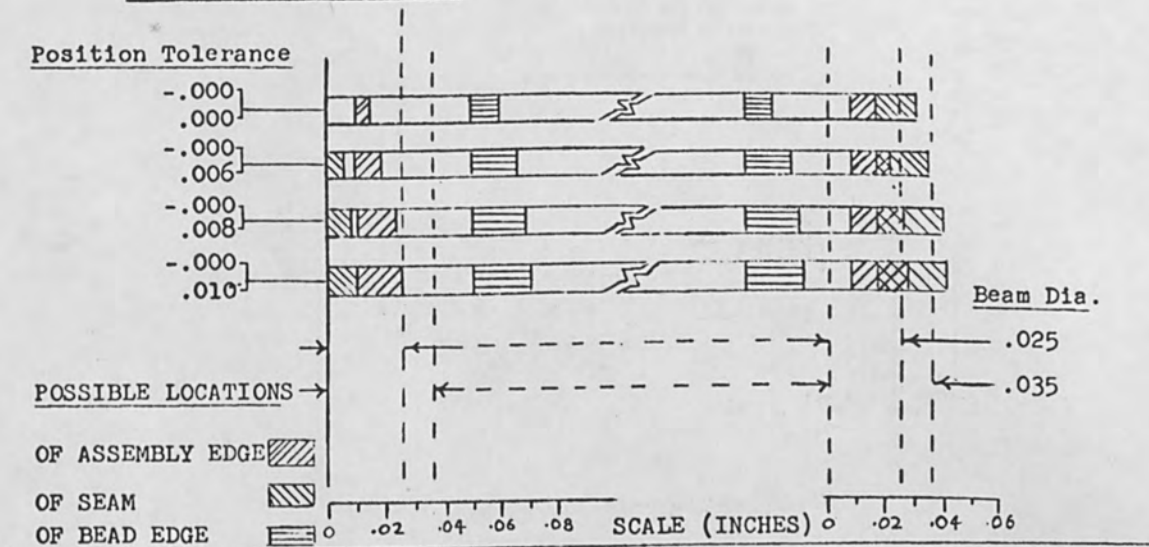


FIG. 5.—(a) Assembly tolerances; (b) partial cross section of assembly.

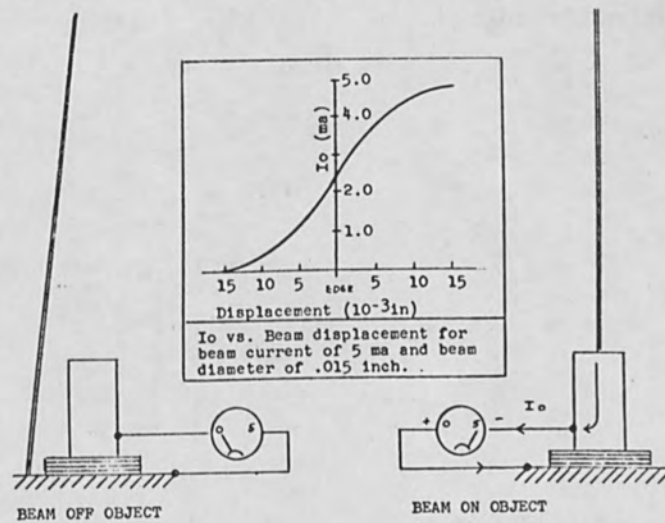


FIG. 6.—Optical states.

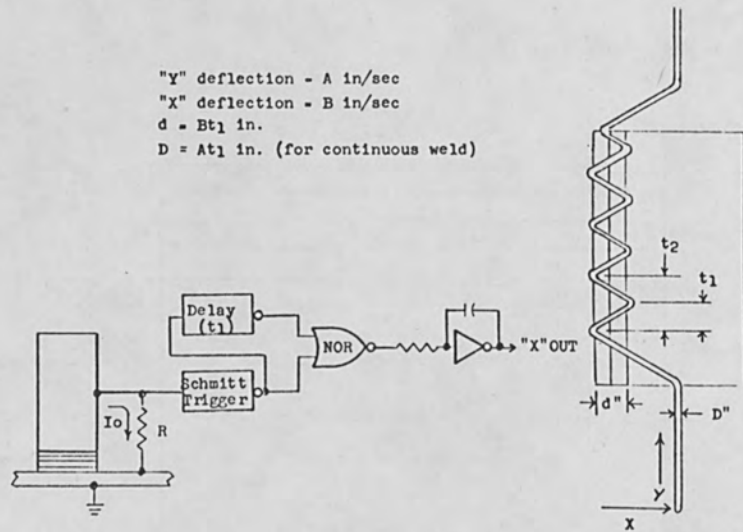


FIG. 7.—Edge-detector operation.

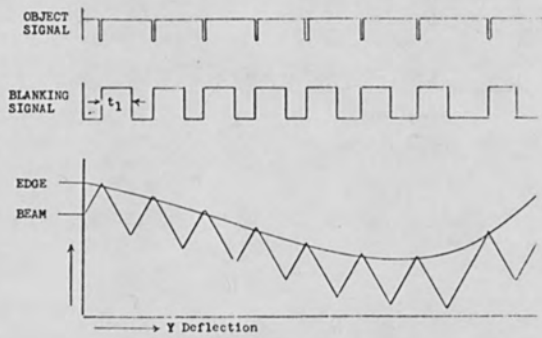


FIG. 8.—Edge-detector signal.

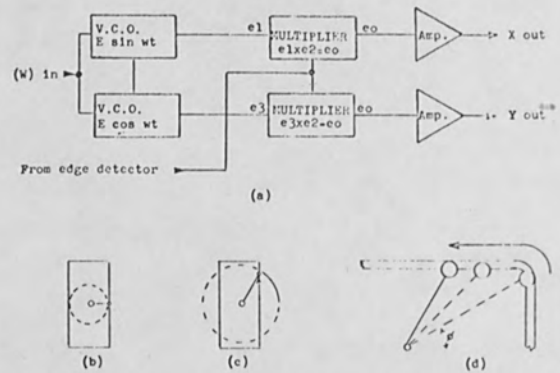


FIG. 9.—Polar coordinate system.

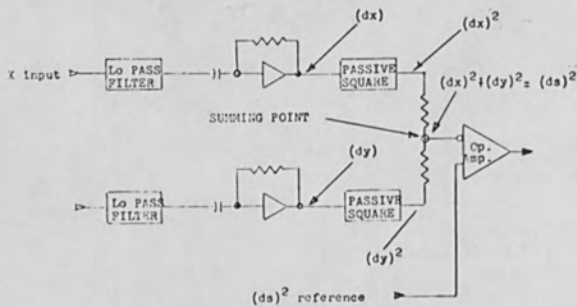


FIG. 10.—Analog computation of linear speed.

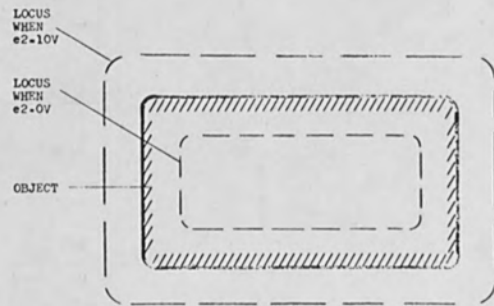


FIG. 11.—Loci of pattern vs. control voltage (e_2).

the relationship $(ds)^2 = (dx)^2 + (dy)^2$ which, when compared with the square of the desired speed, produces a compensating voltage forcing the VCOs to the proper frequency. The low-pass filters remove the modulation component from the function.

A less sophisticated method to accomplish the sweep is to replace the VCOs with one of the previously mentioned function generators. Of course any miscentering of the pattern produces proportionate errors in the welding speed, but a 10% change in the speed causes far less trouble than a 10% positional error. The pattern sizes vs E_0 are shown in Fig. 11. The complete automated system is shown in block diagram in Fig. 12.

Some manufacturers prefer to use a circular modulation of the beam rather than the saw tooth motion to stir the constituents better and produce a more homogeneous alloy at the weld. Edge detection can be applied to such a method, as shown in Fig. 13. Signals of $kE \sin nt$ and $kE \cos nt$ are added just before the coil drivers; kE is then the desired radius of the small circle and n is the frequency, which is high enough to allow overlap of consecutive sweeps. The output of the Schmitt trigger is referred to a voltage E_{ref} , integrated, and applied to the multipliers. The delay is not used. The circle moves outward until the portion of the area on the object is proportional to E_{ref}/E_0 . If E_{ref} is nearly equal to E_0 the circle rests mostly on the object, effecting a weld kE inches from the edge.

As the beam starts some distance within the edge of the object when it is first turned on, it should be blanked out until the edge is reached. Since the beam is a necessary part of the system, it is only defocused and then refocused when it reaches the edge.

A control unit for this purpose is shown in Fig. 14. The control instigated and terminated by a signal from the X axis which occurs at the same point in the sweep. Flip-flop circuit A is set by the start button and the X signal triggers the delay and sets flip-flop B. The beam is turned on defocused until the end of the delay period, where it is focused. When the X signal occurs again the delay holds the beam on until it returns to the point where it was focused and then resets flip-flop A, shutting off the beam. Delayed dropouts on the beam and focus relays assure a slight overlap of the weld.

In cutting and sometimes in welding, the operation must take place at a point where no edge is nearby. Such an operation can be accomplished as shown in Fig. 15 by placing a grounded function template over the object. When the beam reaches the plate the charge is taken away from the object through the template to ground, thereby operating the edge detector. The template must be made of copper so as not to be damaged by the beam, and insulated from the object. The plate can be positioned over the precise area with pins or adhesive or secured to the top of the chamber. If an enclosure has brackets which protrude beyond the edge, the above method must be used to force the beam to follow the seam rather than the bracket. No modulation of the beam is necessary when cutting.

The edge detection method is not restricted to the control of electrons. It can be used for any charged particles, such as ions or plasma.

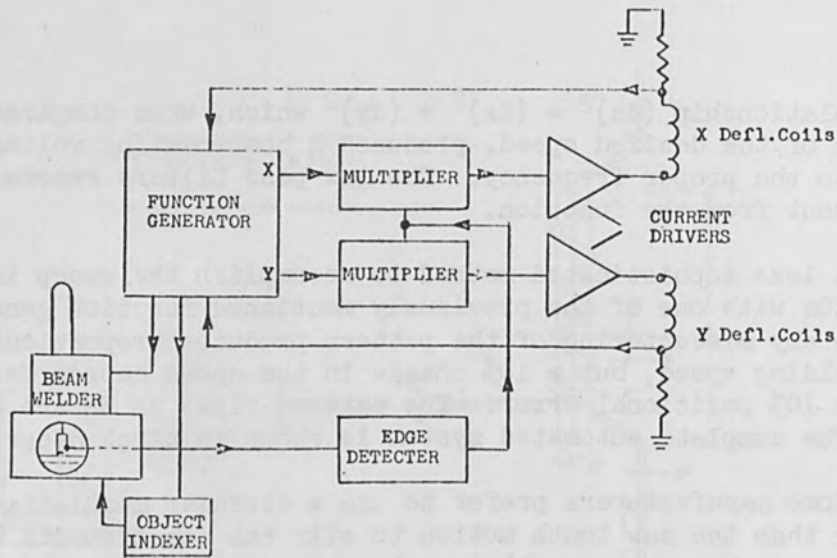


FIG. 12.—Fully automatic welding system.

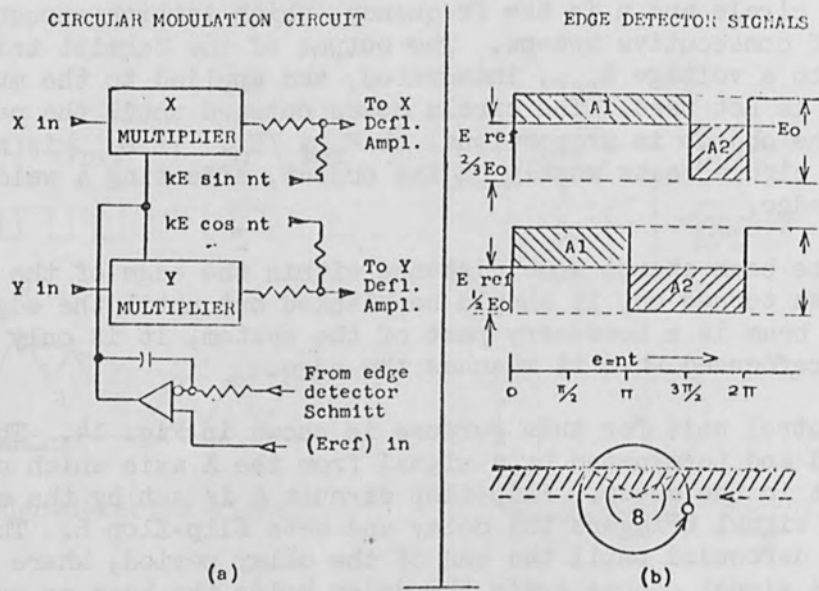


FIG. 13.—Circular modulation.

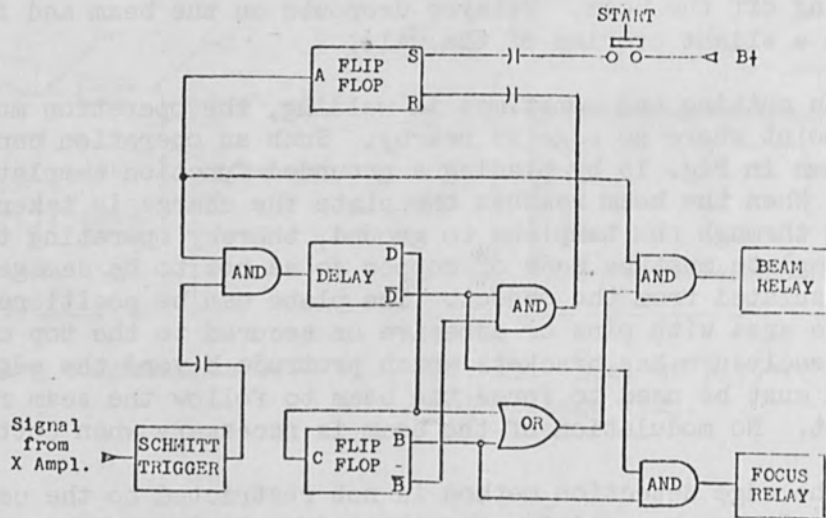


FIG. 14.—Electron-beam control unit.

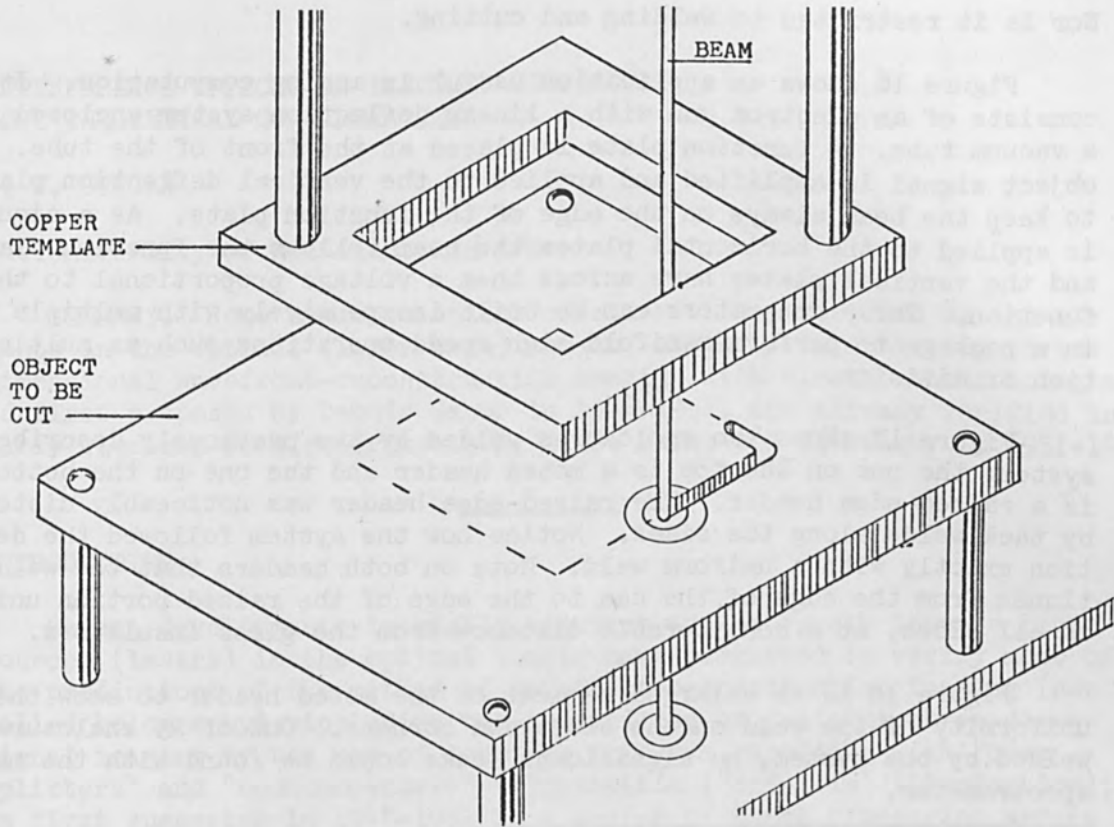


FIG. 15.—Cutting.

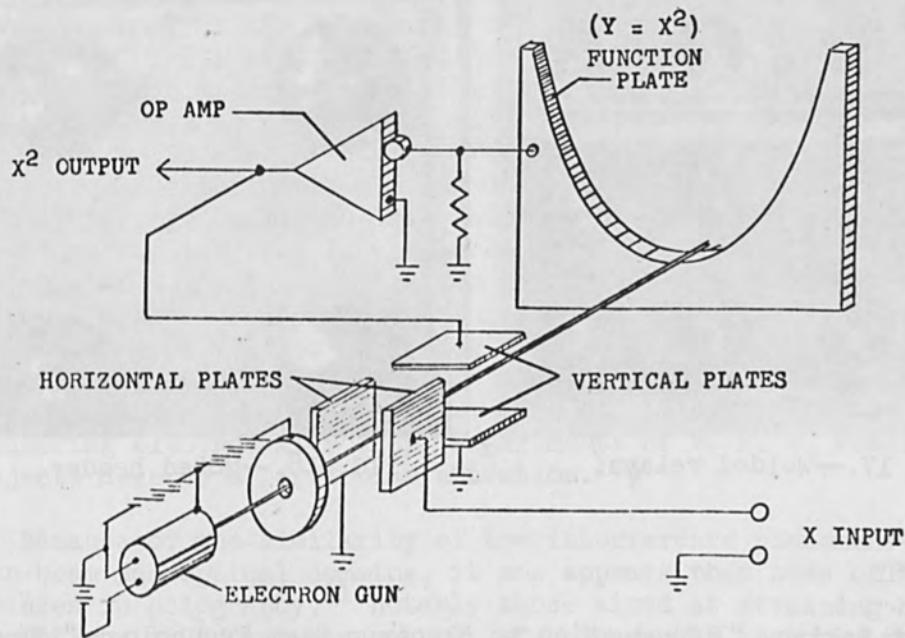


FIG. 16.— $Y = X^2$ function generator.

Nor is it restricted to welding and cutting.

Figure 16 shows an application useful in analog computation. It consists of an electron gun with a linear deflection system enclosed in a vacuum tube. A function plate is placed at the front of the tube. The object signal is amplified and applied to the vertical deflection plates to keep the beam always on the edge of the function plate. As a signal is applied to the horizontal plates the beam follows the function plate, and the vertical plates have across them a voltage proportional to the function. These generators can be built inexpensively with multiple units in a package to perform manifold high speed operations such as multiplication or division.

Figure 17 shows two enclosures welded by the previously described system; the one on the top is a moted header and the one on the bottom is a raised-edge header. The raised-edge header was noticeably distorted by tack welds along the sides. Notice how the system followed the deviation exactly with a uniform weld. Note on both headers that the weld continues from the edge of the can to the edge of the raised portion uniformly on all sides, at a considerable distance from the glass insulators.

Figure 18 is an enlarged segment of the moted header to show the uniformity of the weld on the sides and corners. Out of 25 enclosures welded by the system, no significant leaks could be found with the mass spectrometer.

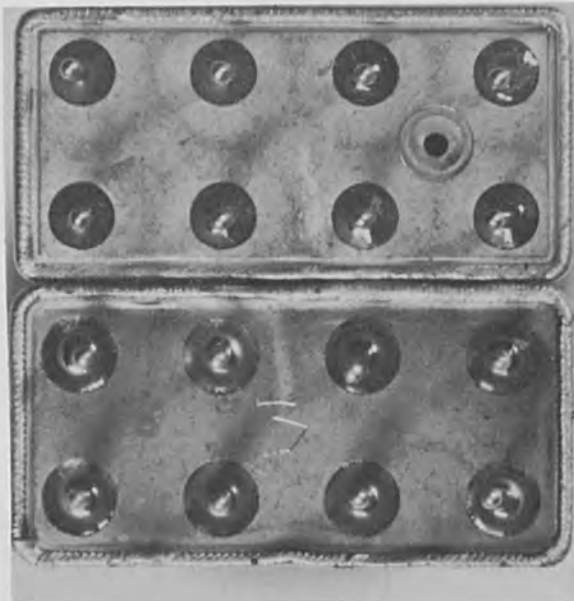


FIG. 17.—Welded relays.



FIG. 18.—Moted header.

BIBLIOGRAPHY

Robert Bakish, "Introduction to Electron Beam Technology," New York, John Wiley & Sons.

J. W. Meier, "Tooling for electron beam metalworking," IEEE Machine Tools Industry Conference, November 1964.

INTERFERENCE EFFECTS IN ELECTRON MICROSCOPY:
SOME THEORETICAL CONSIDERATIONS

G. W. STROKE

The University of Michigan, Ann Arbor

SUMMARY. Some new theoretical considerations, verified by experiments in the optical (laser-beam) domain, may help in achieving three-dimensional wavefront-reconstruction imaging with electron-beam holograms, as first proposed by Dennis Gabor in 1948-1951, and already verified in early electron-beam experiments by M. E. Haine and T. Mulvey in 1951-1952.

INTRODUCTION

Recent developments in highly coherent and extremely intense light sources (lasers) in the optical domain have permitted to verify most of the predictions of the method of wavefront-reconstruction imaging (now called holography), including the possibility of faithful three-dimensional imaging by the use of lensless hologram recording with "beam splitters" and "nonhomocentric" illumination ("off-axis" illumination), as first suggested in 1948-1951 in a series of three pioneering papers by Dennis Gabor.¹⁻³ Images reconstructed from holograms recorded with electron beams were successfully obtained already in 1951-1952 by M. E. Haine and T. Mulvey (using 60-kV electron sources and obtaining 50-Å resolution), who also described some of the conditions required for further improvements.⁴ Recent unpublished experiments by T. E. Everhart and J. Wiesner at the University of California in Berkeley and at the University of Tübingen,⁵ as well as earlier electron beam-splitting experiments initiated in 1952 by L. Marton⁶ (using three single crystal films in tandem to split the amplitudes and then recombine them to produce fringes in a Mach-Zender arrangement) followed by the Fresnel biprism interference experiments performed by Möllenstedt and Düker,⁷ as well as greatly improved electron-beam and electron-microscopy technology⁸ have created a new interest in the three-dimensional wavefront-reconstruction (holographic) imaging application in the electron-beam domain, and hold a new promise for extending to three-dimensional objects the electron-beam microscopy studies of biological subjects, which were initiated by the first electron micrographs of biological subjects, observed in 1934 by L. Marton.⁹ (Even though they were not holographic, the remarkable pioneering electron-microscopy experiments of R. F. W. Pease with living subjects deserve a particular attention.¹⁰)

Because of the similarity of the interference phenomena in the electron-beam and optical domains, it now appears that some of the recent advances in holography,¹¹ notably those aimed at attaining higher-resolutions,¹²⁻¹⁵ and the methods of holographic image synthesis using multiply exposed holograms¹⁶ may prove to be of interest also in the further development of holographic electron-beam microscopy.

Most of the basic considerations regarding these advances have already been given elsewhere¹²⁻¹⁶ and will not be repeated here.

We may recall, in concluding this summary, the two main characteristics of wavefront-reconstruction imaging.

(1) The method of wavefront-reconstruction imaging¹⁻³ is a method of two-step interferometric photography. In the first step, the field scattered by an object, illuminated with coherent light, is made to interfere with "reference field" (coherent background), and the resulting interferogram (hologram) is stored, generally in a photographic emulsion. In the second step, an image of the object may be reconstructed by replacing the hologram into its recording position (or in some equivalent arrangement) and by illuminating it with only the reference beam.

(2) The holograms are wavefront-interferograms, in which the imaging information is generally stored in the form of interference fringes having a diffraction-grating-like appearance (Fig. 1). Clearly, the film grain-spacing in the photographic emulsion must be smaller than the interference-fringe spacing in the hologram. Simple geometric considerations (see Ref. 11, pp. 114-116) permit the computation of the fringe spacing in a hologram recorded by the interference between a wave $\vec{E}_O(x,y,z,t)$ scattered by the object and a plane reference wave $\vec{E}_R(x,y,z,t)$.

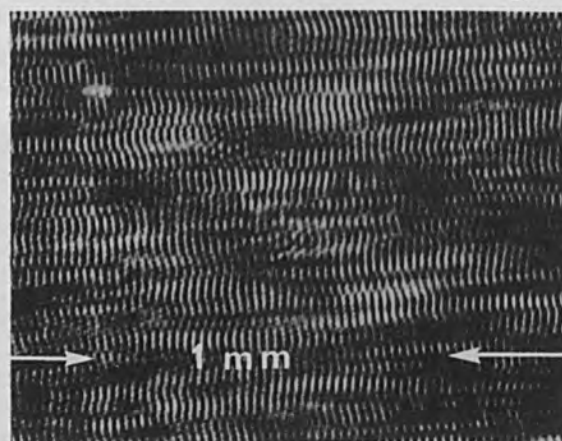


FIG. 1.—Fourier-transform hologram of word HOLOGRAPHY recorded according to Fig. 2(c), in which B = word HOLOGRAPHY and A = point source reference.

The hologram intensity distribution $I(x,y,z)$, written for simplicity in terms of \vec{x} , is equal to

$$I(\vec{x}) = \langle [\vec{E}_O(\vec{x},t) + \vec{E}_R(\vec{x},t)] [\vec{E}_O(\vec{x},t) + \vec{E}_R(\vec{x},t)]^* \rangle \quad (1)$$

$$\text{i.e., } I(\vec{x}) = |\vec{E}_O|^2 + |\vec{E}_R|^2 + \vec{E}_O \vec{E}_R^* + \vec{E}_O^* \vec{E}_R \quad (2)$$

$$\begin{aligned} \text{i.e., } I(\vec{x}) = & |\vec{E}_O|^2 + |\vec{E}_R|^2 + |\vec{E}_O| |\vec{E}_R| e^{i\phi_0} \\ & + |\vec{E}_O| |\vec{E}_R| e^{-i\phi_0} \end{aligned} \quad (3)$$

assuming $\bar{E}_R = |\bar{E}_R| e^{i\phi_R}$ with $\phi_R = 0$ and ϕ_0 the phase of E_0 relative to \bar{E}_R . Equation (3) may be written in the form

$$I(\bar{x}) = |\bar{E}_0|^2 + |\bar{E}_R|^2 + |\bar{E}_0| |\bar{E}_R| 2 \cos \phi_0 \quad (4)$$

The analysis may best be given, according to Toraldo di Francia,¹⁷ as follows. The $\cos \phi_0$ term characterizes the interference fringes, with a phase

$$\phi_0 = \frac{2\pi}{\lambda} \Delta(\bar{x}) \quad (5)$$

The fringe spacing p (along \bar{x}) is given by^{11,17}

$$p = \frac{\lambda}{\partial \Delta(\bar{x}) / \partial \bar{x}} \quad (6)$$

For the case of the Fresnel-transform holograms, obtained by using a plane-wave reference to interfere with the various spherical object waves (Figs. 2a and b), the fringe spacing is generally very close.

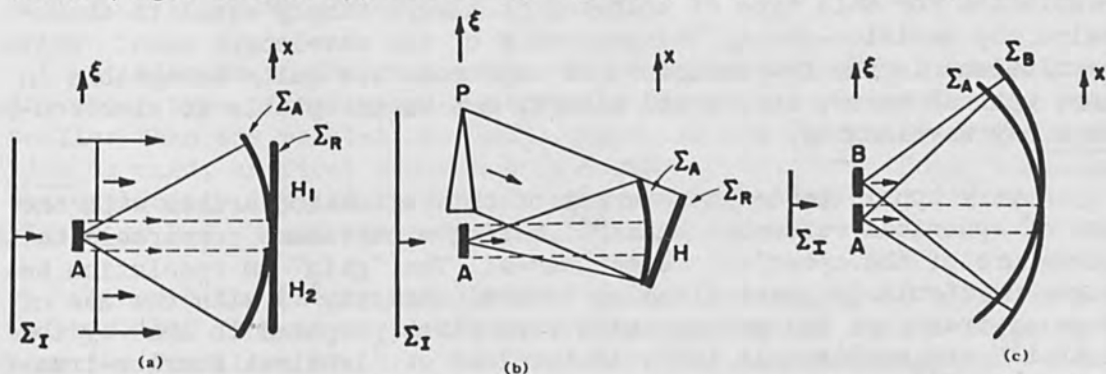


FIG. 2.—HOLOGRAM RECORDING ARRANGEMENTS (after G. W. Stroke et al.²³). (a) and (b) Fresnel-transform hologram-recording arrangements [(a) after D. Gabor,¹ (b) after Cutrona et al.²² and E. N. Leith and J. Upatnieks, *J. Opt. Soc. Am.* 52: 1123, 1962]. Note equivalence of hologram H of Fig. 2(b) with each half H_1 or H_2 of hologram of Fig. 2(a). (In Gabor's original 1948 arrangement,¹ the reference wave was spherical.) (c) Lensless Fourier-transform hologram recording arrangement (after Stroke et al.¹²⁻¹⁵). A = object, B = reference source, P = prism, Σ_I = incident wavefront, Σ_A = object wavefront (described by E_0 in text), Σ_R = reference wavefront (described by E_R in text).

Indeed, one has^{11,17} (apart from constant factors)

$$\Delta_{\text{FRESNEL}} = \sqrt{f^2 + x^2} \quad (7)$$

$$\text{and } p_{\text{FRESNEL}} = \lambda \frac{\sqrt{f^2 + x^2}}{x} \quad (8)$$

$$\text{i.e., } p_{\text{FRESNEL}} = \frac{\lambda}{\sin i'} \quad (9)$$

where i' is the angle of diffraction, as seen from the object, in the usual microscopic sense. Significantly, the fringe spacing is seen to decrease with the wavelength, becoming very small compared to the emulsion grain, at short wavelengths and large angles of diffraction.

For instance, with an emulsion grain of 0.3 micron (3 000 Å) (corresponding to the best available Kodak 649F high-resolution plates) the use of $\lambda = 0.05 \text{ Å}$ (corresponding to 50-kV electrons) and a plane-wave reference wavefront, would limit the angle of diffraction to 1.7×10^{-5} rad, corresponding to a resolution of only 6 000 Å.

In fact, it may be readily shown (Ref. 11, p. 114) that the object resolution for this type of hologram is always simply equal to about twice the emulsion-grain, independently of the wavelength used! While resolutions in the few-thousands of angstroms are quite acceptable in most optical cases, they would clearly not be acceptable at electron-beam or x-ray wavelengths.

A very considerable improvement of this situation arises with the use of spherical reference beams¹⁻⁵ having a curvature comparable to the curvature of the spherical object waves. The "gain" in resolution becomes particularly great (tending towards infinity¹⁷) with the use of Fourier-transform holograms, which were first proposed in 1964 by the author¹² and realized in 1965, in the form of "lensless Fourier-transform holograms."¹³

LENSLESS FOURIER-TRANSFORM HOLOGRAMS

It was first shown by the author¹³ (see also Ref. 11, pp. 116-137) that a very considerable gain in object resolution (exceeding several orders of magnitude) compared to the Fresnel-transform holograms could be obtained if the holograms were recorded with a spherical reference beam centered near the object. Here we give an analysis of the "gain" in resolution recently derived by G. Toraldo di Francia.¹⁷ With reference to Fig. 2(c) one has

$$\Delta_{\text{FOURIER}} = \sqrt{f^2 + x^2} - \sqrt{f^2 + (x - \xi_0)^2} \cong \frac{\xi_0 x}{\sqrt{f^2 + x^2}} \quad (10)$$

to which corresponds a fringe spacing

$$p_{\text{FOURIER}} = \frac{f\lambda}{\xi_0 \cos^3 i'} \quad (11)$$

The "gain" G in object resolution is

$$G = \frac{P_{\text{FOURIER}}}{P_{\text{FRESNEL}}} = \frac{f}{\xi_0} \frac{\sin i'}{\cos^3 i'} \quad (12)$$

where i' is the angle of diffraction, in the usual sense, ξ_0 is the distance of the center of gravity of the object from the center of the reference source, in the ξ plane, and f is the distance of the object plane (ξ plane) from the hologram.

It is readily seen that the "gain" G will tend to infinity for angles of diffraction $i' \rightarrow 90^\circ$. Even for an angle of diffraction slightly greater than 10° , for which $\sin i' / \cos^3 i' \cong 0.18$, the gain may be very considerable. For instance, with $f/\xi_0 = 1\ 000$ —a not unusual value (say $f = 100$ mm, $\xi_0 = 0.1$ mm) the gain will attain 200.

One other result of these investigations may be of interest in view of electron microscopy.

HOLOGRAPHIC IMAGING WITH RESOLUTION-RETRIEVING COMPENSATION FOR THE EFFECT OF EXTENDED REFERENCE SOURCE SIZE

Attainment of the resolution with Fourier-transform as well as with any other type of hologram requires the use of a reference-source diameter smaller than the resolution limit sought, unless "a posteriori" compensation is used, as first described by Stroke et al.^{14,15} Such "compensation" was explicitly implied in Gabor's papers of 1949 and 1951,^{2,3} notably in Fig. 4 of Ref. 3 and the corresponding discussion.

Because the theory involved in the discussion may be given in a form which we now find to be particularly general, we use this section to present the formalism of this "resolution-retrieving compensation"^{11,14,15} for illustration.

The essence of a compact treatment of holography (which may perhaps be considered as a "reformulated general theory of holography") consists in dealing with the electric-field distributions in the hologram plane, i.e., with the wavefronts, without relating them explicitly to the object and reference-source fields, except when this may be necessary (e.g., for purposes of "hologram interferometry"¹⁸).

In terms of the previously defined notation, the hologram intensity distribution is again

$$I(\vec{x}) = |\vec{E}_O|^2 + |\vec{E}_R|^2 + \vec{E}_O \vec{E}_R^* + \vec{E}_O^* \vec{E}_R \quad (2)$$

It may be readily shown¹¹ that the electric field $\vec{E}_T(\vec{x})$, reconstructed by illuminating the hologram with a wave of unit amplitude, has a leading term equal to $I(\vec{x})$, under a wide variety of readily achievable conditions, including the so-called "bleached" or "phase" holograms,¹⁹ and the recently described "white-light reflection" holograms.²⁰

The "images" reconstructed from the holograms are obtained by a spatial Fourier transformation of Eq. (2). It may be readily shown that the three terms ($|\bar{E}_O|^2 + |\bar{E}_R|^2$), $\bar{E}_O\bar{E}_R^*$, and $\bar{E}_O^*\bar{E}_R$ are angularly separated whenever the centers of gravity of the "object" and the "reference source" are spatially separated in the recording. This result was already explicitly shown by Gabor in his 1949 paper² (see the reproduction of the paper in Ref. 11, p. 189) when he discussed nonhomocentric illumination: "In beams which are only approximately homocentric the second image is no longer sharp, but effective separation can always be achieved if the object is sufficiently small, and if certain positions are avoided." Also, regarding the use of beam splitters, Gabor says that "it is very likely that in light optics, where beam splitters are available, methods can be found for providing the coherent background which will allow better separation of object planes, and more effective elimination of the 'twin wave' than the simple arrangements which have been investigated" (Ref. 11, p. 219).

The verification of the "beam-splitter" recording of holograms became particularly spectacular²¹ with the long coherence lengths of lasers, which vastly exceeded the coherence lengths of the ordinary mercury sources available to Gabor, and which follow the introduction of the so-called "off-axis" hologram recording method first described by Cutrona et al. in 1960.²² Stroke et al.²³ finally showed that it was possible to demonstrate with the aid of lasers that no difference existed between the original Gabor "in-line" holograms and the "off-axis" holograms of Cutrona, Leith, et al.^{21,22} inasmuch as each half of a Gabor "in-line" hologram is in effect an "off-axis" hologram (Figs. 2a and b). These considerations are, of course, particularly relevant to electron microscopy, where, for the moment, only low coherence lengths are available, and where "in-line" Gabor holograms rather than Fourier-transform holograms may be preferable. (Because of their very low resolution capability, it is unlikely that "off-axis" Fresnel-transform holograms of the Cutrona-Leith-Upatnieks variety,^{21,22} recorded with plane reference wavefronts, will be of any interest in high-resolution electron microscopy).

We now return to the discussion of the image reconstruction from the hologram described by Eq. (2). We consider, for simplicity, only one of the "separable" terms, e.g., the term

$$\bar{E}_O\bar{E}_R^*$$

If the hologram were to be illuminated with a plane wave, the complex field amplitude in the reconstructed image is equal to

$$T[\bar{E}_O] \star T[\bar{E}_R^*] \quad (13)$$

where $T[\]$ indicates a spatial Fourier transformation and \star a spatial correlation.¹¹

It is immediately clear that the reconstructed image (i.e., its complex amplitude $T[\bar{E}_O]$) is "smeared" out by correlation (similar to a convolution, except for a centro-symmetric rotation about an axis normal to the image "plane"), with the image $T[\bar{E}_R]$ of the source!!

However, if the hologram were to be illuminated with a wave \bar{E}_R , the leading image term would have a separable image-wave term

$$\bar{E}_R, \bar{E}_R^* \bar{E}_O \quad (14)$$

It is clear (as first shown by Stroke et al.^{14,15}) that a completely faithful and theoretically fully resolved (i.e., only "diffraction-limited") image will be reconstructed under the condition that

$$\bar{E}_R, \bar{E}_R^* = 1 \quad (15)$$

This condition may be readily achieved under a wide variety of conditions. For example (Refs. 14, 15, and Ref. 11, pp. 116-127), one can show that the condition of Eq. (15) is equivalent to stating that

$$T[\bar{E}_R,] \times T[\bar{E}_R^*] = \delta \quad (16)$$

a delta function. In other words, resolution-retrieving "compensation" of the image (i.e., diffraction-limited imaging) will be achieved if a hologram recorded with an extended source (rather than a point-source) having a complex-amplitude transmission or reflection $T[\bar{E}_R]$, is illuminated, in the reconstruction, with a wave \bar{E}_R , originating from a source $T[\bar{E}_R,]$. Experiments in the optical domain¹¹ have fully borne out these predictions. For example, in one case, resolution-retrieving compensation was achieved with an extended source having a "diameter" exceeding 2 000 times the resolution limit obtained in the reconstruction.

CONCLUSION AND ACKNOWLEDGMENT

We have given only a few examples of the possibilities of extending to holographic electron microscopy some of the results of our recent investigations of high-resolution holography which were primarily aimed at extensions to x-ray microscopy. Several aspects of our investigations have been and continue to be carried out in collaboration with Prof. Dennis Gabor of Imperial College in London, whose many kind comments and suggestions are here again acknowledged with much gratitude. The assistance of the many students of the author has also already been previously singled out, notably by co-authorship on the papers; it is again acknowledged with much pleasure. The private communication from Prof. G. Toraldo di Francia¹⁷ is also acknowledged with much gratitude, together with an appreciation of his kind interest in our work and his many fruitful comments.

Finally, we wish to acknowledge the kind assistance of the National Science Foundation in granting support for this research.

Early aspects of the ideas in this paper were first presented on 26 May 1966 at the Swiss Federal Institute of Technology, Zürich, upon invitation from Prof. W. F. Berg, director of the ETH Institute for Photography; and some further developments at the Brooklyn Polytechnic Symposium on Modern Optics, in New York, on 24 March 1967.

REFERENCES

1. D. Gabor, *Nature* 161: 777-778, 1948.
2. D. Gabor, *Proc. Roy. Soc. (London)* 197: (A) 454-487, 1949.
3. D. Gabor, *Proc. Phys. Soc. (London)* 64: 449-469, 1951.
4. M. E. Haine and T. Mulvey, *J. Opt. Soc. Am.* 42: 763-773, 1952.
5. T. E. Everhart and J. Wiesner, private communications (1966, 1967).
6. L. Marton, *Phys. Rev.* 85: 1057, 1952.
7. G. Möllenstedt and H. Düker, *Z. Physik* 145: 377-397, 1956.
8. For a general background, see, for instance, R. D. Heidenreich, "Fundamentals of Transmission Electron Microscopy," Interscience Publishers, New York, 1964.
9. L. Marton, *Ann. Bull. Soc. Roy. Sci. Med. Nat. Bruxelles* 92: 106, 1934.
10. R. F. W. Pease, T. L. Hayes, A. S. Camp, and N. M. Amer, *Science* 154: 1185-1186, 1966.
11. For a general background, see, for instance, G. W. Stroke, "An Introduction to Coherent Optics and Holography," Academic Press, New York, 1966, (includes reprints of the three Gabor wavefront-reconstruction imaging papers, Refs. 1-3).
12. G. W. Stroke and D. G. Falconer, *Physics Letters* 13: 306-309, 1964.
13. G. W. Stroke, *Appl. Physics Letters* 6: 201-203, 1965.
14. G. W. Stroke, R. Restrck, A. Funkhouser, and D. Brumm, *Physics Letters* 18: 274-275, 1965.
15. G. W. Stroke, R. Restrck, A. Funkhouser, and D. Brumm, *Appl. Physics Letters* 7: 178-179, 1965.
16. D. Gabor and G. W. Stroke, R. Restrck, A. Funkhouser, and D. Brumm, *Physics Letters* 18: 116-118, 1965.
17. G. Toraldo di Francia, private communication to G. W. Stroke (28 March 1966).
18. K. A. Stetson and R. L. Powell, *J. Opt. Soc. Am.* 56: 1161-1166, 1966.
19. W. T. Cathey, *J. Opt. Soc. Am.* 55: 457, 1965; *ibid.* 56: 1167-1171, 1966.
20. G. W. Stroke and A. Labeyrie, *Physics Letters* 20: 368-370, 1966.
21. E. N. Leith and J. Upatnieks, *J. Opt. Soc. Am.* 54: 1295-1301, 1964.
22. L. J. Cutrona, E. N. Leith, C. J. Palermo, and L. J. Porcello, *IRE Trans. IT-6*: 386-400, 1960.
23. G. W. Stroke, D. Brumm, A. Funkhouser, A. Labeyrie, and R. C. Restrck, *Brit. J. Appl. Phys.* 17: 497-500, 1966.

APPLICATIONS OF FRAUNHOFER HOLOGRAMS

B. J. THOMPSON

Technical Operations, Inc., Mountain View, California

ABSTRACT. Fraunhofer holograms are formed by the coherent addition of the Fraunhofer (far-field) diffraction pattern of an object and a background; the background illumination is usually provided by light transmitted by the area surrounding the object but may be supplied as a separate reference beam. This rather specialized form of holography has important applications in the determination of particle-size distributions in the range from a few microns and upwards. Records of dynamic situations may be captured by using a pulsed ruby laser as a light source. The technique has been applied to a variety of particle sizing problems, including the measurement of naturally occurring fog and test chamber and laboratory aerosols. Other areas of interest are in bubble-chamber photography, small rocket engine studies, and cloud physics research.

INTRODUCTION

Image formation by the holographic or wavefront reconstruction techniques is basically a two-step imaging process in which an intermediate photographic record (hologram) is made. The hologram is not itself an image, but contains all the visual information from the object being recorded. When the hologram is illuminated coherently, an image can be formed that has all the usual properties of an aerial image. The techniques now available are many and varied and a number of possible applications for holography seem to be finally emerging as new and useful technological and scientific tools. The reader is referred to the several popular review articles for details and further references (Leith and Upatnieks,¹ Collier,² Thompson and Parrent³).

It is the purpose of this paper to discuss one particular application of holography that is probably a forerunner of holographic applications since it has already produced useful measurements in a variety of situations. This application is, of course, to the general area of particle sizing. (A bibliography of papers dealing with this application is given in the Appendix.)

The problem under consideration here is the rather special one of measuring the size and shape of particles in a dynamic aerosol. Consider the problem of trying to record with conventional photography the image of two particles, 10 microns in diameter, which are separated longitudinally by 1 cm. It is impossible to build a conventional camera that can record both particles simultaneously. A microscope that can resolve the 10-micron particles would have a depth of field on the order of 100 microns, not 1 cm. Likewise, recording two 1-mm particles separated by several hundred centimeters is an equally difficult problem. But both of these recording problems can be solved by using holography. This is

particularly useful in a dynamic situation when it is not possible to focus and record a sample of particles separately.

FRAUNHOFER HOLOGRAMS

Our particular solution to the problem depends on a development of holography that, of course, stems from the basic concepts of Gabor.⁴ To put this background in its proper perspective we must recall that the original work of Gabor and the subsequent developments at the University of Michigan have used Fresnel diffraction patterns plus a coherent background. The method of adding the coherent background or reference wave has led to many interesting discussions. The key difference in our work is that we have pursued the use of Fraunhofer diffraction patterns with a coherent background—often called Fraunhofer (far-field) holograms to distinguish them from Fresnel holograms—for the solution of the problem posed above.

The terms Fresnel and Fraunhofer diffraction are classical terms in optics to describe different regions of the diffracted field. Often the Fresnel region is called the near field and the Fraunhofer region the far field. For example, for an aperture of diameter $2a$ illuminated with collimated light, the far field is usually considered to be a distance z given by the inequality $z > (2a)^2/\lambda$ in which λ is the wavelength of the incident light. A similar inequality may be stated for an opaque object of diameter $2a$ in an otherwise transparent field.

In Fig. 1 a collimated beam of coherent light illuminates the object. We can again define a near field and a far field for the object. The background light needed to form the hologram is either provided by the undiffracted light as in Fig. 1(a) or by a separate reference beam⁵ provided by the beam splitter and mirror as in Fig. 1(b).

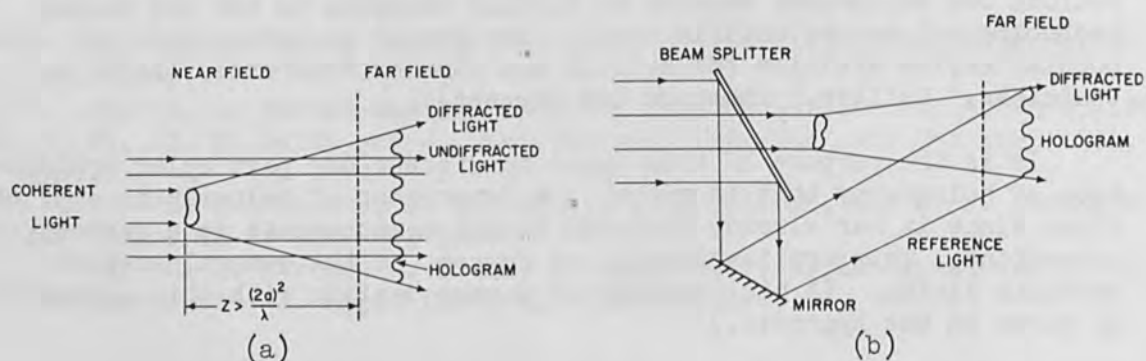


FIG. 1.—Formation of a Fraunhofer (far field) hologram.

Therefore, to form the Fraunhofer holograms, we must expose a photographic medium placed at a distance behind the object that is greater than $(2a)^2/\lambda$. This photographic record is then illuminated again with a coherent beam, and an image is formed at exactly the same distance behind the plate as the plate was from the object. This image shows the cross-sectional shape of the original object.

One of the great drawbacks to the original scheme used by Gabor was the troublesome virtual image that appears as an out-of-focus image in the plane of the real image. This is annoyingly true of Fresnel holograms if they are made with the background light provided in the way indicated in Fig. 1(a). However, with the Fraunhofer holograms formed in the same way the virtual image, although it is still present, contributes only a very small error term because it exists essentially at infinity, since the condition $z > (2a)^2/\lambda$ is an approximation to infinity. The conditions of an off-axis reference (e.g., Fig. 1b) always provide separation of the real and virtual images in the reconstruction since the two images are separated angularly. In fact the system of Fig. 1(b) will produce both types of hologram at the same time. Such a hologram is shown in Fig. 2(a) and the zero-order reconstruction equivalent to the hologram record of the system of Fig. 1(a) in Fig. 2(b); the real image produced by the reference-beam hologram Fig. 2(c). It will be noted that Fig. 2(b) shows very little evidence of the virtual image term.

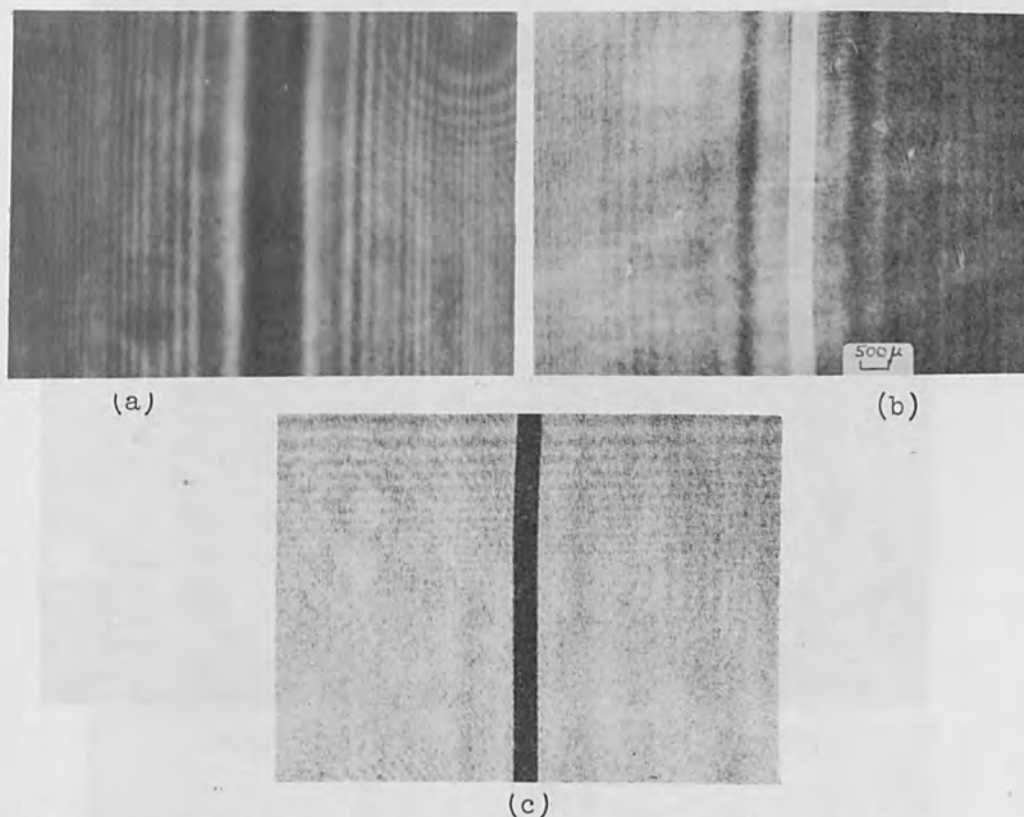


FIG. 2.—Hologram (a) formed by system of Fig. 1(a); (b) reconstruction from hologram formed with coaxial reference beam; (c) reconstruction from hologram formed by off-axis reference beam.

APPLICATIONS OF FRAUNHOFER HOLOGRAMS

Initially this particular branch of holography was developed for the specific purpose of measuring the small dynamic aerosol particles that constitute naturally occurring fog. However, the technique has a much wider application.

SMALL PARTICLE SIZING. The main aim of particle sizing is to deal with dynamic situations with minimum disturbance of the sample. Various types of hologram camera systems using the basic principles of Fraunhofer holography have been built in 1963 and 1964. The first systems were designed to record holograms of naturally occurring fog particles that ranged in size from a few microns to 200 microns in diameter. The system was capable of recording 30 frames a minute on Kodak SO-243 70-mm film. The sample volume was 7 cm^3 and a magnification of 5x was used before the hologram was recorded. The illumination was provided by a 10^6 -W pulsed ruby laser with a pulse length of 0.5×10^{-6} sec. In fact it is of interest to note that this was the first use of a pulsed laser for hologram recording. A typical hologram of an aerosol recorded by this system is shown in Fig. 3. It will be noted that essentially each droplet or particle has associated with it a separate hologram. More highly dynamic aerosols have been studied with a different system using a 10-MW, 20-ns pulsed ruby laser. The duty cycle in this instant was 1 frame/min.

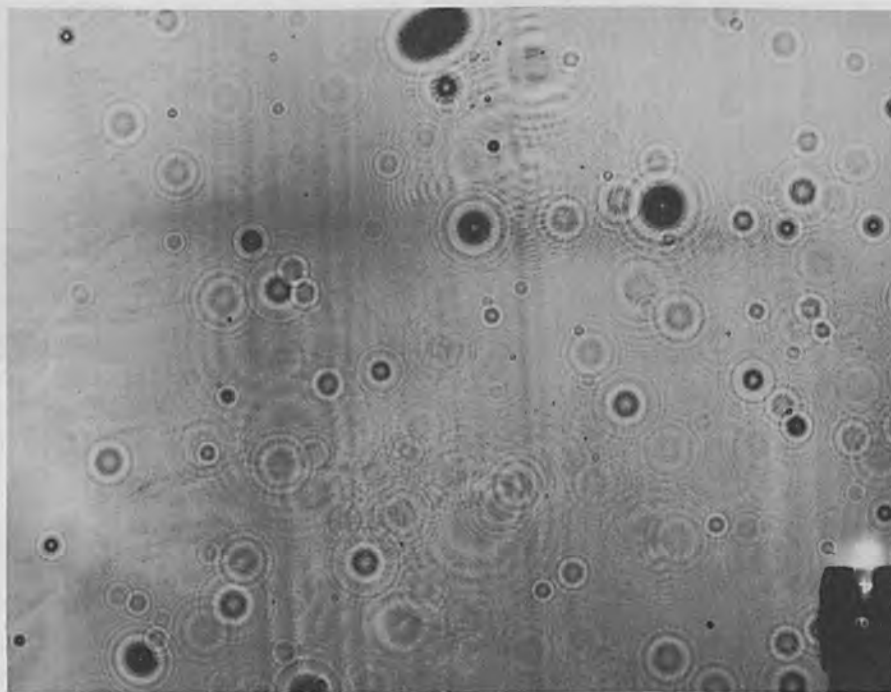
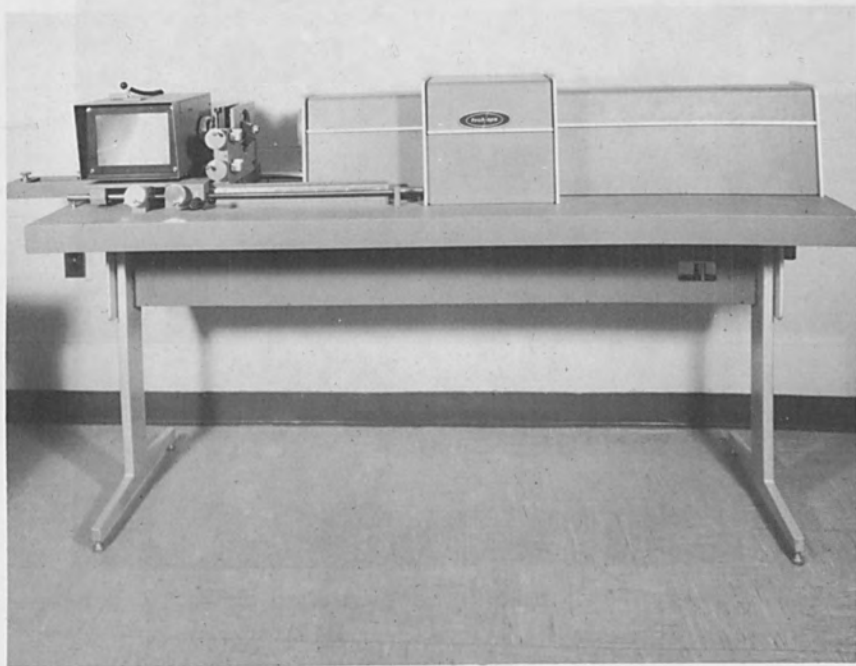
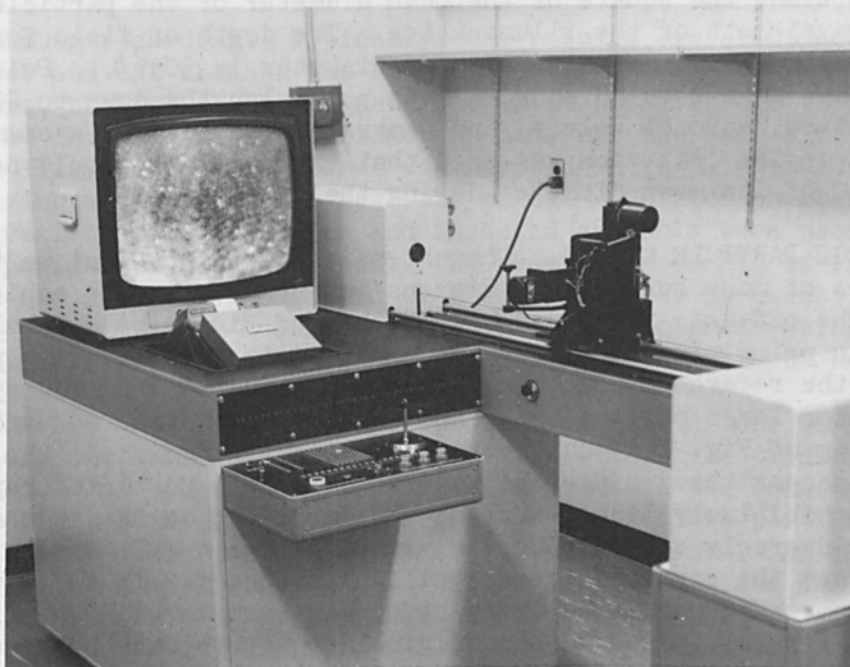


FIG. 3.—Typical hologram of an aerosol.

To produce an image from the hologram record, it is illuminated coherently with the light from a helium neon gas laser and the reconstruction is magnified and displayed on a TV monitor or viewing screen. Two different versions of a reconstruction apparatus are shown in Fig. 4. Figure 4(b) is a semi-automatic system specifically designed for reducing fog particle-size data in which the recording plane is fixed and the hologram is scanned up and down along the axis. A typical reconstruction as photographed off the TV screen is shown in Fig. 5. Each raster line is approximately 2 microns at this enlargement.



(a)



(b)

FIG. 4.—Two hologram readout devices.



FIG. 5.—Typical image photographed from TV screen.

The Fraunhofer hologram camera systems for particle-size analysis have the following characteristics. The hologram is recorded in the far field of the particles at a distance that is effectively infinite from the particle. In a practical camera design, this distance is between 1 and 50 times the square of the mean diameter of the particle divided by the wavelength of the illumination. The depth of field for recording and reconstructing particles of mean diameter is $50d^2/\lambda$. Pulsed ruby lasers have been used as sources with pulse lengths down to 20 ns. The illumination, aerosol volume, and camera are in line on a common optical axis. A design criterion was used that the particle should not move more than 1/10 of its mean diameter during the exposure.

LARGE PARTICLE SIZING. The extension of this technique to larger particles of many hundreds of microns and upwards can be achieved in two ways. The off-axis reference beam method of Fig. 1(b) will always be useful in principle except that in practice it is not always possible to provide the reference beam because of configurations of the system. Of course, for large particles the near-field region will be used. However, the system of Fig. 1(a) can be used if slightly modified; the modification is necessitated since the far field for big particles rapidly becomes prohibitively large. Unless the far field is used the reconstruction is adversely affected by the virtual image term. Before the hologram is recorded the particle is demagnified and the far field is then calculated from the demagnified image size. An example of this principle is shown in Fig. 6; (a) shows the original object (b) the hologram of the demagnified object and (c) the reconstructed image magnified back up to the original scale of the object. This technique could find important applications in such fields as raindrop sizing where sample volumes several meters in depth could be handled in a single exposure.

BUBBLE-CHAMBER PHOTOGRAPHY. Recently feasibility tests have been conducted to determine the applicability of holographic techniques to

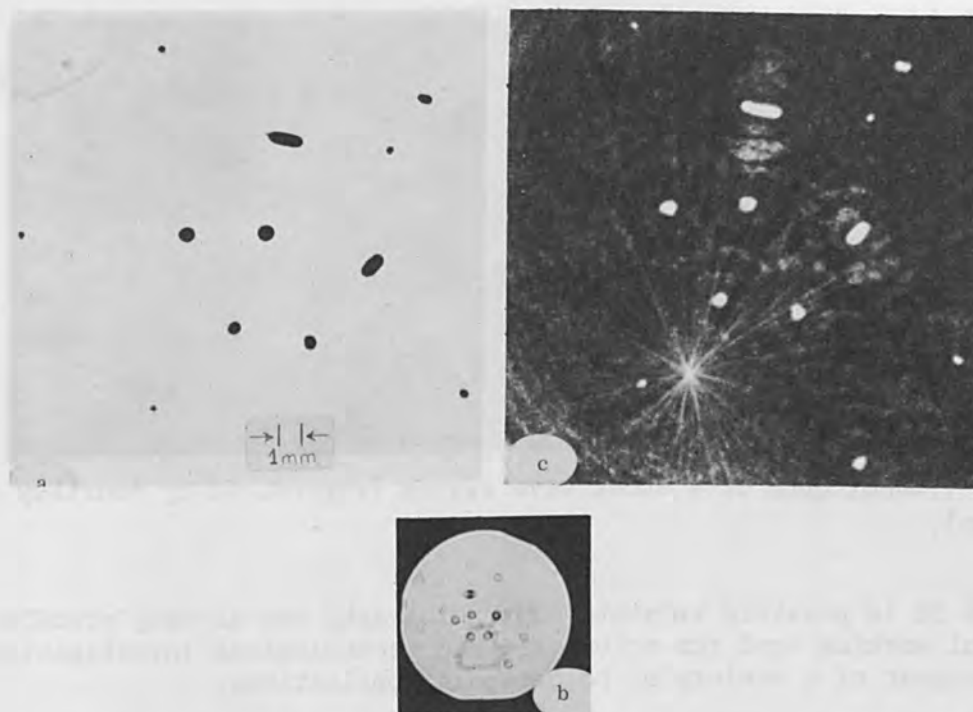


FIG. 6.—Holography of large particles: (a) original object; (b) hologram of demagnified object; (c) reconstructed and magnified image.

bubble-chamber recording. Typically, the bubbles are about 400 microns in diameter and the chamber may be as large as 132 cm or even 200 cm. Furthermore, because of the magnet yoke it is not possible to go straight through the chamber; it is necessary to come out the same side as the source of illumination. A scheme was devised where this could be accomplished using a mirror at the rear end of the simulated chamber. In the tests, a variety of fixed wires and injected aerosols were used to determine the parameters of the system. The resolution ($\pm 3\%$) of individual particles can readily be obtained over sample depths in excess of those required. The location accuracy in depth is not so great being approximately 20 particle diameters; angular accuracy of tracks can be $\pm 4^\circ$.

SHOCK-WAVE RECORDING. As a by-product of some of our work on highly dynamic aerosols, the shock waves associated with their production can be recorded. The optical-density variations across the boundary of the shock wave introduces a path difference between the two portions of the incident beam. Hence an interference pattern is formed. An illustration of this result is shown in Fig. 7. This type of technique has also been suggested by Tanner⁶ and Horman⁷ for interferograms and schlieren photography.

SUMMARY

In this article the field of Fraunhofer holography has been surveyed from the point of view of the applications of this particular technique. Over the last few years these methods have produced useful results in areas that conventional techniques were extremely difficult to apply.



FIG. 7.—Hologram of a shock wave system (reproduced by courtesy of Craig Allen).

Hence it is possible to state that holography has already produced a useful working tool for scientific and technological investigation, the forerunner of a variety of holographic applications.

REFERENCES

1. E. N. Leith and J. Upatnieks, *Scientific American* 212: 6, June 1965.
2. R. J. Collier, *IEEE Spectrum* 4: 67, July 1966.
3. B. J. Thompson and G. B. Parrent, Jr., *Science Journal* 3: 1, 42, 1967.
4. D. Gabor, *Nature* 161: 777, 1948.
5. E. N. Leith and J. Upatnieks, *J. Opt. Soc. Am.* 53: 1377, 1963.
6. L. H. Tanner, *J. Sci. Instr.* 43: 81, 1966.
7. M. H. Horman, *Appl. Optics* 4: 333, 1965.

APPENDIX: FRAUNHOFER HOLOGRAPHY BIBLIOGRAPHY

- B. J. Thompson, "Diffraction by opaque and transparent particles," *SPIE* 2: 43, 1964.
- G. B. Parrent, Jr., and B. J. Thompson, "On the Fraunhofer (far field) diffraction patterns of opaque and transparent objects with coherent background," *Optica Acta* 11: 183, 1964.
- B. A. Silverman, B. J. Thompson, and J. H. Ward, "A laser fog disdrometer," *J. Appl. Met.* 3: 792, 1964.
- B. J. Thompson, "A new method of measuring particle size by diffraction techniques," *Japan J. Appl. Phys. (Suppl. I)* 4: 302, 1965.
- J. B. DeVelis, G. B. Parrent, Jr., and B. J. Thompson, "Image reconstruction with Fraunhofer holograms," *J. Opt. Soc. Am.* 56: 423, 1966.
- B. J. Thompson, G. B. Parrent, Jr., J. H. Ward, and B. Justh, "A readout technique for the laser fog disdrometer," *J. Appl. Met.* 5: 343, 1966.
- B. J. Thompson and J. H. Ward, "Particle sizing—The first direct use of holography," *Sci. Res.* 1: 10, 37, 1966.
- J. H. Ward and B. J. Thompson, "In-line hologram system for bubble-chamber recording," *J. Opt. Soc. Am.* 57: 275, 1967.

THE LASER ALIGNMENT SYSTEM FOR THE
STANFORD 3-km-LONG ACCELERATOR

W. B. HERRMANNSFELDT, J. J. SPRANZA, M. J. LEE, and K. R. TRIGGER

Stanford University, California

INTRODUCTION

The Stanford 3-km-long linear electron accelerator¹ is aligned with a laser system. The system consists of a He-Ne laser, a photoelectric detector, and a large number of lenses, one of which is located at each point to be aligned.

The basic idea of the SLAC alignment system is illustrated in Fig. 1. A straight line is defined between a point source of light L and a detector D. The light source is a helium-neon laser. The detector consists of a mechanical scanning system and a photomultiplier with suitable output equipment capable of resolving a shift of 0.025 mm at any of the 277 support points. At each support point, a target T is supported on a remotely actuated hinge. Three additional targets are mounted on monuments, such as the one at M, which are 60-cm-diameter pillars based on

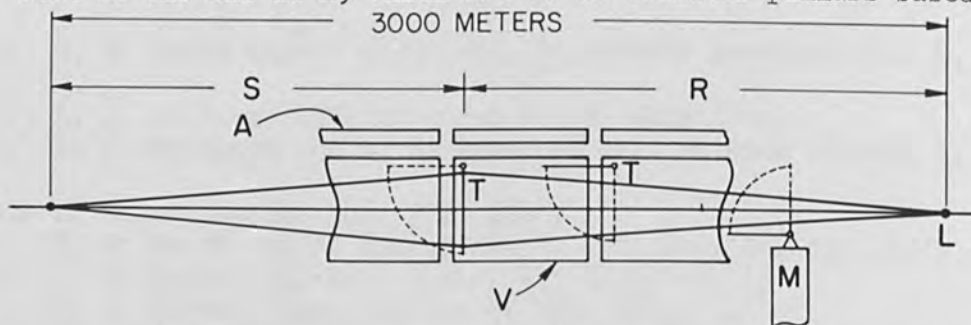


FIG. 1.—Schematic illustration of the SLAC alignment system. A target T, which is actually a rectangular Fresnel lens, focuses the light source L to an image at the detector D. There are 294 adjustable targets and 3 monument targets such as at M, which are attached to deep pillars. V is a vacuum pipe 12 m long and 60 cm in diameter.

bed rock. To check the alignment at a desired point, the target at that point is inserted into the light beam by actuating the hinge mechanism. The target is actually a rectangular Fresnel lens with the correct focal length so that an image of the light source is formed on the plane of the detector. This image is then scanned by the detector in both the vertical and the horizontal directions to determine the displacement of the target from the predetermined line.

The targets are mounted in a 60-cm-diameter aluminum pipe (see Fig. 2) which is the basic support girder for the accelerator. The support girder is evacuated to about 0.01 torr to prevent air refraction effects from distorting or deflecting the alignment image. If any adjustments are required, the support girder is moved by means of a pair of vertical screw jacks and a sidewall screw jack.

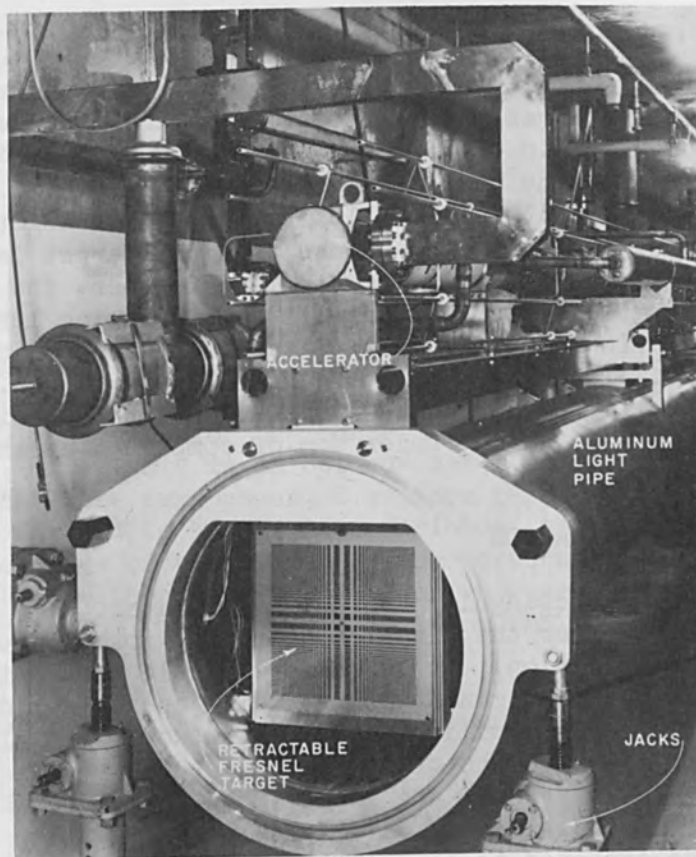


FIG. 2.—Photograph of an installed accelerator segment taken prior to installation of the next segment. Adjacent segments are joined by a welded bellows.

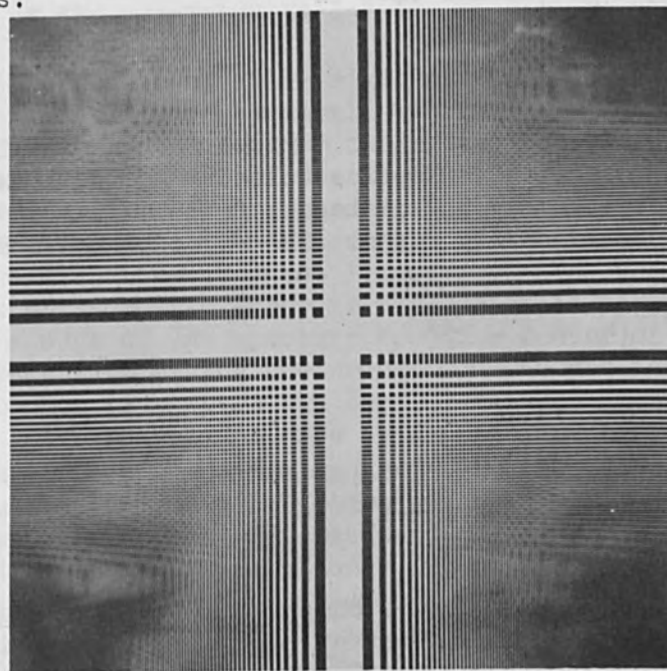


FIG. 3.—The crossed pattern of the rectangular Fresnel lens. The actual lenses have open spaces in the dark areas. The opaque center ribbon, 1 cm in width, provides added structural support.

LIGHT SOURCE

The light source for the alignment system is a standard model of a commercial helium-neon gas laser. The targets are designed for the fundamental visible wavelength of 6328 Å. A short-focal-length lens is mounted on the laser to cause the beam to diverge sufficiently to illuminate fully the closest target, which is about 15 m away. This target has a diagonal dimension of about 15 cm, but to insure that the target is evenly illuminated and to reduce the pointing requirement further, the beam is diverged to about twice that diameter. Even with the diverging lens, the intensity of the images as viewed on a ground glass screen is sufficient to be viewed in subdued light. The laser output is from 1.0 to 3.0 mW. The laser is located in a special room outside of the accelerator housing. The housing and the laser room are buried under 8 m of compacted earth for radiation shielding.

LENS DESIGN AND FABRICATION

The targets are rectangular Fresnel zone plates. The rectangular design is preferred over the classical circular zone plate, primarily for reasons of fabrication. It is easier to rule straight lines than circles, and the circular zones would require special spiders for supports. The basic scheme would of course also work with glass lenses. The overwhelming objection to glass is that ordinary glass turns dark in high radiation fields such as are found along the linear accelerator. Also the cost for glass lenses, particularly of radiation resistant material, could be expected to be much greater.

The Fresnel pattern is shown in Fig. 3. The distance from the center line of the target to the nth slot is

$$X_n = (\lambda rs / 2\ell)^{\frac{1}{2}} (4n)^{\frac{1}{2}} \quad (1)$$

This is the same expression that is derived for the radius of the 2n Fresnel zone in most standard optics texts.² In it, λ is the wavelength, r and s are respectively the distances from the target to the laser and to the detector, and $\ell = r + s$. The edges of the nth slot are at

$$X_{n,i} = \left(\frac{\lambda rs}{2\ell} \right)^{\frac{1}{2}} (4n + d - 1)^{\frac{1}{2}} \quad (2)$$

$$\text{and } X_{n,o} = \left(\frac{\lambda rs}{2\ell} \right)^{\frac{1}{2}} (4n + d + 1)^{\frac{1}{2}}$$

The subscripts "i" and "o" denote the inner and outer edges of a slot, respectively. The arbitrary constant d selects the point at which the slot edge will be located in each Fresnel zone. For example, the values 0.0 and 2.0 for d have the effect of making two patterns which are the inverse or negatives of each other.³

The procedure for choosing an optimum set of design parameters may be illustrated by referring to a Cornu spiral as in Fig. 4. The length along the spiral is measured by the normalized length μ , defined by

$$\mu^2 = \frac{2x^2(r+s)}{\lambda rs} \quad (3)$$

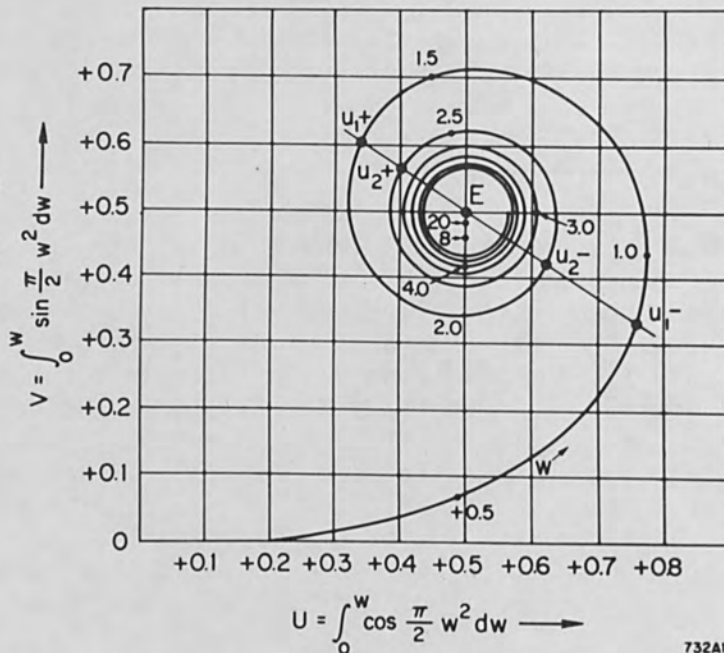
where x is the real length on the target measured in units such that μ is dimensionless. If it is desired to have a central ribbon then μ_{1-} (as shown on the spiral curve) represents the inner edge of the first slot. We then draw a straight line through the end point E of the spiral. The points at which the spiral intersects with the line define a set of μ_{n-} and μ_{n+} for the inner and outer edges, respectively, of the n th slot. That this is an optimum set follows from the fact that all the vectors have the same phase, i.e., are parallel on the spiral plot. If it is not desired to have a center ribbon, then it is noted that the inverse or negative of the above defined pattern is also a solution. The optimum solution without a center ribbon, however, is defined by letting μ_{1-} go to zero; thus the line is drawn from the origin through E .

The first step in fabricating the target is to rule the target pattern by a tape-controlled ruling engine. The punched paper tapes are generated from magnetic tape output from an IBM 7090 computer. After ruling, the pattern is photographed twice at right angles to get the pattern shown in Fig. 3.

The target is made from nickel plated on a copper sheet. The pattern is photographically transferred to the copper blank. After plating on the nickel pattern, the copper is chemically milled from the holes. A cross section of the resulting target is shown in Fig. 5.

Errors in the position of the edges of the apertures can always be divided into symmetric and asymmetric errors. The maximum error that can occur in finding the center of the target is essentially the magnitude of the asymmetric shift of the aperture edges. The tolerance for the aperture edges is 0.025 mm, which is the same as the criteria for the sensitivity of alignment of each target. Symmetric errors can only affect the intensity and sharpness of the image, never its position. The only important type of symmetric error is that which is proportional to the distance of the edge of the aperture from the center of the target. This error is equivalent to having the wrong focal length for the target as calculated from Eq. (2), where the focal length f is given by $f = rs/(r+s)$. The longitudinal distance by which each target can be moved without causing a reduction in alignment sensitivity greater than 10% has been calculated by a digital computer program. In many cases it was found possible to let one target pattern be used in two or more positions without exceeding the 10% limitation. In addition, it is frequently possible to use the same target at an exactly symmetrically located position relative to the center of the accelerator. This procedure is equivalent to exchanging r and s in Eq. (2). As a result, a total of only 121 different patterns are required for the 277 target locations along the accelerator.

FIG. 4.—Cornu spiral used to show graphic method of determining the optimum target design. The point μ_{1-} corresponds to the edge of the central ribbon. Subsequent slot edges correspond to the intersections of successive spirals with the line joining E and μ_{1-} .



732A12



FIG. 5.—A cross section of a target showing how the apertures are formed by the 0.05-mm-thick nickel plating on 0.5-mm-thick copper sheets. Where the holes are small and closely spaced, all the copper may be removed.

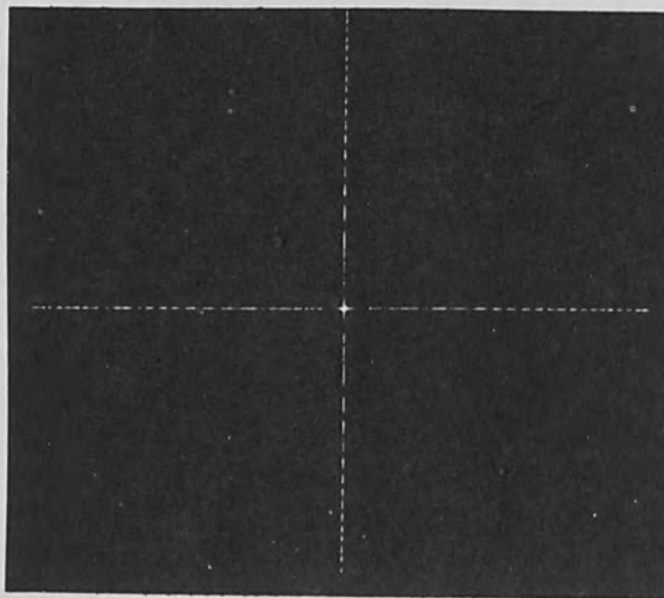


FIG. 6.—Photograph of image pattern from a Fresnel lens. The point to be aligned is the spot at the center of the crossed lines. The width of the center spot corresponds to the diffraction limit of the Fresnel lens.

Most of the patterns are 30 cm square. However, a limit of 250 slots was set and, as a result, at the ends of the accelerator the targets have 250 lines in less than 30 cm. The smallest of the targets, which is the very last one, is only about 10 cm square. The smallest slot in this last target is about 0.1 mm wide. The target with the longest focal length, which is located at the center of the accelerator, has only 46 slots in each direction of the 30 cm square.

DETECTOR

The spot or line width of the image at the detection station varies from about 0.1 mm for the last target to about 10.0 mm for the target nearest the light source. Figure 6 shows a photograph of a typical image pattern. The point to be aligned is the spot at the intersection of the crossed lines. The most difficult targets to align are the ones in the center of the accelerator. In this region, line widths are about 4.0 mm. The desired resolution of the alignment system is 0.025 mm. With a 2-to-1 enlargement ratio of a lens in the center of the accelerator, it is necessary to find the center of the spot to within 0.05 mm, or 1 part in 80 of the line width. This is better than a human operator could be expected to do routinely. Therefore an electro-mechanical scanning system has been devised which generates the derivative of the spot intensity as a function of detector position in the horizontal or vertical directions. The center of the spot is defined by the point where the derivative is zero. The advantage of using this method is that the steep line intersecting the axis gives an unambiguous determination of the image center. Figure 7 shows the actual plot of the differentiated alignment image as obtained from an x-y recorder. The curve was traced twice to establish the reproducibility of the results. Figure 8 shows an artist's cutaway of the detector assembly. The detector can be rotated so that it can scan either horizontally or vertically.

IMAGE PATTERN

The calculation of the image intensity from a pattern of holes in a target plate involves the use of Fresnel integrals. Both Taylor series approximations of the integrals and digital computer programs have been used for calculating the expected images. The analytical approximations were derived in an earlier publication.⁴ It was found that the predicted width of the central spot of an image is given by

$$w \approx \sqrt{5} \frac{\lambda s}{\pi D} \quad (4)$$

where D is the width of the target. Equation (4) is strikingly close to the standard expression for resolution of a lens, s/D . The experimental results have confirmed these predictions.

STABILITY

For the period of operation since April 1966, the accumulated settlement in some areas is up to 2.5 mm. Normal realignment, done every three months, corrects the settlement before it exceeds 1 mm. The largest settlements occurred in areas constructed over filled ground. The

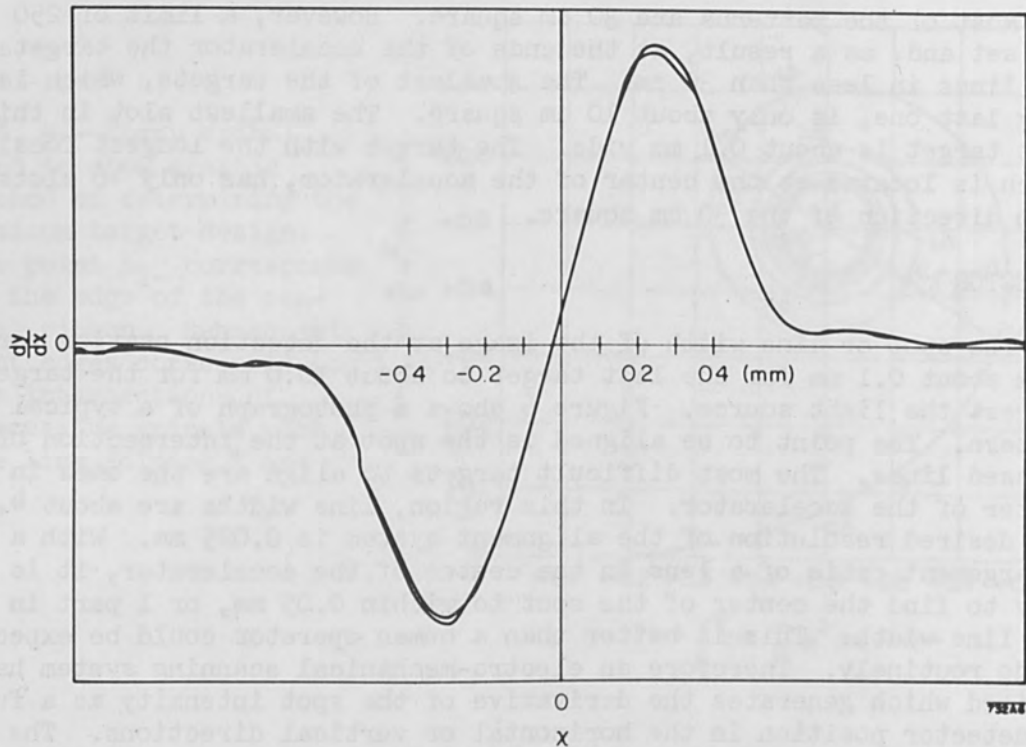


FIG. 7.—Plot of the differentiated signal from the photoelectric scanner. The trace was repeated to show the reproducibility of the output.

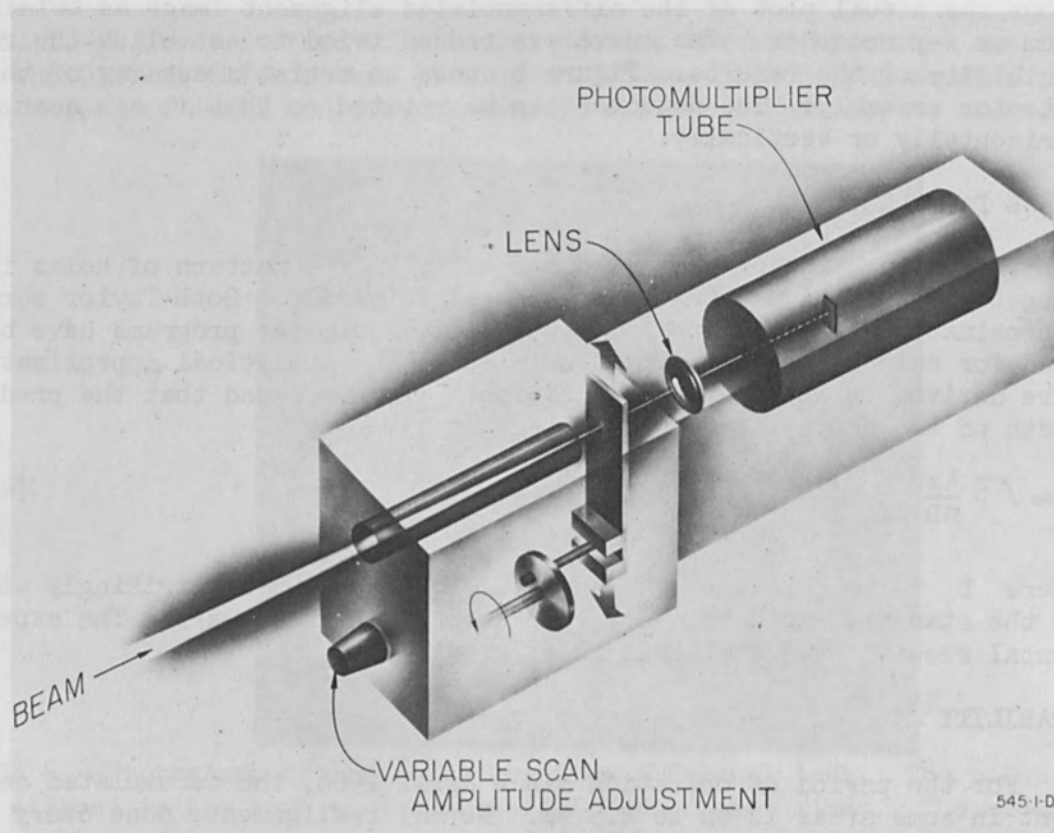


FIG. 8.—The variable-amplitude scanner and photomultiplier. The scanner may be rotated to sweep either vertically or horizontally.

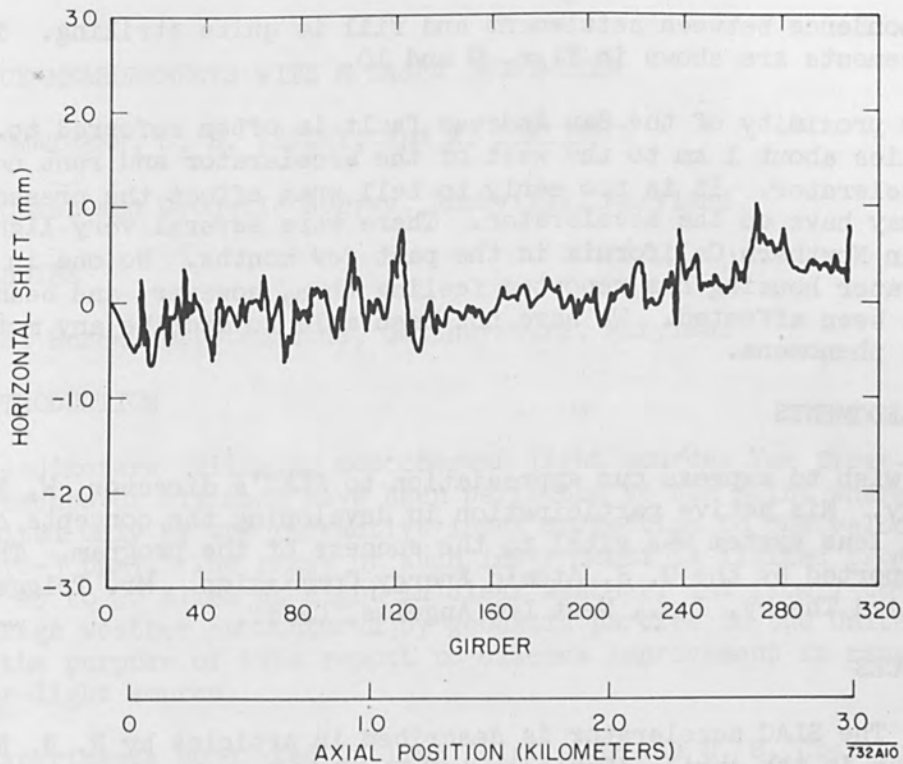


FIG. 9.—Horizontal shift from April 1966 to January 1967. The displacements shown are cumulative totals. Normally the accelerator is realigned before the required adjustment can exceed 1 mm.

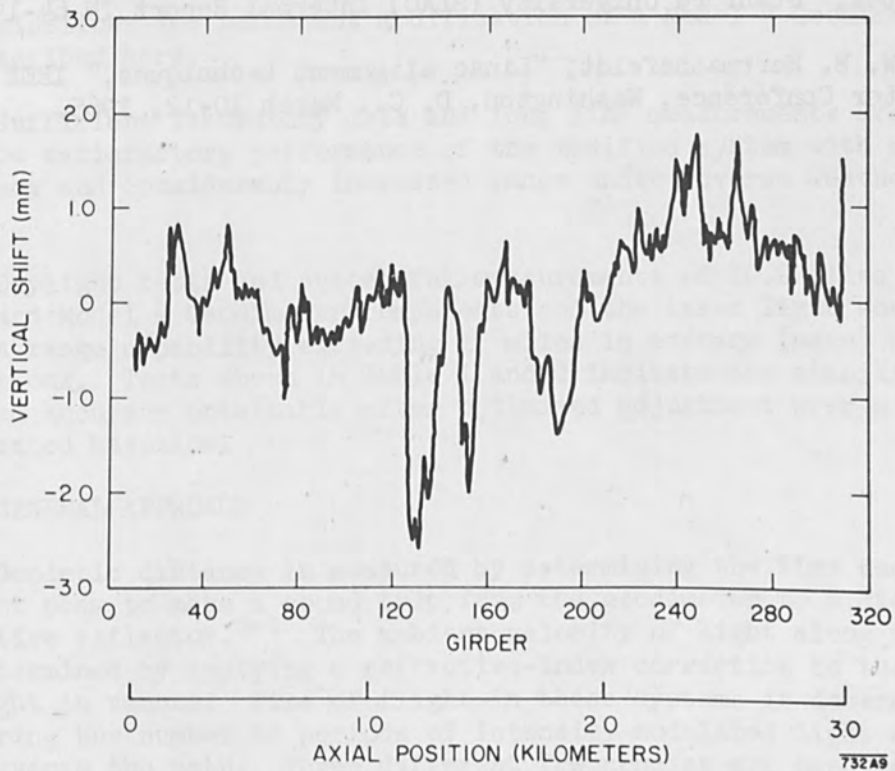


FIG. 10.—Vertical shift from April 1966 to January 1967. The horizontal scale is measured from the west end of the accelerator.

correspondence between settlement and fill is quite striking. The total displacements are shown in Figs. 9 and 10.

The proximity of the San Andreas fault is often referred to. The fault lies about 1 km to the west of the accelerator and runs normal to the accelerator. It is too early to tell what effect the presence of the fault may have on the accelerator. There were several very light tremors in Northern California in the past few months. No one in the accelerator housing has reported feeling them, however, and beam operation has not been affected. We have not been able to ascribe any motion to the seismic phenomena.

ACKNOWLEDGMENTS

We wish to express our appreciation to SLAC's director, W. K. H. Panofsky. His active participation in developing the concepts of the Fresnel lens system was vital to the success of the program. The work was supported by the U. S. Atomic Energy Commission. Mr. Trigger is now at Applied Theory, Inc., West Los Angeles, Calif.

REFERENCES

1. The SLAC accelerator is described in articles by R. B. Neal and J. Ballam in the April, 1967 issue of Physics Today.
2. See, for instance, F. Jenkins and H. White, "Fundamentals of Optics," McGraw-Hill, New York, 1957; 3rd ed.
3. K. R. Trigger, "Approximate Solutions of Images Using Fresnel Zone Plates," Stanford University (SLAC) Internal Report TN 64-19, March, 1964.
4. W. B. Herrmannsfeldt, "Linac alignment techniques," IEEE Particle Accelerator Conference, Washington, D. C., March 10-12, 1965.

DISTANCE MEASUREMENTS WITH A LASER GEODIMETER

S. E. SMATHERS, G. B. LESLEY, and R. TOMLINSON

U. S. Coast and Geodetic Survey, Rockville, Maryland

H. S. BOYNE

National Bureau of Standards, Gaithersburg, Maryland

I. INTRODUCTION

Geodimeters utilizing noncoherent light sources for first-order measurements of distance have been perfected to the point where accuracy is limited only by the refractive index correction to the velocity of light (2-3 ppm). The range of such instruments is limited from approximately 15 to 20 miles at night in clear weather, and from 7 to 8 miles in average weather encountered by geodetic parties in the United States. It is the purpose of this report to discuss improvement in range using a laser light source.

Experiments conducted in 1965 jointly by the U. S. Coast and Geodetic Survey and the National Bureau of Standards¹ with a laser light source resulted in measurements up to 10 miles in moderate haze with power outputs of about 1 mW. There was no loss of accuracy, indicating a possible significant improvement in precision. These results provided the guidelines for permanent modification of a Model 4 Geodimeter which is described here.

Sufficient laboratory data and long line measurements are presented to show satisfactory performance of the modified system with no loss of accuracy and considerably increased range under adverse weather conditions.

Daylight tests and successful measurements of 10.2 miles with the standard Model 4 Geodimeter components and the laser light source indicate a range capability exceeding 15 miles in average (haze) weather conditions. Tests shown in Table 1 and 2 indicate the stability and increased accuracy obtainable after optimized adjustment over a 1-mile calibrated baseline.

II. GENERAL APPROACH

Geodetic distance is measured by determining the time required for a light beam to make a round trip from the geodimeter to a distant retro-directive reflector.²⁻⁴ The ambient velocity of light along the path is determined by applying a refractive-index correction to the velocity of light in vacuum. Time of flight in these systems is determined by measuring the number of periods of intensity-modulated light necessary to traverse the path. Three different frequencies are used to determine unambiguously the whole number of periods, and a phase comparison is made between the outgoing and reflected beam to determine the remaining

fractional period.⁵ The modulation frequencies are near 30 MHz.

The standard Model 4D Geodimeter is equipped with a mercury vapor light source which is focused into an optical shutter consisting of a Kerr cell mounted between crossed polarizers and a Newtonian collimator with a divergence of approximately 5 milliradians. The receiving optics consist of a similar Newtonian collector and a phototube with an S4 spectral response chosen for the green band of a high-pressure mercury-arc lamp.

Earlier experiments showed that the light loss through the Kerr cell can be as much as 90%, and the spectral response of the S4 phototube at 6328 Å is down by a factor of at least 10 from its maximum.¹ It was therefore necessary to redesign both the transmitting and receiving optics, including the Kerr cell and phototube.

III. GEODIMETER MODIFICATIONS

The principal changes to the Geodimeter are shown in schematic form in Fig. 1. The transmitter optics of the Geodimeter were removed to provide space for the laser, KDP cell, and collimator, which were mounted to permit easy access to the components. The receiver change consists of the addition of an S20 photodetector sensitive to 6328 Å.

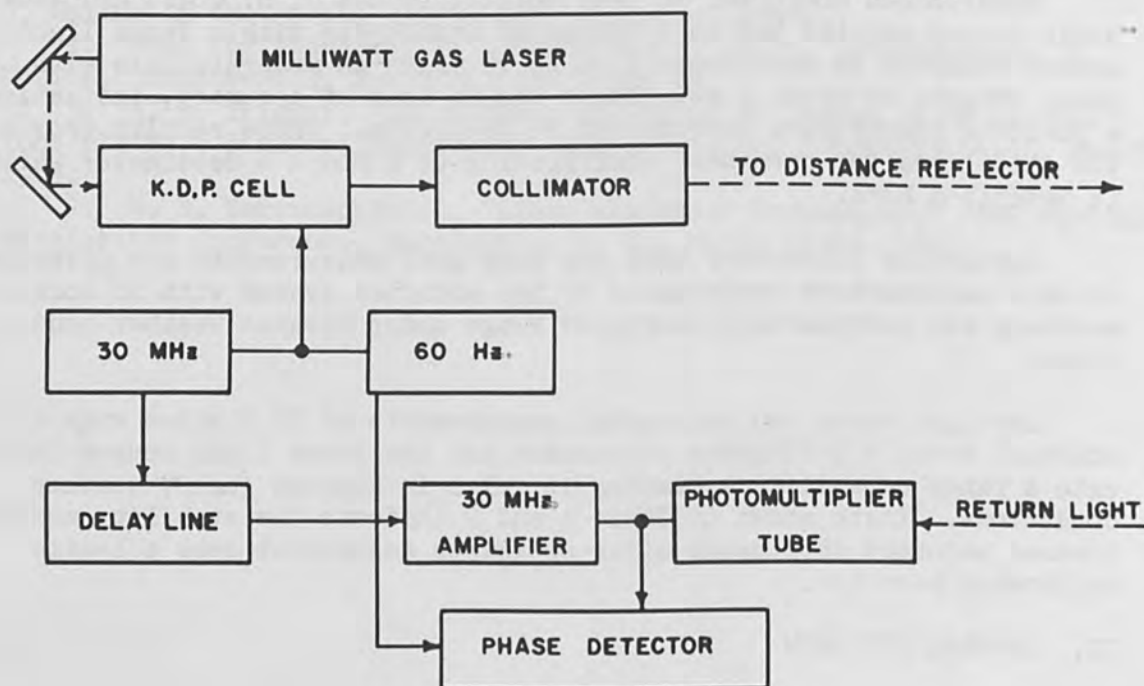


FIG. 1.—Block diagram of modified laser geodimeter.

The laser source is a 1-mW dc-excited, cw, He-Ne gas laser of hemispherical design, approximately 30 cm in length and operating at 6328 Å. The output beam is plane polarized, has a diameter of 2 mm, and has a divergence of 0.03 milliradian.

The KDP cell (potassium dihydrogen phosphate) modulator consisted

of four crystal wafers mounted between two electrodes embedded in an oil-filled cavity. The exit and entrance diameters are 3 mm, and light losses were found to be less than 1% at 6328 Å.

Alignment and adjustment is accomplished by a lock ring adapter with three degrees of freedom with respect to the optical axis.

This cell is designed to operate as an optical shutter with about 90% efficiency at 1000 V. The maximum attainable voltage from the geodimeter at 30 MHz was approximately 50 V, which limited the intensity modulation to about 5%, which is, however, comparable to the percentage modulation obtained with the Kerr cell.

The S4 phototube was replaced with an S20 phototube having a maximum gain of 10^8 and a maximum frequency response of 200 MHz.

This tube was mounted across the front of the geodimeter in a Conetic-shielded case free to move with the receiver optics. The geodimeter gray wedge was used to control the light level. An external 2500-V dc source was used to supply voltage to the S20 phototube.

All transmitting and receiving optics were coated to give maximum response at 6328 Å. The receiving system was relatively insensitive to daylight as measured by the Geodimeter light indicator.

IV. LABORATORY TESTS AND EVALUATION

Relative comparisons of the new modulator and photomultiplier were made with the laser light source and the standard components to insure proper function, maintain sensitivity, and determine the relative noise contribution.

Phase comparison of the 30-MHz intensity-modulated light is accomplished by mixing the return light signal with a 30-MHz signal through a calibrated delay line in a phase detector. A meter at the output of the phase detector indicates a null reading when the relative phase of the signals from the delay line and the return light are in quadrature. In Fig. 2 the null detection signals reflect the total internal geodimeter noise which is inherent in readings of the null indicator. Noise at this point appears as a jitter in the null indicator and adds to the spread of the delay line readings. Comparison of Figs. 2(a) and (b) shows Kerr cell noise and S4 insensitivity to the laser 6328 Å line. Figure 2(c) shows the S4 insensitivity without Kerr cell noise. A comparison of Figs. 2(b) and (d) shows isolated Kerr cell noise.

V. GEODETIC LINE TESTS AND EVALUATION

Comparable distance measurements were made with a standard Model 4D geodimeter and the laser-modified geodimeter with and without the KDP cell and S20 phototube.

The instruments were calibrated and the zero constant determined after each set of measurements in accordance with the U. S. Coast and Geodetic Survey's operational techniques.

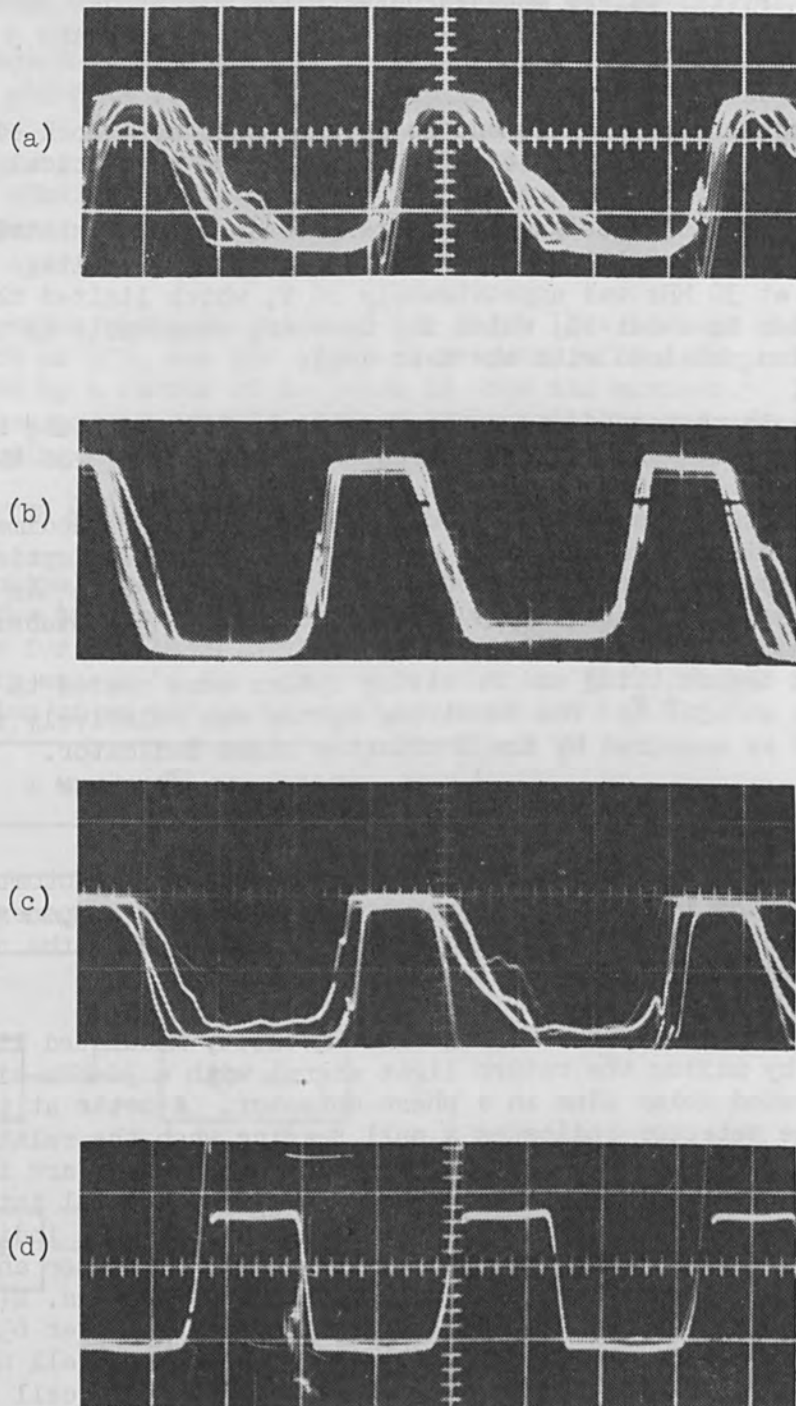


FIG. 2.—Null indicator signals, (a) laser, Kerr cell, S4 phototube, (b) laser, Kerr cell, S20 phototube, (c) laser, KDP cell, S4 phototube, and (d) laser, KDP cell, S20 phototube.

Table 1 is a summary of measurements over the same path of approximately 10.2 miles from the Washington Science Center. These data show a maximum difference of 1.6 cm and are well within the specified requirements placed on first-order triangulation measurements.

TABLE 1.—Summary of geodimeter observations, 16 km.

| Date | Geodimeter No. | Slope Distance (m) |
|--------------------|---|---------------------|
| State: Maryland | | |
| Station: Room 1022 | | |
| | | Locality: Rockville |
| | | To Station: Tysons |
| 3-7-66 | 246 (4-D) | 16,445.695 |
| | | <u>16,445.694</u> |
| | | Mean = 16,445.694 |
| 3-7-66 | 225 (Laser Kerr cell, S4 Phototube) | 16,445.676 |
| | | <u>16,445.700</u> |
| | | Mean = 16,445.688 |
| 8-24-66 | 225 (Laser, KDP cell, S20 Phototube) | 16,445.678 |

TABLE 2.—Summary geodimeter observations, 1.8 km.

| | | | |
|---|-------------------|-------------------------|--------------|
| State: Maryland | | Locality: Beltsville | Date 9-30-66 |
| Station: 150 meters | | To Station: 1800 meters | |
| Geodimeter No. 225 (Laser, KDP cell, S20 Phototube) | | | |
| Geodimeter slope distance = | | 1649.998 | |
| | | 1650.008 | |
| | | 1650.015 | |
| | | <u>1650.009</u> | |
| | | Mean = 1650.008 m | |
| Mean Geodimeter slope distance = | 1650.008 | | |
| Sea level correction | = - 0.013 | | |
| Slope correction | = - 0.008 | | |
| Geodimeter Geodetic distance | = 1649.987 m | | |
| Geodimeter distance | = 1649.987 | | |
| Tape distance | = <u>1649.983</u> | | |
| Difference | = 0.004 | = 1/412,500 | |

Table 2 presents comparable measurements of the laser geodimeter with the taped base line at Beltsville, Maryland. A series of four measurements was made using advanced and retarded phase increments to eliminate error of the delay line. The mean deviation of these four measurements as compared with the taped base is 4 mm.

The delay line readings for these measurements while small in number indicate the order of magnitude of the precision improvement that can be expected with the addition of the laser, KDP cell, and S20 phototube to the geodimeter.

Late in 1966 the laser geodimeter was tested and evaluated over lines measured previously by a geodetic field party in the vicinity of Aurora, Nebraska⁷ (Fig. 3a). To evaluate fully the instrument and determine maximum range, lines of 9.0, 9.7, 18.6, and 26.1 miles were measured at night along the traverse (Fig. 3b). The laser transmitted 2.2 mW of power when these measurements were taken.

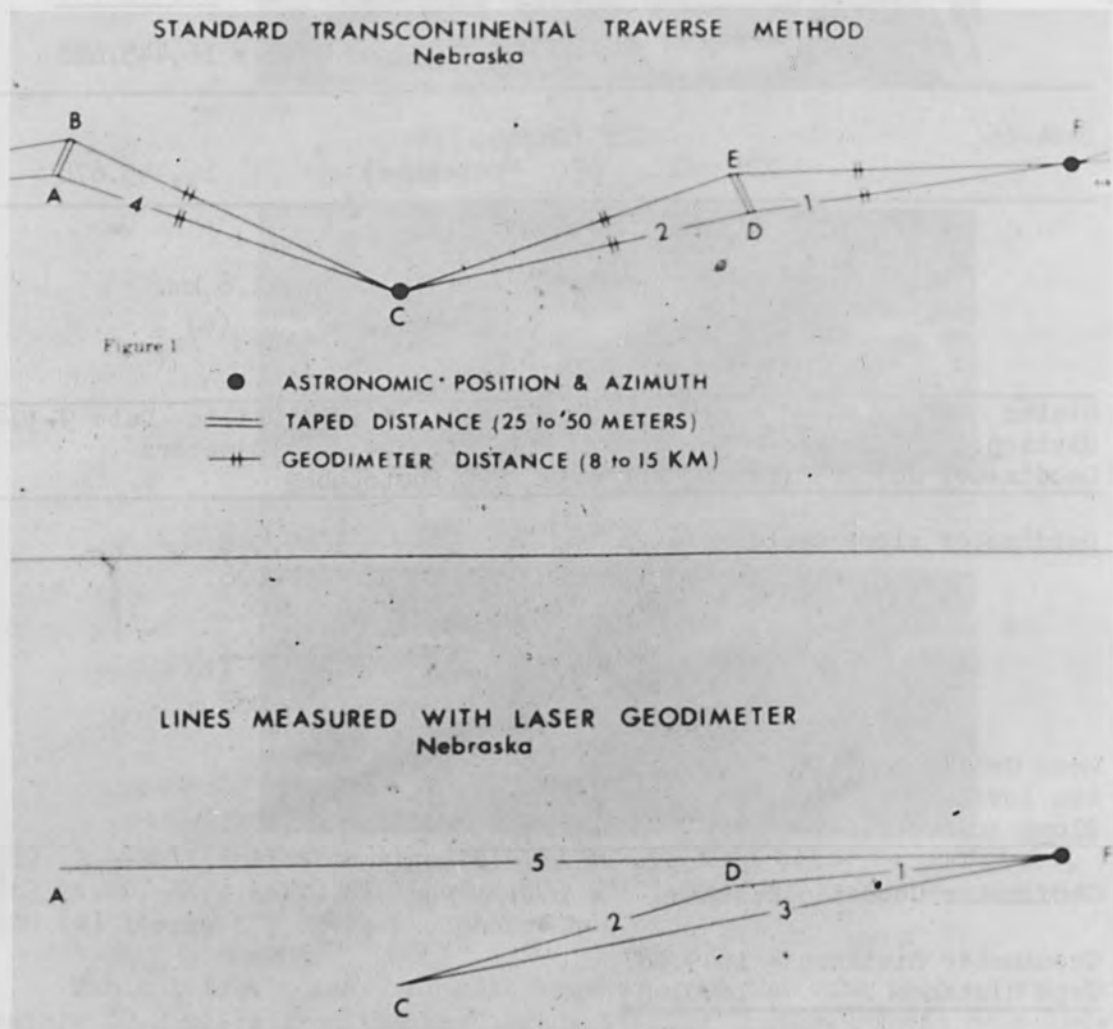


FIG. 3.—Schematic representation of transcontinental field measurements.

Figure 3(a) shows the Model 2A and 4D geodimeter lengths along the transcontinental traverse line, and Figure 3(b) shows the laser geodimeter lengths along the same traverse line. Results obtained with the various instruments are tabulated in Table 3 by line numbers as indicated in Fig. 3(b). The number of complete measurements made on each data is given in column (A), the mean result in column (B), and the weighted mean of each group of measurements in column (C). In column (A), one complete measurement with the laser or 4D geodimeter is a mean result of measurements using each of the three frequencies. Two measurements on each of the three frequencies constitute the six complete measurements with the Model 2A instrument.

TABLE 3

| Line No. | Date | Inst. & No. | (A) | (B) (m) | (C) (m) |
|----------|----------|-------------|-----|------------|------------|
| 1 | 10/05/66 | 4D - 441 | 4 | 14,514.840 | 14,514.839 |
| | 10/11/66 | 4D - 284 | 4 | 14,514.838 | |
| 1 | 11/01/66 | LASER | 5 | 14,514.839 | 14,514.839 |
| | 11/02/66 | LASER | 7 | 14,514.839 | |
| 2 | 10/03/66 | 2A - 114 | 6 | 15,653.487 | 15,653.476 |
| | 10/11/66 | 2A - 151 | 6 | 15,653.466 | |
| 2 | 10/31/66 | LASER | 1 | 15,653.465 | 15,653.470 |
| | 11/02/66 | LASER | 4 | 15,653.471 | |
| 3 | 10/31/66 | LASER | 1 | 29,856.194 | 29,856.205 |
| | 11/01/66 | LASER | 5 | 29,856.213 | |
| | 11/10/66 | LASER | 2 | 29,856.189 | |
| 3* | | | | | 29,856.205 |
| 4 | 10/06/66 | 2A - 114 | 6 | 14,980.279 | 14,980.268 |
| | 10/13/66 | 4D - 284 | 4 | 14,980.252 | |
| | 10/27/66 | 2A - 151 | 6 | 14,980.269 | |
| 5 | 11/10/66 | LASER | 1 | 41,968.662 | 41,968.662 |
| 5** | | | | | 41,968.670 |

* Projected length based on Model 2A and 4D measurements over lines 1 and 2.

** Projected length based on Model 2A and 4D measurements over lines 1, 2, and 4.

VI. DISCUSSION

The modifications which include the laser source, KDP cell, and S20 phototube indicate an improved sensitivity by a factor of 2 over the conventional geodimeter. However, the improvement in range capability during adverse weather conditions and daylight measurements is far more significant. According to the field tests in the Nebraska area, it appears that the maximum range with the Laser Geodimeter with good visibility is about 42 km (26 miles), whereas under average conditions the maximum range is about 30 km (18 miles). Limited tests under similar conditions indicate that the maximum range in daylight is about one-half that at night.

The improvement in range capability is due to the fact that the coherence of the laser source allows for diffraction limited collimation with no loss in intensity. Thus, the geodimeter is transmitting with an intensity of approximately 1.6 mW. The mercury-arc lamp, however, is an extended source and severe intensity losses occur in attempting to achieve a reasonable collimation. Measurements of the output intensity of the conventional Geodimeter show that whereas the mercury lamp emits about 15 mW/Sr, the output intensity through the transmitting optics is only 0.13 mW, which is less by a factor of 10 than that of the laser source. In addition, the KDP cell shows considerable improvement in noise characteristics over the Kerr cell. With the Kerr cell, the laser light scintillated, possibly due to thermal convection currents in the Kerr cell, whereas the light through the KDP cell was uniform in intensity.

REFERENCES

1. S. E. Smathers, A. C. Poling, R. Tomlinson, and H. S. Boyne, "Experiments with Lasers in the Measurements of Precise Distance," U. S. Coast and Geodetic Survey, ESSA, Rockville, Maryland, 20852, September, 1965.
2. R. Scholdström, "The AGA Geodimeter," Reprint from IVA 25 5: 239-251, 1954.
3. E. Bergstrand, J. Geophys. Res. 65: 404, 1960.
4. A. C. Poling, Proc. Am. Soc. Civil Engrs. 84 (No. AUI), April, 1958.
5. A. Bjerhammar, J. Geophys. Res. 65: 412, 1960.
6. A more detailed description of the modifications is described in a paper by S. E. Smathers, G. B. Lesley, R. Tomlinson, and H. S. Boyne (to be published).
7. More detailed results of the Nebraska tests are described in a paper by G. B. Lesley (to be published).

USE OF LASERS IN RAMAN SPECTROSCOPY OF NATURAL PRODUCTS

J. R. SCHERER

U. S. D. A. Western Regional Research Laboratory, Albany, California

DESCRIPTION

Raman spectroscopy, or the study of scattered light whose frequency has been modulated by molecular vibration, has been widely used by molecular spectroscopists to investigate the vibrations of polyatomic molecules. Prior to the introduction of cw gas lasers, Raman scattering was not widely used for general analysis because of the feeble nature of the effect and the relatively large amounts of material (0.2 to 5 ml) which were required to obtain a successful spectrum. Furthermore, investigation of the polarization of Raman scattering was difficult because of intensity attenuation of the source resulting from use of Polaroid and the convergence errors in sample illumination. Additional problems such as absorption and fluorescence encountered with the 4358-Å Hg toronto arc did little to encourage use of the technique.

Use of the cw 6328-Å He/Ne laser has eliminated or, at least to a considerable extent, alleviated the forementioned problems.¹ At the time of this writing, commercial suppliers of Raman instruments have utilized the high intensity of the cw laser to reduce the sample volume to the range of 2 to 20 μ l. As small as this sample size seems, it is not yet small enough to obtain spectra on natural product fractions collected from gas/liquid chromatography.

In the author's laboratory, part of the Western Utilization Research and Development Division of the U. S. Department of Agriculture's Agricultural Research Service, a technique has been devised² for conveniently obtaining Raman spectra with sample volumes (liquids and melts) in the range of 0.04 to 0.4 μ l. The basic principle of the system is to place the sample in a thin-walled Pyrex capillary tube which has a fused end that serves as the collimating lens for a focused laser beam (Fig. 1). In this system a 10-mW laser beam with a 3-mm diameter may be reduced to a parallel beam about 100 microns in diameter whose intensity is of the order of 100 W/cm². Since the Raman intensity per molecule is proportional to the intensity of the incident beam, we achieve a reasonable degree of Raman scattering with fewer molecules. In our optical system, the scattered light from a 3-mm-long by 0.1-mm-diameter cylinder of sample, near the center of the capillary tubing and within 1/2 mm from the capillary lens, is collected over a solid angle (centered 90° from the incident beam direction and normal to the direction of incident beam polarization) of 0.57 steradian. The 90° backscattered light is reflected in the forward direction by an aluminum deposit on the side of the capillary. Assuming an 80% reflection efficiency, the net solid angle of collection is ~1.0 steradian (Fig. 1). A 4:1 magnified image of the illuminated volume is projected on the entrance slit of the monochromator. Under these circumstances the image of the scattering portion of the sample just fills a 0.4-mm slit width corresponding to a spectral slit

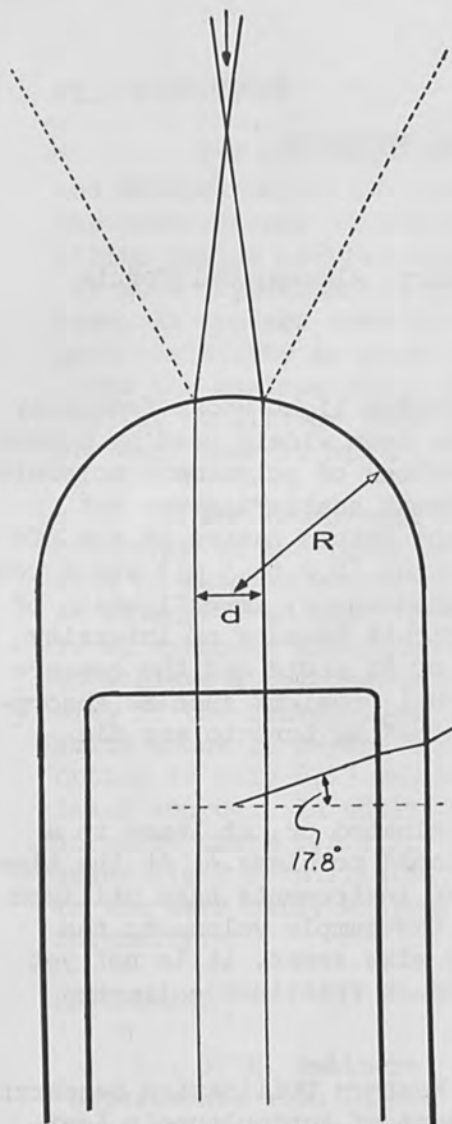


FIG. 2.—Photomicrograph of typical capillary, lens diameter 0.39 mm (oil immersed).

width of 10 cm^{-1} .

Figure 2 shows a photomicrograph of a typical capillary. The capillary is immersed in oil to show the defect-free quality of the lens and the flat inner surface where the sample is in contact with the lens. The capillary lenses are formed by passing a rotating capillary through a gas/oxygen flame at a fast enough rate to prevent formation of bubbles in the glass but to permit fusion to a spherically symmetrical lens. We have found it possible to produce capillaries with sufficient ease so as to consider them disposable after one use. It is noteworthy that samples are easily recovered from the capillaries or that they may be sealed and permanently stored for future measurement.

Successful use of the technique requires that the capillary be accurately positioned at the image of the entrance slit in the sampling area and that the axis of illumination coincide with the length of the slit image. These requirements are met by placing of the capillary in a pin vise that rests on a platform supported by a microscope stage (Fig. 3).



FIG. 1.—Capillary tube showing fused end as collimating lens.

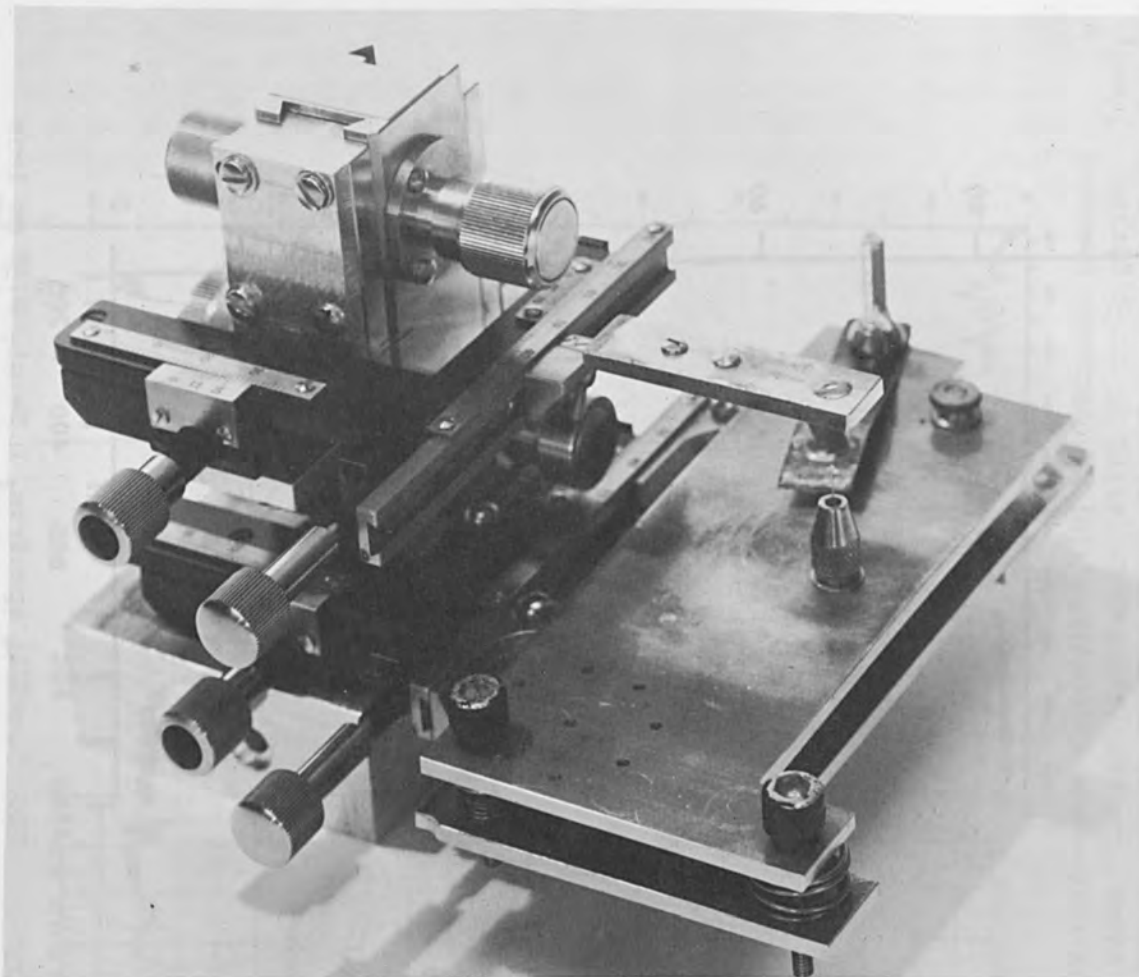


FIG. 3.—Apparatus for holding capillary and focusing lens.

The platform is tilted by means of three leveling screws so that the axis of the capillary coincides with the slit image (vertical). The focusing lens, held by a second microscope stage, is adjustable in the horizontal and vertical planes to insure axial illumination within the capillary.

RESULTS

Figure 4 shows a spectrum of CCl_4 using a 10 cm^{-1} slit width and 0.8-sec time constant. An Ahrens prism analyzer is inserted between the sample and monochromator to determine the normal and parallel components of the scattered radiation. The sample volume was $0.33 \mu\text{l}$ and the laser power was 10 mW. The measured value of C_s , the ratio of parallel to normal components, for the 459 cm^{-1} band is 0.008. The lowest measured value³ for this band is 0.005. Figure 5 shows a spectrum of CCl_4 obtained with $0.04 \mu\text{l}$. The capillary had a lens diameter of 0.32 mm and a tubing ID of $\sim 0.1 \text{ mm}$. In this case 6328 \AA radiation has been scattered from the walls of the capillary and it was necessary to place filters between the monochromator and the photomultiplier to attenuate stray

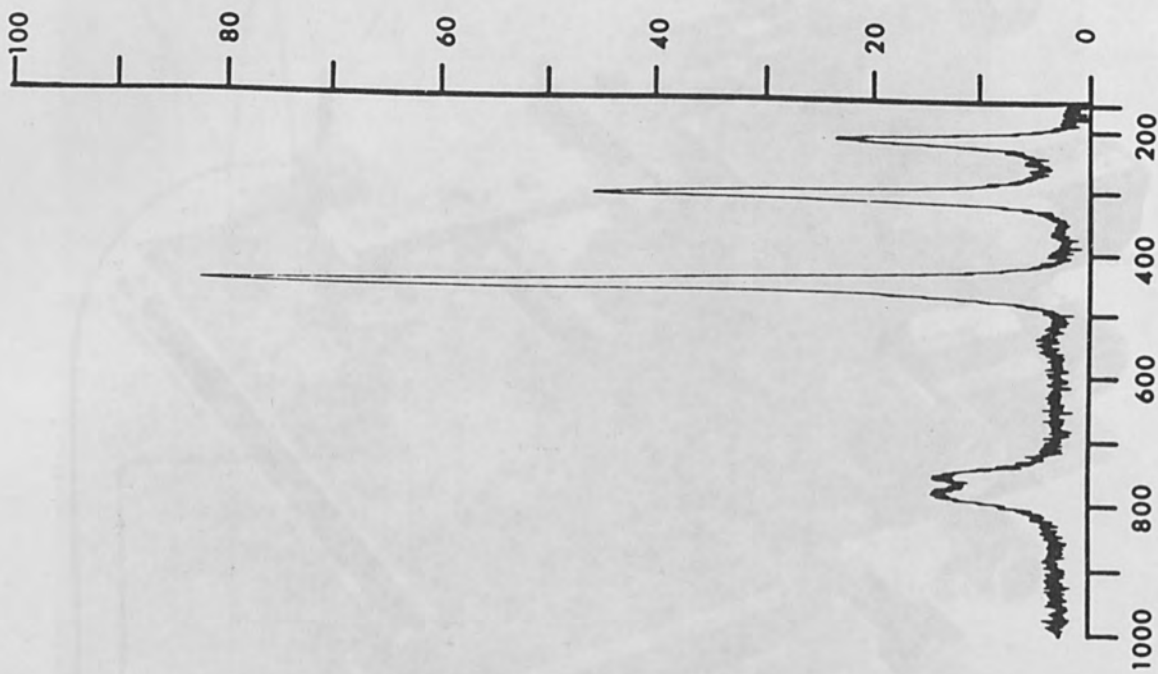


FIG. 5.— CCl_4 spectrum, 0.04 μl , 0.32 mm lens diameter; slit, 10 cm^{-1} ; period, 3 sec; scan rate, 0.9 to 0.8 $\text{cm}^{-1}/\text{sec}$; laser power, 6.7 mW.

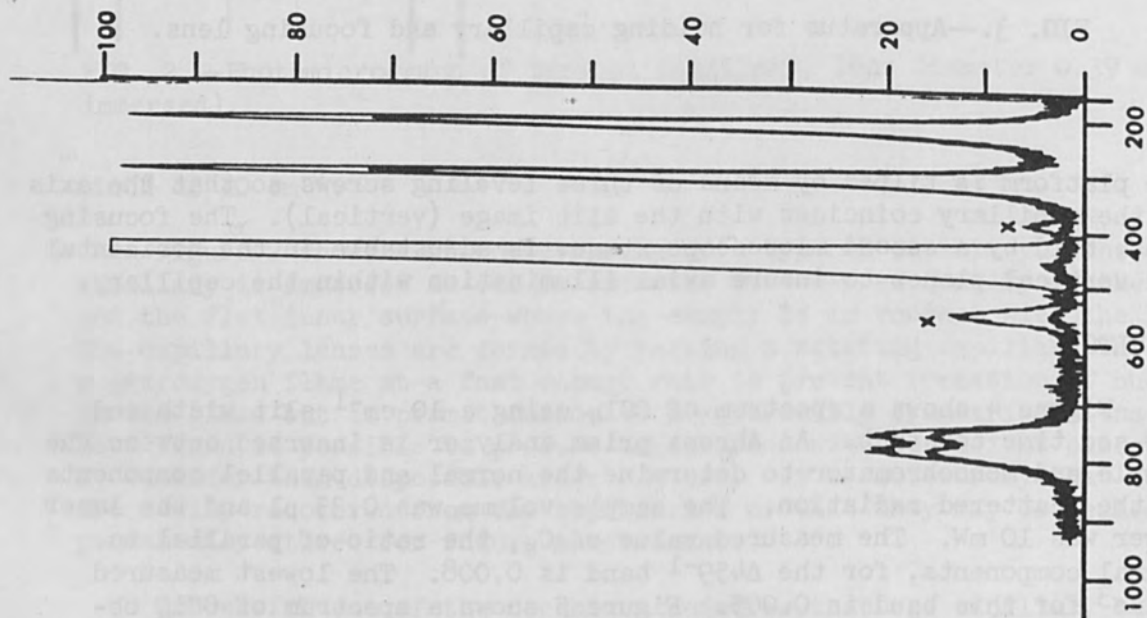


FIG. 4.— CCl_4 spectrum, 0.33 μl , 0.58-mm capillary lens; slit, 10 cm^{-1} ; period, 3 sec; scan rate, 0.9 to 0.8 $\text{cm}^{-1}/\text{sec}$; laser power, 10 mW.

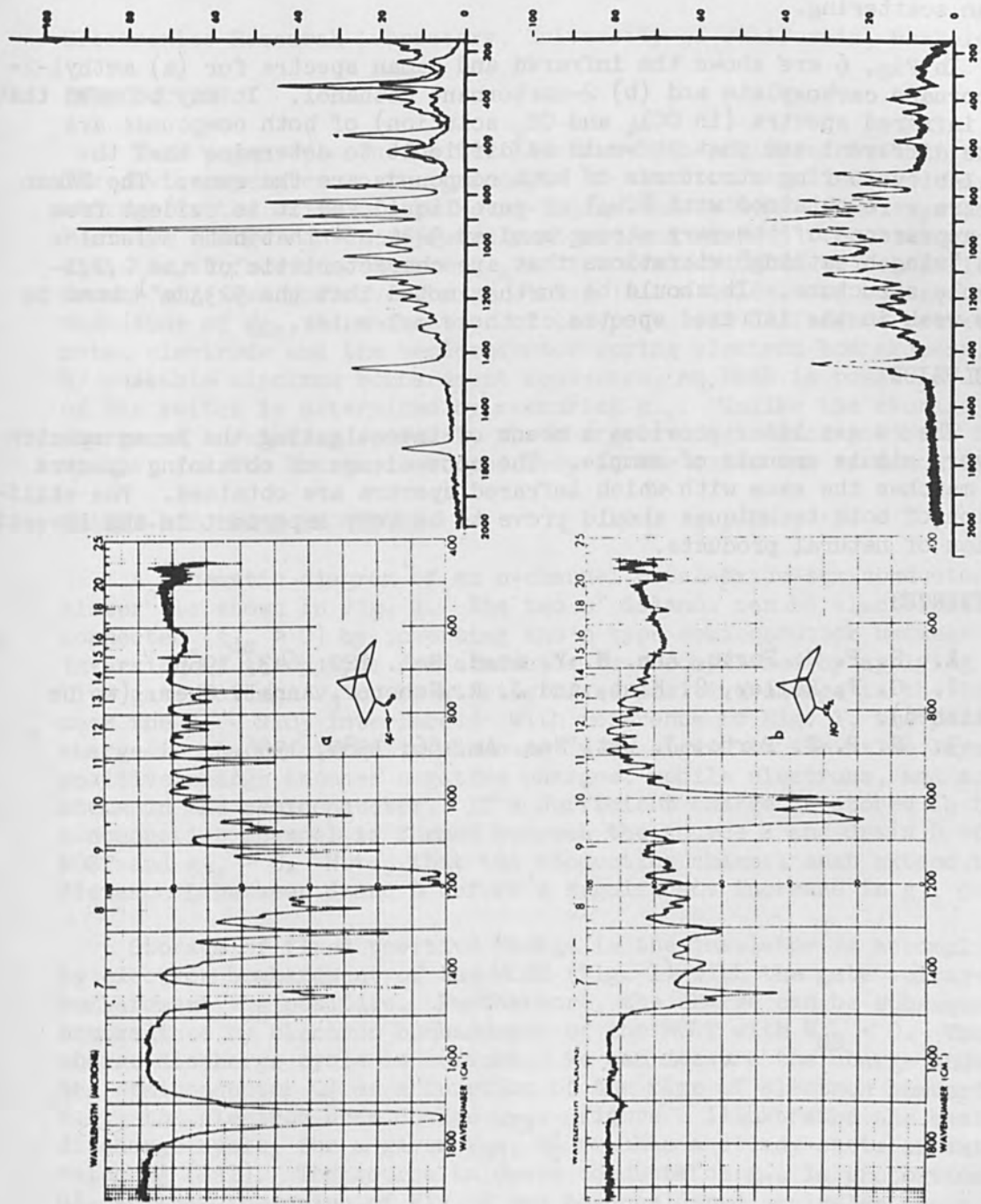


FIG. 6.—Infrared and Raman spectra; (a) methyl-2-norbornane carboxylate, (b) 2-norbornane methanol. (a) Infrared: slit, CBW 2 cm^{-1} ; period, 3 sec; scan: 0.6 $\text{cm}^{-1}/\text{sec}$ Raman: slit, 10 cm^{-1} ; period: 3 sec; scan, 0.9 $\text{cm}^{-1}/\text{sec}$; laser power, 10 mW. (b) Infrared: slit, CBW 2 cm^{-1} ; period, 3 sec; scan, 0.6 $\text{cm}^{-1}/\text{sec}$ Raman: slit, 10 cm^{-1} ; period, 3 sec; scan, 0.9 $\text{cm}^{-1}/\text{sec}$; laser power, 10 mW.

radiation within the monochromator. The two stray peaks at 385 and $555\Delta\text{cm}^{-1}$ (Fig. 4) are caused by stray 6328-Å radiation and are removed by insertion of the filters. The instrument gain and response are the same as in Fig. 4 but the laser power was only 6.7 mW. Of interest is the fact that reducing the sample volume did not significantly reduce the Raman scattering.

In Fig. 6 are shown the infrared and Raman spectra for (a) methyl-2-norbornane carboxylate and (b) 2-norbornane methanol. It may be seen that the infrared spectra (in CCl_4 and CS_2 solution) of both compounds are quite different and that it would be difficult to determine that the 2,2,1-bicyclo ring structures of both compounds are the same. The Raman spectra were obtained with 0.2 μl of pure liquid and it is evident from the appearance of the very strong band at $923\Delta\text{cm}^{-1}$ that both molecules have "ring breathing" vibrations that are characteristic of the 2,2,1-bicyclo structure. It should be further noted that the $923\Delta\text{cm}^{-1}$ band is very weak in the infrared spectra of these molecules.

CONCLUSION

The cw gas laser provides a means of investigating the Raman spectra of very minute amounts of sample. The convenience of obtaining spectra now matches the ease with which infrared spectra are obtained. The utilization of both techniques should prove to be very important in the investigation of natural products.

REFERENCES

1. S. P. S. Porto, Ann. N. Y. Acad. Sci. 122: 643, 1965.
2. G. F. Bailey, S. Kint, and J. R. Scherer, Annal. Chem. (to be published).
3. S. P. S. Porto, J. Opt. Soc. Am. 56: 1585, 1966.

AN ELECTRON-BEAM-ACTIVATED CHARGE STORAGE DEVICE AND MEMORY

N. C. MAC DONALD and T. E. EVERHART

Electronics Research Laboratory, University of California, Berkeley

INTRODUCTION

This paper describes a new Electron-Beam-Activated Switch (EBAS). The device operates on the principle of electron beam induced charge storage in the oxide of the Metal-Oxide-Semiconductor (MOS) system.¹ Positive charge can be repeatedly stored and removed from the oxide, so that the surface conductance g_{ds} of the semiconductor is controlled. The amount of fixed positive charge stored in the oxide, and consequently the magnitude of g_{ds} , is a function of the potential difference between the metal electrode and the semiconductor during electron bombardment. Hence, by suitable electron bombardment sequences, an EBAS is possible; the state of the switch is determined by measuring g_{ds} . Unlike the storage of charge on insulating surfaces, the charge storage discussed here is quite stable, for the charge is stored deep in the oxide and is immobile.

CHARGE-DISCHARGE PROCEDURE

A schematic diagram of an n-channel metal-oxide-semiconductor transistor² is shown in Fig. 1. The two n^+ islands can be electrically connected ($g_{ds} > 0$) by inverting the p type semiconductor between them. Inversion of the p type semiconductor is accomplished by applying a positive gate voltage V_G or by storing fixed positive charge in the insulator near the Si - SiO₂ interface.³ With reference to Fig. 1, the positive charge in the insulator is shown as "plus signs" in the oxide layer. This positive charge induces negative charges, mobile electrons, and acceptor atoms in the semiconductor. If a sufficient charge is stored in the oxide, a conducting channel is formed between the source S and drain D of the MOST and $g_{ds} > 0$. Note, that the conducting channel must extend the entire distance L between S and D before a significant increase in g_{ds} occurs.

Storage of fixed positive charge in the insulator is accomplished¹ by electron bombardment of the MOST (Fig. 1) with the gate voltage during bombardment V_{GB} positive. Furthermore, the charge can be subsequently neutralized by electron bombardment of the MOST with $V_{GB} < 0$. Thus, a charge-discharge cycle is defined. We can measure the charge induced in the semiconductor Q'_S as a function of the time of electron bombardment, i.e., the electron beam dosage Q_{EB} . Figure 2 illustrates the basic charge-discharge cycle; for a given V_{GB} , Q'_S reaches a steady-state or saturated value Q'_S (SAT). The source to drain conductance g_{ds} is proportional to Q'_S , so that the graph of Fig. 2 can be considered equivalent to a graph of g_{ds} vs t. The experimental plot of $Q'_S(t)$ against the time of electron bombardment for $V_{GB} = + 0.8$ V is given by curve (A) of Fig. 2. The value of the ordinate that corresponds to the horizontal portion of curve (A) is Q'_S (SAT). At $t \approx 2.6$ sec a potential $V_{GB} = -0.8$ V is applied to the gate while bombarding the device; the result is a reduction of Q'_S to its initial value at $t = 0$. For the purposes of subsequent discussion, it

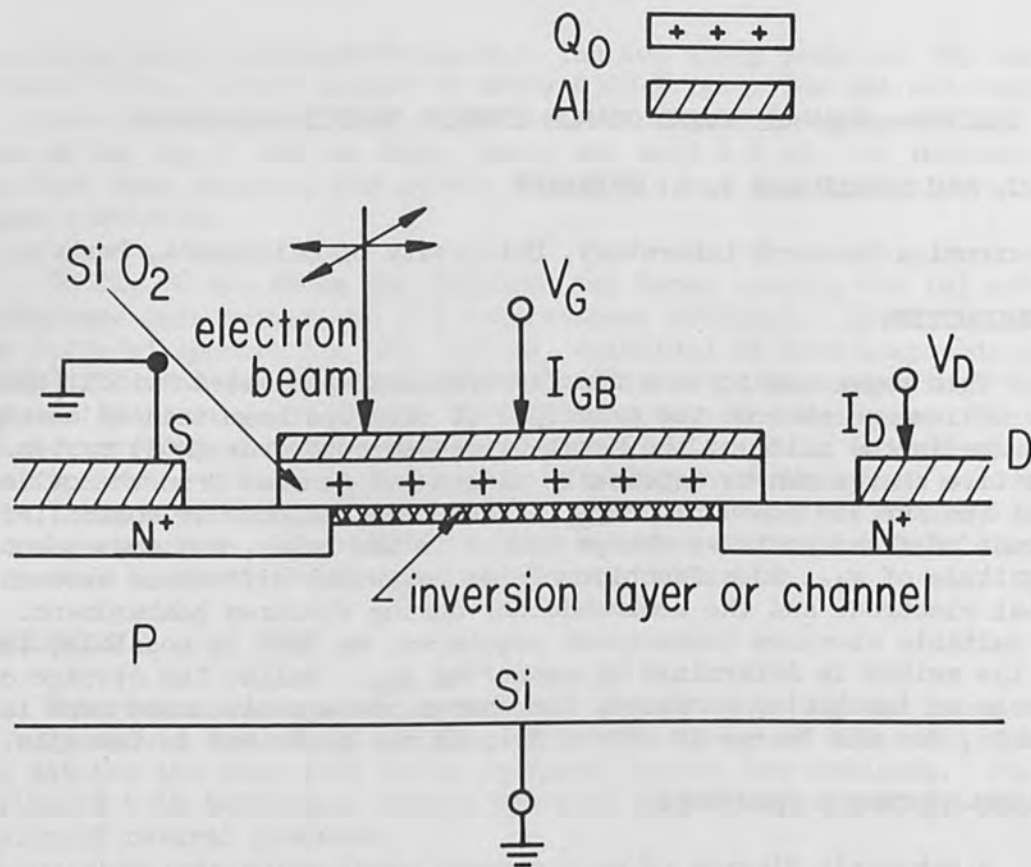


FIG. 1.—Schematic diagram of a cross section of the metal-oxide-semiconductor transistor.

should be emphasized that stopping the electron bombardment at any time during the charging or discharging process preserves the charged state of the oxide at that time. The charged state of the oxide is then changed only by subsequent electron bombardment. In particular, the charged state of the oxide is not altered by a change in the gate voltage unless the gate is being bombarded simultaneously.

THE ELECTRON BEAM ACTIVATED SWITCH

Using the charge storage cycle of Fig. 2, we can reversibly change the source to drain conductance g_{ds} of the MOST. Information is stored and read by electron bombardment of small areas of the gate electrode while the entire gate electrode is at a fixed potential. In particular, a "1" is stored by electron bombardment of a small area of the gate electrode at $V_{GB} > 0$, and the "1" is read by electron bombardment of an adjacent area at $V_{GB} > 0$ and by monitoring the increase in g_{ds} . A "0" is stored by not bombarding a given area of the gate electrode. The "0" is read in the same manner as the "1", but no increase in g_{ds} occurs. A plan view of the MOST structure is shown in Fig. 3. The crosshatched areas of the gate are assumed to be in a high conductance state (by electron bombardment at $V_{GB} > 0$), and the remaining area of the gate is in a low conductance state. The area 1 of Fig. 3 represents a high conductance path between S and D, and this function corresponds to an electron-beam-activated switch.

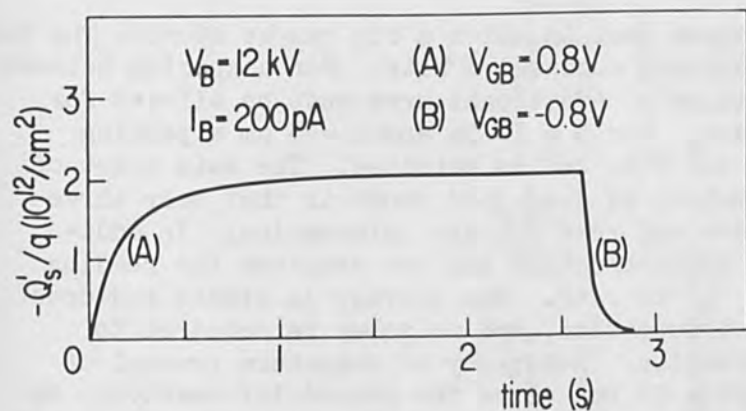


FIG. 2.—Experimental curve showing transient build-up (A) and decay (B) of positive charge Q_{GB} induced in the oxide of a MOST by electron bombardment. The measured parameter is the channel charge Q'_s attracted by Q_{GB} . Electron-beam voltage $V_B = 12$ kV, electron-beam current $I_B = 200$ pA. (A) Charging curve, $V_{GB} = 0.8$ V; (B) discharge curve, $V_{GB} = -0.8$ V.

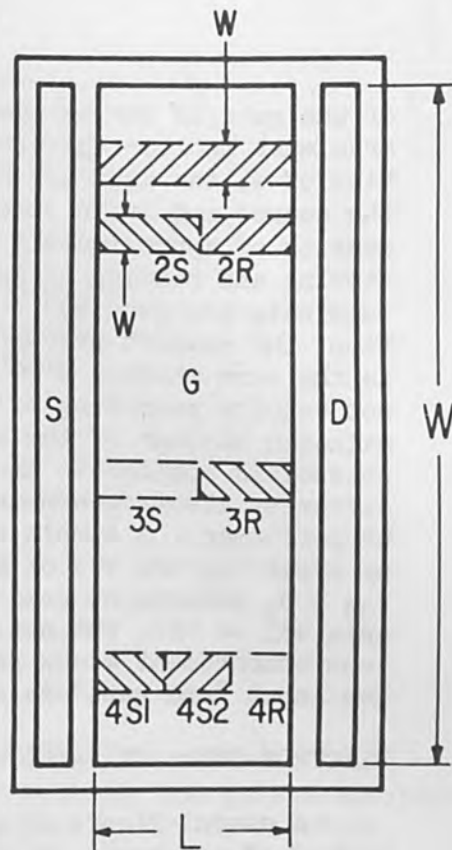


FIG. 3.—Plan view of the MOST. The crosshatched areas of the gate illustrate charge patterns in the oxide such that $V_T = -3$ V. The remainder of the gate is in the state $V_T' = -40$ V.

A storage device with nondestructive readout is obtained by using half the channel, the left side (LS), to store the information, and the remaining half of the channel, the right side (RS), to read the information. The areas 2S and 3S indicate storage of a "1" and a "0", respectively. When the RS of the channel is read by electron bombardment of areas 2R and 3R, adjacent to areas 2S and 3S, an increase in g_{ds} is observed when area 2R is bombarded at $V_{GB} > 0$, but no significant increase in g_{ds} is observed when area 3R is bombarded at $V_{GB} > 0$. To store many bits of information, the electron beam is scanned along the width W of the device on the LS of the channel. With V_{GB} positive, the beam current is pulsed on to store a "1" and off to store a "0" at any desired location; the information is stored in areas $wL/2$. The information is nondestructively retrieved by scanning the electron beam over the RS of the channel. The electron-beam current is pulsed on while $V_{GB} > 0$. Then the electron beam is turned off, V_G is set positive, and g_{ds} is monitored. Next, V_{GB} is set negative, and the electron-beam current is pulsed on once again, in order to discharge the oxide, and hence set $g_{ds} \approx 0$ for this particular area on the RS. This process is repeated for each area on the RS, in order to read information stored on the LS.

The number of bits that can be stored is determined by the total area

of the gate LW and by the minimum area in which a bit can be stored. The latter area must include the space between successive bits. For a spacing between bits of w , the area per bit is $2wL$. Additional area must be allowed for the source and drain electrodes. For $L = 10 \mu\text{m}$ and $w = 5 \mu\text{m}$ a packing density of approximately 2×10^5 bits/cm² is obtained. The main asset of storing and reading of information as described above is that only three terminals are required to store and read all the information. In addition, the readout process is nondestructive and the sequence for reading is the same whether a "0" or "1" is read. The storage is stable and does not require rewriting of the information, and no power is required to maintain storage of the information. Momentary or long-term removal of potentials applied to the device do not alter the stored information. By different electron-bombardment sequences, more complex logic functions can be performed. A simple two-input "and gate" configuration is illustrated by areas 4S1 and 4S2 of Fig. 3. If both 4S1 and 4S2 are bombarded at $V_{GB} < 0$, subsequent reading of 4R produces a large increase in g_{ds} . If area 4S1 or 4S2, but not both, is bombarded, a subsequent reading by electron bombardment of 4R produces only a small increase in g_{ds} ; hence, a two input "and gate" is obtained in this manner.

ELECTRON-BEAM ACTIVATED SWITCHING

A useful figure of merit for electron beam recording devices is the number of electrons per square centimeter necessary to change the state of the device. In terms of the incident charge per unit area, the electron beam dosage Q_{EB} is defined by the expression

$$Q_{EB} = \bar{J}_B \tau_B$$

where \bar{J}_B is the average current density of the electron beam and τ_B is the time the beam irradiates the storage area. The required electron-beam dosage is a characteristic of the storage medium, and its magnitude may vary with \bar{J}_B .

Switching times of the order of a few microseconds or less are usually required in electron beam switching applications. In order to demonstrate 5- μsec switching times, the following experiment was performed. An alternating square wave of voltage (Fig. 4a) was applied to the gate of an n-channel MOST, and a constant potential of $V_{DS} = 20 \text{ mV}$ was applied across the channel. For the devices used for these experiments, V_T was zero. Therefore, if the electron beam is off, $|I_D|$ (or equivalently, g_{ds}) is large during the positive portion of the gate voltage pulse as shown in Fig. 4(b). Then, if the electron beam is pulsed with $V_{GB} > 0$ (Fig. 4c), I_D should increase, because positive charge is stored in the insulator; this increase in I_{DS} is depicted by the level shift 1-2 in Fig. 4(d). Furthermore, the dosage is proportional to the time τ_B that the electron beam is on, since \bar{J}_B for the pulsed electron beam is I_B/A_B , where A_B is the area of the electron beam. Since A_B is approximately 10 times smaller than the total gate area of the n-channel MOST, a significant contribution to I_D is the result of the greater portion of the gate area, being "on" (inverted). The level shift 2-3 of Fig. 4(d) indicates this area of the channel being turned "off" when V_{GB} switches to $-2V$. When $V_{GB} = -2V$ the electron beam is pulsed for a time τ_B , and the charge is removed from the insulator. The area of the channel

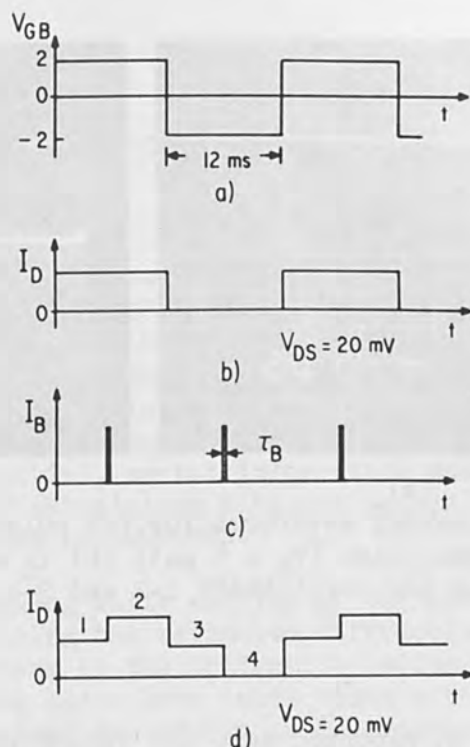


FIG. 4.—Schematic representation of the waveforms for the pulsed electron beam experiment. (a) V_{GB} ; (b) the channel current I_D for no electron bombardment; (c) the electron beam pulses; (d) I_D waveforms for pulsed electron bombardment.

bombarded by the beam is turned "off;" hence, the level shift 3-4 in Fig. 4(d).

Experimental curves showing the duration τ_B of the beam pulse and the I_D level shifts are illustrated in Fig. 5. The $5\ \mu\text{s}$ beam pulse of Fig. 5(a) produces the level shifts (Fig. 5b) 1-2 for $V_{GB} = 2\text{V}$ and 3-4 for $V_{GB} = -2\text{V}$. Both level shifts are approximately three small divisions on the I_D axis. If the dosage is increased by increasing the pulse widths, the level shifts increase. Therefore, for the $10\text{-}\mu\text{s}$ beam pulse, the corresponding traces for I_D indicate level shifts 1-2 and 3-4 of approximately five small divisions along the ordinate. For these measurements, the beam diameter was approximately $10\ \mu\text{m}$ and the beam current was approximately $1.5\ \mu\text{A}$; accordingly, \bar{J}_B was approximately $2\ \text{A}/\text{cm}^2$. The electron beam dosage for the $5\text{-}\mu\text{s}$ pulse illustrated in Fig. 5(a) is $10^{-5}\ \text{C}/\text{cm}^2$.

SUMMARY

Information storage has been demonstrated using an electron-beam induced charge storage phenomenon in the oxide of an MOST. This stored charge is stable at temperatures of 150°C and at room temperature for periods of up to a few months. This stored charge can be erased at will using the electron beam, and new information may be subsequently stored. This method has been demonstrated for 10^6 storage cycles at an electron-beam dosage of $10^{-5}\ \text{C}/\text{cm}^2$ for each cycle, or $10\ \text{C}/\text{cm}^2$ total dosage. The media sensitivity appeared to decrease slightly between the first cycle and the 10^6 cycle. Write times of $5\ \mu\text{s}$ have been demonstrated; these times were limited by available electron-beam equipment.

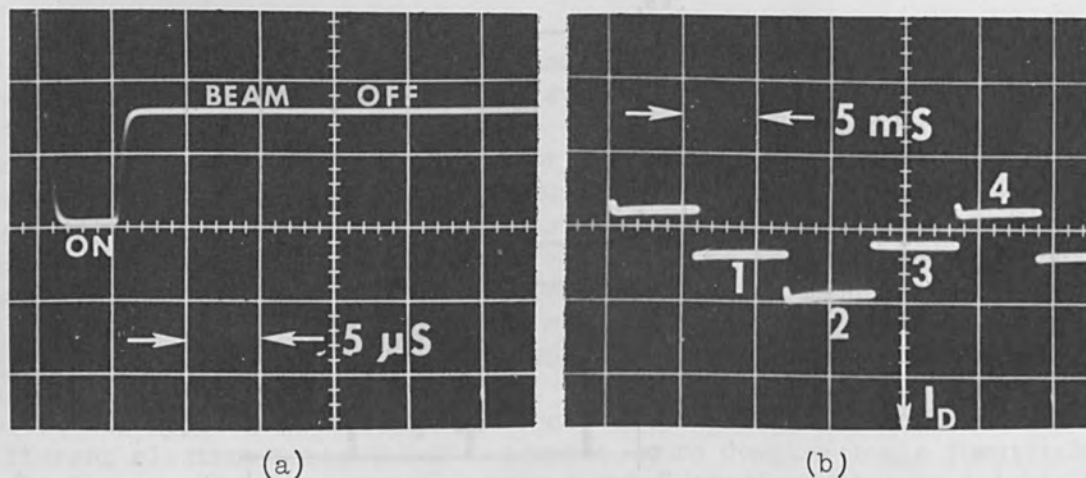


FIG. 5.—Experimental waveforms for the pulsed electron beam experiment. (a) Electron beam pulse ($\tau_B = 5 \mu\text{s}$); (b) I_D waveforms; the electron beam is pulsed during the level shift 1-2 and 3-4.

ACKNOWLEDGMENT

The research reported here was supported wholly by the Electronic Technology Division, Air Force Avionics Laboratory, Research and Technology Division, Wright-Patterson Air Force Base, Ohio, under Contract AF33(615)-3886.

REFERENCES

1. N. C. MacDonald and T. E. Everhart, "An Investigation of the Effects of Electron Beam Irradiation on Metal-Oxide-Semiconductor Transistors," Report ERL 66-16, University of California (Electronics Research Laboratory) Berkeley, California (to be published).
2. C. T. Sah, "Characteristics of MOS transistors," *IEEE Trans. ED-11*: 324-345, 1964.
3. A. S. Grove, B. E. Deal, E. H. Snow, and C. T. Sah, "Investigation of thermally oxidized silicon surfaces using metal-oxide-semiconductor structures," *Solid-State Electronics* 8: 145-163, 1965.

UNICON-COHERENT LIGHT DATA PROCESSING

C. H. BECKER

Precision Instrument Co., Palo Alto, California

ABSTRACT. UNICON represents a radically new data processing system which operates in real time. It is based on two-dimensionally distributed information elements of 1 micron in diameter, created in a special storage medium of optical unidensity. Information is helically positioned across the medium in a time-sequential, serial information pattern with a theoretical packing density of 645 million bits per square inch. UNICON has the potential to be expanded to 1000 MHz.

Instantaneous reproducing while writing of the recorded information occurs in real time, utilizing the reflected diffraction pattern produced from the recording laser beam at the Unidensity medium. Secondary reproducing with the unmodulated laser beam takes place after rewinding, either continuously along the helical recordings or incrementally in single-frame stop-scan fashion.

Depending on its electro-optical modulation characteristics and the time sequential positioning of the information elements, the UNICON operates as a frequency-modulated (FM) video frequency and wideband frequency recording/reproducing and display system, or a pulse-code-modulated (PCM) binary computer mass memory.

I. INTRODUCTION

UNICON represents a radically new approach to real-time data processing. Information is recorded within a special medium of optical unidensity (Fig. 1) utilizing a signal-modulated cw coherent laser beam from an argon II ionic laser to create and detect diffraction-limited "holes" of equal size of 1 micron in diameter in the Unidensity medium. The recorded information elements are helically positioned across the medium in a time-sequential, serial pattern. Depending on the serial-spacing between elements, the UNICON operates either as a wideband recorder/reproducer with time-varying spacing (FM) or as a pulse-code-modulation (PCM) binary serial-bit mass memory with equal spacing.

Transfer of the input signal to the laser beam takes place by means of an electro-optical modulator (Pockel's cell), providing changes of the refractive index of the modulator medium (KD*P) as a function of the sine of the applied electric field intensity.

Instantaneous reproducing with the UNICON utilizes photoelectrical detection of the diffraction pattern reflected back from the Unidensity medium during recording, within a few nanoseconds.

Secondary reproducing with UNICON, after rewinding and reduction of

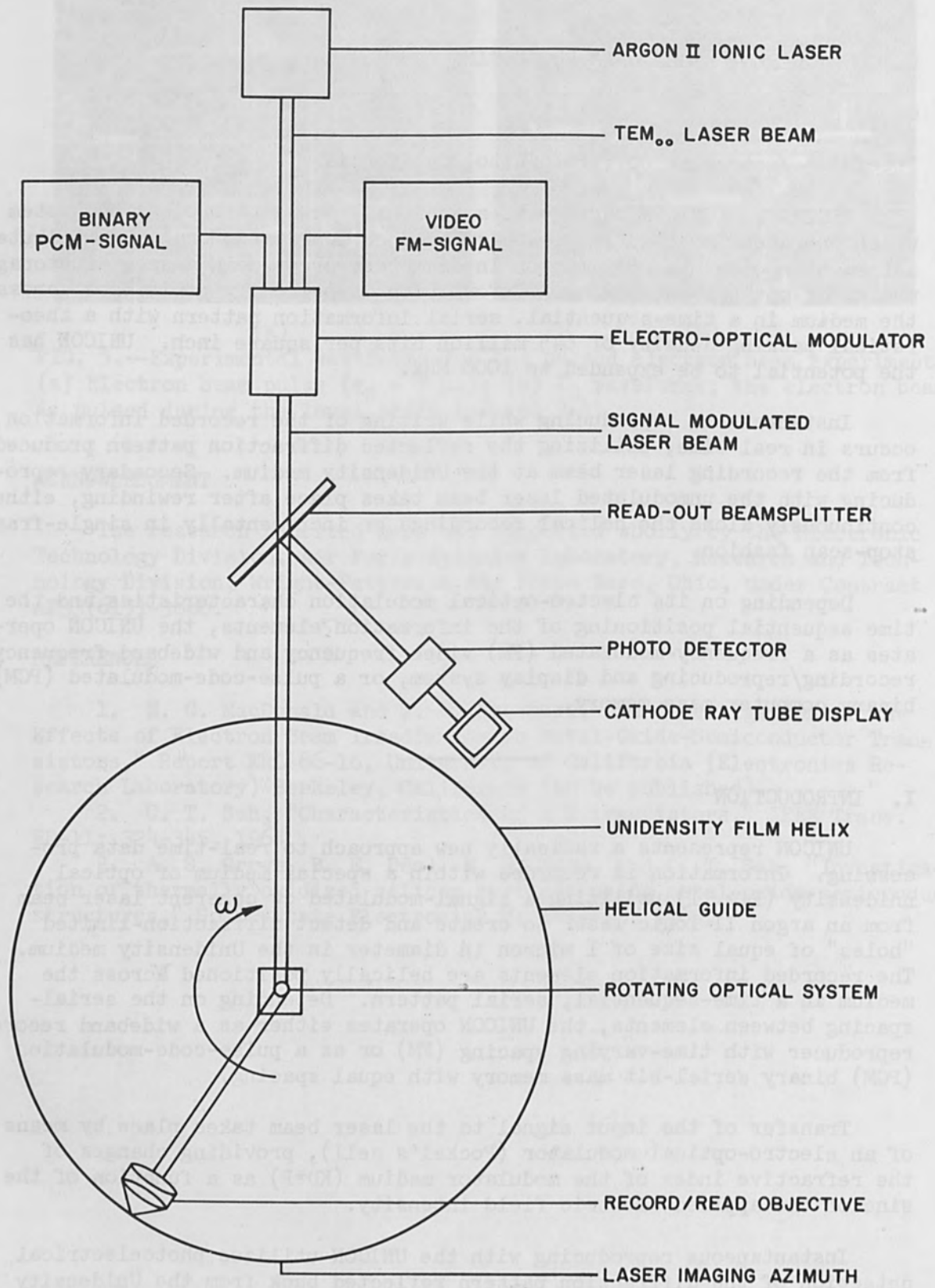


FIG. 1.—UNICON schematics.

laser power by 30 dB (to avoid erasing) reads the "holes," which have been produced in the Unidensity medium during recording, by means of the unmodulated laser beam at strongly reduced power. Secondary reproducing permits continuous reading along the helical recordings, or incremental operation in single-frame stop-scan fashion.

The kinematics of the UNICON are characterized by high-speed relative motion of a rotating optical system without mechanical contact against the Unidensity medium, which moves either continuously at very low speed or in incremental steps (stop-scan). The Unidensity medium can be coated on Mylar tape, disks, or drums, thus yielding helical, transverse, longitudinal, or cylindrical two-dimensional UNICON recording patterns.

The theoretical information packing density of the UNICON is determined by the diffraction limits of the system. It is 645 million "holes" per square inch, assuming 1-micron "holes" and "no-holes" as close as possible adjacent to each other (Fig. 2). The boundaries of a hole are characterized as the first dark Fraunhofer ring of the elementary diffraction pattern of the system.

The practical information packing density of the UNICON is essentially determined by the available laser power and the kinematics of the system. Track widening during recording while reading provides the certainty of tracking during secondary reproducing. The amount of track widening is determined by the available recording laser power, the required rate of the recording process and the mechanical error of the rotary system.

The rate of UNICON data processing depends on the ratio of recording laser power and required energy to produce one hole. Maximum rate of the UNICON is expected to be 1000 MHz.

The main applications of UNICON are wideband frequency recording/reproducing, geophysical exploration, computer mass memory, archival mass information storage, production control and automation. Compared to the present state of the art, UNICON provides real-time read-while-write data processing of more than 100 times over-all improvement in performance.

II. UNICON RECORDING/REPRODUCING PRINCIPLES

UNICON recording/reproducing principles are determined by the optical mode and divergence of the recording/reproducing laser beam, the diffraction limits of the optical system which images the laser aperture on the Unidensity medium, the thermodynamics of the hole-forming process, the signal-modulation principles, as well as the kinematics, which determine optical scanning and medium transport during recording/reproducing.

Assuming the laser emits a zero-order, single-mode (TEM_{00}) coherent light beam at a certain wavelength λ , the laser beam has a diffraction-limited divergence angle α defined by

$$\sin \alpha \approx \alpha = 1.22 (\lambda/D_0)$$

where D_0 is the intrinsic aperture of the laser (Fig. 3).

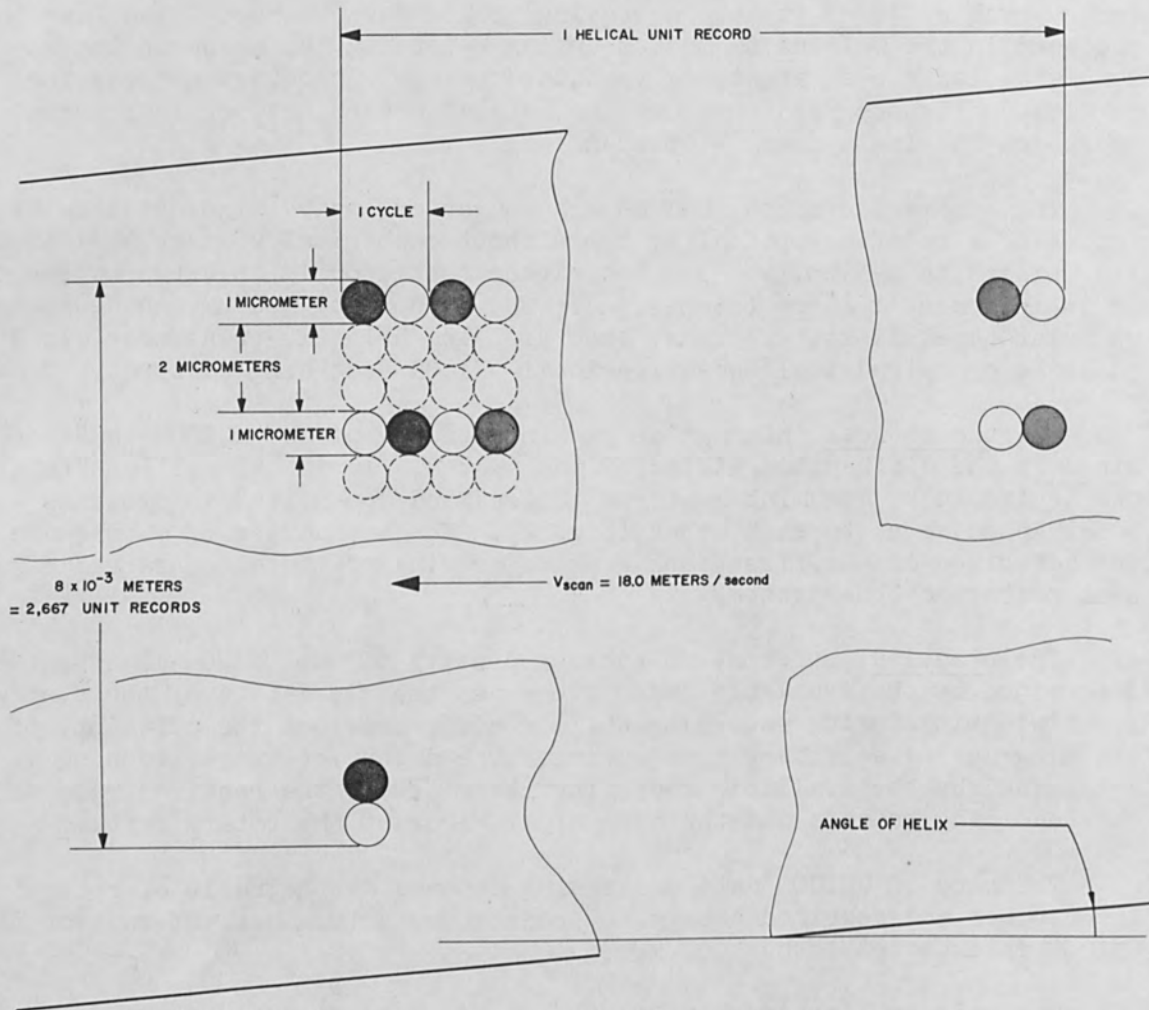


FIG. 2.—UNICON theoretical recording pattern. Theoretical packing density, 6.45×10^8 bits/in.

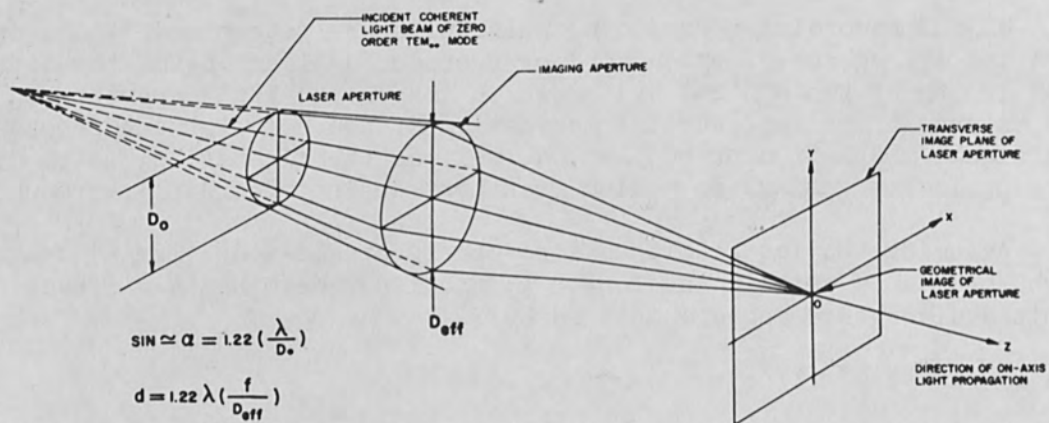


FIG. 3.—Optical rays for theory of imaging of a laser aperture (principles).

The diverging laser beam is "focused" to the Unidensity medium by means of imaging the laser aperture to the Unidensity medium through a diffraction-limited objective. The laser image has a diameter d orthogonal to the direction of laser propagation given by

$$d = 1.22 \lambda (f/D_{\text{eff}})$$

where λ is the laser wavelength, f is the focal length of the objective, and D_{eff} is its effective aperture.

The thermodynamics of the hole-forming process are basically determined by the Stefan-Boltzmann law:

$$S = \sigma T^4 \text{ W/cm}^2$$

yielding the absolute vacuum temperature T at the plane of laser imaging as a function of the laser power density S , which is incident at the laser image; σ is a constant, $5.673 \times 10^{-12} \text{ W cm}^{-2} \text{ }^\circ\text{K}^{-4}$.

UNICON signal modulation is characterized by the fact that the recording laser blows diffraction "holes" in the Unidensity medium, which are instantaneously or secondarily detected by the laser beam. The holes have equal size of 1 micron in diameter. The spacing of holes and no-holes along the recording/reproducing tracks determines the specific information processing characteristics of the UNICON.

When the spacing between holes and no-holes is equal, UNICON represents a pulse code modulation (PCM) serial bit binary mass memory built from binary words of, for example, four time bits plus 36 information bits of equal size (Fig. 4). Thousands of these binary words, in series, represent one unit record, or frame, of the UNICON system.

When spacing between holes and no-holes is alternating as a function of the amplitude of the signal frequency, the UNICON system represents a video-frequency or wideband-frequency (FM) recording/reproducing system (Fig. 5). In that case, information to be recorded/reproduced is converted into the frequency modulation of a square-wave carrier frequency.

UNICON is determined by the kinematics of the following operations:

- (a) UNICON single-frame recording/reproducing (Fig. 6);
- (b) UNICON helical multiple-frame incremental recording/reproducing (see Fig. 7); and
- (c) UNICON helical multiple-frame continuous recording/reproducing (Fig. 8).

The essential element of UNICON single-frame operation is the optical horizon of the system determining the circular azimuth of the laser image in respect to the axis of rotation of the system. Without any error, the height of this azimuth equals the smallest diameter d of the laser image which is determined by the diffraction limits of the system. Instantaneous reproducing of such circular recording takes place without any tracking error, because of the reflective read-while-write characteristics of the

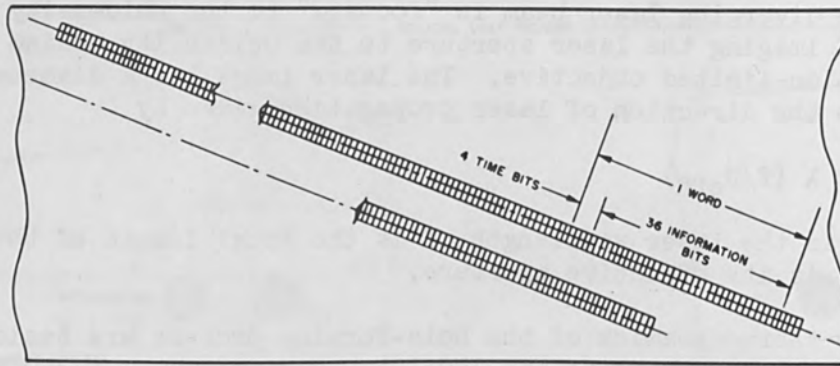


FIG. 4.—UNICON serial-bit pulse-code-modulation (PCM) binary recordings (schematics).

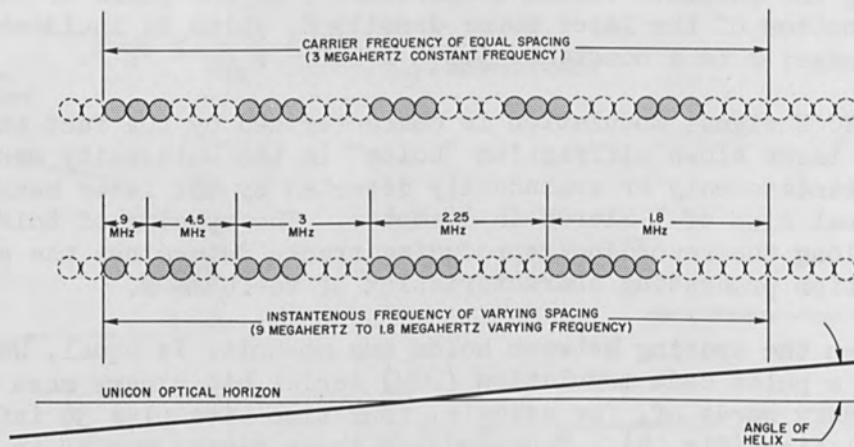


FIG. 5.—UNICON frequency-modulation (FM) recording (schematics).

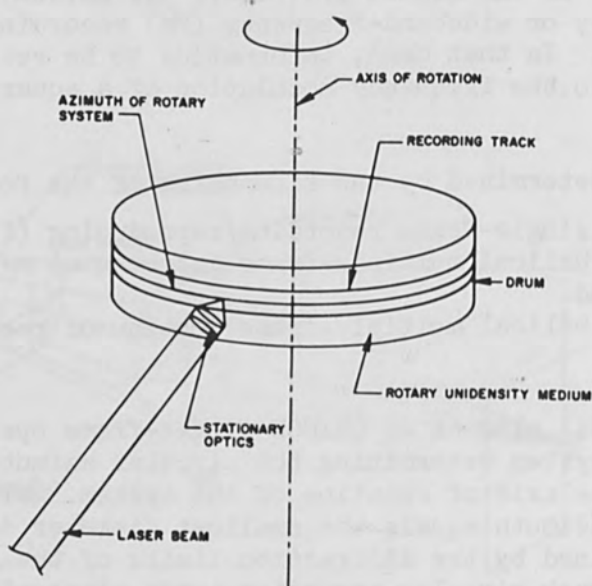


FIG. 6.—UNICON single-frame recording/reproducing schematics.

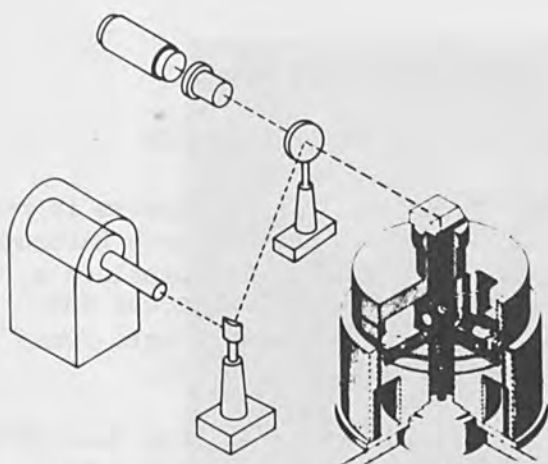


FIG. 7.—UNICON helical multiple-frame incremental recording reproducing.

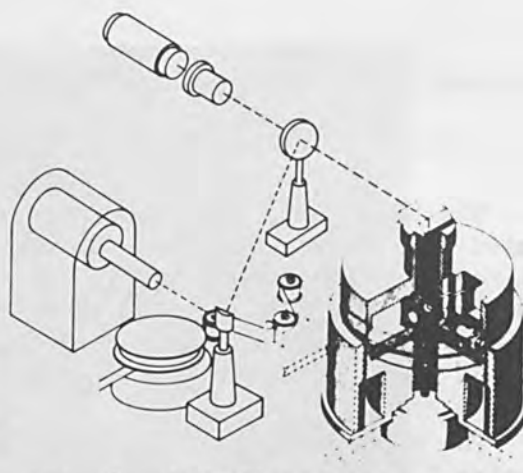


FIG. 8.—UNICON helical multiple-frame continuous recording reproducing.

UNICON. Within nanoseconds the diffraction pattern of the elementary recording process is detected during its creation.

In secondary reproducing, on the other hand, the reading laser beam does not necessarily trace the original recording track, even assuming the reproducing system utilizes the same optics as the recording system. Hence, in order to compensate for secondary readout errors, UNICON provides "track-widening" during recording of such an amount that the reading laser image (without track widening) always stays within the recording track.

The kinematics of the UNICON helical multiple-frame incremental operation (b) utilizes a rotating optical system within two concentric pistons carrying Unidensity film on a helical path around the piston surfaces. Thus, incremental recordings are produced during one revolution of the internal optical system, assuming recording capability is electronically gated to one 360° frame only, utilizing the electro-optical modulator of the system. The Unidensity medium stands still during the recording period, while instantaneous reproducing of the incremental recordings occurs in real time, characterizing the utmost important read-while-write feature of the UNICON system. Between recordings, incremental helical motion of the medium provides space for the next single-frame recording process. When no helical motion occurs after recording, continuous reproducing of one single-frame takes place, again and again, demonstrating the stop-scan fashion of readout during the single-frame recording period.

The kinematics of the UNICON helical multiple-frame continuous recording/reproducing operation (c) determine continuous slow motion of the Unidensity medium during recording/reproducing. Proper selection of the recording pattern assures operation in continuous scan or unlimited incremental stop-scan fashion, a feature which is exclusive with the UNICON, because of the complete elimination of mechanical contact between recording/reproducing optics and Unidensity medium. Of course, as for incremental UNICON recording/reproducing, instantaneous reproducing of the continuous recordings occurs in real-time, thus demonstrating the

continuous read-while-write characteristics of UNICON.

III. UNICON WIDEBAND RECORDING/REPRODUCING AND DISPLAY SYSTEM

The UNICON wideband recording/reproducing and display system is represented by a functional research model operating at the Research Laboratory of Precision Instrument Co. in Palo Alto, California. It comprises a continuous UNICON video drum recording system with instantaneous and secondary continuous reproducing, incorporating stop-scan single-frame readout and a video display on a CRT television tube (Fig. 9).

The experimental UNICON recorder/reproducer is a rotating drum which carries 1/2-in. Unidensity tape at a constant speed. The diffraction-limited objective is continuously or incrementally movable across the drum surface by means of a micromanipulator. Reflective instantaneous and secondary readout is provided by a beam splitter and a photo-electric detector. Video information is picked up by a video camera, the output of which is applied to an electronic AM to FM converter, followed by a special drive amplifier which generates the control voltage for the electro-optical modulation of the laser beam.

To demonstrate the performance characteristics of the experimental UNICON video recording/reproducing system, Fig. 10 shows the reproduction of a Polaroid picture that was made off the monitor screen in real time and instantaneously during continuous recording. The photograph was originally taken from a magazine illustration by means of a television camera, the video output of which was applied to the UNICON.

A microphotograph of instantaneous frequencies of the picture information is shown in Fig. 11, representing a minute part of the actual picture and covering an area of 354 square microns of the corresponding Unidensity tape. The microphotograph was taken with a Polaroid camera utilizing a Leitz research microscope with 100x oil-immersion objective. For comparison, a scale is projected between the recording tracks, with one division corresponding to 1.13 microns.

IV. UNICON COMPUTER MASS MEMORY SYSTEM

The UNICON computer mass memory system was described earlier at the 1966 AFIPS Fall Joint Computer Conference in San Francisco. A functional research model of the system is shown in Fig. 12. An argon II ionic laser provides the recording/reproducing laser beam which enters the UNICON computer mass memory after passing through the electro-optical modulator. Information to be recorded is provided from the computer word generator, which simulates 40-bit standard computer words by means of 4 time bits and 28 information bits at a rate of 2 megabits/sec. The output of the computer word generator is displayed on a double-beam oscilloscope (Tektronix 555) and simultaneously applied to the driver stage of the electro-optical modulator. Electronic gating provides a single-frame 360° recording on the UNICON of the computer words. Reflective instantaneous and secondary readout of the recorded information is applied to a photodetector by means of a beam splitter and detected with a second oscilloscope (Tektronix 547). Reproductions of polaroid pictures of the two oscilloscopes are seen in Fig. 13, showing the identity between input



FIG. 9.—Experimental UNICON video drum recorder/reproducer.

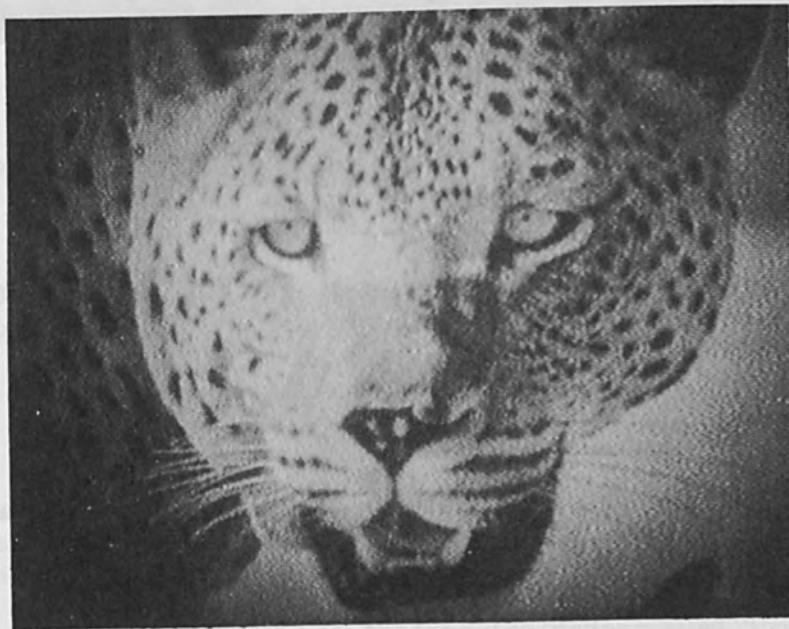


FIG. 10.—UNICON instantaneous real-time video screen picture (Polaroid).

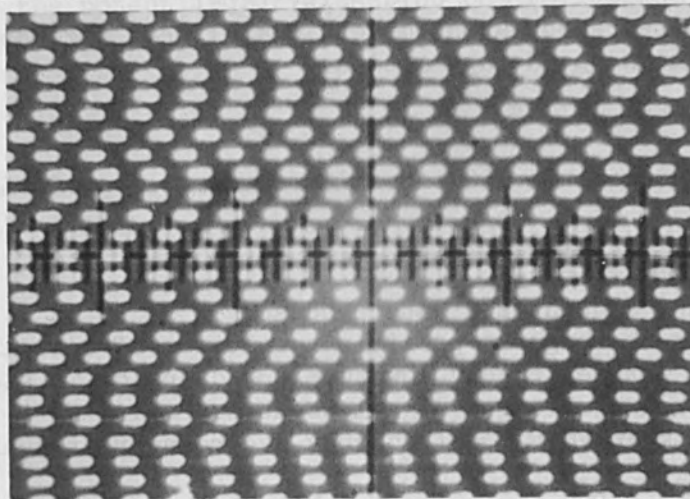


FIG. 11.—UNICON instantaneous video frequency (microphotograph).

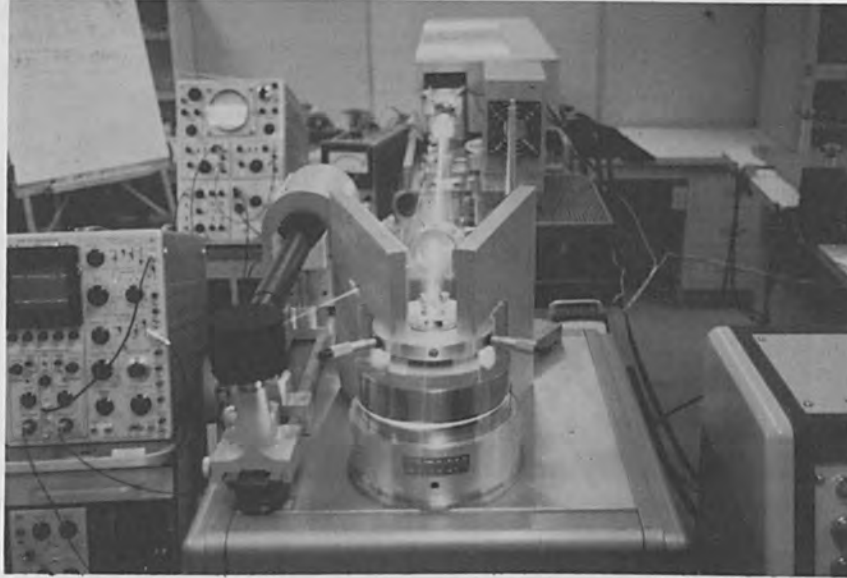


FIG. 12.—UNICON computer mass memory.

and output of the UNICON computer mass memory functional research model.

V. ADVANCEMENT OF THE STATE OF THE ART WITH UNICON

Advancement of the state of the art achieved with the UNICON may best be presented by comparison with present technology in data processing:

The UNICON

- does not operate in vacuum;
- does not represent a magnetic or photographic silver halide process;
- does not possess photographic grain, diffusion, or solarization;
- does not use photographic, photoluminescent, or photochemical development and processing;
- does not have mechanical contact and wear between recording/reproducing head (objective) and Unidensity tape;
- does not represent a one-dimensional linear recording/reproducing process with high-speed tape motion.

However, the UNICON

- provides more than 100 times improvement in performance characteristics;
- operates in real-time;
- reads-while-writing;
- represents a quantized data process;
- possesses the highest possible resolution of optical data processing;
- operates with extremely low tape speed and/or in stop-scan fashion;
- possesses unchallenged signal-to-noise ratio;
- represents an FM video-frequency recording/reproducing and display system;
- represents a PCM binary serial bit mass memory of maximum information

HIGH VOLTAGE POWER SUPPLY

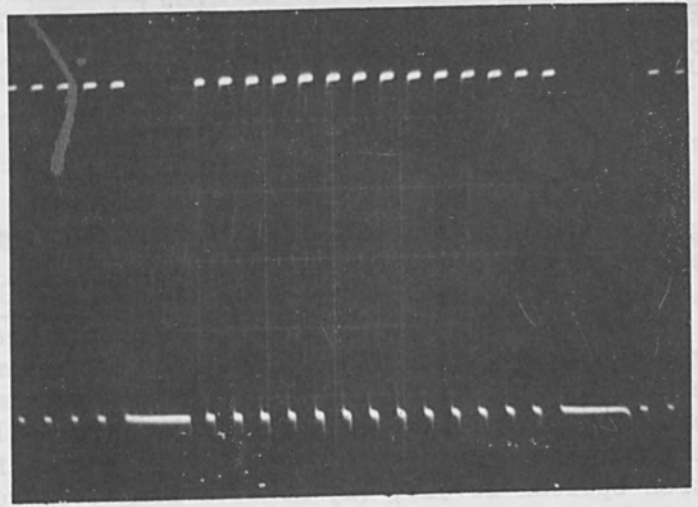
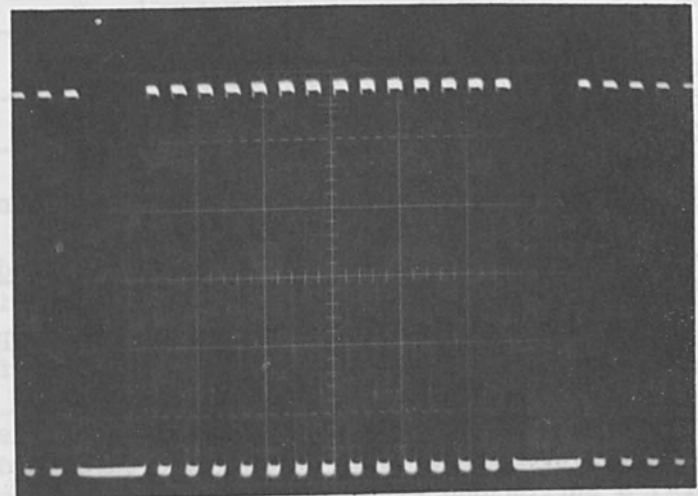


FIG. 13.—UNICON computer word read-in/readout.

packing density and rate;
 possesses the potential for extension to an FM wideband frequency recording/reproducing and display system of up to a frequency bandwidth of 1000 MHz.

AN ELECTRON-BEAM SYSTEM FOR DIGITAL RECORDING

K. H. LOEFFLER

International Business Machines Corp., San Jose, California

ABSTRACT. An electron-beam system has been designed for digital recording in a computer environment. To meet the specifications for reliability, serviceability, and automatic, integrated operation, the electron-optical hardware incorporates: (1) provisions for four feedback control systems to stabilize and monitor the column performance; (2) an easily exchangeable central tube containing all beam-exposed column parts; (3) several indirectly heated apertures and beam current sensors; and (4) a turret gun with a supply of automatically indexed filaments. The system requires no operator attendance for at least two weeks and subsequently only a minimum maintenance time.

INTRODUCTION

In a digital recording system, any instantaneous deterioration of performance beyond levels acceptable to the error coding scheme results in a clearly detectable system malfunction. To preclude such malfunctions in the electron-beam system described here, the design had to conform to the rigid specifications for digital computer hardware with respect to reliability, serviceability, and automatic, integrated operation. The main points of the design philosophy were: (1) automatically monitor and control the operational state of the system tightly on several electron-optical levels; (2) achieve long-term reliability through low contamination rates by intercepting the electron beam with heated surfaces only; (3) reduce any maintenance in the field to a simple exchange of one or two preassembled and pretested units at relatively long intervals.

Accordingly, the following features were incorporated in the electron-optical hardware: (1) provisions for four feedback control systems¹ to stabilize and monitor the column performance; (2) an easily exchangeable central tube containing all beam-exposed column parts; (3) several indirectly heated apertures and beam current sensors; and (4) a turret gun with more than a two-week supply of automatically indexed filaments. These features are presently implemented in a photo-digital mass storage system.² They can be used equally well in other data recording and reading applications, in fabricating and testing electronic microcomponents, or in situations where unattended and reliable operation is convenient or necessary.

Figure 1 illustrates schematically the major electron-optical and electronic components of this system, and Figs. 2 and 3 show cross sections of the electron-optical hardware.

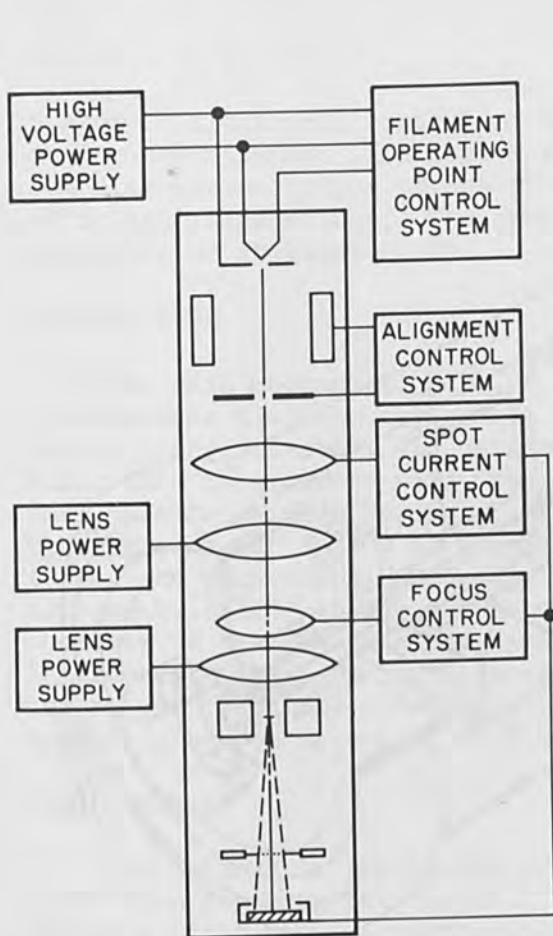


FIG. 1.—Major electron-optical and electronic components.

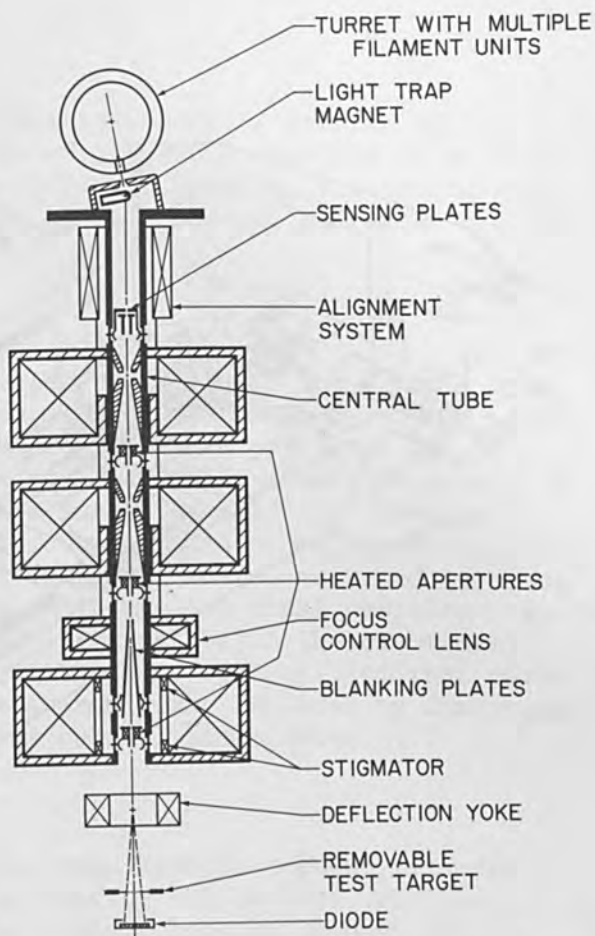


FIG. 2.—Cross section of the electron-optical system.

ELECTRON GUN

The beam is generated in the electron gun which contains 16 expendable filament units in a turret. Primarily, these units have been designed for mechanical ruggedness, thermal stability, and small size. They consist of a tungsten hairpin filament 0.005 in. in diameter, spot-welded to a pair of contact pins which are pressed into a cylindrical alumina insulator (Fig. 4). This subassembly is surrounded by an externally polished grid cylinder of stainless steel, the face of which is 0.016 in. from the filament tip and 0.162 in. from the anode. A special high-voltage power supply with separate terminals for high-voltage power output and high-voltage sensing input has been used to make the auto-bias operation of the gun compatible with long-term stability of the acceleration potential. Accordingly, the power output has been connected to the grid and the sensing input to the filament, thus stabilizing its potential at the operating voltage of -12 kV.

Electron-optical design goals consisted of (1) high gun brightness without space-charge saturation to avoid waste of potential filament life, and (2) moderate field strength between anode and cathode to minimize the danger of high-voltage discharges. Using the theory of Ploke,³ the optimum operating conditions for this system were found to be a grid voltage of -900 V, emission current of 500 μ A, and a brightness of about 8×10^4 A/cm²sr, corresponding to an emission current density of about

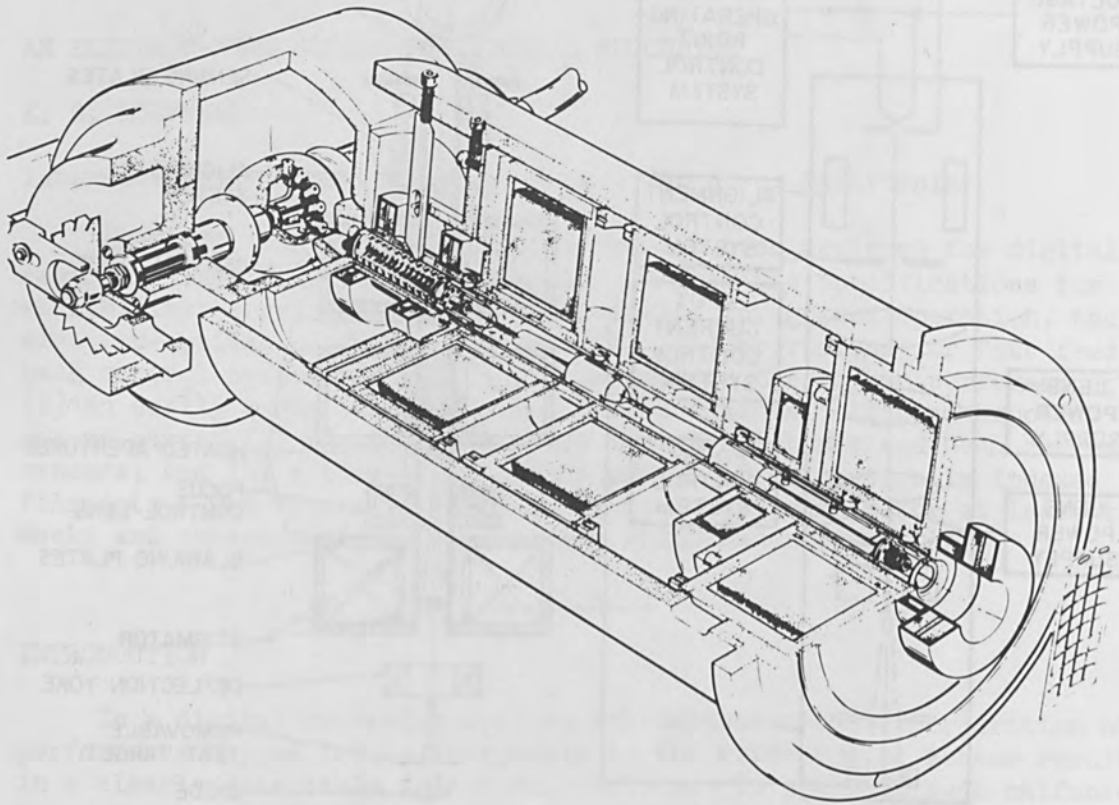


FIG. 3.—Lens assembly and electron gun.

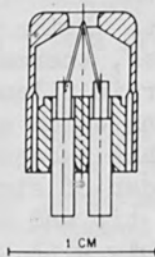


FIG. 4.—Filament unit used in turret gun.

5 A/cm². Electronic control of the heating current, varying typically during the filament life over a range of 3.3-3.0 A, results in a 30 to 40% diameter reduction of the filament before burnout, indicating very efficient filament use. The controls are adjusted to guarantee a filament life of at least 24 hr.

CENTRAL TUBE

The main mechanical part of the lens assembly is the central tube which serves simultaneously as a vacuum wall, alignment reference, electrical interconnector, and maintenance unit. This precision gun-drilled brass tube is provided with internal and external guidance slots and 20 small electrical feedthroughs soldered into its wall. It contains all beam-exposed parts such as the anode, sensing plates, pole pieces, apertures, and beam-blanking plates. The internal parts, machined to close tolerances, slide inside the tube to their precise final position. Spring contacts on the internal and external parts establish the electrical interconnections. During maintenance, the tube with all internal parts can be simply pulled out of the lens assembly and replaced by inserting another cleaned, assembled, and tested tube within minutes.

LENS ASSEMBLY

The cathode is positioned off the tube axis to prevent filament light from reaching the target. Upon leaving the cathode, the beam passes a light trap magnet behind the anode, where it is bent 10° to provide initial alignment with the tube axis. A major part of the beam current is then intercepted by a symmetrical system of four electrically insulated sensing-plate quadrants. These sensing plates provide the error signal for the alignment control system and are beam heated to several hundred degrees centigrade to prevent excessive contamination. The first two of the magnetic lenses have internal pole pieces which allow operation with short focal length (typically around 0.7 in.). A special lens with a short response time used for automatic focus control is located between the second and third lenses. The third lens contains an 8-coil magnetic stigmator in the external lens body and is operated with a focal length of about 2.7 in.

APERTURES

All apertures are indirectly heated to a temperature of 300°C with a power input of about 3 W to reduce the contamination rate by residual organic vapors and to render other contaminants sufficiently conductive.⁴ This feature has proved to be extraordinarily helpful in achieving the required long-term operational reliability. The main parts of the aperture assembly (Fig. 5) are the 0.005-in.-thick platinum-iridium aperture face mounted on a molybdenum base, an alumina bobbin with two heater coils of opposite current direction to reduce magnetic lens effects, and a thermal insulator of cordierite ceramics. The diameter of the central hole is 0.020 in. for all apertures, except for the last one which has a diameter of 0.014 in. Electrical insulation of the apertures allows their use as sensors for the intercepted beam current, to monitor the operational state of the system on several electron-optical levels inside the column.

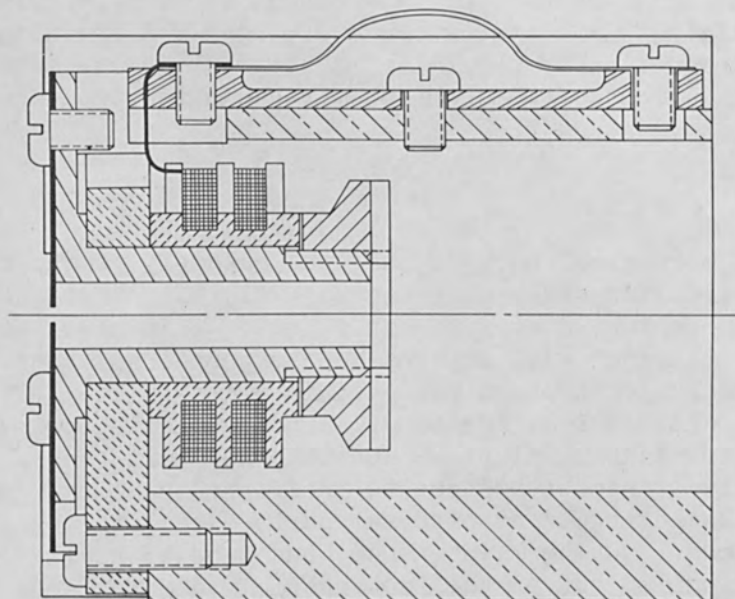


FIG. 5.—Cross section of heated-aperture assembly.

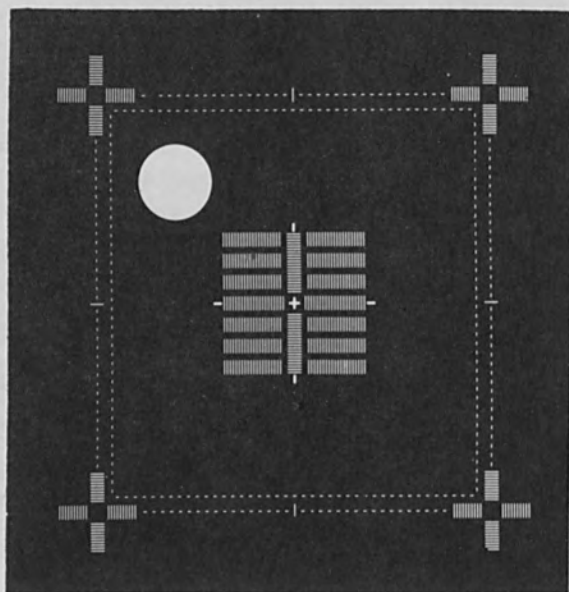


FIG. 6.—Pattern of the test target.

(The hole in the upper left corner provides beam passage to a small Faraday cup for occasional calibration of the semiconductor diode.)

RECORDING CHAMBER

The recording chamber contains the deflection and test elements and the transport mechanism for the recording medium. A working distance of 5 in (from the principal plane of the last lens to the target plane) is used, and the permissible range of the spot diameter is 1 to 2 microns over a field of view 0.25 in. square at a beam current of 5 nA. The beam is deflected by a magnetic yoke for the main deflection and by a pair of electrostatic deflection plates for very high speeds and very small deflection angles. The removable test target (Fig. 6), located in the recording plane, is a thin metal sheet with a special photolithographically produced pattern of openings. By deflecting the beam over these openings and sensing the current passing through the openings with a large-area semiconductor photo diode located beyond the test target, either the error signals for the automatic focusing control system and the spot current control system can be generated or a variety of deflection pattern adjustments and tests can be performed.

SYSTEM CONTROL

The whole electron-beam system is controlled solely by electrical means. Field engineers can check and test the equipment in manual mode on a special control panel. During regular automatic operation, all control, deflection, modulation, power supply, and pumping systems are monitored and sequenced by a central control processor.

ACKNOWLEDGMENT

The author gratefully acknowledges the implementation efforts of many members, both of the Advanced Technology and the Information Storage and Retrieval groups. Mr. C. H. Ting and Mr. M. H. Dost developed the test target, and Mr. E. Salbu contributed the concept of electrical feed-throughs in the central tube.

REFERENCES

1. F. Kurzweil, Jr., R. R. Barber, and M. H. Dost, "Automatic control of an electron-beam column," following paper in the present volume.
2. J. D. Kuehler and H. R. Kerby, "A photo-digital mass storage system," Proc. Fall Joint Computer Conference, 1966; pp. 735-742.
3. M. Floke, "Elementary theory of electron beam formation in a triode system" (in German); I. "Characteristics of the static field in the usual systems," Z. angew. Physik 3: 441-449, 1951; II. "Beam current and structure of the electron beam," *ibid.* 4: 1-12, 1952.
4. K. H. Loeffler, "An electron beam system for unattended reliable operation," 6th Intern. Congr. Electron Microscopy, Kyoto, Japan, 1966; pp. 203-204.

AUTOMATIC CONTROL OF AN ELECTRON-BEAM COLUMN

F. KURZWEIL, JR., R. R. BARBER, and M. H. DOST

International Business Machines Corp., San Jose, California

ABSTRACT. Automatic control techniques have been used to accomplish implementation of a stable, reliable electron-beam recording system for unattended, stand-alone operation. This recording system is an integral part of an IBM photodigital mass memory system. Discussed are the objective, the control concept, and the theory of operation for each of the four electronic control systems which are used to stabilize the important beam parameters: (1) a filament operating-point control system which provides stable, long-life emission from each filament; (2) an alignment control system which maintains the beam on the central axis of the column; (3) a focus control system for periodically refocusing the beam in the recording plane; and (4) a spot current control system for periodically readjusting the spot current in the recording plane.

INTRODUCTION

To realize the high-density recording capabilities of an electron-beam column, an electron-beam recording system has been developed to write data on silver-halide photographic film. As described by J. D. Kuehler and H. R. Kerby,¹ the basic function of the electron-beam recorder used in an IBM photodigital mass memory system is to expose silver halide film to the electron beam and thereby produce data patterns on the film for eventual recovery. The film is transported into the vacuum, exposed, and then withdrawn for further processing. Accordingly, the requirements of the recorder are (1) to assure reliable operation of the electron beam column during the recording intervals and (2) to assure spot characteristics at the target plane essential to data retrieval.

The control systems on the column are the key to providing the long-term column stability which satisfies the above requirements.

Design of the electron-beam column² was oriented toward unattended operation, minimum maintenance, and ease of serviceability. Figure 1 indicates the control systems which were added to the basic column to monitor and stabilize the important beam parameters.

These systems correct for filament variations occurring either during the filament lifetime or as a result of filament exchange, as well as other variations due to environmental influences. The filament operating-point control system controls the filament current to extend the life of the filament at the required brightness. The alignment control system periodically checks the recording spot size (between recording intervals) and automatically refocuses the spot. The spot-current control system periodically checks the recording spot current (between recording intervals) and automatically adjusts the spot current to its desired

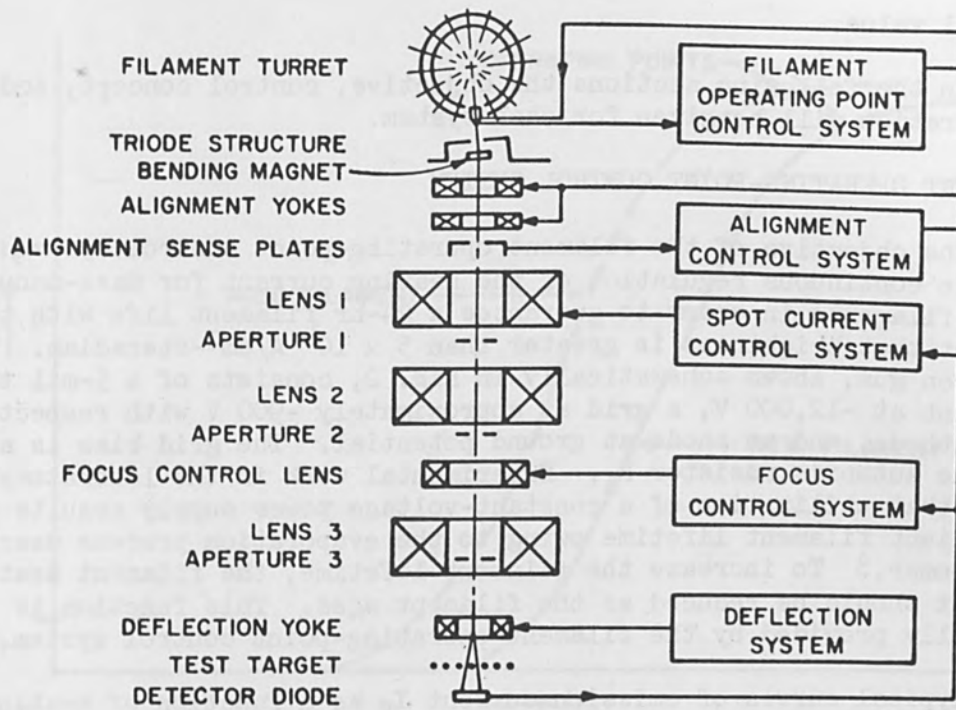


FIG. 1.—Basic electron-beam column and control systems.

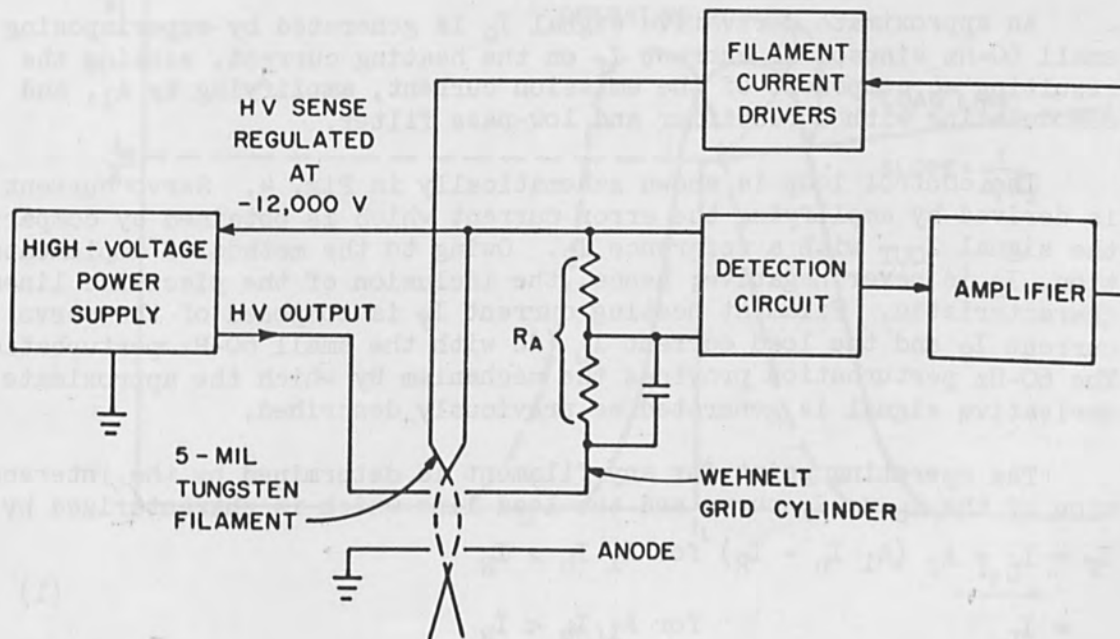


FIG. 2.—Filament operating point control system.

nominal value.

In the following sections the objective, control concept, and theory of operation will be given for each system.

FILAMENT OPERATING-POINT CONTROL SYSTEM

The objective of the filament operating-point control system is to provide continuous regulation of the heating current for mass-manufactured filaments in order to guarantee a 24-hr filament life with the constraint that brightness is greater than 5×10^4 A/cm²-steradian. The electron gun, shown schematically in Fig. 2, consists of a 5-mil tungsten filament at -12,000 V, a grid at approximately -900 V with respect to the cathode, and an anode at ground potential. The grid bias is achieved via the autobias resistor R_A . Experimental work in the laboratory has shown that utilization of a constant-voltage power supply results in insufficient filament lifetime owing to the evaporation process described by Bloomer.³ To increase the filament lifetime, the filament heating current should be reduced as the filament ages. This function is automatically provided by the filament operating-point control system.

Typical curves of emission current I_E as a function of heating current I_F for a new and an aged filament are shown in Fig. 3(a). Experimentally, both filaments have met the brightness criterion when I_F was set such that the operating point is on the knee of the I_E curve. The basic design approach centers around the idea of always operating on the knee of the I_E -vs- I_F curve. The design is implemented by generating a signal I_b which is proportional to the derivative $\Delta I_E / \Delta I_F$ and by servoing to a point on the downward slope of I_b (Fig. 3b).

An approximate derivative signal I_b is generated by superimposing a small 60-Hz sinusoidal current I_p on the heating current, sensing the resulting ac component of the emission current, amplifying by A_1 , and demodulating with a rectifier and low-pass filter.

The control loop is shown schematically in Fig. 4. Servo current I_S is derived by amplifying the error current which is obtained by comparing the signal I_{OUT} with a reference I_R . Owing to the method of implementation, I_S is never negative; hence, the inclusion of the piecewise linear characteristic. Filament heating current I_F is composed of the servo current I_S and the load current I_L (dc with the small 60-Hz perturbation). The 60-Hz perturbation provides the mechanism by which the approximate derivative signal is generated as previously described.

The operating point for any filament is determined by the intersection of the I_b vs I_F curve and the load line which is characterized by

$$\begin{aligned} I_F &= I_L + A_2 (A_1 I_b - I_R) \text{ for } A_1 I_b \geq I_R \\ &= I_L \text{ for } A_1 I_b < I_R \end{aligned} \quad (1)$$

As shown in Fig. 3(b), the heating current is automatically reduced as the filament ages.

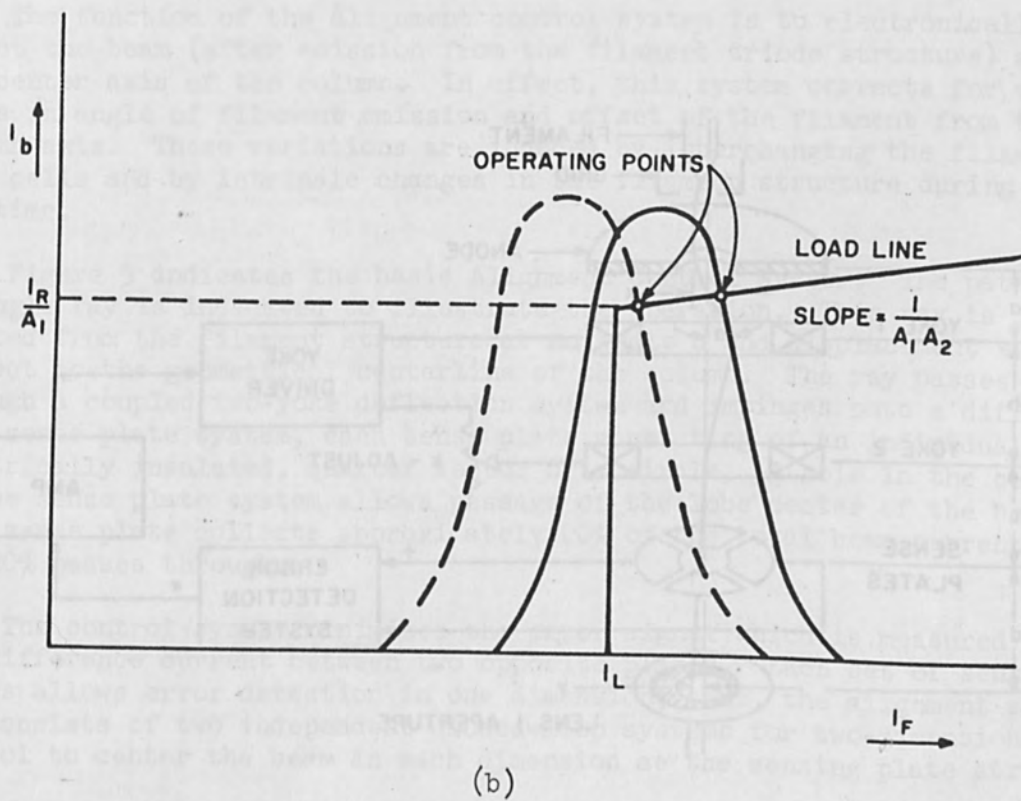
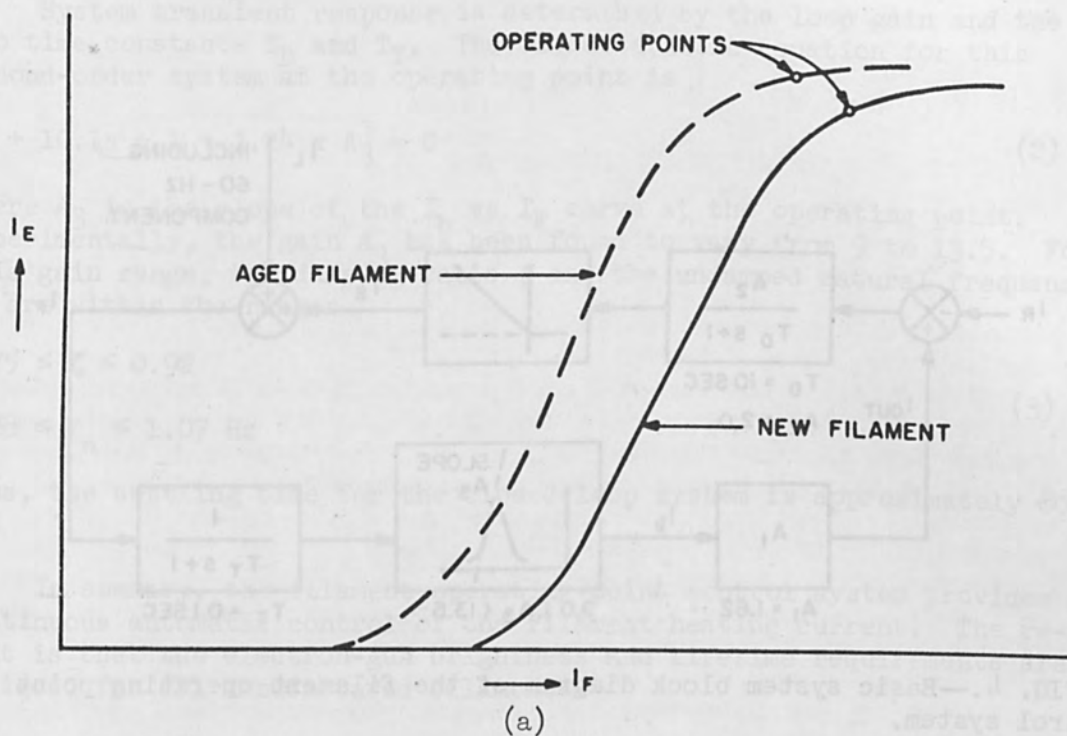


FIG. 3.—(a) Typical emission current vs heating current curves, (b) approximate derivatives of the curves in 3(a) and load line.

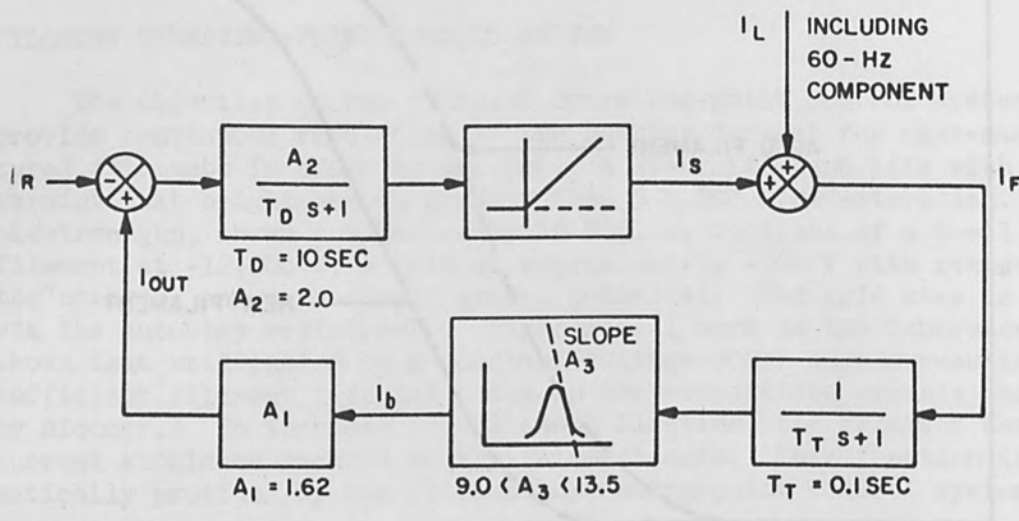


FIG. 4.—Basic system block diagram of the filament operating point control system.

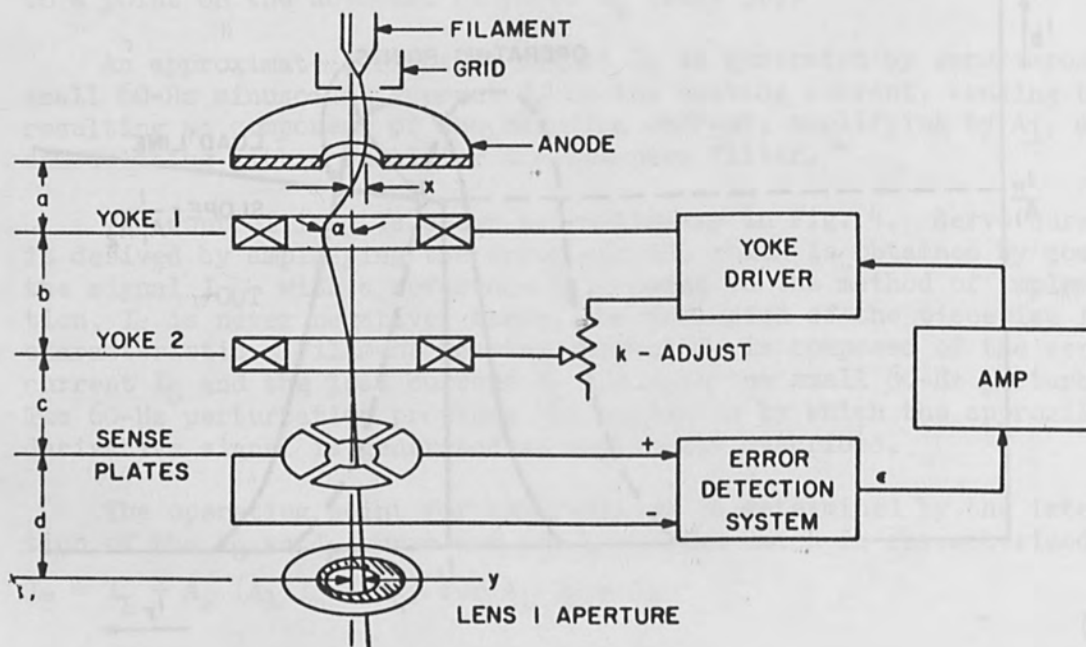


FIG. 5.—One-dimensional representation of the alignment control system.

System transient response is determined by the loop gain and the two time constants T_D and T_T . The characteristic equation for this second-order system at the operating point is

$$s^2 + 10.1s + 1 + 3.24 \times A_3 = 0 \quad (2)$$

where A_3 is the slope of the I_b vs I_T curve at the operating point. Experimentally, the gain A_3 has been found to vary from 9 to 13.5. For this gain range, the damping ratio ζ and the undamped natural frequency f_n are within the ranges

$$0.75 \leq \zeta \leq 0.92 \quad (3)$$

$$0.88 \leq f_n \leq 1.07 \text{ Hz}$$

Thus, the settling time for the closed-loop system is approximately 800 ms.

In summary, the filament operating-point control system provides continuous automatic control of the filament heating current. The result is that the electron-gun brightness and lifetime requirements are achieved for all manufactured filaments.

ALIGNMENT CONTROL SYSTEM

The function of the alignment control system is to electronically direct the beam (after emission from the filament triode structure) along the center axis of the column. In effect, this system corrects for variations in angle of filament emission and offset of the filament from the column axis. These variations are induced by interchanging the filament unit cells and by intrinsic changes in the filament structure during its lifetime.

Figure 5 indicates the basic Alignment Control System. The path of a single ray is indicated to illustrate the operation. This ray is emitted from the filament structure at an angle α and displacement x with respect to the geometrical centerline of the column. The ray passes through a coupled two-yoke deflection system and impinges onto a differential sense plate system, each sense plate consisting of an individual, electrically insulated, quarter sector of a circle. A hole in the center of the sense plate system allows passage of the lobe center of the beam. Each sense plate collects approximately 20% of the total beam current and 20% passes through.

The control system minimizes the error signal which is measured by the difference current between two opposite plates. Each set of sense plates allows error detection in one dimension; thus, the alignment system consists of two independent closed-loop systems for two-dimensional control to center the beam in each dimension at the sensing plate structure.

Mechanical/electronic interaction of this system is evident in Fig. 5. From geometrical considerations it can be shown that in each dimension the displacement y of the ray at aperture 1 due to displacement x and

angular variation α at the cathode, is given by

$$y = \frac{x d (1 - k)}{c (1 - k) - bk} - \alpha \frac{d a (1 - k) + b}{c (1 - k) - bk} \quad (4)$$

The constant k is the ratio of currents of yokes 1 and 2. Thus, the parameter k must be carefully adjusted in each dimension to give the best compromise in α and x variations. Note from Eq. (4) that independence of y from α is achieved for $x = 0$, $k = (a + b)/a$; conversely, y is independent of x for $\alpha = 0$, $k = 1$. A compromise setting of k is achieved by minimizing the y variations for variations in x and α .

From Fig. 5, the closed-loop system consists of the sense plates with an error-detection system, an amplifier, and a yoke driver which couples into the two-yoke system. The error-detection system, because of high gain and high common-mode rejection (5000:1) requirements, employs synchronous detection with chopping at 3 kHz; the bandwidth of the sampled data error detector is approximately 300 Hz. It was determined in the laboratory that, because of variability in the lobar characteristics of the beam at the sensing plates, wide variations in error detector gain would be experienced during actual column operation. A pole of 0.7 Hz was inserted in the low-pass open-loop system to allow for the wide variations in error detector gain without the closed-loop system becoming oscillatory.

The closed-loop system, therefore, was designed as an overdamped two-pole Type 0 control system with the following characteristics:

| | | | |
|----------------------------|-------|----|--------|
| Open loop gain: | 50 | to | 200 |
| Closed-loop bandwidth: | 30 Hz | to | 130 Hz |
| Closed-loop damping ratio: | 1.5 | to | 0.9 |

In summary, the alignment control system provides continuous stable automatic correction to align the central axis of the beam with the central-axis of the column. The correction is provided in two dimensions by two discrete systems, one for each dimension. The result is that dynamic alignment of the beam in the column is achieved for conditions of varying filament-to-filament characteristics, and varying emission characteristics for individual filaments.

FOCUS CONTROL SYSTEM

The purpose of the Focus Control System is automatically to focus the electron beam on the target to compensate for high-voltage supply variation, lens current changes, and thermal expansion. In the recording system environment, periodic refocusing occurs normally three times a minute; the maximum interval between focus adjustments is 5 min, owing to electronic limitations.

The control concept is explained with reference to Fig. 6. By changing the current in the focus control lens, the distance X between final aperture and the beam crossover point near the target is varied. A periodic signal I_D is generated by sweeping the beam at constant speed over a grid pattern in a test target which masks a detector diode from

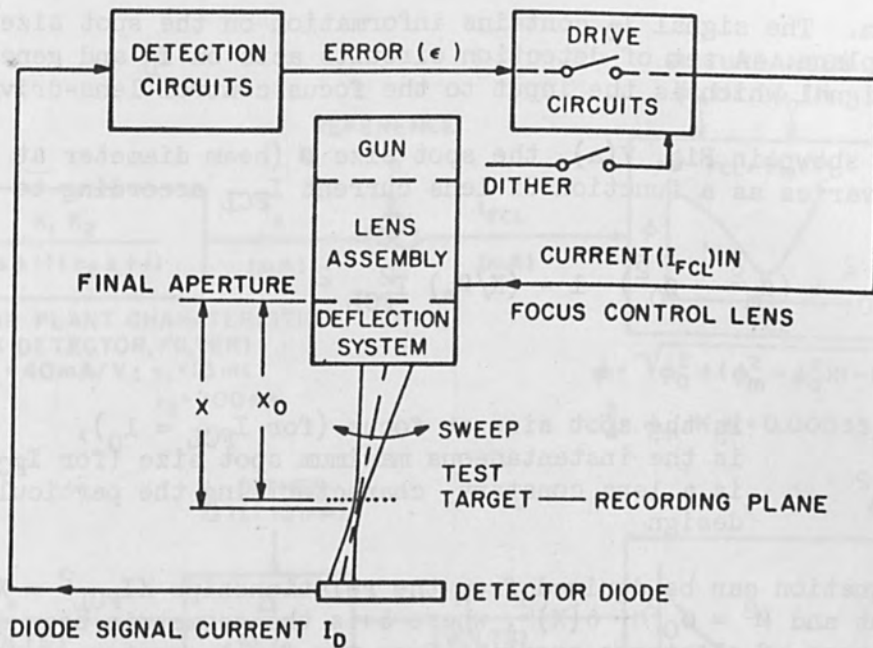


FIG. 6.—Focus control system.

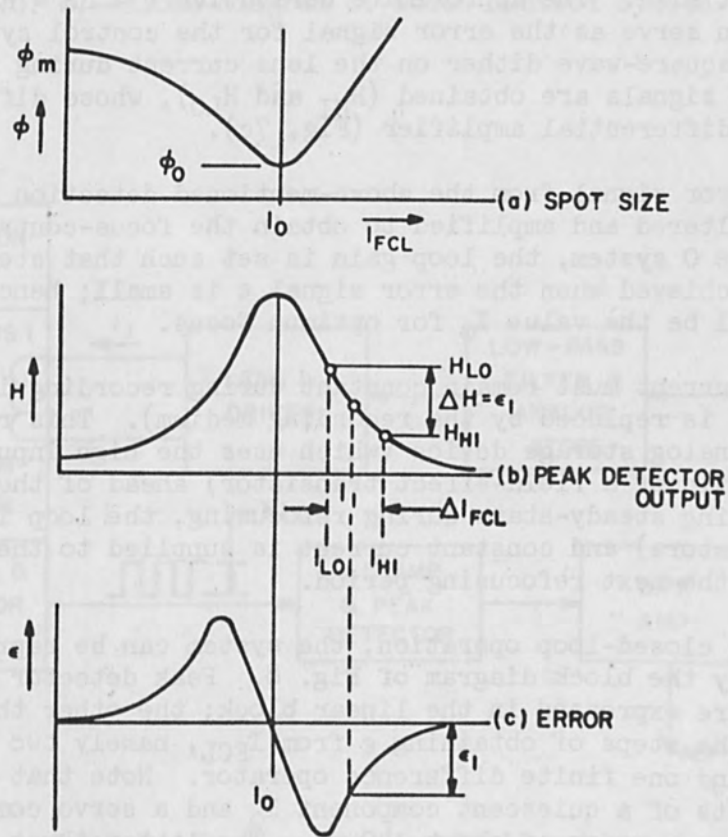


FIG. 7.—Focus control system variables vs lens current.

the beam. The signal I_D contains information on the spot size at the target plane. A set of detection circuits acts on I_D and generates an error signal which is the input to the focus control lens-drive circuitry.

As shown in Fig. 7(a), the spot size ϕ (beam diameter at the target plane) varies as a function of lens current I_{FCL} according to

$$\phi = \phi_0^2 + (\phi_m^2 - \phi_0^2) \left[1 - (K/\phi_m) I_{FCL}^2 \right]^2 \quad (5)$$

where

ϕ_0 is the spot size at focus (for $I_{FCL} = I_0$),
 ϕ_m is the instantaneous maximum spot size (for $I_{FCL} = 0$),
 $K\Delta\phi/\phi_m/I_0^2$ is a lens constant, characterizing the particular lens design

This equation can be derived from the relationships $XI_{FCL}^2 = X_0I_0^2 =$ constant and $\phi^2 = \phi_0^2 + \delta(X)^2$, where δ is the geometric beam diameter of the cone of electrons emerging from the final aperture.

A signal $H(t) \sim 1/\phi(t)$ can be obtained from the diode signal current I_D by differentiation, rectification, and peak detection. When H is plotted as a function of current (Fig. 7b), maximum H corresponds to minimum spot size. The approximate derivative $\epsilon = \Delta H = H_{HI} - H_{LO} \sim \Delta H/\Delta I_{FCL}$ can serve as the error signal for the control system. By superimposing a square-wave dither on the lens current during focusing, two different H signals are obtained (H_{HI} and H_{LO}), whose difference ϵ is taken in a differential amplifier (Fig. 7c).

The error signal from the above-mentioned detection circuitry is low-pass filtered and amplified to obtain the focus-control lens current. In this Type 0 system, the loop gain is set such that steady-state conditions are achieved when the error signal ϵ is small; hence, the lens current will be the value I_0 for optimum focus.

Lens current must remain constant during recording intervals (the test target is replaced by the recording medium). This requirement is met by an analog storage device (which uses the high input impedance characteristic of a field-effect transistor) ahead of the lens driver. After reaching steady-state during refocusing, the loop is opened (within the analog store) and constant current is supplied to the focus control lens until the next refocusing period.

During closed-loop operation, the system can be represented mathematically by the block diagram of Fig. 8. Peak detector and filter time constants are expressed in the linear block; the other three blocks symbolize the steps of obtaining ϵ from I_{FCL} , namely two nonlinear relationships and one finite difference operator. Note that the lens current I_{FCL} consists of a quiescent component I_0 and a servo component I_S , which can vary over a range of about ± 40 mA. The latter three blocks may be lumped into one nonlinearity $\epsilon(I_L)$ if ϕ_0 and ϕ_m are considered constant. For small disturbances around focus, the system can, therefore, be

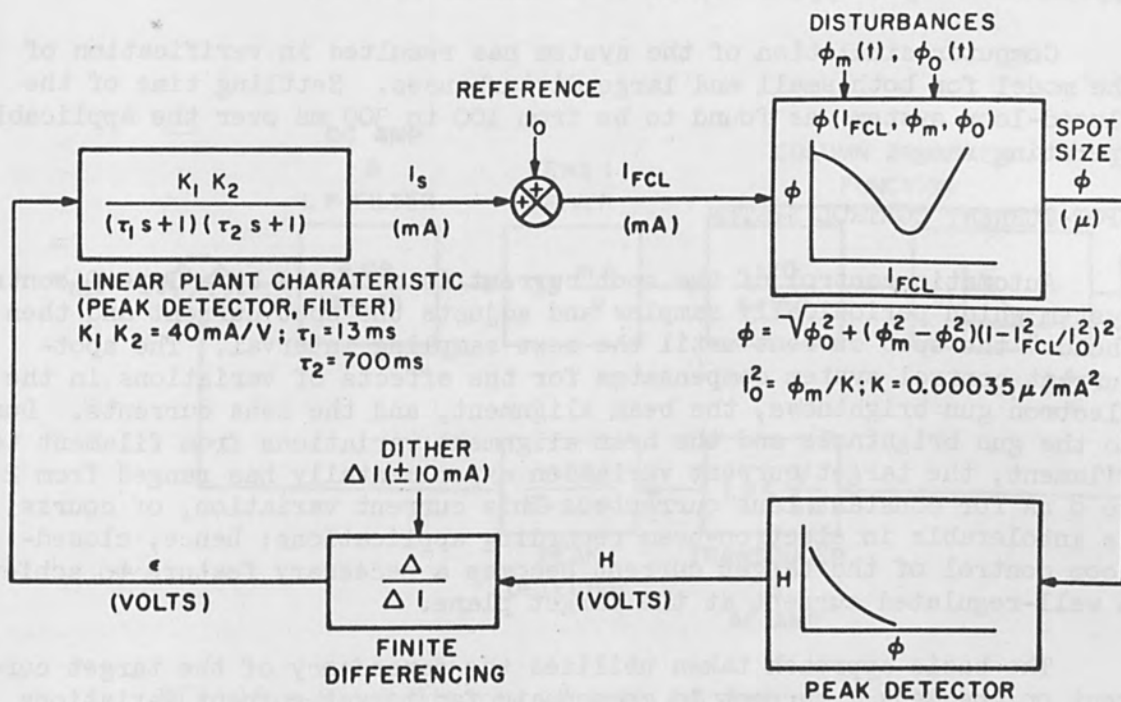


FIG. 8.—Block diagram of focus control system.

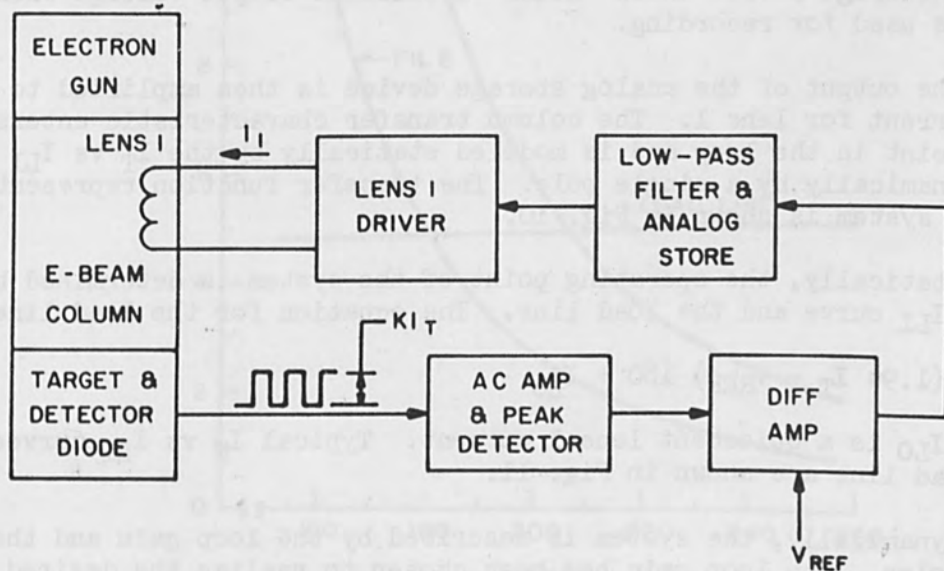


FIG. 9.—Spot current control system.

approximated by a Type 0 second-order linear system.

Computer simulation of the system has resulted in verification of the model for both small and large disturbances. Settling time of the closed-loop system was found to be from 100 to 300 ms over the applicable operating range.

SPOT-CURRENT CONTROL SYSTEM

Automatic control of the spot current is achieved by a Type 0 control system which periodically samples and adjusts the spot current and then "holds" the spot current until the next sampling interval. The spot-current control system compensates for the effects of variations in the electron gun brightness, the beam alignment, and the lens currents. Due to the gun brightness and the beam alignment variations from filament to filament, the target current variation experimentally has ranged from 2 to 8 nA for constant lens currents. This current variation, of course, is intolerable in electron-beam recording applications; hence, closed-loop control of the target current becomes a necessary feature to achieve a well-regulated current at the target plane.

The basic approach taken utilizes the dependency of the target current on the lens 1 current to compensate for target current variations due to changes in any other parameters that affect the target current. With reference to Fig. 9, a pulse train with an amplitude proportional to the spot current is obtained by scanning the beam across the test target. The resultant signal is amplified prior to peak detection. The peak signal detected is compared with a fixed reference signal, and the resultant error signal is amplified to obtain the input to the low-pass filter. The low-pass filter capacitor is also an integral part of the analog storage device which "holds" a constant output voltage when the beam is used for recording.

The output of the analog storage device is then amplified to provide the current for lens 1. The column transfer characteristic enters at this point in the loop and is modeled statically by the I_T vs I_{L1} curve and dynamically by a single pole. The transfer function representation of the system is shown in Fig. 10.

Statically, the operating point of the system is determined by the I_T vs I_{L1} curve and the load line. The equation for the load line is

$$I_{L1} = (1.94 I_T - V_{REF}) 180 + I_{L0} \quad (6)$$

where I_{L0} is a quiescent lens 1 current. Typical I_T vs I_{L1} curves and the load line are shown in Fig. 11.

Dynamically, the system is described by the loop gain and the dominant poles. The loop gain has been chosen to realize the desired control of the spot current ($5 \text{ nA} \pm 10\%$) over the lens 1 current range ($200 \text{ mA} \pm 25\%$), whereas the low-pass filter time constant has been selected to insure a stable system with a transient response which has little or no overshoot. From the block diagram in Fig. 10, the characteristic equation, neglecting the high frequency pole, is

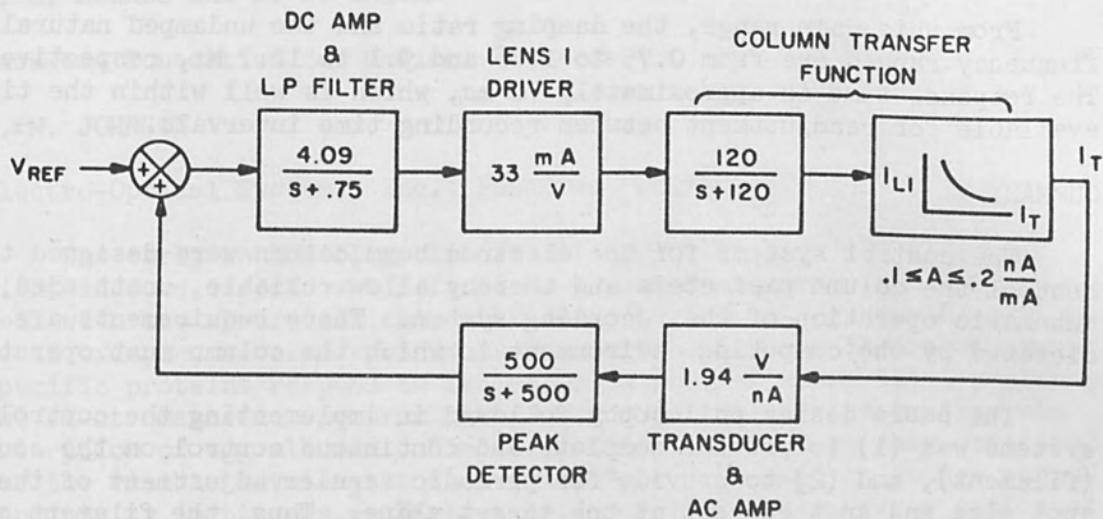


FIG. 10.—Block diagram of spot current control system.

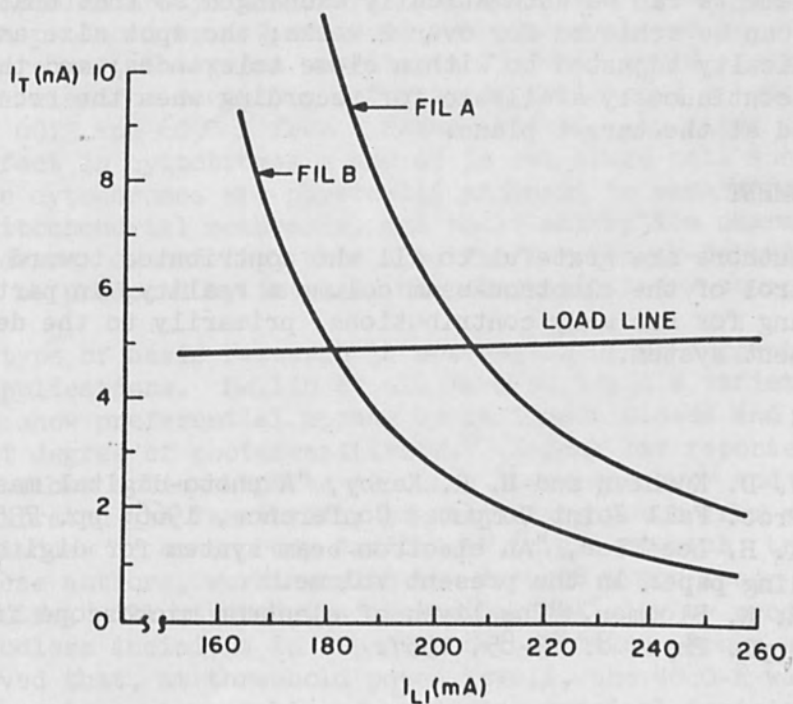


FIG. 11.—Typical I_T vs I_{L1} curves and load line.

$$s^2 + 120s + 90 + 31,400A = 0 \quad (7)$$

where A is the slope of the I_{LL} vs I_T curve at the operating point. This gain A has been measured to range from $0.1 \leq A \leq 0.2$ nA/mA.

From this gain range, the damping ratio and the undamped natural frequency ranges are from 0.75 to 1.06 and 9.1 to 12.7 Hz, respectively. The response time is approximately 70 ms, which is well within the time available for readjustment between recording time intervals.

SUMMARY

The control systems for the electron beam column were designed to control the column parameters and thereby allow reliable, unattended, automatic operation of the recording system. These requirements are dictated by the computing environment in which the column must operate.

The basic design philosophy followed in implementing the control systems was (1) to provide complete and continuous control on the source (filament), and (2) to provide for periodic vernier adjustment of the spot size and spot current at the target plane. Thus, the filament operating-point control system and the alignment control system serve to control the source parameters; the focus control system and the spot-current control system serve to control the spot parameters.

The net result of implementation of the control system on a basic column is that reliable operation of a single filament is assured over 24 hr; filaments can be automatically exchanged so that unattended column operation can be achieved for over 2 weeks; the spot size and spot current are periodically adjusted to within close tolerances; and the composite column is continuously available for recording when the recording medium is inserted at the target plane.

ACKNOWLEDGMENT

The authors are grateful to all who contributed toward making automatic control of the electron-beam column a reality, in particular to Paul C. Lang for his many contributions, primarily to the development of the alignment system.

REFERENCES

1. J. D. Kuehler and H. R. Kerby, "A photo-digital mass storage system," Proc. Fall Joint Computer Conference, 1966; pp. 735-742.
2. K. H. Loeffler, "An electron beam system for digital recording," see preceding paper in the present volume.
3. R. N. Bloomer, "The lives of electron microscope filaments," Brit. J. Appl. Phys. 8: 83-85, 1957.

WAVELENGTH SPECIFICITY OF LASER-INDUCED BIOLOGICAL DAMAGE

D. E. ROUNDS and R. S. OLSON

Pasadena Foundation for Medical Research

F. M. JOHNSON

Electro-Optical Systems, Inc., Pasadena, California

The early photobiology literature indicated that the degree of light-induced effects was defined by an action spectrum which correlated well with the absorption characteristics of the biological material used.¹ As an example, several systems in Paramecia which are dependent upon specific proteins respond to radiation in the far ultraviolet region of the electromagnetic spectrum with degrees of activity resembling the absorption of egg albumin. Similar action spectra have been described for the visible wavelengths when vital dyes were used to induce photosensitivity in tissues.² Early experience with laser energy indicated that analogous phenomena were operational.^{3,4,5} Although a wide variety of wavelengths has not been available, those laser frequencies which were tested indicated that biological damage was produced in proportion to the amount of energy absorbed by either natural chromophores or dyes. It was observed, for example, that hemoglobin within intact human erythrocytes could be bleached with a wavelength of 5300 Å from a frequency-doubled neodymium laser.⁶ An equivalent power density and pulse width produced by a Q-switched ruby laser showed no such bleaching action. Moreover, the green wavelength (5300 Å) could specifically inhibit the electron-accepting activity of cytochrome c, whereas wavelengths of 6013 and 6096 Å from a Raman-shifted ruby laser produced a similar effect in cytochromes a and a₃ in rat brain cell suspension.⁷ Since these cytochromes are physically adjacent to each other within internal mitochondrial membranes, and their absorption characteristics show some degree of overlap, this specific wavelength-dependent activity could only be produced by intense, monochromatic laser sources.

This type of basic research is now beginning to suggest certain clinical applications. Bellin et al. have surveyed a variety of vital dyes which show preferential uptake by malignant tissue and induces a significant degree of photosensitivity.⁸ Kapany has reported on the ability of fiber optics bundles to carry laser energy,⁹ and Bush et al. have demonstrated the feasibility of delivering power from an argon laser into the bladder or other body cavities¹⁰ (e.g., stomach, trachea, colon, etc.). These authors, working with the focused argon laser beam as an "optical knife," illustrated its biological activity by producing essentially bloodless incisions in experimental animals. Brown and Rockwell have observed that, at threshold power levels, the 4880-Å wavelength from an argon laser is capable of producing surgical incisions, but that the 5145-Å wavelength, under comparable conditions, showed no incisional characteristics.¹¹ This result suggests an additional wavelength-dependent phenomenon in the 5000 ± 500 Å region of the spectrum as well. A survey of the natural chromophores that absorb energy in this region of the

spectrum included hemoglobin, myoglobin, cytochrome c, flavin-containing compounds (notably riboflavin), and carotene. The capacity of the argon laser to coagulate blood vessels would appear to be associated with the spectral absorption of hemoglobin. It was noted that when argon laser power was focused through a microscope, a photocoagulation path could be scribed through a monolayer of erythrocytes in a blood smear (Fig. 1). An occasional leucocyte which was located within this path, showed no morphological change. However, hemoglobin, myoglobin, and cytochrome c absorb both the 4880 and 5145-Å wavelengths, and would not be expected to demonstrate the wavelength-specific effect described above.

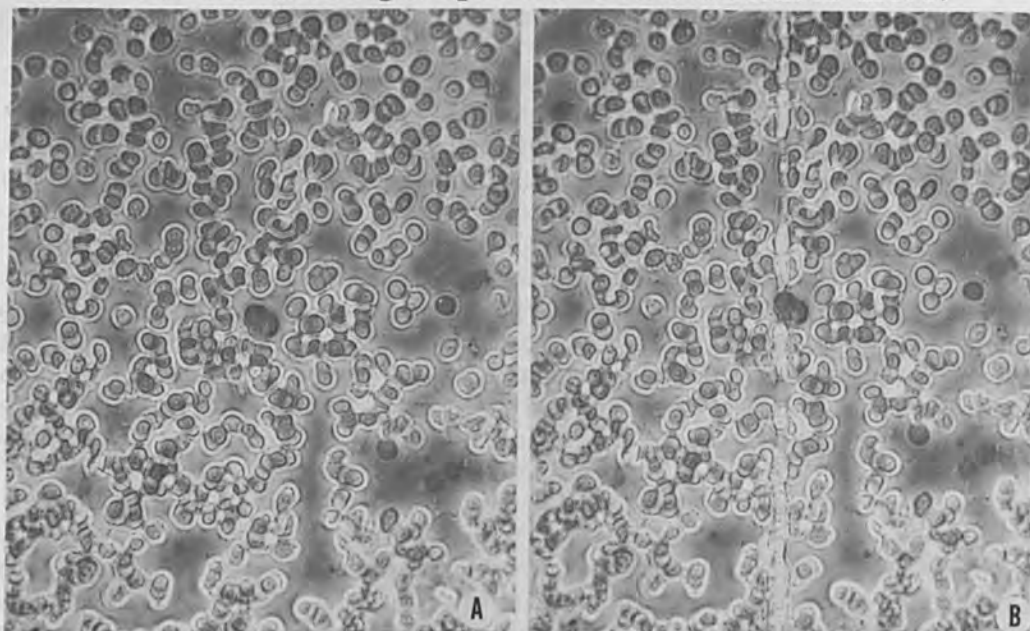


FIG. 1.—(a) Dried smear of red blood cells photographed with phase contrast microscopy; (b) the same field as shown in (a) after scoring with a focused argon ion laser beam. Note the central leucocyte was morphologically unchanged.

Riboflavin is known to be light sensitive. Within the scope of this study, it was observed that 185 mW/cm^2 for 40 min at a wavelength of 4880 Å caused a conversion of riboflavin molecules to lumichrome (Fig. 2). A similar treatment with 5145 Å showed no significant change in the absorption of the riboflavin solution. Blum has indicated that both riboflavin and its breakdown product, lumichrome, act as photosensitizers for the oxidation of ascorbic acid.² Therefore, this vitamin deserves further attention to determine its role as a chromatophore with respect to the argon laser.

Beta carotene was found to be far less light-sensitive (Fig. 3). Instead, treatment with either the 4880 or 5145-Å wavelengths at 185 mW/cm^2 appeared to convert the mixed cis and trans stereoisomers to an all trans form of the molecule.¹² This molecular stability and its ability to bind with cellular membranes¹³ makes carotene an attractive candidate to explain the wavelength-dependent photocoagulation with the argon laser.

The action spectrum which is related to phototropism of plant

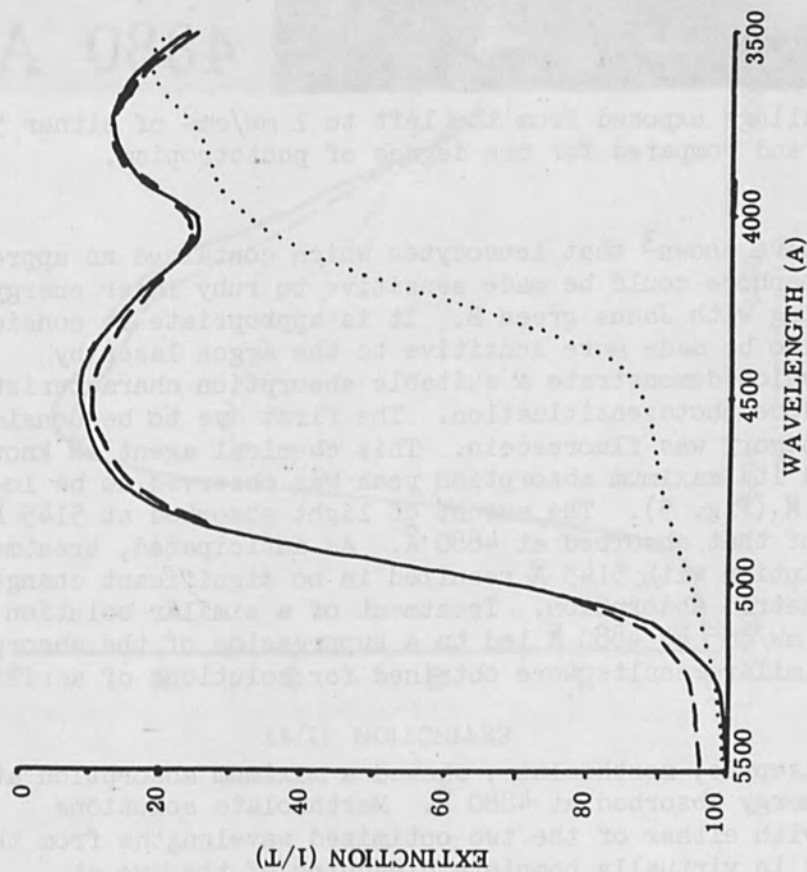


FIG. 2.—The absorption characteristic of riboflavin in water, before and after treatment with 185 mW/cm² for 40 min, using either 5145 Å (dashed line) or 4880 Å (dotted line).

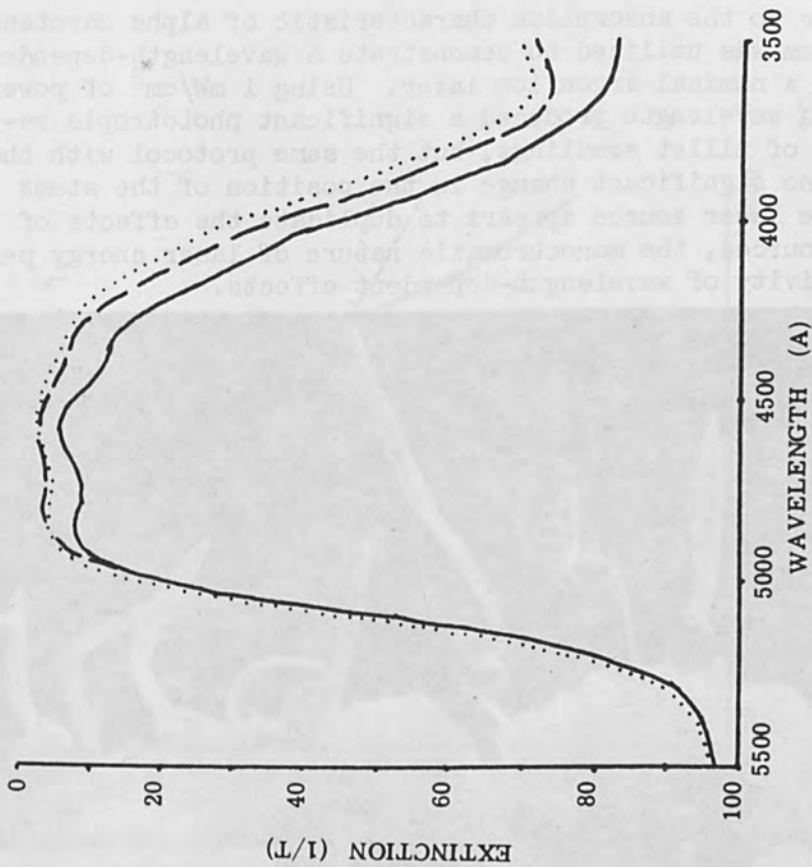


FIG. 3.—The absorption curve for B carotene in methyl alcohol, before and after treatment with 185 mW/cm² for 40 min, using either 5145 Å (dashed line) or 4880 Å (dotted line).

seedlings is similar to the absorption characteristic of alpha carotene.² This sensitive system was utilized to demonstrate a wavelength-dependent effect induced with a nominal argon ion laser. Using 1 mW/cm^2 of power for 2 hr, the $4880\text{-}\text{\AA}$ wavelength produced a significant phototropic response in the stems of millet seedlings, but the same protocol with the $5145\text{-}\text{\AA}$ beam caused no significant change in the position of the stems (Fig. 4). While the laser source appears to duplicate the effects of noncoherent light sources, the monochromatic nature of laser energy permits greater selectivity of wavelength-dependent effects.



FIG. 4.—Millet seedlings exposed from the left to 1 mW/cm^2 of either 5145 \AA or 4880 \AA for 2 hr, and compared for the degree of phototropism.

Bessis et al. have shown³ that leucocytes which contained no appropriate natural chromophore could be made sensitive to ruby laser energy through vital staining with Janus green B. It is appropriate to consider that tissue might also be made more sensitive to the argon laser by staining with dyes which demonstrate a suitable absorption characteristic and are known to induce photosensitization. The first dye to be considered within this category was fluorescein. This chemical agent is known to be nontoxic¹⁴ and its maximum absorption peak was observed to be located at about 4860 \AA (Fig. 5). The amount of light absorbed at 5145 \AA was only about 30% of that absorbed at 4880 \AA . As anticipated, treatment of a fluorescein solution with 5145 \AA resulted in no significant change in its spectrophotometric absorption. Treatment of a similar solution for 40 min with 185 mW/cm^2 at 4880 \AA led to a suppression of the absorption of the dye. Similar results were obtained for solutions of acridine orange (Fig. 6).

The common antiseptic, merthiolate, showed a maximum absorption at 5145 \AA , with less energy absorbed at 4880 \AA . Merthiolate solutions which were treated with either of the two optimized wavelengths from the argon laser resulted in virtually complete bleaching of the dye at

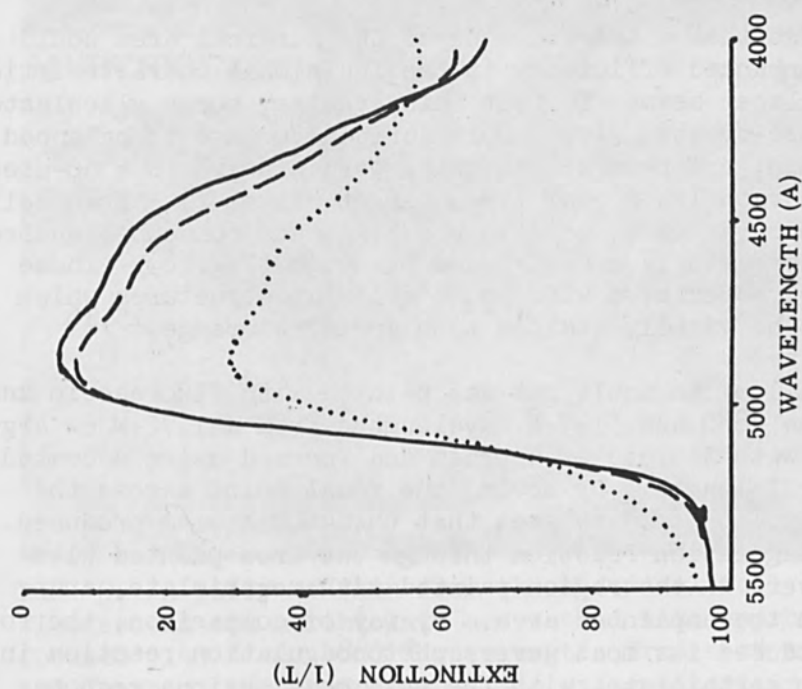


FIG. 5.—The absorption characteristic for fluorescein in water, before and after treatment with 185 mW/cm² for 40 min, using either 5145 Å (dashed line) or 4880 Å (dotted line).

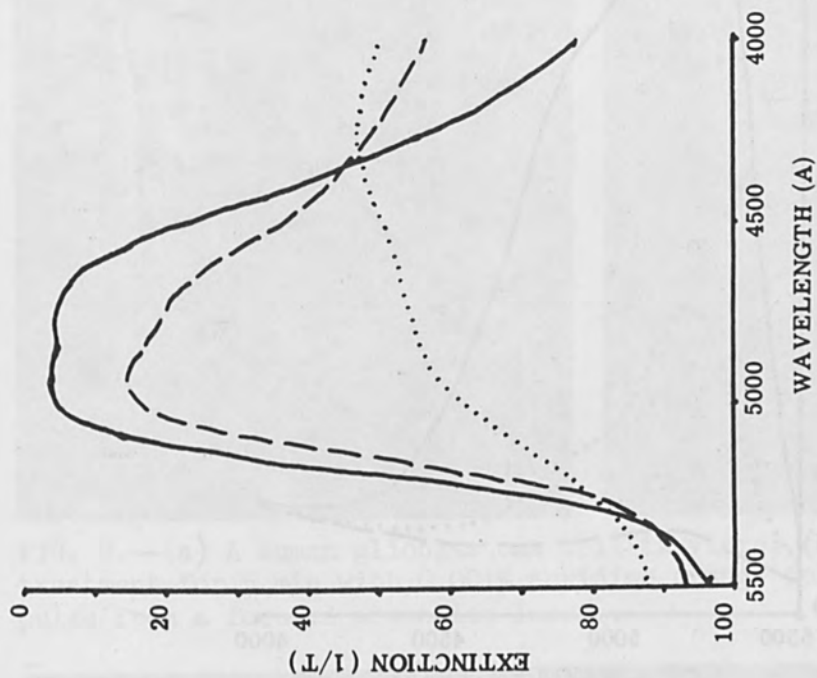


FIG. 6.—The absorption characteristic for acridine orange in water, before and after treatment with 185 mW/cm² for 40 min, using either 5145 Å (dashed line) or 4880 Å (dotted line).

5145 Å, but only a partial bleaching at 4880 Å (Fig. 7).

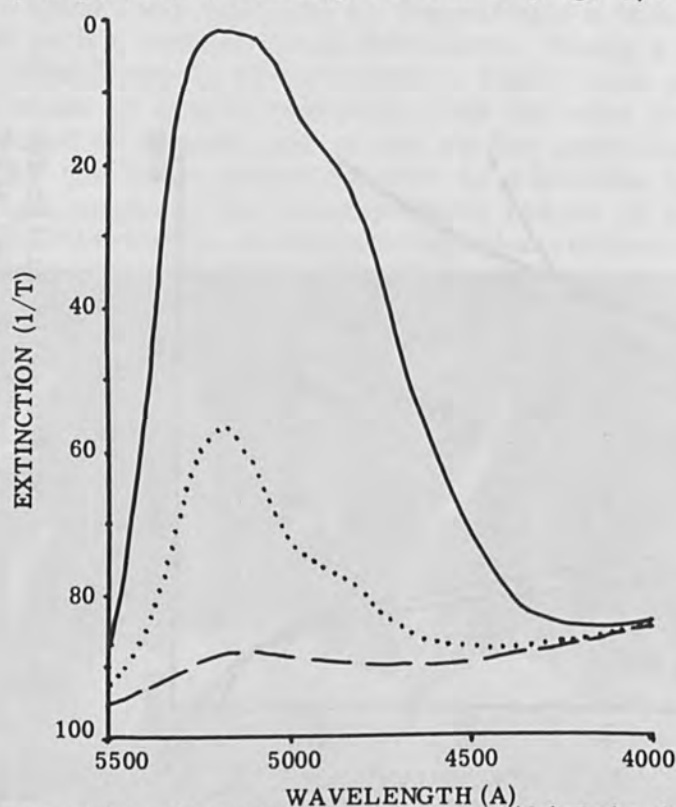


FIG. 7.—The absorption characteristic for merthiolate in water, before and after treatment with 185 mW/cm² for 40 min, using either 5145 Å (dashed line) or 4880 Å (dotted line).

These data suggest that vital staining of the surgical area could result in a greatly enhanced efficiency in the incisional characteristics of the focused argon laser beam. To test this premise, human glioblastoma cells *in vitro* were pre-treated with 0.001% acridine orange in balanced salt solution for 5 min, and then single cells were exposed to a 50-μsec pulse from a focused argon laser beam (12-μ target diameter). Such cells showed fine cytoplasmic vacuoles, zeiotic blebbing, and condensed nucleoli. The nucleus became increasingly granular and pycnotic (Fig. 8). These effects appeared to be associated with those cellular structures which have been reported to be vitally stained with acridine orange.^{15,16}

The abdominal wall of an adult rat was painted with fluorescein and with merthiolate. The 4880 and 5145-Å wavelengths from a 1.72-W cw argon laser were separated with the aid of a prism and focused using a coated lens with a 30-mm focal length. By moving the focal point across the surface of the abdomen, it could be seen that the 4880-Å beam produced a more severe photocoagulation reaction through the area painted with fluorescein, less severe in the region painted with merthiolate, and substantially less in the unpainted area. By way of comparison, the focused 5145-Å beam produced its most severe photocoagulation reaction in the area painted with merthiolate, with the next most obvious response occurring in the fluorescein-treated region, and relatively little effect on the unpainted skin (Fig. 9).

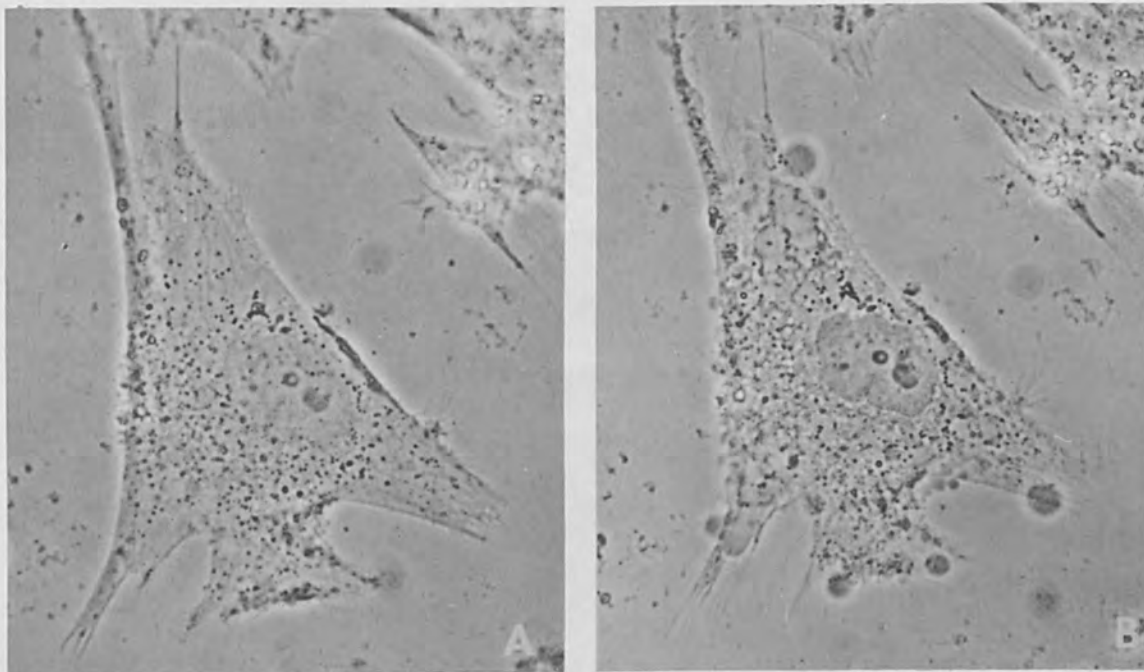


FIG. 8.—(a) A human glioblastoma cell in vitro; (b) the same cell after treatment for 5 min with 0.001% acridine orange followed by a 50- μ sec pulse from a focused argon ion laser.

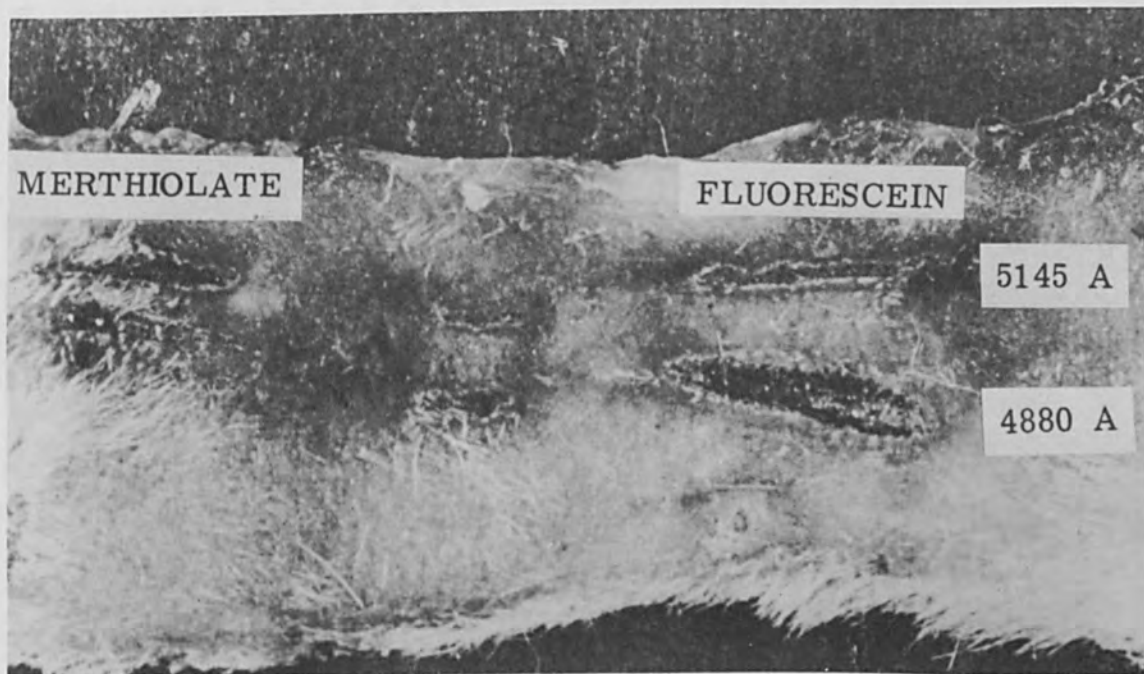


FIG. 9.—A piece of skin from the abdominal wall of a rat, painted with fluorescein and merthiolate and scored with approximately 500 mW each of focused 5145 \AA and 4880 \AA wavelengths from a cw argon laser. The area and depth of the photocoagulation was greatest in the painted regions, with the degree of tissue destruction proportional to the amount of laser power absorbed by each dye.

While these observations are of a qualitative nature, they encourage more definitive studies in the area of photosensitization of tissue to the emitted frequencies from the argon laser. It appears possible to not only gain more effective absorption of the 4880-Å wavelength, but with the aid of a dye such as merthiolate, the 5145-Å wavelength might also be utilized to result in the type of controlled damage which is essential to effective tumor therapy.

ACKNOWLEDGMENT

This research was supported in part by the U. S. Army Medical Research and Development Command, Department of the Army, under Research Grant No. DA-MD-49-193-67-G9220, and the USAF School of Aerospace Medicine (AFSC), Department of the Air Force, under Research Grant No. F41609-67-C-0022.

REFERENCES

1. A. C. Giese, in, "Photophysiology," Academic Press, New York, 1964; vol. 2, p. 220.
2. H. F. Blum, in, "Photodynamic Action and Diseases Caused by Light," Hafner Publishing Company, New York, 1964.
3. M. Bessis, F. Gires, G. Mayer and G. Nomarski, "Irradiation des organites cellulaires a l'aide d'un laser a rubis," Compt. Rend. Acad. Sci. 255: 1010, 1962.
4. R. L. Amy and R. Storb, "Selective mitochondrial damage by a ruby laser microbeam: An electron microscopic study," Science 150: 756, 1965.
5. J. P. Minton, "A Method to determine laser wavelength absorption capabilities of experimental malignant tumors," Life Sciences 3: 1007, 1964.
6. D. E. Rounds, R. S. Olson, and F. M. Johnson, "The laser as a potential tool for cell research," J. Cell Biol. 27: 191, 1965.
7. D. E. Rounds, R. S. Olson, and F. M. Johnson, "The effect of the laser on cellular respiration," IEEE/NEREM Record 7: 106, 1965.
8. J. S. Bellin, S. C. Mohos, and G. Oster, "Dye-sensitized photo-inactivation of tumor cells in vitro," Ca. Res. 21: 1365, 1961.
9. N. S. Kapany, "Fiber optics and the laser," N. Y. Acad. Sci. 122: 615, 1965.
10. I. M. Bush, W. F. Whitmore, Jr., and P. H. Lieberman, "Experimental surgical applications of the laser," Annual Meeting, Assoc. Adv. Med. Instrumentation, Boston, Mass., 27 July 1966.
11. T. E. Brown and R. J. Rockwell, Jr., "The argon laser: Its effects in vascular and neural tissue," p. of present volume.
12. L. Zechmeister, in, "Cis-Trans Isomeric Carotenoids, Vitamins A and Arylpolyenes," Academic Press, New York, 1962; pp. 42-43.
13. D. Chapman, in, "The Structure of Lipids by Spectroscopic and X-ray Techniques," John Wiley and Sons, New York, 1965; p. 50.
14. K. Lange and L. J. Boyd, "The use of fluorescein to determine the adequacy of the circulation," Med. Clin. N. Amer. 26: 943, 1942.
15. A. V. Zelenin, "Fluorescence microscopy of lysosomes and related structures in living cells," Nature 212: 425, 1966.
16. R. B. Hill, Jr., K. G. Bensch, and D. W. King, "Photosensitization of nucleic acids and proteins, the photodynamic action of acridine orange on living cells in culture," Exptl. Cell Res. 21: 106, 1960.

THERMAL DAMAGE TO BIOLOGICAL MATERIALS

C. HU, J. LAURIDSON, and F. BARNES

University of Colorado, Boulder, Colo.

The laser has been used for a number of years as a surgical and microsurgical instrument, and it appears that it is going to have an increasing number of applications to biological and medical problems over the next few years. In order to make this tool more useful, a better understanding of the various damaging mechanisms is needed. It is the purpose of this paper to explore the nature of thermochemical damage in some detail.

There are four principal means by which a laser damages biological material. The first is photochemical. This damaging mechanism is of primary importance at the shorter visible wavelengths and involves the oxidation of material such as proteins with the help of photoactive catalyts such as porphyrin or riboflavin.¹

The second form of damage is vaporization of a portion of the biological material; since most of the biological material is largely water, it is relatively easy to make an approximate calculation of the maximum volume of material that can be vaporized. The third form of damage is acoustical or mechanical and results from a combination of the rapid thermal expansion of the heated material and the evaporation of material from the surface. In the case of Q-switched lasers, the shockwave amplitudes may exceed 50 atm in the immediate vicinity of the laser impact, and the pressure gradients may be extremely sharp.^{2,3} However, in the microsurgical situation using ordinary ruby and neodymium lasers with millisecond pulse lengths, the shock amplitudes appear to be less than 1 atm and are seldom of major importance.

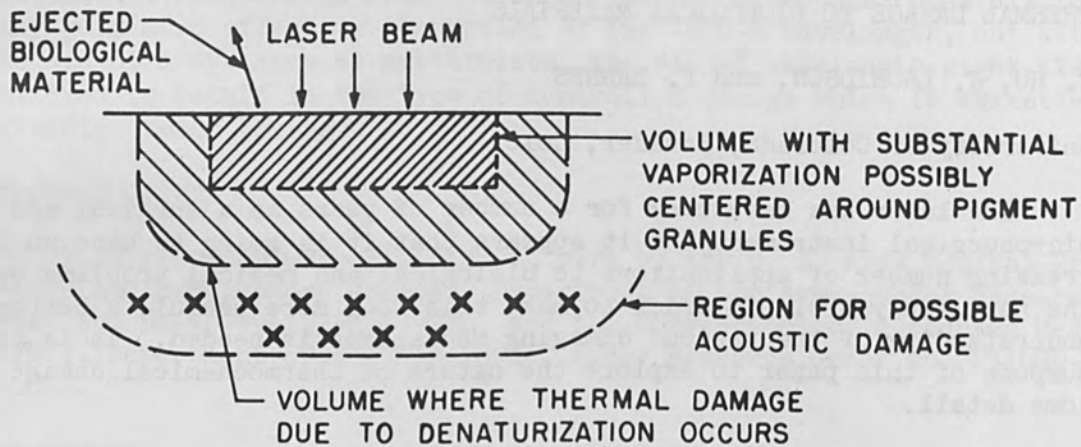
The fourth damaging mechanism results from thermochemical changes which may be induced by the transient thermal wave and its form of damage, which is the subject of this paper.

Figure 1 shows an idealization of the two configurations that most frequently occur in surgical situations. The first is the semi-infinite surface, which is an approximation for problems such as the removal of a skin cancer. The second is an approximation of the situation with which we have been working in microsurgery, where the object is to destroy one of a group of cells. It is for this configuration that we have worked out the heat transfer equation and the corresponding radii of damage.

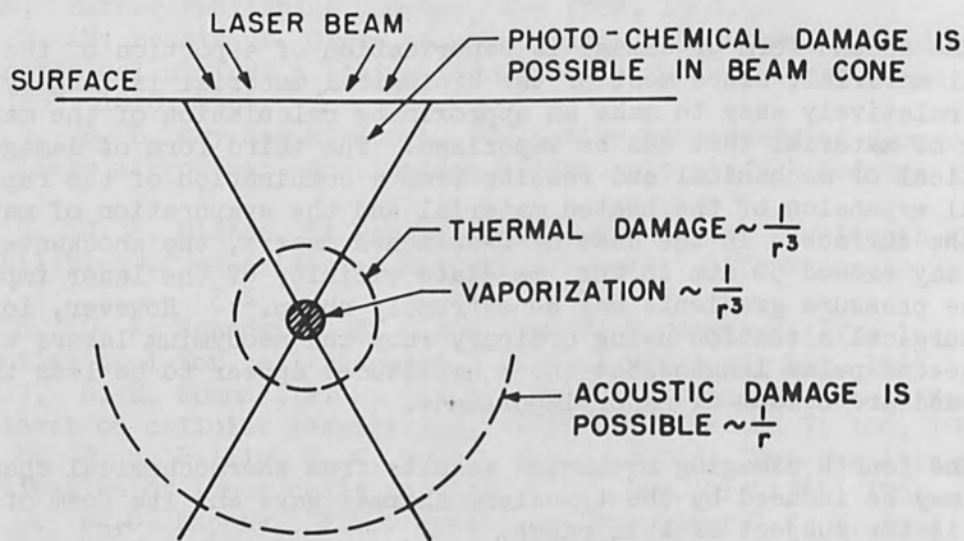
Equations for heat transfer in spherical coordinates have been solved and tabulated by Carslaw and Jaeger.⁴

$$T = \frac{1}{2} T_0 \left\{ \operatorname{erf} \left[\frac{r+a}{2(\alpha t)^{\frac{1}{2}}} \right] - \operatorname{erf} \left[\frac{r-a}{2(\alpha t)^{\frac{1}{2}}} \right] - \frac{2(\alpha t)^{\frac{1}{2}}}{r\pi^{\frac{1}{2}}} \left[e^{-\frac{(r-a)^2}{4\alpha t}} - e^{-\frac{(r+a)^2}{4\alpha t}} \right] \right\}$$

(1)



(a)



(b)

FIG. 1.—(a) Semi-infinite homogeneous biological material; (b) focused laser beam and immersed absorption center.

where $\alpha = K\nu^{-1}$ (K is the thermal conductivity), $\nu = \rho C_p$, ρ is the density, and C_p is the heat capacity of the material.

An approximate plot of this equation where R is much greater than a is shown in Fig. 2. The thermal damage to many biological materials is described by a simple first order rate equation of the form⁵

$$\frac{dS}{dt} = -K'S \quad (2)$$

where $S = N/N_0$ and $K' = (kT/h) \exp [- (\Delta H - T\Delta S)/RT]$, S is the surviving fraction of the active biological material, and N_0 is the initial concentration, k is Boltzman's constant, T is the absolute temperature, h is Plank's constant, ΔH and ΔS are constants of the biological material and functions of the environment, and R is the gas constant.

GENERAL EQUATION FOR POINT SOURCE

$$\bar{T} = \bar{r}^{\frac{3}{2}} e^{-\frac{1}{\bar{r}}}$$

NORMALIZATION PARAMETERS

$$\bar{r} = \frac{T - T_0}{A} \quad A = \frac{Q}{\rho C \pi^{3/2} r^3}$$

$$\bar{r} = \frac{4Kt}{r^2}$$

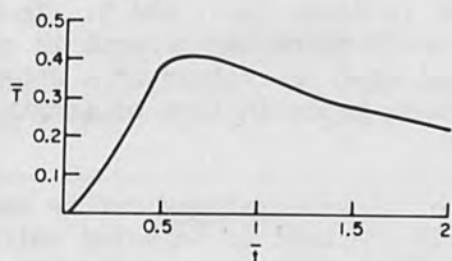


FIG. 2.—Temperature wave for normalized spherical case.

Equation (2) applies to processes which in radiation chemistry are called single-hit processes, meaning that there is one critical bond or one critical event which needs to take place in order to make the observed chemical change. Unfortunately, many biological processes are considerably more complicated than that. However, the denaturizations of many proteins and enzymes may be approximated by this simple rate equation over appropriately small ranges of temperature and under conditions that other important chemical factors including pH are constant. (These equations can become very complicated, as shown, for instance, in Ref. 6.) In order for the constants ΔH and ΔS to be significant, the environmental conditions for the laser experiments have to be reproducible and the same as the steady-state experiments that are used to evaluate these constants.

In order to obtain the survival probability S for the biological material, we need to substitute Eq. (1) into (2) and integrate. We should like to have a result for each r as a function of the laser input parameters. In order to reduce the amount of work required to get answers that we hope will be useful, we arbitrarily decide to limit our interests to that radius r which corresponds to a survival fraction of one half of

the population. In that case the equation that we wish to solve becomes

$$-\log 1/2 = \int_0^{\infty} K' dt \quad (3)$$

Unfortunately, as formulated this way Eq. (3) is too simple: K' does not approach zero as t approaches infinity, since we have not taken the reverse reaction into account. However, if we limit our integral to that period of time at which the change in temperature to the heat impulse is relatively large, usable answers are still obtained. If K' is plotted as a function of T , it is found to be such a rapidly varying function that it may be considered to have a threshold which we shall arbitrarily label as a critical temperature T_c above which the reaction occurs rather rapidly and below which, for the time scale involved in a heat impulse, essentially no damage occurs. This critical temperature is approximately 63°C for hemoglobin and provides a convenient point above which to normalize our solutions. In Figs. 3, 4, and 5 a convenient normalization factor, ΔT_c is defined as $\Delta T_c \equiv T_c - \text{surrounding temperature}$, or, for this curve, $63 - 25 = 38^\circ\text{C}$.

The results of calculations for a variety of laser input conditions on hemoglobin are shown in Figs. 3, 4, and 5. In calculating these curves, we have to assume that the entire laser input is converted to heat which is uniformly distributed over the volume of a sphere of radius a and delivered by a rectangular pulse in time of length τ ; H is the total energy of the pulse.

The general form of these equations can be checked by looking at some limiting cases. If the heat is injected uniformly in zero time, then the maximum temperature decreases in the far zone as the cube of the radius, as shown in Fig. 6, and the radius to which we would expect damage is formed by the intersection of this curve and T_c . If the input volume of the sphere is increased by increasing a , then r_c increases until it falls below T_c , as shown in Fig. 7. If the length of the pulse τ is increased, it has a tendency to round off the corners as the diffusion of heat occurs most rapidly where the gradient is the largest. The variation for r versus a with constant H and τ is shown in Fig. 8. The curves calculated in Figs. 3 through 5 are more accurate representations of this situation, which also take into account the fact that the threshold at T_c is not absolutely sharp.

Experimental verifications of the accuracy of these transient solutions to the rate equations have only been carried out over a small range in a preliminary fashion so far. Our experimental apparatus has consisted of a small ruby laser with a maximum output of approximately 0.8 joule mounted on a microscope. The energy delivered to this microscope is of the order of 10 millijoules and is concentrated into an area of about 100 microns. Since our facilities for doing microchemical analysis on denaturation of materials such as hemoglobin were negligible, we chose to use a combination of carbon specks and egg white as the material from which we could get visual indications of approximate radii of damage for various laser input energies and spot sizes. The energy used in heating the carbon specks was estimated by first measuring the energy

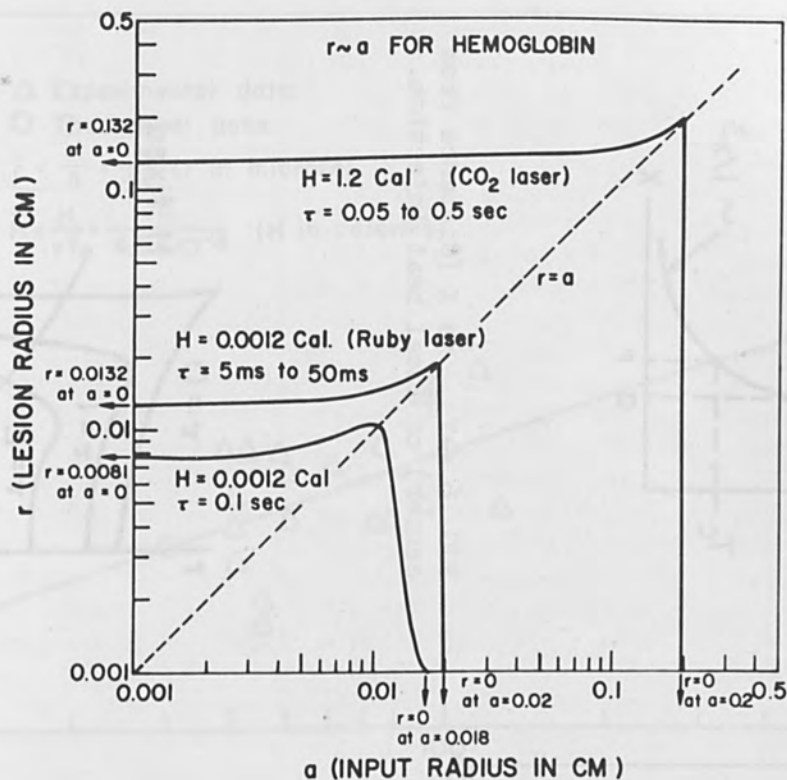


FIG. 3.—Damage radius r as function of input spot radius a for hemoglobin with the input energy H and light pulse lengths τ .

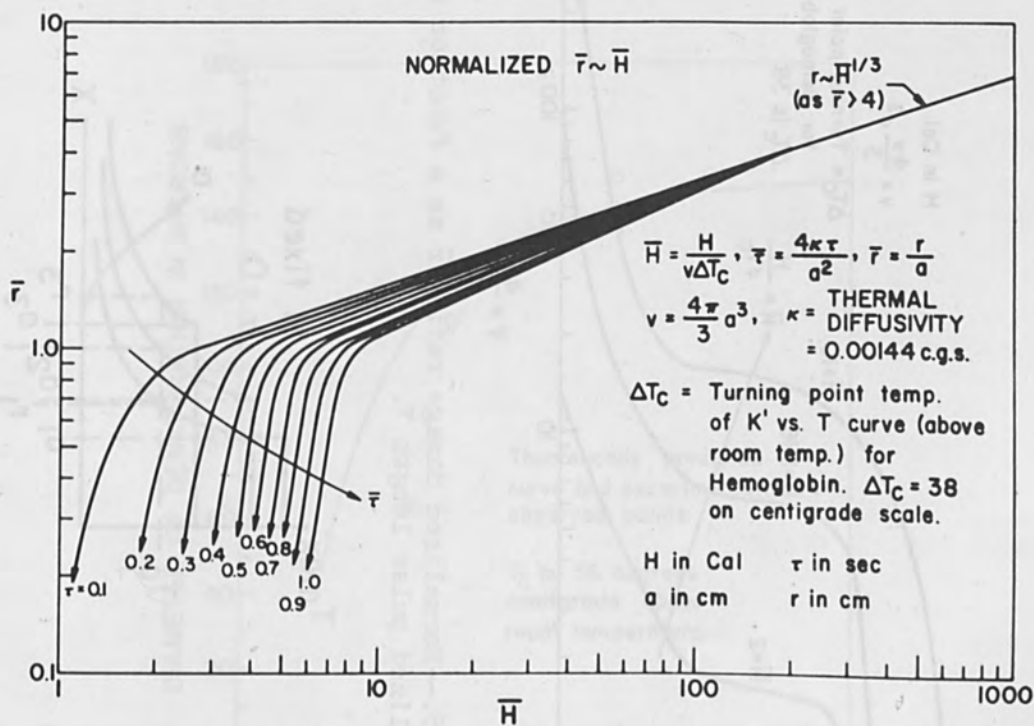


FIG. 4.—Normalized damage radius \bar{r} as a function of the heat input per unit volume and the critical temperature T_c .

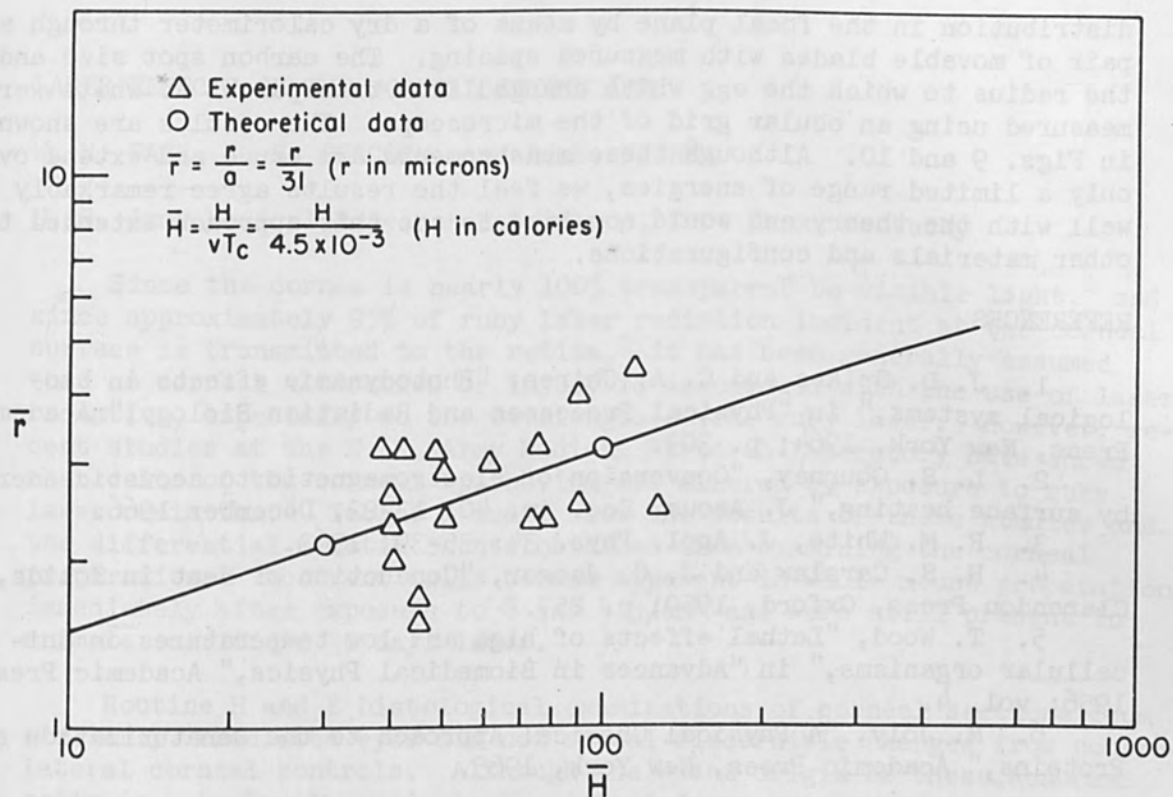


FIG. 9.—Comparison of experimental and theoretical denaturation radii of egg albumen irradiated by ruby laser.

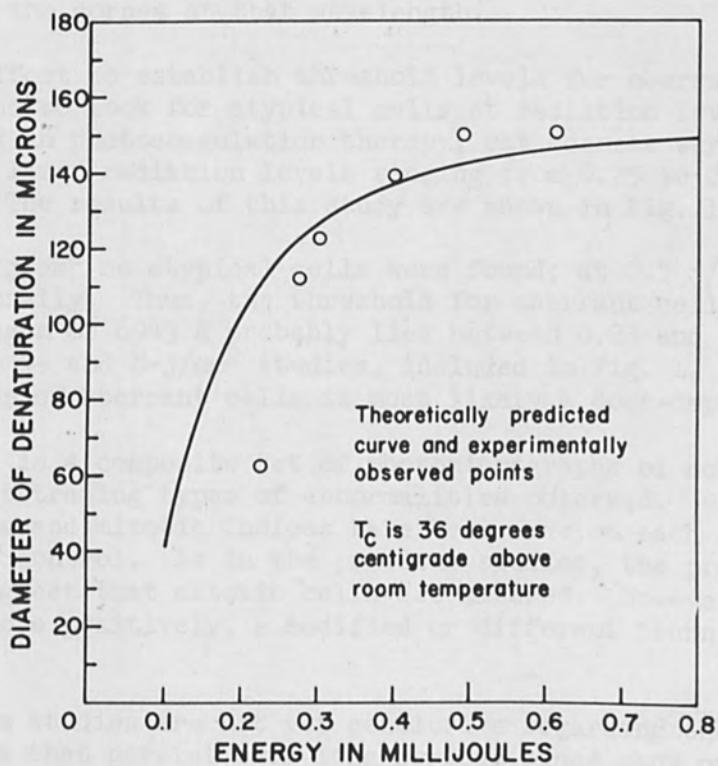


FIG. 10.—Denaturation of egg albumen.

distribution in the focal plane by means of a dry calorimeter through a pair of movable blades with measured spacing. The carbon spot size and the radius to which the egg white changed from transparent to white were measured using an ocular grid of the microscope. The results are shown in Figs. 9 and 10. Although these measurements are crude and extend over only a limited range of energies, we feel the results agree remarkably well with the theory and would now like to see this approach extended to other materials and configurations.

REFERENCES

1. J. D. Spikes and C. A. Ghiren, "Photodynamic effects in biological systems," in "Physical Processes and Radiation Biology," Academic Press, New York, 1964; p. 309.
2. L. S. Gournay, "Conversion of electromagnetic to acoustic energy by surface heating," J. Acous. Soc. Am. 40: 13-22, December 1966.
3. R. M. White, J. Appl. Phys. 34: 35-39, 1963.
4. H. S. Carslaw and J. C. Jaeger, "Conduction of Heat in Solids," Clarendon Press, Oxford, 1959; p. 257.
5. T. Wood, "Lethal effects of high and low temperatures on unicellular organisms," in "Advances in Biomedical Physics," Academic Press, 1956; vol. 4.
6. M. Joly, "A Physical Chemical Approach to the Denaturation of Proteins," Academic Press, New York, 1965.

LASER EFFECTS ON THE CORNEAL EPITHELIUM

W. H. PARR, G. R. PEACOCK, and R. S. FISHER

U. S. Army Medical Research Laboratory, Fort Knox, Kentucky

Since the cornea is nearly 100% transparent to visible light,¹ and since approximately 95% of ruby laser radiation incident at the corneal surface is transmitted to the retina,² it has been generally assumed that no corneal alteration or injury is associated with the use of laser radiation, especially at the wavelength of the ruby laser. However, recent studies at the U. S. Army Medical Research Laboratory have shown that cells of the corneal epithelium are altered by exposure to ruby laser radiation.³ Tables 1 and 2 show the results of these studies and the differential mitotic counts obtained from examining the corneal preparations. Aberrant cells became apparent in whole mount preparations immediately after exposure to 8 and 4 j/cm² and were still present in animals sacrificed 30 days later.

Routine H and E histological examinations of corneal sections from similarly irradiated eyes did not reveal discernible changes from contralateral corneal controls. Although the exact origin of these abnormal cells is not clearly evident, the data indicate that cells in active mitosis are preferentially affected. This effect may be significant as a long-term hazard from either ruby laser radiation, or more importantly, from laser radiation at 10.6 microns because of the high absorption coefficient of the cornea at that wavelength.

In an effort to establish threshold levels for aberrant corneal cell production and to look for atypical cells at radiation levels comparable to those used in photocoagulation therapy, rat corneas were exposed in vivo to ruby laser radiation levels ranging from 0.25 to 2 j/cm² for a 3-ms pulse. The results of this study are shown in Fig. 1.

At 0.25 j/cm² no atypical cells were found; at 0.5 j/cm² they may occur occasionally. Thus, the threshold for aberrant cell production for a wavelength of 6943 Å probably lies between 0.25 and 1.0 j/cm². The data from the 4- and 8-j/cm² studies, included in Fig. 1, suggest that the production of aberrant cells is most likely a dose-dependent effect.

Figure 2 is a composite set of photomicrographs of normal and atypical cells illustrating types of abnormalities observed. Differential mitotic counts and mitotic indices have been made on each sample and its contralateral control. As in the previous studies, the present evaluations also suggest that mitotic cells are altered. However, to decide this matter more positively, a modified or different technique will be required.

Long-term studies are not yet conclusive regarding the number of atypical cells that persist over long periods since many of the animals died before sacrifice time. They have shown, however, that atypical cells apparently persist after a year in rats exposed to 4 j/cm²; the

TABLE 1.—Differential mitotic cell counts on epithelial cells of rat corneas exposed to laser energy. (8 J/cm² - immediate sacrifice; all values expressed in percentages.)

| RAT # | LASED EYE | | | | | CONTRALATERAL EYE | | | | |
|---------|-----------|-----------|----------|-----------|----------|-------------------|-----------|----------|-----------|----------|
| | PROPHASE | METAPHASE | ANAPHASE | TELOPHASE | ATYPICAL | PROPHASE | METAPHASE | ANAPHASE | TELOPHASE | ATYPICAL |
| 6 | 22 | 18 | 14 | 3 | 43 | 47 | 33 | 16 | 4 | -- |
| 7 | 31 | 18 | 11 | 7 | 33 | 43 | 40 | 11 | 6 | -- |
| 8 | 26 | 30 | 6 | 2 | 36 | 43 | 28 | 19 | 10 | -- |
| 9 | 27 | 14 | 6 | 8 | 45 | 41 | 29 | 21 | 9 | -- |
| 10 | 47 | 34 | 1 | 1 | 17 | 47 | 37 | 10 | 6 | -- |
| AVERAGE | 30.60 | 22.80 | 7.60 | 4.20 | 34.80 | 43.60 | 33.40 | 15.20 | 7.00 | -- |

TABLE 2.—Differential mitotic cell counts on epithelial cells of rat corneas exposed to laser energy. (4 J/cm²; all values expressed in percentages.)

IMMEDIATE SACRIFICE - 12 ANIMALS

| EYE EXAMINED | PROPHASE | METAPHASE | ANAPHASE | TELOPHASE | ATYPICAL |
|--------------------|----------|-----------|----------|-----------|----------|
| Lased Eye | 37.27 | 21.91 | 16.46 | 12.00 | 12.33 |
| Adjusted Lased Eye | 42.5 | 25.0 | 18.77 | 13.68 | -- |
| Contralateral Eye | 42.83 | 29.0 | 16.75 | 11.33 | -- |

24 HOUR SACRIFICE - 6 ANIMALS

| | | | | | |
|--------------------|-------|-------|-------|-------|-------|
| Lased Eye | 33.80 | 22.60 | 23.20 | 9.80 | 10.60 |
| Adjusted Lased Eye | 37.80 | 25.30 | 25.95 | 10.96 | -- |
| Contralateral Eye | 40.83 | 25.33 | 21.50 | 12.17 | 0.17 |

48 HOUR SACRIFICE - 5 ANIMALS

| | | | | | |
|--------------------|-------|-------|-------|-------|-------|
| Lased Eye | 35.20 | 24.80 | 19.00 | 9.80 | 11.20 |
| Adjusted Lased Eye | 39.64 | 27.92 | 21.80 | 11.03 | -- |
| Contralateral Eye | 43.00 | 29.20 | 18.00 | 9.40 | 0.40 |

15 DAY SACRIFICE - 5 ANIMALS

| | | | | | |
|--------------------|------|------|------|-----|------|
| Lased Eye | 38.8 | 27.0 | 16.6 | 5.0 | 12.6 |
| Adjusted Lased Eye | 44.4 | 30.9 | 19.0 | 5.7 | -- |
| Contralateral Eye | 46.2 | 33.2 | 14.6 | 5.6 | -- |

30 DAY SACRIFICE - 6 ANIMALS

| | | | | | |
|--------------------|-------|-------|-------|-------|------|
| Lased Eye | 37.00 | 24.33 | 17.66 | 10.33 | 7.33 |
| Adjusted Lased Eye | 41.40 | 27.28 | 19.78 | 11.57 | -- |
| Contralateral Eye | 42.20 | 25.60 | 22.60 | 9.60 | -- |

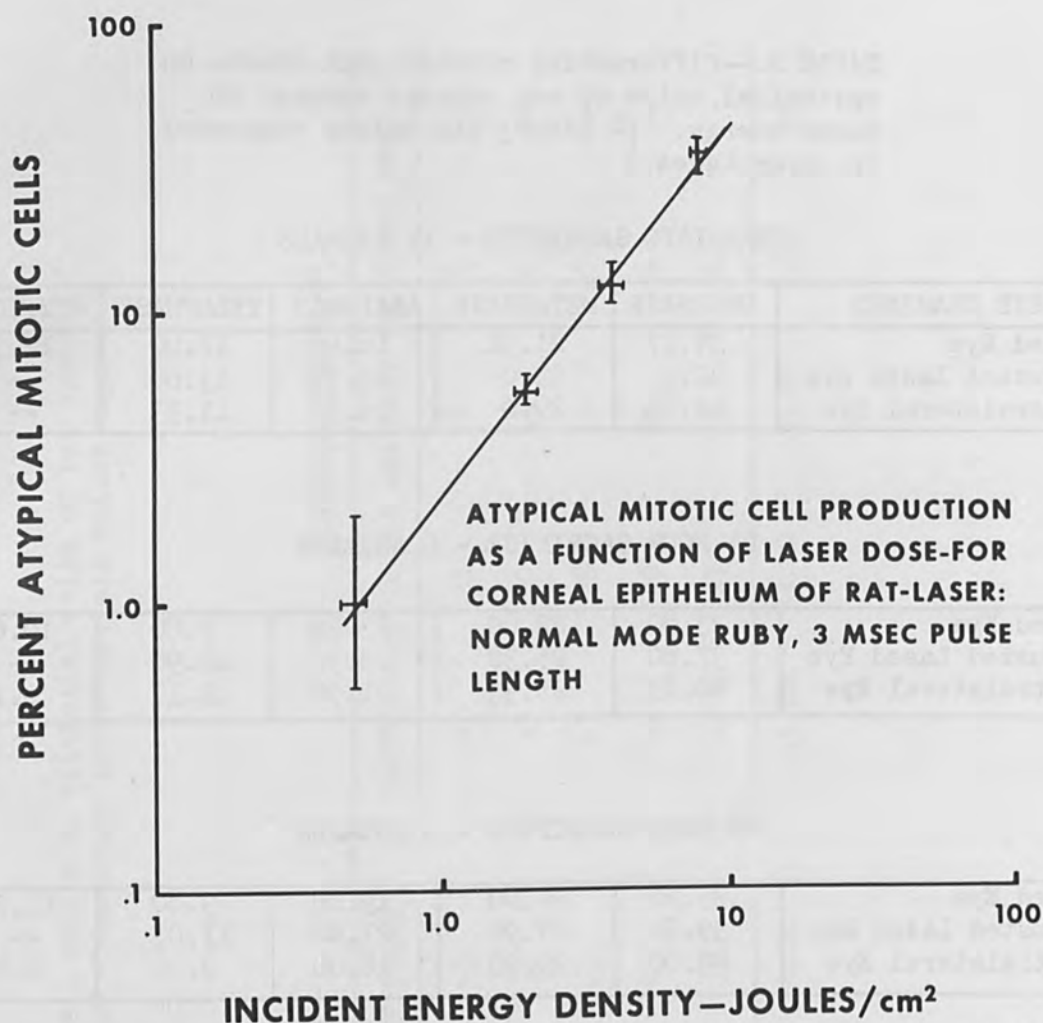


FIG. 1.—Atypical mitotic cell production as a function of laser dose.

life span of the normal dividing cell is between 5-10 days. Considering that the threshold value for aberrant cell production lies somewhere between 0.25 and 1.0 j/cm^2 , this effect may be a source of long-term problems in photocoagulation therapy using ruby lasers.

Our studies with CO_2 laser radiation have shown cellular abnormalities similar to those found with the ruby laser. Fine et al. have shown that the CO_2 laser can cause opacities, severe burns, and charring of the cornea as power densities are increased.⁴ Our data are based on radiation doses of a considerably lower level. In fact, in our studies no gross observable change of the cornea or corneal epithelium was evident in irradiated eyes.

Preliminary data indicate that the threshold for atypical cell production at 10.6 microns lies in the neighborhood of 7.0 W/cm^2 for a 0.1-sec exposure time. However, the threshold varies both with power density and exposure time.

Since CO_2 laser radiation is totally absorbed in the cornea, it appears reasonable to assume that a thermal mechanism underlies the observed changes. Also, there are little data to suggest that the atypical

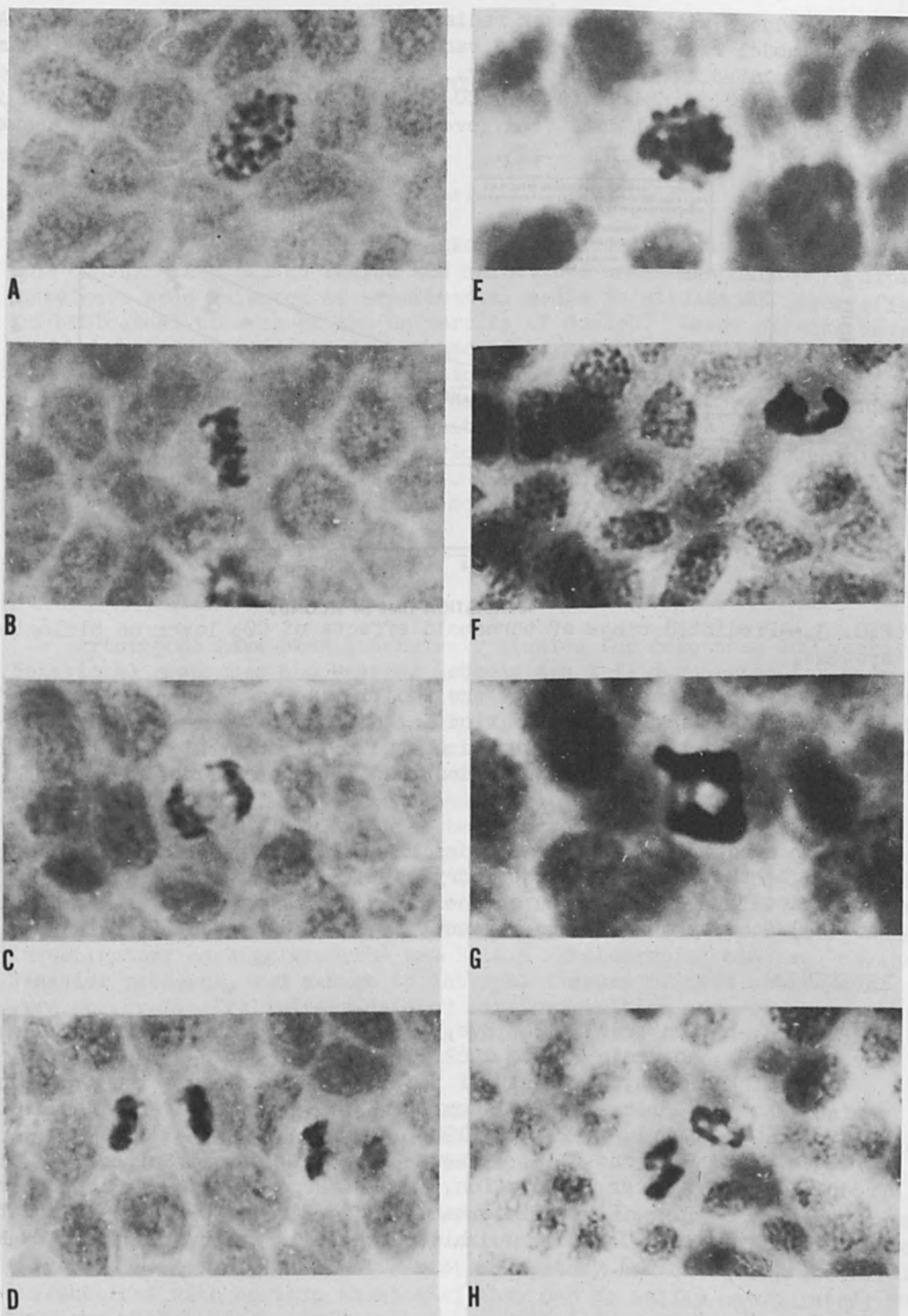


FIG. 2.—Normal mitotic stages of cells in the corneal epithelium: (A, prophase; B, metaphase; C, anaphase; D, telophase); and examples of various types of abnormalities that occur following exposure to ruby laser radiation (E through H).

cells produced with ruby laser radiation is not a thermal effect. A thermal model relating threshold range to dose and irradiation time has been formulated at this Laboratory. The predictions of this model, along with some experimental data from CO₂ laser experiments, are presented in Fig. 3. Experimental data from several burn studies are included as well.

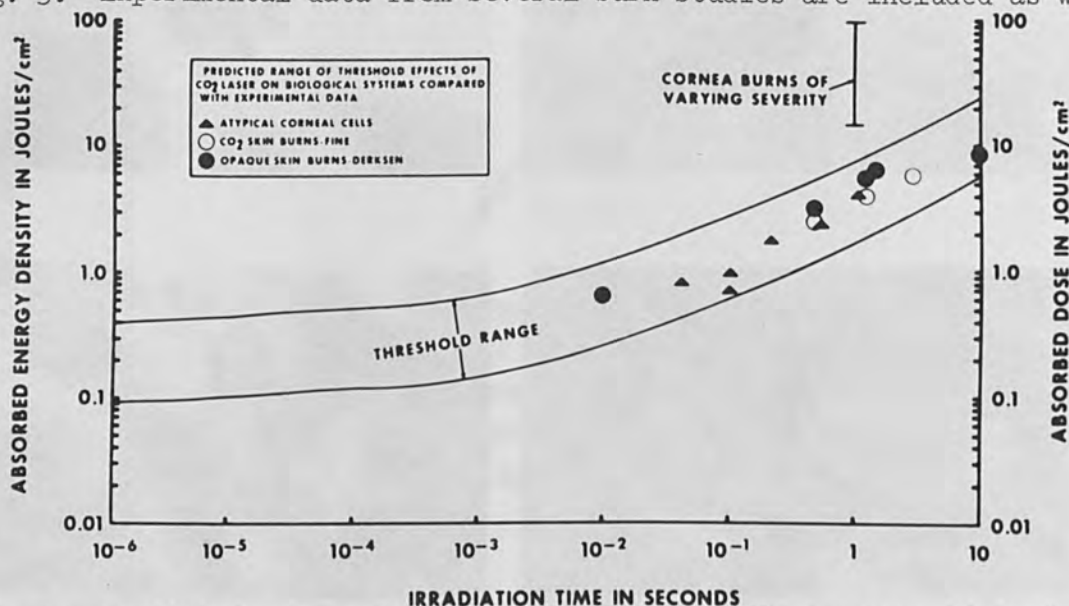


FIG. 3.—Predicted range of threshold effects of CO₂ laser on biological systems.

The range of values included by the two limits shown are necessarily wide. This model is a first approximation and needs further refinement. Perhaps the most interesting features of the model are that the experimental data fit the shape of the curves and that all the experimental data lie above the lower limit curve.

(In conducting the research described in this paper, the investigators adhered to the "Guide for Laboratory Animal Facilities and Care," as promulgated by the Committee on the Guide for Laboratory Animal, Resources, National Academy of Sciences-National Research Council.)

REFERENCES

1. H. Davson (ed.), "The Eye," Vegetative Physiology and Biochemistry, New York, Academic Press, 1962.
2. M. M. Zaret, "Analysis of factors of laser radiation producing retinal damage," Proc. 1st Ann. Conf. on Biol. Effects of Laser Radiation, Fed. Proc. 24 (Suppl. 14-2): 62, 1965.
3. W. H. Parr and R. S. Fisher, "Aberrant Corneal Epithelial Cells Produced by Ruby Laser Irradiation," USAMRL Report No. 698, 31 October 1966.
4. B. S. Fine, L. E. Zimmerman, and S. Fine, "CO₂ laser irradiation of the rabbit eye: Clinical and histopathologic observations," IEEE NEREM Record, November 1960.

ARTHROPODS AS EXPERIMENTAL MEDIA FOR LASER INVESTIGATIONS

W. H. A. WILDE and R. W. KOBYLNYK

University of Guelph, Guelph, Ontario, Canada

ABSTRACT. Because so much data are available on many arthropods, and because they can be reared and maintained under laboratory conditions, they have been selected as experimental media in studies of laser effects on biological tissues at the University of Guelph. Laser effects have been observed on pigmentation, shape, internal anatomy, and behavioral responses of mites Tetranychus urticae (Koch), dermestid beetles Trogoderma versicolor (Creutzer), cockroaches Periplaneta americana (Linne), aphids Myzus persicae (Sulzer), whiteflies Trialeurodes vaporariorum (Westwood), pear psylla Psylla pyricola Foerster, and the European pine sawfly Neodiprion sertifer (Geoff). Responses to these laser effects have been compared with responses documented in untreated specimens.

INTRODUCTION

Arthropods have been intensively studied for more than 100 years. Behavioral responses and rearing methods are well documented for many species. Because of the availability of such information, arthropods in five major orders were chosen as experimental animals for laser studies at the Zoology Department of the University of Guelph in Ontario. Life histories and rearing methods for mites, dermestid beetles, cockroaches, aphids, pear psylla, whiteflies, and pine sawflies enabled numbers of these arthropods to be reared for test purposes throughout the year. Unknown requirements of diapause in the pear psylla and lack of a suitable diet or artificial food host other than Pyrus (pear) made psylla rearing more difficult than any of the other species tested. Behavioral responses of aphids and cockroaches were compared with responses reported by such investigators as Wigglesworth¹ and Roth.² Phototropic changes, "escape" behavior patterns, and damage to internal tissues of test arthropods were observed. Preliminary data on mite oviposition and effects on the F₁ generation is discussed although investigations on actual genetic material has not been initiated.

Parr and Fisher have already shown mitotic changes can occur in mammalian tissues.³ Laser influences on arthropod genetic material may be as pronounced as that on chordate material.

Terrestrial arthropods are convenient for experimentation for several reasons. Large populations can be maintained under controlled conditions; they have relatively short life histories; they can be easily and safely anesthetized with certain chemicals; they can be easily manipulated; and they can withstand surgical procedures well.^{1,4}

MATERIALS AND METHODS

Test arthropods were reared in conventional greenhouses, screenhouses, and a standard growth chamber. Various types of cages, some of which are described by Peterson, were used to confine these test arthropods such as whiteflies, psyllids, aphids, sawflies, and cockroaches. Mites were reared in isolation in the open on Phaseolus (bean) hosts, psyllids were reared exclusively on Pyrus (pear), aphids and whiteflies were reared on bean, and sawflies were reared on Scots pine (Pinus sylvestris). Cockroaches did not require plant hosts in their rearing and reproduced well under low-humidity caged conditions in near darkness. Part of the cockroach diet was similar to commercial dog food.

Test arthropods were treated with varying numbers (1-3) of focused or unfocused laser pulses from a ruby laser of 4,000 V capacity which delivered 0.45 j for 0.7 ms. The intensity of a focused pulse was 3.75×10^4 W/cm² in an area of 0.0177 cm², and the intensity of an unfocused pulse was 1.06×10^3 W/cm² in an area of 0.624 cm². The total energies per unit area were 25.48 j/cm² and 0.72 j/cm², respectively. Convex glass lenses were used in holders attached to an optical bench for focusing the pulses. Arthropods, held in position for lasering by the use of masking tape, putty, or cellulose tape, were sometimes anesthetized or chilled to facilitate handling. Pulse impact areas were determined by the carbon or photographic paper method⁵⁻⁸ or by a pulse-sighter⁹ before arthropod placement on target areas.

Laser effects were observed under both stereoscopic and compound microscopes and internal effects were observed in sectioned, stained, and slide-mounted tissues from test arthropods. Check arthropods were maintained in all tests; also, check material for internal effects were reared and stored in the same manner as the treated material.

Scots pine (P. sylvestris), infested with N. sertifer eggs were maintained in screenhouses and greenhouses to ensure availability of sawfly material. When sawfly life stages were to be lasered, various procedures were used. Eggs in pine needles were lasered after being positioned on a laboratory jack with tape and strips of paper. Twelve to sixteen eggs comprised each test group; 300 eggs were maintained as checks. Eggs were observed weekly for developmental changes.

Pronymphal larvae within cocoons of N. sertifer were mass-reared in the summer of 1965 and stored at 3°C until treatment. Each test and check group consisted of 20 males and 20 females.

For internal histological studies, additional pine needles bearing N. sertifer eggs were prepared in test and in check groups. Two needles from each group were cut into 5-mm lengths each containing two eggs immediately after lasering and two needles were similarly cut 24 hr later. These lengths were then stored for 9 months in Karpenchenko fixative which was similar to Randolph's Modified Navashin Fluid.¹⁰ They were then embedded in paraffin¹⁰ and sectioned transversely at 10 microns.¹¹ Slides were stained in Mayer's haematoxylin for 5 min and counterstained in eosin-Y for 30 sec.

RESULTS

Behavioral responses such as antennal stroking, negative phototaxis, and cessation of feeding were observed in cockroaches, aphids, and psyllids. Neural damage is assumed in the cockroaches as laser damage on external surfaces in close proximity to recurrent nerve tissue was observed.

Degrees of sterility resulted from mite and white fly egg lasering even when minimal surface effect on eggs was observed. Adults from 9 lasered mite eggs laid only two eggs in 8 days, whereas each adult from 10 check eggs laid 35-78 eggs in 5 days.

Loss of mobility occurred in white flies because of leg and tarsi excision. Also, immobility and uncoordinated movement was observed in otherwise undamaged white flies. These latter two phenomena lasted for periods of 10 min to $2\frac{1}{2}$ hr.

Aphids, usually sluggish in movement, often remained immobile for as long as 30 min even when stimulated by a soft hair brush. Feeding in some experimental specimens did not resume for 6 hr. Lasered aphids turned on their dorsal surfaces were unable to reorient to normal walking positions for up to 3 hr. Feeble leg movements and antennal movement were observed throughout the 3-hr period in the latter tests.

Moulting in some dermestid larvae occurred soon after laser treatment. Germ layer damage was severe as up to 14 succeeding moults still showed original laser damage. Moulting was not prevented in any of the lasered specimens and moulting of test specimens occurred sooner than any moulting in the checks.

In the pine sawfly, a single focused pulse caused immediate discoloration of eggs and the surrounding pine needle tissue. All eggs exposed to a single focused pulse and most eggs exposed to three and six unfocused pulses failed to hatch. In the focused eggs, separations occurred between the endochorion and the serosa, and the endochorion was darkened and thickened at the egg pole opposite the embryo. However, no external or histological changes were observed in the eggs exposed to three and six unfocused pulses.

A single focused pulse removed part of the wall of cocoons containing pronymphal larvae or pupae. Two to six focused pulses produced a hole through the entire cocoon wall which was not repaired one month later. Focused pulses produced areas of depigmented cuticle in pronymphal larvae and clear droplets were usually formed in these lesions. Larvae appeared to avoid the focused pulses by moving away from the impact area. Lesions and adjacent segments darkened and swelled after 24 hr. These changes were similar to changes in larvae with lesions produced by a heated pin. The viscosity of haemolymph of lasered larvae also appeared to increase after 24 hr. Specimens exposed to single focused pulses also lost body weight in the first 16 days at faster rates than check specimens. Ninety per cent of larvae exposed to one and two focused pulses died as larvae. All larvae exposed to three, four, five, and six focused pulses died similarly. Adult emergence was high from the check larvae and larvae

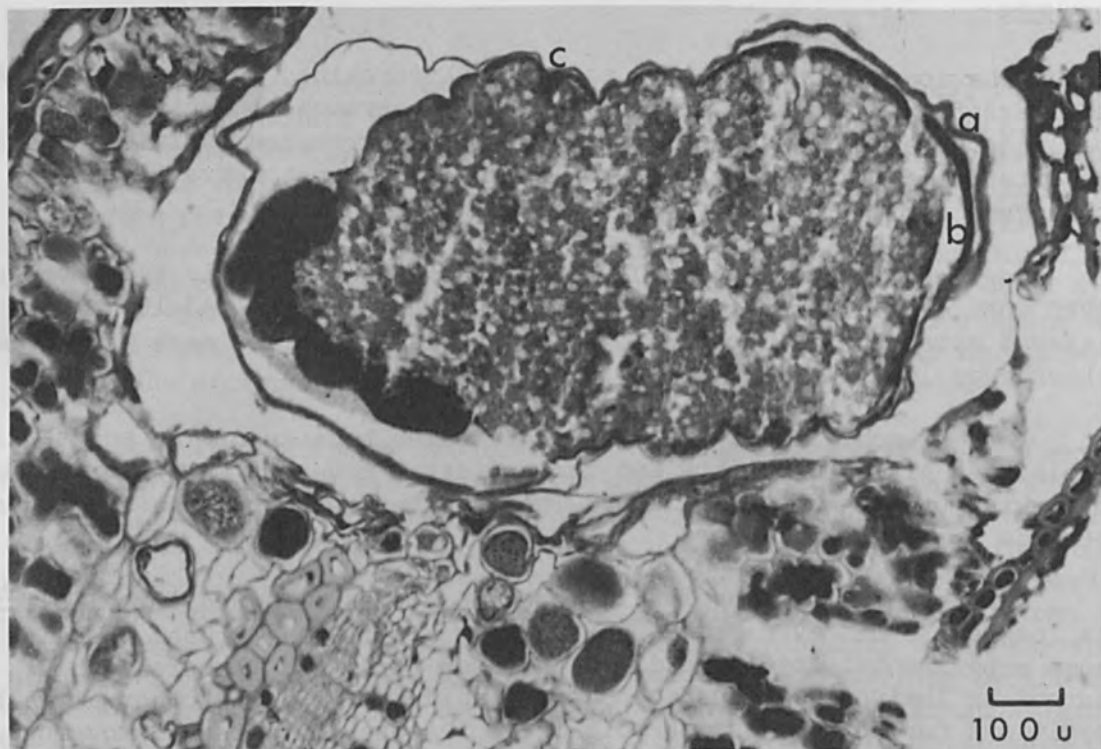


FIG. 1.—Transverse section of an *N. sertifer* egg within a *P. sylvestris* needle exposed to one focused pulse showing separation of (a) endochorion from (b) the serosa layer. Unaffected tissue is shown at (c).



FIG. 2.—Transverse section of cuticle of an *N. sertifer* pronymphal larva exposed to one focused pulse showing (a) separation in the cuticle, (b) yellow cuticle, (c) vacuolized epidermis, and (d) unaffected cuticle. (Magnification 200 x.)

exposed to six unfocused pulses. Immediately after focused lasering, separations occurred between the epicuticle and the endocuticle as well as separations between the cuticle and the epidermis. Clear areas were observed in the epidermis. After 24 hr, the epicuticle was aggregated into lumps or impregnated into the endocuticle, and the cuticle became yellow, darkened, and thickened.

DISCUSSION

Laser effects on biological tissues should include comparisons between vertebrate and invertebrate tissues, and responses of the respective test specimens. When arthropods are used as test hosts, laser effects can be compared with effects documented or recorded by entomologists on many life processes in many species of arthropods. One of the principal life processes and one easiest to work with would be comparisons of gross physical responses in laser-treated arthropods with arthropod responses induced by chemical, temperature, tactile, and olfactory stimulants. Other life process easily investigated would be oviposition and reproduction responses to lasering including detailed studies of the effects on chromosomal material. In this instance, the intensively studied vinegar fly Drosophila melanogaster (Meig.) would make an excellent laser study host. Internal physiological changes and effects on lymphatic, excretory, digestive, olfactory, audio, and visual systems caused by laser pulsing could be compared with much existing and accurate data already available.

Comparisons of laser effects on both gametic and parthenogenetic species and on holometabolic and hemimetabolic specimens would permit detailed study of laser effects on many types of life stages. Associated with direct effects on arthropods would be the indirect effects of laser treatment on commensal organisms of arthropods such as nematodes, virus, and other parasitic life forms existing as internal or external biota. Laser effects on insect vectors of plant or animal diseases could also be compared with known documented effects.

Histological results on pine sawfly life stages indicates lasering of eggs and pronymphal larvae of N. sertifer caused coagulation necrosis in the form of heat denaturation of proteins in the outer tissue layers. This effect probably led to uncontrolled dehydration of tissues and death.

Because arthropods can be readily reared and easily handled, because their behavioral patterns are well documented, and because their feeding and ovipositing effects on plant hosts are well known, arthropods make ideal laser experimental material for the physiologist, the biophysicist, the plant pathologist, the virologist, and the entomologist. Test data could in many instances be compared with vertebrate results or could provide data useful for similar laser investigations of vertebrate tissue.

ACKNOWLEDGMENT

The writers acknowledge with thanks the financial assistance provided by the National Research Council of Canada.

REFERENCES

1. V. B. Wigglesworth, "The Principles of Insect Physiology, Methuen, London, 1950.
2. L. M. Roth and E. R. Willis, "The biotic association of cockroaches, 141 *Smithson. Misc. Coll.* 4422: 345-347, 1960.
3. W. H. Parr and R. S. Fisher, "Aberrant Corneal Epithelial Cells Produced by Ruby Laser Irradiation. Rept. No. 698, Biophysics Division, U. S. Army Medical Res. Laboratory, Fort Knox, Ky., 1966.
4. R. D. O'Brien and L. S. Wolfe, "Radiation, Radioactivity, and Insects," Academic Press, New York, 1964.
5. L. Goldman and P. L. Owens, "Chromosome studies in dermatology," *Acta Derm.-Venereol.* 44: 68-75, 1964.
6. J. M. Igelman and T. Rotte, "Effects of tyrosinase," *Federation Proc.* 24(1 Part III, Suppl. 14) S-94-96, 1965.
7. W. H. A. Wilde, "Laser effects on two insects," *Can. Entomol.* 97: 88-92, 1965.
8. W. H. A. Wilde, "Laser effects on some phytophagous arthropods and their hosts," *Ann. Entomol. Am.* 60: 1, 1967.
9. R. W. Kobylnyk, "Candling and sighting techniques used in laser investigations of the European pine sawfly, Neodiprion sertifer Geoff. (Hymenoptera: Diprionidae)," *Can. Ent.* 99 (6): 670-672, 1967.
10. D. A. Johansen, "Plant Microtechnique," McGraw-Hill, New York, 1940; pp. 45, 126-134.
11. W. Brygider, "In what embryonic stage do the eggs of Neodiprion enter the winter diapause?" *Can. J. Zool.* 30 (2): 99-108, 1952.

RUBY LASER MICRO-IRRADIATION OF SINGLE TISSUE CULTURE CELLS VITALLY STAINED WITH JANUS GREEN B: AN ELECTRON MICROSCOPE STUDY

R. STORB, R. L. AMY, R. K. WERTZ, and M. BESSIS

Institut de Pathologie Cellulaire, Hôpital de Bicêtre, Paris

It is known that low-intensity irradiation with the light of a pulsed ruby laser does not produce readily perceptible reactions in living non-pigmented cells. By contrast, in naturally pigmented cells, such as erythrocytes, certain infusoria and plant cells, or in vitally stained cells, a visible morphological effect is produced, presumably because of the absorption of laser light by appropriate chromophores. It has been shown that extremely small, invisible amounts of dye are sufficient to produce such an effect. When choosing adequately selective vital stains, proper stain concentrations, and laser light intensities, one might expect a selective interaction of the laser beam with stained sub-cellular structures in living cells.

The effect produced in a living cell by coherent monochromatic light concentrated in a very small cytoplasmic area is of interest also, both with respect to primary effects produced at the irradiation site and with respect to secondary effects produced in nonirradiated parts of the cell. In the present study, single cells subjected to localized ruby laser irradiation of the cytoplasm were examined with the electron microscope to explore the four following questions: (1) primary radiation effects in cells stained with Janus green B, which is known for its mitochondrial specificity; (2) primary radiation effects in cells stained with other basic vital stains; (3) secondary radiation effects induced in parts of the cell that had not been subjected directly to the micro-beam; and (4) morphology of treated cells at different times after irradiation.

The air-cooled laser used in these experiments consisted of a ruby rod, 40 mm long and 3 mm in diameter, and an excitation xenon flash tube, and was mounted on a phase contrast microscope. The maximum energy output of the laser was 0.5 joule with a pulse duration of 500 μ sec. The emitted wavelength was 6943 Å. The energy could be varied by means of a graded neutral density filter placed between the ruby rod and ocular. The spot size in the focal plane depended on the ocular and objective used and was, in the present study, approximately 5.8 μ in diameter. The beam was focused in the target area by means of a spot of visible light traveling the same optical path as the laser beam. Observation of the cells during the irradiation procedure was possible by integrally mounted television and cinema camera equipment.

The tissue culture cells used in these experiments were either KB epithelial or C13 fibroblast cells growing in a monolayer on small glass slides. Prior to each experiment the cells were incubated with vital stains in concentrations ranging from 10^{-5} to 10^{-7} which were virtually nontoxic. After 30 min of incubation at 37°C the cells were covered with a coverslip and placed on the microscope stage. Then, cells were

selected for treatment and irradiated in the granuloplasm, an area rich in mitochondria. With low laser light intensity and low stain concentrations a small black mass characterized as light primary damage was produced at the irradiation site. The surface area of this mass averaged $2 \mu^2$. When increasing the laser flux, one or two larger black granules were produced averaging 5 to $10 \mu^2$ in area. This was arbitrarily termed moderate primary damage.

Still higher levels of laser flux caused heavy damage. Either a light zone with a blackend rim or cell fragmentation appeared at the irradiation site.

To study these cells under the electron microscope, we used the following technique. The cells were grown on slides whose surface was coated with a thin layer of formvar. Prior to use, three circles approximately 200 microns in diameter were made on the upper slide surface by means of a diamond scribe. The approximate position of these circles was marked by readily visible guide circles inscribed on the lower slide surface. The cells were covered by a coverslip and under low magnification 1 to 2 cells lying adjacent to one of the 200μ circles were selected for irradiation. After irradiation which was photographically recorded, the coverslip was floated off in Tyrode's solution and processing for electron microscopy was carried out directly on the slide. For final inclusion, an Epon-filled half of a gelatine capsule was inverted over the circle containing the irradiated cells. After polymerization of the Epon, capsule and slide were separated by thermoshock. On the surface of the freed capsule the impression of the circle and the irradiated cells, now in mirror image, could easily be identified. Subsequently, a truncated pyramid with the irradiated cells on its surface was trimmed from the capsule, followed by serial sectioning of the cells and examination under the electron microscope.

A modification of this technique made possible vertical sections through irradiated cells to study depth and size of the primary lesion and to determine whether the cell membranes were affected.

The electron microscope revealed striking changes at the irradiation site in Janus green B-stained cells having sustained light primary damage. Mitochondria along the microbeam's path were converted into electron-opaque material in which a few cristae and double membranes were distinguishable. Some mitochondria were only partially affected by this alteration. Restriction of the laser damage to the mitochondria was evident. Other cell structures in the immediate vicinity of the altered organelles—i.e., parts that had been exposed to the laser light—appeared to be intact. In unexposed portions of the cell, no secondary radiation damage could be detected.

Thus, a selective conversion of the mitochondria at the irradiation site into electron-opaque material was the only demonstrable change in cells with light primary damage. This alteration is almost certainly due to absorption of laser energy by Janus green B. present in the mitochondria. In contrast, irradiation of nonvitaly stained cells with a 50-times greater laser flux did not produce structural changes. The electron-opaque material in the mitochondria probably consisted of denatured lipids or

proteins produced by heat development as a consequence of energy transfer in the area of laser light absorption. Temperature and duration of the induced heat in our system, however, remain unknown.

Most of the cells survived the irradiation, but only 55% of them underwent later division as compared to about 80% in control cells indicating a disturbance of cell metabolism which was undetected by morphological criteria. The cells showed some decrease in RNA synthesis, whereas several mitochondrial and nuclear enzyme systems appeared to be intact.

The ultrastructural changes observed at the irradiation site in Janus green-B stained cells with moderate primary damage were similar to those found in cells with light primary damage. However, a greater number of mitochondria appeared to be altered. Organelles other than the mitochondria showed typical morphology. Vertical sections through cells with moderate primary damage revealed that the cell membranes above and below the irradiation site were intact. Most cell structures in the unirradiated cell portions did not exhibit signs of secondary radiation damage. By contrast the mitochondria had undergone a striking change, being greatly swollen and having lost their cristae. The matrix of each was light or had been transformed into granular electron-opaque masses condensed on the smooth inner membrane.

The mechanism evoking such secondary mitochondrial damage in these cells remains obscure. Rupture of the cell membrane was excluded on a morphologic basis as well as by trypan blue exclusion tests. A "spreading" of the beam to an area greater than 6μ in diameter should affect adjacent cells, which indeed were perfectly normal. The role of heat conduction in secondary damage remains unclear. The fact that development of heat by energy transfer is restricted to the area of primary damage, which constitutes only about $1/200$ to $1/400$ of the cell volume, makes a significant rise of temperature unlikely. Also, there was no morphologic evidence for a heat gradient, which one would expect.

Pressure waves emanating from the irradiated site have been observed after exposure of living tissue to high intensity ruby laser light. In our system, one would expect that the adjacent portions of control cells would be more affected than the distal pole of the irradiated cell. This argument is valid only if one assumes that conduction through two cell membranes is as efficient as conduction through or around the cell nucleus.

Since the diffusion distance of eventually formed free radicals is very small, in the $20\text{-}\text{\AA}$ range, secondary mitochondrial damage can hardly be attributed to that phenomenon.

It remains to mention possible changes of pH as a consequence of short-term heat development at the irradiation site. In addition, ammonia, CO, and CO₂ together with H₂O vapor may be present in the temporary gas bubble often produced at the site of laser light-stain interaction. The rapid diffusion of these substances may account for the mitochondrial changes seen in the whole cell.

Despite the extensive mitochondrial damage in cells with moderate primary damage, there was a normal histochemical activity of a series of oxidative enzymes in such cells. However, the observed mitochondrial alterations are probably accompanied by a temporary uncoupling of phosphorylation and oxidation which may be one explanation for a significant decrease of RNA synthesis in these cells.

Long-term studies showed that the majority of the cells with moderate primary damage died within 24 hr of irradiation and less than 10% survived but failed to divide. To explore primary and secondary damage as a function of survival times, we studied treated cells at different times. A number of cells were fixed for electron microscopy 4 hr after irradiation. When compared with the results obtained immediately after irradiation, two differences were evident. First, the electron-opaque material in the area of primary damage was scattered over a larger zone rather than occurring in clumps. It was found in slightly vacuolized mitochondria with or without cristae or in loose contact with membrane fragments. The second difference was found in the mitochondria of the unirradiated cell portions. The secondary damage observed immediately after irradiation was missing, and the majority of the organelles were normal in structure. Only a small number of mitochondria showed slight vacuolization. Other cell organelles were also found to have typical structure.

Such cells studied 24 hr after irradiation could not be distinguished from controls. Despite the morphological recovery these cells failed to divide. These findings suggest irreversible cell damage at the molecular level. Indeed, when studying the incorporation of H^3 -uridine in such cells 4 hr after irradiation we found that about 60% of the cells showed virtually no RNA synthesis.

In Janus green B-stained cells sustaining heavy primary damage not only mitochondria but also other organelles at the irradiation site were converted into electron-opaque masses. In most cases, the cell membrane was disrupted. This result probably reflects absorption of laser light by minute quantities of stain also present in nonmitochondrial cell structures. In such cells, virtually all cell structures showed drastic secondary alterations. Most cells exhibited decreased or no oxidative enzyme activity, the RNA synthesis averaged only about 25% of that of unirradiated cells, and cell death usually occurred within 2 hr of irradiation. The massive secondary damage in these cells seems to be associated with the rupture of the cell membrane which allowed water and ions to enter the cell and proteins to leave it. The resulting change of the internal cell milieu probably caused the irreversible secondary damage.

In most cells stained with other basic vital stains such as Nile blue, toluidine blue, or methylene blue, no selective alterations of organelles were observed. By contrast, the irradiation site was uniformly covered with loose electron-opaque material. This finding agrees with the concept that these dyes undergo adsorptive bindings with all electro-negative cell constituents such as nucleic acids, mucopolysaccharides, and phospholipids. Only in a single fibroblast, stained with cresyl blue, did we find a selective conversion of the Golgi lamellae into electron-opaque material while adjacent cell structures were apparently not affected.

The secondary damage found in cells of this group was similar to that reported for the Janus green B-sensitized cells indicating that the secondary alterations are a general phenomenon resulting from localized laser irradiation of the cytoplasm and are not linked to the use of a certain vital stain.

NOTE: R. Storb is now at the University of Washington School of Medicine, Seattle, Washington; R. L. Amy is at the Biology Department, Southwestern at Memphis, Tennessee; and R. K. Wertz is in Sacramento, Calif.

CLINICAL EXPERIENCE WITH LASER PHOTOCOAGULATION OF OCULAR TISSUE

H. C. ZWENG

Palo Alto Medical Clinic and Stanford University School of Medicine,
Palo Alto, Calif.

ABSTRACT. Photocoagulation of ocular tissues by noncoherent white light had been demonstrated to be a practical therapeutic measure in the 1950s. Therefore, ophthalmologists in the field of photocoagulation were in an excellent position to apply coherent light sources to ocular problems. Our own experience embraces over 200 patients treated with long-pulsed ruby pulses. Laser energy has been found completely feasible in sealing off retinal holes and tears to prevent retinal detachment; to wall off and prevent the spread of retinoschisis; and to wall off areas of peripheral retinal degeneration. Its usefulness in the treatment of diabetic retinopathy is being evaluated with especial emphasis on the obliteration of the microaneurysms of diabetic retinopathy and the sealing down of retinal areas threatened with detachment by retinitis proliferans.

One of the most exciting applications of laser energy to ocular disease is the treatment of macular edema secondary to central serous retinopathy, following cataract surgery, central chorioretinitis, diabetic microcystic edema of the macula, early senile macular degeneration, and following incomplete closure of the central retinal vein. All these problems are very difficult to treat and represent great threats to the patient's central (reading) vision. The demonstration of leakage of intravenous fluorescein dye into the macula gives a way to demonstrate the leakage of blood vessels which laser photocoagulation attempts to seal.

The use of the laser in the treatment of ocular tumors and glaucoma remain possible applications that are being investigated.

TREATMENT OF MACULAR DISEASE

R. R. PEABODY

Stanford University School of Medicine, Palo Alto, Calif.

The macular area of the retina is the area of greatest visual sensitivity. Vision in the healthy macula is 20/20 or better; if the macula is destroyed by any disease process, vision is reduced to 20/200, or less. Diseases of the macula have been difficult to treat by any means usually, and impossible to treat with conventional photocoagulation because of the large amount of damage produced by the treatment itself.

However, histologic studies of pulsed ruby laser lesions of the human retina show that the ganglion cell and the nerve fiber layers are not damaged.¹

In Fig. 1, a photomicrograph of a human retina, the laser damage is seen to be limited to the outer layers of the retina, with spreading of the outer nuclear cells, dispersion of pigment from the pigment epithelium, and infiltration of lymphocytes in the choroid. The lesion edges are sharp. The inner layers show no morphological or histological evidence of disturbance. The absence of damage of the inner layer containing transmission fibers gave rise to speculation that one might treat diseased areas near the optic disk and in the macula without producing extensive new fiber-bundle defects in the visual field. This has proven to be the case clinically and has permitted clinical evaluation of laser photocoagulation in a variety of diseases affecting the macula.²

The use of fluorescein retinal angiography has provided a means for understanding the pathologic physiology and for localizing vascular leaks in macular diseases.³ The dye is injected into the antecubital vein of the arm and is observed through a Wrattan No. 47 cobalt filter as it circulates through the eye. Diseased areas fluoresce as fluid flows from vascular leaks into the retina. Photographs may be taken to record the leaks.

Laser photocoagulation provides a means to treat the localized vascular leaks with a discrete beam.

Patients treated during the past two years may be grouped into the following six categories:

- (1) Breaks in Bruch's membrane with leakage from the choriocapillaries into the macula in central serous retinopathy.
- (2) Macular edema in diabetic retinopathy.
- (3) Inflammatory lesions of the macula associated with infectious diseases, such as histoplasmosis and toxoplasmosis.
- (4) Macular edema following cataract extraction.
- (5) Macular cysts of unknown etiology.
- (6) Senile macular degenerations.

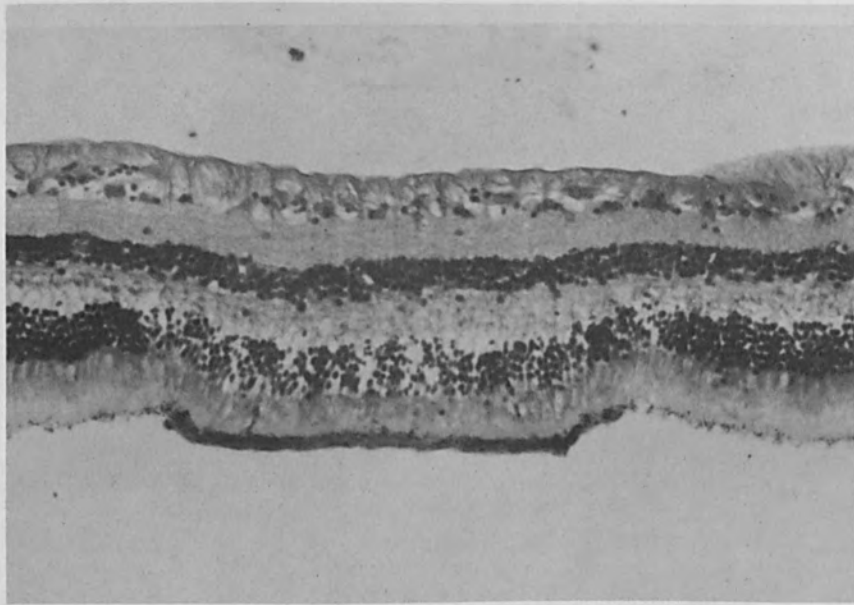


FIG. 1.—Laser damage to human retina.

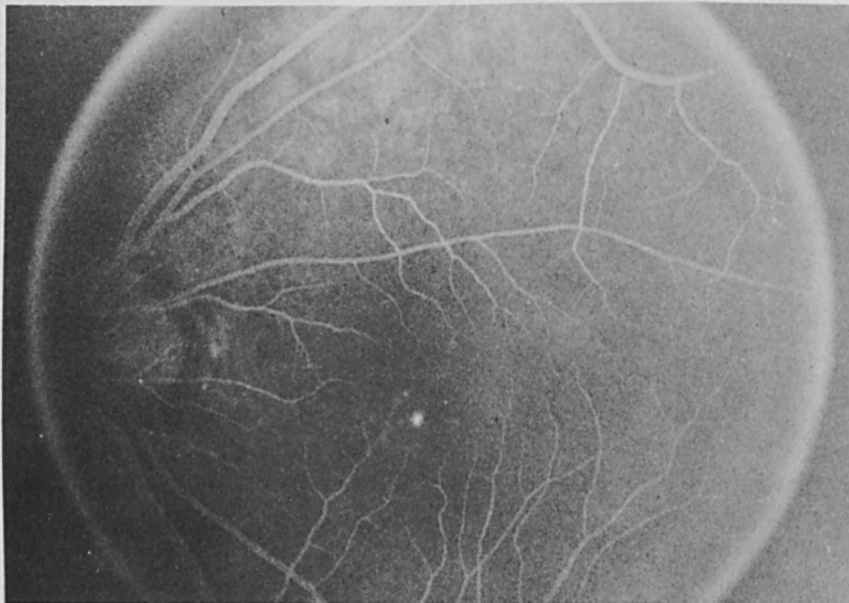


FIG. 2.—Angiography shows discrete white leak in a diseased retina.

All patients described here were treated with the laser photocoagulator described previously,⁴ manufactured by Optics Technology, Inc., Palo Alto, Calif.

Patients who are diagnosed as having leaks by angiography are given usual medical therapy before any laser therapy is given. If the medical treatment fails to improve vision and decreases the macular edema, the discrete leaks are treated with the laser photocoagulator using the narrow beam and just enough energy to produce a minimal change, usually about 25 millijoules at the cornea. The results are described in what follows.

1. PERSISTENT CENTRAL SEROUS RETINOPATHY. Most patients with central serous retinopathy get better spontaneously. For that reason, all patients were observed at least 3 months before laser treatment was considered, and most much longer. The response to laser photocoagulation has been good to excellent to date. Areas of disease are localized with fluorescein (Fig. 2) and are sealed off with small applications of energy delivered with the narrow beam. Visual improvement may take place as soon as 24 hr after treatment with several patients improving from 20/80 to 20/20-2 in that time span. Many of the patients treated, however, took up to 14 days for improvement of vision. To date eighteen patients with persistent central serous retinopathy have been treated. The duration of the disease ranged from 6 to 24 months pretreatment. All patients had visual improvement, with 95 per cent returning to 20/20 vision. Visual acuities before treatment ranged from 20/40 to 20/200. Follow-up periods of up to 2 years have shown only two recurrences, both of which responded to retreatment with the laser.

2. MACULAR LEAKS IN DIABETIC RETINOPATHY. Some diabetic patients have visual loss because of microcystic edema of the macula. Angiography has delineated areas of leakage in three eyes. All three have responded well to laser photocoagulation.

One patient had 20/100 vision in one eye and 20/200 in the other eye before treatment; 20/20 and 20/25, 1 week after.

3. CHORIORETINITIS OF THE MACULA. This inflammatory disease has many causes. One of the most commonly identified is histoplasmosis, a fungus infection. It causes a lesion which often gives bleeding and scar formation in the macula with permanent central vision loss. The rationale for treatment with laser photocoagulation has been to burn the lesion and thus destroy the causative agent. Five patients with small paramacular lesions have been treated; three had a regression of the disease, one stayed the same, and one progressed in her disease. Four weeks after treatment, the latter patient had some bleeding in the macula with resultant visual decrease.

Four more advanced cases of macula hemorrhage, edema, and scar tissue accumulation secondary to chorioretinitis were treated, with resulting resolution of hemorrhage and regression of edema. In two cases an increase in visual acuity resulted, from 20/200 to 20/50, and from 20/200 to 20/60.

4. EDEMA OF THE MACULA AFTER CATARACT EXTRACTION. Cataract surgery

that has been well done may still result in decreased vision due to post-operative edema of the macula with vision down to 20/200. The disease is somewhat resistant to treatment; but some of these patients improve on steroids, Diamox, and time. However, many patients go on to form macular cysts and when the cysts rupture, holes are formed with permanent loss of central vision. In the resistant group which has not responded to medication, laser photocoagulation has been used to attempt to seal off the leaks as demonstrated with fluorescein. Of ten patients treated five have improved, four have remained the same, and one has worsened.

The results on the five improved are listed below:

| Pretreatment | Posttreatment |
|--------------|---------------|
| 20/80 | 20/30 |
| 20/50 | 20/25 |
| 20/100 | 20/40 |
| 20/60 | 20/25 |

It is less likely that laser photocoagulation will benefit this group of patients, as the fluid leakage in the macula is more diffuse rather than discrete.

5. MACULAR CYSTS. Macular cysts that are small and limited in extent have been treated with laser photocoagulation with disappearance of the cyst in three cases. If the cysts go on to hole formation in the macula, vision is limited to 20/200 (legal blindness). Hence, early detection and possible treatment is of importance. This limited experience indicates that this mode of therapy might be useful.

6. SENILE DEGENERATION OF THE MACULA. In this disease of the macular circulation, there is very diffuse macular edema and sometimes hemorrhage. Early work with narrow-beam laser photocoagulation failed to limit progression of the disease. More recently, the use of wide beam-lesions and higher-energy inputs (up to 100 millijoules) has been of some value. In general, because of the widespread basic pathology, the laser has been of little help to date. However, of twelve eyes treated, vision has been improved in two eyes.

In conclusion, the pulsed ruby laser appears to be useful in treatment of selected macular lesions. All patients treated had macular disturbance with demonstrable fluorescein leaks.

The choice of the laser for photocoagulation of macular lesions is based upon the advantages listed below:

(1) Small energy quantum needed for coagulation, usually about 25 millijoules.

(2) Small spot size with sharp edges to the lesions, giving limited damage horizontally.

(3) 200- to 400- μ sec delivery time.

(4) No inner retina damage at clinical levels of energy inputs with no arcuate scotomas (blind spots).

(5) Patient acceptance, owing to lack of pain and inconvenience.

It must be emphasized that this work is in its preliminary phases and much evaluation needs to be done before it finds its place in the ophthalmological armamentarium.

REFERENCES

1. H. C. Zweng, M. Flocks, and R. Peabody, "Histology of human ocular laser coagulation," Arch. Ophth. 76: 11-15, 1966.
2. H. C. Zweng, "Laser photocoagulation of the retina," Proc. 20th Intern. Congr. Ophth. (in preparation).
3. J. D. Gass, "The pathogenesis of disciform detachment of the neuroepithelium," Am. J. Ophth. 63 (Suppl.): 1-139, 1967.
4. H. C. Zweng and M. Flocks, "Retinal laser photocoagulation," Trans. Am. Acad. Ophth. and Oto. 71: 39-45, 1967.

LASER-INDUCED ALTERATION OF SURFACE ENAMEL

R. H. STERN and R. F. SOGNAES

School of Dentistry, University of California at Los Angeles

ABSTRACT. It was previously reported that laser beam exposure of the intact dental enamel surface showed glass-like fusion which exhibited reduced birefringence under polarized light. The present study investigates the changes that occur on the surface of laser-exposed dental enamel. Extracted human teeth were subjected to the ruby laser at various energy levels. The enamel was then demineralized to simulate in vitro the development of incipient in vivo caries. Microradiographic examination revealed reduced subsurface enamel decalcification of the lased enamel, whereas unlased control sections demonstrated comparatively greater subsurface enamel demineralization. It may be inferred that lasing the enamel imparts to it a degree of resistance to demineralization. If this result is borne out in further studies, it may be possible to achieve such resistance in vivo and, in so doing, reduce caries susceptibility.

INTRODUCTION

The investigation of laser effect on oral hard and soft tissues and various commonly used dental materials has been carried out on a superficial basis by several investigators.¹⁻⁸

A more profound approach was taken by Taylor et al., who studied the effect of comparatively high energy intensities on Syrian hamster teeth;⁹ by Gordon, who described the plume that occurs on laser impact of the tooth;¹⁰ by Lobene and Fine, who observed no changes in radiodensity, hydroxyapatite configuration, or microhardness of human enamel but did find alterations in the enamel rod structure after laser exposure;¹¹ and by Kinersly et al., who describe the use of a low-powered ruby laser as a transilluminator to diagnose dental disease.¹²

GENERAL

An understanding of the effect of laser on the surface of human dental enamel must be preceded by the realization that the incipient stage of in vivo dental caries consists of a pronounced subsurface demineralization of the enamel. Such demineralization may be as deep as 1000 microns prior to the invasion and advanced destruction of the tooth structure by oral microorganisms (Fig. 1a).¹³⁻¹⁴

The precise origin, nature, and microstructural pathways of the initial dissolving agents are not fully understood; nor are the exact escape routes and interactions of the dissolved tooth minerals.

The effect of laser on the surface of the enamel of extracted human

teeth was studied by comparing the in vivo incipient dental carious lesion (Fig. 1a) to an in vitro incipient carious lesion (Fig. 1b). Microradiographic examination—as well as other comparisons—shows the in vitro incipient carious lesion to simulate its in vivo counterpart.

METHOD AND MATERIAL

Extracted human teeth with clinically intact enamel were exposed to a defocused laser beam with 45 joules of output energy focused to a spot size of 5 mm with a pulse duration of 1 msec. At this energy level there was no macroscopically visible change in the appearance of the enamel surface. The teeth so treated were prepared for in vitro demineralization so that the relative resistance of superficially lased enamel could be compared to unlased control areas of the same tooth specimen. The teeth were placed for 7 to 14 days in a demineralizing solution consisting of 0.1 M lactic acid, 6% hydroxyethylcellulose, and brought to a pH of 4.5 with sodium hydroxide.¹⁵ This method has been found to produce in vitro the characteristic subsurface demineralization patterns of enamel which appear in in vivo incipient human enamel caries (Fig. 1). After the appearance of changes in the surface opacity of the enamel (white spot), which is indicative of subsurface demineralization, the teeth were removed from the solution, sectioned to a thickness of 80 to 115 microns, and microradiographed. High-resolution microradiography was accomplished by placing the tooth sections on Kodak plates (type 649-0) for transmission of soft x rays at 25 to 40 kV and 16 mA for 10-20 minutes.

OBSERVATIONS

The response of unlased (Fig. 2a) compared to lased enamel surfaces (Fig. 2b) following in vitro demineralization is shown. It will be noted that the unlased control surface shows the typical subsurface demineralization as seen in vivo in Fig. 1(a) and in vitro in Fig. 1(b). By contrast the lased enamel subsurface, which was exposed to identical demineralizing conditions, has retained a high microdensity with very little mineral leakage from the subsurface area.

DISCUSSION

The effect of laser on human enamel apparently causes a change which is reflected in lesser subsurface demineralization when compared to unlased enamel.¹⁶ Whether this effect is a purely physical one of making enamel more amorphous by fusion of certain preformed pathways, or whether other changes occur with laser exposure, remains to be determined. The observed resistance to subsurface demineralization—an apparently physical change induced by laser exposure—is being further studied by determining the penetrability of the lased enamel surface to fluoride ions.

Consideration must also be given to the related problems of temperature increase at the dental pulp and increasing the enamel surface absorption of laser energy. If the enamel surface can be made to absorb more laser energy rather than transmit it, then lower energies might be sufficient and heat transfer to the pulp minimized. An increased enamel surface interaction has been observed by coating the enamel with India ink.¹¹

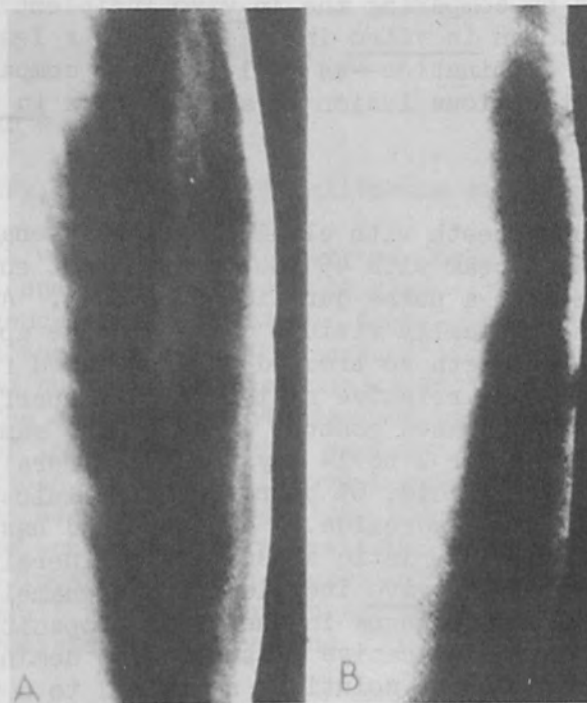


FIG. 1.—Microradiographs of human dental enamel: (a) in vivo demineralization typical of incipient enamel caries, (b) in vitro demineralization where enamel has been exposed to the demineralizing solution. (Note similar loss of subsurface microdensity.)

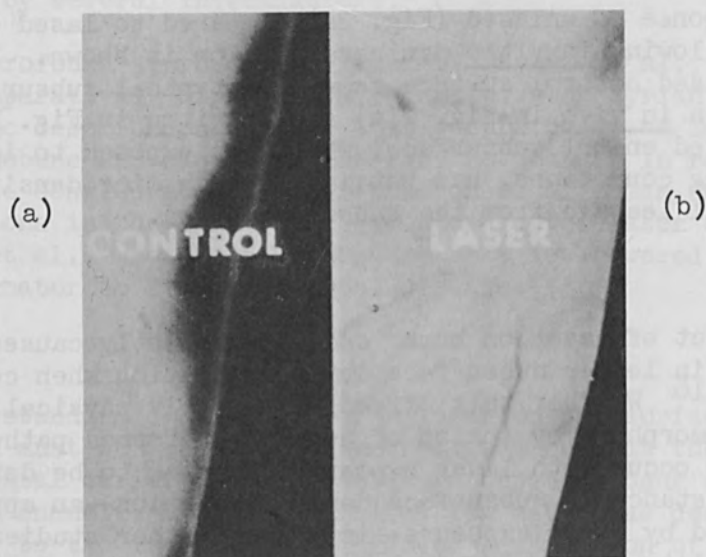


FIG. 2.—Microradiographs of human dental enamel which has been exposed to the demineralizing solution to create in vitro the effect of incipient enamel caries (white spot): (a) control unexposed enamel, (b) laser exposed enamel—45-joule exposure focused to 5-mm spot size. (Note dissimilar subsurface microdensity.)

Also, it is possible that enamel may absorb more energy from lasers operating at wavelengths different from that of the ruby laser.

At present many obstacles stand in the way of even the most superficial potential clinical laser application. The effect of laser on organic and inorganic constituents of enamel and dentin must be investigated; the effect of temperature changes on the dental pulp at various energy levels must be considered; the effect of impact or pressure waves on the dental pulp—which might under such stress behave like a closed liquid system—must be considered; and finally, the long-term effects of exposing vital hard and soft tissues to laser energy must be considered. Clinical application of lasers in dentistry is currently premature. Furthermore, limitation imposed by laser technology, dental materials, and understanding of the effects of laser make an absurdity of statements proposing the use of laser as a substitute for the dental drill.

CONCLUSION

The in vitro effect of laser impact on the surface of dental enamel has been described. It was shown that lasing imparts to the enamel surface a degree of impenetrability which reduces the characteristic subsurface demineralization that is seen in the in vitro precarious lesion. The observed impenetrability is significant in that it presents a means whereby the caries process can for the first time be affected by other than chemical means.

ACKNOWLEDGMENT

This research was supported through General Research Grant 1-SO-1 FR 05 304.

REFERENCES

1. R. H. Stern and R. F. Sognaes, "Laser beam effect on dental hard tissues," *J. Dent. Res.* 43: 873, 1964.
2. R. H. Stern and R. F. Sognaes, "Laser effect on dental hard tissues," *J. South. Calif. State Dent. Assoc.* 33: 17-19, 1965.
3. T. Kinersly, J. P. Jarabak, N. M. Phatak, and J. De Ment, "Laser effects on tissue and materials related to dentistry," *Jour. Amer. Dent. Assoc.* 70: 593-600, 1965.
4. L. Goldman, J. A. Gray, J. Goldman, B. Goldman, and R. Meyer, "Effect of laser beam impacts on teeth," *J. Amer. Dent. Assoc.* 70: 601-606, 1965.
5. R. F. Sognaes and R. H. Stern, "Laser effect on resistance of human dental enamel to demineralization in vitro," *J. South. Calif. State Dent. Assoc.* 33: 328-329, 1965.
6. T. E. Gordon, Jr., "Laser interaction with extracted human teeth: A preliminary report," *Dental Digest* 72: 155-158, 1966.
7. S. Peck and H. Peck, "Laser radiation: Some specific dental effects and an evaluation of its potential in dentistry," *J. Pros. Dent.* 17: 195-203, 1967.
8. T. Kinersly, J. P. Jarabak, N. M. Phatak, and J. DeMent, "Laser-induced microperforations in teeth sections," *J. Dent. Res.* 45: 199-203, 1966.

9. R. Taylor, G. Shklar, and F. Roeber, "The effects of laser radiation teeth, dental pulp, and oral mucosa of experimental animals," *Oral Surg., Oral Med., and Oral Path.* 19: 776-785, 1965.

10. T. E. Gordon, Jr., "Some effects of laser impacts on extracted teeth," *J. Dent. Res.* 45: 372-375, 1966.

11. R. R. Lobene and S. Fine, "Interaction of laser radiation with oral hard tissues," *Jour. Pros. Den.* 16: 589-597, 1966.

12. T. Kinersly, J. P. Jarabak, N. M. Phatak, and J. DeMent, "Tooth transillumination with laser radiation," *Med. and Biol. Illus.* 17: 5-6, January, 1967.

13. A. I. Darling, "Microstructural changes in early dental caries," in "Mechanisms of Hard Tissue Destruction," (R. F. Sognaes, ed.) Amer. Assoc. Adv. Sci. 1963; Chap. 6.

14. R. F. Sognaes, ed., "Chemistry and Prevention of Dental Caries," Thomas Publishing Co., Springfield, Ill., 1962.

15. J. A. Gray and M. D. Francis, "Physical chemistry of enamel dissolution," in "Mechanisms of Hard Tissue Destruction," (R. F. Sognaes, ed.), Amer. Assoc. Adv. Sci., 1963; Chap. 8.

16. R. H. Stern, R. F. Sognaes, and F. Goodman, "Laser effect on in vitro permeability and solubility," *Jour. Amer. Dent. Assoc.* 73: 838-843, 1966.

THE ARGON LASER: ITS EFFECTS IN VASCULAR AND NEURAL TISSUE

T. E. BROWN and R. J. ROCKWELL, JR.

The Children's Hospital Research Foundation, Cincinnati, Ohio

This paper describes two aspects of study with the argon laser:

- (1) Description of a new and flexible method for beam delivery in biological studies, and
- (2) A discussion of whether the argon beam displays selective effect on certain biological tissues.

Emphasis will be placed on the relationship to, and effect upon, the vascular content of the tissues.

Delivery of laser radiation with precision and ease has remained a problem for biomedical applications. The laser instrument itself is heavy, bulky, and consequently not easily maneuverable. At present, pulsed laser energy is delivered either as an unfocused beam, through a focusing lens, or by light guides fabricated from high-quality quartz rods. Such delivery methods impose hazards to the eye because of scattering and reflection of radiation from the target area. Protection must be provided to the subject and the laser workers at the time of the laser pulse.

Continuous-wave lasers, such as the argon ion laser, introduce the additional demand for constant eye protection. Safety glasses of amber plexiglas can provide for the eye safety problem for the argon laser. As with the pulsed laser systems, the aspects of beam delivery are also cumbersome. A Gimbal-mounted mirror has provided a means by which a continuous beam may be reflected with up to three degrees of freedom in beam directionality. Flexible fiber optics bundles have also been tested, but have thus far proved incapable of delivering significant magnitudes of cw laser power. Such devices have inherent high absorption in long lengths, and the very nature of their flexibility can substantially reduce the spatial coherence of the laser beam.

Recently, scientists at the Bell Telephone Laboratories developed a freely maneuverable, flexible light transmitting arm. It is constructed of six equal segments, joined at right angles by a 360° rotation joint. Internally, quartz prisms located at each elbow reflect the beam optically from one joint to the next. Antireflection coatings placed on the prism faces have minimized transmission losses to only 6% of the total beam power. This design permits a full range of beam delivery with six degrees of freedom. A lens attached to its distal end permits focusing of the beam. Counterbalancing was also provided to reduce the apparent weight in the operator's hand. Its present length of 2 ft is too short for present biomedical endeavors. Future designs could improve its maneuverability by addition of a telescoping arm in the first stage of the system. This instrument can be easily sterilized by conventional means. The flexible light pipe has provided a reasonably useful solution to the

problem of beam delivery for experimental studies.

The argon laser used in these studies produced multimode beam powers up to a total of 5 W. The 4880- and 5145-Å transitions accounted for approximately 80% of the total beam. The relative content of these two wavelengths could be altered by interchanging dump mirrors of different wavelength-reflection characteristics. At discharge tube currents above the threshold for both of the wavelengths, a 92% reflector peaked at 4880 Å and less than 89% at 5145 Å produced a predominantly blue beam. A second 92% reflector peaked at 5145 Å and less than 89% at 4880 Å produced a predominantly green beam. The mirrors were at a radius of curvature 10 m.

Single-mode, single-wavelength operation at lower powers (2.5 W total) was achieved by replacing the 100% mirror with a quartz prism with a 100% broad-band coating on its rear surface. The front face of the prism was aligned at Brewster's angle. Power measurements were made with a Coherent Radiation Laboratories thermopile.

Study of the reaction in tissues with this laser permits the following general conclusions:

- (1) Generally, beam powers below 3W incise tissues too slowly,
- (2) The resultant char of tissue edges reduces the efficacy of the cutting process,
- (3) The greater the local char formation, the less confined will be the local tissue damage along the path of the beam.

Higher powers up to 10 W will probably be required for cleaner, more rapid incisions. So far as charring is concerned, one technique has been developed to minimize its amount. When the tissue being cut is placed on tension, char is lessened or eliminated; this technique would be useful only where the tissue being cut could be so manipulated.

One of the more interesting biological effects of the argon ion laser is its selective effect in tissues. Vascularity of the tissue plays a direct role in the argon tissue effects. The more vascular the tissue, the more readily does the mixed frequency argon beam incise the tissue. This observation led us to study whether one of the predominant wavelengths in the mixed-frequency beam could account for the correlation with vascularity. By means of the quartz prism wavelength selector, the laser was operated at either of the two major wavelengths of the argon beam—the 4880 Å and 5145 Å—so that their specific effects could be tested in biological tissues. Initially, studies were carried out on the brain surface.

At power levels of 0.5 W, the brain surface was incised by the 4880-Å beam; the 5145-Å beam proved ineffective. Similarly, surface vessels of the brain were transected by the 4880 Å but not the 5145 Å beam. It is interesting to note that these two wavelengths differ by less than 300 Å within the visible spectrum.

Studies on other organ systems revealed further differences in the effect of these two wavelengths. These results were obtained with 1-W powers at both wavelengths. Skin was incised by either beam, but somewhat

more rapidly by the 4880 Å, although the 5145-Å beam provided a cleaner cut—i.e., less char formation. Similar effects were seen in the liver, spleen, kidney, and skeletal muscle. But in each instance, the tissue path of the 5145-Å beam appeared quite clean. But then a different problem was encountered. In the highly vascular tissues of the liver, kidney, and spleen, the 4880-Å beam initially incised the tissues more rapidly but bleeding frequently occurred. However, bleeding proved minimal or absent with the 5145 Å beam.

In order to study this difference more closely, these two beams were trained onto the vessels of the brain surface. Because of the transparency of the adjacent brain tissue, these vessels could be easily observed. The reason for this difference now became more obvious. Vessels in the path of the 4880-Å beam were affected almost immediately, showing vaporization of the enclosed blood column and consequent disruption of the vessel wall. Bleeding then ensued. However, the 5145-Å beam initially caused vaso-constriction only, presumably because it less readily passed through the vessel wall into the blood column. As a result, the vessel constriction literally emptied itself of blood and, therefore, subsequent collapse and thrombosis of the vessel occurred. Therefore, it appears likely that the more bloodless cutting characteristic of the 5145-Å beam is caused by its stronger absorption at the vessel wall.

It is interesting that the absorption spectrum of hemoglobin has a peak absorption at 5145 Å with a very small fall off to 4880 Å. Therefore, in view of the closeness of the absorption spectrum of these two points, it is doubtful that hemoglobin accounts for the vascular effects of the 5145-Å and 4880-Å beams. More plausible is the explanation that this difference in effect is due to absorption and transmission characteristics of either the vascular wall, the plasma, or the red cell membrane itself.

Two additional wavelengths were also studied—4765 Å and 4965 Å. Since together these comprise about 10% of the mixed-frequency beam, and because of the relatively low power output, comparisons could be made only at 0.2 W. The 4765-Å and 4965-Å beams showed similar effects in all tissues to the 4880 Å.

That the vessel wall does, in part, control the argon tissue effect was easily seen in heart muscle. Heart muscle is incised by either wavelength, 4880 Å or 5145 Å, more readily than any other tissue that was tested. However, as one would expect from the above observations, the 4880 Å, which was more effective initially in its rate of incision, caused more bleeding along its tract than the 5145 Å. When the circulating blood is removed by exsanguination, the beam now incises the same heart muscle at very rapid rates even with use of low powers. Therefore, it is safe to presume that a specific component of muscle tissue enhances the argon-beam absorption. The nature of this substance is as yet unknown.

The surface of the brain again demonstrated a difference in interaction to these two wavelengths. Here, the 5145-Å beam did not cause observable char, although its incision rate was slower than the 4880-Å

beam which did cause char. This finding implies that a substance is present in the cerebral cortex which interacts selectively with the 4880-Å wavelength to a much greater extent than to the 5145 Å. Because of the sparsity of blood supply to the cerebral cortex, it is doubtful we could account for the observed differences of these two beams simply by relating the wavelengths to the absorption characteristics of the vascular tree. If, in fact, such a relationship were found, the rate of incision from the 5145 Å in vascular areas of the brain should be comparable to that of the 4880 Å. This result was not seen when tested.

Lightly colored and avascular tissues—such as the dural covering of the brain, or fascial layers of the body—are poorly incised by the 4880 Å although any vessels in its path are readily cauterized. The 5145-Å beam proves much more effective in incising such tissues, again demonstrating the biological significance caused by a small difference in the wavelength of laser radiation.

A brief note will be made in this final section on the study of the argon beam in hemophilic beagles. Hemophilia is an inherited bleeding disorder characterized by absence of a specific blood clotting factor, namely factor VII. Certain strains of dogs carry the identical disorder. Our studies with such animals have only recently begun, but it is worthy to note that the 4880-Å and 5145-Å argon beams have identical tissue effects in these animals as compared to normal animals. This suggests strongly that the coagulating effect of an argon laser is independent of a specific blood factor and may, therefore, someday have clinical application in the treatment of such disorders. However, results are premature and must await further studies of the relationship of all blood clotting factors to laser radiation.

In summary, it is obvious that selection of a specific wavelength might be required if one desires selective lasing of a given tissue. This specificity of tissue response seen by comparison of these two argon wavelengths was unexpected. It is suggested that there may be some optimum combination of these two wavelengths to provide a maximum incision rate with only minimal charring. This result implies the need to establish the exact gain conditions in the argon laser at both wavelengths in order to achieve a mixed frequency beam of correct proportions. This goal may be accomplished by appropriate selection of resonator mirror reflectors at these two wavelengths.

An explanation for the difference observed in the beam effects can be offered. It appears that the 4880-Å beam effect depends greatly on the local vascular tree. Therefore, the less vascular a structure, the less effective this particular beam. The 5145-Å wavelength affects tissues in a manner not necessarily correlated with the vascular supply. This result indicates that a specific photochemical interaction exists between the cell membrane or cellular organelles and this precise laser wavelength under study. It is a problem of specificity that should be given due concern in future biologic studies with the argon laser and, perhaps, with all lasers.

ACKNOWLEDGMENT

The work reported here was done at the Laser Laboratory of The Children's Hospital Research Foundation in Cincinnati, Ohio, and was supported by grants from The John A. Hartford Foundation and from the U. S. Public Health Service (No. OH-00118-04).

TOPICS COVERED

References to the literature have been included in this bibliography. The subjects of "scanning electron microscopy" and "laser light scattering" are treated in which the laser light is used as a probe. The subjects of "scanning electron microscopy" and "laser light scattering" are treated in which the laser light is used as a probe. The subjects of "scanning electron microscopy" and "laser light scattering" are treated in which the laser light is used as a probe.

INTRODUCTION AND ACKNOWLEDGMENTS

The scanning electron microscope was developed in the late 1950's and early 1960's. It has become one of the most important tools in the field of electron microscopy. The scanning electron microscope is a type of electron microscope that uses a beam of electrons to create an image of a specimen. The scanning electron microscope is a type of electron microscope that uses a beam of electrons to create an image of a specimen. The scanning electron microscope is a type of electron microscope that uses a beam of electrons to create an image of a specimen.

BIBLIOGRAPHY ON THE SCANNING ELECTRON MICROSCOPE

O. C. WELLS

IBM Watson Research Center, Yorktown Heights, N. Y.

ABSTRACT. Approximately 200 literature references to the scanning electron microscope are cited in this bibliography. Instrumental aspects and applications are both covered. Applications include studies of newsprint, metal fractures, metal whiskers, thermionic cathodes, semiconductors, insulating thin films, biological and cathodoluminescent specimens. References are indexed by subject matter. Co-authors are cross-indexed.

INTRODUCTION AND ACKNOWLEDGMENTS

This bibliography was compiled with the assistance of a large number of persons. If any readers can detect omissions, then I shall be very grateful for details to be included in updated versions. (Update sheets will be produced from time to time.) I would like to acknowledge the assistance of the Watson Research Laboratory librarians in locating papers, often from inadequate references. I would like to thank the correspondents who answered questions on points of detail and who in many cases kindly supplied reprints of their work. In particular, I would like to thank A. Rezanovich (Pulp and Paper Research Institute of Canada), D. Green and M. Larkin (Westinghouse), R. F. M. Thornley and E. J. Walker (IBM), W. C. Nixon (Cambridge University), P. R. Thornton (Bangor University), E. J. Dwornik (U. S. Geological Survey), P. Whitcombe (Engis Equipment Co) and several others, all of whom sent references.

BIBLIOGRAPHY ON THE SCANNING ELECTRON MICROSCOPE

This was prepared using TEXT90. This program is listed in the SHARE Reference Library as program number 7090-IBM-0022. It is described by V. S. Mercer, F. E. Franklin and R. A. Lowenstein, "The TEXT90 System," *Datamation*, vol. 12, October 1966, pp. 41, 43, 45 and 47. I am grateful to W. A. Lethbridge for advice on TEXT90, and to M. C. Grove and F. Gracer for edit programs that were used with it.

TOPICS COVERED

References to x-ray microanalysis have been excluded from this bibliography. The definition of "scanning electron microscopy" has been taken to include only those cases in which the modulating signal was taken from the specimen in the form of secondary electrons, backscattered electrons, transmitted electrons, carrier recombination radiation or as signals from p-n junctions. In some cases, a note has been added to indicate the relevance of a reference. References to electron beam fabrication are restricted to cases in which the scanning electron microscope was used either to observe or to control the process. A related topic, which has also been included, is the (nonthermal) effects on semiconductors of electron irradiation in the energy range up to 20 keV. References that include more than six authors are listed by the first three authors "and x others." An index of the references by subject matter precedes the main bibliography.

CONFERENCE PROCEEDINGS

Conference proceedings are listed under editor(s) and year of publication. They are included as a separate entry if they contain more than two references to the scanning microscope. Papers published in these proceedings are listed by the author of the paper and by the date of publication of the proceedings, which in some cases is 1 year or more later than the date of the conference.

A list of these conferences by location and year is as follows:

- Leeds (1956): Challice and Sikorsky (1957).
- Stockholm (1956): Sjostrand and Rhodin (1957).
- Denver (1957 et seq.): Mueller (or Mueller et al) (1957 et seq.).
- Berlin (1958): Bargmann et al (1960).
- Delft (1960): Houwink and Spit (1961).
- Boston (1961): Bakish (1961).
- Oxford (1961): Bolam (1962).

BIBLIOGRAPHY ON THE SCANNING ELECTRON MICROSCOPE

- Philadelphia (1962): Breese (1962).
Prague (1964): Titlebach (1965).
Princeton, N.J. (1964): Kurshan (1964).
Toronto (1964): Bakish (1965).
Washington (1964): McKinley et al (1966).
Cambridge (1965): Bolam (1966).
Kyoto (electron microscope conference, 1966): Uyeda (1966).
Kyoto (semiconductors, 1966): was published without an editor's name; it is cited in the reference Wittry (1966).
London (IERE and IEE, 1966): was published without an editor's name; it is cited in the reference Chang and Nixon (1966b).
Michigan (1966): Haddad (1966).

INDEX OF REFERENCES BY SUBJECT

- Applications (see also Image):
Biological (see Papermaking):
-teeth: Boyde and Quilliam (1966), Boyde and Stewart (1962 and 1963), Stewart and Boyde (1962).
-insects: Oatley (1966), Pease, Hayes, Camp and Amer (1966), Smith and Oatley (1955).
-other specimens: (algae) Dwornik (1966), (blood corpuscle) Hayes, Pease and McDonald (1966), (human Jaques, Coalson and Zervins (1965), (house cricket eggshell) McFarlane (1965), (spinach leaf) Pease and Hayes (1966), (pollen grains) Thornhill, Matta and Wood (1965), (rat villi) Thornley (1960b), (shore crab) Thornton (1965).
-preparing biological material: Jaques, Coalson and Zervins (1965), Thornley (1960b), Washburn and Buchanan (1964).
Cathodes, thermionic: Ahmed (1962), Ahmed and Beck (1963), Beck and Ahmed (1963).
Ceramics, see Low Voltage Method.
Cement Fracture: Chatterji and Jeffery (1966).
Crystals (see Graphite Crystals, Phosphor Crystals):
-decomposing by heat: Bowden and McAuslan (1956), McAuslan and Smith (1957), Oatley (1966).
-defects in: see Semiconductors.
-quartz crystals: Dwornik (1966).
Dielectric Films (see Semiconductors, integrated circuits; and Low Voltage Method):
-iron oxide on iron: Knoll (1941b).
-examined by induced signal method: Green (1966).

BIBLIOGRAPHY ON THE SCANNING ELECTRON MICROSCOPE

- Diffusion Couple: Shirai, Onoguchi and Ichinokawa (1967).
Electron Beam Fabrication (involving principles of SEM):
-formation of structure: Broers (1965a, b and c), Chang and Nixon (1967), Pease and Nixon (1965b).
-registration using induced signal method: Wells, Everhart and Matta (1963 and 1965).
Fabrics and Fibres: Bobkowicz (1963), Challice and Sikorsky (1957), Culpin and Dunderdale (1965), Smith and Oatley (1955).
Geological Samples:
-Dwornik (1966).
-by luminescent method: Long (1962).
Glass Ceramics: Majumdar et al (1966).
Graphite Crystals: Minkoff (1966a and b), Minkoff and Nixon (1966).
Gravure Cells: Goode (1966).
Insulators, see Low Voltage Method.
Iron Oxide Particles: Themelis (1961), Themelis and Gauvin (1962 and 1963).
Metal Alloys, examined by luminescent method: Heinrich (1962).
Metal Fractures: Tipper, Dagg and Wells (1959), McGrath, Buchanan and Thurston (1962), Morris (1965).
Metals Under Strain: Davoine (1957).
Nylon Spinneret: Wells (1959).
Papermaking:
-initial evaluation: Atack and Smith (1956).
-wood fracture, chipping and pulping: Atack, May, Morris and Sproule (1961), Buchanan and Smith (1960), Debaise, Porter and Pentoney (1966), Forgacs (1961 and 1963), Green, H. V., (1962), Smith (1959), Teder (1964a and b).
-paper: Baker and Sepall (1965), Buchanan and Lindsay (1961), Buchanan and Washburn (1961, 1962 and 1964), Forgacs and Atack (1961), Pye, Washburn and Buchanan (1966), Smith (1959), Washburn and Buchanan (1964).
Phosphor Crystals:
-by secondary electron method: Pinard, Paris and Matteudi (1964).
-by luminescent method: Bernard, Davoine and Pinard (1959), Davoine, Bernard and Pinard (1960), Davoine and Pinard (1964 and 1965), Davoine, Pinard and Martineau (1960), Korda, Pruden and Williams (1967), Pinard (1964), Shaw, Wayte and Thornton (1966), Smith and Oatley (1955).
Semiconductors (see Image, secondary electron, to determine surface potentials):
-breakdown of junctions: Davies, Hughes, Sulway and

BIBLIOGRAPHY ON THE SCANNING ELECTRON MICROSCOPE

- Thornton (1966), Gaylord (1966), Neve et al (1966a, b and c), Sulway et al (1966).
- crystal defects in: Czaja (1966a and b), Czaja and Wheatley (1964), Czaja and Patel (1965), Lander, Schreiber, Buck and Mathews (1963), Thornton (1965).
 - depletion layer observation: MacDonald and Everhart (1965), Everhart (1966a).
 - device fabrication (non-thermal): Wells, Everhart and Matta (1963 and 1965), Matta, Green and Larkin (1965).
 - effect of bombardment: Green, D., Sandor, O'Keefe and Matta (1965), Nealey, Laakso and Hagon (1966), Ovsyuk and Smirnov (1965), Speth and Fang (1965), Szedon and Sandor (1965), Thornton, Hughes, Kyaw, Millward and Sulway (1967).
 - gallium arsenide (by secondary electron method): Drummond and Thornton (1965), Northrop, Thornton and Trezise (1964), Shaw, Hughes, Neve, Sulway, Thornton and Gooch (1966), Thornton (1965), Thornton, Culpin and Drummond (1963).
 - gallium arsenide (by luminescent method): Casey (1966), Casey and Kaiser (1966), Kyser and Wittry (1966), Wittry (1966), Wittry and Kyser (1964, 1965 and 1966).
 - gallium phosphide: Everhart, Smith, Wells and Oatley (1960).
 - germanium: Allen and Smith (1956), Everhart (1958), Everhart, Wells and Oatley (1959), Oatley and Everhart (1957), Ovsyuk and Smirnov (1965).
 - integrated circuits: Everhart, Wells and Matta (1963, 1964a and 1964b), Kimura, Higuchi, Maki and Tamura (1966), Mackintosh (1965), te Gude (1965), Thornhill and Mackintosh (1965), Thornton, Hughes, Kyaw, Millward and Sulway (1967).
 - inversion layers: Green, D., and Nathanson (1965), Higuchi and Maki (1965), Lander, Schreiber, Buck and Mathews (1963), Sulway, Hughes, Evans and Thornton (1966).
 - measurements by induced signal method (see also crystal defects and integrated circuits): Higuchi, Tauchi and Kimura (1964), Higuchi and Tamura (1965), Munakata (1965, 1966a, 1966b, 1966c, 1966d, 1967a and 1967b), Munakata and Todokoro (1966), Thornton, Hughes, Sulway and Wayte (1966).
 - time-varying effects: Northrop, Thornton and Trezise (1964), Saporin, Spivak and Stepanov (1966).
 - other: Wells (1961, 1962 and 1964).
- Surfaces:
- chemically etched: (aluminum) Everhart, Wells and Oatley (1959); (germanium) Allen and Smith (1956).

BIBLIOGRAPHY ON THE SCANNING ELECTRON MICROSCOPE

- electron beam machined: Chang and Nixon (1966a and b).
- ion etched: Broers (1965), Stewart (1962), Stewart and Boyde (1962), Pease, Broers and Ploc (1965).
- spark machined: Cole, Bucklow and Grigson (1961).
- thermally etched: Thornley (1960a).
- Whisker Growth: Morris (1965), Pease, Broers and Ploc (1965), Pease and Ploc (1965), Gardner and Cahn (1966), Thornton, James, Lewis and Bradford (1966).
- Wood Fractures, see Papermaking.
- Bibliographies: Heinrich (1966).
- Display, methods of:
 - cathode ray tube: Knoll (1935), Heinrich (1962).
 - storage tube: Brookshier and Gilroy (1965).
 - deflection modulated: Everhart (1966b), Wittry and Vancouvering (1967).
- Electron Collector, see Instrument Design.
- Field Emission Cathode:
 - in sealed-off SEM: Zworykin, Hillier and Snyder (1942).
 - in demountable system: Crewe (1963, 1964, 1965 and 1966).
- Image, backscattered electron:
 - discussed: McMullan (1952, 1953a and 1953b), Heinrich (1963), Shirai, Onoguchi and Ichinokawa (1966).
 - compared with secondary electron image: Everhart (1958), Everhart, Wells and Oatley (1959), Kimoto, Hashimoto and Sato (1966).
 - escape area measured: Pease (1965).
 - applied to study of diffusion couple: Shirai, Onoguchi and Ichinokawa (1967).
- Image, induced signal, see Applications: Semiconductors, crystal defects in; Semiconductors, integrated circuits; Dielectric Films and Electron Beam Fabrication.
- Image, luminescent, see Applications: Metal alloys; Phosphor crystals; Semiconductors, gallium arsenide; (construction of instrument) Davey (1965). See also (Applications, biological) Pease and Hayes (1966);
- Image, secondary electron:
 - to examine surface topography: Knoll (1935), Knoll and Theile (1939), Zworykin, Hillier and Snyder (1942), Smith (1956 and 1959), Smith and Oatley (1955), Everhart, Wells and Oatley (1959); see also Applications.
 - to determine surface potentials ("voltage contrast"): Knoll (1941a), Oatley and Everhart (1957), Everhart, Wells and Oatley (1959), Spivak, Saparin and Pereverzev (1962), Thornton, Neve and Sulway (1966); (high field voltage contrast) Drummond and Thornton (1965), Spivak et al (1965).
 - to reveal mechanical strain: Davoine (1957).
 - to reveal crystal orientations: Bernard and Davoine

BIBLIOGRAPHY ON THE SCANNING ELECTRON MICROSCOPE

- (1960).
- to detect magnetic fields (insensitive): Thornley (1960a), Everhart (1958), Dorsey (1966).
- Image, transmitted electron: von Ardenne (1938a and b), Crewe (1963, 1964, 1965 and 1966), McMullan (1952), Smith and Oatley (1955).
- Instrument Design (see Display, methods of; and Field Emission Cathode):
- method proposed: Stintzing (1929), Knoll (1935).
 - resolution calculated: Brachet (1946), Zworykin et al (1945), Smith and Oatley (1955), Everhart (1958), Smith (1961), Pease and Nixon (1965a).
 - made from glass: Knoll (1935), Theile (1938), te Gude (1945).
 - metal, oil pumped: von Ardenne (1938a and b), Zworykin, Hillier and Snyder (1942), McMullen (1952, 1953a and 1953b), Bernard and Davoine (1957), Smith (1960), Stewart and Snelling (1965), Kimura, Higuchi, Tamura and Maki (1966).
 - ultra-high vacuum: Crewe (1963, 1964, 1965 and 1966), Haas and Thomas (1963 and 1966).
 - combined with x-ray microanalyser: Cosslett and Duncumb (1957), Kushnir et al (1961 and 1963).
 - electron gun: Wittry (1957).
 - electron collector: Everhart and Thornley (1960), Kimoto and Hashimoto (1966).
 - best resolution: Pease and Nixon (1965a).
- Low Voltage Method:
- to examine insulators: Thornley (1960a and b), Thornley and Cartz (1962).
 - to reduce electron penetration: Bernard and Davoine (1960), Davoine, Bernard and Pinard (1960).
 - to measure work functions: Haas and Thomas (1963 and 1966).
 - to examine dielectric films: Da Silva and White (1961), Harris (1964).
- Resolution, see Instrument Design; Image.
- Stereomicrographs, calculations of: Wells (1960).
- Survey Papers (most recent): Mollenstedt and Lenz (1963), Nixon (1964), Oatley (1958), Oatley, Nixon and Pease (1965), Smith (1961), Thornton (1965).
- Voltage Contrast, see Image, secondary electron.
- Water Vapor, specimens examined in: Smith (1956), Thornley (1960a).

BIBLIOGRAPHY ON THE SCANNING ELECTRON MICROSCOPE

LIST OF REFERENCES:

- Ahmed, H., (1962). "Studies on high current density thermionic cathodes," Ph.D. Dissertation, Cambridge University.
- Ahmed, H., and A. H. W. Beck (1963). "Thermionic emission from dispenser cathodes," *J. Appl. Phys.*, vol. 34, pp. 997-998.
- Ahmed, H., see Beck and Ahmed (1963).
- Allen, J. W., and K. C. A. Smith (1956). "Electron microscopy of etched germanium surfaces," *J. Electronics*, vol. 1, pp. 439-443.
- Amer, N. M., see Pease, Hayes, Camp and Amer (1966).
- Ardenne, M. von, (1938a). "The scanning electron microscope. Practical construction" (in German), *Z. Techn. Physik*, vol. 19, pp. 407-416.
- Ardenne, M. von, (1938b). "The scanning electron microscope. Theoretical fundamentals" (in German), *Z. Physik*, vol. 109, pp. 553-572.
- Atack, D., and K. C. A. Smith (1956). "The scanning electron microscope - A new tool in fibre technology," *Pulp Paper Magazine Canada*, vol. 57, pp. 245-251; convention issue.
- Atack, D., W. D. May, E. L. Morris and R. N. Sproule (1961). "The energy of tensile and cleavage fracture of black spruce," *Tappi*, vol. 44, pp. 555-567.
- Atack, D., see Forgacs and Atack (1961).
- Baker, D. L., and D. Sepall (1965). "A new dimension in papermaking - carboxyethylation," *Pulp Paper Mag. Canada (Technical Section)*, vol. 66, pp. T449-T455. (Has 4 SEM images.)
- Bakish, R., (1961). *Proc. Third Symposium on Electron Beam Technology*, Alloyd Electronics Corp., Boston.
- Bakish, R., (1965). *First Int. Conf. Electron and Ion Beam Science Tech.* Toronto, May 1964. John Wiley and Sons, New York, 1965.
- Bargmann, W., G. Mollenstedt, H. Niehrs and 3 others (1960). *Proc. Fourth Int. Conf. on Electron Microscopy*, Berlin, Sept. 1958. Springer Verlag, Berlin, 1960.
- Beck, A. H. W., and H. Ahmed (1963). "The activation process in dispenser cathodes," *J. Electronics and Control*, vol. 14, pp. 623-627.
- Beck, A. H. W., see Ahmed and Beck (1963).
- Bernard, R., and F. Davoine (1957). "The scanning electron microscope" (in French), *Ann. de L'Univ. de Lyon*, Third Series, Sciences, Section B, vol. 10, pp. 78-86 and 4 plates.
- Bernard, R., and F. Davoine (1960). "Scanning electron microscopy" (in French), pp. 273-276 in Bargmann et

BIBLIOGRAPHY ON THE SCANNING ELECTRON MICROSCOPE

- al (1960). (Describes low-voltage SEM.)
- Bernard, R., F. Davoine and P. Pinard (1959). "Extension of the technique of scanning electron microscopy to the observation of fluorescent substances" (in French), C. R. Acad. Sci., vol. 248, pp. 2564-2566.
- Bernard, R., see Davoine, Bernard and Pinard (1960).
- Bikov, M. V., see Spivak, Saporin, Massarani and Bikov (1965).
- Bobkowicz, A. J., (1963). "The effects of turbulence on the flow characteristics of model fibre suspensions," Ph.D. Dissertation, McGill University. (Contains SEM images of damaged fibres.)
- Bolam, F., (1961). "The Formation and Structure of Paper," Trans. Oxford Symp., Sept. 1961, Technical Section of British Paper and Board Makers Association, London, E.C.4, England.
- Bolam, F., (1966). "Consolidation of the paper web," Trans. of the Symposium held at Cambridge, Sept. 1966, Technical Section of British Paper and Board Makers Association, London, E.C.4, England.
- Bowden, F. B., and J. McAuslan (1956). "Slow decomposition of explosive crystals," Nature (London), vol. 178, pp. 408-410.
- Boyde, A., and T. A. Quilliam (1966). "The scanning electron microscope," Medical and Biological Illustration, vol. 16, pp. 116-117. (Shows SEM images of developing African elephant molar tooth enamel.)
- Boyde, A., and A. D. G. Stewart (1962). "A study of the etching of dental tissues with argon ion beams," J. Ultrastructure Research, vol. 7, pp. 159-172.
- Boyde, A., and A. D. G. Stewart (1963). "Scanning electron microscopy of the surface of developing mammalian dental enamel," Nature (London), vol. 198, pp. 1102-1103.
- Boyde, A., see Stewart and Boyde (1962).
- Brachet, C., (1946). "Note on the resolution of the scanning electron microscope" (in French), Bull. L'Assoc. Tech. Mar. et Aero., No. 45, pp. 369-378.
- Bradford, A., see Thornton, James, Lewis and Bradford (1966).
- Breese, S. S., (1962). Proc. Fifth Int. Cong. for Electron Microscopy, Philadelphia, Aug./Sept. 1962. Academic Press, New York, 1962.
- Broers, A. N., (1965a). "Selective ion beam etching in the scanning electron microscope," Ph. D. Dissertation, Cambridge University.
- Broers, A. N., (1965b). "Micromachining by sputtering through a mask of contamination laid down by an electron beam," pp. 191-204 in Bakish (1965).

BIBLIOGRAPHY ON THE SCANNING ELECTRON MICROSCOPE

- Broers, A. N., (1965c). "Combined electron and ion beam processes for microelectronics," *Microelectronics and Reliability*, vol. 4, pp. 103-104 and 1 plate.
- Broers, A. N., see Pease, Broers and Ploc (1965).
- Brookshier, W. K., and J. Gilroy (1965). "Display system for use with a scanning electron energy analyzing microscope," *IEEE Trans. on Nuclear Science*, vol. NS-12, pp. 104-110.
- Buchanan, J. G., and R. A. Lindsay (1961). "A note on structure of paper as revealed by the scanning electron microscope," pp. 101-117 in Bolam (1961).
- Buchanan, J. G., and K. C. A. Smith (1960). "Preliminary studies of damage in papermaking wood chips using the scanning electron microscope," pp. 547-550 in Houwink and Spit (1960).
- Buchanan, J. G., and D. V. Washburn (1961). "Some experimental observations with a bearing on the paper 'A new theory of the shrinkage, structure and properties of paper'," pp. 422-425 in Bolam (1961).
- Buchanan, J. G., and D. V. Washburn (1962). "The surface and tensile fractures of chemical fibre handsheets as observed with the scanning electron microscope," *Pulp Paper Magazine Canada (Technical Section)*, vol. 63, pp. T485-T493.
- Buchanan, J. G., and D. V. Washburn (1964). "The surface and tensile fractures of groundwood handsheets as observed with the scanning electron microscope," *Pulp Paper Magazine Canada (Technical Section)*, vol. 65, pp. T52-T60.
- Buchanan, J. G., see McGrath, Buchanan and Thurston (1962), Pye, Washburn and Buchanan (1966) and Washburn and Buchanan (1964).
- Buck, T. M., see Lander, Schreiber, Buck and Mathews (1963).
- Bucklow, I. A., see Cole, Bucklow and Grigson (1961).
- Cahn, R. W., see Gardner and Cahn (1966).
- Camp, A. S., see Pease, Hayes, Camp and Amer (1966).
- Cartz, L., see Thornley and Cartz (1962).
- Casey, H. C., (1966). "Investigation of inhomogeneities in GaAs by electron beam excitation," *J. Electrochem. Soc.*, vol. 114, pp. 153-158.
- Casey, H. C., and R. H. Kaiser (1966). "Analysis of n-type GaAs with electron beam excited radiative recombination," *J. Electrochem. Soc.*, vol. 114, pp. 149-153.
- Challice, C. E., and J. Sikorski (1957). "Summarised proceedings of a conference on the electron microscopy of fibres - Leeds, January 1956," *Brit. J. Appl. Phys.*, vol. 8, pp. 1-26. (Has SEM image of wool fibre surface.)
- Chang, T. H. P., and W. C. Nixon (1966a). "Scanning electron microscopy and electron beam effects on silicon

BIBLIOGRAPHY ON THE SCANNING ELECTRON MICROSCOPE

- surfaces," pp. 193-194 in Uyeda (1966).
- Chang, T. H. P., and W. C. Nixon (1966b). "Electron beam machining of silicon observed with the scanning electron microscope," Paper 23 (3 pages) in Proc. Joint IERE-IRE Conf. on Applications of Thin Films in Electronic Engineering, London 1966. (IERE Conf. Proc. no. 7.)
- Chang, T. H. P., and W. C. Nixon (1967). "Electron beam formation of 800 AU wide aluminium lines," J. Sci. Inst., vol. 44, pp. 231-234.
- Chatterji, S., and J. W. Jeffery (1966). "Three-dimensional arrangement of hydration products in set cement paste," Nature (London), vol. 209, pp. 1233-1234. (Shows SEM images of fractured cement surfaces.)
- Chatterji, S., see Majumdar, Nurse, Chatterji and Jeffrey (1966).
- Coalson, J., see Jaques, Coalson and Zervins (1965).
- Cole, M., I. A. Bucklow and C. W. B. Grigson (1961). "Technique for the rapid, accurate and strain-free machining of metallic single crystals," Brit. J. Appl. Phys., vol. 12, pp. 296-297.
- Cosslett, V. E., and P. Duncumb (1957). "A scanning microscope with either electron or x-ray recording," pp. 12-14 in Sjostrand and Rhodin (1957).
- Crewe, A. V., (1963). "A new kind of scanning microscope," J. Microscopie (Societe Francaise de Microscopie Electronique, Paris), vol. 2, pp. 369-371.
- Crewe, A. V., (1964). "Scanning techniques for high voltage microscopes," pp. 63-81 in Proc. AMU-ANL High Voltage Electron Microscope Meeting, Argonne National Laboratory, Ill., U. S. A., W. C. Bigelow et al, Ed., Conf - 640204 available from USAEC Div. of Tech. Info., P. O. Box 62, Oak Ridge, Tenn.
- Crewe, A. V., (1965). Abstracts A9, A10 and A25 in the Program for the 23rd. Annual Meeting of the Electron Microscope Society of America, New York, Aug. 1965.
- Crewe, A. V., (1966). "Scanning electron microscopes: is high resolution possible?" Science, vol. 154, pp. 729-738. (Shows SEM images of thin films obtained by collecting electrons with specified energy loss.)
- Culpin, M. J., and K. F. Dunderdale (1965). "Studies of fibre surfaces in a scanning electron microscope," pp. 421-422 in Titlebach (1965).
- Culpin, M. J., see Thornton, Culpin and Drummond (1963).
- Czaja, W., (1966a). "Detection of partial dislocations in silicon with the scanning electron beam technique," J. Appl. Phys., vol. 37, pp. 918-919.
- Czaja, W., (1966b). "Response of Si and GaP p-n junctions to a 5- to 40-keV electron beam," J. Appl. Phys., vol. 37,

BIBLIOGRAPHY ON THE SCANNING ELECTRON MICROSCOPE

- pp. 4236-4248.
- Czaja W., and G. H. Wheatley (1964). "Simultaneous observation of diffusion-induced dislocation slip patterns in silicon with electron beam scanning and optical means," *J. Appl. Phys.*, vol. 35, pp. 2782-2783.
- Czaja W., and J. R. Patel (1965). "Observations of individual dislocations and oxygen precipitates in silicon with a scanning electron beam method," *J. Appl. Phys.*, vol. 36, pp. 1476-1482.
- Dagg, D. I., see Tipper, Dagg and Wells (1959).
- Da Silva, E. M., and P. White (1961). "A method for detecting imperfections in thin insulating films," pp. 830-835 in 1961 *Trans. of the Eighth National Vacuum Symp. (American Vacuum Society) combined with Second Int. Cong. on Vacuum Science* Pergamon Press, New York, N. Y.
- Davey, J. P., (1965). "Electron microprobe scanning system for the study of luminescence," Ph. D. Dissertation, Cambridge University.
- Davies, I. G., K. A. Hughes, D. V. Sulway, and P. R. Thornton (1966). "The direct observation of electrical leakage paths due to crystal defects by use of the scanning electron microscope," *Solid-State Electronics*, vol. 9, pp. 275-279.
- Davies, I. G., see Sulway, Davies, Hughes, Thornton and Holeman (1966).
- Davoine, F., (1957). "Secondary electron emission of metals under mechanical strain" (in French), Ph. D. Dissertation, L'University de Lyon.
- Davoine, F., R. Bernard and P. Pinard (1960). "Fluorescence of alkali halides observed with a scanning electron microscope" (in French), pp. 165-168 in Houwink and Spit (1960).
- Davoine, F., P. Pinard, and M. Martineau (1960). "Observation of cadmium sulfide bombarded with electrons of 5 kev energy" (in French), *J. Phys. Rad.*, vol. 21, pp. 121-124.
- Davoine, F., and P. Pinard (1965). "Study of cathodoluminescence by scanning electron microscopy" (in French), pp. 113-114 in Titlebach (1965).
- Davoine, F., see Bernard and Davoine (1957 and 1960) and Bernard, Davoine and Pinard (1959).
- Debaise, G. R., A. W. Porter and R. E. Pentoney (1966). "Morphology and mechanics of wood fracture," *Materials Research and Standards*, vol. 6, pp. 493-499.
- Der-Shvarts, G. V., see Kushnir, Fetisov, Der-Shvarts and 9 others (1963).
- Dorsey, J. R., (1966). "Scanning electron probe measurement of magnetic fields," abstract no. 10, First National

BIBLIOGRAPHY ON THE SCANNING ELECTRON MICROSCOPE

- Conf. on Electron Probe Microanalysis, available from L. Marton, ed., College Park, Maryland.
- Drummond, I. W., and P. R. Thornton (1965). "Studies of electrical high-field regions in high resistivity GaAs with the scanning electron microscope," pp. 287-288 in Titlebach (1965).
- Drummond, I. W., see Thornton, Culpin and Drummond (1963).
- Duncumb, P., see Cosslett and Duncumb (1957).
- Dunderdale, K. F., see Culpin and Dunderdale (1965).
- Dwornik, E. J., (1965). "Use of the scanning electron microscope in geologic studies," U. S. Geol. Survey Prof. Paper 550-D, pp. D209-D213.
- Evans, W. A., see Sulway, Hughes, Evans and Thornton (1966).
- Everhart, T. E., (1958). "Contrast formation in the scanning electron microscope," Ph. D. Dissertation, Cambridge University. (Available as Memorandum ERL-M161 from Electronics Research Laboratory, College of Engineering, University of California, Berkeley, Calif. 94720.)
- Everhart, T. E., (1966a). "Certain semiconductor applications of the scanning electron microscope," pp. 665-676 in McKinley et al (1966).
- Everhart, T. E., (1966b). "Deflection-modulation CRT display," Proc. IEEE, vol. 54, pp. 1480-1482.
- Everhart, T. E., K. C. A. Smith, O. C. Wells, and C. W. Oatley (1960). "Recent developments in scanning electron microscopy," pp. 269-273 in Bargmann et al (1960).
- Everhart, T. E., and R. F. M. Thornley (1960). "Wide-band detector for micro-microampere low-energy electron currents," J. Sci. Inst., vol. 37, pp. 246-248.
- Everhart, T. E., O. C. Wells and R. K. Matta (1963). "Evaluation of passivated integrated circuits using the scanning electron microscope," Extended abstracts, (Electrochemical Society) Electronics Division, vol. 12, no. 2, pp. 2-4. (New York Meeting, Oct. 1963.)
- Everhart, T. E., O. C. Wells and R. K. Matta (1964a). "Evaluation of passivated integrated circuits using the scanning electron microscope," J. Electrochem. Soc., vol. 111, pp. 929-936.
- Everhart, T. E., O. C. Wells and R. K. Matta (1964b). "A novel method of semiconductor device measurements," Proc. IEEE, vol. 52, pp. 1642-1647.
- Everhart, T. E., O. C. Wells and C. W. Oatley (1959). "Factors affecting contrast and resolution in the scanning electron microscope," J. Electron and Control, vol. 7, pp. 97-111.
- Everhart, T. E., see MacDonald and Everhart (1965), Oatley and Everhart (1957) and Wells, Everhart and Matta (1963)

BIBLIOGRAPHY ON THE SCANNING ELECTRON MICROSCOPE

- and 1965).
- Fang, F. F., see Speth and Fang (1965).
- Fetisov, D. V., see Kushnir, Fetisov, Raspletin and 4 others (1961) and Kushnir, Fetisov, Der-Shvarts and 9 others (1963).
- Forgacs, O. L., (1961). "Structural weaknesses in softwood pulp tracheids," *Tappi*, vol. 44, pp. 112-119.
- Forgacs, O. L., (1963). "The characterization of mechanical pulps," *Pulp Paper Mag. Canada (Technical Section)*, pp. T89-T118; Convention issue.
- Forgacs, O. L., and D. Atack (1961). "Distribution of chemical woodpulp and groundwood through the thickness of newsprint," pp. 721-747 in Bolam (1961).
- Gardner, Mrs. G. A., and R. W. Cahn (1966). "The use of a scanning electron microscope to examine whisker growth on an iron-aluminium alloy," *J. Materials Science*, vol. 1, pp. 211-212.
- Gauvin, W. H., see Themelis and Gauvin (1962 and 1963).
- Gaylord, J. W., (1966). "Microplasma observations in silicon junctions using a scanning electron beam," *J. Electrochem. Soc.*, vol. 113, pp. 753-754.
- Gilroy, J., see Brookshier and Gilroy (1965).
- Gooch, C., see Shaw, Hughes, Neve, Sulway, Thornton and Gooch (1966).
- Goode, F. N., (1966). "New views of gravure cells," *Gravure Magazine*, vol. 12, pp. 26-29 in issue for October.
- Green, D., (1966). "A method of examination of semiconductor oxides with a scanning electron microscope," pp. 375-384 in Haddad (1966).
- Green D., and H. C. Nathanson (1965). "Observation of inversion layers under insulated-gate electrodes using a scanning electron microscope," *Proc. IEEE*, vol. 53, pp. 183-184.
- Green D., J. E. Sandor, T. W. O'Keeffe and R. K. Matta (1965). "Reversible changes in transistor characteristics caused by scanning electron microscope examination," *Appl. Phys. Letters*, vol. 6, pp. 3-4.
- Green, D., see Matta, Green and Larkin (1965).
- Green, H. V., (1962). "Compression-caused transverse discontinuities in tracheids," *Pulp Paper Mag. Canada, (Technical Section)*, vol. 63, pp. T155-T168.
- Grigson, C. W. B., see Cole, Bucklow and Grigson (1961).
- Gude, H. te, See te Gude, H.
- Haas, G. A., and R. E. Thomas (1963). "Investigation of the patch effect in uranium carbide," *J. Appl. Phys.*, vol. 34, pp. 3457-3465. (These workers used a scanning electron beam of very low energy in ultra-high vacuum.)

BIBLIOGRAPHY ON THE SCANNING ELECTRON MICROSCOPE

- Haas, G. A., and R. E. Thomas (1966). "Electron beam scanning technique for measuring surface work function variations," *Surface Science* (Holland), vol. 4, pp. 64-88. (These workers used a scanning electron beam of very low energy in ultra-high vacuum.)
- Haddad, G. I., (1966). *Proc. Eighth Annual Electron and Laser Beam Symp., Univ. of Michigan, April 1966.*
- Hagon, P. J., see Nealey, Laakso and Hagon (1966).
- Harris, F. H., (1964). "Low velocity electron probe investigation of thin dielectric films," pp. 227-232 in *Proc. National Electronic Conf., Chicago.*
- Hashimoto, H., see Kimoto and Hashimoto (1966) and Kimoto, Hashimoto and Sato (1966).
- Hayes, T. L., R. F. W. Pease and L. W. McDonald (1966). "Applications of the scanning electron microscope to biologic investigations," *Laboratory Investigation*, vol. 15, pp. 1320-1326.
- Hayes, T. L., see Pease and Hayes (1966) and Pease, Hayes, Camp and Amer (1966).
- Heinrich, K. F. J., (1962). "Oscilloscope readout of electron microprobe data," pp. 291-300 in *Mueller and Fay (1962).*
- Heinrich, K. F. J., (1963). "Interrelationships of sample composition, backscatter coefficient, and target current measurement," pp. 325-339 in *Mueller, Mallett and Fay (1963).*
- Heinrich, K. F. J., (1966). "Bibliography on electron probe microanalysis and related subjects," pp. 979-1030 in *McKinley et al (1966).*
- Heinrich, K. F. J., see McKinley, Heinrich and Wittry (1966).
- Higuchi, H., and M. Maki (1965). "Observations of channels of MOS field-effect transistors using the scanning electron microscope," *Japan. J. Appl. Phys.*, vol. 4, pp. 1021-1022.
- Higuchi, H., and H. Tamura (1965). "Measurement of the lifetime of minority carriers in semiconductors with a scanning electron microscope," *Japan. J. Appl. Phys.* vol. 4, pp. 316-317.
- Higuchi, H., S. Tauchi and H. Kimura (1964). "Amplification of bombarding electron beam current in transistors," *Electrochemical Society Extended Abstracts, Electronics Division*, vol. 13, No. 1, pp. 140-141 (Toronto Meeting, May 1964).
- Higuchi, H., see Kimura, Higuchi, Maki and Tamura (1966), Kimura, Higuchi, Maki and Tamura (1966) and Kimura, Higuchi, Tamura and Maki (1966).

BIBLIOGRAPHY ON THE SCANNING ELECTRON MICROSCOPE

- Hillier, J., see Zworykin, Hillier and Snyder (1942) and Zworykin, Morton, Ramberg, Hillier and Vance (1945).
- Holeman, B. R., see Sulway, Davies, Hughes, Thornton and Holeman (1966).
- Houwink, A. L., and B. J. Spit (1961). Proc. European Regional Conf. on Electron Microscopy, Delft, Aug. 1960. De Nederlandse Vereniging Voor Electronenmicroscopie, Delft, 1961.
- Hughes, K. A., see Sulway, Davies, Hughes, Thornton and Holeman (1966), Neve, Hughes and Thornton (1966), Neve, Sulway, Hughes and Thornton (1966), Shaw, Hughes, Neve, Sulway, Thornton and Gooch (1966), Sulway, Davies, Hughes and Thornton (1966), Sulway, Hughes, Evans and Thornton (1966), Thornton, Hughes, Sulway and Wayte (1966), Thornton, Hughes, Kyaw, Millward and Sulway (1967).
- Ichinokawa, T., see Shirai, Onoguchi and Ichinokawa (1967).
- James, D. W. F., see Thornton, James, Lewis and Bradford (1966).
- Jaques, W. E., J. Coalson, and A. Zervins (1965). "Application of the scanning electron microscope to human tissues - A preliminary survey," Exp. and Molecular Pathology, vol. 4, pp. 576-580.
- Jeffery, J. W., see Chatterji and Jeffery (1966) and Majumdar, Nurse, Chatterji and Jeffrey (1966).
- Kaiser, R. H., see Casey and Kaiser (1966).
- Kimoto, S., and H. Hashimoto (1966). "Stereoscopic observation in scanning microscopy using multiple detectors," pp. 480-489 in McKinley et al (1966).
- Kimoto, S., H. Hashimoto and M. Sato (1966) "On a scanning electron microscope," pp. 197-198 in Uyeda (1966). (Compares backscattered image and secondary electron image from same area.)
- Kimura, H., H. Higuchi, M. Maki and H. Tamura (1966). "Observation of semiconductor elements using scanning electron microscope," J. Electron Microscopy (Japan), vol. 15, pp. 21-25.
- Kimura, H., H. Higuchi, H. Tamura and M. Maki (1966). "New scanning electron microscope and its applications," pp. 195-196 in Uyeda (1966).
- Kimura, H., see Higuchi, Tauchi and Kimura (1964).
- Knoll, M., (1935). "Static potential and secondary emission of bodies under electron irradiation" (in German), Z. Techn. Phys., vol. 11, pp. 467-475.
- Knoll, M., (1941a). "Deflecting action of a charged particle in the electric field of a secondary emitting cathode" (in German), Naturwiss., vol. 29, pp. 335-336.
- Knoll, M., (1941b). "Demonstration of the existence of

BIBLIOGRAPHY ON THE SCANNING ELECTRON MICROSCOPE

- oxidised layers on iron with the scanning electron microscope" (in German), *Phys. Z.*, vol. 42, pp. 120-122 and one plate.
- Knoll, M., and R. Theile (1939). "Scanning electron microscope for determining the topography of surfaces and thin layers" (in German), *Z. Phys.*, vol. 113, pp. 260-280.
- Korda, E. J., L. H. Pruden and J. P. Williams (1967). "Scanning electron microscopy of a P-16 phosphor - cathodoluminescent and secondary electron emission modes," *Appl. Phys. Letters*, vol. 10, pp. 205-206.
- Kurshan, J., (1964). *Proc. Symp. on Analytical Characterization of Materials* (available from RCA Laboratories, Princeton, New Jersey).
- Kushnir, Yu. M., D. V. Fetisov, K. K. Raspletin and 4 others (1961). "Scanning electron microscope and x-ray microanalyser," *Bulletin of the Academy of Sciences USSR, Physical Series (USA)*, vol. 25, pp. 709-714, 1962. Translated from *Izv. Akad. Nauk USSR, Ser. Fiz.*, vol. 25, pp. 695-700; (1961).
- Kushnir, Yu. M., D. V. Fetisov, G. V. Der-Shvarts and 9 others (1963). "Scanning electron microscope-x-ray microanalyser with magnetic electron optics," *Bulletin of the Academy of Sciences USSR, Physical Series (USA)*, vol. 27, pp. 1146-1151. Translated from *Izv. Acad. Nauk USSR, Ser. Fiz.*, vol. 27, pp. 1166-1172.
- Kyaw, Htin, see Thornton, Hughes, Kyaw, Millward and Sulway (1967).
- Kyser, D. F., and D. B. Wittry (1966). "Cathodoluminescence in gallium arsenide," pp. 691-714 in McKinley et al (1966).
- Kyser, D. F., see Wittry and Kyser (1964, 1965 and 1966).
- Laakso, C. W., see Nealey, Laakso and Hagon (1966).
- Lander, J. J., H. Schreiber, T. M. Buck and J. R. Mathews (1963). "Microscopy of internal crystal imperfections in silicon p-n junction diodes by use of electron beams," *Appl. Phys. Letters*, vol. 3, pp. 206-207.
- Larkin, M. W., see Matta, Green and Larkin (1965).
- Lenz, F., see Mollenstedt and Lenz (1963).
- Lindsay, R. A., see Buchanan and Lindsay (1961).
- Lewis, C., see Thornton, James, Lewis and Bradford (1966).
- Long, J. V. P., (1962). "Recent advances in electron-probe analysis," pp. 276-290 in Mueller and Fay (1962).
- MacDonald, N. C., and T. E. Everhart (1965). "Direct measurement of the depletion layer width variation vs applied bias for a p-n junction," *Appl. Phys. Letters*, vol. 7, pp. 267-269.
- Mackintosh, I. M., (1965). "Applications of the scanning electron microscope to solid-state devices," *Proc. IEEE*,

BIBLIOGRAPHY ON THE SCANNING ELECTRON MICROSCOPE

- vol. 53, pp. 370-377.
- Mackintosh, I. M., see Thornhill and Mackintosh (1965).
- Majumdar, A. J., R. W. Nurse, S. Chatterji and J. W. Jeffrey (1966). "Three-dimensional view of phase separation in glass ceramics," *Nature* (London), vol. 211, pp. 622-624.
- Maki, M., see Higuchi and Maki (1965), Kimura, Higuchi, Maki and Tamura (1966) and Kimura, Higuchi, Tamura and Maki (1966).
- Martineau, M., see Davoine, Pinard and Martineau (1960).
- Massarani, B., see Spivak, Saparin, Massarani and Bikov (1965).
- Mathews, J. R., see Lander, Schreiber, Buck and Mathews (1963).
- Matta, R. K., D. Green and M. W. Larkin (1965). "The use of the scanning electron microscope in the fabrication of an integrated circuit," *Extended Abstracts (Electrochemical Society), Electrothermics and Metallurgy Division*, vol. 3, no. 1, pp. 32-33. (San Francisco Meeting, May 1965.)
- Matta, R. K., see Everhart, Wells and Matta (1963, 1964a and 1964b), Green, D., Sandor, O'Keefe and Matta (1965), Thornhill, Matta and Wood (1965) and Wells, Everhart and Matta (1963 and 1965).
- Matteudi, G., see Pinard, Paris and Matteudi (1964).
- May, W. D., see Atack, May, Morris and Sproule (1961).
- McAuslan, J. H. L., and K. C. A. Smith (1957). "The direct observation in the scanning microscope of chemical reactions," pp. 343-345 in Sjostrand and Rhodin (1957).
- McAuslan, J., see Bowden and McAuslan (1956).
- McDonald, L. W., see Hayes, Pease and McDonald (1966).
- McFarlane, J. E., (1965). "The surface structures of various layers of the house cricket eggshell as seen in the scanning electron microscope," *Canadian J. Zool.*, vol. 43, pp. 911-913.
- McGrath, J. T., J. G. Buchanan and R. C. A. Thurston (1962). "A study of fatigue and impact fractures with the scanning electron microscope," *J. Inst. Metals* (England), vol. 91, Pt 1, pp. 34-39.
- McKinley, T. D., K. F. J. Heinrich and D. B. Wittry (1966). *The Electron Microprobe*. Proc. Symp. held in Washington, D. C., Oct. 1964. John Wiley and Sons, New York, 1966.
- McMullan, D., (1952). "Investigations relating to the design of electron microscopes," Ph. D. Dissertation, Cambridge University.
- McMullan, D., (1953a). "The scanning electron microscope and the electron-optical examination of surfaces," *Electronic Engineering* (England), vol. 25, pp. 46-50.
- McMullan, D., (1953b). "An improved scanning electron microscope for opaque specimens," *Proc. IEE* (England),

BIBLIOGRAPHY ON THE SCANNING ELECTRON MICROSCOPE

- vol. 100, Pt II, pp. 245-259.
- Millward, C., see Thornton, Hughes, Kyaw, Millward and Sulway (1967).
- Minkoff, I., (1966a). "Observations of spherulitic graphite growth with the scanning electron microscope," *Acta Metallurgica*, vol. 14, pp. 551-552.
- Minkoff, I., (1966b). "Hole formation in crystal growth by surface adsorption of an impurity," *Phil. Mag.*, vol. 12, pp. 1083-1086.
- Minkoff, I., and W. C. Nixon (1966). "Scanning electron microscopy of graphite growth in iron and nickel alloys," *J. Appl. Phys.*, vol. 37, pp. 4848-4855.
- Mollenstedt, G., and F. Lenz (1963). "Electron emission microscopy," pp. 251-329 in *Advances in Electronics and Electron Physics*, L. Marton and C. Marton, ed., Academic Press, N. Y.
- Mollenstedt, G., see Bargmann, Mollenstedt, Niehrs and 3 others (1960).
- Morris, E. L., see Atack, May, Morris and Sproule (1961).
- Morris, W. G., (1965). "Scanning electron microscopy of the surface structure of iron whiskers," Ph. D. Dissertation, MIT.
- Morton, G. A., see Zworykin, Morton, Ramberg, Hillier and Vance (1945).
- Mueller, W. M., (or Mueller et al) (1957 et seq). *Advances in X-Ray Analysis, Proc. Sixth et seq. Annual Conferences on Application of X-Ray Analysis, Univ. of Denver. Plenum Press, New York, N. Y.*
- Munakata, C., (1965). "Measurement of the homogeneity of a semiconductor with an electron beam," *Japan. J. Appl. Phys.*, vol. 4, p. 815.
- Munakata, C., (1966a). "Detection of resistivity striations in a Ge crystal with an electron beam," *Japan. J. Appl. Phys.*, vol. 5, p. 336.
- Munakata, C., (1966b). "On the voltage induced by an electron beam in a bulk semiconductor crystal," *Japan. J. Appl. Phys.*, vol. 5, pp. 756-763.
- Munakata, C., (1966c). "Applications of the barrier electron voltaic effect," pp. 357-374 in Haddad (1966).
- Munakata, C., (1966d). "Measurement of minority carrier lifetime with a non-ohmic contact and an electron beam," *Microelectronics and Reliability*, vol. 5, pp. 267-270 and 2 plates.
- Munakata, C., (1967a). "Detection of resistivity variation in a semiconductor pellet with an electron beam," *Microelectronics and Reliability*, vol. 6, pp. 27-33 and 2 plates.
- Munakata, C., (1967b). "An electron beam method of measur-

BIBLIOGRAPHY ON THE SCANNING ELECTRON MICROSCOPE

- ing diffusion voltage in semiconductors," Japan. J. Appl. Phys., vol. 6, p. 274.
- Munakata, C., and H. Todokoro (1966). "A method of measuring lifetime for minority carriers induced by an electron beam in germanium," Japan. J. Appl. Phys., vol. 5, p. 249.
- Nathanson, H. C., see Green, D., and Nathanson (1965).
- Nealey, C. C., C. W. Laakso and P. J. Hagon (1966). "Planar silicon device analyses with the electron microprobe microanalyser," pp. 748-783 in McKinley, Heinrich and Wittry (1966). (Has data on irradiated planar transistors.)
- Neve, N. F. B., K. A. Hughes and P. R. Thornton (1966). "Scanning electron microscope as a means of studying microplasmas at high resolution," J. Appl. Phys., vol. 37, pp. 1704-1709.
- Neve, N. F. B., D. V. Sulway, K. A. Hughes and P. R. Thornton (1966). "The scanning electron microscope as a means of investigating second breakdown and similar phenomena," IEEE Trans. on Electron Devices, vol. ED-13, pp. 639-642.
- Neve, N. F. B., and P. R. Thornton (1966). "Electrical effects of crystal imperfections studied by scanning electron microscopy," Solid-State Electronics, vol. 9, pp. 900-901 and 2 plates.
- Neve, N. F. B., see Shaw, Hughes, Neve, Sulway, Thornton and Gooch (1966) and Thornton, Neve and Sulway (1966).
- Niehrs, H., see Bargmann, Mollenstedt, Niehrs and 3 others (1960).
- Nixon, W. C.; (1964). "Scanning electron microscopy," J. Royal Microscopical Soc., vol. 83, pts. 1 and 2, pp. 213-216. Reprinted in Microelectronics and Reliability, vol. 4, pp. 55-57; 1965.
- Nixon, W. C., see Chang and Nixon (1966a, 1966b and 1967), Oatley, Nixon and Pease (1965) and Pease and Nixon (1965a and b).
- Northrop, D. C., P. R. Thornton and K. W. Trezise (1964). "Electrical transients in high resistivity gallium arsenide," Solid-State Electron., vol. 7, pp. 17-30.
- Nurse, R. W., see Majumdar, Nurse, Chatterji and Jeffrey (1966).
- Oatley, C. W., (1958). "The scanning electron microscope," New Scientist (England), pp. 153-155 in issue for 12 June.
- Oatley, C. W., (1966). "New electron-probe instruments," Electronics and Power, vol. 12, pp. 282-285.
- Oatley, C. W., and T. E. Everhart (1957). "The examination of p-n junctions with the scanning electron microscope," J. Electron., vol. 2, pp. 568-570 and 1 plate.
- Oatley, C. W., W. C. Nixon and R. F. W. Pease (1965). "Scanning electron microscopy," pp. 181-247 in Advances in Electronics and Electron Physics, vol. 21, L. Marton, ed.,

BIBLIOGRAPHY ON THE SCANNING ELECTRON MICROSCOPE

- Academic Press, New York, N. Y.
- Oatley, C. W., see Everhart, Smith, Wells and Oatley (1960), Everhart, Wells and Oatley (1959) and Smith and Oatley (1955).
- O'Keefe, T. W., see Green, D., Sandor, O'Keefe and Matta (1965).
- Onoguchi, A., see Shirai, Onoguchi and Ichinokawa (1967).
- Ovsiuk, V. N., and L. S. Smirnov (1965). *Soviet Physics - Solid State (USA)*, vol. 6, pp. 2413-2418. "Effect of electron bombardment on the surface states of germanium," Paris, J-P., see Pinard, Paris and Matteudi (1964).
- Patel, J. R., see Czaja and Patel (1965).
- Pease, R. F. W., (1963). "High resolution scanning electron microscopy," Ph. D. Dissertation, Cambridge University.
- Pease, R. F. W., (1965). "The determination of the area of emission of reflected electrons in a scanning electron microscope," *J. Sci. Inst.*, vol. 42, pp. 158-159.
- Pease, R. F. W., A. N. Broers and R. A. Ploc (1965). "Scanning electron microscopy of the growth and subsequent sectioning by sputtering of iron oxide films," pp. 389-390 in Titlebach (1965).
- Pease, R. F. W., and T. L. Hayes (1966). "Scanning electron microscopy of biological material," *Nature (London)*, vol. 210, p. 1049. (Observes selectively absorbed cathodoluminescent dyes by the luminescent method.)
- Pease, R. F. W., T. L. Hayes A. S. Camp and N. M. Amer (1966). "Electron microscopy of living insects," *Science*, vol. 154, pp. 1185-1186.
- Pease, R. F. W., and W. C. Nixon (1965a). "High resolution scanning electron microscopy," *J. Sci. Inst.* vol. 42, pp. 81-85.
- Pease, R. F. W., and W. C. Nixon (1965b). "Microformation of Filaments," pp. 220-230 in Bakish (1965).
- Pease, R. F. W., and R. A. Ploc (1965). "Scanning electron microscopy as applied to the oxidation of iron," *Trans. Met. Soc. AIME*, vol. 233, pp. 1949-1954.
- Pease, R. F. W., see Hayes, Pease and McDonald (1966) and Oatley, Nixon and Pease (1965).
- Pentoney, R. E., see Debaise, Porter and Pentoney (1966).
- Pereverzev, N. A., see Spivak, Saparin and Pereverzev (1962).
- Pinard, P., (1964). "Study of cathodoluminescence using the scanning electron microscope" (in French), Ph. D. Dissertation, L'Universite de Lyon.
- Pinard, P., J-P. Paris and G. Matteudi (1964). "Secondary electron emission from cadmium sulfide" (in French), *C. R. Acad. Sc. Paris*, vol. 259, pp. 2187-2189.
- Pinard, P., see Bernard, Davoine and Pinard (1959), Davoine,

BIBLIOGRAPHY ON THE SCANNING ELECTRON MICROSCOPE

- Bernard and Pinard (1960), Davoine, Pinard and Martineau (1960) and Davoine and Pinard (1965).
- Ploc, R. A., see Pease, Broers and Ploc (1965) and Pease and Ploc (1965).
- Porter, A. W., see Debaise, Porter and Pentoney (1966).
- Pruden, L. H., see Korda, Pruden and Williams (1967).
- Pye, I. T., O. V. Washburn and J. G. Buchanan (1966). "Structural changes in paper on pressing and drying," pp. 353-367 in Bolam (1966).
- Quilliam, T. A., see Boyde and Quilliam (1966).
- Ramberg, E. G., see Zworykin, Morton, Ramberg, Hillier and Vance (1945).
- Raspletin, K. K., see Kushnir, Fetisov, Raspletin and 4 others (1961).
- Rhodin, J., see Sjostrand and Rhodin (1957).
- Sandor, J. E., see Green, D., Sandor, O'Keeffe and Matta (1965) and Szedon and Sandor (1965).
- Saparin, G. V., G. V. Spivak and S. S. Stepanov (1966). "Observation of the p-n junction at small constant and alternating bias with the scanning electron microscope," pp. 609-610 in Uyeda (1966).
- Saparin, G. V., see Spivak, Saparin and Pereverzev (1962) and Spivak, Saparin, Massarani and Bikov (1965).
- Sato, M., see Kimoto, Hashimoto and Sato (1966).
- Schreiber, H., see Lander, Schreiber, Buck and Mathews (1963).
- Sepall, O., see Baker and Sepall (1965).
- Shaw, D. A., K. A. Hughes, N. F. B. Neve, D. V. Sulway, P. R. Thornton and C. Gooch (1966). "Crystal mosaic structures and the lasing properties of GaAs laser diodes," *Solid-State Electronics*, vol. 9, pp. 664-665 and 2 plates.
- Shaw, D. A., R. C. Wayte and P. R. Thornton (1966). "Scanning electron microscopy observations of ZnS phosphor grains at high resolution," *Appl. Phys. Letters*, vol. 8, pp. 289-291.
- Shirai, S., A. Onoguchi and T. Ichinokawa (1966). "Atomic number analysis by specimen current in scanning electron microscope," pp. 199-200 in Uyeda (1966).
- Shirai, S., A. Onoguchi and T. Ichinokawa (1967). "Absorbed specimen current anomaly of Cu-Zn diffusion couple in electron scanning microscope," *Japan. J. Appl. Phys.*, vol. 6, pp. 277-278.
- Sikorski, J., see Challice and Sikorski (1957).
- Sjostrand, F. S., and J. Rhodin (1957). *Electron Microscopy*. Proc. Stockholm Conf. Sept. 1960. Almquist and Wiksells, Uppsala; Academic Press, New York, 1957.
- Smirnov, L. S., see Ovsyuk and Smirnov (1965).

BIBLIOGRAPHY ON THE SCANNING ELECTRON MICROSCOPE

- Smith, K. C. A., (1956). "The scanning electron microscope and its fields of application," Ph. D. Dissertation, Cambridge University.
- Smith, K. C. A., (1959). "Scanning electron microscopy in pulp and paper research," Pulp and Paper Mag. Canada (Technical Section), vol. 60, pp. T366-T371.
- Smith, K. C. A., (1960). "A versatile scanning electron microscope," pp. 177-180 in Houwink and Spit (1960).
- Smith, K. C. A., (1961). "Scanning," pp. 241-251 in "Encyclopedia of Microscopy," G. L. Clark, Ed., Reinhold Publishing Corp., New York, N. Y.
- Smith, K. C. A., and C. W. Oatley (1955). "The scanning electron microscope and its fields of application," Brit. J. of Appl. Phys., vol. 6, pp. 391-399.
- Smith, K. C. A., see Allen and Smith (1956), Atack and Smith (1956), Buchanan and Smith (1960), Everhart, Smith, Wells and Oatley (1960) and McAuslan and Smith (1957).
- Snelling, M. A., see Stewart and Snelling (1965).
- Snyder, R. L., see Zworykin, Hillier and Snyder (1942).
- Speth, A. J., and F. F. Fang (1965). "Effects of low-energy electron irradiation on Si-insulated gate FET's," Applied Physics Letters, vol. 7, pp. 145-146.
- Spit, B. J., see Houwink and Spit (1961).
- Spivak, G. V., G. V. Saparin, B. Massarani, and M. V. Bikov (1965). "Contrast of images of a p-n junction in the scanning electron microscope" (in German), pp. 285-286 in Titlebach (1965).
- Spivak, G. V., G. V. Saparin and N. A. Pereverzev (1962). "Potential distribution in a p-n junction as observed by electron-optical scanning," Bulletin of the Academy of Sciences USSR, Physical Series (USA), vol. 26, pp. 1362-1365; 1962. Translated from Izvest. Akad. Nauk, Ser. Fiz., USSR, vol. 26, pp. 1339-1342; 1962.
- Spivak, G. V., see Saparin, Spivak and Stepanov (1966).
- Sproule, R. N., see Atack, May, Morris and Sproule (1961).
- Stepanov, S. S., see Saparin, Spivak and Stepanov (1966).
- Stewart, A. D. G., (1962). "Investigation of the topography of ion bombarded surfaces with a scanning electron microscope," pp. D12-D13 in Breese (1962).
- Stewart, A. D. G. and A. Boyde (1962). "Ion etching of dental tissues in a scanning electron microscope," Nature (London), vol. 196, pp. 81-82.
- Stewart, A. D. G., and M. A. Snelling (1965). "A new scanning electron microscope," pp. 55-56 in Titlebach (1965).
- Stewart, A. D. G., see Boyde and Stewart (1962) and Boyde and Stewart (1963).
- Stintzing, H., (1929). German Patent No. 485,155. "Method and device for automatically assessing, measuring and

BIBLIOGRAPHY ON THE SCANNING ELECTRON MICROSCOPE

- counting particles of any type, shape and size," Date of application - 13 May 1927. Granted Oct. 1929.
- Sulway, D. V., I. G. Davies, K. A. Hughes, P. R. Thornton and B. R. Holeman (1966). "Localized breakdown in Ge mesa diodes due to inclusions," *Microelectronics and Reliability*, vol. 5, pp. 323-327 and 3 plates.
- Sulway, D. V., see Thornton, Hughes, Kyaw, Millward and Sulway (1967), Thornton, Neve and Sulway (1966), Thornton, Hughes, Sulway and Wayte (1966), Davies, Hughes, Sulway and Thornton (1966), Neve, Sulway, Hughes and Thornton (1966) and Shaw, Hughes, Neve, Sulway, Thornton and Gooch (1966).
- Sulway, D. V., K. A. Hughes, W. A. Evans and P. R. Thornton (1966). "Direct observation of MOS transistor channel pinch-off by scanning electron microscopy," *Appl. Phys. Letters*, vol. 8, pp. 296-298.
- Szedon, J. R., and J. E. Sandor (1965). "The effect of low-energy electron irradiation of metal-oxide-semiconductor structures," *Appl. Phys. Letters*, vol. 6, pp. 181-182.
- Tauchi, S., see Higuchi, Tauchi and Kimura (1964).
- Tamura, H., see Higuchi and Tamura (1965), Kimura, Higuchi, Maki and Tamura (1966) and Kimura, Higuchi, Tamura and Maki (1966).
- Teder, A., (1964a). "The properties of spruce pulps as related to paper structures observed with the scanning electron microscope," *Svensk Papperstidn*, vol. 67, pp. 670-685.
- Teder, A., (1964b). "The effect of drying, heat treatment and beating on the papermaking properties of birch pulps," *Svensk Papperstidn*, vol. 67, pp. 911-923.
- te Gude, H., (1945). "The scanning electron microscope - an imaging method using secondary electrons" (in German), *Funk und Ton*, vol. 7, pp. 373-383.
- te Gude, H., (1965). "Automatic inspection and fabrication of integrated circuits with the scanning electron microscope" (in German), *Internationale Elektronische Rundschau*, vol. 19, pp. 479-482, 567 and 570.
- Theile, R., (1938). "Resistance-sensitive scanning electron tubes" (in German), *Die Telefunken Rohre*, number 13, pp. 90-126 in the August issue.
- Theile, R., see Knoll and Theile (1939).
- Themelis, N. J., (1961). "Studies in the reduction of iron oxides in particulate systems," Ph. D. Dissertation, McGill University. (Contains SEM images of iron oxide particles.)
- Themelis, N. J., and W. H. Gauvin (1962). "Reduction of iron oxide in gas-conveyed systems," *A. I. Ch. E. J.*,

BIBLIOGRAPHY ON THE SCANNING ELECTRON MICROSCOPE

- vol. 8, pp. 437-444.
- Themelis, N. J., and W. H. Gauvin (1963). "A generalized rate equation for the reduction of iron oxides," *Trans. Met. Soc. of AIME*, vol. 227, pp. 290-300. (Figures 4 through 7 show SEM images of iron oxide particles.)
- Thomas, R. E., see Haas and Thomas (1963 and 1966).
- Thornhill, J. W., R. K. Matta and W. H. Wood (1965). "Examining three-dimensional microstructures with the scanning electron microscope," *Grana Palynologica* (Almquist and Wiksells), vol. 6, pp. 3-6 and 2 plates. (Contains SEM images of pollen grains.)
- Thornhill, J. W., and I. M. Mackintosh (1965). "Application of the scanning electron microscope to semiconductor device structures," *Microelectronics and Reliability*, vol. 4, pp. 97-100.
- Thornley, R. F. M., (1960a). "New applications of the scanning electron microscope," Ph. D. Dissertation, Cambridge University.
- Thornley, R. F. M., (1960b). "Recent developments in scanning electron microscopy," pp. 173-176 in Houwink and Spit (1960).
- Thornley, R. F. M., and L. Cartz (1962). "Direct examination of ceramic surfaces with the scanning electron microscope," *J. Amer. Ceramic Soc.*, vol. 45, pp. 425-428.
- Thornley, R. F. M., see Everhart and Thornley (1960).
- Thornton, P. R., (1965). "The scanning electron microscope," *Science Journal* (London), pp. 66-71 in the Nov. issue.
- Thornton, P. R., M. J. Culpin and I. W. Drummond (1963). "Direct observation of the high-field regions in GaAs," *Solid-State Electronics*, vol. 6, pp. 532-533 and 2 plates.
- Thornton, P. R., K. A. Hughes, D. V. Sulway and R. C. Wayte (1966). "Quantitative measurements by scanning electron microscopy - 1, the use of conductivity maps," *Microelectronics and Reliability*, vol. 5, pp. 291-298 and 2 plates.
- Thornton, P. R., D. W. F. James, C. Lewis and A. Bradford (1966). "Silicon whisker growth by the vapor-liquid-solid process," *Phil. Mag.*, vol. 14, pp. 165-177.
- Thornton, P. R., N. F. B. Neve and D. V. Sulway (1966). "Quantitative measurements by scanning electron microscopy - 2, the use of emissive micrographs," *Microelectronics and Reliability*, vol. 5, pp. 299-303 and 3 plates.
- Thornton, P. R., K. A. Hughes, Htin Kyaw, C. Millward and D. V. Sulway (1967). "Failure analysis of microcircuitry by scanning electron microscopy," *Microelectronics and Reliability*, vol. 6, pp. 9-16 and 4 plates.
- Thornton, P. R., see Sulway, Hughes, Evans and Thornton (1966), Sulway, Davies, Hughes and Thornton (1966), Sul-

BIBLIOGRAPHY ON THE SCANNING ELECTRON MICROSCOPE

- way, Davies, Hughes, Thornton and Holeman (1966), Shaw, Wayte and Thornton (1966), Neve and Thornton (1966), Drummond and Thornton (1965), Neve, Sulway, Hughes and Thornton (1966), Neve, Hughes and Thornton (1966), Northrop, Thornton and Trezise (1964) and Shaw, Hughes, Neve, Sulway, Thornton and Gooch (1966).
- Thurston, R. C. A., see McGrath, Buchanan and Thurston (1962).
- Tipper, C. F., D. I. Dagg and O. C. Wells (1959). "Surface fracture markings on alpha iron crystals," J. Iron and Steel Institute, vol. 193, pp. 133-141.
- Titlebach, M., (1965). Electron Microscopy. Proc. Third European Regional Conf. Prague, Sept. 1964. Pub. House of Czechoslovak Academy of Sciences, Prague.
- Todokoro, H., see Munakata and Todokoro (1966).
- Trezise, K. W., see Northrop, Thornton and Trezise (1964).
- Uyeda, R., (1966). "Electron Microscopy 1966," Sixth Int. Cong. Electron Microscopy, Kyoto, Aug./Sept. 1966. Vol. 1, Non-Biology; Vol. 2, Biology. Maruzen Co., Tokyo, 1966.
- Vance, A. W., see Zworykin, Morton, Ramberg, Hillier and Vance (1945).
- VanCouvering, A., see Wittry and Vancouvering (1967).
- von Ardenne, M. See Ardenne, M. von.
- Washburn, O. V., and J. G. Buchanan (1964). "Changes in web structure on pressing and drying," Pulp Paper Mag. Canada. (Technical Section), vol. 65, pp. T400-T408.
- Washburn, O. V., see Buchanan and Washburn (1961, 1962 and 1964) and Pye, Washburn and Buchanan (1966).
- Wayte, R. C., see Thornton, Hughes, Sulway and Wayte (1966) and Shaw, Wayte and Thornton (1966).
- Wells, O. C., (1957). "The construction of a scanning electron microscope and its application to the study of fibres," Ph. D. Dissertation, Cambridge University.
- Wells, O. C., (1959). "Examination of nylon spinneret holes by scanning electron microscopy," J. Electronics and Control, vol. 7, pp. 373-376.
- Wells, O. C., (1960). "Correction of errors in electron stereomicroscopy," Brit. J. Appl. Phys., vol. 11, pp. 199-201. (Refers to case when the lines of sight are separated by a large angle.)
- Wells, O. C., (1961). "Electron beams in microelectronics," pp. 291-321 in Bakish (1961).
- Wells, O. C., (1962). "Electron beams in microelectronics," pp. 354-381 in Introduction to Electron Beam Technology, R. Bakish, Ed., J. Wiley and Sons, New York, N. Y.
- Wells, O. C., (1964). "Scanning electron microscope," pp. 32-34 in Kurshan (1964).

BIBLIOGRAPHY ON THE SCANNING ELECTRON MICROSCOPE

- Wells, O. C., T. E. Everhart and R. K. Matta (1963). "Automatic positioning of device electrodes using the scanning electron microscope," *Extended Abstracts (Electrochemical Society), Electronics Division*, vol. 12, no. 2, pp. 5-10. (New York Meeting, Oct. 1963.)
- Wells, O. C., T. E. Everhart and R. K. Matta (1965). "Automatic positioning of device electrodes using the scanning electron microscope," *IEEE Trans. on Electron Devices*, vol. ED-12, pp. 556-563.
- Wells, O. C., see Everhart, Smith, Wells and Oatley (1960), Everhart, Wells and Matta (1963, 1964a and 1964b), Everhart, Wells and Oatley (1959) and Tipper, Dagg and Wells (1959).
- Wheatley, G. H., see Czaja and Wheatley (1964).
- White, P., see Da Silva and White (1961).
- Williams, J. P., see Korda, Pruden and Williams (1967).
- Wittry, D. B., (1957). "Two improvements in electron sources for electron probes," *Rev. Sci. Inst.*, vol. 28, p. 58.
- Wittry, D. B., (1966). "Cathodoluminescence and impurity variations in Te-doped GaAs," *Appl. Phys. Letters*, vol. 8; pp. 142-144.
- Wittry, D. B., and D. F. Kyser (1964). "Use of electron probes in the study of recombination radiation," *J. Appl. Phys.*, vol. 35, pp. 2439-2442.
- Wittry, D. B., and D. F. Kyser (1965). "Cathodoluminescence at p-n junctions in GaAs," *J. Appl. Phys.*, vol. 36, pp. 1387-1389.
- Wittry, D. B., and D. F. Kyser (1966). "Surface recombination velocities and diffusion lengths in GaAs," pp. 312-316 in *Proc. Int. Conf. on the Physics of Semiconductors*, Kyoto, 1966. Published in *J. Physical Society Japan*, vol. 21, Supplement, 1966.
- Wittry, D. B., and A. VanCouvering (1967). "Stereoscopic display system for electron microprobe instruments," *J. Sci. Inst.*, vol. 44, pp. 294-295.
- Wittry, D. B., see Kyser and Wittry (1966) and McKinley, Heinrich and Wittry (1966).
- Wood, W. H., see Thornhill, Matta and Wood (1965).
- Zervins, A., see Jaques, Coalson and Zervins (1965).
- Zworykin, V. K., J. Hillier and R. L. Snyder (1942). "A scanning electron microscope," *ASTM Bull.*, no. 117, pp. 15-23.
- Zworykin, V. K., G. A. Morton, E. G. Ramberg, J. Hillier and A. W. Vance (1945). "Electron optics and the electron microscope," John Wiley and Sons, New York, N. Y.

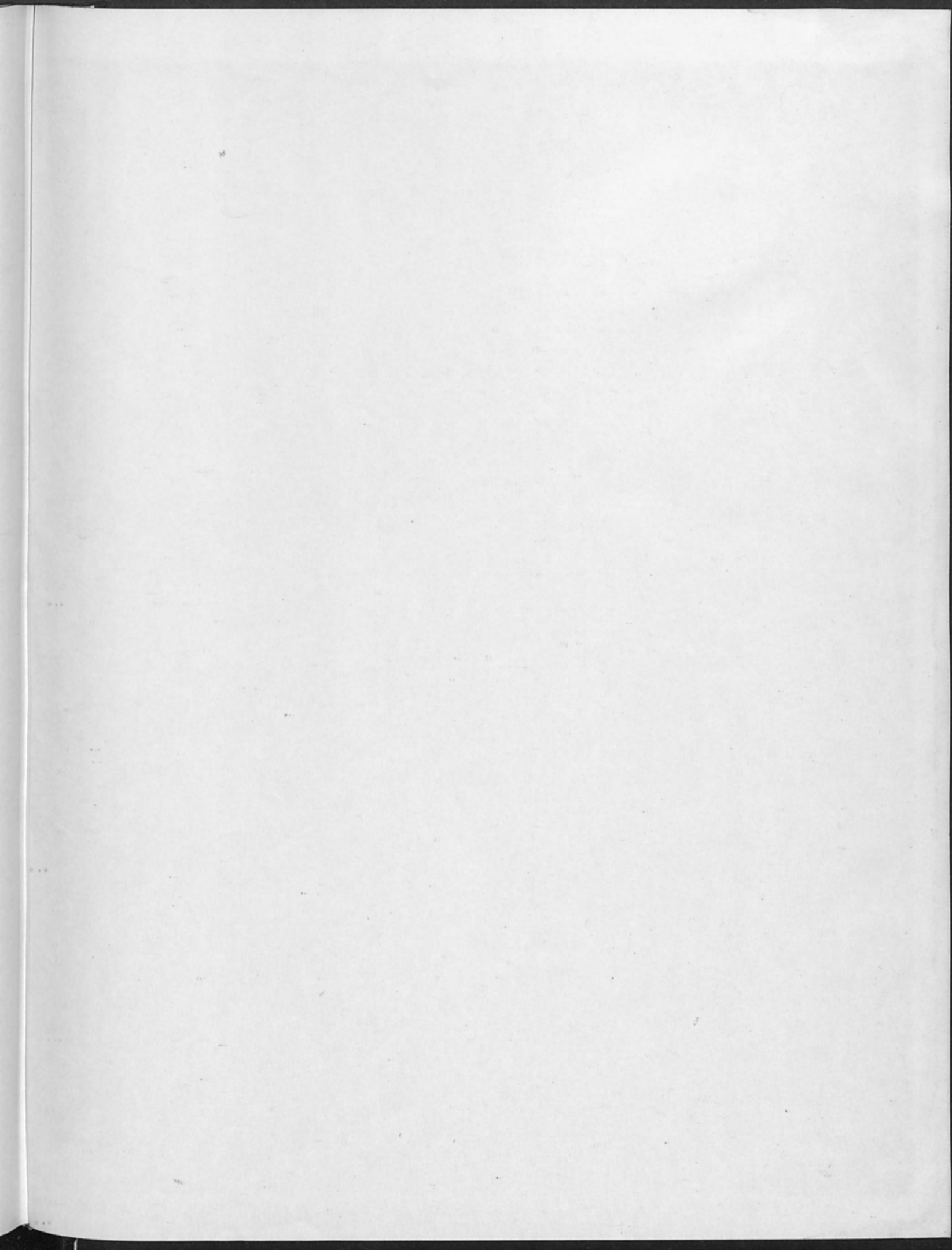
AUTHOR INDEX

| AUTHOR | PAGE | AUTHOR | PAGE |
|----------------------------|---------|---------------------------|---------|
| Amy, R. L. | 391 | Lauridson, J. | 371 |
| Arai, T. | 86 | Lee, M. J. | 304 |
| Banas, C. M. | 42 | Leitten, C. F., Jr. | 262 |
| Barber, R. R. | 350 | Lesley, G. B. | 313 |
| Barbour, J. P. | 7 | Levy, M. F. | 206 |
| Barnes, F. | 371 | Lienau, H. | 239 |
| Becker, C. H. | 333 | Link, W. T. | 77 |
| Benedick, W. B. | 70 | Loeffler, K. H. | 344 |
| Bessis, M. | 391 | Lowry, J. F. | 239 |
| Boyne, H. S. | 313 | Miller, D. E. | 118 |
| Brewster, J. L. | 7 | Motz, J. W. | 34 |
| Broers, A. N. | 1 | MacDonald, N. C. | 327 |
| Brown, C. O. | 42 | McDonald, R. E. | 262 |
| Brown, T. E. | 407 | Namba, S. | 86 |
| Chang, T. H. P. | 123 | Neve, N. F. B. | 145 |
| Charbonnier, F. M. | 7 | Nixon, W. C. | 123 |
| Davis, N. M. | 254 | Olson, R. S. | 363 |
| Dean, C. W. | 262 | Parr, W. H. | 379 |
| Dost, M. H. | 350 | Peabody, R. R. | 397 |
| Dreikorn, R. E. | 206 | Peacock, G. R. | 379 |
| Emery, A. | 278 | Pease, R. F. W. | 118,176 |
| Everhart, T. E. | 15,327 | Penner, S. | 50 |
| Fisher, R. S. | 379 | Rockwell, R. J., Jr. | 407 |
| Gibbons, J. F. | 101,108 | Rounds, D. E. | 363 |
| Gonzales, A. J. | 188 | Saunders, T. F. | 206 |
| Graham, R. A. | 70 | Scherer, J. R. | 321 |
| Grundhauser, F. J. | 7 | Schollhammer, F. R. | 215 |
| Hassan, C. B. | 239 | Schwarz, H. | 86 |
| Hatzakis, M. | 94 | Sloan, D. H. | 77 |
| Herrmannsfeldt, W. B. | 304 | Smathers, S. E. | 313 |
| Hu, C. | 371 | Smith, J. F. | 268 |
| Hutchison, R. E. | 70 | Sognaes, R. F. | 402 |
| Itoh, T. | 86 | Sparrow, J. H. | 34 |
| Johnson, F. M. | 363 | Spranza, J. J. | 304 |
| Johnson, W. S. | 101,108 | Stern, R. H. | 402 |
| Juleff, E. M. | 157 | Storb, R. | 391 |
| Kim, P. H. | 86 | Stroke, G. W. | 287 |
| Kimura, H. | 62,198 | Sulway, D. V. | 145 |
| Kleinfelder, W. J. | 101,108 | Tamura, H. | 62,198 |
| Kobylnyk, R. W. | 385 | Thompson, A. | 268 |
| Kurzweil, F., Jr. | 350 | Thompson, B. J. | 295 |
| | | Thornley, R. F. M. | 94 |
| | | Thornton, P. R. | 145 |

AUTHOR INDEX (Cont'd)

| AUTHOR | PAGE |
|----------------------|------|
| Tomlinson, R. | 313 |
| Trigger, K. R. | 304 |
| Varker, C. J. | 157 |
| Wayte, R. C. | 145 |
| Wells, O. C. | 412 |
| Wertz, R. K. | 391 |
| Wilde, W. H. A. | 385 |
| Wilson, R. G. | 22 |
| Wolf, E. D. | 135 |
| Zweng, H. C. | 396 |

dmh



| | |
|--|----------|
| ANNALS OF THE ENTOMOLOGICAL SOCIETY OF AMERICA | 1956 |
| CONTENTS | |
| | 1-10 |
| | 11-20 |
| | 21-30 |
| | 31-40 |
| | 41-50 |
| | 51-60 |
| | 61-70 |
| | 71-80 |
| | 81-90 |
| | 91-100 |
| | 101-110 |
| | 111-120 |
| | 121-130 |
| | 131-140 |
| | 141-150 |
| | 151-160 |
| | 161-170 |
| | 171-180 |
| | 181-190 |
| | 191-200 |
| | 201-210 |
| | 211-220 |
| | 221-230 |
| | 231-240 |
| | 241-250 |
| | 251-260 |
| | 261-270 |
| | 271-280 |
| | 281-290 |
| | 291-300 |
| | 301-310 |
| | 311-320 |
| | 321-330 |
| | 331-340 |
| | 341-350 |
| | 351-360 |
| | 361-370 |
| | 371-380 |
| | 381-390 |
| | 391-400 |
| | 401-410 |
| | 411-420 |
| | 421-430 |
| | 431-440 |
| | 441-450 |
| | 451-460 |
| | 461-470 |
| | 471-480 |
| | 481-490 |
| | 491-500 |
| | 501-510 |
| | 511-520 |
| | 521-530 |
| | 531-540 |
| | 541-550 |
| | 551-560 |
| | 561-570 |
| | 571-580 |
| | 581-590 |
| | 591-600 |
| | 601-610 |
| | 611-620 |
| | 621-630 |
| | 631-640 |
| | 641-650 |
| | 651-660 |
| | 661-670 |
| | 671-680 |
| | 681-690 |
| | 691-700 |
| | 701-710 |
| | 711-720 |
| | 721-730 |
| | 731-740 |
| | 741-750 |
| | 751-760 |
| | 761-770 |
| | 771-780 |
| | 781-790 |
| | 791-800 |
| | 801-810 |
| | 811-820 |
| | 821-830 |
| | 831-840 |
| | 841-850 |
| | 851-860 |
| | 861-870 |
| | 871-880 |
| | 881-890 |
| | 891-900 |
| | 901-910 |
| | 911-920 |
| | 921-930 |
| | 931-940 |
| | 941-950 |
| | 951-960 |
| | 961-970 |
| | 971-980 |
| | 981-990 |
| | 991-1000 |

..... 304

